Modeling and Control of Thermomechanical Systems

Managing Heat-Induced Deformation in Extreme Ultraviolet Lithography

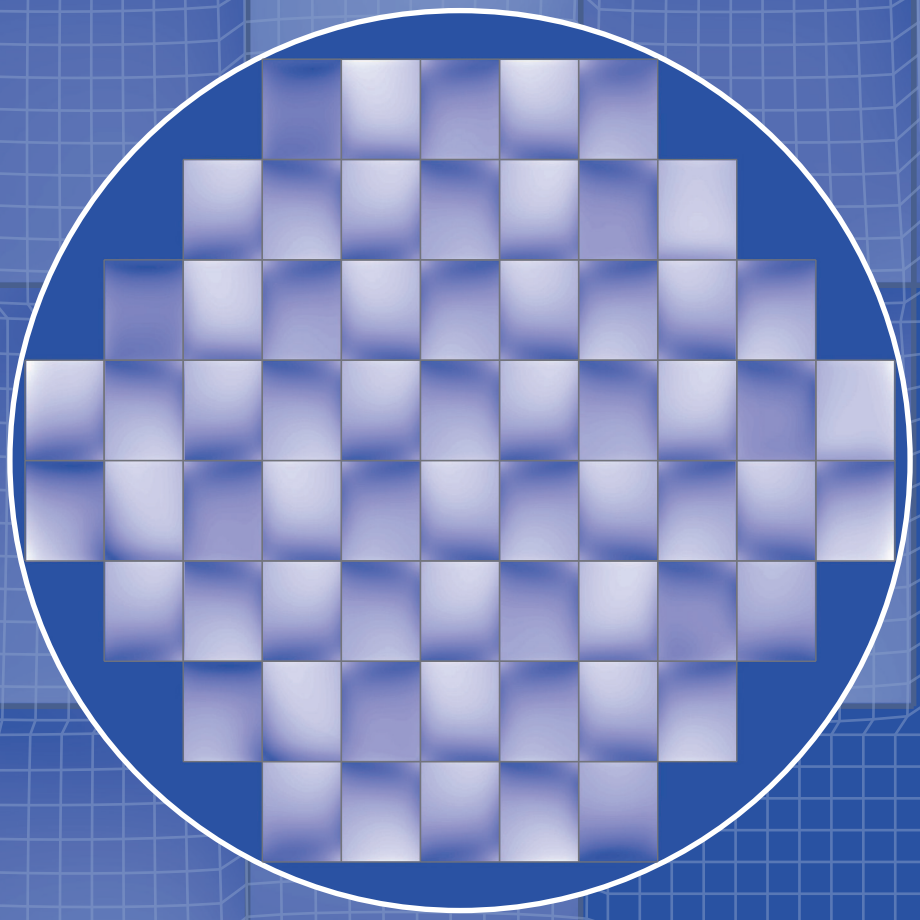

Daniël Veldman

Modeling and Control of Thermomechanical Systems

Managing Heat-Induced Deformation in Extreme Ultraviolet Lithography

Daniël Veldman

The research reported in this thesis is part of the research program of the Dutch Institute of Systems and Control (DISC). The author has successfully completed the educational program of the Graduate School DISC.

This work has been performed within the Impulse II research program of the Eindhoven University of Technology and was financially supported by ASML, Veldhoven, The Netherlands.

A catalogue record is available from the Eindhoven University of Technology Library.
ISBN: 978-90-386-5091-3

Typeset using LaTeX.

Reproduction: ProefschriftMaken.
Cover design: Daniël Veldman.

Modeling and Control of Thermomechanical Systems

Managing Heat-Induced Deformation in Extreme Ultraviolet Lithography

PROEFSCHRIFT

ter verkrijging van de graad van doctor aan de Technische Universiteit Eindhoven, op gezag van de rector magnificus prof.dr.ir. F.P.T. Baaijens, voor een commissie aangewezen door het College voor Promoties, in het openbaar te verdedigen op vrijdag 11 september 2020 om 16:00 uur

door

Daniël Willem Maria Veldman

geboren te Nijmegen

Dit proefschrift is goedgekeurd door de promotoren en de samenstelling van de promotiecommissie is als volgt:

voorzitter:	prof.dr. L.P.H. de Goey
1e promotor:	prof.dr. H. Nijmeijer
2e promotor:	prof.dr. H.J. Zwart
co-promotor:	dr.ir. R.H.B. Fey
leden:	prof.dr. E. Zuazua (Friedrich-Alexander Universität Erlangen-Nürnberg)
	prof.dr.ir. A. van Keulen (TUD)
	prof.dr. S. Weiland
adviseur:	dr.ir. M.M.J. van de Wal (ASML)

Het onderzoek dat in dit proefschrift wordt beschreven is uitgevoerd in overeenstemming met de TU/e Gedragscode Wetenschapsbeoefening.

Summary

Modeling and Control of Thermomechanical Systems:
Managing Heat-Induced Deformation in Extreme Ultraviolet Lithography

In the past four decades, the number of electrical components that can be fitted into a single integrated circuit has increased exponentially. This trend has enabled the production of smaller, more efficient, and cheaper computer chips which can be found everywhere in today's society.

The ever decreasing feature sizes of components on computer chips have led to ever stricter positioning tolerances for the wafer scanners that produce these chips. With positioning tolerances approaching the subnanometer range, new technological challenges are appearing. One of them is that the previously neglected coupling from the thermal to the mechanical domain is now a determining factor for the overall system performance.

In the latest generation wafer scanners, a set of mirrors is used to project a beam of extreme ultraviolet (EUV) light through a mask onto a silicon wafer. The mask contains the desired pattern of electronic connections that should be projected accurately onto the wafer. The wafer is coated with a material in which a chemical reaction occurs under the influence of the EUV light. The difference between exposed and unexposed areas can then be used to etch the projected pattern into the wafer at a later stage of the production process. The imaging quality of the latest generation of wafer scanners is significantly affected by wafer heating and mirror heating, i.e. by the thermal expansion of the wafer and mirrors in the optical path due to the heat deposited by the EUV light.

One currently used technique to reduce the effect of wafer heating on the imaging quality is called error correction. In this technique, an accurate physical model is used to predict the thermal expansion of the wafer. Based on this prediction the positions of the wafer and mirrors are adjusted to reduce the optical error. Since the predictions of the wafer deformation are needed in real time, a computationally efficient simulation method is needed. However, obtaining an accurate and computationally efficient model for the thermal expansion of the

wafer is challenging because the applied heat source travels with a high velocity. The first part of the thesis addresses this problem by proposing new numerically efficient techniques based on the form of the applied heat load and the structure of the underlying partial differential equation.

For the next generation wafer scanners error correction alone will not be sufficient and more advanced control systems will be needed to achieve the required imaging quality. An important question during the design of such control system is where thermal actuators, i.e. additional heaters and/or coolers, should be placed and how these should be controlled. In the second part of the thesis, an optimization method to answer this question is proposed. Because there is a significant amount of information about the projection pattern available, perfect knowledge of the heat load induced by the EUV light is assumed to design the optimal shape of the actuation heat load. The obtained shape has a clear physical interpretation and gives a good indication for the optimal placement of actuators. A modification of the proposed technique has also been applied to a mirror heating problem, for which valuable insights in the effective configuration of heaters were obtained.

Sufficient robustness against modeling errors can be achieved by feedback control based on local temperature measurements of the wafer. However, the locations where these temperature measurements are taken can significantly influence the achievable performance of the resulting closed-loop control system. In the third part of the thesis, the placement of temperature sensors is addressed based on analytic expressions for (irrational) transfer functions. The approach yields simple analytic expressions for the optimal placement of sensors in heat conduction problems on one-dimensional and two-dimensional spatial domains that can be used as guidelines for control system design.

Summarizing, this thesis contains several new techniques for the increasingly important control of heat-induced deformation in EUV lithography systems. Specifically, new computationally efficient simulation methods and new methods for control system design, in particular methods for the placement of actuators for feedforward control and sensors for feedback control, are presented.

Contents

Part I

Opening

Chapter 1

Introduction

1.1 Thermomechanical systems

Thermomechanical systems have been studied since antiquity. Probably the oldest known example is accredited to Philo of Byzantium (280 - 220 BC), who conducted the following experiment [McGee, 1988]. He took a tube with one open and one closed end and placed the open end in a jug of water. When the tube was placed in the sun, the water level in the tube dropped and when the tube was placed back into the shade, the water level rose again. Philo's experiment shows that there is an interaction between temperature and deformation, i.e. that substances, like air, contract and expand under the influence of temperature. Systems like this in which there is an interaction between temperature and deformation are thermomechanical systems.

A mathematical theory that describes the deformation of a body under the influence of temperature was not developed until the nineteenth century. The first paper in this field is [Duhamel, 1837]. In this purely mathematical paper, Duhamel develops the first theory of thermoelasticity by combining Navier's elasticity theory and Fourier's theory of heat conduction [Maugin, 2014]. The theory of thermoelasticity was further developed together with the theory of elasticity at the end of the nineteenth century and the beginning of the twentieth century by several others.

Up to the twentieth century, the theory of thermomechanical systems only considered the deformation of a body induced by temperature variations. However, the reverse effect also exists, i.e. deformations of a body also induce temperature changes. This effect was first observed in [Zener, 1937; Zener, 1938] as thermoelastic damping, i.e. the loss of mechanical energy due to irreversible thermodynamic processes. The observations of Zener were fully integrated into

the theory of thermodynamics and elasticity by [Biot, 1956]. The temperature increases induced by deformations are mainly relevant at the micro and nano scale, for example in Micro Electromechanical Systems (MEMS) and Nano Electromechanical Systems (NEMS) [Mestrom, 2009].

Since the beginning of the 1960s, the first textbooks on thermoelasticity began to appear, see e.g. [Boley and Weiner, 1960; Nowacki, 1962; Parkus, 1976; Nowinski, 1978] and, more recently, [Hetnarski and Eslami, 2009]. Since the 1960s, there have been many developments in the field of thermomechanical systems but their discussion falls outside the scope of this thesis. The interested reader is referred to [Hetnarski and Eslami, 2009].

The theory of thermoelasticity was mainly of theoretical interest until the years before the second world war. Around that time, many applications appeared in which high temperatures (which lead to a reduction in strength) and temperature gradients (which lead to high thermal stresses) could result in structural failure. Examples are aircrafts, nuclear reactors, jet and rocket engines, space vehicles and missiles, and large steam turbines in ships [Nowacki, 1962]. In the past decades, many methods have been developed for the thermal control of these structures. In most cases, passive control (e.g. fluid loops and advanced materials and coatings) are used to avoid structural failure, see e.g. [Hengeveld et al., 2010].

More recently, thermomechanical effects in high-precision systems are also receiving significant interest. With the precision of these systems now approaching the subnanometer range, thermal expansion is becoming increasingly important for the overall machine performance. A few examples of such systems are milling machines [Ramesh et al., 2000], electron microscopes [Evers et al., 2019a], and wafer scanners [Subramany et al., 2016]. The latter will be discussed in more detail in the next section.

1.2 Extreme ultraviolet lithography

1.2.1 The semiconductor industry

The rapid technological developments in the semiconductor industry in the past 60 years have had an enormous impact on our society. They have enabled the creation of modern electronic devices, such as televisions, personal computers, laptops, smartphones, and many others, which can now be found almost everywhere. In the coming years, the expected development of the internet of things (see e.g. [Wortmann and Flüchter, 2015]) will integrate electronics in even more areas, such as manufacturing, mobility, healthcare, and household products. The production of smaller and better computer chips by the semiconductor industry will therefore remain important.

The fundamental building block of all modern electronic devices is the transistor. The first transistor was built at Bell Telephone Laboratories in 1947

[Riordan and Hoddeson, 1997] by William Shockley, John Bardeen, and Walter Brattain. For their discovery they received the Nobel prize in physics in 1956. However, the real potential of the technology is to be found in the creation of Integrated Circuits (ICs), i.e. in the creation of many transistors on a single chip. One of the first people that saw this potential was Gordan Moore, the later co-founder of Intel. In his famous paper [Moore, 1965], he predicted that the minimization of the cost per individual transistor would lead to a doubling of the number of transistors that could be fitted in an IC every year. The rate predicted by Moore turned out to be a bit too optimistic and he later corrected it to a doubling every two years [Moore, 1975]. This trend has been surprisingly stable over the past five decades, see Figure 1.1.

The trend in Figure 1.1 has been enabled by the ongoing scaling down of components on chips, which comes with great benefits. Scaling down allows higher operating speeds, leads to lower energy consumption, improves the reliability of electrical circuits, and reduces the cost per component [Moore, 1995]. However, producing smaller and smaller components becomes more and more difficult. In the 1990s, the minimum feature sizes started to fall below 1 micron (10^{-6} m) and following Moore's law was becoming increasingly difficult. Since then Moore's law is no longer a natural phenomenon, but the result of careful planning of the whole semiconductor industry. This planning is formalized in roadmaps such as the International Roadmap for Semiconductors (ITRS). Instead of a prediction of the future, Moore's law has thus become the production plan for the semiconductor industry [Grier, 2006].

Moore's law has been followed up to this decade due to continuing technical innovations. The smallest feature sizes have now shrunk to only a few nanometres (10^{-9} m). Figure 1.2 shows an example of such features on a processor in a modern smartphone.

Despite the increasing complexity and manufacturing costs, the semiconductor industry keeps growing, with global sales reaching $469 billion in 2018 and increasing about 13% every year [SIA, 2019]. ASML, one of the main manufacturers of the lithography machines used to produce these chips, reached almost €11 billion sales in 2018 [ASML, 2019a].

Of course the scaling down of components cannot continue indefinitely. With the diameter of silicon atoms being 0.2 nm and chips produced with 7-nm node technology currently on the market, it is clear that the physical limits are approaching. At some point the increasing manufacturing costs will outweigh the added value of chips with even smaller features. Many researchers have therefore predicted the end of Moore's law (see e.g. [Schaller, 1997; Waldrop, 2016; Theis and Wong, 2017]), and some of these predictions have already been proven wrong by the continuing innovation. With Samsung announcing 5-nm, 4-nm, and 3-nm nodes [Shilov, 2018], scaling down will continue in the near future. It therefore seems likely that a quote of Gordan Moore remains accurate for the next decade: "No exponential is forever: but 'Forever' can be delayed!" [Moore, 2003].

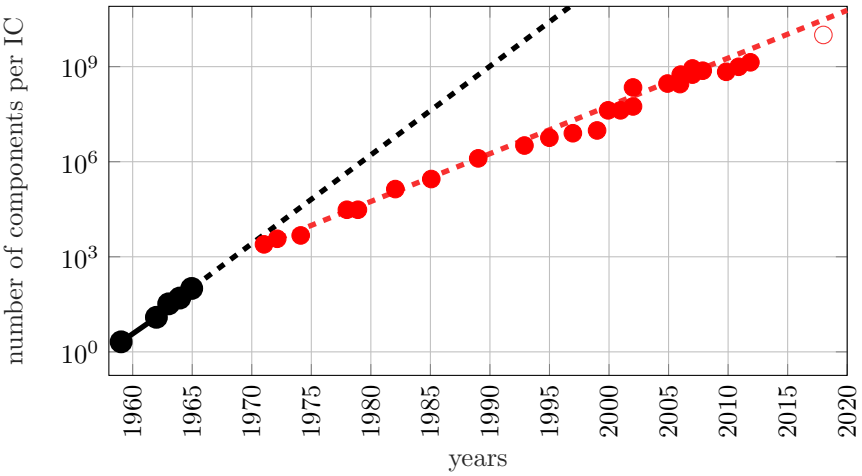

Figure 1.1. Data available in [Moore, 1965] (black filled dots), the original trend predicted in [Moore, 1965] (black dashed line), the corrected trend from [Moore, 1975] (red dashed line), the number of components in some actually produced ICs (filled red dots, data from [Waldrop, 2016]), and of one of the latest processors on the market (open red dot, [Wikichip, 2018])

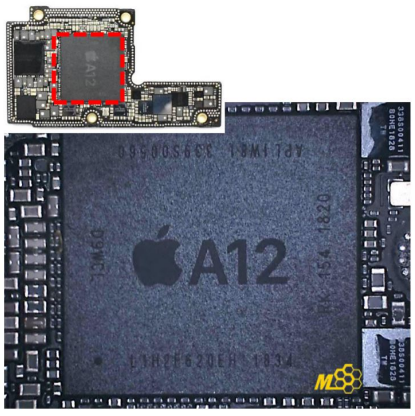

(a) Apple's A12 Bionic processor from a 2018 iPhone XS

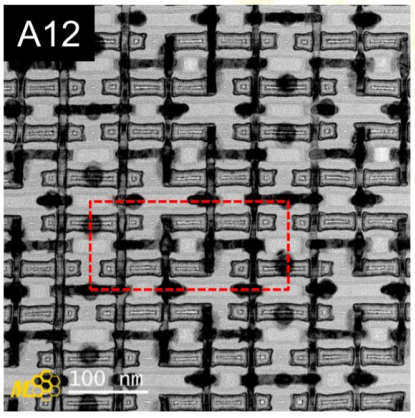

(b) Transmission Electron Microscopy image of the RAM area (dashed red area is the repeated unit cell)

Figure 1.2. The features on Apple's A12 Bionic processor [MSS, 2019]

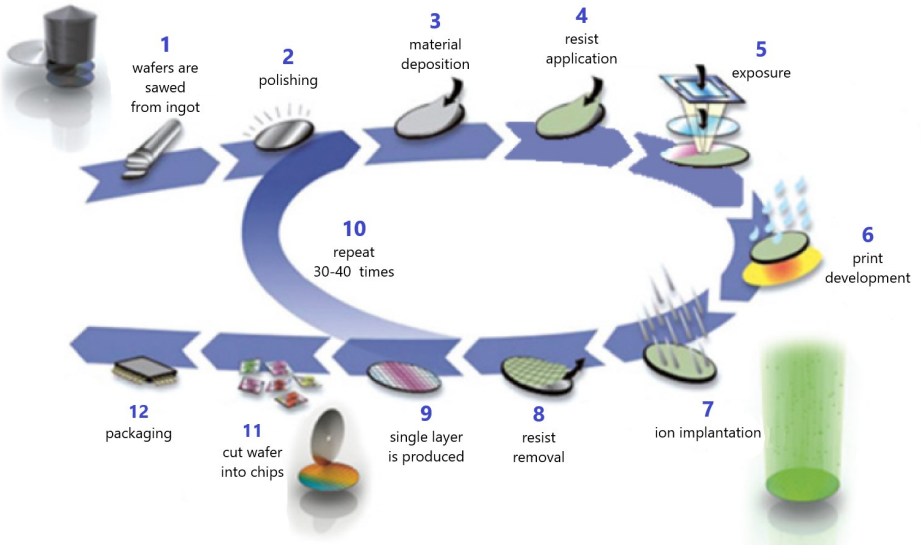

Figure 1.3. The IC manufacturing process [van Gerven, 2016a]

1.2.2 IC manufacturing

The production of ICs consists of several production steps which are displayed in Figure 1.3.

First, an ingot of crystalline silicon is cut into thin slices that are called wafers or substrates (step 1). After the wafers have been cut, they are polished to obtain a smooth surface on which the chips can be created (step 2). It is worth noting that the base material silicon (Si) is one of the most common elements in the earth crust [Anderson, 1989] and is thus widely and cheaply available. Over the years, the wafer diameter has been continually increased. Today, wafers typically have a diameter of 300 mm and a thickness of 0.775 mm. Major companies have been planning the transition to 450 mm wafers, but this transition is not expected to happen soon [Rulison, 2017].

To create new structures on the wafer first a new layer of material is created on the top surface of the wafer (step 3). This can be done by various deposition techniques such as (physical or chemical) vapor decomposition, but it can also include modification of the top surface, typically by thermal oxide formation. In order to create patterns in the newly deposited layer, the wafer is coated with a photoresist (step 4) on which a light source projects the pattern of desired electronic connections (step 5). This crucial step forms the heart of the lithography process and is performed by wafer scanners that will be discussed in more detail in Subsection 1.2.3. The photoresist is then dissolved in either the exposed or unexposed areas, depending on the type of photoresist that is used (step 6).

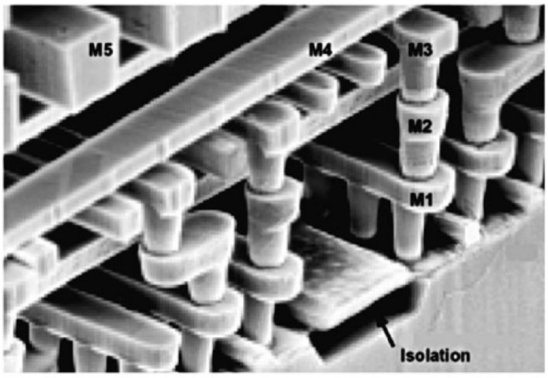

Figure 1.4. Stacking of multiple layers in a chip [Veendrick, 2017]

The difference between areas with and without photoresist can now be used to create patterns in the layer below the photoresist created in step 3. This can be done by etching processes which remove material or by ion implantation which modifies electrical properties. After the desired patterns have been created the photoresist is removed from the whole wafer surface (step 8). This completes the production of a single layer of the chip (step 9).

This process is repeated several times to create several layers on the chip (step 10), which allows to create three-dimensional (3-D) structures on the chips (see Figure 1.4). Modern chips typically contain 30 to 40 layers. For correct functioning of the chip it is crucial that the next layer is well aligned with the previous layers. This motivates the definition of the *overlay error*, which measures the misalignment between two consecutive layers and is an important performance indicator for a lithography system. In the latest wafer scanners the overlay error is below 2 nm [ASML, 2019c].

After all layers have been created, the wafer is cut into individual chips (step 11), which are also called *dies*. Depending on their size, several hundred dies can fit on a 300 mm wafer. After they have been cut out, the functionality of the chips is tested and they are fitted with a plastic packaging to make them less sensitive to contamination (step 12).

1.2.3 The wafer scanner

A crucial step in the IC manufacturing process in Figure 1.3 is the exposure of the photoresist to the light that projects the pattern onto the wafer (step 5). This process largely determines the minimal size of features that can be created on chips. The projection of the pattern of electronic connections is usually done by wafer scanners. One of the latest wafer scanners is shown in Figure 1.5. The main function of this machine is to project light generated at the source through

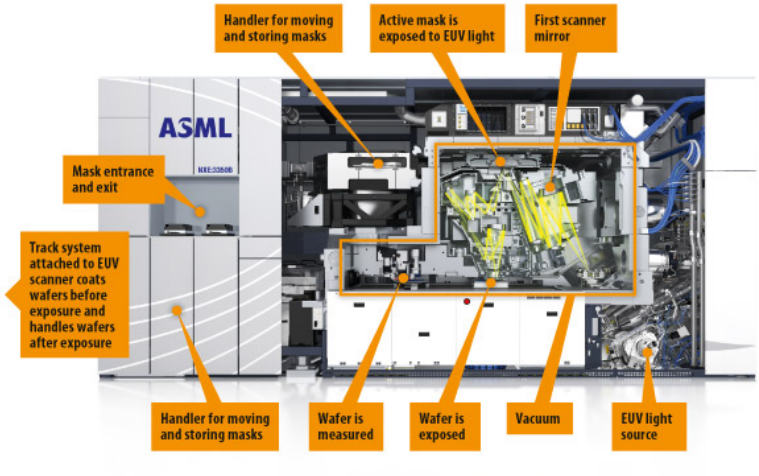

Figure 1.5. ASML's EUV lithography machine [van Gerven, 2016b]

a sequence of mirrors onto the mask and then through another set of mirrors onto the wafer. The mask or reticle contains the desired pattern that is projected four times smaller on the wafer. The area on which the image of the reticle is projected is called a *field*. Note that fields are not necessarily the same as the dies in which the wafer is cut. A wafer typically contains about 100 fields.

A whole field is not exposed to the EUV light at once. Instead, a step-and-scan procedure is followed (Figure 1.6), in which the EUV light is focused in a smaller area called the *slit* that moves with a constant velocity along the length of the field (this process is called a *scan*). To achieve this scanning motion, the wafer and reticle are placed on stages that move through the projection light. After a scan is complete, the position of the wafer is changed such that the next field can be exposed (this process is called a *step*). Figure 1.7 shows a typical expose pattern that results from this procedure. Note that two consecutive fields are always scanned in opposite directions. This is done such that no sudden changes in the position of the reticle stage are required.

The maximal resolution that can be achieved by a certain lithographic system is characterized by the Critical Dimension (CD). The CD is the smallest feature that can be projected with the optical system and is limited by Rayleigh's criterion [Levinson, 2010]

$$\mathrm{CD} = k_1 \frac{\lambda}{\mathrm{NA}}, \tag{1.1}$$

where λ is the wave length of the projection light, NA is the Numerical Aperture, and k_1 is the resolution factor. There are theoretical and practical limits on the decrease in CD that can be achieved by improving k_1 and NA. The theoretical

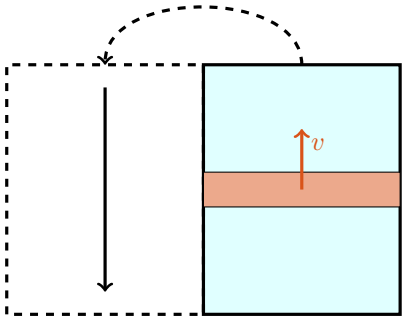

Figure 1.6. Scanning of a field (the light blue rectangle indicates the field, the red area indicates the slit, the dashed and solid black arrows indicate the step to the next field and the scan of the next field, respectively)

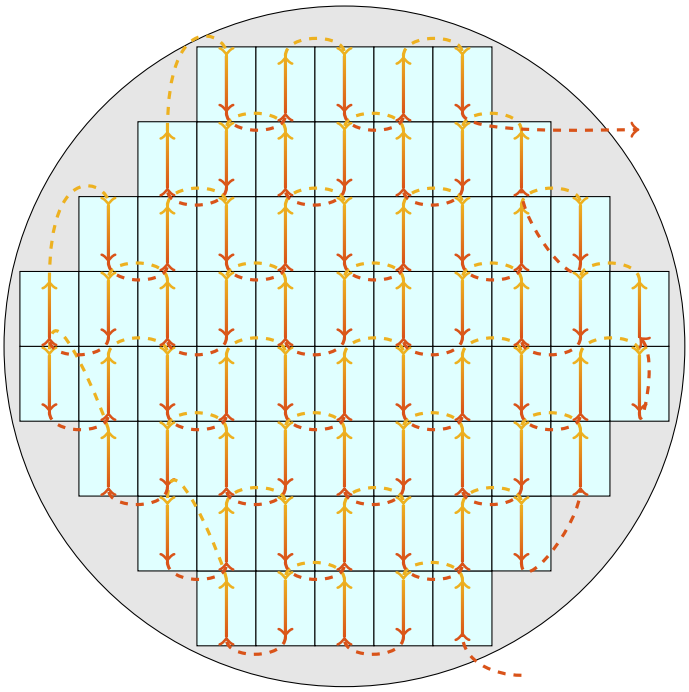

Figure 1.7. A typical expose pattern (gray disk indicates the wafer, light blue rectangles indicate fields, solid arrows indicate scans, and dashed arrows indicate steps)

lower limit on k_1 is 0.25 [Levinson, 2010], but due to rapidly increasing costs k_1 cannot be reduced to much more than 0.3 in practice [Rubingh, 2007]. For projection in air, the theoretical upper limit on NA is 1 while in practice NA cannot exceed 0.93 [Rubingh, 2007]. The most effective way to decrease CD is thus decreasing the wave length λ, but this has also the biggest impact. It, for example, requires the developments of new light sources, photoresists, and lenses. Over the years, the wave length has been reduced in steps from ultraviolet (UV) light with a wavelength of $\lambda = 436$ nm in the 1980s to Deep Ultraviolet (DUV) light with a wavelength of $\lambda = 193$ nm in the 2000s. The next step is EUV light with a wave length of $\lambda = 13.5$ nm, which is currently being introduced in the semiconductor industry [ASML, 2018; Samsung, 2019; TSMC, 2019].

Because the introduction of EUV has been delayed several times [Tallents et al., 2010], DUV technology has been pushed far beyond the CD of 62 nm that could be expected from Rayleigh's criterion (1.1). For example, the theoretical limit NA < 1 has been circumvented by immersion lithography [Levinson, 2010], in which there is water instead of air between the lens and the wafer. This allowed to increase the NA to 1.35 and to improve the CD to 38 nm [ASML, 2019c]. Features smaller than the CD of the optical process can be created using multiple patterning techniques [Levinson, 2010]. In these techniques, the patterns projected in multiple exposure steps are combined using a more advanced etching strategy. This technique has enabled the creation of patterns below 38 nm (such as the ones in Figure 1.2b) without EUV light. However, multiple patterning techniques require many processing steps to create a single layer, and are therefore more complex, time consuming, and expensive compared to a conventional (single-pattern) lithography step. Apart from the possibility to create even smaller features, EUV lithography therefore offers a way to simplify the production and reduce the cost of certain layers that are now created by multiple patterning [Samsung, 2019].

The wavelength of $\lambda = 13.5$ nm for EUV has been chosen by the industry as the next step after the 193-nm wavelength for DUV. The reduction of the wave length by a factor 15 clearly offers the possibility to achieve a significant reduction in the CD. In 2006, ASML and Nikon built the first operational prototypes of commercial EUV tools. Since then, the technology was further developed by ASML [Rice, 2014]. The first EUV systems for high volume manufacturing are currently available and major manufacturers are building and testing EUV production lines [Samsung, 2019; TSMC, 2019].

The development of these EUV systems posed tremendous technical challenges. A major difficulty is that EUV light is absorbed strongly by almost all materials. This makes the construction of EUV wafer scanners significantly different from all previous generations such as DUV wafer scanners. In particular, EUV light cannot be transmitted through air, which means that the whole optical system needs to be placed in a (near) vacuum environment. Furthermore, transmissive optics like the glass lenses in DUV scanners will also absorb the

EUV light and have to be replaced by reflective optics (mirrors). However, even very advanced molybdenum and silicon (Mo/Si) mirrors can only reach a reflexivity of about 70%, which means that each mirror absorbs 30% of the light it receives [Rice, 2014]. With six mirrors between the reticle and the wafer, only 12% of the light reflected from the reticle will reach the wafer.

Because a large portion of the EUV light is absorbed during the projection process, the creation of a light source with sufficient power was one of the main problems in the development of EUV wafer scanners. Because of their very high costs, the throughput of a wafer scanner, i.e. the number of processed wafers per hour, should be sufficiently high. Therefore, the scanning velocity should be high as well. However, the available source power limits the maximal scan speed because a sufficient amount of light is required to create a pattern in the photoresist. Due to these considerations, a cost-effective wafer scanner requires a source power of 100-250 W [Rice, 2014]. Such levels have only been obtained recently and the latest EUV wafer scanners can now process more than 125 wafers per hour [ASML, 2019b].

1.2.4 The increasing importance of thermomechanical control

The high source power of 100 W and more leads to significant thermal loads on machine components. Furthermore, the total overlay error in current machines is specified as 1.4 nm [ASML, 2019b], which means that the overlay error introduced by thermal effects must be in the subnanometer range. Consideration of thermomechanical effects is therefore already crucial to achieve the required imaging tolerances.

In the coming years, the importance of these effects will only increase. In the next-generation wafer scanners, the source power will be increased to 500 W, while the total overlay error will decrease to 1.1 nm or lower [De Young, 2019]. Achieving these targets requires a significant performance improvement for which modeling and control of thermomechanical effects are necessary. For example, in the next-generation wafer scanners, the heat-induced deformation of the wafer alone can easily lead to an overlay error of 4 nm (see Chapter 5), which clearly demonstrates that effective strategies to reduce the overlay error induced by wafer heating are absolutely necessary.

Much of the heat-induced deformation in wafer scanners is currently being reduced by passive control strategies. For example, the deformation of the reticle and the mirrors are reduced by using materials with a very small Coefficient of Thermal Expansion (CTE) such as Zerodur and Ultra Low Expansion glass (ULE). However, it is clear that the positioning tolerances in next-generation wafer scanners cannot be achieved with passive control alone and that active control strategies will be necessary.

In current wafer scanners, most advanced active control strategies are applied

to the motion control of the wafer and reticle stages. This has been an active field of research for the past two decades, see e.g. [de Roover and Bosgra, 2000; van de Wal et al., 2002; van der Meulen et al., 2008; Oomen et al., 2014; Heertjes et al., 2016; Evers et al., 2019b]. These continued efforts have now reduced the overlay errors due to the positioning of the wafer and reticle stage to the subnanometer range [Evers et al., 2019b].

Modeling and control of thermomechanical effects in wafer scanners has received less attention, although the interest has been growing in the past decade. The research on heat-induced deformation in wafer scanners is concentrated on three machine components: the reticle, the mirrors, and the wafer. Because the mirrors and the reticle receive the largest heat loads, the research initially focused on the heat-induced deformation of these components and the propagation of the resulting optical error through the sequence of mirrors [Saathof, 2013; Bikcora, 2013; Bikcora et al., 2014; Saathof et al., 2016; Habets et al., 2016]. However, the deformation of the wafer is becoming more and more significant and is considered in recent works as well, often using relatively simple one-dimensional models [Hanema, 2018; van den Hurk et al., 2018; Merks, 2019].

Summarizing, thermomechanical control of the reticle, mirrors, and wafer is less developed than the motion control of the reticle and wafer stages. This is potentially problematic because the errors introduced by thermomechanical effects can easily exceed the remaining errors in the motion control of the stages. For example, simulations in Chapter 5 show that the overlay errors introduced by wafer heating can easily exceed 4 nm, whereas the overlay errors due to positioning of the wafer and reticle stages are already in the subnanometer range.

1.3 Challenges in thermomechanical control for EUV lithography

At first sight, thermomechanical systems might seem similar to mechanical systems. After all, both are derived from underlying Partial Differential Equations (PDEs), whose discretization typically results in large-scale Finite Element (FE) models, see e.g. [Zienkiewicz et al., 2013]. However, the thermomechanical systems that need to be controlled in wafer scanners pose several specific challenges that require special attention.

1.3.1 Slow system dynamics

The considered thermal and thermomechanical systems are typically slow, i.e. the time constants of these systems are typically much longer than the time window of interest. This means that (during the relevant time window) the response of thermomechanical systems is dominated by transient effects, and that the steady-state response is less relevant for the performance of the system.

An example of this problem occurs in the mirror heating problem. Here, the slowest time constant of the mirror is several hours which is much longer than the time it takes to scan a whole wafer (approximately 10 s) or a single field on the wafer (approximately 0.1 s).

Interpretation of frequency response functions

When the slowest time constant is much longer than the time window of interest, care should be taken when interpreting Frequency Response Functions (FRFs). The FRF of a Linear Time Invariant (LTI) system captures the information about the steady-state response under harmonic excitation. Although this characterizes the long-term input-output behavior of the system, it is important to note that the response in the time window of interest will be dominated by transient effects and not by steady-state behavior. An example were this problem plays a role can be found in [Evers et al., 2018]. There it is shown that FRF identification techniques developed for mechanical systems required modifications before they could be effectively applied to thermal systems, because transient effects dominated the measurements from the thermal system.

This observation also impacts the design of feedback controllers in the frequency domain. For example, commonly used $\mathcal{H}_2$- or $\mathcal{H}_\infty$-optimal controller designs might not lead to an optimal closed-loop response in the time window of interest.

Modal analysis

The importance of transient effects makes modal analysis less effective. In modal analysis, the complexity of the FE model is reduced by considering only the first few eigenmodes. Modal analysis has proven to be extremely effective for applications in structural dynamics, see e.g. [Gawronski, 2004; de Kraker, 2004] and is also commonly applied in thermal analysis, see e.g. [van Gils et al., 2012]. However, when the considered process window is much smaller than the slowest time constants, many eigenmodes need to be considered to obtain an accurate model and modal analysis becomes less effective.

Another indication that modal analysis is problematic appears in the wafer heating problem. Here, an infinite spatial domain approximation is very effective (see Chapter 3), but eigenmodes do not exist on the infinite domain.

1.3.2 Moving sources

As discussed in Subsection 1.2.3, the scanning motion of the EUV light results in moving heat sources on the wafer and the reticle. The velocities of these moving sources are high in order to maximize the throughput of the wafer scanner.

Fast moving heat loads make simulation challenging. In particular, the higher the velocity of the load, the smaller the mesh size of the FE model should be

to avoid discretization artefacts, see e.g. [Zienkiewicz et al., 2014]. Because the spatial and temporal domain are related by the velocity of the moving load, this also limits the maximal time step that can be used. A small mesh size and time step are thus required in all areas that are exposed to the moving EUV light. Because the heat load travels through a large spatial domain (see Figure 1.7), the simulation of the wafer heating problem is especially challenging.

1.3.3 Nonlinear material behavior

To reduce the thermal expansion of the reticle and the mirrors, these components are made from ultra low expansion materials such as ULE and Zerodur. An inherent property of these materials is that the Coefficient of Thermal Expansion (CTE) is strongly temperature dependent. This results in a nonlinear relation between the temperature fields and displacement fields (see Chapter 2).

This complicates the modeling and control of these structures significantly. First of all, the nonlinearity should be included in the FE analysis, which complicates the modeling procedure. A second problem is that the performance of the wafer scanner is determined by the displacement field, which depends nonlinearly on the applied heat loads. This complicates the design of feedback controllers because controller design techniques for nonlinear systems need to be used.

1.3.4 Unmeasurable performance variables

A well-known problem in lithography is that the optical performance cannot be measured directly. Only after the wafer has been exposed, the projected pattern can be measured. Prediction and control of the optical performance therefore largely rely on high-fidelity models. Some research regarding this problem has been done in the context of motion control of the stages (see e.g. [Oomen et al., 2015; Dorosti et al., 2018b; Dorosti et al., 2018a]). For thermomechanical systems the problem could be even more challenging than for motion control.

First of all, there is the problem that temperature measurements are often the easiest to obtain but that the actual performance is determined by the resulting displacement field. Temperature measurements provide only information about the thermal model. The translation from the temperature field to the resulting deformation then still relies on accurate (FE) models.

Another problem is that the temperature increase and deformation introduced by thermal loads is typically concentrated in the area where these loads are applied. This localized character means that sensors should be close to the optical surface in order to get a good indication of the heat-induced deformation. However, it is often impossible to place sensors near the optical surface because this will block the EUV light or degrade the imaging quality in another way.

It is worth noting that the solutions proposed in [Dorosti et al., 2018b] and

[Dorosti et al., 2018a] for flexible structures are based on eigenmodes. Because modal analysis is a less effective tool for the considered thermomechanical systems, it seems unlikely that the same approach would be effective to predict heat-induced deformation of the reticle, the mirrors, and the wafer.

1.3.5 Control system design

As argued in Subsection 1.2.4, active thermomechanical control will be necessary to achieve the ever decreasing positioning tolerances. However, current wafer scanners do not contain sufficient actuation and sensing possibilities and new control systems will have to be designed. This comes with several challenges.

A central question, that is also commonly encountered during the design of many other control systems, is where actuators and sensors should be placed. There is a large amount of literature on this topic, see [van de Wal and de Jager, 2001] for an overview. Apart from this question, there are several other challenges specific for the considered application.

Control inputs in different physical domains

A thermomechanical system can be controlled using inputs in the thermal (i.e. by adding or extracting heat) or in the mechanical domain (i.e. by applying forces). Both thermal and mechanical actuation are being considered in mirror and wafer heating problems. For mirror heating, thermal control has been used to control mirror deformations, see [Saathof et al., 2016] and simulations indicate that mechanical control (i.e. the control of rigid body modes of the mirrors) can significantly improve the imaging quality, see [Habets et al., 2016]. For wafer heating, both thermal control, see [van Schoot et al., 2017], and mechanical control, see [van den Hurk et al., 2018], are being considered as well. Combinations of thermal and mechanical control are likely to be most effective, but this requires the coordination of control inputs from different physical domains.

Limitations of thermal actuators

The type of thermal actuators that is used typically introduces significant limitations on the heat loads that can be generated. A clear example of this problem are actuators based on Joule heating such as thin film heaters, which can only supply heat and not extract heat. The maximum power that can be generated by these actuators has to be limited to prevent burn out. Thermal actuation by additional light sources such as IR heaters can also only add heat. Peltier elements can both heat and cool, but experience significant nonlinear input/output behavior that complicates their use for feedback control, see [Bos et al., 2018].

The above mentioned input constraints are especially problematic to incorporate in feedback controller design. Most of the existing feedback control techniques (see e.g. [Skogestad and Postlethwaite, 2007]) cannot take these con-

straints on the actuator output into account. Model Predictive Control can consider such limitations and is therefore considered a promising technique for advanced feedback control of thermomechanical systems, see e.g. [Hanema, 2018]. Also more pragmatic approaches are being considered. For example, feedback controllers can be designed around an operation point where heaters produce an offset power, which allows the control signal to become negative w.r.t. to the offset power but keep the net applied heat load positive (provided that the deviations from the offset power are not too large).

It is worth noting that the (spatial) shape of the heat loads generated using these thermal actuators allows significant design freedom. For example, the density of electric windings in a thin film heater could be varied and the distribution of IR light can be shaped using lenses.

Mechanical actuation

Heat-induced deformation can also be reduced by mechanical actuation. An advantage of this approach is that mechanical actuation is typically very fast compared to the slow dynamics of the thermomechanical system and can be applied almost instantaneously. Naturally, mechanical actuation is applied to control the rigid body modes of the reticle, mirrors, and wafer. However, further reduction of heat-induced deformation using mechanical actuation comes with significantly more complications than thermal actuation.

First of all, mechanical actuation cannot be applied directly to the optical surfaces because the actuators will block the EUV light. Mechanical actuators should therefore be integrated in the structure below the optical surface. Some thermal actuators do not suffer from this limitation. For example, IR heating can be applied directly to the optical surface without interfering with the projection of the EUV light.

A second problem is that heat loads are typically concentrated. Mechanical actuation therefore typically requires a fine grid of actuators. This observation has led to the development of an 'active wafer clamp', i.e. a wafer clamp containing a fine grid of mechanical actuators [Steur, 2017; van den Hurk et al., 2018]. However, the development, construction, and control of an active wafer clamp are very complex.

Limitations in sensing possibilities

Several types of sensors could be considered for the control of thermomechanical systems. Temperature sensors like Negative Temperature Coefficient thermistors (NTCs) and thermocouples should be integrated below the optical surface. Optical temperature sensors could be used to measure the temperature of the optical surface directly, without interfering with the projection of EUV light. As the performance is determined in the mechanical domain, sensors that measure quantities in the mechanical domain are also of interest. The best candidate

for such sensors are strain gauges. These should also be integrated somewhere below the optical surface.

As touched upon in Subsection 1.3.4, sensing possibilities are often limited. This is inherent to the considered application where the disturbance enters at the optical surface which also determines the imaging quality. The most useful measurements should thus be taken near this optical surface. However, it is not straightforward to take such measurements without reducing the optical performance. For example, it is clearly not possible to place sensors on the optical surface itself.

1.4 Research objective and contributions

1.4.1 Research objective

As indicated in Subsection 1.2.1, the number of components that can be fitted on a single IC has increased exponentially during the past five decades. This trend has been enabled for a large part by improvements in lithography, particularly by improvements in the wafer scanners used to project a pattern of electronic connection onto a silicon wafer, see Subsection 1.2.3. With the features of the projected patterns now approaching the subnanometer range, the performance of wafer scanners is more and more determined by thermomechanical effects and the next-generation wafer scanners will require active control to reduce the effects of heat-induced deformation on the imaging quality, see Subsection 1.2.4. Because the development of such control systems poses many challenges (as discussed in Section 1.3), the objective of this thesis is as follows.

Objective: To develop effective and efficient methods for the modelling and control of thermomechanical systems.

This objective is addressed in the context of the three control configurations shown in Figure 1.8 which are relevant for EUV lithography. In these figures, the thermomechanical plant P has mechanical inputs and outputs labeled by 'M' and thermal inputs and outputs labeled by 'T'. The optical performance of the plant is determined by the deformation of the optical surface d_{OS}. In most problems considered in this thesis, the plant P is a thermomechanical model of the wafer only. However, eventually the heat-induced deformation of all components in the optical chain (i.e. the reticle, the mirrors, and the wafer) and the propagation of the induced optical errors to the wafer surface should be considered. The heat induced by the EUV light Q_{EUV} is the only considered disturbance. Eventually, it might be necessary to consider other heat loads as well, but the heat induced by the EUV light is expected to be the most dominant disturbance.

The first control configuration in Figure 1.8a is called error correction. Only the rigid body modes d_{rb} of the reticle, the mirrors, and the wafer are adjusted

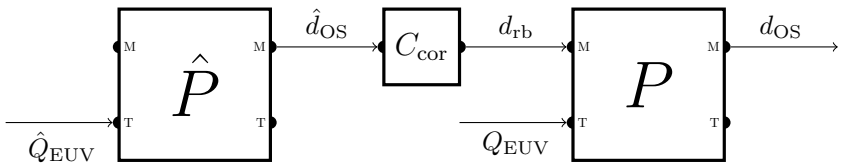

(a) Error correction

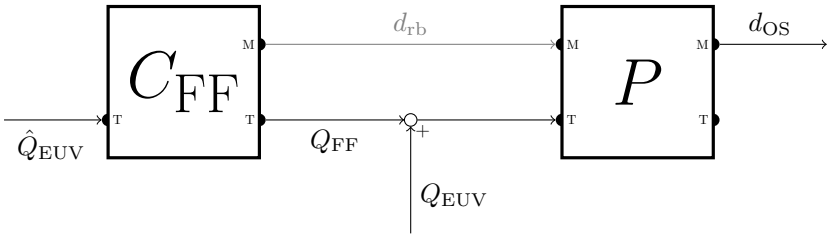

(b) Feedforward control

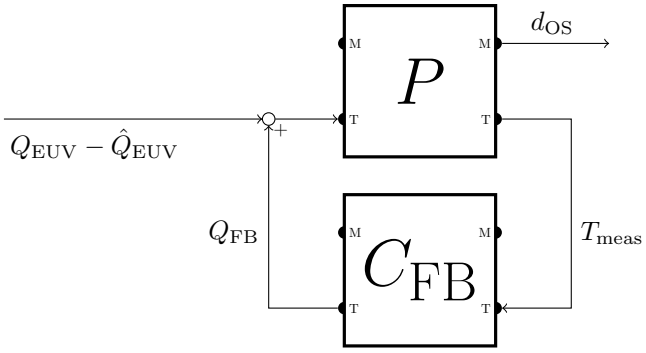

(c) Feedback control

Figure 1.8. The three control configurations considered in this thesis

to improve the imaging quality. The required corrections are computed by the corrector C_{cor} based on the predicted deformations of the optical surfaces $\hat{d}_{\text{OS}}$, which are computed based on a plant model $\hat{P}$ and the expected heat deposited by the EUV light $\hat{Q}_{\text{EUV}}$.

The second control configuration in Figure 1.8b shows a more standard feedforward control configuration. Here, a feedforward controller C_{FF} computes a thermal actuation heat load Q_{FF} based on the expected heat generated by the EUV light $\hat{Q}_{\text{EUV}}$ and the plant model $\hat{P}$. The performance of this system can be improved further when C_{FF} may also adjust the rigid-body modes that were also considered in the error correction scheme (gray arrow). In that case, the configuration in Figure 1.8b is an extension of the configuration in Figure 1.8a.

The schemes in Figures 1.8a and 1.8b are not robust to modeling errors in $\hat{Q}_{\text{EUV}}$ and $\hat{P}$. The third control configuration in Figure 1.8c shows a feedback control that increases the robustness against modeling errors in $\hat{Q}_{\text{EUV}}$. In this configuration, the feedback controller C_{FB} uses temperature measurements T_{meas} to compute a heat load Q_{FB} that should reduce the influence of the modeling error $Q_{\text{EUV}} - \hat{Q}_{\text{EUV}}$ on the performance variables d_{OS}. Note that such controller is designed based on a plant model $\hat{P}$, but implemented on the real plant P.

1.4.2 Contribution 1

The first contribution of this thesis is motivated by the error correction scheme in Figure 1.8a. The main challenge for the control scheme in Figure 1.8a lies in the computation of $\hat{d}_{\text{OS}}$ based on $\hat{P}$ and $\hat{Q}_{\text{EUV}}$. Another problem is of course the computation of d_{rb} based on $\hat{d}_{\text{OS}}$, but this problem has already been addressed in [Habets et al., 2016]. Because the area where the pattern is projected moves with a high velocity over the wafer surface, the computation of the deformation of the wafer due to this heat load is most challenging. The main problem is that the wafer scanner can be used for a large variety of EUV loads $\hat{Q}_{\text{EUV}}$. For example, the scan velocity, the order in which fields are scanned (see Figure 1.7), and the time required to 'step' to the next field (i.e. the time it takes to position the wafer at the next field after the scanning of a field has been completed) may vary from wafer to wafer. It is therefore not possible to precompute $\hat{d}_{\text{OS}}$ off line. This is problematic because $\hat{d}_{\text{OS}}$ is typically computed as the solution of a large FE model and the computational power and memory available in a wafer scanner are limited. Therefore, efficient numerical techniques are needed to compute $\hat{d}_{\text{OS}}$. This forms the first contribution of this thesis.

Contribution 1: Computationally efficient methods for the simulation of thermomechanical systems subject to repetitive moving heat loads.

This contribution consists of two techniques. The first technique exploits the repetitive nature of a heat load such as the one in Figure 1.7. It is shown that

the temperature and displacement fields resulting from such a heat load can be reconstructed by considering the temperature and displacement fields that result from the heat load applied to a single field only. This yields a significant reduction in the required computational time and memory. Variations in the order in which fields are exposed and varying 'step'-times can be incorporated easily in this technique. The second technique addresses the computation of the temperature field resulting from the moving heat load applied to a single field. It is demonstrated that the temperature field on a two-dimensional spatial domain can be accurately approximated based on the solutions of three problems on one-dimensional spatial domains. Especially because moving heat loads require a fine mesh (see Subsection 1.3.2), this yields a significant reduction in the required computational time and memory. The two proposed techniques might also be valuable for other applications in which moving heat loads occur such as welding and additive manufacturing.

1.4.3 Contribution 2

The second contribution of this thesis is based on the thermal feedforward control configuration in Figure 1.8b. Obviously, the actuation heat load Q_{FF} should be realized by thermal actuators. However, (almost) no thermal actuators are present in current wafer scanners. Designing an effective actuator layout for the next-generation wafer scanners is an important problem because the design can strongly influence the achievable performance of the resulting control system. To aid the design of such actuator layout, a method to compute the optimal shapes of the actuation heat load is proposed. In particular, the method computes a fixed number of actuation heat load shapes and the intensities with which these should be applied to satisfy certain deformation constraints. Input constraints that are typical for thermal actuators (see Subsection 1.3.5) can be easily incorporated in this approach. The development of this method forms the second contribution of this thesis.

Contribution 2: A method to compute the optimal actuation heat load shapes for feedforward control of thermomechanical systems.

The proposed method has been applied to a wafer heating and mirror heating application. In both applications, the computed actuation heat load shapes give a good impression about an effective placement of thermal actuators. Control of the transient response is considered in the wafer heating application whereas steady-state temperature fields are controlled in the mirror heating application. The mirror heating application also demonstrates that nonlinear material behavior, such as a temperature-dependent CTE (see Subsection 1.3.3), can be included in the optimization procedure. The actuation heat load shapes can also be computed while simultaneously considering the effect of corrections in

rigid-body modes (gray arrow in Figure 1.8b).

1.4.4 Contribution 3

The third contribution of this thesis considers the feedback control configuration in Figure 1.8c. The actuators and sensors required to control thermomechanical effects are both (almost) not present in current wafer scanners. Since Contribution 2 has given some insight in an effective actuator layout (although not specifically for feedback control), the main problem is where the sensors should be placed.

In order to obtain a better understanding of this problem, thermal and thermomechanical systems have been considered on one- and two-dimensional (unbounded) spatial domains. Given locations of a (point) disturbance, (point) actuator, and (point) performance variable, the question is where the (point) sensor should be placed to achieve the best closed-loop disturbance rejection. It is shown that the considered systems do not have any fundamental performance limitations, i.e. for any chosen sensor location the closed-loop transfer function can be made arbitrarily small if the order of the controller C_{FB} is not limited. Furthermore, analytic expressions for the optimal sensor locations for the case of proportional feedback control (i.e. a controller of order zero) are determined. This forms the third contribution of this thesis.

Contribution 3: Guidelines for the placement of sensors and actuators in feedback-controlled thermal systems.

Numerical results indicate that these guidelines accurately predict the optimal sensor locations under proportional feedback control. The results can also be used to accurately predict the optimal (point) actuator locations for given locations of the (point) sensor, disturbance, and performance variable.

1.5 Outline

This thesis is divided into five parts.

Part I forms the opening of the thesis and contains two chapters. After a general introduction, Chapter 2 contains a more specific introduction to the modeling of the thermomechanical systems that will be considered in the remainder of this thesis.

Part II covers Contribution 1 and also contains two chapters. In Chapter 3, a method to obtain the temperature and displacement fields resulting from repetitive heat loads such as the expose pattern in Figure 1.7 is presented. Chapter 4 contains a semi-analytic approximation method for the temperature field resulting from moving heat loads. In this method, the temperature field on a

two-dimensional spatial domain is approximated in terms of three solutions on one-dimensional spatial domains.

Part III covers Contribution 2 and again contains two chapters. In Chapter 5, the method to compute the optimal actuation heat load shapes for transient problems is described and applied to the scanning of a single field on the wafer. In Chapter 6, a modification of the method from Chapter 5 for the mirror heating problem is presented. In this problem, the steady-state temperature fields resulting from multiple illumination patterns are considered instead of a transient response.

Part IV covers Contribution 3 and contains one chapter. In Chapter 7, guidelines for sensor and actuator placement in thermal and thermomechanical systems on one- and two-dimensional unbounded spatial domains are derived.

Part V, consisting only of Chapter 8, contains the conclusions and recommendations for future research.

Chapters 4, 5, and 7 are based on journal papers that have been published or are accepted for publication. The papers are indicated at the beginning of these chapters. A journal paper based on Chapter 3 is is preparation.

All chapters can be read independently, but the introduction to the modeling of thermomechanical systems in Chapter 2 might aid understanding of the models used in the other chapters.

Chapter 2

Modeling of thermomechanical systems

This chapter introduces the models of thermomechanical systems considered in this thesis. After the introduction of some notation in Section 2.1, the general equations for a thermoelastic solid are derived in Section 2.2. Two commonly used simplifications of the general theory are presented in the following two sections: Section 2.3 introduces the equations for linear thermoelasticity and Section 2.4 introduces the equations for quasi-static thermoelasticity. The equations for linear quasi-static thermoelasticity are used to model wafer heating in Section 2.5. This chapter ends with a short conclusion in Section 2.6.

2.1 Notation

The following notation will be used in this chapter. Scalars are denoted by italic letters, e.g. a and J denote a scalar. Vectors are denoted by bold lower-case letters, e.g. $\mathbf{a}$ and $\boldsymbol{\theta}$ denote a vectors. Unless otherwise specified, vectors are column vectors. Matrices are denoted by bold capital Roman letters or bold Greek letters, e.g. $\mathbf{A}$ and $\boldsymbol{\sigma}$ denote matrices. A bold lower-case Greek letter can thus denote a vector or a matrix. Components of vectors and matrices are again scalars and are thus denoted by lower-case italic letters, e.g.

$$\mathbf{a} = \begin{bmatrix} a_1 \\ a_2 \\ \vdots \\ a_n \end{bmatrix}, \qquad \mathbf{A} = \begin{bmatrix} a_{11} & a_{12} & \cdots & a_{1m} \\ a_{21} & a_{22} & \cdots & a_{2m} \\ \vdots & \vdots & & \vdots \\ a_{n1} & a_{n2} & \cdots & a_{nm} \end{bmatrix}. \tag{2.1}$$

The same conventions are used with respect to functions, e.g. $a(t)$, $\mathbf{a}(t)$, and $\mathbf{A}(t)$ denote scalar-valued, vector-valued, and matrix-valued functions depending on the scalar variable t, respectively.

The transpose of a matrix $\mathbf{A}$ is denoted by $\mathbf{A}^\top$ and $\mathbf{AB}$ denotes the matrix-product of $\mathbf{A}$ and $\mathbf{B}$. The inverse of an invertible matrix $\mathbf{A}$ is denoted by $\mathbf{A}^{-1}$. The inverse of $\mathbf{A}^\top$ is equal to the transpose of $\mathbf{A}^{-1}$ and is denoted by $\mathbf{A}^{-\top}$.

The (Euclidean) inner product of two real vectors with n components is

$$\mathbf{a} \cdot \mathbf{b} := \mathbf{a}^\top \mathbf{b} = a_1 b_1 + a_2 b_2 + \ldots + a_n b_n, \tag{2.2}$$

and the corresponding (Euclidean) norm is denoted by

$$\|\mathbf{a}\| := \sqrt{\mathbf{a} \cdot \mathbf{a}} = \sqrt{a_1^2 + a_2^2 + \ldots + a_n^2}. \tag{2.3}$$

The double inner product of two real $n \times m$-matrices $\mathbf{A}$ and $\mathbf{B}$ is defined as

$$\mathbf{A} : \mathbf{B} = \sum_{i=1}^{n} \sum_{j=1}^{m} a_{ij} b_{ij} = \operatorname{trace}(\mathbf{A}^\top \mathbf{B}). \tag{2.4}$$

Remark 2.1. *The double inner product notation is adopted from tensor calculus. In this setting, the matrices* $\mathbf{A}$ *and* $\mathbf{B}$ *are interpreted as second-order tensors w.r.t. an orthonormal basis, see e.g. [Lebedev et al., 2010].*

The derivative of a matrix-valued function $\mathbf{A}(t)$ w.r.t. the scalar variable t is obtained by taking the derivatives of the components and yields a matrix of the same size as $\mathbf{A}$. Taking the derivative of a vector-valued function $\mathbf{f}(\mathbf{x})$ w.r.t. the vector $\mathbf{x}$ yields the matrix of partial derivatives

$$\frac{\partial \mathbf{f}}{\partial \mathbf{x}}(\mathbf{x}) = \begin{bmatrix} \frac{\partial f_1}{\partial x_1}(\mathbf{x}) & \frac{\partial f_1}{\partial x_2}(\mathbf{x}) & \cdots & \frac{\partial f_1}{x_n}(\mathbf{x}) \\ \frac{\partial f_2}{\partial x_1}(\mathbf{x}) & \frac{\partial f_2}{\partial x_2}(\mathbf{x}) & \cdots & \frac{\partial f_2}{x_n}(\mathbf{x}) \\ \vdots & \vdots & & \vdots \\ \frac{\partial f_m}{\partial x_1}(\mathbf{x}) & \frac{\partial f_m}{\partial x_2}(\mathbf{x}) & \cdots & \frac{\partial f_m}{x_n}(\mathbf{x}) \end{bmatrix}. \tag{2.5}$$

It is important to note that the matrix of partial derivatives is not the same as the gradient $\nabla_{\mathbf{x}} \mathbf{f}(\mathbf{x})$ but equal to its transpose, i.e.

$$\nabla_{\mathbf{x}} \mathbf{f}(\mathbf{x}) := \left(\frac{\partial \mathbf{f}}{\partial \mathbf{x}}(\mathbf{x}) \right)^\top. \tag{2.6}$$

By a slight abuse of notation, the derivative of a scalar-valued function $f(\mathbf{X})$ w.r.t. an $n \times m$-matrix $\mathbf{X}$ is defined as

$$\frac{\partial f}{\partial \mathbf{X}}(\mathbf{X}) = \begin{bmatrix} \frac{\partial f}{\partial x_{11}}(\mathbf{X}) & \frac{\partial f}{\partial x_{12}}(\mathbf{X}) & \cdots & \frac{\partial f}{x_{1m}}(\mathbf{X}) \\ \frac{\partial f}{\partial x_{21}}(\mathbf{X}) & \frac{\partial f}{\partial x_{22}}(\mathbf{X}) & \cdots & \frac{\partial f}{x_{2m}}(\mathbf{X}) \\ \vdots & \vdots & & \vdots \\ \frac{\partial f}{\partial x_{n1}}(\mathbf{X}) & \frac{\partial f}{\partial x_{n2}}(\mathbf{X}) & \cdots & \frac{\partial f}{x_{nm}}(\mathbf{X}) \end{bmatrix}. \tag{2.7}$$

Note that for the composition $f(\mathbf{X}(t))$ of a scalar-valued function $f(\mathbf{X})$ with a matrix-valued function $\mathbf{X}(t)$, the chain rule for differentiation shows that

$$\frac{\partial}{\partial t}\left(f(\mathbf{X}(t))\right) = \sum_{i=1}^{n}\sum_{j=1}^{m}\frac{\partial f}{\partial x_{ij}}(\mathbf{X}(t))\frac{\partial x_{ij}}{\partial t}(t) = \frac{\partial f}{\partial \mathbf{X}}(\mathbf{X}(t)) : \frac{\partial \mathbf{X}}{\partial t}(t), \tag{2.8}$$

where : denotes the inner product of matrices as in (2.4).

When $\mathbf{f}(\mathbf{x})$ and $\mathbf{x}$ are both of length n, the inner product of the gradient operator $\nabla_{\mathbf{x}}$ and $\mathbf{f}(\mathbf{x})$ can be defined as the scalar-valued function

$$\left(\nabla_{\mathbf{x}} \cdot \mathbf{f}\right)(\mathbf{x}) := \frac{\partial f_1}{\partial x_1}(\mathbf{x}) + \frac{\partial f_2}{\partial x_2}(\mathbf{x}) + \ldots + \frac{\partial f_n}{\partial x_n}(\mathbf{x}). \tag{2.9}$$

For a vector $\mathbf{x}$ of length n and an $n \times m$-matrix valued function $\mathbf{A}(\mathbf{x})$ with columns $\mathbf{a}_1(\mathbf{x})$, $\mathbf{a}_2(\mathbf{x})$, $\ldots$, $\mathbf{a}_m(\mathbf{x})$, the inner product of $\nabla_{\mathbf{x}}$ and $\mathbf{A}$ yields a vector-valued function of length m

$$\left(\nabla_{\mathbf{x}} \cdot \mathbf{A}\right)(\mathbf{x}) := \begin{bmatrix} \left(\nabla_{\mathbf{x}} \cdot \mathbf{a}_1\right)(\mathbf{x}) \\ \left(\nabla_{\mathbf{x}} \cdot \mathbf{a}_2\right)(\mathbf{x}) \\ \vdots \\ \left(\nabla_{\mathbf{x}} \cdot \mathbf{a}_m\right)(\mathbf{x}) \end{bmatrix}. \tag{2.10}$$

2.2 General thermoelasticity

The theory of general thermoelasticity presented in this section is mainly based on [Parkus, 1976]. This theory partially overlaps with elasticity theory, for which [Geers et al., 2011] is used as standard reference.

Consider the solid in a three-dimensional (3-D) space as shown in Figure 2.1. The spatial coordinates w.r.t. a Cartesian basis are denoted by $\mathbf{x} = [x_1, x_2, x_3]^\top$. Time is denoted by t. It is assumed that there exists an undeformed or reference situation in which the solid has a uniform temperature T_0 and is stress free. Note that T_0 denotes the absolute temperature in Kelvin.

The volume occupied by the solid in this reference configuration is denoted by $\Omega_0 \subseteq \mathbb{R}^3$ and the volume occupied by the solid occupied at time t is denoted by $\Omega(t) \subseteq \mathbb{R}^3$. The Lagrangian description of deformation is used. A point originally located at the position $\mathbf{x}$ in the undeformed solid Ω_0 is located at the position $\mathbf{p} = \mathbf{p}(\mathbf{x}, t) \in \mathbb{R}^3$ at time t. At time t, the displacement of the point originally located at $\mathbf{x}$ is thus

$$\mathbf{d}(\mathbf{x}, t) = \mathbf{p}(\mathbf{x}, t) - \mathbf{x}. \tag{2.11}$$

The temperature increase w.r.t. the reference temperature T_0 of a point originally located at $\mathbf{x}$ (which is located at $\mathbf{p}(\mathbf{x}, t)$ at time t) is denoted by $T(\mathbf{x}, t)$. The absolute temperature at a point originally located at $\mathbf{x}$ is thus $T_0 + T(\mathbf{x}, t)$.

In the remainder of this section, four equations for $T(\mathbf{x}, t)$ and the three components of $\mathbf{d}(\mathbf{x}, t)$ will derived.

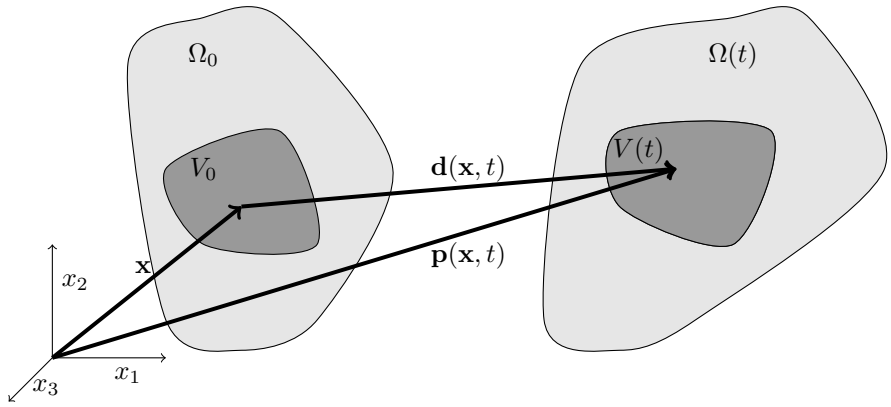

Figure 2.1. The solid occupies a volume Ω_0 in the reference configuration and a volume $\Omega(t)$ at time t. Points in a volume $V_0 \subseteq \Omega_0$ occupy the volume $V(t) \subseteq \Omega(t)$ at time t. The point originally located at $\mathbf{x} \in \Omega_0$ is located at $\mathbf{p}(\mathbf{x},t)$ at time t and has been displaced over $\mathbf{d}(\mathbf{x},t)$.

2.2.1 Mass and strain

First, introduce the deformation gradient $\mathbf{J}$ and the displacement gradient $\mathbf{D}$ as

$$\mathbf{J} := \frac{\partial \mathbf{p}}{\partial \mathbf{x}} = (\nabla_{\mathbf{x}} \mathbf{p})^{\top}, \qquad \mathbf{D} := \frac{\partial \mathbf{d}}{\partial \mathbf{x}} = \mathbf{J} - \mathbf{I}, \tag{2.12}$$

where $\mathbf{I}$ denotes the identity matrix. Note that the dependence on $(\mathbf{x},t)$ will be omitted for brevity throughout this section. The absolute value of the determinant of $\mathbf{J}$ is denoted by J and has the following interpretation. Consider a volume V_0 which is deformed into a volume $V(t) := \{\mathbf{y} \in \mathbb{R}^3 \mid \exists \mathbf{x} \in V_0 \text{ s.t. } \mathbf{y} = \mathbf{p}(\mathbf{x},t)\}$ at time t. The mass of this volume can then be written using integration by substitution as

$$\iiint_{V(t)} \rho \, \mathrm{d}V = \iiint_{V_0} (\rho \circ \mathbf{p}) \, J \, \mathrm{d}V_0 = \iiint_{V_0} \rho_0 \, \mathrm{d}V_0, \tag{2.13}$$

where $\rho(\cdot,t) : \Omega(t) \to \mathbb{R}$ denotes the mass density in the deformed configuration at time t, $\rho \circ \mathbf{p}$ denotes the composition $\rho(\mathbf{p}(\mathbf{x},t),t)$, and $\rho_0 : \Omega_0 \to \mathbb{R}$ denotes the mass density in the reference situation given by $\rho_0(\mathbf{x}) = J(\mathbf{x},t)\rho(\mathbf{p}(\mathbf{x},t),t)$. It thus follows that J is never zero, which implies that $\mathbf{J}$ is invertible for all $(\mathbf{x},t)$ and that $\mathbf{x} \mapsto \mathbf{p}(\mathbf{x},t)$ is a diffeomorphism for all t. The inverse of the map $\mathbf{x} \mapsto \mathbf{p}(\mathbf{x},t)$ is denoted by $\mathbf{p}^{-1}(\cdot,t) : \Omega(t) \to \Omega_0$ and satisfies $\mathbf{p}^{-1}(\mathbf{p}(\mathbf{x},t),t) = \mathbf{x}$ for every $\mathbf{x} \in \Omega_0 \subset \mathbb{R}^3$ at every time instant t.

The strain $\boldsymbol{\varepsilon}(\cdot,t) : \Omega_0 \to \mathbb{R}^{3\times 3}$ describes the stretching of the solid at the time instant t. To introduce the strain, consider a curve $\boldsymbol{\gamma}(\tau) : [0,1] \to \Omega_0 \subset \mathbb{R}^3$

in the undeformed situation. The length of this curve is

$$L_0 = \int_0^1 \left\| \frac{\mathrm{d}\boldsymbol{\gamma}}{\mathrm{d}\tau}(\tau) \right\| \, \mathrm{d}\tau, \tag{2.14}$$

where $\|\cdot\|$ denotes the Euclidean norm. At time t, the curve $\boldsymbol{\gamma}$ is deformed into the curve $\tau \mapsto \mathbf{p}(\boldsymbol{\gamma}(\tau), t)$. The length of the curve at time t is therefore given by

$$L(t) = \int_0^1 \left\| \frac{\partial}{\partial \tau} \left(\mathbf{p}(\gamma(\tau), t) \right) \right\| \, \mathrm{d}\tau = \int_0^1 \left\| \mathbf{J}(\boldsymbol{\gamma}(\tau), t) \frac{\mathrm{d}\boldsymbol{\gamma}}{\mathrm{d}\tau}(\tau) \right\| \, \mathrm{d}\tau. \tag{2.15}$$

The Green strain $\boldsymbol{\varepsilon} = \boldsymbol{\varepsilon}(\mathbf{x}, t)$ is now defined such that the length of every curve $\boldsymbol{\gamma} : [0, 1] \to \Omega_0$ can be expressed as

$$L(t) = \int_0^1 \sqrt{\left(\frac{\mathrm{d}\boldsymbol{\gamma}}{\mathrm{d}\tau}(\tau) \right)^\top (\mathbf{I} + 2\boldsymbol{\varepsilon}(\boldsymbol{\gamma}(\tau), t)) \frac{\mathrm{d}\boldsymbol{\gamma}}{\mathrm{d}\tau}(\tau)} \, \mathrm{d}\tau. \tag{2.16}$$

Comparing (2.15) and (2.16), it follows that

$$\boldsymbol{\varepsilon} = \frac{1}{2} \left(\mathbf{J}^\top \mathbf{J} - \mathbf{I} \right) = \frac{1}{2} \left((\mathbf{D} + \mathbf{I})^\top (\mathbf{D} + \mathbf{I}) - \mathbf{I} \right) = \frac{1}{2} \left(\mathbf{D} + \mathbf{D}^\top + \mathbf{D}^\top \mathbf{D} \right), \tag{2.17}$$

where the second identity follows from the definition of $\mathbf{D}$ in (2.12). Note that the strain $\boldsymbol{\varepsilon}(\mathbf{x}, t)$ is symmetric and therefore has six independent components.

Remark 2.2. *The factor 2 in* (2.16) *is inserted such that the strain* $\boldsymbol{\varepsilon}$ *can be interpreted as the relative elongation* $(L(t) - L_0)/L_0$*. To see that this is the case, consider the situation where* $\boldsymbol{\varepsilon} = \varepsilon \mathbf{I}$ *with* $\varepsilon \in \mathbb{R}$ *constant. In that case* (2.16) *and* (2.14) *show that* $L(t) = \sqrt{1 + 2\varepsilon} L_0$*, which means that the relative elongation* $(L(t) - L_0)/L_0 = \sqrt{1 + 2\varepsilon} - 1 \approx \varepsilon + \mathcal{O}(\varepsilon^2)$.

2.2.2 The force balance

Consider a subset $V_0 \subset \Omega_0$ with boundary S_0. At time t, the subset V_0 is deformed into the subset $V(t) := \{\mathbf{y} \in \mathbb{R}^3 \mid \exists \mathbf{x} \in V_0 \text{ s.t. } \mathbf{y} = \mathbf{p}(\mathbf{x}, t)\} \subseteq \Omega(t)$ with boundary $S(t)$. The force $\mathbf{F}_{V(t)}$ acting on $V(t)$ is the result of surface forces $\mathbf{t} : S(t) \to \mathbb{R}^3$, also called tractions, and forces per unit mass $\mathbf{f}_{\text{ext}}(\cdot, t) : \Omega(t) \to \mathbb{R}^3$. The force $\mathbf{F}_{V(t)}$ is thus

$$\mathbf{F}_{V(t)} = \iint_{S(t)} \mathbf{t} \, \mathrm{d}S + \iiint_{V(t)} \rho \mathbf{f}_{\text{ext}} \, \mathrm{d}V. \tag{2.18}$$

A famous theorem of Cauchy (see e.g. [Geers et al., 2011]) shows that there exists a matrix-valued function $\boldsymbol{\sigma}^{\mathrm{C}}(\cdot, t) : \Omega(t) \to \mathbb{R}^{3\times 3}$ called the Cauchy or true stress such that the traction $\mathbf{t}$ (on any surface $S(t)$) can be written as

$$\mathbf{t} = \left(\boldsymbol{\sigma}^{\mathrm{C}} \right)^\top \mathbf{n}, \tag{2.19}$$

where $\mathbf{n} : S(t) \to \mathbb{R}^3$ denotes the outward-pointing normal of the surface $S(t)$. Because $\mathbf{d}$ and T are functions of the coordinates $\mathbf{x}$ in the reference state, it will be more convenient to transform the integrals over $S(t)$ and $V(t)$ in (2.18) to integrals over S_0 and V_0. This yields [Geers et al., 2011]

$$\mathbf{F}_{V(t)} = \iint_{S_0} \left(\boldsymbol{\sigma}^{\mathrm{PK1}}\right)^{\top} \mathbf{n}_0 \, \mathrm{d}S_0 + \iiint_{V_0} \rho_0 \mathbf{f}_{0,\mathrm{ext}} \, \mathrm{d}V_0, \tag{2.20}$$

where $\mathbf{n}_0 : S_0 \to \mathbb{R}^3$ denotes the outward pointing normal to S_0, $\boldsymbol{\sigma}^{\mathrm{PK1}}(\cdot, t) : \Omega_0 \to \mathbb{R}^{3\times 3}$ denotes the first Piola-Kirchhoff stress defined as

$$\boldsymbol{\sigma}^{\mathrm{PK1}}(\mathbf{x}, t) = J(\mathbf{x}, t)\mathbf{J}^{-1}(\mathbf{x}, t)\boldsymbol{\sigma}^{\mathrm{C}}(\mathbf{p}(\mathbf{x}, t), t), \tag{2.21}$$

and $\mathbf{f}_{0,\mathrm{ext}}(\cdot, t) : \Omega_0 \to \mathbb{R}^3$ is defined as $\mathbf{f}_{0,\mathrm{ext}}(\mathbf{x}, t) = \mathbf{f}_{\mathrm{ext}}(\mathbf{p}(\mathbf{x}, t), t)$. By the divergence theorem, it follows that (2.20) can be rewritten as

$$\mathbf{F}_{V(t)} = \iiint_{V_0} \left(\nabla_{\mathbf{x}} \cdot \boldsymbol{\sigma}^{\mathrm{PK1}} + \rho_0 \mathbf{f}_{0,\mathrm{ext}}\right) \, \mathrm{d}V_0. \tag{2.22}$$

Newton's second law now asserts that

$$\mathbf{F}_{V(t)} = \frac{\partial^2}{\partial t^2} \left(m_{V(t)} \bar{\mathbf{p}}_{V(t)}\right), \tag{2.23}$$

where $m_V(t)$ denotes the mass of the volume $V(t)$ and $\bar{\mathbf{p}}_{V(t)}$ denotes the center of mass of $V(t)$. The definition of the center of mass now gives that

$$m_{V(t)} \bar{\mathbf{p}}_{V(t)} = \iiint_{V(t)} \rho \, \mathrm{d}V \frac{\iiint_{V(t)} \rho \mathbf{x} \, \mathrm{d}V}{\iiint_{V(t)} \rho \, \mathrm{d}V} = \iiint_{V(t)} \rho \mathbf{x} \, \mathrm{d}V. \tag{2.24}$$

Transforming the latter integral back to an integral over $V_0 = \mathbf{p}^{-1}(V(t), t)$ and inserting this result back into (2.23) yields

$$\mathbf{F}_{V(t)} = \frac{\partial^2}{\partial t^2} \iiint_{V_0} \rho_0 \mathbf{p} \, \mathrm{d}V_0 = \iiint_{V_0} \rho_0 \frac{\partial^2 \mathbf{p}}{\partial t^2} \, \mathrm{d}V_0 = \iiint_{V_0} \rho_0 \frac{\partial^2 \mathbf{d}}{\partial t^2} \, \mathrm{d}V_0, \tag{2.25}$$

where the last identity follows from (2.11). Combining (2.22) and (2.25) yields

$$\iiint_{V_0} \left(\nabla_{\mathbf{x}} \cdot \boldsymbol{\sigma}^{\mathrm{PK1}} + \rho_0 \mathbf{f}_{0,\mathrm{ext}}\right) \, \mathrm{d}V_0 = \iiint_{V_0} \rho_0 \frac{\partial^2 \mathbf{d}}{\partial t^2} \, \mathrm{d}V_0. \tag{2.26}$$

Since (2.26) holds for any $V_0 \subseteq \Omega_0$, it follows that

$$\nabla_{\mathbf{x}} \cdot \boldsymbol{\sigma}^{\mathrm{PK1}} + \rho_0 \mathbf{f}_{0,\mathrm{ext}} = \rho_0 \frac{\partial^2 \mathbf{d}}{\partial t^2}. \tag{2.27}$$

Note that $\boldsymbol{\sigma}^{\mathrm{PK1}}$ still needs to be expressed in terms of $\mathbf{d}$ and T, which will be done at a later stage.

Apart from the Cauchy stress $\boldsymbol{\sigma}^{\mathrm{C}}(\cdot,t) : \Omega(t) \to \mathbb{R}^{3\times3}$ and the first Piola-Kirchhoff stress $\boldsymbol{\sigma}^{\mathrm{PK1}}(\cdot,t) : \Omega_0 \to \mathbb{R}^{3\times3}$, there is also a second Piola-Kirchhoff stress $\boldsymbol{\sigma}^{\mathrm{PK2}}(\cdot,t) : \Omega_0 \to \mathbb{R}^{3\times3}$ defined as [Geers et al., 2011]

$$\boldsymbol{\sigma}^{\mathrm{PK2}}(\mathbf{x},t) = \boldsymbol{\sigma}^{\mathrm{PK1}}(\mathbf{x},t)\mathbf{J}^{-\top}(\mathbf{x},t). \tag{2.28}$$

The conservation of angular momentum shows that $\boldsymbol{\sigma}^{\mathrm{C}}$ and $\boldsymbol{\sigma}^{\mathrm{PK2}}$ must be symmetric, see e.g. [Geers et al., 2011]. The second Piola-Kirchhoff stress $\boldsymbol{\sigma}^{\mathrm{PK2}}$ is the energy conjugate of the Green strain $\boldsymbol{\varepsilon}$, i.e. $\boldsymbol{\sigma}^{\mathrm{PK2}} : \boldsymbol{\varepsilon}$ represents energy, and will therefore appear in the energy balance in the following subsection.

2.2.3 The energy balance

The first law of thermodynamics is an energy balance. It states that in any thermodynamic system it must hold that

$$\frac{\partial K}{\partial t} + \frac{\partial U}{\partial t} = \frac{\partial W}{\partial t} + \frac{\partial Q}{\partial t}, \tag{2.29}$$

where K denotes the kinetic energy (due to macroscopic motion), U denotes the internal energy, W denotes the work done by external forces, and Q denotes the applied heat.

Now consider again a volume $V_0 \subseteq \Omega_0$ with boundary S_0. At time t, this volume is deformed into a volume $V(t)$ with boundary $S(t)$. For this volume, the quantities in (2.29) can be expressed as

$$K = \iiint_{V_0} \frac{\rho_0}{2} \left\| \frac{\partial \mathbf{d}}{\partial t} \right\|^2 \mathrm{d}V_0, \tag{2.30}$$

$$U = \iiint_{V_0} \rho_0 u \, \mathrm{d}V_0, \tag{2.31}$$

$$\frac{\partial W}{\partial t} = \iint_{S(t)} \frac{\partial \mathbf{d}}{\partial t} \cdot \left(\left(\boldsymbol{\sigma}^{\mathrm{C}}\right)^{\top} \mathbf{n} \right) \mathrm{d}S + \iiint_{V(t)} \frac{\partial \mathbf{d}}{\partial t} \cdot \rho \mathbf{f}_{\mathrm{ext}} \, \mathrm{d}V, \tag{2.32}$$

$$\frac{\partial Q}{\partial t} = -\iint_{S(t)} \mathbf{q} \cdot \mathbf{n} \, \mathrm{d}S + \iiint_{V(t)} \rho Q_{\mathrm{ext}} \, \mathrm{d}V, \tag{2.33}$$

where $u(\cdot,t) : \Omega_0 \to \mathbb{R}$ denotes the internal energy per unit mass, $\mathbf{q}(\cdot,t) : \Omega(t) \to \mathbb{R}^3$ denotes the heat flux, and $Q_{\mathrm{ext}}(\cdot,t) : \Omega(t) \to \mathbb{R}$ denotes the applied heat load per unit mass. Recall that $\mathbf{n} : S(t) \to \mathbb{R}^3$ denotes the outward pointing normal, so that the the first term on the right hand side (RHS) of (2.33) denotes the heat flux *into* $V(t)$. Note that (2.30) and (2.31) are already expressed as integrals over the undeformed volume V_0, but that (2.32) and (2.37) are still written as integrals over the deformed volume $V(t)$. To write (2.29) as a Partial Differential Equation (PDE) in the coordinates $\mathbf{x}$ in the undeformed configuration, (2.32)

and (2.37) need to be rewritten as integrals over V_0. Using the previously derived force balance (2.27), it can be shown that [Parkus, 1976; Geers et al., 2011]

$$\frac{\partial W}{\partial t} - \frac{\partial K}{\partial t} = \iiint_{V_0} \boldsymbol{\sigma}^{\mathrm{PK2}} : \frac{\partial \boldsymbol{\varepsilon}}{\partial t} \, \mathrm{d}V_0, \tag{2.34}$$

where $\boldsymbol{\sigma}^{\mathrm{PK2}}$ denotes the second Piola-Kirchhoff stress as defined in (2.28). It thus remains to rewrite $\partial Q/\partial t$ as an integral over the original volume V_0. To this end, we use that the surface integral can be transformed to

$$\iint_{S(t)} \mathbf{q} \cdot \mathbf{n} \, \mathrm{d}S = \iint_{S_0} \mathbf{q}_0 \cdot \mathbf{n}_0 \, \mathrm{d}S_0, \tag{2.35}$$

where $\mathbf{q}_0(\cdot, t) : \Omega_0 \to \mathbb{R}^3$ denotes the equivalent heat flux for the surface S_0 and is given by [Geers et al., 2011]

$$\mathbf{q}_0(\mathbf{x}, t) = J(\mathbf{x}, t)\mathbf{J}^{-1}(\mathbf{x}, t)\mathbf{q}(\mathbf{p}(\mathbf{x}, t), t). \tag{2.36}$$

Note that the conversion of $\mathbf{q}$ to $\mathbf{q}_0$ in (2.36) is similar to the conversion of $\boldsymbol{\sigma}^{\mathrm{C}}$ to $\boldsymbol{\sigma}^{\mathrm{PK1}}$ in (2.21). Using (2.35), the heat flux into the volume $V(t)$ in (2.33) can be rewritten as

$$\begin{aligned} \frac{\partial Q}{\partial t} = &- \iint_{S_0} \mathbf{q}_0 \cdot \mathbf{n}_0 \, \mathrm{d}S_0 + \iiint_{V_0} \rho_0 Q_{0,\mathrm{ext}} \, \mathrm{d}V_0 \\ &= \iiint_{V_0} \left(-\nabla_{\mathbf{x}} \cdot \mathbf{q}_0 + \rho_0 Q_{0,\mathrm{ext}}\right) \, \mathrm{d}V_0, \end{aligned} \tag{2.37}$$

where $Q_{0,\mathrm{ext}}(\mathbf{x}, t) = Q_{\mathrm{ext}}(\mathbf{p}(\mathbf{x}, t), t)$. Substituting (2.31), (2.34), and (2.37) into (2.29) and removing the integral over V_0 now yields

$$\rho_0 \frac{\partial u}{\partial t} = \boldsymbol{\sigma}^{\mathrm{PK2}} : \frac{\partial \boldsymbol{\varepsilon}}{\partial t} - \nabla_{\mathbf{x}} \cdot \mathbf{q}_0 + \rho_0 Q_{0,\mathrm{ext}}. \tag{2.38}$$

Equation (2.38) is thus the PDE formulation of the first law of thermodynamics (2.29), where the LHS represents the rate of change in the internal energy U, the first term on the RHS represents the rate of change in the difference between the work W and the kinetic energy K, and the last two terms on the RHS represent the rate at which the heat Q is applied.

2.2.4 The Helmholtz free energy

To obtain governing equations for the temperature field T and the displacement field $\mathbf{d}$ from the force balance (2.27) and the energy balance (2.38), u, $\boldsymbol{\sigma}^{\mathrm{PK2}}$, and $\mathbf{q}_0$ need to be expressed in terms of T and $\mathbf{d}$. Note that an expression for $\boldsymbol{\sigma}^{\mathrm{PK2}}$ in terms of T and $\mathbf{d}$ also leads to an expression for σ^{PK1} through (2.28)

and (2.12). In this subsection, a first step in this direction is made by expressing $\partial u/\partial t$ in (2.38) in terms of T, $\boldsymbol{\varepsilon}$, and $\boldsymbol{\sigma}^{\mathrm{PK2}}$. Note that the strain $\boldsymbol{\varepsilon}$ is already expressed in terms of the displacement field $\mathbf{d}$ through (2.17) and (2.12).

Note that $\boldsymbol{\varepsilon}$ and T are thermodynamic state variables. Because two state variables are sufficient to describe the state of a thermodynamic system, all other thermodynamic state variables such as σ^{PK2} and u can be written as a function of $\boldsymbol{\varepsilon}$ and T, see e.g. [Turns, 2006]. The Helmholtz free energy per unit mass f is also a thermodynamic state variable and can thus be written as a function of $\boldsymbol{\varepsilon}$ and T. In particular, f is defined as

$$f(\boldsymbol{\varepsilon}, T) = u(\boldsymbol{\varepsilon}, T) - (T_0 + T)s(\boldsymbol{\varepsilon}, T), \tag{2.39}$$

where s denotes the mass density of entropy, which is also a thermodynamic state variable which can thus be written as a function of $\boldsymbol{\varepsilon}$ and T.

Remark 2.3. *Here the choice is made to consider all thermodynamic state variables as functions of $\boldsymbol{\varepsilon}$ and T. This choice is natural because the aim of this chapter is to obtain equations in terms of $\mathbf{d}$ and T, but other choices could be made as well. The introduction of the Helmholtz free energy is related to the choice for $\boldsymbol{\varepsilon}$ and T as independent state variables. When $\boldsymbol{\sigma}^{\mathrm{PK2}}$ and T are used as independent thermodynamic state variables, it is more natural to introduce the Gibbs free energy, see e.g. [Lubarda, 2004] for details.*

It can be shown using the energy balance (2.38) and the second law of thermodynamics that [Parkus, 1976]

$$\frac{\partial f}{\partial \boldsymbol{\varepsilon}} = \frac{1}{\rho_0}\boldsymbol{\sigma}^{\mathrm{PK2}}, \qquad \frac{\partial f}{\partial T} = -s. \tag{2.40}$$

Using that f is a function of $\boldsymbol{\varepsilon}$ and T, differentiating f w.r.t. t yields

$$\frac{\partial f}{\partial t} = \frac{\partial f}{\partial \boldsymbol{\varepsilon}} : \frac{\partial \boldsymbol{\varepsilon}}{\partial t} + \frac{\partial f}{\partial T}\frac{\partial T}{\partial t} = \frac{1}{\rho_0}\boldsymbol{\sigma}^{\mathrm{PK2}} : \frac{\partial \boldsymbol{\varepsilon}}{\partial t} - s\frac{\partial T}{\partial t}, \tag{2.41}$$

where the first identity was obtained using (2.8). Recall that : denotes the inner product of matrices as in (2.4). On the other hand, differentiating the definition (2.39) w.r.t. t yields

$$\frac{\partial f}{\partial t} = \frac{\partial u}{\partial t} - \frac{\partial T}{\partial t}s - (T_0 + T)\frac{\partial s}{\partial t}. \tag{2.42}$$

Rearranging (2.42) now shows that

$$\frac{\partial u}{\partial t} = \frac{\partial f}{\partial t} + \frac{\partial T}{\partial t}s + (T_0 + T)\frac{\partial s}{\partial t} = \frac{1}{\rho_0}\boldsymbol{\sigma}^{\mathrm{PK2}} : \frac{\partial \boldsymbol{\varepsilon}}{\partial t} + (T_0 + T)\frac{\partial s}{\partial t}, \tag{2.43}$$

where the second identity follows after inserting (2.41). Substituting the found expression for $\partial u/\partial t$ in (2.38) yields

$$\rho_0(T_0 + T)\frac{\partial s}{\partial t} = -\nabla_{\mathbf{x}} \cdot \mathbf{q}_0 + \rho_0 Q_{0,\mathrm{ext}}. \tag{2.44}$$

It remains to find an expression for $\partial s/\partial t$ in terms of T, $\boldsymbol{\varepsilon}$, and $\boldsymbol{\sigma}^{\mathrm{PK2}}$. Because s is also a thermodynamic state variable, $s = s(\boldsymbol{\varepsilon}, T)$ holds and

$$\frac{\partial s}{\partial t} = \frac{\partial s}{\partial \boldsymbol{\varepsilon}} : \frac{\partial \boldsymbol{\varepsilon}}{\partial t} + \frac{\partial s}{\partial T}\frac{\partial T}{\partial t}. \tag{2.45}$$

The partial derivatives of s can be expressed as

$$\frac{\partial s}{\partial \boldsymbol{\varepsilon}} = -\frac{\partial^2 f}{\partial \boldsymbol{\varepsilon} \partial T} = -\frac{1}{\rho_0}\frac{\partial \boldsymbol{\sigma}^{\mathrm{PK2}}}{\partial T}, \qquad \frac{\partial s}{\partial T} = -\frac{\partial^2 f}{\partial T^2} = \frac{c}{T_0 + T}, \tag{2.46}$$

where the first set of equations follows from (2.40) and the latter set of equations from (2.40) and from the definition of the heat capacity per unit mass c (at constant strain). Inserting (2.45) and (2.46) back into (2.44) yields

$$\rho_0 c \frac{\partial T}{\partial t} = (T_0 + T)\frac{\partial \boldsymbol{\sigma}^{\mathrm{PK2}}}{\partial T} : \frac{\partial \boldsymbol{\varepsilon}}{\partial t} - \nabla_{\mathbf{x}} \cdot \mathbf{q}_0 + \rho_0 Q_{0,\mathrm{ext}}. \tag{2.47}$$

Equation (2.47) is thus a rewritten form of the PDE formulation of the first law of thermodynamics (2.38), from which the internal energy per unit mass u has been removed using the Helmholtz free energy and the second law of thermodynamics. Note that (2.47) nicely shows that the first term on the RHS disappears when the stress does not depend on the temperature, i.e. when the displacement field $\mathbf{d}$ is independent of the temperature.

2.2.5 Constitutive relations

To write the force balance (2.27) and the energy balance (2.47) in terms of $\mathbf{d}$ and T, the stress $\boldsymbol{\sigma}^{\mathrm{PK2}}$, the heat capacity c, and the heat flux $\mathbf{q}_0$ still need to be expressed in terms of $\mathbf{d}$ and T.

Expressions for the stress $\boldsymbol{\sigma}^{\mathrm{PK2}}$ and the heat capacity c are typically obtained by specifying a formula for the Helmholtz free energy function f in terms of $\boldsymbol{\varepsilon}$ and T and differentiating this according to (2.40), see e.g. [Parkus, 1976; Kovalenko, 1969; Lubarda, 2004]. Typically, f is chosen as a polynomial in the components of $\boldsymbol{\varepsilon}$ and T. For an isotropic material, f can only be a function of the temperature T and the three invariants (under orthogonal transformations) of the strain $I_1 = \varepsilon_{11} + \varepsilon_{22} + \varepsilon_{33} = \boldsymbol{\varepsilon} : \mathbf{I}$, $I_2 = \boldsymbol{\varepsilon} : \boldsymbol{\varepsilon}$, and $I_3 = \det(\boldsymbol{\varepsilon})$. A commonly used choice for f that leads to the stress-strain relations for a linear isotropic material is [Parkus, 1976]

$$f(\boldsymbol{\varepsilon}, T) = \frac{1}{\rho_0}\left(\frac{E}{2(1+\nu)}I_2 + \frac{E\nu}{2(1+\nu)(1-2\nu)}I_1^2 + \frac{-E}{1-2\nu}I_1\varepsilon_T(T)\right) + f_T(T), \tag{2.48}$$

where E denotes the Young's modulus, ν denotes Poisson's ratio, $\varepsilon_T(T)$ denotes the thermal strain, and

$$f_T(T) = -c_0(T_0 + T)\log(T_0 + T) + (c_0 - s_0)T, \tag{2.49}$$

where c_0 and s_0 denote the heat capacity and entropy density per unit mass in the reference state, respectively.

Differentiating f according to the first identity in (2.40) yields the stress components of $\boldsymbol{\sigma}^{\mathrm{PK2}}$ as

$$\begin{bmatrix} \sigma_{11}^{\mathrm{PK2}} \\ \sigma_{22}^{\mathrm{PK2}} \\ \sigma_{33}^{\mathrm{PK2}} \\ \sigma_{12}^{\mathrm{PK2}} \\ \sigma_{13}^{\mathrm{PK2}} \\ \sigma_{23}^{\mathrm{PK2}} \end{bmatrix} = \frac{E}{(1+\nu)} \begin{bmatrix} \varepsilon_{11} \\ \varepsilon_{22} \\ \varepsilon_{33} \\ \varepsilon_{12} \\ \varepsilon_{13} \\ \varepsilon_{23} \end{bmatrix} + \frac{E\nu(\varepsilon_{11}+\varepsilon_{22}+\varepsilon_{33})}{(1+\nu)(1-2\nu)} \begin{bmatrix} 1 \\ 1 \\ 1 \\ 0 \\ 0 \\ 0 \end{bmatrix} + \frac{-\varepsilon_T(T)E}{1-2\nu} \begin{bmatrix} 1 \\ 1 \\ 1 \\ 0 \\ 0 \\ 0 \end{bmatrix}. \tag{2.50}$$

According to the last identity in (2.46), the heat capacity c is

$$c = -(T_0+T)\frac{\partial^2 f}{\partial T^2} = \frac{(T_0+T)E}{(1-2\nu)\rho_0} I_1 \frac{\partial^2 \varepsilon_T}{\partial T^2} + c_0. \tag{2.51}$$

The heat capacity c may thus depend on both the thermal strain and the temperature.

The thermal strain $\varepsilon_T(T)$ accounts for the thermal expansion of the material. Since it was assumed that the solid is stress free in the reference state, it is required that the thermal strain is zero in the reference state, i.e. $\varepsilon_T(0) = 0$. For most materials such as silicon the thermal strain is a linear function, i.e.

$$\varepsilon_T(T) = \alpha T, \tag{2.52}$$

where α denotes the Coefficient of Thermal Expansion (CTE). However, for ultra low expansion materials such as ultra low expansion glass (ULE) and Zerodur the CTE is a nonlinear function of temperature. The CTE (defined as the derivative of $\varepsilon_T(T)$ w.r.t. T) therefore depends on temperature and vanishes near $T = 0$. The temperature at which the CTE becomes equal to zero is called the zero crossing temperature and is denoted by T_{ZC}. The thermal strain $\varepsilon_T(T)$ is a quadratic function of T near $T = T_{\mathrm{ZC}}$. Figure 2.2 shows the dependence on temperature of the thermal strain ε_T and the CTE α for silicon (a linear material) and ULE (an ultra low expansion material).

The heat flux $\mathbf{q}(\cdot, t) : \Omega(t) \to \mathbb{R}^3$ is typically described by Fourier's law of heat conduction. For an isotropic material this takes the form

$$\mathbf{q} = -\boldsymbol{\kappa}\nabla T = -\boldsymbol{\kappa}\mathbf{J}^{-\top}\nabla_{\mathbf{x}} T, \tag{2.53}$$

where $\boldsymbol{\kappa}(\cdot, t) : \Omega(t) \to \mathbb{R}^{3\times 3}$ denotes the heat conduction matrix, and ∇T denotes the temperature gradient in the deformed configuration, which is equal to $\mathbf{J}^{-\top}\nabla_{\mathbf{x}} T$ (see e.g. [Geers et al., 2011]). According to (2.36), the corresponding heat flux $\mathbf{q}_0(\cdot, t) : \Omega_0 \to \mathbb{R}^3$ is

$$\mathbf{q}_0(\mathbf{x}, t) = \boldsymbol{\kappa}_0(\mathbf{x}, t)\nabla_{\mathbf{x}} T(\mathbf{x}, t). \tag{2.54}$$

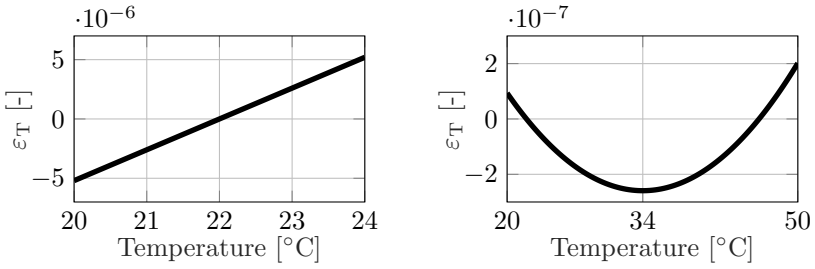

(a) ε_{T} for silicon

(b) ε_{T} for ULE

(c) CTE of silicon

(d) CTE of ULE

Figure 2.2. The dependence of the thermal strain ε_{T} and the CTE α on temperature for silicon and ULE ($T_0 = 22$ °C, $T_{\mathrm{ZC}} = 34$ °C)

where

$$\boldsymbol{\kappa}_0(\mathbf{x},t) = J(\mathbf{x},t)\mathbf{J}^{-1}(\mathbf{x},t)\boldsymbol{\kappa}(\mathbf{p}(\mathbf{x},t),t)\mathbf{J}^{-\top}(\mathbf{x},t). \tag{2.55}$$

The heat conduction matrix $\boldsymbol{\kappa}_0$ depends on the considered material. For the models in this thesis, heat conduction is isotropic and the heat conduction matrix is chosen as $\boldsymbol{\kappa}_0 = k\mathbf{I}$, where k denotes the (scalar) thermal conductivity.

Remark 2.4. *The choice of* $\mathbf{q}$ *as in* (2.53) *is closely related to the second law of thermodynamics. For the subvolume* $V(t) \subseteq \Omega(t)$ *which was originally located at* V_0*, the second law of thermodynamics in the form of the Clausius-Duhem inequality takes the form (see e.g. [Parkus, 1976; Hetnarski and Eslami, 2009])*

$$\frac{\partial}{\partial t}\iiint_{V_0} \rho_0 s \,\mathrm{d}V_0 = -\iint_{S_0} \frac{\mathbf{q}_0\cdot\mathbf{n}_0}{T_0+T}\,\mathrm{d}S_0 + \iiint_{V_0}\left(\frac{\rho_0 Q_{0,\mathrm{ext}}}{T_0+T} + \rho_0\frac{\partial s_p}{\partial t}\right)\,\mathrm{d}V_0. \tag{2.56}$$

where $\partial s_p/\partial t \geq 0$ *denotes the rate of entropy production per unit mass which is nonnegative. Again, the surface integral is converted to a volume integral using the divergence theorem. This yields*

$$\begin{aligned}\iint_{S_0}\frac{\mathbf{q}_0\cdot\mathbf{n}_0}{T_0+T}\,\mathrm{d}S_0 &= \iiint_{V_0}\nabla_{\mathbf{x}}\cdot\left(\frac{\mathbf{q}_0}{T_0+T}\right)\,\mathrm{d}V_0 \\ &= \iiint_{V_0}\left(\frac{1}{T_0+T}\nabla_{\mathbf{x}}\cdot\mathbf{q}_0 - \frac{1}{(T_0+T)^2}\mathbf{q}_0\cdot\nabla_{\mathbf{x}}T\right)\,\mathrm{d}V_0.\end{aligned} \tag{2.57}$$

Inserting this result back into (2.56) *yields an equality only involving volume integrals. Since this equality holds for any volume* $V_0 \subseteq \Omega_0$ *the integral over* V_0 *can be removed. After multiplication by* T_0+T*, it follows that*

$$\rho_0(T_0+T)\frac{\partial s}{\partial t} = -\nabla_{\mathbf{x}}\cdot\mathbf{q}_0 + \frac{1}{T_0+T}\mathbf{q}_0\cdot\nabla_{\mathbf{x}}T + \rho_0 Q_{\mathrm{ext}} + \rho_0(T+T_0)\frac{\partial s_p}{\partial t}. \tag{2.58}$$

Subtracting (2.44)*, dividing by* T_0+T*, and rearranging the resulting terms yields*

$$\rho_0\frac{\partial s_p}{\partial t} = \frac{-1}{(T_0+T)^2}\mathbf{q}_0\cdot\nabla_{\mathbf{x}}T = \frac{1}{(T_0+T)^2}\left(\nabla_{\mathbf{x}}T\right)^{\top}\boldsymbol{\kappa}_0\nabla_{\mathbf{x}}T, \tag{2.59}$$

where the second identity follows from (2.54)*. The rate of entropy production per unit mass* $\partial s_p/\partial t$ *should be nonnegative. This is the case if and only if* $\boldsymbol{\kappa}_0$ *is a positive definite matrix. The relation between* $\boldsymbol{\kappa}$ *and* $\boldsymbol{\kappa}_0$ *in* (2.55) *shows that* $\boldsymbol{\kappa}_0$ *is positive definite if and only if* $\boldsymbol{\kappa}$ *is positive definite.*

2.2.6 Governing equations

The governing equations for a thermoelastic solid thus consist of the force balance (2.27), i.e.

$$\nabla_{\mathbf{x}}\cdot\boldsymbol{\sigma}^{\mathrm{PK1}} + \rho_0\mathbf{f}_{0,\mathrm{ext}} = \rho_0\frac{\partial^2\mathbf{d}}{\partial t^2}, \tag{2.60}$$

and the energy balance (2.47), i.e.

$$\rho_0 c \frac{\partial T}{\partial t} = (T_0 + T) \frac{\partial \boldsymbol{\sigma}^{\mathrm{PK2}}}{\partial T} : \frac{\partial \boldsymbol{\varepsilon}}{\partial t} - \nabla_{\mathbf{x}} \cdot \mathbf{q}_0 + \rho_0 Q_{0,\mathrm{ext}}. \tag{2.61}$$

These two equations can be expressed in terms of the displacement field $\mathbf{d}(\mathbf{x}, t)$ and the temperature field $T(\mathbf{x}, t)$ using the strain-displacement relations (2.17) and (2.12)

$$\boldsymbol{\varepsilon} = \frac{1}{2} \left(\mathbf{D} + \mathbf{D}^\top + \mathbf{D}^\top \mathbf{D} \right), \qquad \mathbf{D} = \frac{\partial \mathbf{d}}{\partial \mathbf{x}}, \tag{2.62}$$

the stress-strain-temperature relations (2.50) and (2.28)

$$\begin{bmatrix} \sigma_{11}^{\mathrm{PK2}} \\ \sigma_{22}^{\mathrm{PK2}} \\ \sigma_{33}^{\mathrm{PK2}} \\ \sigma_{12}^{\mathrm{PK2}} \\ \sigma_{13}^{\mathrm{PK2}} \\ \sigma_{23}^{\mathrm{PK2}} \end{bmatrix} = \frac{E}{(1+\nu)} \begin{bmatrix} \varepsilon_{11} \\ \varepsilon_{22} \\ \varepsilon_{33} \\ \varepsilon_{12} \\ \varepsilon_{13} \\ \varepsilon_{23} \end{bmatrix} + \frac{E\nu(\varepsilon_{11} + \varepsilon_{22} + \varepsilon_{33})}{(1+\nu)(1-2\nu)} \begin{bmatrix} 1 \\ 1 \\ 1 \\ 0 \\ 0 \\ 0 \end{bmatrix} + \frac{-\varepsilon_T(T) E}{1-2\nu} \begin{bmatrix} 1 \\ 1 \\ 1 \\ 0 \\ 0 \\ 0 \end{bmatrix}, \tag{2.63}$$

$$\boldsymbol{\sigma}^{\mathrm{PK1}} = \boldsymbol{\sigma}^{\mathrm{PK2}} \mathbf{J}^\top, \qquad \mathbf{J} = \mathbf{I} + \mathbf{D}, \tag{2.64}$$

Fourier's law (2.54)

$$\mathbf{q}_0 = \boldsymbol{\kappa}_0 \nabla_{\mathbf{x}} T, \tag{2.65}$$

and the expression for the heat capacity at constant strain (2.51)

$$c = \frac{(T_0 + T)E}{(1-2\nu)\rho_0} (\varepsilon_{11} + \varepsilon_{22} + \varepsilon_{33}) \frac{\partial^2 \varepsilon_T}{\partial T^2} + c_0. \tag{2.66}$$

2.3 Linear thermoelasticity

For small deviations from the reference state $\mathbf{d}(\mathbf{x}, t) \equiv \mathbf{0}$ and $T(\mathbf{x}, t) \equiv 0$, the equations derived in the previous section may be linearised. This yields the equations for linear thermoelasticity. The perturbations from the reference state $\mathbf{d}(\mathbf{x}, t) \equiv \mathbf{0}$ and $T(\mathbf{x}, t) \equiv 0$ are denoted by $\tilde{\mathbf{d}}(\mathbf{x}, t)$ and $\tilde{T}(\mathbf{x}, t)$.

First the linearization of the force balance (2.60) will be determined. To this end, note that the linearization of the strain-displacement relations (2.62) around $\mathbf{d} \equiv \mathbf{0}$ yields

$$\tilde{\boldsymbol{\varepsilon}} = \frac{1}{2} \left(\tilde{\mathbf{D}} + \tilde{\mathbf{D}}^\top \right), \qquad \tilde{\mathbf{D}} = \frac{\partial \tilde{\mathbf{d}}}{\partial \mathbf{x}}. \tag{2.67}$$

For the linearization of (2.64), note that (2.63) shows that $\boldsymbol{\sigma}^{\mathrm{PK2}}$ is zero in the reference state. Because $\mathbf{J} = \mathbf{I}$ in the reference state, the linearization of (2.64) becomes

$$\tilde{\boldsymbol{\sigma}}^{\mathrm{PK1}} = \tilde{\boldsymbol{\sigma}}^{\mathrm{PK2}} =: \tilde{\boldsymbol{\sigma}}, \tag{2.68}$$

where $\tilde{\boldsymbol{\sigma}}$ now simply denotes the (linearised) stress because the linearizations of the first and second Piola-Kirchhoff stress are equal. An explicit expression for $\tilde{\boldsymbol{\sigma}}$ follows after linearization of (2.63), which yields

$$\begin{bmatrix} \tilde{\sigma}_{11} \\ \tilde{\sigma}_{22} \\ \tilde{\sigma}_{33} \\ \tilde{\sigma}_{12} \\ \tilde{\sigma}_{13} \\ \tilde{\sigma}_{23} \end{bmatrix} = \mathbf{H} \begin{bmatrix} \tilde{\varepsilon}_{11} - \alpha_0 T \\ \tilde{\varepsilon}_{22} - \alpha_0 T \\ \tilde{\varepsilon}_{33} - \alpha_0 T \\ 2\tilde{\varepsilon}_{12} \\ 2\tilde{\varepsilon}_{13} \\ 2\tilde{\varepsilon}_{23} \end{bmatrix}, \tag{2.69}$$

where $\alpha_0 := \frac{\partial \varepsilon_T}{\partial T}(0)$ and

$$\mathbf{H} = \frac{E}{(1+\nu)(1-2\nu)} \begin{bmatrix} 1-\nu & \nu & \nu & 0 & 0 & 0 \\ \nu & 1-\nu & \nu & 0 & 0 & 0 \\ \nu & \nu & 1-\nu & 0 & 0 & 0 \\ 0 & 0 & 0 & \frac{1-2\nu}{2} & 0 & 0 \\ 0 & 0 & 0 & 0 & \frac{1-2\nu}{2} & 0 \\ 0 & 0 & 0 & 0 & 0 & \frac{1-2\nu}{2} \end{bmatrix}. \tag{2.70}$$

The linearization of the force balance (2.60) thus takes the form

$$\nabla_{\mathbf{x}} \cdot \tilde{\boldsymbol{\sigma}} + \rho_0 \mathbf{f}_{0,\text{ext}} = \rho_0 \frac{\partial^2 \tilde{\mathbf{d}}}{\partial t^2}. \tag{2.71}$$

Next, the linearization of the energy balance (2.61) is considered. For the term on the left hand side (LHS) of (2.61), note that (2.66) shows that the heat capacity c is equal to c_0 in the reference state. The linearization of the LHS of (2.61) thus becomes $\rho_0 c_0 \partial \tilde{T}/\partial t$. For the first term on the RHS of (2.61), note that

$$(T_0 + T) \frac{\partial \boldsymbol{\sigma}^{\text{PK2}}}{\partial T}\bigg|_{\mathbf{d}=0, T=0} = \frac{-T_0 E \alpha_0}{1-2\nu} \mathbf{I}, \tag{2.72}$$

where the expression for $\boldsymbol{\sigma}^{\text{PK2}}$ in (2.63) was used. The linearization of the first term on the RHS of (2.47) thus becomes

$$\frac{T_0 E \alpha_0}{1-2\nu} \mathbf{I} : \frac{\partial \tilde{\boldsymbol{\varepsilon}}}{\partial t} = \frac{-T_0 E \alpha_0}{1-2\nu} \frac{\partial}{\partial t} \left(\tilde{\varepsilon}_{11} + \tilde{\varepsilon}_{22} + \tilde{\varepsilon}_{33} \right). \tag{2.73}$$

Since Fourier's law (2.65) is already linear, the linearization of (2.61) becomes

$$\rho_0 c_0 \frac{\partial \tilde{T}}{\partial t} = \frac{-T_0 E \alpha_0}{1-2\nu} \frac{\partial}{\partial t} \left(\tilde{\varepsilon}_{11} + \tilde{\varepsilon}_{22} + \tilde{\varepsilon}_{33} \right) + \nabla_{\mathbf{x}} \cdot \boldsymbol{\kappa}_0 \nabla_{\mathbf{x}} \tilde{T} + \rho_0 Q_{0,\text{ext}}. \tag{2.74}$$

The governing equations for linear thermoelasticity are now given by (2.71) and (2.74). These equations can be written explicitly in terms of the perturbations $\tilde{\mathbf{d}}(\mathbf{x}, t)$ and $\tilde{T}(\mathbf{x}, t)$ using the strain-displacement relations (2.67) and the stress-strain-temperature relations (2.69). The equations for linear thermoelasticity can be found in many standard textbooks, see e.g. [Boley and Weiner, 1960; Nowacki, 1962; Kovalenko, 1969; Hetnarski and Eslami, 2009].

2.4 Quasi-static thermoelasticity

From (2.74) it is clear that temperature variations can be introduced by external heat sources or by strain rates. The former cause is most common and is also relevant for the models considered in this thesis where the heat induced by the EUV light is the main disturbance. In this case, the first term on the RHS of (2.74) may be neglected, see [Kovalenko, 1969]. This yields

$$\rho_0 c_0 \frac{\partial \tilde{T}}{\partial t} = \nabla_{\mathbf{x}} \cdot \boldsymbol{\kappa}_0 \nabla_{\mathbf{x}} \tilde{T} + \rho_0 Q_{0,\text{ext}}. \tag{2.75}$$

The temperature field $\tilde{T}(\mathbf{x}, t)$ thus satisfies a heat equation (a parabolic PDE) and can be computed independently of the displacement field $\mathbf{d}(\mathbf{x}, t)$. This is significantly simpler than solving the coupled equations (2.71) and (2.74).

In many applications, the evolution of the temperature field is slow compared to the evolution of the displacement field. It is therefore reasonable to assume that the displacement field reacts instantaneously to changes in the temperature field. In other words, the inertia term $\rho_0 \partial^2 \tilde{\mathbf{d}} / \partial t^2$ in (2.71) is negligible. With this assumption, (2.71) reduces to

$$\nabla_{\mathbf{x}} \cdot \tilde{\boldsymbol{\sigma}} + \rho_0 \mathbf{f}_{0,\text{ext}} = \mathbf{0}. \tag{2.76}$$

Note that $\tilde{\boldsymbol{\sigma}}$ depends on the first-order differentials of $\mathbf{d}$, see (2.69) and (2.67). This means that instead of the hyperbolic PDE (2.71), now the elliptic PDE (2.76) needs to be solved (at every time instant) where the source term results from the external force $\mathbf{f}_{0,\text{ext}}$ and the dependence of $\tilde{\boldsymbol{\sigma}}$ on the temperature field $\tilde{T}(\mathbf{x}, t)$.

The equations for linear quasi-static thermoelasticity are thus given by (2.75) and (2.76). These equations can be expressed explicitly in terms of $\tilde{\mathbf{d}}(\mathbf{x}, t)$ and $\tilde{T}(\mathbf{x}, t)$ using the linear strain-displacement relations (2.67) and the stress-strain-temperature relations (2.69).

Remark 2.5. *Note that the quasi-static assumption can be applied to the equations for general thermoelasticity* (2.60) *and* (2.61) *as well. In this case, the first term of the RHS of the energy balance* (2.61) *and the inertia term on the RHS of the force balance* (2.60) *are neglected.*

2.5 Wafer heating

In this section, the linear quasi-static theory developed in the previous sections will be used to develop a wafer heating model. The linear quasi-static theory is used in all ASML applications that do not involve ultra low expansion materials, see e.g. [Viganò, 2013; Feng and van de Wal, 2014; Hekner, 2016; van den Hurk et al., 2018; Hooijkamp and van Keulen, 2018]. This section is divided in five

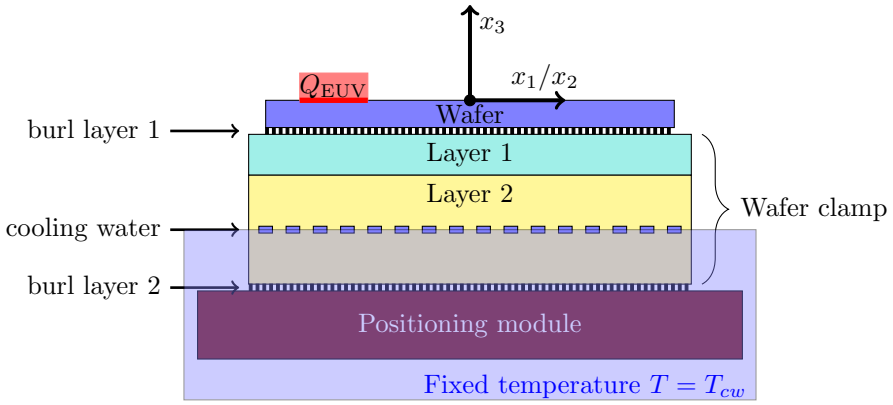

Figure 2.3. Cross section of the wafer and its supporting structure

subsections. In the first subsection, the wafer heating model is formulated as a set of Partial Differential Equations (PDEs). In the second subsection, the FE discretization of these PDEs is discussed. In the third and fourth subsections, the FE model is analyzed by computing thermal eigenmodes and by transient simulations. Based on the observations in two previous subsections, the fifth subsection introduces a simplified two-dimensional (2-D) model that will be used throughout this thesis.

2.5.1 Model description

A cross section of a typical wafer heating model from [Hekner, 2016] is shown in Figure 2.3. Note that the thickness of the layers displayed in Figure 2.3 is not to scale. The wafer is placed on a wafer clamp (consisting of layer 1 and layer 2), which is again placed on a positioning module (also called the chuck). The wafer, the wafer clamp, and the positioning module are separated by two thin layers that consist of many small bumps, called burls. Halfway Layer 2, water cooling is present. Note that the cross section in Figure 2.3 does not show that the positioning module layer is a square in the (x_1, x_2)-plane and that all other layers are circular. The dimensions of the different layers are given in Table 2.1. The dimensions of the positioning module in the x_1- and x_2-directions are both 400 mm. Recall that the cooling channels are located halfway Layer 2, so at 4.15 mm from the bottom of Layer 1.

Layer 1 is used to create an electrostatic force that pulls the wafer onto the wafer clamp. This force is necessary to keep the wafer attached to the wafer clamp during the high accelerations of the positioning module.

There are roughly 29,000 burls supporting the wafer, which are typically 1.5 mm apart, see [Steur, 2017]. The main advantage of the burl layer is that

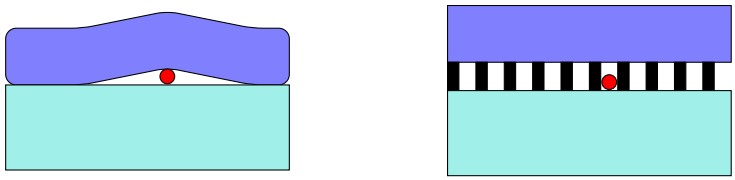

(a) Without burl layer **(b)** With burl layer

Figure 2.4. A burl layer (black) between the wafer (blue) and the wafer clamp (turquoise) improves the flatness of the wafer surface in the presence of contamination particles (red)

Table 2.1. Dimensions of the layers in Figure 2.3

Layer	Diameter [mm]	Thickness [mm]
Wafer	300	0.775
Burls 1	300	0.01
Layer 1	325	0.8
Layer 2	325	8.3
Burls 2	325	0.01
Positioning module	-	70

it improves the flatness of the wafer because contamination particles will fall between the burls, see Figure 2.4. However, disadvantages are that the burl layer also leads to a smaller contact area and a high thermal resistance between the wafer and wafer clamp. To improve the thermal conditioning of the wafer, a backfill gas is inserted in the burl layer which conducts heat between the wafer and the wafer clamp.

The thermoelastic behavior of the wafer and its supporting structure will be modeled using the equations for linear quasi-static thermoelasticity (2.75)–(2.76). The different layers are modeled using piecewise constant material properties. Recall that the heat conduction matrix is chosen as $\boldsymbol{\kappa}_0 = k\mathbf{I}$.

The wafer, Layer 1, Layer 2, and the positioning module are modeled as linear isotropic materials, satisfying the stress-strain-temperature relations in (2.69). The material properties for these layers are given Table 2.2.

The burl layers create a mechanical and thermal coupling between the adjacent layers. The thermal coupling is mainly due to the backfill gas that is present between the burls (heat conduction through the burls themselves is neglected because the contact area between the burls and the wafer is very small). The heat capacity of the backfill gas will be neglected, so that the burl layer acts as a thermal resistance only. The mechanical coupling is due to the out-of-plane (axial) stiffness and an in-plane (transversal) stiffness of the burls. The burls are not modeled individually. Instead, the whole burl layer is modeled as an or-

Table 2.2. Material properties for the layers in Figure 2.3

Symbol	Substrate	Layer 1	Layer 2	Pos. mod.	Unit
ρ_0	2329	2230	3070	2530	kg/m^3
E	167	64	373	90.3	GPa
ν	0.30	0.20	0.18	0.30	-
c_0	705	830	700	800	J/kg/K
k	149	1.2	120	1.5	W/m/K
α_0	2.4	3.25	2.5	0.02	10^{-6} 1/K

Table 2.3. Material properties of the burl layers in Figure 2.3

Symbol	Burl layer 1	Burl layer 2	Unit
ρ_0	0	0	kg/m^3
E_{33}	12.8	80.7	MPa
$G_{13} = G_{23}$	12.8	48.6	MPa
c_0	0	0	J/kg/K
k	0.015	0.015	W/m/K
α_0	0	0	1/K

thotropic material without Poisson effect (also called 'shear layer', see [de Best, 2015]), meaning the matrix $\mathbf{H}$ in (2.69) is diagonal with E_{11}, E_{22}, E_{33}, G_{12}, G_{13}, and G_{23} on the diagonal. The out-of-plane stiffness of the burl layer is modeled through the Young's modulus E_{33} and the in-plane stiffness through the shear moduli G_{13} and G_{23}. The other parameters E_{11}, E_{22}, and G_{12} are zero. The used material properties for the burl layers are given in Table 2.3.

The applied boundary conditions are as follows. The part of the structure below the cooling channels is assumed to have a fixed temperature and is thus not relevant for the thermal behavior. However, the material below the cooling channels is important for the mechanical stiffness of the assembly. The heat induced by the EUV light is applied to the top surface of the wafer in a rectangular area called the slit that moves with a velocity v in the x_2-direction, see Figure 2.5. Parameter values for the applied heat load are given in Table 2.4. The applied heat load at the top surface $x_3 = 0$ can thus be written as

$$Q_{\text{exp}}(x_1, x_2, t) = B_{\text{exp}}(x_1, x_2, t)\bar{u}_{\text{exp}}, \tag{2.77}$$

where $\bar{u}_{\text{exp}} = P_{\text{EUV}}$ is the applied heat load in Watts and B_{exp} describes the location where the heat load is applied. The boundary condition at the top surface of the wafer can thus be written as

$$-\tilde{\mathbf{q}}_0 \cdot \mathbf{n}_0\Big|_{x_3=0} = \left(\boldsymbol{\kappa}_0 \nabla_{\mathbf{x}} \tilde{T}\right) \cdot \mathbf{n}_0\Big|_{x_3=0} = Q_{\text{exp}}. \tag{2.78}$$

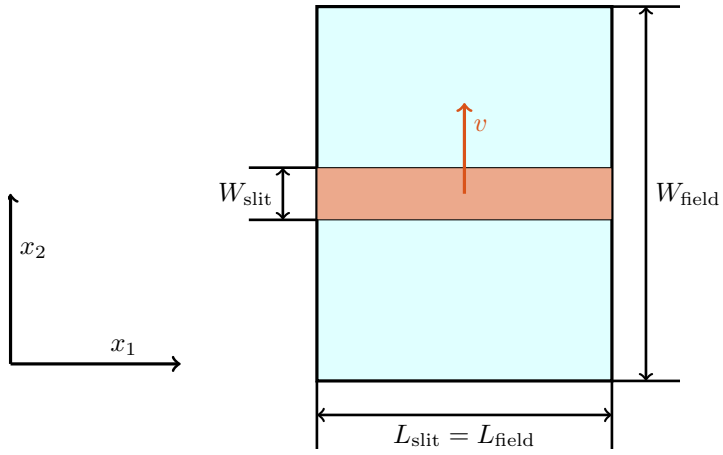

Figure 2.5. Applied heat load

Table 2.4. Properties of the applied heat load

Description	Symbol	Value	Unit	Formula
Dose	E_{dose}	450	J/m^2	
Scan speed	v	0.276	m/s	
Slit length in x_1-direction	L_{slit}	26	mm	
Slit length in x_2-direction	W_{slit}	4.6	mm	
Exposure time / point	t_{exp}	0.0167	s	W_{slit}/v
EUV power at substrate	P_{EUV}	3.2292	W	$E_{\text{dose}} L_{\text{slit}} v$
Field length in x_1-direction	L_{field}	26	mm	
Field length in x_2-direction	W_{field}	33	mm	
Exposure time / field	t_{field}	0.1362	s	$(W_{\text{field}} + W_{\text{slit}})/v$

All material below the cooling channels halfway Layer 2 has a fixed temperature. Because the wafer clamp is placed in a nearly vacuum environment, a perfectly insulated boundary condition (i.e. zero heat flux) is applied to all other edges. There are no constraints applied in the mechanical domain, i.e. all edges are stress free. The rigid body modes are removed by constraining the center of the bottom of the positioning module.

2.5.2 Finite element model

The finite element model for the linear quasi-static theory (2.75)–(2.76) is derived via the weak form of the force and energy balances. The weak form of the energy balance (2.75) is obtained after multiplication of (2.75) by a test function

$\tilde{w} = \tilde{w}(\mathbf{x})$ and integrating over the considered domain Ω_0. After application of Green's first identity it follows that at every time instant t,

$$\iiint_{\Omega_0} \rho_0 c_0 \tilde{w} \frac{\partial \tilde{T}}{\partial t} \, \mathrm{d}V_0 = - \iiint_{\Omega_0} (\nabla_{\mathbf{x}} \tilde{w})^\top \boldsymbol{\kappa}_0 \nabla_{\mathbf{x}} \tilde{T} \, \mathrm{d}V_0 + \iiint_{\partial\Omega_0} \tilde{w} \left(\boldsymbol{\kappa}_0 \nabla_{\mathbf{x}} \tilde{T} \right) \cdot \mathbf{n}_0 \, \mathrm{d}S_0 + \iiint_{\Omega_0} \tilde{w} \rho_0 Q_{0,\mathrm{ext}} \, \mathrm{d}V_0, \quad (2.79)$$

where $\partial\Omega_0$ denotes the boundary of Ω_0. Also note that $\left(\boldsymbol{\kappa}_0 \nabla_{\mathbf{x}} \tilde{T} \right) \cdot \mathbf{n}_0 = \tilde{\mathbf{q}}_0 \cdot \mathbf{n}_0$ is the (outgoing) heat flux through the boundary, which is specified in the boundary conditions. In particular, $\tilde{\mathbf{q}}_0 \cdot \mathbf{n}$ is zero except at the top surface of the wafer where the heat load induced by the EUV light is applied as in (2.78). The heat load $Q_{0,\mathrm{ext}}$ per unit mass is zero in the considered application.

For the weak form of the force balance (2.76) the test function $\tilde{\mathbf{w}} = \tilde{\mathbf{w}}(\mathbf{x})$ has three components. After multiplication of (2.76) with $\tilde{\mathbf{w}}^\top$, integrating over the considered domain Ω_0, and application of Green's first identity, the weak form of the force balance is obtained as [Zienkiewicz et al., 2013]

$$- \iiint_{\Omega_0} (\underline{\boldsymbol{\partial}} \tilde{\mathbf{w}})^\top \mathbf{H} \left(\underline{\boldsymbol{\partial}} \tilde{\mathbf{d}} - \boldsymbol{\alpha} \tilde{T} \right) \, \mathrm{d}V_0 + \iint_{\partial\Omega_0} \tilde{\mathbf{w}}^\top \tilde{\boldsymbol{\sigma}}^\top \mathbf{n}_0 \, \mathrm{d}S_0 + \iiint_{\Omega_0} \tilde{\mathbf{w}}^\top \rho_0 \mathbf{f}_{0,\mathrm{ext}} \, \mathrm{d}V_0 = \mathbf{0}, \quad (2.80)$$

where

$$\underline{\boldsymbol{\partial}} = \begin{bmatrix} \frac{\partial}{\partial x_1} & 0 & 0 \\ 0 & \frac{\partial}{\partial x_2} & 0 \\ 0 & 0 & \frac{\partial}{\partial x_3} \\ \frac{\partial}{\partial x_2} & \frac{\partial}{\partial x_1} & 0 \\ 0 & \frac{\partial}{\partial x_3} & \frac{\partial}{\partial x_2} \\ \frac{\partial}{\partial x_3} & 0 & \frac{\partial}{\partial x_1} \end{bmatrix}, \qquad \boldsymbol{\alpha} = \alpha_0 \begin{bmatrix} 1 \\ 1 \\ 1 \\ 0 \\ 0 \\ 0 \end{bmatrix}. \quad (2.81)$$

Note that $\underline{\boldsymbol{\partial}} \tilde{\mathbf{d}}$ is the vectorized strain as it appears on the RHS of (2.69), and that $\mathbf{H} \left(\underline{\boldsymbol{\partial}} \tilde{\mathbf{d}} - \boldsymbol{\alpha} \tilde{T} \right)$ is the vectorized stress on the LHS of (2.69). Also note that $\tilde{\boldsymbol{\sigma}}^\top \mathbf{n}_0$ are the traction forces applied to the boundary, which are zero because no forces are applied to the outside of the structure. The main goal of the model is to predict the in-plane (overlay) deformation. The electrostatic clamping force, the backfill gas pressure, and gravity are therefore not considered and the force per unit mass $\mathbf{f}_{0,\mathrm{ext}}$ is zero.

The FE model is now obtained by approximating the temperature field $\tilde{T}(\mathbf{x}, t)$, the displacement field $\tilde{\mathbf{d}}(\mathbf{x}, t)$, and the test functions $\tilde{w}(\mathbf{x})$ and $\tilde{\mathbf{w}}(\mathbf{x})$ in terms of FE element shape functions

$$\tilde{T}(\mathbf{x}, t) = \mathbf{N}(\mathbf{x}) \boldsymbol{\theta}(t), \quad (2.82)$$

$$\tilde{\mathbf{d}}(\mathbf{x},t)=\begin{bmatrix}d_1(t)\\d_2(t)\\d_3(t)\end{bmatrix}=\begin{bmatrix}\mathbf{N}(\mathbf{x}) & \mathbf{0} & \mathbf{0}\\ \mathbf{0} & \mathbf{N}(\mathbf{x}) & \mathbf{0}\\ \mathbf{0} & \mathbf{0} & \mathbf{N}(\mathbf{x})\end{bmatrix}\begin{bmatrix}\boldsymbol{\zeta}_1(t)\\\boldsymbol{\zeta}_2(t)\\\boldsymbol{\zeta}_3(t)\end{bmatrix}=\underline{\mathbf{N}}(\mathbf{x})\boldsymbol{\zeta}(t), \tag{2.83}$$

$$\tilde{w}(\mathbf{x})=\mathbf{c}^\top\mathbf{N}^\top(\mathbf{x}),\qquad \tilde{\mathbf{w}}(\mathbf{x})=\underline{\mathbf{c}}^\top\underline{\mathbf{N}}^\top(\mathbf{x}). \tag{2.84}$$

where $\mathbf{N}(\mathbf{x})$ denotes the row vector of finite element shape functions, $\boldsymbol{\theta}(t)$ denotes the column vector of nodal temperatures, and $\boldsymbol{\zeta}_1(t)$, $\boldsymbol{\zeta}_1(t)$, and $\boldsymbol{\zeta}_1(t)$ denote the column vectors of nodal displacements in the x_1, x_2, and x_3-directions, respectively, and $\mathbf{c}$ and $\underline{\mathbf{c}}$ denote the vectors with the nodal values of the test functions. Note that the same FE shape functions are used to approximate the temperature field and displacement field. Also note that the Galerkin method is used, i.e. the same shape functions are used for the test functions $\tilde{w}$ and $\tilde{\mathbf{w}}$ as for the temperature and displacement fields.

The expressions (2.82)–(2.84) are then inserted into the weak form of the energy balance (2.79) and the weak form of the force balance (2.80). Noting the resulting equations should hold for any choice of $\mathbf{c}$ and $\underline{\mathbf{c}}$ and that these vectors may thus be removed from these equations, the following FE model is obtained

$$\mathbf{E}\dot{\boldsymbol{\theta}}(t)=\mathbf{A}\boldsymbol{\theta}(t)+\mathbf{B}_{\text{exp}}(t)\bar{u}_{\text{exp}}, \tag{2.85}$$

$$\mathbf{0}=-\mathbf{K}\boldsymbol{\zeta}(t)+\mathbf{L}\boldsymbol{\theta}(t), \tag{2.86}$$

where the dot denotes differentiation w.r.t. time,

$$\mathbf{E}=\iiint_{\Omega_0}\rho_0 c_0\mathbf{N}^\top\mathbf{N}\,\mathrm{d}V_0,\quad \mathbf{A}=-\iiint_{\Omega_0}k(\boldsymbol{\partial}\mathbf{N})^\top\boldsymbol{\partial}\mathbf{N}\,\mathrm{d}V_0, \tag{2.87}$$

$$\boldsymbol{\partial}\mathbf{N}=\begin{bmatrix}\frac{\partial\mathbf{N}}{\partial x_1}^\top & \frac{\partial\mathbf{N}}{\partial x_2}^\top & \frac{\partial\mathbf{N}}{\partial x_3}^\top\end{bmatrix}^\top,\qquad \mathbf{B}_{\text{exp}}(t)=\iint_{\partial\Omega_{\text{top}}}\mathbf{N}^\top B_{\text{exp}}\,\mathrm{d}S_0, \tag{2.88}$$

$$\mathbf{K}=\iiint_{\Omega_0}(\underline{\boldsymbol{\partial}\mathbf{N}})^\top\ \mathbf{H}\ \underline{\boldsymbol{\partial}\mathbf{N}}\,\mathrm{d}V_0,\qquad \mathbf{L}=\iiint_{\Omega_0}(\underline{\boldsymbol{\partial}\mathbf{N}})^\top\mathbf{H}\boldsymbol{\alpha}\ \mathbf{N}\,\mathrm{d}V_0. \tag{2.89}$$

The temperature and displacement constraints can be implemented in the usual manner by partitioning the thermal and mechanical DOFs in free and constrained DOFs, see e.g. [Zienkiewicz et al., 2013] for details.

Remark 2.6. *A FE model for the equations for linear thermoelasticity* (2.71) *and* (2.74) *can be obtained similarly. The most critical step is to account for the first term on the RHS of the energy balance* (2.74)*. This term leads to an additional term on the RHS of the weak form of the energy balance* (2.79)

$$\begin{aligned}&\iiint_{\Omega_0}\tilde{w}\frac{T_0E\alpha_0}{(1-2\nu)}\frac{\partial}{\partial t}\left(\tilde{\varepsilon}_{11}+\tilde{\varepsilon}_{22}+\tilde{\varepsilon}_{33}\right)\,\mathrm{d}V_0 \\ &\quad=T_0\iiint_{\Omega_0}\tilde{w}\frac{E\boldsymbol{\alpha}^\top}{(1-2\nu)}\frac{\partial}{\partial t}\left(\underline{\boldsymbol{\partial}}\tilde{\mathbf{d}}\right)\,\mathrm{d}V_0=T_0\iiint_{\Omega_0}\tilde{w}\boldsymbol{\alpha}^\top\mathbf{H}^\top\underline{\boldsymbol{\partial}}\frac{\partial\tilde{\mathbf{d}}}{\partial t}\,\mathrm{d}V_0,\end{aligned} \tag{2.90}$$

where the first identity follows from the definitions in (2.81) *and the second identity by noting that* $\mathbf{H}\boldsymbol{\alpha} = \frac{E}{1-2\nu}\boldsymbol{\alpha}$, *see* (2.70). *Inserting the approximations for* $\tilde{w}$ *and* $\tilde{\mathbf{d}}$ *from* (2.84) *and* (2.83) *in this expression now yields*

$$T_0\mathbf{c}^\top \iiint_{\Omega_0} \mathbf{N}^\top \boldsymbol{\alpha}^\top \mathbf{H}^\top \underline{\boldsymbol{\partial}\mathbf{N}} \, \mathrm{d}V_0 \dot{\boldsymbol{\zeta}} = T_0\mathbf{c}^\top \mathbf{L}^\top \dot{\boldsymbol{\zeta}}, \tag{2.91}$$

with $\mathbf{L}$ *as in* (2.89). *From* (2.91) *it is now easy to see that a FE model for the linear theory* (2.71) *and* (2.74) *based on the approximations in* (2.82)–(2.84) *takes the form*

$$\mathbf{E}\dot{\boldsymbol{\theta}}(t) = \mathbf{A}\boldsymbol{\theta}(t) - T_0\mathbf{L}^\top\dot{\boldsymbol{\zeta}}(t) + \mathbf{B}_{\mathrm{exp}}(t)\bar{u}_{\mathrm{exp}}, \tag{2.92}$$

$$\mathbf{M}\ddot{\boldsymbol{\zeta}}(t) = -\mathbf{K}\boldsymbol{\zeta}(t) + \mathbf{L}\boldsymbol{\theta}(t), \tag{2.93}$$

where $\mathbf{M} := \iiint_{\Omega_0} \rho_0 \underline{\mathbf{N}}^\top \underline{\mathbf{N}} \, \mathrm{d}V_0$ *is the mass matrix.*

Remark 2.7. *The equations* (2.92)–(2.93) *form a port-Hamiltonian system. A (finite-dimensional) port-Hamiltonian system can be written in the form [van der Schaft, 2006]*

$$\dot{\mathbf{x}}(t) = (\mathcal{J} - \mathcal{R})\,\mathcal{H}\mathbf{x}(t), \tag{2.94}$$

where $\mathcal{J}^\top = -\mathcal{J}$, $\mathcal{R}^\top = \mathcal{R}$, $\mathcal{R} \geq 0$, $\mathcal{H}^\top = \mathcal{H}$, $\mathcal{H} > 0$. *The function* $h(t) = \frac{1}{2}\mathbf{x}^\top(t)\mathcal{H}\mathbf{x}(t)$ *is the Hamiltonian and can be considered as the energy of the system. Because* $\dot{h}(t) = -\mathbf{x}^\top(t)\mathcal{H}\mathcal{R}\mathcal{H}\mathbf{x}(t)$, *it follows that* $\mathcal{R}$ *accounts for energy dissipating mechanisms and* $\mathcal{J}$ *for energy preserving mechanisms.*

Without the source term $\mathbf{B}_{\mathrm{exp}}(t)\bar{u}_{\mathrm{exp}}$, *the equations* (2.92)–(2.93) *can be written in the form* (2.94) *by setting*

$$\mathbf{x}(t) = \begin{bmatrix} \boldsymbol{\zeta}(t) \\ \mathbf{M}\dot{\boldsymbol{\zeta}}(t) \\ \frac{1}{T_0}\mathbf{E}\boldsymbol{\theta}(t) \end{bmatrix}, \qquad \mathcal{J} = \begin{bmatrix} \mathbf{0} & \mathbf{I} & \mathbf{0} \\ -\mathbf{I} & \mathbf{0} & \mathbf{L} \\ \mathbf{0} & -\mathbf{L}^\top & \mathbf{0} \end{bmatrix}, \tag{2.95}$$

$$\mathcal{R} = \begin{bmatrix} \mathbf{0} & \mathbf{0} & \mathbf{0} \\ \mathbf{0} & \mathbf{0} & \mathbf{0} \\ \mathbf{0} & \mathbf{0} & \frac{-1}{T_0}\mathbf{A} \end{bmatrix}, \qquad \mathcal{H} = \begin{bmatrix} \mathbf{K} & \mathbf{0} & \mathbf{0} \\ \mathbf{0} & \mathbf{M}^{-1} & \mathbf{0} \\ \mathbf{0} & \mathbf{0} & T_0\mathbf{E}^{-1} \end{bmatrix}. \tag{2.96}$$

Now observe that 1) the matrix $\mathbf{A}$ *only appears in* $\mathcal{R}$, *showing that heat conduction decreases the Hamiltonian* h, *and 2) the thermal load matrix* $\mathbf{L}$ *only appears in* $\mathcal{J}$, *meaning interconnection between the thermal and mechanical domain through* $\mathbf{L}$ *conserves the Hamiltonian* h.

It seems a similar result holds in infinite dimensional equations of linear thermoelasticty (2.71) *and* (2.74). *For example, the infinite dimensional equivalent of the Hamiltonian* h *is used in [Racke and Jiang, 2000], but the connection to port-Hamiltonian systems is not made there.*

Remark 2.8. *The time derivative of the Hamiltonian* $\dot{h}(t) = \frac{1}{T_0}\boldsymbol{\theta}^\top(t)\mathbf{A}\boldsymbol{\theta}(t)$ *has a close relation to the rate of entropy production. To see this, note that a quadratic approximation around the reference state* $T(\mathbf{x},t) \equiv 0$ *of the entropy production rate* (2.59) *is*

$$\rho_0 \frac{\partial s_p}{\partial t} = \frac{1}{T_0^2}\left(\nabla_{\mathbf{x}}\tilde{T}\right)^\top \boldsymbol{\kappa}_0 \nabla_{\mathbf{x}}\tilde{T} = \frac{k}{T_0^2}\left(\nabla_{\mathbf{x}}\tilde{T}\right)^\top \nabla_{\mathbf{x}}\tilde{T}. \tag{2.97}$$

By approximating $\tilde{T}$ *in FE shape functions using* (2.82)*, integrating over the volume* Ω_0*, and using the definition of* $\mathbf{A}$ *in* (2.87)*, the entropy production in the discretized model becomes* $S_p(t) := \frac{-1}{T_0^2}\boldsymbol{\theta}^\top(t)\mathbf{A}\boldsymbol{\theta}(t) \geq 0$*. The time derivative of the Hamiltonian can thus be expressed as* $\dot{h}(t) = -T_0 S_p(t)$*.*

2.5.3 Thermal modes

In order to obtain more insight in the dynamics of the thermomechanical system under consideration, it is insightful to compute the thermal modes, which are solutions to the eigenvalue problem

$$\left(\mathbf{A} - \frac{1}{\tau_k}\mathbf{E}\right)\boldsymbol{\theta}_k = \mathbf{0}, \tag{2.98}$$

where τ_k denote the thermal time constants and $\boldsymbol{\theta}_k$ denote the corresponding thermal modes.

The used mesh is shown in Figure 2.6 and consists of 8-node brick linear elements. The mesh contains two elements along the thickness of the wafer and layer 1, and four elements along the thickness of layer 2 and the positioning module. The burl layers are modeled using a single layer of elements. The resulting mesh contains 21,652 elements and 25,443 nodes. The finite element matrices are constructed using a MATLAB tool based on [de Best, 2015].

The largest 12 thermal time constants τ_k and their inverses $1/\tau_k$ are shown in Table 2.5. Observe that the $1/\tau_k$ are concentrated in a relatively narrow frequency band between 0.5 and 0.65 Hz and that the τ_k are significantly longer than the time it takes to expose one field $t_{\text{field}} = 0.1362$ s, see also Table 2.4. This observation indicates that a standard modal truncation will not be effective for the wafer heating problem because many modes will be needed to accurately capture the response in the short time window of interest. It is also worth noting that the first mechanical eigenfrequency is above 1000 Hz, which indicates that the quasi-static approximation is reasonable for this application.

The six thermal modes $\boldsymbol{\theta}_k$ corresponding to the six largest time constants τ_k are shown in Figure 2.7. Recall that the temperature below the cooling channels half way Layer 2 is constrained. Due to the rotational symmetry of the resulting model, the modes $\boldsymbol{\theta}_2$ and $\boldsymbol{\theta}_3$ only differ by a rotation over 90 degrees and the corresponding time constants τ_2 and τ_3 in Table 2.5 are equal. The pairs $\boldsymbol{\theta}_4$ and

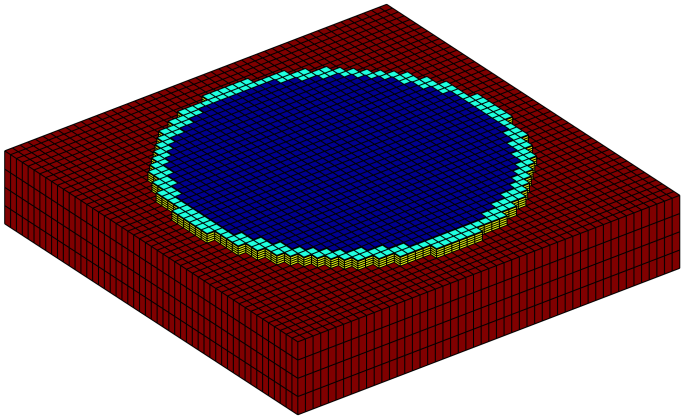

Figure 2.6. The mesh used for the eigenvalue analysis (the colors of the layers are the same as in Figure 2.3).

Table 2.5. Thermal time constants and their reciprocal values

k	1	2	3	4	5	6
τ_k [s]	1.9378	1.8809	1.8809	1.7992	1.7956	1.7447
$1/\tau_k$ [Hz]	0.5160	0.5317	0.5317	0.5558	0.5569	0.5732

k	7	8	9	10	11	12
τ_k [s]	1.6957	1.6957	1.5978	1.5978	1.5883	1.5785
$1/\tau_k$ [Hz]	0.5897	0.5897	0.6259	0.6259	0.6296	0.6335

θ_5, θ_7 and θ_8, θ_9 and θ_{10}, and θ_{11} and θ_{12} also differ only by a rotation and their time constants only differ due to the used discretization.

The cross sections in Figure 2.7 show that hardly any temperature changes in Layer 1 and the top half of Layer 2 are visible. This indicates that the thermal resistance of the burl layer is significant and partially motivates the consideration of the 2-D model for the wafer alone in Subsection 2.5.5.

2.5.4 Transient simulation

Next, the transient simulation for the scanning of a single field on the wafer with center at $(x_1, x_2) = (52, -115.5)$ mm is considered. It is assumed that the whole structure is initially at the reference temperature $T_0 = 22$ °C, i.e. the initial condition for (2.85) is $\boldsymbol{\theta}(0) = \mathbf{0}$. Recall that the scanning of a single field takes approximately 0.14 s (see Table 2.4). The time interval between $t = 0$ and $t = 0.3$ s is discretized with $N = 300$ equidistant time points t_k. The temperature

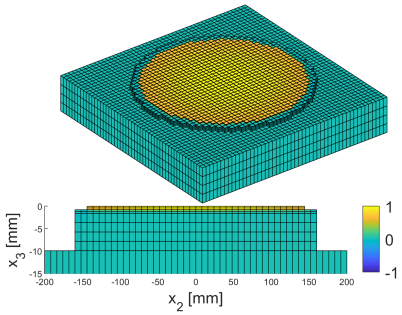

(a) Thermal mode for $k = 1$

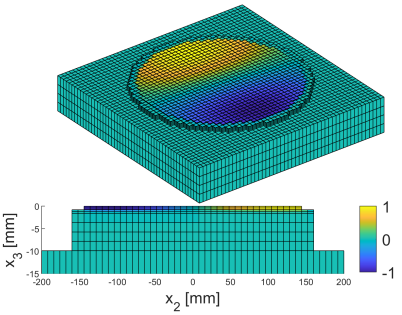

(b) Thermal mode for $k = 2$

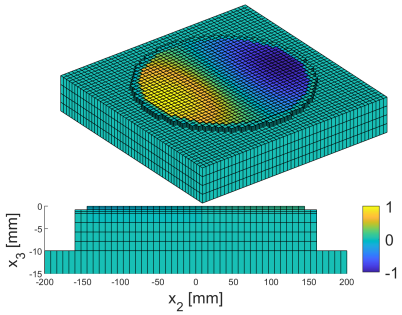

(c) Thermal mode for $k = 3$

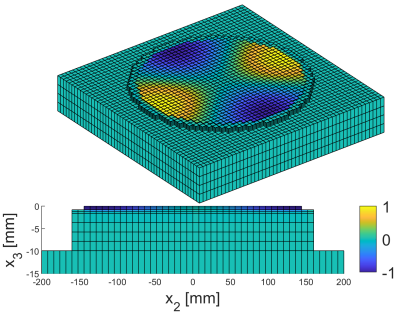

(d) Thermal mode for $k = 4$

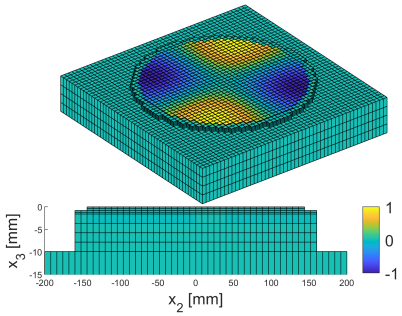

(e) Thermal mode for $k = 5$

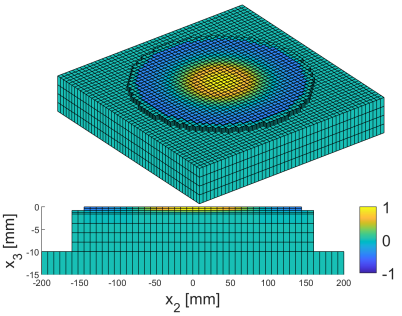

(f) Thermal mode for $k = 6$

Figure 2.7. Thermal modes corresponding to the six longest time constants. The lower parts of the subfigures show the cross section along the plane $x_1 = 0$.

field is computed by solving (2.85) using the Crank-Nicolson method [Crank and Nicolson, 1947] as

$$\frac{1}{2\Delta t}\mathbf{E}\left(\boldsymbol{\theta}_{k+1}-\boldsymbol{\theta}_k\right)=\mathbf{A}\left(\boldsymbol{\theta}_{k+1}+\boldsymbol{\theta}_k\right)+\mathbf{B}_{\exp}\left(\frac{t_{k+1}+t_k}{2}\right)\bar{u}_{\exp}, \tag{2.99}$$

where Δt denotes the spacing of the time grid and $\boldsymbol{\theta}_k$ is the approximation of the nodal temperatures at the k-th time instant $t_k = k\Delta t$. A snapshot from the simulation using the mesh in Figure 2.6 is shown in Figure 2.8a. Note that the temperature increase occurs only in a few elements and the element size of 8 mm × 8 mm in x_1- and x_2-directions is large compared to the slit of 26 mm × 4.6 mm.

Because only a single field is considered, it is natural to truncate the spatial domain in Figure 2.8b. For this model the mesh size in x_1- and x_2-directions can be reduced to 2 mm × 2 mm without severe computational problems. The displacement of the node in the center of the field (at the top surface of the wafer) is computed by solving (2.86) (after removal of the six rigid body modes by constraining nodes near the center of the considered domain at the bottom of the positioning module). Because the number of mechanical DOFs of interest (3) is much smaller than the number of time steps (300), this computation is most efficiently done as

$$\mathbf{d}_{\mathrm{c},k}=(\mathbf{S}_{\mathrm{c}}\mathbf{K}_{\mathrm{ff}}^{-1})\mathbf{L}_{\mathrm{f}}\boldsymbol{\theta}_k, \tag{2.100}$$

where $\mathbf{d}_{\mathrm{c},k}$ denotes the displacement vector of the node at the center of the field, $\mathbf{S}_{\mathrm{c}}$ selects the free mechanical DOFs of interest, $\mathbf{K}_{\mathrm{ff}}$ and $\mathbf{L}_{\mathrm{f}}$ are the parts of $\mathbf{K}$ and $\mathbf{L}$ corresponding to the free mechanical DOFs. Since $\mathbf{S}_{\mathrm{c}}$ has only three rows, this computation requires the solution of only three linear systems.

Some results of the simulation on the 3-D truncated domain for the 8 mm and 2 mm meshes are indicated by the solid lines in Figure 2.9. The number of DOFs and the computational times for these simulations are given in Table 2.6. Figure 2.9a shows the temperature increase at the top of the wafer in the center of the considered field. Note that before and after the rapid temperature increase due to the passing of the moving heat load, spurious oscillations are observed and that these oscillations, although to a lower extend, are still visible on the 2 mm mesh. The displacement in x_1-direction of the same node is shown in Figure 2.9b. Because the considered node lies on the symmetry line of the considered field, the displacement in x_1-direction is relatively small compared to the displacement in x_2-direction in Figure 2.9c (the displacement in the x_1-direction would be zero if the geometry in Figure 2.8b would be symmetric in the center line of the field). The displacement in the x_2-direction in Figure 2.9c increases until the heat load has passed the center of the field, after which it decreases until the scanning of the field is completed at $t_{\mathrm{field}} = 0.1362$ s. Figure 2.9d shows the increase in the thickness of the wafer, i.e. the difference between the deformation in z-direction of the top and bottom of the wafer. Note that the

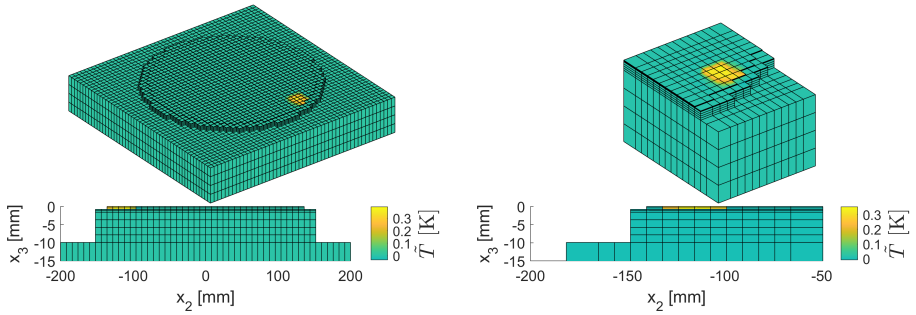

(a) Complete domain **(b)** Truncated domain

Figure 2.8. Snapshots from the transient simulation at $t = 0.1134$ s for the complete wafer model and for the truncated domain. The lower part of the figures shows the cross section in the plane $x_1 = \text{const}$ that passes through the center of the field that is being scanned.

spurious oscillations in the temperature increase in Figure 2.9a are also visible in Figure 2.9d.

The results on the 8 mm $\times$ 8 mm and 2 mm $\times$ 2 mm meshes in Figure 2.9 differ significantly. However, decreasing the mesh size further leads to large FE models with 100,000 nodes and more, even on the truncated domain. Especially due to the size of the stiffness matrix $\mathbf{K}$, the computation of the resulting displacements on finer meshes requires the use of iterative solvers [van der Vorst, 2003], possibly in combination with multigrid methods [Wesseling, 1992]. This path is not investigated further in this thesis.

The computational times in Table 2.6 are relatively small, but it should be noted that these are times for the simulation of a single field on a truncated domain. As a wafer contains typically 100 fields and considering the full domain increases the number of DOFs by roughly a factor 8 (see Table 2.6), it is clear that solving the 3-D wafer heating problem on the complete spatial domain for the exposure of all fields is very challenging. Furthermore, it should be noted that the computational times for the mechanical part now consider the computation of the displacement of a single node which requires the computation of only one row in $\mathbf{K}_{\text{ff}}^{-1}$, see (2.100). As the deformation inside the slit determines the imaging quality and the slit moves over almost the whole wafer surface, the displacement of practically all nodes in the wafer surface will be of interest. This increases the computational complexity even more.

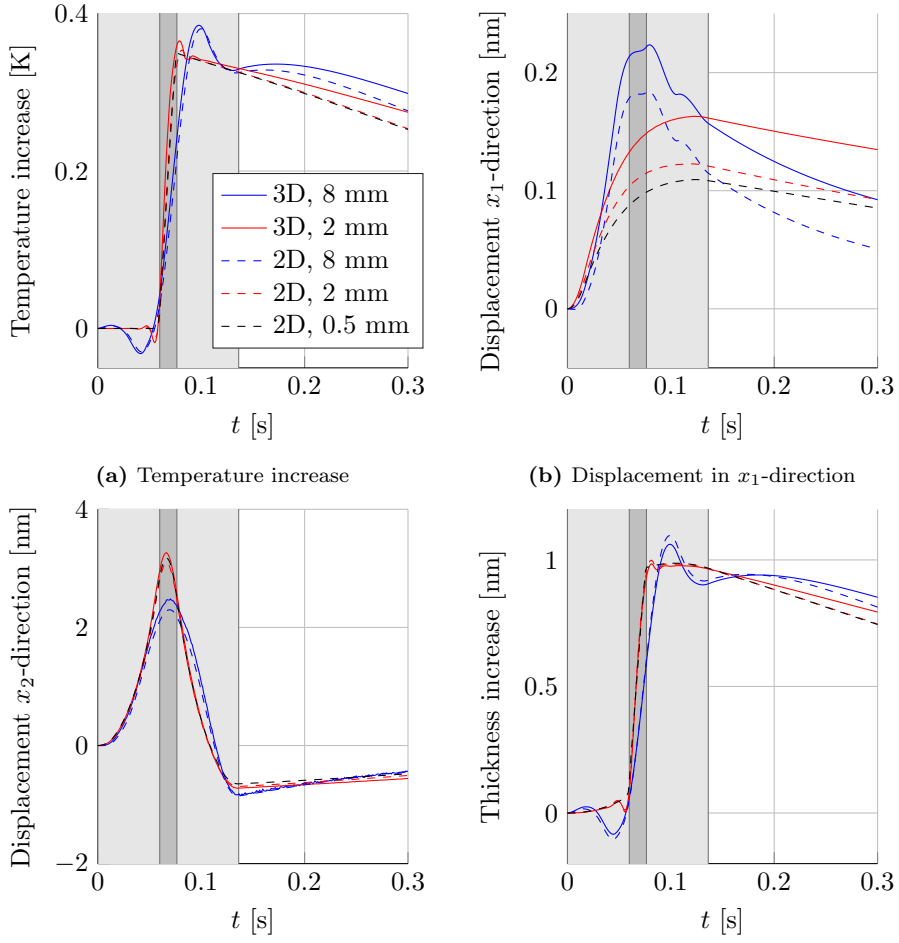

(a) Temperature increase

(b) Displacement in x_1-direction

(c) Displacement in x_2-direction

(d) Increase in thickness

Figure 2.9. Temperature increase, displacement in x_1- and x_2-direction, and the increase in thickness of the wafer at the center of the field for several 3-D and 2-D meshes. The light gray area indicates the time interval $[0, t_{\text{field}}]$ during which the heat load is applied to the wafer, and the dark gray area the time interval during which the heat load is applied to the center of the field.

Table 2.6. The number of (free) DOFs and the computational times for the thermal and mechanical parts of the 3-D FE model of the full wafer clamp (3-D full, mesh in Figure 2.8a), the 3-D model on the truncated domain (3-D trunc., mesh in Figure 2.8b), and the 2-D model on the truncated domain (2-D trunc.) for several element sizes

	Element size [mm]	Thermal part		Mechanical part	
		# DOFs	time [s]	# DOFs	time [s]
3-D full	8	8,523	11.7	76,323	–
3-D trunc.	8	1,007	0.8	7,308	1.1
3-D trunc.	2	14,354	18.0	103,878	487.0
2-D trunc.	8	133	0.1	266	<0.1
2-D trunc.	2	1,874	0.7	3,784	<0.1
2-D trunc.	0.5	30,372	16.7	60,744	0.5

2.5.5 Two-dimensional model

In this subsection, a 2-D wafer heating model will be derived. The development of this model is motivated by the observation that the temperature increase in the layers below the wafer is small compared to the temperature increase in the wafer (see Figures 2.7 and 2.8) and the high computational complexity of the 3-D model in the previous subsection.

The 2-D model is derived under the following main assumptions:

- Layer 1 has a constant temperature T_0 and does not deform.
- The temperature and displacement fields in the wafer do not depend on the out-of-plane coordinate x_3.

Under these assumptions, the temperature field $T_{2\mathrm{D}}(x_1, x_2, t)$ in the wafer can be found by integrating (2.75) over the thickness of the wafer H from $x_3 = -H$ to $x_3 = 0$. This yields

$$\rho_0 c_0 H \frac{\partial T_{2\mathrm{D}}}{\partial t} = kH \left(\frac{\partial^2 T_{2\mathrm{D}}}{\partial x_1^2} + \frac{\partial^2 T_{2\mathrm{D}}}{\partial x_2^2} \right) + k \frac{\partial T}{\partial x_3}\bigg|_{x_3=-H}^{0}, \tag{2.101}$$

where ρ_0, c_0, and k now denote the (constant) mass density, specific heat capacity, and thermal conductivity of the wafer. The boundary condition (2.78) and the zero heat capacity of the burl layer give that

$$k \frac{\partial T}{\partial x_3}\bigg|_{x_3=0} = Q_{\mathrm{exp}}, \qquad -k \frac{\partial T}{\partial x_3}\bigg|_{x_3=-H} = -\frac{1}{R_t} T_{2\mathrm{D}}. \tag{2.102}$$

Here, R_t denotes the thermal resistance of the (first) burl layer which can be expressed as $R_t = H_{\mathrm{burl},1}/k_{\mathrm{burl},1}$, where $H_{\mathrm{burl},1}$ and $k_{\mathrm{burl},1}$ denote the thickness and thermal conductivity of the burl layer, see Tables 2.1 and 2.2.

In the mechanical part of the 2-D model, the in-plane displacement field components $d_{2\mathrm{D},1}(x_1, x_2, t)$ and $d_{2\mathrm{D},2}(x_1, x_2, t)$ are independent of the out-of-plane coordinate x_3. The linear strain-displacement relation (2.67) now yields the in-plane strain components as

$$\varepsilon_{2\mathrm{D},11} = \frac{\partial d_{2\mathrm{D},1}}{\partial x_1}, \quad \varepsilon_{2\mathrm{D},22} = \frac{\partial d_{2\mathrm{D},2}}{\partial x_2}, \quad \varepsilon_{2\mathrm{D},12} = \frac{1}{2}\left(\frac{\partial d_{2\mathrm{D},1}}{\partial x_2} + \frac{\partial d_{2\mathrm{D},2}}{\partial x_1}\right). \tag{2.103}$$

To find the stress-strain-temperature relations for the 2-D model, note that the stress-strain-temperature relations for the 3-D model in (2.69) can be rewritten by taking the inverse of matrix $\mathbf{H}$ in (2.70) as

$$\begin{bmatrix} \tilde{\varepsilon}_{11} - \alpha_0 T \\ \tilde{\varepsilon}_{22} - \alpha_0 T \\ \tilde{\varepsilon}_{33} - \alpha_0 T \\ \tilde{\varepsilon}_{12} \\ \tilde{\varepsilon}_{13} \\ \tilde{\varepsilon}_{23} \end{bmatrix} = \frac{1}{E} \begin{bmatrix} 1 & -\nu & -\nu & 0 & 0 & 0 \\ -\nu & 1 & -\nu & 0 & 0 & 0 \\ -\nu & -\nu & 1 & 0 & 0 & 0 \\ 0 & 0 & 0 & 1+\nu & 0 & 0 \\ 0 & 0 & 0 & 0 & 1+\nu & 0 \\ 0 & 0 & 0 & 0 & 0 & 1+\nu \end{bmatrix} \begin{bmatrix} \tilde{\sigma}_{11} \\ \tilde{\sigma}_{22} \\ \tilde{\sigma}_{33} \\ \tilde{\sigma}_{12} \\ \tilde{\sigma}_{13} \\ \tilde{\sigma}_{23} \end{bmatrix}. \tag{2.104}$$

Because no forces are applied at the top surface of the wafer, $\tilde{\sigma}_{33} = 0$ at the top surface of the wafer. As the wafer is thin, it reasonable to neglect $\tilde{\sigma}_{33}$ throughout the wafer. This is a standard assumption for the modeling of thin plates, see e.g. [Hetnarski and Eslami, 2009; Zienkiewicz et al., 2013]. Using that $\tilde{\sigma}_{33} = 0$, the relations for the in-plane stress components of the 2-D model $\sigma_{2\mathrm{D},11}$, $\sigma_{2\mathrm{D},22}$, and $\sigma_{2\mathrm{D},12}$ now follow from the first, second, and fourth row of (2.104) as

$$\begin{bmatrix} \varepsilon_{2\mathrm{D},11} - \alpha_0 T_{2\mathrm{D}} \\ \varepsilon_{2\mathrm{D},22} - \alpha_0 T_{2\mathrm{D}} \\ \varepsilon_{2\mathrm{D},12} \end{bmatrix} = \frac{1}{E} \begin{bmatrix} 1 & -\nu & 0 \\ -\nu & 1 & 0 \\ 0 & 0 & 1+\nu \end{bmatrix} \begin{bmatrix} \sigma_{2\mathrm{D},11} \\ \sigma_{2\mathrm{D},22} \\ \sigma_{2\mathrm{D},12} \end{bmatrix}. \tag{2.105}$$

Inverting this relation yields the plane-stress stress-strain-temperature relations for the 2-D model

$$\begin{bmatrix} \sigma_{2\mathrm{D},11} \\ \sigma_{2\mathrm{D},22} \\ \sigma_{2\mathrm{D},12} \end{bmatrix} = \frac{E}{1-\nu^2} \begin{bmatrix} 1 & \nu & 0 \\ \nu & 1 & 0 \\ 0 & 0 & 1-\nu \end{bmatrix} \begin{bmatrix} \varepsilon_{2\mathrm{D},11} - \alpha_0 T_{2\mathrm{D}} \\ \varepsilon_{2\mathrm{D},22} - \alpha_0 T_{2\mathrm{D}} \\ \varepsilon_{2\mathrm{D},12} \end{bmatrix}. \tag{2.106}$$

The 2-D mechanical model is completed by integrating the first two equations of the force balance (2.76) from $x_3 = -H$ to $x_3 = 0$. This yields

$$H\frac{\partial \sigma_{2\mathrm{D},11}}{\partial x_1} + H\frac{\partial \sigma_{2\mathrm{D},21}}{\partial x_2} + \sigma_{31}|_{x_3=-H}^{0} = 0, \tag{2.107}$$

$$H\frac{\partial \sigma_{2\mathrm{D},12}}{\partial x_1} + H\frac{\partial \sigma_{2\mathrm{D},22}}{\partial x_2} + \sigma_{32}|_{x_3=-H}^{0} = 0. \tag{2.108}$$

Now note that the σ_{31} and σ_{32} are zero on the top surface $x_3 = 0$ because no forces are applied to the top surface. By the continuity of the stress, the stress

on the bottom of the wafer is the same as the stress at the top surface of the burl layer. In view of the very small thickness of the burl layer (see Table 2.1), it is reasonable to approximate the strains in the burl layer as $\varepsilon_{31} = d_{2\mathrm{D},1}/H_{\mathrm{burl},1}$ and $\varepsilon_{32} = d_{2\mathrm{D},2}/H_{\mathrm{burl},1}$, where $H_{\mathrm{burl},1}$ denotes the thickness of the burl layer, see Table 2.1. Recall that the burl layer was modeled as an isotropic material without Poisson effect, meaning that the matrix $\mathbf{H}$ in (2.69) is diagonal with elements E_{11}, E_{22}, E_{33}, G_{12}, G_{13}, and G_{23} on the diagonal (the nonzero elements are given in Table 2.3). The shear stresses at the top of the burl layer σ_{31} and σ_{32} are thus given by

$$\sigma_{31}|_{x_3=-H} = G_{31,\mathrm{burl},1}\frac{d_{2\mathrm{D},1}}{H_{\mathrm{burl},1}}, \qquad \sigma_{32}|_{x_3=-H} = G_{32,\mathrm{burl},1}\frac{d_{2\mathrm{D},2}}{H_{\mathrm{burl},1}}. \tag{2.109}$$

The force balance (2.107)–(2.108) thus becomes

$$H\frac{\partial\sigma_{2\mathrm{D},11}}{\partial x_1} + H\frac{\partial\sigma_{2\mathrm{D},21}}{\partial x_2} - \frac{G_{31,\mathrm{burl},1}}{H_{\mathrm{burl},1}}d_{2\mathrm{D},1} = 0, \tag{2.110}$$

$$H\frac{\partial\sigma_{2\mathrm{D},12}}{\partial x_1} + H\frac{\partial\sigma_{2\mathrm{D},22}}{\partial x_2} - \frac{G_{32,\mathrm{burl},1}}{H_{\mathrm{burl},1}}d_{2\mathrm{D},2} = 0. \tag{2.111}$$

The 2-D model can also be used to predict the increase in thickness of the wafer, see e.g. [Kovalenko, 1969]. To see how, note that the third row of (2.104) with $\tilde{\sigma}_{33} = 0$ shows that

$$\frac{\partial d_3}{\partial x_3} = \varepsilon_{33} = -\frac{\nu}{E}\left(\sigma_{2\mathrm{D},11} + \sigma_{2\mathrm{D},22}\right) + \alpha_0 T_{2\mathrm{D}}. \tag{2.112}$$

Inserting the expressions for $\sigma_{2\mathrm{D},11}$ and $\sigma_{2\mathrm{D},22}$ from (2.106) and integrating from $x_3 = -H$ to $x_3 = 0$ now yields an expression for the increase in thickness of the wafer

$$d_3|_{x_3=0} - d_3|_{x_3=-H} = H\left(\left(1 + \frac{2\nu}{1-\nu}\right)\alpha_0 T_{2\mathrm{D}} - \frac{\nu}{1-\nu}\left(\varepsilon_{2\mathrm{D},11} + \varepsilon_{2\mathrm{D},22}\right)\right). \tag{2.113}$$

The FE discretization of the 2-D model is derived in a similar way as in Subsection 2.5.2 and yields a system of equations of the form (2.92)–(2.93).

The dashed lines in Figure 2.9 show the simulation results for the 2-D model. Note that the 2-D model can be solved on a 0.5 mm × 0.5 mm mesh because the computational times for the 2-D model are significantly smaller than for the 3-D model, see Table 2.6.

As can be seen from Figure 2.9a, the temperature responses of the 2-D model matches the temperature response of the 3-D model well around the rapid temperature increase due to passing of the moving heat load. However, the temperatures computed based on the 2-D and 3-D model start to differ after the heat load has passed. In the 2-D model the temperature of Layer 1 is fixed (i.e. the

heat capacity of Layer 1 is infinite), but in the 3-D model Layer 1 has a finite heat capacity and heats up. The temperature increase in the wafer predicted by the 2-D model is thus lower than for the 3-D model. Also note that the spurious oscilations that were still visible on the 2 mm mesh are no longer present on the 0.5 mm mesh. This observation matches the results in [Zienkiewicz et al., 2014] which show that spurious oscillations in advection-diffusion equations do not exist if the mesh size is smaller than

$$\frac{2k}{\rho c v} = 0.66 \text{ mm}. \tag{2.114}$$

Remark 2.9. *The results in Figure 2.9a indicate that the accuracy of the 2-D model can be improved by considering the temperature increase of layer 1. A possible way to do this is introducing a second heat equation in two spatial dimensions to model the temperature of Layer 1 and couple it to* (2.101) *through the thermal resistance of the burl layer. Modeling Layer 1 (and Layer 2) with one or more sublayers, each described by a 2-D heat equation, can improve the accuracy further. Models of this type are referred to as 2.5D models.*

Figures 2.9b and 2.9c show the in-plane displacement fields predicted by the 2-D model. The relative difference between the 2-D and 3-D model for the displacement in the x_1-direction is significant. However, it should be noted that the absolute error is around 0.05 nm which is relatively small compared to the displacement of 4 nm in x_2-direction.

Figure 2.9d also shows that the increase in thickness is accurately predicted by the 2-D model. Just as for the temperature in Figure 2.9a, the effect of the temperature increase of layer 1 becomes more important after the scanning of the field has been completed.

2.6 Conclusions

In this chapter, the theory for the modeling of thermomechanical systems has been presented and applied to a wafer heating problem. In particular, two important simplifications of the general theory for a thermoelastic solid presented in Section 2.2 have been considered: 1) linear thermoelasticity (see Section 2.3), which follows after linearization of the equations for general thermoelasticity, and 2) quasi-static thermoelasticity (see Section 2.4), in which the response of the mechanical model is assumed to be quasi-static. The equations for linear quasi-static thermoelasticity have then been applied to a wafer heating problem in Section 2.5. A closer look at this problem showed that the original 3-D problem could be further simplified to a 2-D model. The results from the 2-D and 3-D models match quite well, especially during the time interval up to $t_{\text{field}} = 0.1362$ s during which a single field is scanned.

Because the computational cost of the 2-D model is significantly lower than that of the 3-D model, the use of the 2-D model enables the computation of accurate reference solutions which are not easy or even impossible to obtain for the 3-D models. Therefore, the 2-D model will be used to develop and verify the methods in the remaining chapters of this thesis. Furthermore, note that the scanning of only a singe field has been considered up to now, but that a wafer typically contains about 100 fields. In the next chapter, it will be shown how the response for a single field can be used to efficiently construct the thermomechanical response for the scanning of all fields on the wafer.

Part II

Simulation of moving heat source problems

Chapter 3

The method of images for thermomechanical systems

3.1 Introduction

The method of images relates the solution of the heat equation with constant coefficients on $\mathbb{R}^n$, typically $n = 2$ or $n = 3$, to solutions of the heat equation on certain subdomains $\Omega \subset \mathbb{R}^n$. Analytic expressions for the solution on $\mathbb{R}^n$ can be obtained using the fundamental solution of the heat equation, see e.g. [Carslaw and Jaeger, 1959; Evans, 2010]. The method of images is therefore typically used to derive analytic and semi-analytic expressions for the solution of heat conduction problems on bounded domains, see e.g. [Rosenthal, 1946; Fachinotti et al., 2011; Dias, 2015; Dias, 2016; Flint et al., 2018]. In most cases, the method is applied for zero Neumann boundary conditions (i.e. the heat flux through the boundary is zero), but the method has been extended to a variety of other boundary conditions such as (zero) Dirichlet or Robin boundary conditions, see [Carslaw and Jaeger, 1959; Dias, 2015; Dias, 2016]. The method of images dates back at least to the nineteenth century, see [Bryan, 1890], but might well be even older.

As will be demonstrated in this chapter, the method of images can be used to reduce the computational cost for the simulation of heat conduction problems with repetitive sources. For such processes, the temperature field on the unbounded domain $\mathbb{R}^n$ can be constructed effectively by exploiting the translation, rotation, and time invariance of the heat equation on $\mathbb{R}^n$. The method of images

This chapter formed the basis of D. W. M. Veldman et al. (2020b). The method of images in thermoelasticity with an application to wafer heating. *In preperation*, which contains a slightly more general formulation than this chapter also applicable to 3-D spatial domains.

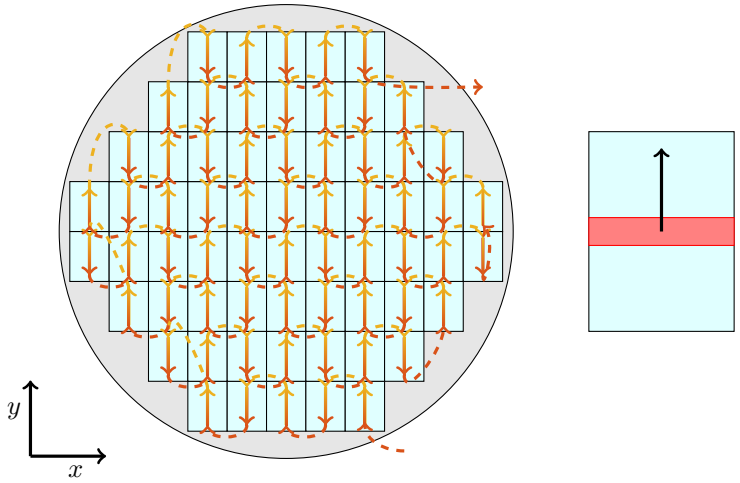

Figure 3.1. A typical expose pattern in lithography (left) with a detailed view of a single passing of the heat load (right). The heat load (red rectangle) scans multiple fields (blue rectangles) on a silicon wafer (gray disk) which results in a meandering path (red and orange arrows).

is then applied to obtain the solution on the subdomain $\Omega \subset \mathbb{R}^n$ of interest.

Repetitive heat loads occur in many industrial applications where a surface is treated by the (small) spot of a laser beam. In these applications, multiple passings of the laser over the surface occur. The heat load applied during each passing is very similar. Examples of such processes are the laser hardening of metals [Komanduri and Hou, 2001; Majumdar and Manna, 2011; Oh and Ki, 2017], additive manufacturing [Frazier, 2014; King et al., 2015; Schwalbach et al., 2019], and wafer heating [Subramany et al., 2016; van den Hurk et al., 2018]. In the latter application, a pattern of electronic connections is projected onto a silicon wafer following a meandering path, see Figure 3.1. The light used to project the pattern heats up the wafer which leads to thermal expansion and a degraded imaging quality. Fast and sufficiently accurate simulation of this process is needed to improve the imaging quality of the latest generation wafer scanners.

It should be noted that the assumption of constant material properties is problematic when temperature increases are large. However, semi-analytic models have also been developed for applications where the material properties are certainly not constant such as welding [Fachinotti et al., 2011; Flint et al., 2018] and additive manufacturing [Schwalbach et al., 2019]. In contrast to these applications, the temperature increases encountered in wafer heating are small, i.e. smaller than one Kelvin, and the material properties can assumed to be constant. This makes the method of images particularly suitable for the wafer

heating application.

However, the wafer heating application comes with two specific difficulties. The first difficulty is that the spatial domain is circular (see Figure 3.1) and that, to the best of our knowledge, the method of images has only been applied to box-shaped (also called orthogonal) domains. The second difficulty is that not only the temperature field, but also the heat-induced deformation are of interest because this eventually determines the imaging quality of the lithographic process. To the best of our knowledge, the method of images has only been applied to the temperature field and not to the heat-induced deformations.

This chapter addresses these two difficulties by extending the well-known method of images in two ways. First of all, the method of images is reformulated by writing the solution on the subdomain $\Omega \subset \mathbb{R}^2$ as the convolution of the solution on $\mathbb{R}^2$ with a kernel. This kernel should satisfy a certain Partial Differential Equation (PDE) which can be solved analytically for several orthogonal subdomains and for the circular subdomain. Secondly, it is shown how the method of images can be used to compute the heat-induced deformation in a subdomain $\Omega \subset \mathbb{R}^2$ based on the heat-induced deformation on $\mathbb{R}^2$. This extension is made using the displacement potential function, see e.g. [Nowacki, 1962; Kovalenko, 1969; Hetnarski and Eslami, 2009], which means that in almost all cases an additional correction is needed to satisfy the mechanical boundary conditions.

This chapter thus provides an extension of the method of images that enables the efficient simulation of thermomechanical systems on circular domains. Application of the proposed methods to the wafer heating application indeed shows that the method leads to a significant reduction in computational time.

The remainder of this chapter is organized as follows. Section 3.2 introduces some preliminaries, such as the considered thermomechanical system with a repetitive heat load and the displacement potential. In Section 3.3, the method of images is reformulated in terms of a convolution kernel, which enables the extension of the method of images to a circular domain. Section 3.4 presents the extension of the method of images to the heat-induced deformations and the developed techniques are applied to a wafer heating application in Section 3.5. Finally, Section 3.6 contains the conclusions and recommendations.

3.2 Preliminaries

3.2.1 Thermomechanical model

The considered thermomechanical model for a thin plate consists of a thermal and mechanical part. The thermal part models heat conduction and the mechanical part the resulting thermal expansion.

At time $t = 0$, the plate has a constant temperature equal to T_0 and is stress-free. In this reference state, the plate occupies a volume $(x, y, z) \in$

$\Omega \times [-H, 0] \subseteq \mathbb{R}^2 \times [-H, 0]$, where (x, y, z) are Cartesian coordinates and H denotes the thickness of the plate. Because the plate is thin, the temperature increase $T_\Omega(x, y, t)$ and the in-plane displacement field $\mathbf{d}_\Omega(x, y, t) = [d_{\Omega,x}(x, y, t), d_{\Omega,y}(x, y, t)]^\top$ (both w.r.t. the reference situation at $t = 0$) are only a function of the in-plane coordinates (x, y) and time t.

The temperature increase $T_\Omega(x, y, t)$ w.r.t. T_0 satisfies, see e.g. [Veldman et al., 2018; van den Hurk et al., 2018] or Subsection 2.5.5,

$$\rho c H \frac{\partial T_\Omega}{\partial t} = kH\nabla^2 T_\Omega - hT_\Omega + Q_\Omega, \qquad (x, y) \in \Omega, t \geq 0, \tag{3.1}$$

where ρ, c, k, are the (constant) mass density, specific heat capacity, and thermal conductivity of the plate, respectively, h denotes the convection coefficient for the heat losses to the surroundings, $Q_\Omega(x, y, t)$ denotes the applied heat load, and ∇^2 denotes the Laplacian. In the considered Cartesian coordinates

$$\nabla^2 = \frac{\partial^2}{\partial x^2} + \frac{\partial^2}{\partial y^2}. \tag{3.2}$$

In the wafer heating application, the coefficient h models the heat losses to the water-cooled supporting structure and Q_Ω is the heat load induced by the expose light that travels along the wafer surface as in Figure 3.1.

The mechanical part of the plate model is based on linear strain-displacement relations and Hooke's law for an isotropic material in a state of plane stress. Inertia effects are neglected. These are common assumptions for the modeling of thin plates under thermal loading, see e.g. [Kovalenko, 1969; Hetnarski and Eslami, 2009; Zienkiewicz et al., 2013] or Subsection 2.5.5. Under these assumptions, the force balance takes the form

$$\frac{EH}{2(1+\nu)}\nabla^2 \mathbf{d}_\Omega + \frac{EH}{2(1-\nu)}\nabla\left(\nabla \cdot \mathbf{d}_\Omega\right) + \mathbf{f} = \frac{\alpha EH}{1-\nu}\nabla T_\Omega, \tag{3.3}$$

for $(x, y) \in \Omega$ and $t \geq 0$ and where E, ν, and α are the (constant) Young's modulus, Poisson's ratio, and Coefficient of Thermal Expansion (CTE) of the plate, respectively, $\mathbf{d}_\Omega = [d_{\Omega,x}, d_{\Omega,y}]^\top$ denotes the displacement field, $\mathbf{f} = [f_x, f_y]^\top$ denotes the applied force per unit area, the Laplacian is applied component-wise, and the gradient and divergence operators are defined as

$$\nabla = \begin{bmatrix} \frac{\partial}{\partial x} \\ \frac{\partial}{\partial y} \end{bmatrix}, \qquad \nabla \cdot \mathbf{d}_\Omega = \frac{\partial d_{\Omega,x}}{\partial x} + \frac{\partial d_{\Omega,y}}{\partial y}. \tag{3.4}$$

The applied forces $\mathbf{f}$ are assumed to be of the form

$$\mathbf{f} = -k_\mathrm{s}\mathbf{d}_\Omega, \qquad (x, y) \in \Omega, t \geq 0, \tag{3.5}$$

where $k_\mathrm{s} > 0$ denotes the additional in-plane stiffness per unit area due to the surroundings of the plate. In the wafer heating application, k_s models the in-plane stiffness of the connection between the supporting structure and the wafer.

Remark 3.1. *Since* (3.3) *is linear, deformations resulting from external forces that do not depend on* $\mathbf{d}_\Omega$ *can be computed independently of the temperature field* T_Ω*. In this chapter, only heat-induced deformation is considered.*

On subdomains $\Omega \subset \mathbb{R}^2$, thermal and mechanical boundary conditions are needed to complete the model. Motivated by the wafer heating application, perfectly insulated boundary conditions (i.e. no heat flux) and stress-free boundary conditions (i.e. no in-plane traction forces) are applied at the edge $\partial\Omega$ of Ω. These boundary conditions take the form

$$k\frac{\partial T_\Omega}{\partial n}(x,y,t) = 0, \qquad (x,y) \in \partial\Omega, t \geq 0, \tag{3.6}$$

$$\begin{bmatrix} \sigma_{\Omega,xx}(x,y,t) & \sigma_{\Omega,xy}(x,y,t) \\ \sigma_{\Omega,xy}(x,y,t) & \sigma_{\Omega,yy}(x,y,t) \end{bmatrix} \begin{bmatrix} n_x(x,y) \\ n_y(x,y) \end{bmatrix} = \begin{bmatrix} 0 \\ 0 \end{bmatrix}, \quad (x,y) \in \partial\Omega, t \geq 0, \tag{3.7}$$

where $\mathbf{n}(x,y) = [n_x(x,y), n_y(x,y)]^\top$ is the outward pointing normal to the edge $\partial\Omega$, $\partial T_\Omega/\partial n = \nabla T_\Omega \cdot \mathbf{n}$ denotes the derivative of T_Ω in the $\mathbf{n}$-direction, and σ_{xx}, σ_{xy}, and σ_{yy} denote the stress components

$$\sigma_{\Omega,xx} = \frac{E}{1-\nu^2}\left(\frac{\partial d_{\Omega,x}}{\partial x} + \nu\frac{\partial d_{\Omega,y}}{\partial y} - (1+\nu)\alpha T_\Omega\right), \tag{3.8}$$

$$\sigma_{\Omega,xy} = \frac{E}{2(1+\nu)}\left(\frac{\partial d_{\Omega,x}}{\partial y} + \frac{\partial d_{\Omega,y}}{\partial x}\right), \tag{3.9}$$

$$\sigma_{\Omega,yy} = \frac{E}{1-\nu^2}\left(\frac{\partial d_{\Omega,y}}{\partial y} + \nu\frac{\partial d_{\Omega,x}}{\partial x} - (1+\nu)\alpha T_\Omega\right). \tag{3.10}$$

Equations (3.1), (3.3), and (3.5) with boundary conditions (3.6)–(3.7) will be considered on several spatial domains $\Omega \subseteq \mathbb{R}^2$. The solutions on the unbounded spatial domain $\Omega = \mathbb{R}^2$ are denoted by T_∞ and $\mathbf{d}_\infty = [d_{\infty,x}, d_{\infty,y}]^\top$. For the wafer heating application, the solutions T_D and $\mathbf{d}_D = [d_{D,x}, d_{D,y}]^\top$ on the disk $D := \{(x,y) \in \mathbb{R}^2 \mid x^2 + y^2 < R^2\}$ with radius R are especially of interest. To illustrate and validate the developed method, other subdomains $\Omega \subset \mathbb{R}^2$ will be considered as well.

3.2.2 The method of images

For certain spatial domains Ω and boundary conditions, the method of images expresses the solution T_Ω on a subdomain $\Omega \subset \mathbb{R}^2$ that results from zero initial conditions and the heat load $Q_\Omega : \Omega \times \mathbb{R}_+ \to \mathbb{R}$ in terms of a solution $T_{\Omega,\infty}$ on the unbounded domain $\mathbb{R}^2$ that results from zero initial conditions and a heat load $Q_{\Omega,\infty} : \mathbb{R}^2 \times \mathbb{R}_+ \to \mathbb{R}$, see e.g. [Carslaw and Jaeger, 1959; Dias, 2015]. In this section, only the perfectly insulated boundary conditions (3.6) will be considered, but other types of boundary conditions can be considered as well, see also Remark 3.2 later on.

The method is best illustrated for a one-dimensional spatial domain. Therefore, the dependence on y is neglected for a moment and the spatial domain of interest is chosen as the semi-infinite line $\ell := \{x \in \mathbb{R} \mid x \leq x_e\}$. On ℓ, a certain heat load $Q_\ell : \ell \times \mathbb{R}_+ \to \mathbb{R}$ is applied.

There are two equivalent view points on the method of images that lead to a different definition of $Q_{\ell,\infty}$. In the first viewpoint, the heat load $Q_{\ell,\infty}$ is obtained by adding the mirror image in the edge $x = x_e$ of the heat load Q_ℓ, i.e.

$$Q^{(1)}_{\ell,\infty}(x,t) = \begin{cases} Q_\ell(x,t) & \text{for } x \leq x_e, \\ Q_\ell(2x_e - x, t) & \text{for } x \geq x_e. \end{cases} \tag{3.11}$$

The construction of $Q^{(1)}_{\ell,\infty}$ is illustrated in Figure 3.2a. The solution $T_\ell(x,t)$ can then be obtained by truncating the temperature field $T^{(1)}_{\ell,\infty}$ resulting from $Q^{(1)}_{\ell,\infty}$ to ℓ, i.e.

$$T_\ell(x,t) = T^{(1)}_{\ell,\infty}(x,t), \qquad x \leq x_e. \tag{3.12}$$

In the second viewpoint, the heat load $Q_{\ell,\infty}$ is constructed by setting $Q_{\ell,\infty}$ to zero outside ℓ, i.e. by defining

$$Q^{(2)}_{\ell,\infty}(x,y,t) = \begin{cases} Q_\ell(x,y,t) & \text{for } x \leq x_e, \\ 0 & \text{for } x \geq x_e. \end{cases} \tag{3.13}$$

The solution T_ℓ can then be obtained by mirroring the part of the temperature field $T^{(2)}_{\ell,\infty}$ that results from $Q^{(2)}_{\ell,\infty}$ in the edge $x = x_e$, i.e.

$$T_\ell(x,t) = T^{(2)}_\infty(x,t) + T^{(2)}_\infty(2x_e - x, t), \qquad x \leq x_e. \tag{3.14}$$

This construction of $T_\ell(x,t)$ is illustrated in Figure 3.2b. By noticing that $Q^{(1)}_{\ell,\infty}$ is equal to the sum of $Q^{(2)}_{\ell,\infty}$ and its mirror image and observing that the mirror image of $T^{(2)}_{\ell,\infty}$ is the temperature field resulting from the mirror image of $Q^{(2)}_{\ell,\infty}$, it is easy to see that T_ℓ in (3.12) should be equal to T_ℓ in (3.14). The second viewpoint in (3.13)–(3.14) will be adopted in the remainder of this chapter.

Remark 3.2. *Formulas similar to* (3.14) *exist for Dirichlet and Robin boundary conditions. For a Dirichlet boundary condition $T_\ell = 0$ on $\partial\Omega$,*

$$T_\ell(x,t) = T^{(2)}_{\ell,\infty}(x,t) - T^{(2)}_{\ell,\infty}(2x_e - x, t), \qquad x \leq x_e. \tag{3.15}$$

For a Robin boundary condition $\partial T_\ell/\partial x = bT_\ell$ at $x = x_e$, the formula becomes, see e.g. [Carslaw and Jaeger, 1959; Dias, 2016]

$$\begin{aligned} T_\ell(x,t) = {} & T^{(2)}_{\ell,\infty}(x,t) + T^{(2)}_{\ell,\infty}(2x_e - x, t) \\ & - 2\int_0^\infty be^{-bx'} T^{(2)}_{\ell,\infty}(2x_e - x + x', t)\, \mathrm{d}x', \qquad x \leq x_e. \end{aligned} \tag{3.16}$$

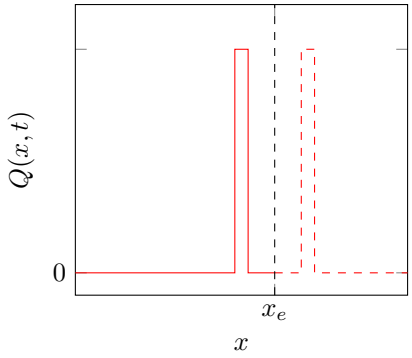

(a) The heat load Q_Ω (solid red line) and the extension $Q_\infty^{(1)}$ (both red lines) obtained by mirroring Q_Ω in the edge $x = x_e$.

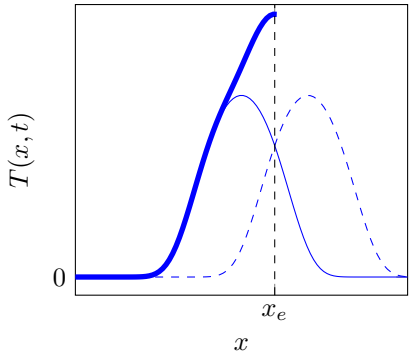

(b) The temperature field $T_\Omega(x,t)$ (thick solid line), $T_\infty^{(2)}$ (thin solid line) and its mirror image (dashed line).

Figure 3.2. An illustration of the method of images on $x \leq x_e$.

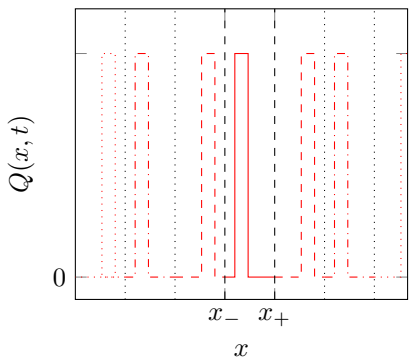

(a) The heat load Q_Ω (solid red line) and its mirror images (dashed red lines).

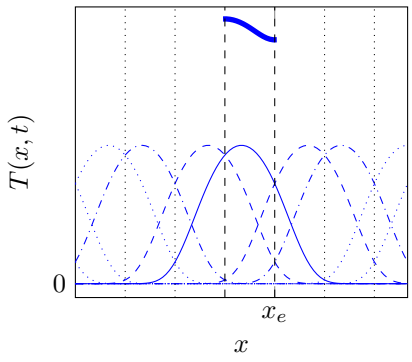

(b) The temperature field $T_\Omega(x,t)$ (thick solid line), $T_\infty^{(2)}$ (thin solid line) and its mirror images (dashed and dotted lines).

Figure 3.3. An illustration of the method of images on $x \in (x_-, x_+)$. Dashed lines indicate the reflections in the edges, dashed-dotted lines indicate the reflections of these reflections, and the dotted lines indicate higher-order reflections.

Now that the basics of the method of images have been introduced, the spatial coordinate y is again considered. For any domain $\Omega \subset \mathbb{R}^2$ inside which a heat load Q_Ω is applied, the heat load $Q_{\Omega,\infty}$ is thus defined by

$$Q_{\Omega,\infty}(x,y,t) := \begin{cases} Q_\Omega(x,y,t) & \text{for } (x,y) \in \Omega, \\ 0 & \text{for } (x,y) \notin \Omega. \end{cases} \tag{3.17}$$

The temperature field resulting from zero initial conditions and $Q_{\Omega,\infty}$ is denoted by $T_{\Omega,\infty}$. Expressions for T_Ω in terms of $T_{\Omega,\infty}$ are known for several choices of the spatial domain Ω.

A straightforward extension of the result for the semi-infinite line ℓ considers the semi-infinite plane $P := \{(x,y) \in \mathbb{R}^2 \mid x \leq x_e\}$. In this case

$$T_P(x,y,t) = T_{P,\infty}(x,y,t) + T_{P,\infty}(2x_e - x, y, t). \tag{3.18}$$

For the strip $S := \{(x,y) \in \mathbb{R}^2 \mid x_- \leq x \leq x_+\}$, there are infinitely many mirror images as Figure 3.3 illustrates for a similar one-dimensional problem. From this figure it is now easy to verify that, see also e.g. [Flint et al., 2018]

$$\begin{aligned} T_S(x,y,t) = &\sum_{n\in\mathbb{Z}} T_{S,\infty}(x + 2n(x_+ - x_-), y, t) \\ &+ \sum_{n\in\mathbb{Z}} T_{S,\infty}(2x_+ - x + 2n(x_+ - x_-), y, t). \end{aligned} \tag{3.19}$$

Note that if the strip S is wide enough, the solution $T_{S,\infty}$ will decay rapidly outside S and only a few terms in the infinite summation are needed to achieve an acceptable accuracy. For the rectangle $B := \{(x,y) \in \mathbb{R}^2 \mid x_- \leq x \leq x_+, y_- \leq y \leq y_+\}$, there are more types of reflections to consider, see e.g. [Flint et al., 2018]

$$\begin{aligned} T_B(x,y,t) = &\sum_{n,m\in\mathbb{Z}} T_{B,\infty}(x + 2n(x_+ - x_-), y + 2m(y_+ - y_-), t) \\ &+ \sum_{n,m\in\mathbb{Z}} T_{B,\infty}(2x_+ - x + 2n(x_+ - x_-), y + 2m(y_+ - y_-), t) \\ &+ \sum_{n,m\in\mathbb{Z}} T_{B,\infty}(x + 2n(x_+ - x_-), 2y_+ - y + 2m(y_+ - y_-), t) \\ &+ \sum_{n,m\in\mathbb{Z}} T_{B,\infty}(2x_+ - x + 2n(x_+ - x_-), 2y_+ - y + 2m(y_+ - y_-), t). \end{aligned} \tag{3.20}$$

However, it seems no such formulas are known for the disk D. In Section 3.3, a generalization of the method of images will be introduced such that it can be applied to the disk D as well.

3.2.3 The displacement potential

The displacement field $\mathbf{d}_\Omega(x,y,t)$ resulting from a temperature field $T_\Omega(x,y,t)$ can be obtained using the displacement potential $\Phi_\Omega(x,y,t)$, see e.g. [Nowacki, 1962; Kovalenko, 1969; Hetnarski and Eslami, 2009]. In this method, the displacement field $\mathbf{d}_\Omega$ is decomposed into two parts

$$\mathbf{d}_\Omega = \mathbf{d}_\Omega^{(T)} + \mathbf{d}_\Omega^{(BC)}, \tag{3.21}$$

where $\mathbf{d}_\Omega^{(T)}$ is equal to the gradient of the displacement potential Φ_Ω, i.e.

$$\mathbf{d}_\Omega^{(T)} = \nabla\Phi_\Omega. \tag{3.22}$$

It will be demonstrated later that the decomposition (3.21) is generally not unique.

Remark 3.3. *The curl associated to the displacement field* $\mathbf{d}_\Omega^{(T)}$ *is*

$$\frac{1}{2}\left(\frac{\partial d_{\Omega,y}^{(T)}}{\partial x} - \frac{\partial d_{\Omega,y}^{(T)}}{\partial x}\right) = \frac{1}{2}\left(\frac{\partial^2\Phi_\Omega}{\partial x\partial y} - \frac{\partial^2\Phi_\Omega}{\partial y\partial x}\right) = 0. \tag{3.23}$$

The part $\mathbf{d}_\Omega^{(T)}$ *is thus curl-free. At first sight,* (3.21) *thus resembles a Helmholtz-Hodge decomposition in a curl-free and divergence-free part, see e.g. [Bhatia et al., 2013]. However, the part* $\mathbf{d}_\Omega^{(BC)}$ *is typically not divergence-free, so that* (3.21) *does* not *represent a Helmholtz-Hodge decomposition.*

When substituting (3.5) into (3.3) and then substituting $\mathbf{d}_\Omega = \nabla\Phi_\Omega$, it follows that

$$\frac{EH}{2(1+\nu)}\nabla^2\nabla\Phi_\Omega + \frac{EH}{2(1-\nu)}\nabla\nabla^2\Phi_\Omega - k_\mathrm{s}\nabla\Phi_\Omega = \frac{\alpha EH}{1-\nu}\nabla T_\Omega, \tag{3.24}$$

where it was used that $\nabla\cdot\nabla = \nabla^2$ by definition. Using that $\nabla^2\nabla = \nabla\nabla^2$, this equation can be rewritten as

$$\frac{EH}{1-\nu^2}\nabla\nabla^2\Phi_\Omega - k_\mathrm{s}\nabla\Phi_\Omega = \frac{\alpha EH}{1-\nu}\nabla T_\Omega. \tag{3.25}$$

This equation is satisfied if Φ_Ω satisfied

$$\nabla^2\Phi_\Omega - \tilde{k}_\mathrm{s}\Phi_\Omega = (1+\nu)\alpha T_\Omega, \tag{3.26}$$

where

$$\tilde{k}_\mathrm{s} = \frac{k_\mathrm{s}(1-\nu^2)}{EH}. \tag{3.27}$$

It is thus possible to obtain a particular solution $\mathbf{d}_\Omega^{(T)}$ of (3.3) and (3.5) for a given temperature field T_Ω by finding a solution Φ_Ω of (3.26).

Note that (3.26) is a second-order PDE for Φ_Ω, which means that one boundary condition can be specified for Φ_Ω. However, there are two mechanical boundary conditions needed to define a unique displacement field $\mathbf{d}_\Omega$, see e.g. the boundary conditions (3.7). There is thus not sufficient freedom in the boundary conditions for (3.26) to assure that the displacement field $\mathbf{d}_\Omega^{(T)}$ resulting from Φ_Ω satisfies both mechanical boundary conditions. It is therefore not clear how the boundary conditions for (3.26) should be chosen (it seems this is also not addressed in the literature). As different choices for the boundary condition of Φ_Ω will typically lead to different decompositions (3.21), it is clear that the decomposition (3.21) is generally not unique. Typical choices for the boundary condition are the Dirichlet boundary condition $\Phi_\Omega = 0$ or the Neumann boundary condition $\partial\Phi_\Omega/\partial n = 0$, which correspond to zero tangential and normal components of $\mathbf{d}^{(T)}$, respectively, see (3.22). The choice of boundary conditions for (3.26) will be further addressed in Section 3.4.

Because the displacement field $\mathbf{d}_\Omega^{(T)}$ will typically not satisfy the boundary conditions, an additional correction $\mathbf{d}_\Omega^{(BC)}$ is used to assure that the resulting displacement field $\mathbf{d}_\Omega$ in (3.21) satisfies the desired boundary conditions. Because $\mathbf{d}_\Omega^{(T)}$ has been constructed to satisfy (3.3) and (3.5), it is easy to see that $\mathbf{d}_\Omega^{(BC)}$ is the solution of (3.3) and (3.5) with $T_\Omega \equiv 0$. The boundary conditions for $\mathbf{d}_\Omega^{(BC)}$ follow after substitution of (3.21) into the (mechanical) boundary conditions. For the boundary conditions (3.7), this leads to

$$\begin{bmatrix} \sigma_{\Omega,xx}^{(BC)} & \sigma_{\Omega,xy}^{(BC)} \\ \sigma_{\Omega,xy}^{(BC)} & \sigma_{\Omega,yy}^{(BC)} \end{bmatrix} \begin{bmatrix} n_x \\ n_y \end{bmatrix} = - \begin{bmatrix} \sigma_{\Omega,xx}^{(T)} & \sigma_{\Omega,xy}^{(T)} \\ \sigma_{\Omega,xy}^{(T)} & \sigma_{\Omega,yy}^{(T)} \end{bmatrix} \begin{bmatrix} n_x \\ n_y \end{bmatrix}, \tag{3.28}$$

where $\sigma_{\Omega,xx}^{(T)}, \sigma_{\Omega,xy}^{(T)}$, and $\sigma_{\Omega,yy}^{(T)}$ are the stress components resulting from $\mathbf{d}_\Omega^{(T)}$ and $\sigma_{\Omega,xx}^{(BC)}, \sigma_{\Omega,xy}^{(BC)}$, and $\sigma_{\Omega,yy}^{(BC)}$ are the stress components resulting from $\mathbf{d}_\Omega^{(BC)}$, see (3.8)–(3.10), and $\mathbf{n} = [n_x, n_y]^\top$ denotes the outward pointing normal.

On the unbounded domain $\Omega = \mathbb{R}^2$, the solution Φ_∞ of (3.26) is unique, see e.g. [Evans, 2010], and no correction for the boundary conditions is needed. Therefore, $\mathbf{d}_{\Omega,\infty}^{(BC)} = \mathbf{0}$ and

$$\mathbf{d}_{\Omega,\infty} = \nabla\Phi_{\Omega,\infty}. \tag{3.29}$$

3.2.4 Response to repetitive heat loads

In many manufacturing processes such as the wafer heating problem in Figure 3.1, the applied heat load Q_Ω consists of multiple similar passings. The only difference between two passings is a translation and/or rotation in space and a shift in time. Such translations and rotations are best described on $\mathbb{R}^2$ and not on a subdomain $\Omega \subset \mathbb{R}^2$. A heat load Q_Ω is thus called repetitive if its extension

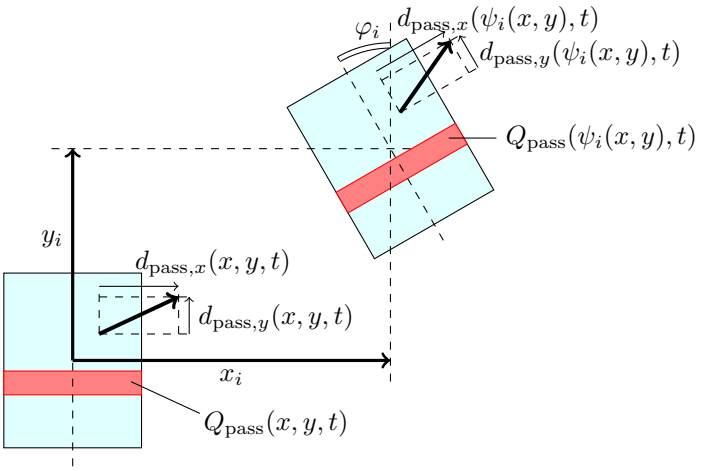

Figure 3.4. The mapping ψ_i represents a translation along (x_i, y_i) followed by a rotation over over φ_i.

$Q_{\Omega,\infty}$ to $\mathbb{R}^2$ as defined in (3.17) can be written as

$$Q_{\Omega,\infty}(x,y,t) = \sum_{i=1}^{N} Q_{\text{pass}}(\psi_i(x,y), t-\tau_i), \tag{3.30}$$

where $Q_{\text{pass}} : \mathbb{R}^2 \times \mathbb{R}_+ \to \mathbb{R}$ represents the heat load applied during one passing of the heat load, N is the total number of passings, τ_i describes a shift in time, and ψ_i describes a translation over (x_i, y_i) followed by a rotation over an angle φ_i, i.e.

$$\psi_i : \begin{bmatrix} x \\ y \end{bmatrix} \mapsto \begin{bmatrix} \cos(\varphi_i) & \sin(\varphi_i) \\ -\sin(\varphi_i) & \cos(\varphi_i) \end{bmatrix} \begin{bmatrix} x - x_i \\ y - y_i \end{bmatrix}. \tag{3.31}$$

The mapping ψ_i is illustrated in Figure 3.4. For the wafer heating application in Figure 3.1, Q_{pass} represents the heat load applied to a single field (one blue rectangle in Figure 3.1) that is scanned in the positive y-direction centered at $(x, y) = (0, 0)$, (x_i, y_i) is the center of i-th field, and $\varphi_i = i\pi \mod 2\pi$.

Because the heat equation (3.1) is linear and translation, rotation, and time invariant on $\mathbb{R}^2$, the temperature field $T_{\Omega,\infty}(x,y,t)$ resulting from zero initial conditions and the repetitive heat load $Q_{\Omega,\infty}(x,y,t)$ in (3.30) can be written as

$$T_{\Omega,\infty}(x,y,t) = \sum_{i=1}^{N} T_{\text{pass}}(\psi_i(x,y), t-\tau_i), \tag{3.32}$$

where $T_{\text{pass}}(x,y,t)$ is the temperature field resulting from zero initial conditions and the heat load $Q_{\text{pass}}(x,y,t)$.

The displacement field $\mathbf{d}_{\Omega,\infty}$ that results from the temperature field $T_{\Omega,\infty}$ in (3.32) can also be expressed in terms of the displacement field $\mathbf{d}_{\text{pass}}$ that results from T_{pass}. Recall from Subsection 3.2.3 that any heat-induced displacement field on $\mathbb{R}^2$ corresponds to a unique displacement potential. The displacement potentials that correspond to $\mathbf{d}_{\Omega,\infty}$ and $\mathbf{d}_{\text{pass}}$ are denoted by $\Phi_{\Omega,\infty}$ and Φ_{pass}, respectively. Recall that $\Phi_{\Omega,\infty}$ and Φ_{pass} are the solutions of (3.26) with T_Ω replaced by $T_{\Omega,\infty}$ and T_{pass}, respectively. Since equation (3.26) is also linear and invariant under translations and rotations in space and under shifts in time,

$$\Phi_{\Omega,\infty}(x,y,t) = \sum_{i=1}^{N} \Phi_{\text{pass}}(\psi_i(x,y), t-\tau_i). \tag{3.33}$$

Differentiating both sides of (3.33) w.r.t. (x,y) using the chain rule yields

$$\begin{aligned}\left[\tfrac{\partial \Phi_{\Omega,\infty}}{\partial x}(x,y,t) \quad \tfrac{\partial \Phi_{\Omega,\infty}}{\partial y}(x,y,t)\right] &= \left[d_{\Omega,\infty,x}(x,y,t) \quad d_{\Omega,\infty,y}(x,y,t)\right] = \\ \sum_{i=1}^{N} \left[d_{\text{pass},x}(\psi_i(x,y),t-\tau_i) \quad d_{\text{pass},y}(\psi_i(x,y),t-\tau_i)\right] &\begin{bmatrix} \cos(\varphi_i) & \sin(\varphi_i) \\ -\sin(\varphi_i) & \cos(\varphi_i)\end{bmatrix},\end{aligned} \tag{3.34}$$

where it was used that $\nabla \Phi_{\Omega,\infty} = \mathbf{d}_{\Omega,\infty} = [d_{\Omega,\infty,x}, d_{\Omega,\infty,y}]^\top$ and $\nabla \Phi_{\text{pass}} = \mathbf{d}_{\text{pass}} = [d_{\text{pass},x}, d_{\text{pass},y}]^\top$, see (3.29), and that ψ_i is given by (3.31). Taking the transpose of this equation now yields

$$\begin{bmatrix} d_{\Omega,\infty,x}(x,y,t) \\ d_{\Omega,\infty,y}(x,y,t)\end{bmatrix} = \sum_{i=1}^{N} \begin{bmatrix} \cos(\varphi_i) & -\sin(\varphi_i) \\ \sin(\varphi_i) & \cos(\varphi_i)\end{bmatrix} \begin{bmatrix} d_{\text{pass},x}(\psi_i(x,y),t-\tau_i) \\ d_{\text{pass},y}(\psi_i(x,y),t-\tau_i)\end{bmatrix}. \tag{3.35}$$

The appearance of the rotation matrix in (3.35) can also be understood because $d_{\text{pass},x}(\psi_i(x,y),t-\tau_i)$ and $d_{\text{pass},y}(\psi_i(x,y),t-\tau_i)$ denote the components of the displacement field w.r.t. a basis that is rotated over an angle φ_i, see Figure 3.4.

Note that it is often much easier to compute T_{pass} and $\mathbf{d}_{\text{pass}}$ resulting from Q_{pass} than the solution $\mathbf{d}_{\Omega,\infty}$ resulting from the complete heat load $Q_{\Omega,\infty}$ because $\mathbf{d}_{\text{pass}}$ typically needs to be computed over a smaller time window and requires a mesh of a smaller part of the spatial domain than $\mathbf{d}_{\Omega,\infty}$. This makes the construction of $T_{\Omega,\infty}$ and $\mathbf{d}_{\Omega,\infty}$ through (3.32) and (3.35) attractive in many applications such as the wafer heating problem considered in Section 3.5.

The problem that remains is to convert the solutions $T_{\Omega,\infty}$ and $\mathbf{d}_{\Omega,\infty}$ to solutions T_Ω and $\mathbf{d}_\Omega$ on the subdomain $\Omega \subset \mathbb{R}^2$. In Subsection 3.2.2, it was already demonstrated that the method of images describes how to convert $T_{\Omega,\infty}$ to T_Ω for certain subdomains Ω, but not for the circular domain in Figure 3.1. This question forms the main motivation for the developments in Sections 3.3 and 3.4.

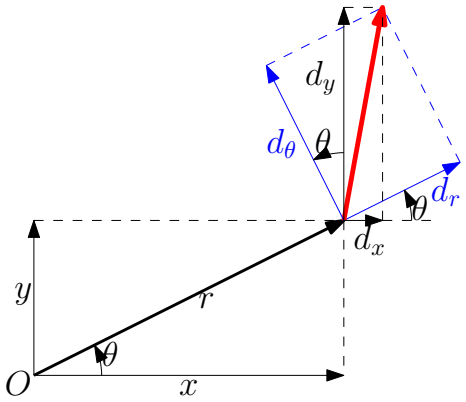

Figure 3.5. The displacement of a point $(x, y) = (r\cos(\theta), r\sin(\theta))$ (red arrow) can be described in terms of the Cartesian components $d_x(x, y)$ and $d_y(x, y)$ or in terms of the radial and transverse components $d_r(r, \theta)$ and $d_\theta(r, \theta)$.

3.2.5 Polar coordinates

To extend the method of images to the circular domain D, it will be convenient to use polar coordinates. These are related to the Cartesian coordinates (x, y) by

$$x = r\cos(\theta), \qquad y = r\sin(\theta). \tag{3.36}$$

The definition of these coordinates is also illustrated in Figure 3.5. The components of the displacement field $\mathbf{d}_\Omega$ in the radial and transversal directions are denoted by $d_{\Omega,r}(r, \theta)$ and $d_{\Omega,\theta}(r, \theta)$, respectively, and are related to the Cartesian components of the displacement field $d_{\Omega,x}(x, y)$ and $d_{\Omega,y}(x, y)$ by (see Figure 3.5)

$$\begin{bmatrix} d_{\Omega,r}(r,\theta) \\ d_{\Omega,\theta}(r,\theta) \end{bmatrix} = \begin{bmatrix} \cos(\theta) & \sin(\theta) \\ -\sin(\theta) & \cos(\theta) \end{bmatrix} \begin{bmatrix} d_{\Omega,x}(r\cos(\theta), r\sin(\theta)) \\ d_{\Omega,y}(r\cos(\theta), r\sin(\theta)) \end{bmatrix}. \tag{3.37}$$

Note that the equations for the thermomechanical model in (3.1), (3.3), and (3.5) have been written in terms of the Laplacian, gradient, and divergence operators, which can be expressed in the polar coordinate system as

$$\nabla^2 = \frac{1}{r}\frac{\partial}{\partial r}\left(r\frac{\partial}{\partial r}\right) + \frac{1}{r^2}\frac{\partial^2}{\partial\theta^2}, \quad \nabla = \begin{bmatrix} \frac{\partial}{\partial r} \\ \frac{1}{r}\frac{\partial}{\partial\theta} \end{bmatrix}, \quad \nabla\cdot\mathbf{d} = \frac{\partial d_r}{\partial r} + \frac{d_r}{r} + \frac{1}{r}\frac{\partial d_\theta}{\partial\theta}. \tag{3.38}$$

Equations (3.1), (3.3), and (3.5) thus remain valid when T_Ω, Q_Ω, $\mathbf{d}_\Omega$, and $\mathbf{f}$ are expressed in polar coordinates. This means that T_Ω and Q_Ω should be expressed in polar coordinates as $T_r(r, \theta, t) = T_\Omega(r\cos(\theta), r\sin(\theta), t)$ and $Q_r(r, \theta, t) = Q_\Omega(r\cos(\theta), r\sin(\theta), t)$, respectively, and that the displacement field $\mathbf{d}_\Omega$ and force vector $\mathbf{f}$ are now expressed in terms of their radial and transversal components, i.e. $\mathbf{d}_\Omega = [d_{\Omega,r}(r, \theta, t), d_{\Omega,\theta}(r, \theta, t)]^\top$ and $\mathbf{f} = [f_r(r, \theta, t), f_\theta(r, \theta, t)]^\top$.

Equation (3.22) can also be used to compute the radial and transverse components of $\mathbf{d}_\Omega^{(T)}$ when Φ_Ω is considered as a function of (r, θ, t) and the gradient is computed according to (3.38).

On the disk $D = \{(r, \theta) \in \mathbb{R} \times [0, 2\pi) \mid r < R\}$, the boundary conditions (3.6) and (3.7) become

$$kH\frac{\partial T}{\partial r}(r, \theta, t) = 0, \quad \sigma_{rr}(r, \theta, t) = \sigma_{r\theta}(r, \theta, t) = 0, \quad r = R, t \geq 0, \tag{3.39}$$

where the stress components σ_{rr} and $\sigma_{r\theta}$ are [Zienkiewicz et al., 2013]

$$\sigma_{rr} = \frac{E}{1-\nu^2}\left(\frac{\partial d_r}{\partial r} + \nu\frac{d_r}{r} + \nu\frac{1}{r}\frac{\partial d_\theta}{\partial \theta} - (1+\nu)\alpha T\right), \tag{3.40}$$

$$\sigma_{r\theta} = \frac{E}{2(1+\nu)}\left(\frac{1}{r}\frac{\partial d_r}{\partial \theta} - \frac{d_\theta}{r} + \frac{\partial d_\theta}{\partial r}\right). \tag{3.41}$$

3.3 A kernel representation for the method of images

The objective of this section is to express the solution T_Ω that satisfies (3.1) on the subdomain $\Omega \subset \mathbb{R}^2$ and the boundary condition (3.6) on $\partial\Omega$ in terms of the solution $T_{\Omega,\infty}$ that satisfies (3.1) on $\mathbb{R}^2$. Recall that T_Ω is the temperature field resulting from the heat load Q_Ω on Ω and that $T_{\Omega,\infty}$ is the temperature field resulting from $Q_{\Omega,\infty}$ which is the extension of Q_Ω to $\mathbb{R}^2$ according to (3.17). Since $Q_{\Omega,\infty}$ is equal to Q_Ω on Ω, the restriction of $T_{\Omega,\infty}$ to Ω will satisfy (3.1) but not the boundary condition (3.6). It is therefore natural to write

$$T_\Omega(x, y, t) = T_{\Omega,\infty}(x, y, t) + \tilde{T}_\Omega(x, y, t), \qquad (x, y) \in \Omega, \tag{3.42}$$

where the function $\tilde{T}_\Omega(x, y, t)$ is needed to satisfy the boundary condition (3.6). In particular, it is now easy to see that $\tilde{T}_\Omega$ is the solution of

$$\rho cH\frac{\partial \tilde{T}_\Omega}{\partial t} = kH\nabla^2\tilde{T}_\Omega - h\tilde{T}_\Omega, \qquad (x, y) \in \Omega, \tag{3.43}$$

$$\frac{\partial \tilde{T}_\Omega}{\partial n} = -\frac{\partial T_{\Omega,\infty}}{\partial n}, \qquad (x, y) \in \partial\Omega. \tag{3.44}$$

On the subdomains $\Omega \subset \mathbb{R}^2$ for which it is known how to apply the method of images, the correction $\tilde{T}_\Omega$ can be expressed in terms of $T_{\Omega,\infty}$, see (3.18)–(3.20).

3.3.1 Kernel representations

The idea is now to generalize this observation by writing

$$\tilde{T}_\Omega(x, y, t) = \iint_{\mathbb{R}^2\setminus\Omega} W_\Omega(x, y, x', y')T_{\Omega,\infty}(x', y', t)\ \mathrm{d}x'\ \mathrm{d}y', \tag{3.45}$$

for some kernel $W_\Omega : \Omega \times (\mathbb{R}^2 \backslash \Omega) \to \mathbb{R}$.

Proposition 3.4 now gives conditions on the kernel W_Ω that assure that $\tilde{T}_\Omega$ in (3.45) is indeed the solution of (3.43)–(3.44).

Proposition 3.4. *If the the kernel $W_\Omega : \Omega \times (\mathbb{R}^2 \backslash \Omega) \to \mathbb{R}$ satisfies*

$$\nabla'^2 W_\Omega(x, y, x', y') = \nabla^2 W_\Omega(x, y, x', y'), \tag{3.46}$$

for $(x, y) \in \Omega$ and $(x', y') \in \mathbb{R}^2 \backslash \Omega$,

$$W_\Omega(x, y, x', y') = \nabla' W_\Omega(x, y, x', y') \cdot \mathbf{n}(x', y') = 0, \tag{3.47}$$

for $(x, y) \in \Omega$ and $(x', y') \in \partial\Omega$, and

$$\nabla W_\Omega(x, y, x', y') \cdot \mathbf{n}(x, y) = \nabla' \left(\delta(x - x')\delta(y - y')\right) \cdot \mathbf{n}(x, y), \tag{3.48}$$

for $(x, y) \in \partial\Omega$ and $(x', y') \in \Omega$, then $\tilde{T}_\Omega$ in (3.45) satisfies (3.43)–(3.44).

Here, ∇' and ∇'^2 denote the gradient and Laplacian w.r.t. (x', y'). Note that this result involves the gradient of the Dirac delta in (3.48). As will become clear from the proof below, this expression should be interpreted in the weak sense, meaning that for any $\Omega' \subseteq \mathbb{R}^2$ and any test function $f : \Omega' \to \mathbb{R}$

$$\iint_{\Omega'} f(x', y') \nabla' \left(\delta(x')\delta(y')\right) \, \mathrm{d}x' \, \mathrm{d}y' = -\iint_{\Omega'} \left(\nabla' f(x', y')\right) \delta(x')\delta(y') \, \mathrm{d}x' \, \mathrm{d}y'. \tag{3.49}$$

Proof. It will be shown that substitution of (3.45) in the LHS and RHS of (3.43) and (3.44) yields the same results when (3.46)–(3.48) hold.

Substitution of (3.45) in the LHS of (3.43) yields

$$\begin{aligned}
\rho c H \frac{\partial \tilde{T}_\Omega}{\partial t}(x, y, t) &= \iint_{\mathbb{R}^2 \backslash \Omega} W_\Omega(x, y, x', y') \rho c H \frac{\partial T_{\Omega,\infty}}{\partial t}(x', y', t) \, \mathrm{d}x' \, \mathrm{d}y' \\
&= \iint_{\mathbb{R}^2 \backslash \Omega} W_\Omega(x, y, x', y') \left(kH \nabla'^2 T_{\Omega,\infty}(x', y', t) - h T_{\Omega,\infty}(x', y', t)\right) \, \mathrm{d}x' \, \mathrm{d}y' \\
&= kH \iint_{\mathbb{R}^2 \backslash \Omega} W_\Omega(x, y, x', y') \nabla'^2 T_{\Omega,\infty}(x', y', t) \, \mathrm{d}x' \, \mathrm{d}y' - h\tilde{T}_\Omega(x, y, t),
\end{aligned} \tag{3.50}$$

where the second identity follows because $T_{\Omega,\infty}$ satisfies (3.1) with the heat load $Q_{\Omega,\infty}$ which is zero outside Ω by its definition in (3.17). Inserting (3.45) in the RHS of (3.43) yields

$$\begin{aligned}
&kH \nabla^2 \tilde{T}_\Omega(x, y, t) - h\tilde{T}_\Omega(x, y, t) = \\
&\qquad kH \iint_{\mathbb{R}^2 \backslash \Omega} \nabla^2 W_\Omega(x, y, x', y') T_{\Omega,\infty}(x', y', t) \, \mathrm{d}x' \, \mathrm{d}y' - h\tilde{T}_\Omega(x, y, t).
\end{aligned} \tag{3.51}$$

To see that the expressions on the RHS of (3.50) and (3.51) are equal, note that one of Green's identities, see e.g. [Evans, 2010], shows that

$$\begin{aligned}
&\iint_{\mathbb{R}^2\setminus\Omega} W_\Omega \nabla'^2 T_{\Omega,\infty}\, \mathrm{d}x'\, \mathrm{d}y' = \\
&\quad \int_{\partial\Omega} (W_\Omega \nabla' T_{\Omega,\infty} - T_{\Omega,\infty}\nabla' W_\Omega)\cdot \mathbf{n}\, \mathrm{d}\ell' + \iint_{\mathbb{R}^2\setminus\Omega} \left(\nabla'^2 W_\Omega\right) T_{\Omega,\infty}\, \mathrm{d}x'\, \mathrm{d}y' \\
&\qquad = \iint_{\mathbb{R}^2\setminus\Omega} (\nabla'^2 W_\Omega) T_{\Omega,\infty}\, \mathrm{d}x'\, \mathrm{d}y' = \iint_{\mathbb{R}^2\setminus\Omega} (\nabla^2 W_\Omega) T_{\Omega,\infty}\, \mathrm{d}x'\, \mathrm{d}y', \quad (3.52)
\end{aligned}$$

where the dependence of W_Ω on (x, y, x', y') and of $T_{\Omega,\infty}$ on (x', y', t) has been omitted, and $\mathbf{n} = \mathbf{n}(x', y')$ denotes the outward pointing normal of Ω which is the inward pointing normal of $\mathbb{R}^2\setminus\Omega$. The second identity in (3.52) follows because (3.47) shows that the boundary terms vanish and the last identity in (3.52) follows from (3.46). It thus follows that $\tilde{T}_\Omega$ in (3.45) satisfies (3.43).

For the boundary condition (3.44), note that the LHS of (3.44) can be rewritten as

$$\begin{aligned}
\frac{\partial \tilde{T}_\Omega}{\partial n}(x, y, t) &= \nabla \tilde{T}_\Omega(x, y, t)\cdot \mathbf{n}(x, y) \\
&= \iint_{\mathbb{R}^2\setminus\Omega} T_{\Omega,\infty}(x', y', t) \nabla W_\Omega(x, y, x', y')\cdot \mathbf{n}(x, y)\, \mathrm{d}x'\, \mathrm{d}y' \\
&= \iint_{\mathbb{R}^2\setminus\Omega} T_{\Omega,\infty}(x', y', t) \nabla'(\delta(x - x')\delta(y - y'))\, \mathrm{d}x'\, \mathrm{d}y' \cdot \mathbf{n}(x, y). \quad (3.53)
\end{aligned}$$

For the RHS of (3.44), note that

$$\begin{aligned}
-\frac{\partial T_{\Omega,\infty}}{\partial n}(x, y, t) &= -\nabla T_{\Omega,\infty}(x, y, t)\cdot \mathbf{n}(x, y) \\
&= -\iint_{\mathbb{R}^2\setminus\Omega} \delta(x - x')\delta(y - y') \nabla' T_{\Omega,\infty}(x', y', t)\, \mathrm{d}x'\, \mathrm{d}y' \cdot \mathbf{n}(x, y) \\
&= \iint_{\mathbb{R}^2\setminus\Omega} T_{\Omega,\infty}(x', y', t) \nabla'(\delta(x - x')\delta(y - y'))\, \mathrm{d}x'\, \mathrm{d}y' \cdot \mathbf{n}(x, y), \quad (3.54)
\end{aligned}$$

where the last identity follows from the definition of the derivative of the Dirac delta. The function $\tilde{T}_\Omega$ in (3.45) thus satisfies the boundary condition (3.44). □

Remark 3.5. *It is easy to verify that for the Dirichlet boundary condition* $T_\Omega(x, y, t) = 0$ *for* $(x, y) \in \partial\Omega$, (3.44) *changes to* $\tilde{T}_\Omega(x, y, t) = -T_{\Omega,\infty}(x, y, t)$ *for* $(x, y) \in \partial\Omega$ *and that the condition* (3.48) *changes to*

$$W_\Omega(x, y, x', y') = -\delta(x - x')\delta(y - y'), \qquad (x, y) \in \partial\Omega. \quad (3.55)$$

An equation of the form (3.46) is called ultrahyperbolic. For the case considered here where the W_Ω depends on four variables, it is also known as John's equation after the paper [John, 1938]. There is a correspondence between solutions of (3.46) and functions $\mathbb{R}^3 \to \mathbb{R}$ through the Radon transform and a mapping from the lines in $\mathbb{R}^3$ to points in $\mathbb{R}^4$ [John, 1938; Kurusa, 1991]. This implies that the existence and uniqueness of solutions for certain boundary conditions is not guaranteed. In particular, it is generally *not* possible to prescribe the values of W_Ω on an arbitrary 3-dimensional manifold.

Because the considered domains Ω possesses certain symmetries, physical insight allows the elimination of one of the independent variables. This reduces the ultrahyperbolic equation to a (normal) hyperbolic equation for which the existence and uniqueness of solutions is well understood, see e.g. [Evans, 2010]. This approach will now be demonstrated for the semi-infinite plane, the strip, and the rectangle, for which it is known how to apply the method of images, see (3.18)–(3.20). After that, the problem for the disk will be studied.

3.3.2 Solutions for specific domains

The semi-infinite plane

Since the semi-infinite plane $P = \{(x, y) \in \mathbb{R}^2 \mid x \leq x_e\}$ is invariant under translation in the y-direction, the kernel W_P is only a function of x, x', and $\hat{y} := y - y'$, i.e. $W_P = W_P(x, y - y', x')$. The conditions (3.46)–(3.48) become

$$\frac{\partial W_P}{\partial x'^2}(x, \hat{y}, x') = \frac{\partial^2 W_P}{\partial x^2}(x, \hat{y}, x'), \qquad x < x_e, \hat{y} \in \mathbb{R}, x' > x_e, \quad (3.56)$$

$$W_P(x, \hat{y}, x_e) = \frac{\partial W_P}{\partial x'}(x, \hat{y}, x_e) = 0, \qquad x < x_e, \hat{y} \in \mathbb{R}, \quad (3.57)$$

$$\frac{\partial W_P}{\partial x}(x_e, \hat{y}, x') = \frac{\partial \delta}{\partial x'}(x_e - x')\delta(\hat{y}), \qquad \hat{y} \in \mathbb{R}, x' \geq x_e. \quad (3.58)$$

These equations can now be viewed as a wave equation where x' has the role of time and x and $\hat{y}$ are the coordinates for the spatial domain. Equation (3.56) shows that the wave speed is 1, equation (3.57) that the initial conditions are zero, and equation (3.58) that a pulse is applied at the initial time $x' = x_e$ in the point $(x, \hat{y}) = (x_e, 0)$. To understand the result of the applied pulse with the shape of the derivative of a Dirac delta better, it is useful to first consider the following finite-dimensional example.

Example 3.6. *Consider the following mass-spring-damper system*

$$m\ddot{x}(t) + b\dot{x}(t) + kx(t) = F(t), \qquad x(0) = \dot{x}(0) = 0, \quad (3.59)$$

where $x(t)$ denotes the position of the mass, the dot denotes differentiation w.r.t. the time t, m, b, and k are the mass, the damping coefficient, and the spring

constant, respectively, and $F(t) = F_0\dot{\delta}(t)$ *is the applied force in the shape of the derivative of the Dirac delta. Because* (3.59) *contains a Dirac delta, solutions have to be considered in the weak sense. The first equation in* (3.59) *is therefore multiplied by a test function* $f(t)$ *and integrated over the time interval* $t \in [0, \varepsilon]$

$$\int_0^\varepsilon f(t)\left(m\ddot{x}(t) + b\dot{x}(t) + kx(t)\right)\,\mathrm{d}t = \int_0^\varepsilon f(t)F(t)\,\mathrm{d}t. \tag{3.60}$$

By definition of the derivative of the Dirac delta, the RHS of (3.60) *is equal to* $-\dot{f}(0)F_0$*. The LHS of* (3.60) *can be rewritten using integration by parts twice*

$$\begin{aligned} &f(t)\left(m\dot{x}(t) + bx(t)\right)\Big|_{t=0}^{\varepsilon} + \int_0^\varepsilon \left(-\dot{f}(t)m\dot{x}(t) + \left(-b\dot{f}(t) + kf(t)\right)x(t)\right)\,\mathrm{d}t \\ &= \left(f(t)\left(m\dot{x}(t) + bx(t)\right) - \dot{f}(t)mx(t)\right)\Big|_{t=0}^{\varepsilon} \\ &\quad + \int_0^\varepsilon \left(m\ddot{f}(t) - b\dot{f}(t) + kf(t)\right)x(t)\,\mathrm{d}t = -\dot{f}(0)F_0. \end{aligned} \tag{3.61}$$

The initial conditions in (3.59) *show that the boundary terms in* $t = 0$ *vanish. Since* $f(t)$ *is a smooth test function, the integrand is bounded. The remaining integral over* t *thus vanishes when taking the limit* $\varepsilon \downarrow 0$*. Using that* $f(t)$ *and* $\dot{f}(t)$ *are continuous in* $t = 0$*, it now follows that*

$$f(0)\left(m\lim_{\varepsilon\downarrow 0}\dot{x}(\varepsilon) + b\lim_{\varepsilon\downarrow 0}x(\varepsilon)\right) - \dot{f}(0)m\lim_{\varepsilon\downarrow 0}x(\varepsilon) = -\dot{f}(0)F_0. \tag{3.62}$$

Since this equation must hold for any test function $f(t)$*, the factors in front of* $\dot{f}(0)$ *and* $f(0)$ *should match, which implies that*

$$\lim_{\varepsilon\downarrow 0}x(\varepsilon) = \frac{F_0}{m}, \qquad \lim_{\varepsilon\downarrow 0}\dot{x}(\varepsilon) = \frac{-b}{m}\lim_{\varepsilon\downarrow 0}x(\varepsilon) = \frac{-bF_0}{m^2}. \tag{3.63}$$

The applied force in the shape of the derivative of a Dirac delta is thus equivalent to a jump in the state $(x(t), \dot{x}(t))$*. Note that without damping, i.e. when* $b = 0$*, the jump occurs only in the position* $x(t)$ *and does not affect the velocity* $\dot{x}(t)$ *and that for a first-order system, i.e. when* $m = 0$*, the solution is not well-defined.*

The result of the Dirac delta in the boundary condition (3.58) can be studied in a similar way as in Example 3.6. To this end, (3.56) is multiplied by a test function $f = f(x, \hat{y}, x')$ and integrated over $(x, \hat{y}, x') \in P \times [x_e, x_e + \varepsilon]$. This leads to

$$\begin{aligned} &\iint_P \left(f\frac{\partial W_P}{\partial x'} - \frac{\partial f}{\partial x'}W_P\right)\mathrm{d}x\,\mathrm{d}\hat{y}\Big|_{x'=x_e}^{x_e+\varepsilon} + \int_{x_e}^{x_e+\varepsilon}\iint_P \frac{\partial^2 f}{\partial x'^2}W_P\,\mathrm{d}x\,\mathrm{d}\hat{y}\,\mathrm{d}x' \\ &= -\int_{\mathbb{R}} \frac{\partial f}{\partial x'}\Big|_{(x,x')=(x_e,x_e)}\delta(\hat{y})\,\mathrm{d}\hat{y} - \int_{x_e}^{x_e+\varepsilon}\iint_P \frac{\partial f}{\partial x}\frac{\partial W_P}{\partial x}\,\mathrm{d}x\,\mathrm{d}\hat{y}\,\mathrm{d}x', \end{aligned} \tag{3.64}$$

where the LHS $f\partial^2 W_P/\partial x'^2$ has been rewritten by applying integration by parts over x' twice and the RHS $f\partial^2 W_P/\partial x^2$ has been rewritten using one integration by parts over x, the boundary condition (3.58), and the definition of derivative of the Dirac delta in (3.49). When taking the limit $\varepsilon \downarrow 0$, the integrals over x' converge to zero. Since (3.64) must hold for any test function f, the factors in front of f and $\partial f/\partial x'$ must be zero. Using (3.57) it thus follows that

$$\lim_{\varepsilon\downarrow 0} W_P(x,\hat{y},x_e+\varepsilon) = \delta(x-x_e)\delta(\hat{y}), \qquad \lim_{\varepsilon\downarrow 0} \frac{\partial W_P}{\partial x'}(x,\hat{y},x_e+\varepsilon) = 0. \quad (3.65)$$

For $x' > x_e$, the boundary condition (3.58) is equivalent to

$$\frac{\partial W_P}{\partial x}(x_e,\hat{y},x') = 0, \qquad \hat{y}\in\mathbb{R}, x' \geq x_e. \quad (3.66)$$

It thus follows that after the application of the Dirac delta, (3.57) and (3.58) are equivalent to (3.65) and (3.66).

The solution of (3.56), (3.65), and (3.66) is thus given by a pulse travelling in the negative x-direction, i.e.

$$W_P(x,\hat{y},x') = \delta((x_e-x)+(x_e-x'))\delta(\hat{y}). \quad (3.67)$$

Inserting this expression into (3.45) using that $\hat{y} = y - y'$ shows that $\tilde{T}_P(x,y,t) = T_{P,\infty}(2x_e - x, y, t)$, so that (3.42) is indeed the same as (3.18).

The strip

The strip $S = \{(x,y)\in\mathbb{R}^2 \mid x_- \leq x \leq x_+\}$ is also invariant under translation in the y-direction. Therefore, $W_S = W_S(x,\hat{y},x')$, where, just as before, $\hat{y} = y - y'$. Inspired by the form of W_P in (3.67), it is attempted to write W_S as

$$W_S(x,\hat{y},x') = W_{S,x}(x,x')W_{S,y}(\hat{y}). \quad (3.68)$$

On the boundary $x\in\{x_-,x_+\}$, condition (3.48) takes the form

$$\frac{\partial W_S}{\partial x} = \frac{\partial}{\partial x'}\left(\delta(x-x')\delta(\hat{y})\right) = \frac{\partial\delta}{\partial x'}(x-x')\delta(\hat{y}), \quad (3.69)$$

so that substitution of (3.68) into (3.69) shows that $W_{S,y}(\hat{y}) = \delta(\hat{y})$. The conditions (3.46)–(3.48) now lead to the following initial value problem for $W_{S,x}(x,x')$

$$\frac{\partial W_{S,x}}{\partial x'^2}(x,x') = \frac{\partial^2 W_{S,x}}{\partial x^2}(x,x'), \qquad x\in(x_-,x_+), x'\in\mathbb{R}\backslash(x_-,x_+) \quad (3.70)$$

$$W_{S,x}(x,x') = \frac{\partial W_{S,x}}{\partial x'}(x,x') = 0, \qquad x\in(x_-,x_+), x'\in\{x_-,x_+\}, \quad (3.71)$$

$$\frac{\partial W_{S,x}}{\partial x}(x,x') = \frac{\partial\delta}{\partial x'}(x-x'), \qquad x\in\{x_-,x_+\}, x'\in\mathbb{R}\backslash(x_-,x_+). \quad (3.72)$$

Note that the 'time' x' is now an element of a disconnected set which consists of two connected parts $x' < x_-$ and $x' > x_+$. Solutions on these two parts can be constructed independently. The solution on $x' < x_-$ is denoted by $W_- = W_-(x, \hat{y}, x')$ and the solution on $x' > x_+$ is denoted by $W_+ = W_+(x, \hat{y}, x')$. By considering the weak form of (3.70)–(3.72) similarly as for the semi-infinite plane P in (3.64), it can be shown that pulse in (3.72) is equivalent to a change in initial conditions. The solution W_+ is thus a δ-pulse starting in the point $x = x_+$ at time $x' = x_+$ which travels in the negative x-direction. This wave is reflected at the other boundary $x = x_-$ at time $x' = 2x_+ - x_-$, which is again reflected at $x = x_+$ at time $x' = 3x_+ - 2x_-$, and so on. The solution is also illustrated in the top part of Figure 3.6. It thus follows that

$$W_+(x, x') = \sum_{n=0}^{\infty} \delta(2x_+ - x - x' + 2n(x_+ - x_-)) + \sum_{n=1}^{\infty} \delta(x - x' + 2n(x_+ - x_-)), \quad (3.73)$$

Similarly, the solution W_- is also a Dirac delta pulse that starts traveling in the positive x-direction in the point $x = x_-$ at time $x' = x_-$. This pulse arrives at $x = x_+$ at time $x' = x_- - (x_+ - x_-)$, and its reflection again arrives at $x = x_-$ at time $x' = x_- - 2(x_+ - x_-)$, and so on. The solution W_- is thus obtained as (see also the lower part of Figure 3.6)

$$W_-(x, x') = \sum_{n=1}^{\infty} \delta(2x_+ - x - x' - 2n(x_+ - x_-)) + \sum_{n=1}^{\infty} \delta(x - x' - 2n(x_+ - x_-)). \quad (3.74)$$

Combining the two solutions W_+ and W_- on the disconnected parts yields

$$W_{S,x}(x, x') = \sum_{n\in\mathbb{Z}} \delta(2x_+ - x - x' + 2n(x_+ - x_-)) + \sum_{n\in\mathbb{Z}, n\neq 0} \delta(x - x' - 2n(x_+ - x_-)). \quad (3.75)$$

The kernel W_S can now be obtained from (3.68) using that $W_{S,y}(\hat{y}) = \delta(\hat{y})$. It is now easy to verify that the substitution of the resulting expression for W_S into (3.45) and the thus obtained expression for $\tilde{T}_S$ into (3.42) yields the expression for T_S as in (3.19).

The rectangle

For the rectangle $B = \{(x, y) \in \mathbb{R}^2 \mid x_- \leq x \leq x_+, y_- \leq y \leq y_+\}$, there is no translation invariance. It is therefore not possible to reduce the PDE (3.46) to a PDE in three or less spatial variables. Explicitly solving the PDEs (3.46)-(3.47)

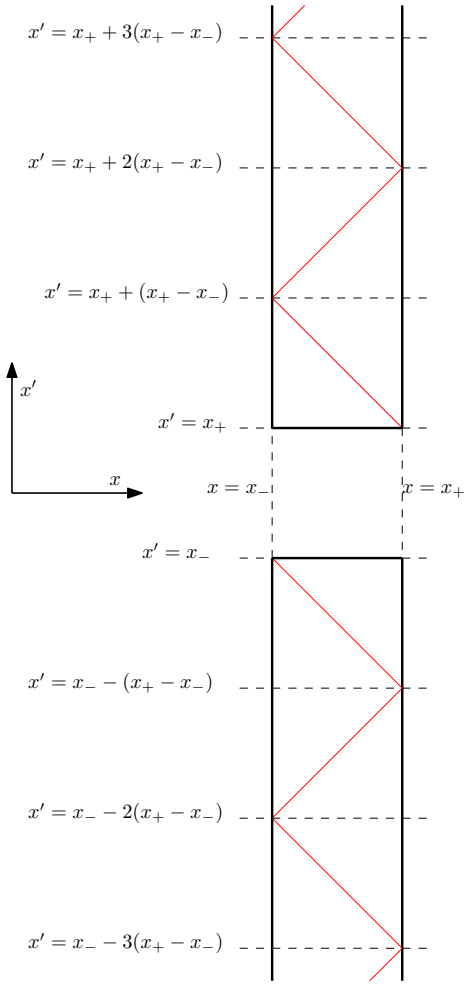

Figure 3.6. The waves $W_+(x, x')$ and $W_-(x, x')$ reflecting within $x \in (x_-, x_+)$

and (3.48) is thus difficult. However, based on the expression for T_B in (3.20) the kernel W_B is known to be obtained easily. It can be verified that this kernel indeed satisfies the conditions (3.46)–(3.48).

3.3.3 Solution for the disk

For the disk $D = \{(x, y) \in \mathbb{R}^2 \mid x^2 + y^2 < R^2\}$, it is more convenient to use the polar coordinates (r, θ) as defined in (3.36). Because the disk $r < R$ is invariant under rotations (i.e. shifts in the θ-direction), it follows that $W_D(r, \theta, r', \theta') = W_D(r, \hat{\theta}, r')$ with $\hat{\theta} := \theta - \theta'$. Conditions (3.46)–(3.47) and (3.48) now become

$$\frac{1}{r'}\frac{\partial}{\partial r'}\left(r'\frac{\partial W_D}{\partial r'}\right) + \frac{1}{r'^2}\frac{\partial^2 W_D}{\partial \hat{\theta}^2} = \frac{1}{r}\frac{\partial}{\partial r}\left(r\frac{\partial W_D}{\partial r}\right) + \frac{1}{r^2}\frac{\partial^2 W_D}{\partial \hat{\theta}^2}, \tag{3.76}$$

$$W_D(r, \hat{\theta}, R) = \frac{\partial W_D}{\partial r'}(r, \hat{\theta}, R) = 0, \tag{3.77}$$

$$\frac{\partial W_D}{\partial r}(R, \hat{\theta}, r') = \frac{1}{r'}\frac{\partial \delta}{\partial r'}(R - r')\delta(\hat{\theta}), \qquad r < R, 0 \le \hat{\theta} \le 2\pi, r' > R. \tag{3.78}$$

Remark 3.7. *The factor* $1/r'$ *in* (3.78) *appears because of the transformation to polar coordinates, see e.g. [Grubb, 2009]. One can see that this factor is necessary because it now holds that for any test function* $f = f(r, \theta)$

$$\begin{aligned}\int_0^\infty \int_0^{2\pi} f(r', \theta')\frac{1}{r'}\frac{\partial \delta}{\partial r'}(r - r')\delta(\theta - \theta')r' \,\mathrm{d}\theta' \,\mathrm{d}r' = \\ -\int_0^\infty \int_0^{2\pi} \frac{\partial f}{\partial r}(r', \theta')\delta(r - r')\delta(\theta - \theta') \,\mathrm{d}r' \,\mathrm{d}\theta' = -\frac{\partial f}{\partial r}(r, \theta).\end{aligned} \tag{3.79}$$

To remove the derivative of the Dirac delta in (3.78), the weak form of (3.76)–(3.78) is derived by multiplying (3.76) by $f(r, \hat{\theta}, r')r'r$, where f is a test function, and then integrating over $(r, \hat{\theta}, r') \in (0, R) \times (0, 2\pi) \times (R, R + \varepsilon)$. This leads to

$$\begin{aligned}\int_0^{2\pi} \int_0^R \left[f\frac{\partial W_D}{\partial r'} - \frac{\partial f}{\partial r'}W_D\right] r'r \,\mathrm{d}r \,\mathrm{d}\hat{\theta}\Big|_{r'=R}^{R+\varepsilon} \\ + \int_R^{R+\varepsilon} \int_0^{2\pi} \int_0^R \left[\frac{1}{r'}\frac{\partial}{\partial r'}\left(r'\frac{\partial f}{\partial r'}\right) + \frac{1}{r'^2}\frac{\partial^2 f}{\partial \hat{\theta}^2}\right] W_D r'r \,\mathrm{d}r \,\mathrm{d}\hat{\theta} \,\mathrm{d}r' \\ = -\int_0^{2\pi} \frac{\partial f}{\partial r'}\Big|_{(r,r')=(R,R)} R\delta(\hat{\theta}) \,\mathrm{d}\hat{\theta} \\ - \int_R^{R+\varepsilon} \int_0^{2\pi} \int_0^R \left(\frac{\partial f}{\partial r}\frac{\partial W_D}{\partial r} + \frac{1}{r^2}\frac{\partial f}{\partial \hat{\theta}}\frac{\partial W_D}{\partial \hat{\theta}}\right) r'r \,\mathrm{d}r \,\mathrm{d}\hat{\theta} \,\mathrm{d}r',\end{aligned} \tag{3.80}$$

where the terms on the LHS have been rewritten integrating by parts twice over r' and $\hat{\theta}$ (the boundary terms for the integration by parts over $\hat{\theta}$ vanish

because of the periodicity in the $\hat{\theta}$-direction), and the terms on the RHS have been rewritten using one integration by parts, the boundary condition (3.78), and the definition of the derivative of the Dirac delta. Similarly as before, the integrals over r' vanish when taking the limit $\varepsilon \downarrow 0$. Matching the boundary terms multiplied by $\partial f/\partial r'$ and f using (3.77), it follows that

$$\lim_{\varepsilon \downarrow 0} W_D(r, \hat{\theta}, R+\varepsilon) = \frac{1}{R}\delta(r-R)\delta(\hat{\theta}), \qquad \lim_{\varepsilon \downarrow 0} \frac{\partial W_D}{\partial r'}(r, \hat{\theta}, R+\varepsilon) = 0. \quad (3.81)$$

Furthermore, for $r' > R$ the boundary condition (3.78) becomes

$$\frac{\partial W_D}{\partial r}(R, \hat{\theta}, r') = 0. \quad (3.82)$$

The initial and boundary conditions (3.77) and (3.78) are thus equivalent to (3.81) and (3.82) for $r' > R$.

To compute the solution to (3.76) with boundary conditions (3.81) and (3.82), r and $\hat{\theta}$ are considered as the 'spatial' coordinates and r' as the 'temporal' coordinate. A closed-form analytic expression can now be obtained by writing the kernel W_D as linear combination of the eigenfunctions of the Laplacian on the disk $r \leq R$, $0 \leq \hat{\theta} \leq 2\pi$ satisfying zero Neumann boundary conditions. To avoid very narrow features that are not clearly visible and to improve convergence, the Dirac delta in the initial condition (3.81) is replaced by the function $\delta_\gamma(r-R, \hat{\theta})$ where $\gamma > 0$ is a smoothing parameter. In particular, $\delta_\gamma(r-R, \hat{\theta})$ is defined as

$$\delta_\gamma(r-R, \hat{\theta}) = \frac{1}{2\gamma^2 R^2}\left(1+\cos\left(\frac{\pi(r-R)}{\gamma R}\right)\right)\left(1+\cos\left(\frac{\pi\hat{\theta}}{\gamma}\right)\right), \quad (3.83)$$

for $r \in [(1-\gamma)R, R]$ and $\hat{\theta} \in [-\gamma, \gamma]$ and zero otherwise. Note that $\delta_\gamma(r, \hat{\theta})$ approaches the Dirac in (3.81) for $\gamma \downarrow 0$. The derivation in Appendix A.1 now shows that the kernel $W_{D,\gamma}(r, \hat{\theta}, r')$ satisfying (3.76), (3.81), and (3.82) with the Dirac delta is replaced by $\delta_\gamma(r-R, \hat{\theta})$ in (3.83) can be written as

$$W_{D,\gamma}(r, \hat{\theta}, r') = \sum_{n=0}^{\infty}\sum_{m=1}^{\infty} A_{n,m}(\gamma) J_n\left(\beta_{n,m}\frac{r}{R}\right)\cos(n\hat{\theta}) J_n\left(\beta_{n,m}\frac{r'}{R}\right), \quad (3.84)$$

where J_n is the Bessel function of the first kind of order n, $\beta_{n,m}$ is the m-th (nonnegative real) root of $\partial J_n(r)/\partial r = 0$, and the coefficients $A_{n,m}(\gamma)$ depend on the smoothing parameter γ. It is shown in Appendix A.1 that the coefficients $A_{n,m}(\gamma)$ in (3.84) in $\gamma = 0$ are for $(n, m) = (0, 1)$

$$A_{0,1}(0) = \frac{1}{\pi R^2}, \quad (3.85)$$

and for $(n, m) \neq (0, 1)$

$$A_{n,m}(0) = \frac{1}{\pi R^2}\frac{2\beta_{n,m}^2}{\epsilon_n J_n^2(\beta_{n,m})\left(\beta_{n,m}^2 - n^2\right)}, \quad (3.86)$$

where $\epsilon_n = 2$ for $n = 0$ and $\epsilon_n = 1$ for $n \neq 0$. Expressions for $A_{n,m}(\gamma)$ for $\gamma > 0$ can be found in Appendix A.1

The cross sections in Figures 3.7 and 3.8 give an impression of the obtained kernel $W_{D,\gamma}$. These figures have been obtained by setting $\gamma = 0.05$ and truncating the infinite summation in (3.84) to 31,250 terms ($n \in \{0, 1, \ldots, 249\}$ and $m \in \{1, 2, \ldots, 125\}$). The difference between the solution obtained by considering four times more terms (i.e. $n \in \{0, 1, \ldots, 499\}$ and $m \in \{1, 2, \ldots, 250\}$) is less than 1% for all considered snapshots.

The cross sections for r' constant in Figure 3.7 help to understand the behaviour of the solution of the PDE (3.76) with initial conditions (3.81) and boundary conditions (3.82). As Figure 3.7 shows, the solution starts as a Dirac delta at $(r, \hat{\theta}) = (R, 0)$ which then propagates through the spatial domain as the 'time' r' increases. Note the wave front is not circular but that the propagation speed in r-direction is initially higher than in $\hat{\theta}$-direction, see e.g. Figure 3.7b. This can be understood from the PDE (3.76) which shows that the two terms involving derivatives w.r.t. $\hat{\theta}$ cancel each other for $r = R$ and $r' = R$. At the initial 'time' $r' = R$, there is thus no diffusion in $\hat{\theta}$-direction and the wave propagates only in the r-direction. However, as $r' \to \infty$ the LHS of (3.76) approaches $\partial^2 W_D / \partial r'^2$ and so that (3.76) approaches a standard wave equation and the wave fronts for larger r' more and more approach a circular shape. Note that Figures 3.7e and 3.7f also show reflections from the boundary.

Some cross sections of $W_{D,\gamma}$ for r constant are displayed in Figure 3.8 (the axes in this figure show $x' = r' \cos(\hat{\theta})$ and $y' = r' \sin(\hat{\theta})$). The cross sections in Figure 3.8 are relevant for the computation of $\tilde{T}_D$ as the convolution of W_D and $T_{D,\infty}$, see (3.45). In particular, the cross section of W_D for $r = r_0$ shows the function that should be multiplied with $T_{D,\infty}$ and integrated over $\mathbb{R}^2 \backslash D$ to obtain $\tilde{T}_D$ in the point $(r, \theta) = (r_0, 0)$. Subfigure 3.8a shows the approximation of the initial Dirac delta that propagates and diffuses in subfigures 3.8b–3.8d. For r closer to 0 the kernel $W_{D,\gamma}$ approaches a circular shape, see Subfigures 3.8e and 3.8f. It should be noted that the cross section for $r = 0$ in Subfigure 3.8f does not consist of a single circle at $r' = 2R$ but of multiple concentric circles at $r' = 2kR$ with $k \in \mathbb{N}$. The circle at $r' = 4R$ is visible in the corners of Subfigure 3.8f. The other cross sections in Figure 3.8 also contain other fronts, but these are not visible on the displayed domains. Note, however, that if the radius R is sufficiently large these other circles will not influence the resulting $\tilde{T}_D$ in (3.45) much because $T_{D,\infty}$ will then decrease rapidly outside D.

The computation of the convolution of W_D and $T_{D,\infty}$ typically requires a numerical approximation of the integral in (3.45). Using more integration points for this approximation increases the computational cost. Therefore, an one-point approximation of this convolution will be used to generate the numerical results in Section 3.5. This approximation is obtained as follows. Because $T_{D,\infty}$ will typically decrease rapidly outside D, the focus is on the behavior of W_D for r

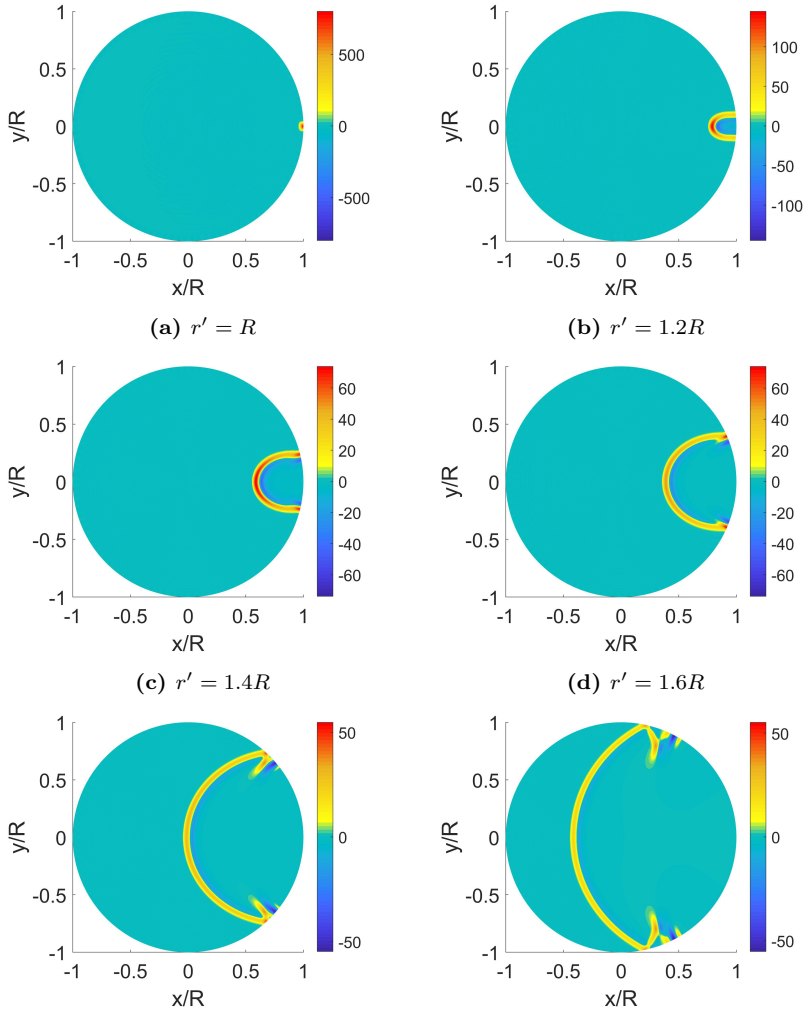

(a) $r' = R$ **(b)** $r' = 1.2R$

(c) $r' = 1.4R$ **(d)** $r' = 1.6R$

(e) $r' = 2R$ **(f)** $r' = 2.4R$

Figure 3.7. Six cross sections for r' constant of the kernel $W_{D,\gamma}$ with $\gamma = 0.05$

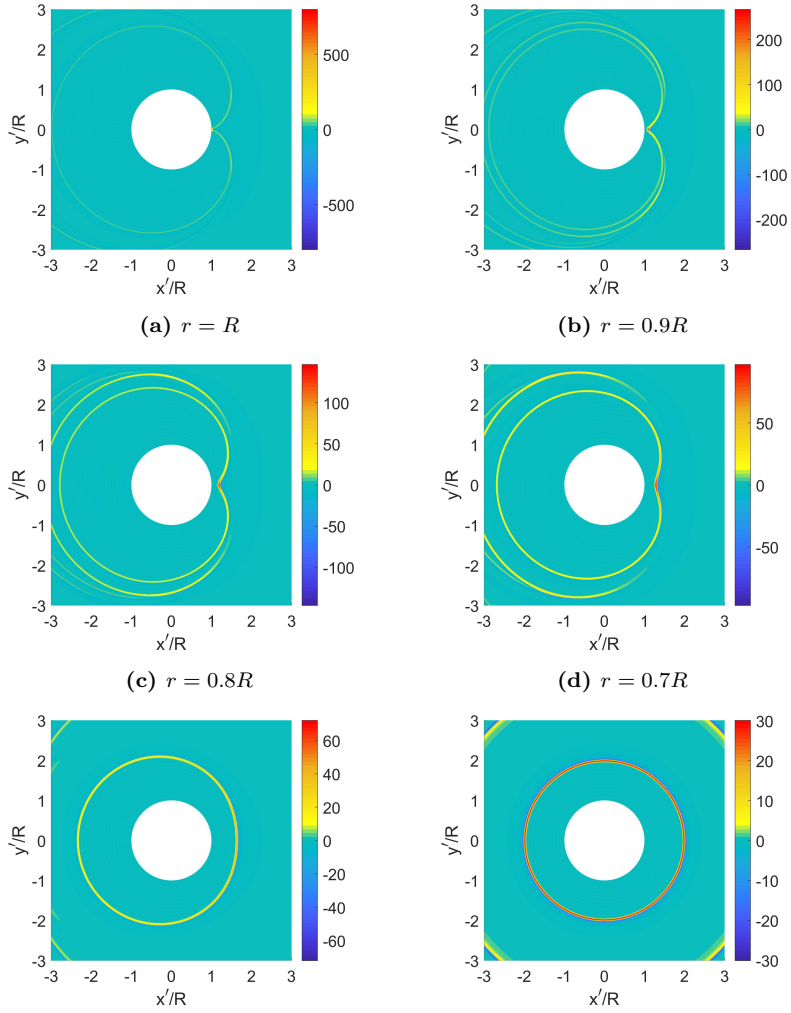

(a) $r = R$ **(b)** $r = 0.9R$

(c) $r = 0.8R$ **(d)** $r = 0.7R$

(e) $r = 0.35R$ **(f)** $r = 0$

Figure 3.8. Six cross sections for r constant of the kernel $W_{D,\gamma}$ with $\gamma = 0.05$

and r' near R. In this case, (3.76) can be approximated by

$$\frac{\partial^2 W_{D,\text{appr}}}{\partial r'^2} + \frac{1}{R}\frac{\partial W_{D,\text{appr}}}{\partial r'} = \frac{\partial^2 W_{D,\text{appr}}}{\partial r^2} + \frac{1}{R}\frac{\partial W_{D,\text{appr}}}{\partial r}. \tag{3.87}$$

The solution of (3.87) with the initial and boundary conditions (3.81) and (3.82) is

$$W_{D,\text{appr}}(r, \hat{\theta}, r') = \frac{1}{R}\delta((r-R)+(r'-R))\delta(\hat{\theta}). \tag{3.88}$$

The kernel $W_{D,\text{appr}}$ is thus a good approximation for W_D for r and r' near R. Inserting the kernel $W_{D,\text{appr}}$ in (3.88) into (3.42) and (3.45) and again using the approximation $r' \approx R$ yields

$$\begin{aligned} &T_{D,\text{appr}}(r,\theta,t) \\ &= T_{D,\infty}(r,\theta,t) + \int_R^\infty \int_0^{2\pi} T_{D,\infty}(r',\theta',t) W_{D,\text{appr}}(r,\theta-\theta',r') R \,\mathrm{d}\theta' \,\mathrm{d}r' \\ &= T_{D,\infty}(r,\theta,t) + T_{D,\infty}(2R-r,\theta,t), \end{aligned} \tag{3.89}$$

where $T_{D,\text{appr}}(r,\theta,t)$ is thus a good approximation $T_D(r,\theta,t)$ near the edge $r = R$ when the radius R is large enough. Note that it is indeed much easier to compute $T_{D,\text{appr}}(r,\theta,t)$ from $T_{D,\infty}(r,\theta,t)$ than the exact solution $T_D(r,\theta,t)$ using the kernel $W_{D,0}$ in (3.84)–(3.86). The numerical results in Section 3.5 demonstrate that the difference between the approximation $T_{D,\text{appr}}$ and the exact solution T_D is very small in the considered wafer heating application.

3.4 Heat-induced deformation

In the previous section, it has been demonstrated how the temperature field T_Ω on the subdomain $\Omega \subset \mathbb{R}^2$ can be obtained from the temperature field $T_{\Omega,\infty}$ on $\mathbb{R}^2$ using a convolution kernel W_Ω. This approach will be extended to heat-induced deformations in this section. Recall from Section 3.2.3 that the displacement field $\mathbf{d}_\Omega$ can be decomposed into two parts $\mathbf{d}_\Omega^{(T)}$ and $\mathbf{d}_\Omega^{(BC)}$ as in (3.21). The part $\mathbf{d}_\Omega^{(T)}$ is the gradient of the displacement potential Φ_Ω and is a particular solution of (3.3) for the given temperature field T_Ω. Because $\mathbf{d}_\Omega^{(T)}$ typically does not satisfy the boundary conditions, a correction $\mathbf{d}_\Omega^{(BC)}$ is needed. This correction is a homogeneous solution of (3.3) with $T_\Omega \equiv 0$. This is a standard elasticity problem for which many solution methods are available, e.g. the FE method [Zienkiewicz et al., 2013], that will not be addressed further in this section. The computation of $\mathbf{d}_D^{(BC)}$ for the circular domain D is addressed further in Section 3.5 and Appendix A.2. This section focuses on the computation $\mathbf{d}_\Omega^{(T)}$ based on $\mathbf{d}_{\Omega,\infty}$ and the same kernel W_Ω that was used to obtain the temperature field T_Ω in the previous section.

3.4.1 A kernel representation for the displacement potential

Recall from Section 3.2.3 that a displacement potential Φ_Ω resulting from a temperature field T_Ω should satisfy (3.26) on $\Omega \subseteq \mathbb{R}^2$. On $\mathbb{R}^2$, this requirement defines a unique solution $\Phi_{\Omega,\infty}$ resulting from $T_{\Omega,\infty}$. On a subdomain $\Omega \subset \mathbb{R}^2$, the solution Φ_Ω resulting from T_Ω is not unique, but a unique solution can be obtained by specifying proper boundary conditions for Φ_Ω on the edge $\partial\Omega$.

In the previous section, it has been shown that the temperature field T_Ω can be constructed from $T_{\Omega,\infty}$ using the kernel W_Ω and equations (3.42) and (3.45). Because (3.26) is linear in Φ_Ω and T_Ω, it is natural to construct Φ_Ω in a similar way as

$$\Phi_\Omega(x,y,t) = \Phi_{\Omega,\infty}(x,y,t) + \tilde{\Phi}_\Omega(x,y,t), \tag{3.90}$$

where the $\Phi_{\Omega,\infty}$ is the (unique) displacement potential resulting from $T_{\Omega,\infty}$ defined on $\mathbb{R}^2$ and

$$\tilde{\Phi}_\Omega(x,y,t) = \iint_{\mathbb{R}^2\setminus\Omega} W_\Omega(x,y,x',y')\Phi_{\Omega,\infty}(x',y',t)\ \mathrm{d}x'\ \mathrm{d}y', \tag{3.91}$$

where W_Ω is the same kernel as was used to obtain $\tilde{T}_\Omega$ in (3.45) which thus satisfies the conditions (3.46)–(3.48) in Proposition 3.4. For the displacement potential $\tilde{\Phi}_\Omega$ defined in (3.91), the following result can be obtained.

Lemma 3.8. *Assume that the kernel W_Ω satisfies* (3.46)–(3.48) *and that $\tilde{T}_\Omega$ is defined in terms of W_Ω and $T_{\Omega,\infty}$ as in* (3.45)*. Let $\Phi_{\Omega,\infty}$ be the (unique) solution of* (3.26) *with $T_\Omega = T_{\Omega,\infty}$, then the function $\tilde{\Phi}_\Omega$ defined in* (3.91) *satisfies*

$$\nabla^2\tilde{\Phi}_\Omega - \tilde{k}_\mathrm{s}\tilde{\Phi}_\Omega = (1+\nu)\alpha\tilde{T}_\Omega, \qquad \text{on } \Omega, \tag{3.92}$$

$$\frac{\partial\tilde{\Phi}_\Omega}{\partial n} = -\frac{\partial\Phi_{\Omega,\infty}}{\partial n}, \qquad \text{on } \partial\Omega. \tag{3.93}$$

Proof. To see that $\tilde{\Phi}_\Omega$ defined by (3.91) indeed satisfies (3.92), note that the definition (3.91) shows that

$$\begin{aligned}
\nabla^2\tilde{\Phi}_\Omega &= \iint_{\mathbb{R}^2\setminus\Omega} (\nabla^2 W_\Omega)\Phi_{\Omega,\infty}\ \mathrm{d}x'\ \mathrm{d}y' = \iint_{\mathbb{R}^2\setminus\Omega} (\nabla'^2 W_\Omega)\Phi_{\Omega,\infty}\ \mathrm{d}x'\ \mathrm{d}y' \\
&= \iint_{\mathbb{R}^2\setminus\Omega} W_\Omega(\nabla'^2\Phi_{\Omega,\infty})\ \mathrm{d}x'\ \mathrm{d}y' + \int_{\partial\Omega} (W_\Omega\nabla'\Phi_{\Omega,\infty} - \Phi_{\Omega,\infty}\nabla' W_\Omega)\cdot\mathbf{n}\ \mathrm{d}\ell', \\
&= \iint_{\mathbb{R}^2\setminus\Omega} W_\Omega(\tilde{k}_\mathrm{s}\Phi_{\Omega,\infty} + (1+\nu)\alpha T_{\Omega,\infty})\ \mathrm{d}x'\ \mathrm{d}y' = \tilde{k}_\mathrm{s}\tilde{\Phi}_\Omega + (1+\nu)\alpha\tilde{T}_\Omega,
\end{aligned} \tag{3.94}$$

where the second identity follows from (3.46), the third identity follows from Green's identities, the fourth identity because the boundary terms vanish due

to (3.47) and because $\Phi_{\Omega,\infty}$ is defined as the solution of (3.26), and the last identity from the definitions of $\tilde{\Phi}_\Omega$ and $\tilde{T}_\Omega$ in (3.91) and (3.45). It thus follows that $\tilde{\Phi}_\Omega$ in (3.91) satisfies (3.92).

For the boundary condition (3.93), note that for $(x, y) \in \partial\Omega$

$$\begin{aligned}
\frac{\partial\tilde{\Phi}_\Omega}{\partial n}(x,y,t) &= \nabla\left(\iint_{\mathbb{R}^2\setminus\Omega} \Phi_{\Omega,\infty}(x',y',t) W_\Omega(x,y,x',y')\ \mathrm{d}x'\ \mathrm{d}y'\right)\cdot\mathbf{n}(x,y)\\
&= \iint_{\mathbb{R}^2\setminus\Omega} \Phi_{\Omega,\infty}(x',y',t)\nabla W_\Omega(x,y,x',y')\ \mathrm{d}x'\ \mathrm{d}y'\cdot\mathbf{n}(x,y)\\
&= \iint_{\mathbb{R}^2\setminus\Omega} \Phi_{\Omega,\infty}(x',y',t)\nabla'(\delta(x-x')\delta(y-y'))\ \mathrm{d}x'\ \mathrm{d}y'\cdot\mathbf{n}(x,y)\\
&= -\iint_{\mathbb{R}^2\setminus\Omega} \nabla'\Phi_{\Omega,\infty}(x',y',t)\delta(x-x')\delta(y-y')\ \mathrm{d}x'\ \mathrm{d}y'\cdot\mathbf{n}(x,y)\\
&= -\nabla\Phi_{\Omega,\infty}(x,y,t)\cdot\mathbf{n}(x,y) = -\frac{\partial\Phi_{\Omega,\infty}}{\partial n}(x,y,t), \quad (3.95)
\end{aligned}$$

where the first identity follows from the definition of the derivative in the normal direction and the definition of $\tilde{\Phi}_\Omega$ in (3.91), the second identity by moving the gradient inside the integral, the third identity from (3.48), and the fourth identity from the definition of the derivative of a Dirac delta in (3.49). The boundary condition (3.93) is thus indeed satisfied by $\tilde{\Phi}_\Omega$ defined as in (3.91). □

By differentiating (3.90) and using (3.93), it follows that

$$\frac{\partial\Phi_\Omega}{\partial n}(x,y,t) = 0, \qquad (x,y) \in \partial\Omega, t \geq 0. \quad (3.96)$$

Noting that the solution of (3.26) with boundary condition (3.96) is unique, the following corollary of Lemma 3.8 is obtained.

Corollary 3.9. *The displacement potential Φ_Ω defined in terms of $\Phi_{\Omega,\infty}$ and the kernel W_Ω is the unique solution of* (3.26) *with boundary condition* (3.96)*.*

Using that $\mathbf{d}_\Omega^{(T)} = \nabla\Phi_\Omega$ (see (3.22)), it follows from (3.96) that the resulting displacement in the direction normal to the edge $\mathbf{d}_\Omega^{(T)}\cdot\mathbf{n}$ is zero on the edge $\partial\Omega$.

Remark 3.10. *To construct the temperature field T_Ω such that the Dirichlet boundary condition $T_\Omega = 0$ on $\partial\Omega$ is satisfied, the kernel W_Ω should satisfy* (3.55) *instead of* (3.48)*. For this case, it is easy to see from* (3.91) *and* (3.55) *that $\tilde{\Phi}_\Omega = -\Phi_{\Omega,\infty}$ on $\partial\Omega$, so that* (3.90) *shows that $\Phi_\Omega = 0$ on $\partial\Omega$. This implies that the derivative of Φ_Ω parallel to the edge will be zero, so that the component of the resulting displacement field $\mathbf{d}_\Omega^{(T)}$ along the edge is zero on $\partial\Omega$ when T_Ω satisfies zero Dirichlet boundary conditions.*

3.4.2 Solutions for specific domains

The results from the previous subsection can now be applied to the specific domains that were also studied for the temperature field T_Ω in Section 3.3.

The semi-infinite plane

For the semi-infinite plane $P = \{(x, y) \in \mathbb{R}^2 \mid x \leq x_e\}$, the kernel W_P is given by (3.67). Inserting this expression into (3.90)–(3.91) gives

$$\Phi_P(x, y, t) = \Phi_{P,\infty}(x, y, t) + \Phi_{P,\infty}(2x_e - x, y, t). \tag{3.97}$$

Taking the gradient of this expression shows that

$$\begin{bmatrix} d^{(T)}_{P,x}(x, y, t) \\ d^{(T)}_{P,y}(x, y, t) \end{bmatrix} = \begin{bmatrix} d_{P,\infty,x}(x, y, t) - d_{P,\infty,x}(2x_e - x, y, t) \\ d_{P,\infty,y}(x, y, t) + d_{P,\infty,y}(2x_e - x, y, t) \end{bmatrix}. \tag{3.98}$$

The displacement field $\mathbf{d}^{(T)}_P$ on the semi-infinite plane P is thus obtained by subtracting the mirror image of the x-component $d_{P,\infty,x}(2x_e - x, y, t)$ and adding the mirror image of the y-component $d_{P,\infty,y}(2x_e - x, y, t)$. From (3.98) it is easy to verify that $d^{(T)}_{P,x} = 0$ for $x = x_e$. This is in agreement with the observation that Φ_P should satisfy the boundary condition (3.96), which implies that the displacement normal to the edge should be zero on the edge. Furthermore, inserting the expressions for $d^{(T)}_{P,x}$ and $d^{(T)}_{P,y}$ from (3.98) into (3.9) shows that

$$\begin{aligned} \sigma^{(T)}_{P,xy}(x, y, t) = \frac{E}{1 + \nu} \Bigg(& \frac{\partial d_{P,\infty,x}}{\partial y}(x, y, t) - \frac{\partial d_{P,\infty,x}}{\partial y}(2x_e - x, y, t) \\ & + \frac{\partial d_{P,\infty,y}}{\partial x}(x, y, t) - \frac{\partial d_{P,\infty,y}}{\partial x}(2x_e - x, y, t) \Bigg). \end{aligned} \tag{3.99}$$

One easily verifies that the shear force is zero on the edge $x = x_e$ meaning that the traction force parallel to the edge resulting from $\mathbf{d}^{(T)}_P$ is thus zero. Note that the boundary conditions $d^{(T)}_{P,x} = 0$ and $\sigma^{(T)}_{P,xy} = 0$ on the edge $x = x_e$ define a unique displacement field $\mathbf{d}^{(T)}_P$ on P.

The strip

For the strip $S = \{(x, y) \in \mathbb{R}^2 \mid x_- \leq x \leq x_+\}$, the kernel W_S is given by (3.68) with $W_{S,x}$ as in (3.75) and $W_{S,y}(\hat{y}) = \delta(\hat{y})$. The displacement potential Φ_S is now obtained from (3.90)–(3.91) as

$$\begin{aligned} \Phi_S(x, y, t) = & \sum_{n \in \mathbb{Z}} \Phi_{S,\infty}(x + 2n(x_+ - x_-), y, t) \\ & + \sum_{n \in \mathbb{Z}} \Phi_{S,\infty}(2x_+ - x + 2n(x_+ - x_-), y, t). \end{aligned} \tag{3.100}$$

Taking the gradient on both sides of this expression shows that

$$\begin{bmatrix} d_{S,x}^{(T)}(x,y,t) \\ d_{S,y}^{(T)}(x,y,t) \end{bmatrix} = \sum_{n\in\mathbb{Z}} \begin{bmatrix} d_{S,\infty,x}(x+2n(x_+-x_-),y,t) \\ d_{S,\infty,y}(x+2n(x_+-x_-),y,t) \end{bmatrix} + \sum_{n\in\mathbb{Z}} \begin{bmatrix} -d_{S,\infty,x}(2x_+-x+2n(x_+-x_-),y,t) \\ d_{S,\infty,y}(2x_+-x+2n(x_+-x_-),y,t) \end{bmatrix}. \quad (3.101)$$

Again, one easily verifies that $d_{S,x}^{(T)}$ is zero at the two edges $x = x_-$ and $x = x_+$, which is in agreement with the observation that the boundary condition (3.96) implies that the displacement normal to the edge should be zero. Furthermore, it can be verified similarly as for the semi-infinite plane P that the shear stress $\sigma_{S,xy}^{(T)}$ resulting from $\mathbf{d}_S^{(T)}$ is zero at the edges $x = x_-$ and $x = x_+$, meaning that the traction force parallel to both boundaries is zero.

The rectangle

For the rectangle $B = \{(x,y) \in \mathbb{R}^2 \mid x_- \le x \le x_+, y_- \le y \le y_+\}$ the kernel W_B can be inferred from (3.20). The displacement potential Φ_B can thus be expressed in terms of $\Phi_{B,\infty}$ similarly as in the previous examples by a formula similar to (3.20). Taking the gradient of the obtained expression then yields

$$\begin{aligned} \begin{bmatrix} d_{B,x}^{(T)}(x,y,t) \\ d_{B,y}^{(T)}(x,y,t) \end{bmatrix} &= \sum_{n,m\in\mathbb{Z}} \begin{bmatrix} d_{B,\infty,x}(x+2n(x_+-x_-),y+2m(y_+-y_-),t) \\ d_{B,\infty,y}(x+2n(x_+-x_-),y+2m(y_+-y_-),t) \end{bmatrix} \\ &+ \sum_{n,m\in\mathbb{Z}} \begin{bmatrix} -d_{B,\infty,x}(2x_+-x+2n(x_+-x_-),y+2m(y_+-y_-),t) \\ d_{B,\infty,y}(2x_+-x+2n(x_+-x_-),y+2m(y_+-y_-),t) \end{bmatrix} \\ &+ \sum_{n,m\in\mathbb{Z}} \begin{bmatrix} d_{B,\infty,x}(x+2n(x_+-x_-),2y_+-y+2m(y_+-y_-),t) \\ -d_{B,\infty,y}(x+2n(x_+-x_-),2y_+-y+2m(y_+-y_-),t) \end{bmatrix} \\ &+ \sum_{n,m\in\mathbb{Z}} \begin{bmatrix} -d_{B,\infty,x}(2x_+-x+2n(x_+-x_-),2y_+-y+2m(y_+-y_-),t) \\ -d_{B,\infty,y}(2x_+-x+2n(x_+-x_-),2y_+-y+2m(y_+-y_-),t) \end{bmatrix}. \end{aligned} \quad (3.102)$$

Again, one easily verifies that the displacement normal to the edge and shear force on the edge (i.e. the traction force parallel to the edge) are zero.

The disk

As stated at the end of Subsection 3.3.3, the convolution with the kernel is W_D in (3.84) cannot be computed easily for the disk $D = \{(x,y) \in \mathbb{R}^2 \mid x^2+y^2 < R^2\}$. However, for r and r' near R we may approximate W_D by $W_{D,\text{appr}}$ in (3.88).

The displacement potential $\Phi_{D,\mathrm{appr}}$ obtained based on $W_{D,\mathrm{appr}}$ in (3.88) using (3.90) and (3.91) and the approximation $r' \approx R$ is

$$\begin{aligned}
&\Phi_{D,\mathrm{appr}}(r,\theta,t) \\
&= \Phi_{D,\infty}(r,\theta,t) + \int_R^\infty \int_0^{2\pi} \Phi_{D,\infty}(r',\theta',t) W_{D,\mathrm{appr}}(r,\theta-\theta',r') R \,\mathrm{d}\theta' \,\mathrm{d}r' \\
&= \Phi_{D,\infty}(r,\theta,t) + \Phi_{D,\infty}(2R-r,\theta,t).
\end{aligned} \tag{3.103}$$

Taking the gradient (in polar coordinates as in (3.38)) on both sides yields expressions for the displacement fields resulting from this approximation

$$\begin{aligned}
\begin{bmatrix} d^{(T)}_{D,\mathrm{appr},r}(r,\theta,t) \\ d^{(T)}_{D,\mathrm{appr},\theta}(r,\theta,t) \end{bmatrix} &= \begin{bmatrix} \frac{\partial \Phi_{D,\mathrm{appr}}}{\partial r}(r,\theta,t) \\ \frac{1}{r}\frac{\partial \Phi_{D,\mathrm{appr}}}{\partial \theta}(r,\theta,t) \end{bmatrix} \\
&= \begin{bmatrix} d_{D,\infty,r}(r,\theta,t) - d_{D,\infty,r}(2R-r,\theta,t) \\ d_{D,\infty,\theta}(r,\theta,t) + \frac{2R-r}{r} d_{D,\infty,\theta}(2R-r,\theta,t) \end{bmatrix}.
\end{aligned} \tag{3.104}$$

The formula for the θ-component follows because (3.29) shows that

$$d_{D,\infty,\theta}(2R-r,\theta,t) = \frac{1}{2R-r} \frac{\partial \Phi_{D,\infty}}{\partial \theta}(2R-r,\theta,t). \tag{3.105}$$

Based on the previous examples one might expect that the shear stress $\sigma^{(T)}_{D,\mathrm{appr},r\theta}$ resulting from $\mathbf{d}_{D,\mathrm{appr}}$ will be zero on the edge. However, it is shown in Appendix A.2 that this is not the case.

3.5 Application to wafer heating

In this section, a part of the theory developed in the previous sections will be applied to a wafer heating problem. In this application, a thin circular silicon disk, called the wafer, is exposed to a light source which creates a pattern of electronic connections. The whole wafer surface is not exposed to the light source simultaneously. Instead the heat load is applied only in a small area, called the slit, which moves over the wafer. The slit is modeled as a rectangular area in which a uniform heat load is applied. The scanning of the wafer is illustrated in Figure 3.1, which shows how the heat load scans consecutively several rectangular areas, called fields. During the scanning of each field the slit moves with a constant velocity v. It is assumed that after the scanning of one field is completed, the heat load instantly moves to the next field. The parameter values considered in this section are given in Table 3.1.

Because the wafer is thin, the temperature and displacement fields are considered as functions of the in-plane Cartesian coordinates x and y only, see e.g. [Veldman et al., 2018; van den Hurk et al., 2018] or Subsection 2.5.5.

Table 3.1. Considered parameter values

Description	Symbol	Value	Unit
Radius of the wafer	R	150	mm
Thickness of the wafer	H	0.775	mm
Slit length in x-direction	L_{slit}	26	mm
Slit length in y-direction	W_{slit}	4.6	mm
Field length in x-direction	L_{field}	26	mm
Field length in y-direction	W_{field}	33	mm
Mass density	ρ	2329	kg/m^3
Specific heat capacity	c	705	J/kg/K
Thermal conductivity	k	149	W/m/K
Convection coefficient	h	1500	$\text{W/m}^2\text{/K}$
Young's modulus	E	167	GPa
Poisson's ratio	ν	0.3	–
Stiffness of supporting structure	k_{s}	1209	N/mm^3
Scan speed	v	0.276	m/s
Applied heating power	P_{EUV}	3.229	W

The accurate and efficient computation of the resulting temperature field T_D satisfying (3.1) and displacement field $\mathbf{d}_D$ satisfying (3.3) on the circular disk $D = \{(x, y) \in \mathbb{R}^2 \mid x^2 + y^2 < R^2\}$ is important, because such predictions can be used to improve the quality of the lithography process significantly.

Note that the heat load applied to each field is identical for the scanning pattern in Figure 3.1, only the location, the scanning direction, and the time at which the slit arrives varies for the different fields. This means that (the extension to $\mathbb{R}^2$ of) the applied heat load $Q_{D,\infty}$ can be written in the form (3.30), where Q_{pass} denotes the heat load applied to a single field centered at $(x, y) = (0, 0)$ starting at time $t = 0$. On the unbounded domain $\mathbb{R}^2$, the temperature field $T_{D,\infty}$ and displacement field $\mathbf{d}_{D,\infty}$ resulting from the applied heat load $Q_{D,\infty}$ according to (3.1) and (3.3) can thus be constructed from the responses T_{pass} and $\mathbf{d}_{\text{pass}}$ that result from Q_{pass} using the formulas (3.32) and (3.35), respectively. The solutions T_D and $\mathbf{d}_D$ on the disk D can then be approximated by $T_{D,\text{appr}}$ and $\mathbf{d}_{D,\text{appr}}$ in (3.89) and (3.104), respectively.

The method will first be employed for the construction of the temperature and displacement fields at one particular time instant (and at all points in the considered spatial domain) because this illustrates the proposed method clearly. After that, a more practical case will be considered in which the method is used to compute overlay maps. These show the deformation that is observed at each point in the wafer surface at the moment it is scanned and thus provide the information relevant for the quality of the lithography process.

3.5.1 Snapshots at a particular time instant

First, the construction of the temperature and displacement fields T_D and $\mathbf{d}_D$ at a particular time instant $t_1 = 0.628$ s will be considered. At this time instant, the fifth field in the expose pattern in Figure 3.1 is being scanned. The temperature and displacement fields $T_{D,\text{appr}}$ and $\mathbf{d}_{D,\text{appr}}$ obtained using the method of images and the approximation of the kernel $W_{D,\text{appr}}$ in (3.88) will be compared to temperature and displacement fields T_D and $\mathbf{d}_D$ obtained through a standard FE analysis. The solutions T_D, $\mathbf{d}_D$, $T_{D,\text{appr}}$, and $\mathbf{d}_{D,\text{appr}}$ will be computed on several spatial and temporal grids, which are distinguished based on L_e, the smallest element size in the spatial grid.

Considered grids

Figure 3.9a shows the coarsest spatial grid that is used for the computation of T_D and $\mathbf{d}_D$ by a standard FE analysis with an element size of $L_e = 2$ mm. This mesh has been obtained by defining a rectangular mesh and discarding the elements in the mesh that (partially) fall outside the considered domain D. Meshes for smaller values of L_e are obtained by subdividing each element in the initial rectangular grid into 2×2 smaller ones and then discarding the elements that fall outside D. The circular edge is thus better approximated on finer meshes. The construction of the FE matrices is implemented in MATLAB (version 2019a) and is based on the FE tooling developed at ASML [de Best, 2015]. Linear Lagrangian shape functions are used, which means that the number of spatial grid points in Table 3.2 is equal to the number of nodes in the FE model. The number of spatial grid points in each of the considered meshes are shown in the fourth column of Table 3.2. The time integration is implemented using the Crank-Nicolson scheme [Crank and Nicolson, 1947]. A Lower-Upper (LU) decomposition is used to speed up the solution of the linear systems that need to be solved at every time step. For the spatial grid with mesh size $L_e = 2$ mm, a fixed time step of 4 ms is used. This time step is chosen such that the heat load never travels over the length of more than one element during one time step. Each time step is therefore also subdivided into two smaller ones with each refinement of the spatial grid. The number of temporal grid points for each of the considered meshes is shown in the last column of Table 3.2.

Figures 3.9b and 3.9c show the grids used for the computation of $T_{D,\text{appr}}$ and $\mathbf{d}_{D,\text{appr}}$ by the method of images. Recall that the temperature and displacement fields $T_{D,\infty}$ and $\mathbf{d}_{D,\infty}$ on $\mathbb{R}^2$ can be constructed based on the responses T_{pass} and $\mathbf{d}_{\text{pass}}$ resulting from the heat load applied to a single field according to (3.32) and (3.35). Figure 3.9b shows the grid used for the computation of T_{pass} and $\mathbf{d}_{\text{pass}}$ for the largest mesh size $L_e = 2$ mm. Grids for smaller element sizes are obtained by subdividing each element in the initial grid into 2×2 smaller ones. The number of spatial grid points in the thus obtained meshes is shown in the second column of Table 3.2. The FE matrices are again based on linear Lagrangian elements

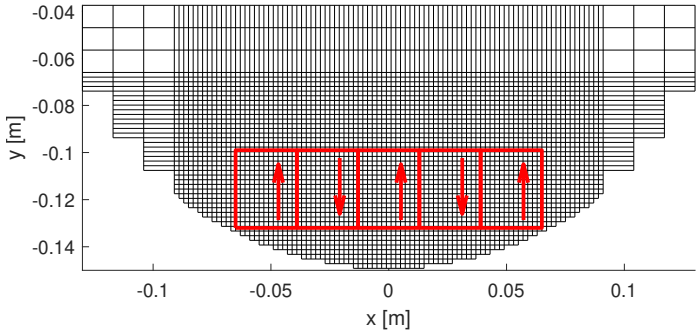

(a) Standard FE solution

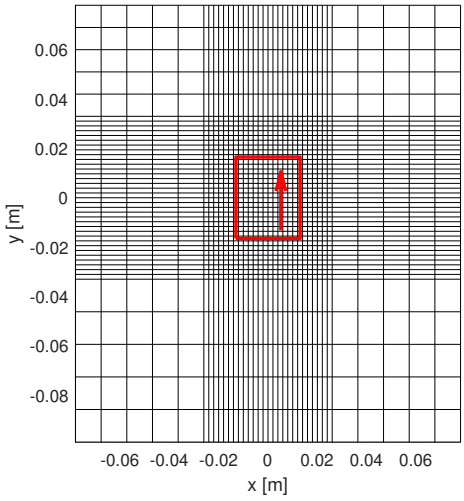

(b) Single field

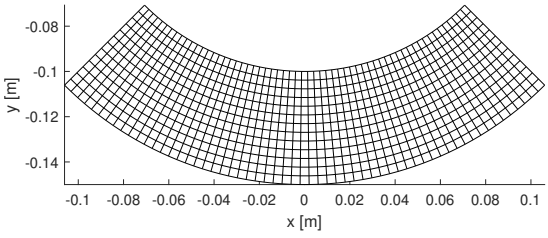

(c) Edge correction

Figure 3.9. The meshes used to compute the response for the standard FE solution, a single field, and the edge correction for $L_e = 2$ mm. The red rectangles with arrows indicate the considered fields with their scanning directions.

Table 3.2. The number of spatial and temporal grid points used to compute the snapshots of the temperature and displacement field at $t = t_1 = 0.628$ s

L_e [mm]	# spatial grid points			# temporal grid points	
	single field	edge correction	standard FEM	single field	standard FEM
2	1,665	840	3,860	58	158
1	6,497	3,213	15,323	115	315
1/2	25,665	12,561	61,100	229	629
1/4	102,017	49,665	243,958	457	1,257
1/8	–	–	974,899	–	2,513

and are again constructed in MATLAB using the FE tooling developed at ASML [de Best, 2015]. For the $L_e = 2$ mm mesh, a 4 ms time step is used from $t = 0$ to $t = 0.148$ s (the time interval during which the field is scanned) and a 24 ms in the time interval from $t = 0.148$ s to $t = 0.628$ s (the time interval in which no heat load is applied to the field). With each subdivision of the spatial mesh, each time step is also subdivided into two smaller ones to assure that the heat load does not travel over a length of more than one element during every time step. The number of temporal grid points in each of these grids are given in the fifth column of Table 3.2. Figure 3.9c shows a grid used for the edge correction $\mathbf{d}^{(BC)}_{D,\text{appr}}$, which will be discussed in detail later. The solutions $T_{D,\text{appr}}$ and $\mathbf{d}_{D,\text{appr}}$ are evaluated in the same spatial grid points that are used for T_D and $\mathbf{d}_D$ computed by a standard FE approach. This simplifies the comparison of the solutions obtained by both methods.

Graphical illustration

The temperature field $T_{D,\infty}$ and the displacement field $\mathbf{d}_{D,\infty}$ on the infinite domain $\mathbb{R}^2$ can now be constructed from T_{pass} and $\mathbf{d}_{\text{pass}}$ according to (3.32) and (3.35). The resulting temperature and displacement field at the time instant $t = t_1 = 0.628$ s are shown in Figure 3.10.

Using the obtained responses on the infinite domain $T_{D,\infty}$ and $\mathbf{d}_{D,\infty}$ in Figure 3.10, the approximations $T_{D,\text{appr}}$ and $\mathbf{d}^{(T)}_{D,\text{appr}}$ can now be computed according to (3.89) and (3.104). Figures 3.11 and 3.12a show the snapshots of $T_{D,\text{appr}}$ and $\mathbf{d}^{(T)}_{D,\text{appr}}$ at the time instant $t = t_1 = 0.628$ s. The approximations $T_{D,\text{appr}}$ and $\mathbf{d}^{(T)}_{D,\text{appr}}$ in these figures are evaluated on the $L_e = 1/4$ mm grid used for the reference solution (the grid obtained after three subdivisions of the grid in Figure 3.9a). Because the reflections along radial lines are not compatible with the used rectangular grids, this step requires the interpolation of the FE solutions T_{pass} and $\mathbf{d}_{\text{pass}}$ which is implemented using MATLAB's `griddedInterpolant` function.

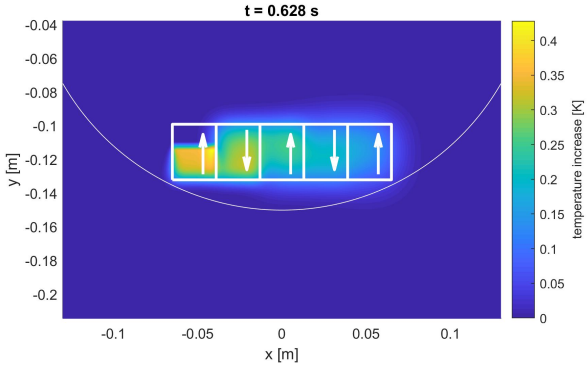

(a) Temperature field

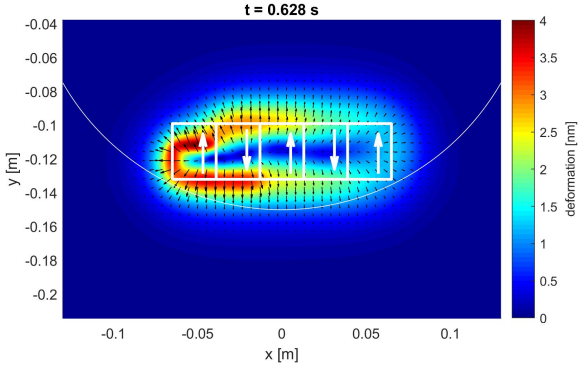

(b) Displacement field

Figure 3.10. The temperature field $T_{D,\infty}(x, y, t_1)$ and the displacement field $\mathbf{d}_{D,\infty}(x, y, t_1)$ on $\mathbb{R}^2$ constructed from $T_{\text{pass}}(x, y, t)$ and $\mathbf{d}_{\text{pass}}(x, y, t)$. The thin white line shows the location of the edge of the wafer and the white rectangles with arrows indicate the considered fields with their scanning directions.

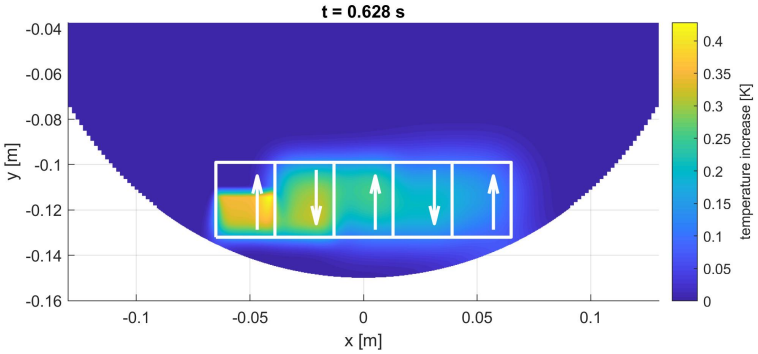

Figure 3.11. Temperature field $T_{D,\text{appr}}$ at $t = t_1 = 0.628$ s. The white rectangles with arrows indicate the considered fields with their scanning directions.

The construction of the resulting displacement field $\mathbf{d}_{D,\text{appr}}$ still requires the computation of $\mathbf{d}^{(BC)}_{D,\text{appr}}$, which is computed by solving a standard elasticity problem in which $T_{D,\infty}$ and $\mathbf{d}_{D,\infty}$ appear in the boundary conditions. Explicit expressions for these boundary conditions can be found in Appendix A.2. The elasticity problem is solved in polar coordinates. The mesh used in combination with the $L_e = 2$ mm grids is shown in Figure 3.9c and is chosen such that elements near the edge are approximately 4×4 mm^2. The mesh for $\mathbf{d}^{BC}_{D,\text{appr}}$ is thus coarser than the mesh on which T_{pass} and $\mathbf{d}_{\text{pass}}$ are computed. Meshes for smaller element sizes are again obtained by subdividing all elements in the original mesh. The resulting displacement field $\mathbf{d}^{(BC)}_{D,\text{appr}}$ is shown in Figure 3.12b and is indeed concentrated near the edge. The complete approximation of the displacement field $\mathbf{d}_{D,\text{appr}}$ is now obtained as $\mathbf{d}_{D,\text{appr}} = \mathbf{d}^{(T)}_{D,\text{appr}} + \mathbf{d}^{(BC)}_{D,\text{appr}}$ and is shown in Figure 3.12c.

Computational times

The computational times required to construct the snapshots at $t = t_1 = 0.628$ s by a standard FE analysis and by the method of images are shown in Tables 3.3 and 3.4. All computational times in this section have been obtained with MATLAB (version 2019a) on a laptop with an Intel core i7 processor and 8 GB RAM. Table 3.3 shows the computational times for the standard FE method. Note that the computation of T_D is significantly more time consuming than the computation of the resulting displacement field $\mathbf{d}_D$ because T_D needs to be computed at all considered time steps whereas the displacement field $\mathbf{d}_D$ at $t = t_1 = 0.628$ s can be computed based on the temperature field at the final time instant only. Observe that the FE solution is also computed on the $L_e = 1/8$

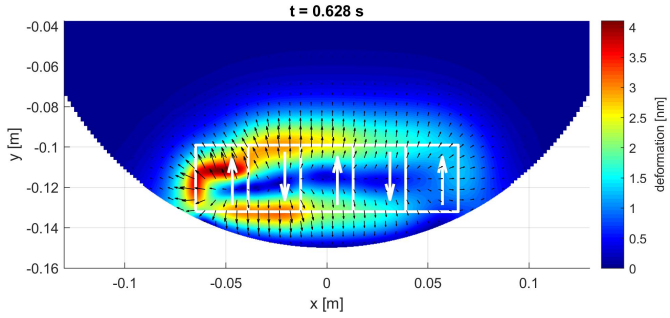

(a) $\mathbf{d}_{D,\mathrm{appr}}^{(T)}$

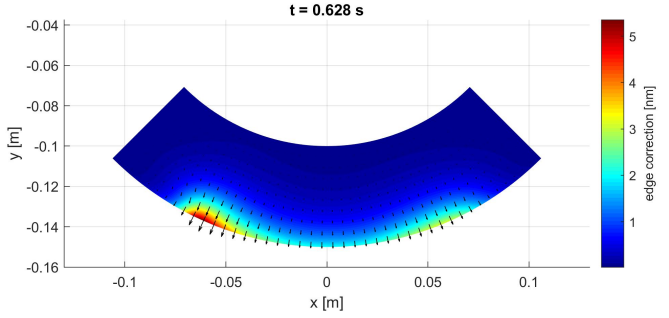

(b) $\mathbf{d}_{D,\mathrm{appr}}^{(BC)}$

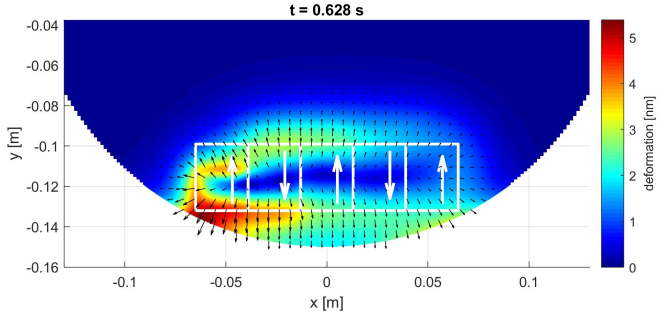

(c) $\mathbf{d}_{D,\mathrm{appr}} = \mathbf{d}_{D,\mathrm{appr}}^{(T)} + \mathbf{d}_{D,\mathrm{appr}}^{(BC)}$

Figure 3.12. Construction of the displacement field $\mathbf{d}_{D,\mathrm{appr}}$ at $t = t_1 = 0.628$ s. The white rectangles with arrows indicate the considered fields with their scanning directions.

Table 3.3. Times in seconds for the computation of the temperature and displacement fields T_D and $\mathbf{d}_D$ at $t = t_1 = 0.628$ s by a standard FE approach

L_e [mm]	T_D	$\mathbf{d}_D$	total
2	0.3	<0.1	0.8
1	3.4	0.1	4.9
1/2	27.6	0.6	33.5
1/4	256.1	3.8	281.4
1/8	2293.4	42.7	2427.5

Table 3.4. Times in seconds for the computation of the temperature and displacement fields $T_{D,\text{appr}}$ and $\mathbf{d}_{D,\text{appr}}$ at $t = t_1 = 0.628$ s

L_e	single field			$T_{D,\text{appr}}$		$T_{D,\text{appr}}$
[mm]	T_{pass}	$\mathbf{d}_{\text{pass}}$	total	& $\mathbf{d}^{(T)}_{D,\text{appr}}$	$\mathbf{d}^{(BC)}_{D,\text{appr}}$	& $\mathbf{d}_{D,\text{appr}}$
2	0.1	0.1	0.5	0.6	0.7	1.8
1	0.4	0.6	1.6	0.6	1.5	3.7
1/2	4.4	4.8	11.8	2.4	4.8	19.0
1/4	35.2	40.7	89.0	9.5	18.1	116.7

mm mesh. This solution will be used as a reference to assess the error in the other solutions.

The computational times for the construction of $T_{D,\text{appr}}$ and $\mathbf{d}_{D,\text{appr}}$ using the method of images are given Table 3.4. The second, third, and fourth columns in this table show the time required to compute the solutions T_{pass}, $\mathbf{d}_{\text{pass}}$, and the total time which also includes the time to construct the FE matrices and other overheads. Note that the time to compute T_{pass} and $\mathbf{d}_{\text{pass}}$ are of similar magnitude because $\mathbf{d}_{\text{pass}}$ is computed at all considered time instances to enable the construction of $\mathbf{d}_{D,\infty}$ according to (3.35). This was not required for the standard FE solution for which the computation of $\mathbf{d}_D$ is relatively fast compared to the computation of T_D, see Table 3.3. The fourth column of Table 3.4 gives the time required to compute the solutions $T_{D,\text{appr}}$ and $\mathbf{d}^{(T)}_{D,\text{appr}}$ from T_{pass} and $\mathbf{d}_{\text{pass}}$ according to the superposition principles in (3.32) and (3.35) and the method of images in (3.89) and (3.104). Obtaining the displacement field $\mathbf{d}_{D,\text{appr}}$ then still requires the computation of the edge correction $\mathbf{d}^{(BC)}_{D,\text{appr}}$, for which the computational times is given in the sixth column of Table 3.4. The last column of Table 3.4 gives the total time required to compute $T_{D,\text{appr}}$ and $\mathbf{d}_{D,\text{appr}}$, i.e. the sum of the fourth, fifth, and sixth column.

When comparing the total times in the last columns of Tables 3.3 and 3.4, it is clear that the times for both methods are of a similar magnitude, although the construction by the method of images is faster for smaller element sizes L_e. It should be noted here that the comparison of the computational times in Tables

Table 3.5. Accuracy of the solutions computed using the Method of Images (MoI) and using the conventional Finite Element Method (FEM) at $t = t_1 = 0.628$ s

L_e	Temperature error [mK]				Deformation error [nm]			
[mm]	MoI		FEM		MoI		FEM	
2	13.1	(3.1%)	48.5	(11.3%)	0.53	(10.0%)	1.41	(26.8%)
1	6.1	(1.4%)	21.3	(5.0%)	0.20	(3.8%)	0.61	(11.6%)
1/2	2.3	(0.5%)	7.7	(1.8%)	0.15	(2.9%)	0.24	(4.6%)
1/4	2.4	(0.6%)	2.7	(0.6%)	0.15	(2.9%)	0.09	(1.8%)

3.3 and 3.4 can be a bit deceiving. First of all, the computational times for the mechanical part in Table 3.3 only consider the computation of the displacement field at the final time $t = t_1 = 0.628$ s, whereas the computational times for T_{pass} and $\mathbf{d}_{\text{pass}}$ in Table 3.4 contain the computation of the displacement field at all time instances in the used time grids. Furthermore, the mesh in Figure 3.9a does not cover the whole wafer, so that a FE simulation for the whole wafer with a similar mesh size will require significantly more DOFs and will thus be significantly more time consuming. More insightful comparisons of the computational times will be presented in the next subsection.

Accuracy

Using the solution computed on the $L_e = 1/8$ mm mesh as a reference, the accuracy of the approximations $T_{D,\text{appr}}$ and $\mathbf{d}_{D,\text{appr}}$ obtained using the method of images can now be compared to the accuracy of the conventional FE analysis on the coarser grids. The resulting errors (measured in the sup-norm over space and time) are given in Table 3.5. It is remarkable to see that the solutions computed using the method of images are often more accurate than the solutions computed using the FE method, especially on the coarser meshes. This clearly indicates that the error introduced by the approximation of the kernel W_D by $W_{D,\text{appr}}$ is very small. It even seems that the error reported for the method of images on the $L_e = 1/4$ mm mesh is significantly influenced by remaining errors in the reference solution. In particular, it is remarkable to see that the error in the temperature field computed by the standard FE method on the $L_e = 1/4$ mm mesh, has a shape very similar to the error in the temperature field constructed by the method of images on the $L_e = 1/4$ mm mesh, see Figure 3.13. For the $L_e = 1/4$ mm mesh, a more accurate reference solution is thus required to see the error introduced by the approximation of W_D by $W_{D,\text{appr}}$. However, with the number of nodes in the $L_e = 1/8$ mm mesh already approaching 1 million, see Table 3.2, the computation of a more accurate reference solution was unfeasible.

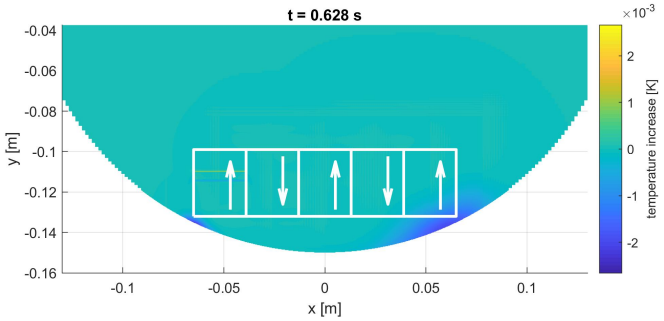

(a) $T_{D,\mathrm{appr}} - T_{D,\mathrm{ref}}$

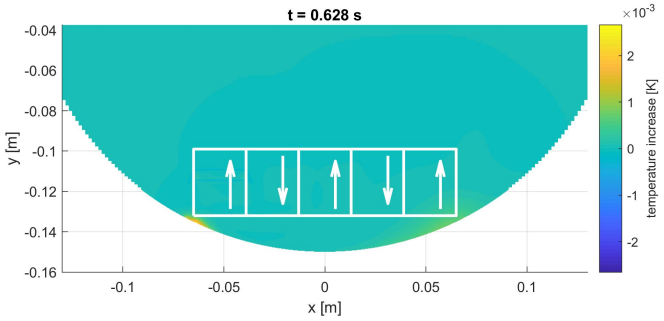

(b) $T_{D,\mathrm{FEM}} - T_{D,\mathrm{ref}}$

Figure 3.13. The difference between $T_{D,\mathrm{appr}}$, the solution constructed by the method of images on the $L_e = 1/4$ mm mesh, and $T_{D,\mathrm{ref}}$, the solution computed by the FE method on the $L_e = 1/8$ mm mesh that is used as reference solution, and the difference between $T_{D,\mathrm{FEM}}$, the solution computed by the FE method on the $L_e = 1/4$ mm mesh, and the same reference solution. The white rectangles with arrows indicate the considered fields with their scanning directions.

3.5.2 Overlay maps

The construction of the temperature and displacement fields at a particular time instant in the previous subsection was mainly used to illustrate the proposed method. In this subsection, the construction of overlay maps using the proposed method will be demonstrated. In particular, the moving-average (MA) overlay e at a point (x, y) on the wafer is defined as

$$e(x,y) = \frac{1}{t_+(x,y) - t_-(x,y)} \int_{t_-(x,y)}^{t_+(x,y)} \sqrt{d_{D,x}^2(x,y,t) + d_{D,y}^2(x,y,t)}\ \mathrm{d}t, \quad (3.106)$$

where $t_-(x, y)$ and $t_+(x, y)$ denote the starting point and end point of the time interval during which the point (x, y) is exposed to the projection light, i.e. the applied heat load $Q_D(x, y, t)$ is nonzero precisely during the time interval $[t_-(x, y), t_+(x, y)]$. For points (x, y) that are never exposed to the projection light, $e(x, y)$ is set to zero. The MA overlay $e(x, y)$ thus gives a good indication of the degradation in imaging quality due to wafer heating. To get some indication of the occurring deformation, the figures in this subsection will also display

$$\mathbf{e}(x,y) = \frac{1}{t_+(x,y) - t_-(x,y)} \int_{t_-(x,y)}^{t_+(x,y)} \mathbf{d}_D(x,y,t)\ \mathrm{d}t. \quad (3.107)$$

Note, however, that the norm of $\mathbf{e}(x, y)$ is not equal to $e(x, y)$ and that $\mathbf{e}(x, y)$ not always gives a good indication of the quality of the lithography process because changes in the direction of $\mathbf{d}_D(x, y, t)$ during $[t_-(x, y), t_+(x, y)]$ can be averaged out in $\mathbf{e}(x, y)$. The MA overlay $e_{\mathrm{appr}}(x, y)$ and the MA deformation $\mathbf{e}_{\mathrm{appr}}(x, y)$ are defined based on the displacement field $\mathbf{d}_{D,\mathrm{appr}}(x, y, t)$ instead of $\mathbf{d}_D(x, y, t)$.

The first five fields

The overlay map is first computed on the same time interval considered in the previous subsection, so from $t = 0$ to $t = t_1 = 0.628$ s. This means that the same spatial and temporal grids as in the previous subsection can be used, see Table 3.2. However, the mesh used to compute the edge correction $\mathbf{d}_{D,\mathrm{appr}}^{(BC)}$ in Figure 3.9c is now rotated along the edge of the wafer such that it is centred around the currently considered field. In particular, if (r_i, θ_i) denotes the location of the center of the i-th field in the considered cylindrical coordinate system with its origin at the center of the wafer, the mesh in Figure 3.9c) is rotated over an angle $\theta_i + \pi/2$.

The obtained overlay map is shown in Figure 3.14. Note that for all fields except the first one, $\mathbf{e}(x, y)$ has a significant component in the negative x-direction due to thermal expansion in the previously scanned fields.

The overlay maps $e_{\mathrm{appr}}(x, y)$ and $\mathbf{e}_{\mathrm{appr}}(x, y)$ obtained using the method of images will be compared to the overlay maps $e(x, y)$ and $\mathbf{e}(x, y)$ obtained by

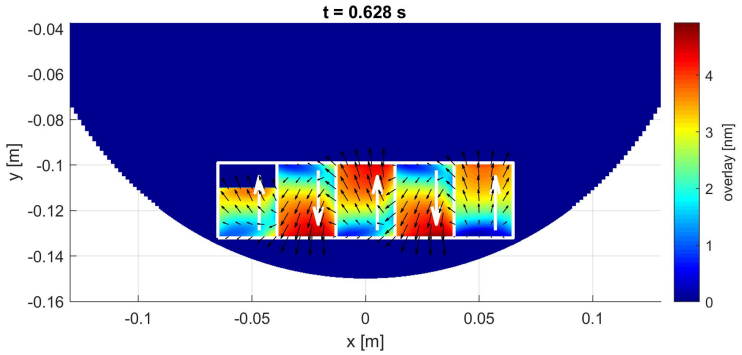

Figure 3.14. Overlay map constructed using the method of images for the $L_e = 1/4$ mm mesh. The color scale shows $e_{\text{appr}}(x, y)$, the black arrows indicate the direction of $\mathbf{e}_{\text{appr}}(x, y)$, and the white rectangles with arrows indicate the considered fields with their scanning directions.

Table 3.6. Computational times in seconds for the construction of the overlay maps using the Method of Images (MoI) and the standard Finite Element Method (FEM) from $t = 0$ s to $t = t_1 = 0.628$ s

L_e [mm]	$\mathbf{d}_{\text{pass}}$	e_{appr} & $\mathbf{e}_{\text{appr}}$	MoI	FEM
2	0.4	1.7	2.2	3.2
1	1.6	4.1	5.6	20.8
1/2	11.5	22.7	34.2	163.7
1/4	89.6	162.2	251.7	1,453.7
1/8	–	–	–	160,675.2

Table 3.7. Accuracy of the overlay maps computed using the Method of Images (MoI) and a standard Finite Element Method (FEM) up to $t = t_1 = 0.628$ s

L_e [mm]	Error in $e(x, y)$ [nm]				Error in $\mathbf{e}(x, y)$ [nm]			
	MoI		FEM		MoI		FEM	
2	0.25	(5.0%)	0.28	(5.6%)	0.26	(5.2%)	0.39	(7.9%)
1	0.08	(1.6%)	0.11	(2.3%)	0.11	(2.2%)	0.12	(2.5%)
1/2	0.06	(1.2%)	0.06	(1.1%)	0.08	(1.6%)	0.06	(1.2%)
1/4	0.07	(1.4%)	0.02	(0.3%)	0.07	(1.4%)	0.02	(0.3%)

standard FE approach (again on the same meshes that were considered in the previous subsection).

The times required to compute $e(x, y)$ and $\mathbf{e}(x, y)$ using the method of images and the standard finite element approach are compared in Table 3.6. Especially for smaller element sizes L_e, the constructions based on the method of images is significantly faster. Note that the computational times for the method of images in the fourth column of Table 3.6 have been split into the time required to compute the solution $\mathbf{d}_{\text{pass}}$ in the second column for one field and the other steps required for the construction of $e_{\text{appr}}(x, y)$ and $\mathbf{e}_{\text{appr}}(x, y)$ in the third column. Also note that the construction of the overlay map using the standard FE approach (see Table 3.6) takes significantly more time than the computation of the snapshot at $t = t_1 = 0.628$ s (see Table 3.3) because the computation of the overlay map requires the computation of the deformation at all considered time instances and not just at the final time instance. The construction of the overlay map for $L_e = 1/8$ mm is very time consuming because there was not enough memory available to compute an LU decomposition of the stiffness matrix.

The accuracy of $e_{\text{appr}}(x, y)$ and $\mathbf{e}_{\text{appr}}(x, y)$ computed using the method of images and $e(x, y)$ and $\mathbf{e}(x, y)$ computed by the standard FE approach are compared in Table 3.7. Just as for the construction of the snaphots in the previous subsection, the accuracy of both methods is similar on most of the considered grids. However, the solution obtained by the standard FE approach on the $L_e = 1/4$ mm grid seems to be more accurate than the solution obtained using the method of images on the same grid. Note that on the $L_e = 1/4$ mm grid, the solutions computed by both methods are already below 0.1 nm, which is the typical accuracy for wafer heating models currently required at ASML.

All fields on the wafer

To demonstrate the true potential of the proposed method, the overlay map is now constructed for all fields on the wafer. This requires a modification of the grid in Figure 3.9a, which is replaced by a uniform $L_e \times L_e$ grid. Elements that partially fall outside D are discarded. For the $L_e = 2$ mm grid, a uniform temporal grid with a time step of 4 ms is used. The time step is halved each time L_e is halved to assure that the heat load does not travel over more than one element in every time step. The resulting number of spatial and temporal grid points are given in the fourth and in the last column of Table 3.8. The solution for one field $\mathbf{d}_{\text{pass}}$ is still computed on subdivisions of the spatial grid in Figure 3.9b, but the temporal grid is now extended up to $t = 3$ s after which T_{pass} (and thus also $\mathbf{d}_{\text{pass}}$) is approximately zero due to the cooling of the environment. For the $L_e = 2$ mm mesh, a time step of 4 ms is used during the scanning of the field (i.e. from $t = 0$ to $t = 0.148$ s) and a time step of 24 ms after that (i.e. from $t = 0.148$ s to $t = 3$ s). The time steps are again subdivided into two smaller time steps with each refinement of the spatial grid. The resulting

Table 3.8. The number of spatial and temporal grid points used to compute the overlay map for all fields on the wafer

L_e [mm]	# spatial grid points			# temporal grid points	
	single field	edge correction	standard FEM	single field	standard FEM
2	1,665	840	17,661	198	2181
1	6,497	3,213	70,766	395	4361
1/2	25,665	12,561	282,693	789	8721
1/4	102,017	49,665	1,130,909	1577	17441
1/8	–	–	974,899	–	2,513

Table 3.9. Times in seconds needed to compute the overlay map for the whole wafer using the Method of Images (MoI) and the conventional Finite Element Method (FEM)

L_e [mm]	$\mathbf{d}_{\text{pass}}$	e_{appr} & $\mathbf{e}_{\text{appr}}$	MoI	FEM
2	0.4	13.1	13.5	138.6
1	1.6	32.9	34.5	1,195.3
1/2	11.5	137.8	149.3	10,376.2
1/4	89.6	867.0	956.6	–

number of temporal grid points used for the computation of $\mathbf{d}_{\text{pass}}$ is given in the fifth column of Table 3.8. Note that the number of spatial grid points for the solutions for a single field and for the edge correction in Table 3.8 are the same as in Table 3.2.

The overlay map computed on the $L_e = 1/4$ mm grid is shown in Figure 3.15. Note that the overlay error due to wafer heating is about 5.5 nm, which clearly indicates that modelling and control are necessary to obtain the required subnanometer accuracy, see e.g. [ASML, 2019b].

To get an idea of the reduction in computational cost achieved by the proposed method, the times required for the computation of $e(x, y)$ and $\mathbf{e}(x, y)$ based on the method of images and a standard FE solution are compared in Table 3.9. The standard FE solution could not be computed within a reasonable amount of time on the $L_e = 1/4$ mm grid because there was not enough memory available to compute an LU decomposition of the stiffness matrix. Consequently, the computation of the resulting displacements becomes very time consuming. The number of DOFs involved in the computation using the method of images is much lower. The reduction in computational time achieved by the proposed method compared to a standard FE approach is thus significant, especially on fine grids. It is worth noting that almost all of the computational time for the method of images in Table 3.9 is spent during the evaluation of the infinite do-

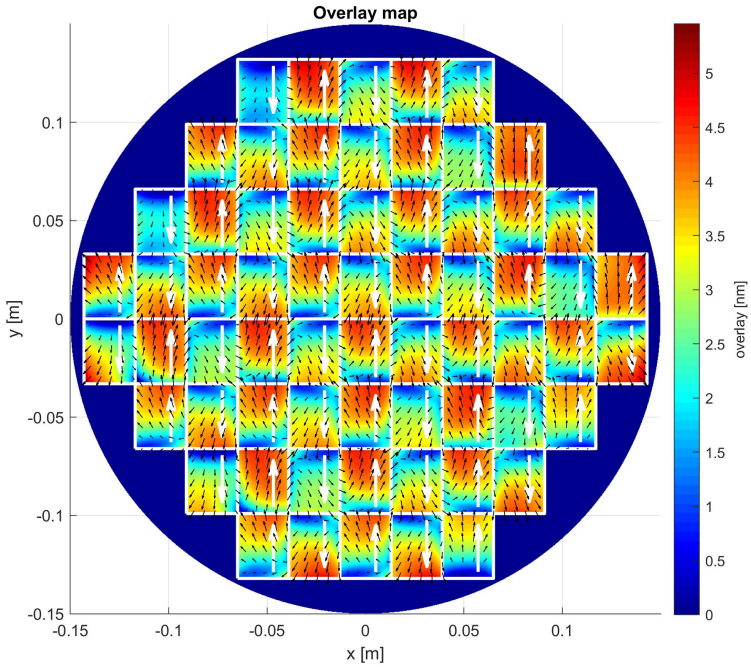

Figure 3.15. Overlay map constructed using the method of images on a uniform $L_e = 1/4$ mm mesh. The color scale shows $e_{\mathrm{appr}}(x, y)$, the black arrows indicate the direction of $\mathbf{e}_{\mathrm{appr}}(x, y)$, and the white rectangles with arrows indicate the considered fields with their scanning directions.

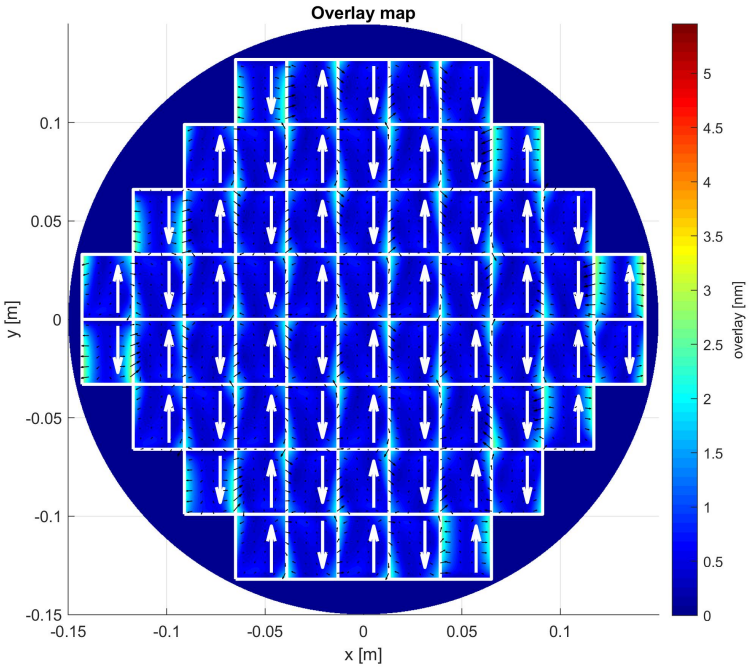

Figure 3.16. Overlay map obtained when the rigid-body translations in the x- and y-direction of the wafer stage are used reduce the overlay error, constructed using the method of images on a uniform spatial grid with spacing $L_e = 1/4$ mm. The color scale shows $e_{\text{appr}}(x, y)$, the black arrows indicate the direction of $\mathbf{e}_{\text{appr}}(x, y)$, and the white rectangles with arrows indicate the considered fields with their scanning directions.

main solutions $T_{D,\infty}$ and $\mathbf{d}_{D,\infty}$ according to (3.32) and (3.35), which involves interpolation of the solutions T_{pass} and $\mathbf{d}_{\text{pass}}$. It might be possible to reduce this time further with a smarter choice of spatial grids and/or a different (and more efficient) interpolation method.

With rigid-body corrections

The overlay error can be reduced by adapting the rigid body modes of the wafer stage and the rigid body modes of the mirrors that are used to project the light onto the wafer, see [Merks, 2015] or Section 1.4. The overlay map in Figure 3.16 shows results of such an approach in which only the two translations of the wafer stage are used to reduce the overlay error. In particular, the overlay errors $e(x, y)$ and $\mathbf{e}(x, y)$ in this figure are obtained by replacing $\mathbf{d}_D(x, y, t)$ in (3.106) and (3.107) by

$$\mathbf{d}_D(x, y, t) - \iint_{\Omega_{\text{slit}}(t)} \mathbf{d}_D(x, y, t) \, \mathrm{d}x \, \mathrm{d}y, \tag{3.108}$$

where $\Omega_{\text{slit}}(t) \subset \mathbb{R}^2$ denotes the area of the slit (i.e. the area in which the heat load is applied) at time t. These rigid-body corrections reduce the maximal overlay error from 5 nm without corrections to less than 3.5 nm. The computational times for the corrections are very similar to the times required without corrections given in Table 3.9. The method of images thus provides an efficient way to test various correction strategies. This efficiency is particularly important because these corrections should eventually be implemented in the wafer scanner, which means they will have to be computed just before or during the exposure of the wafer.

3.6 Conclusions and discussions

The results in this chapter extend the original method of images in two ways. First, it has been shown how the method can be applied to circular domains, which was not possible before. This extension has been obtained by reformulating the method of images for arbitrary spatial domains $\Omega \subset \mathbb{R}^2$ in terms of a convolution kernel that should satisfy the conditions of Proposition 3.4. By exploiting the radial symmetry of the circular domain, a kernel satisfying the conditions in Proposition 3.4 can be determined explicitly. Because the convolution with this kernel is expensive to compute, an approximation with lower computational cost has been derived as well. Secondly, the method of images has been extended such that it can be applied not only to the temperature field, but also to the heat-induced deformations. This extension is based on the displacement potential, which means that in most cases an additional elasticity problem needs to be solved to satisfy the mechanical boundary conditions.

The developed extensions have been applied to a wafer heating problem. Using the proposed approximation of the convolution kernel for the circular domain and by exploiting the repetitive nature of the applied heat load, the proposed method results in a significantly lower computational cost than a conventional FE analysis. On a 2 mm grid, the overlay map can be computed 10 times faster than a conventional FE approach. On finer grids, the relative reduction in computational time becomes even larger. On coarser grids, the results constructed based on the proposed method are even more accurate than a standard FE method on a similar grid. On finer grids for which the absolute errors in the predicted overlay are already below 0.1 nm for both methods, the standard FE method appears to be more accurate, but this observation could be influenced by the used reference solution.

The total time to construct the overlay map with the method of images on a 2 mm grid is now 13.5 seconds. This is still slightly more than the time it takes to expose the whole wafer (about 9 s). A real-time implementation of the proposed method thus requires some further improvements. These can be sought in various directions. One possibility is to improve the available hardware, i.e. to use a faster processor, but this approach might be problematic because the computational power available at the wafer scanner is typically rather limited. Improving the implementation of the proposed method might also reduce to the required computational time further. Most of the remaining computational cost is now spent during the construction of the temperature and displacement fields resulting from all considered passings of the heat load based on the solutions resulting from a single passing according to (3.32) and (3.35). This step involves an interpolation of the single-passing solutions. A different choice for the spatial and temporal grids or the use of a different interpolation function in MATLAB might reduce the cost of this step. The solutions resulting from all considered passings also enter in the boundary conditions for the computation of the edge correction, see Appendix A.2. Limiting the number of nodes on the edge of the mesh on which the edge correction is computed can thus potentially reduce the computational cost further.

Also simply limiting the amount of data that needs to be interpolated can potentially reduce the computational cost further. For example, the solutions for a single passing on the $L_e = 1/4$ mm grid require more than 1 GB of memory. Reducing the amount of simulation data for a single field may thus further speed up the other steps in the construction of the temperature and displacement fields as well. The following chapter contains a semi-analytic approach that reduces the computational cost and memory required for the computation of the temperature field. Another approach is based on Model Order Reduction (MOR) techniques, see e.g. [Antoulas, 2005; Besselink et al., 2013]. Since these techniques have been developed mainly for time-invariant systems, an attractive approach is to perform the simulation for a single field in a coordinate system fixed to the moving heat load (such a coordinate change is also used in Chapter

5). Because the solution for the single field is computed on $\mathbb{R}^2$, this coordinate change results in a time-invariant system to which standard MOR techniques can be applied. Some preliminary results for a representative one-dimensional model in [van der Heijden, 2018] suggest that a model with 20 states obtained by such an approach can already lead to satisfactory results.

Although a closed-form analytic formula for the kernel on the circular domain has been derived, an approximation consisting of a single Dirac delta has been used in the numerical example in Section 3.5. This did not lead to a significant error in the considered example. However, in other applications more accurate approximations might be necessary. It is desirable that such approximations can be written as a sum of Dirac deltas to facilitate efficient computation of the convolution with the approximation of the kernel. However, such an approximation problem is challenging and is considered a topic for future research. It is worth mentioning that such kernel approximation problems appear in many other situations. For example, a similar approximation of the full-state feedback control kernel appearing in an infinite-dimensional Linear-Quadratic (LQ) optimal control problem can be used to solve sensor placement problems, see [Demetriou, 2017].

The results in this chapter have been presented for 2-D spatial domains, but most of the ideas generalize to three-dimensional (3-D) spatial domains as well. For example, the equations for 3-D thermoelasticity (with constant coefficients) are essentially of the same form as (3.1) and (3.3), only the coefficients are different, see e.g. [Kovalenko, 1969]. This means that a displacement potential can be introduced in a similar way as for the two-dimensional (2-D) problem, see e.g. [Nowacki, 1962; Hetnarski and Eslami, 2009]. The reformulation of the method of images in terms of a convolution kernel also generalizes rather straightforwardly to 3-D problems. In particular, Proposition 3.4 and Lemma 3.8 can be generalized easily to 3-D spatial domains. However, the convolution kernel will now depend on six variables which means that finding a kernel that satisfies the conditions in Proposition 3.4 for particular subdomains will be even more challenging than in the 2-D case.

For the wafer heating problem, this extension is interesting because it is the first step towards the application of the proposed method to 3-D wafer heating models, such as the one presented in Section 2.5. As these models are significantly more complex than the considered 2-D model, the reduction in computational cost achieved by the proposed method can be even more significant for these models. However, an additional problem is that the physical parameters and the radii of the different layers depend on the out-of-plane direction in this application. Some additional work is thus required to apply the method of images to 3-D wafer heating problems.

Two additional difficulties in the simulation of wafer heating that have not been considered in Section 3.5 should be mentioned. First of all, it has been assumed that the heat load moves instantaneously to the next field after the

scanning the previous field has been completed. In reality, this process will take some time that is not known exactly before the exposure of the wafer. Such uncertain timings can be incorporated easily in the proposed method by modifying the time instances τ_i in (3.32) and (3.35) and can thus be incorporated after the solutions for the single field have been computed. Secondly, it should be noted that all fields in the heat load in Figure 3.1 fit fully on the wafer. However, to maximize the number of integrated circuits on each wafer, wafers often also contain fields that do not fit completely on the wafer. Such 'half fields' have not been considered. As each of these half fields will typically have a different position w.r.t. the edge of the wafer, the exposure of each half field will typically require an additional simulation.

Finally, it should be noted that the overlay clearly depends on the order in which the fields on the wafer are being scanned. The ordering considered in the example in Section 3.5 is constructed such that the next field is always close to the previous field because this keeps the time required to step to the next field small. A different scanning order could lead to an improved imaging quality, but could also significantly increase the time required to scan the wafer. This trade off makes the design of a different scanning order an interesting problem for future research. The proposed method can be used in such a design process to evaluate the overlay resulting from various potential designs quickly and accurately.

Chapter 4

Semi-analytic approximation of the temperature field resulting from moving heat loads

4.1 Introduction

Moving heat load problems occur in many manufacturing processes, such as welding [Rosenthal, 1946; Goldak et al., 1984; Prasad and Narayanan, 1996; Runnemalm and Hyun, 2000; Nguyen et al., 1999; Nguyen, 2004; Fachinotti et al., 2011; Flint et al., 2018], grinding [Moulik et al., 2001; Doman et al., 2009], metal cutting [Bunting and Cornfield, 1975; Nemchinsky, 2016], laser hardening of metals [Komanduri and Hou, 2001; Oh and Ki, 2017], and additive manufacturing [Zhang et al., 2004; Roberts et al., 2009; Patil et al., 2015; Irwin and Michaleris, 2015]. More recently, moving heat load problems are also studied in precision engineering because of their emerging relevance in lithography systems for the semiconductor industry. Because this is still an emerging problem only a few introductory references are available [Bikcora et al., 2014; Morishima et al., 2015; Subramany et al., 2016]. In the lithography application, it is customary to consider a two-dimensional (2-D) spatial domain, see [Morishima et al., 2015; Subramany et al., 2016], whereas three-dimensional (3-D) spatial domains are typical for the other applications.

This chapter is based on D. W. M. Veldman et al. (2018). 'Semi-analytic approximation of the temperature field resulting from moving heat loads'. *International Journal of Heat and Mass Transfer*, volume 122, pages 128 –137. However, the methods for the simulation of repetitive scanning patterns in Section 4 of the original paper are not presented in this chapter because a more in depth discussion of these ideas can be found in Chapter 3.

The basis of the theory for moving heat sources was developed in [Rosenthal, 1946], see also [Hahn and Ozisik, 2012], who observed that when the path of the heat load is long enough, the temperature distribution around the source soon becomes quasi-stationary. Assuming constant material properties, Rosenthal developed closed-form analytic expressions for these quasi-stationary temperature fields resulting from point, line, and plane heat sources. Although Rosenthal's analysis provides valuable estimates, transient effects and position or temperature dependent coefficients are important in many applications. In these situations, the problem is solved by Finite Element (FE) analysis, see for example [Goldak et al., 1984; Prasad and Narayanan, 1996; Roberts et al., 2009].

Solving a moving heat load problem by the FE method poses several numerical challenges. One problem is that by fixing the coordinate frame to the heat load, a convection-diffusion problem arises. It is well known that the FE discretization of such problems may result in spurious oscillations [Zienkiewicz et al., 2014]. Spurious oscillations can be prevented in two ways. In the first approach, the mesh size in the direction of the velocity of the moving load is chosen smaller than $2D/v$, where D [m^2/s] denotes the thermal diffusivity of the material and v [m/s] denotes the velocity of the moving load, see e.g. [Zienkiewicz et al., 2014]. Note that this approach is computationally demanding when the velocity v is high. In the second approach, upwinding schemes, see e.g. [Ozisik, 1994], are used. These schemes prevent spurious oscillations at the cost of an increased discretization error.

Another problem is that the area in which the heat load is applied is typically small. This makes both the spatial and temporal discretization of such problems computationally demanding. For example, for a Gaussian heat distribution the mesh size should be at least twice as small as the radius of the heat distribution and at least two time steps are needed for the time that the heat load travels along one element [Zhang et al., 2004].

Because of these considerations, many problems require a small mesh size. For a static mesh, this mesh size needs to be used in the whole region through which the heat load travels, which results in models with many Degrees of Freedom (DOFs). To keep the number of DOFs limited, adaptive meshing strategies have been proposed, see e.g. [Prasad and Narayanan, 1996; Runnemalm and Hyun, 2000; Patil et al., 2015], which lead to significant reduction in computational effort. Note that these schemes require some cost for updating the mesh and that the temporal discretization remains challenging, since the adaptive mesh will keep the mesh size near the source small.

For problems with constant coefficients on simple spatial domains, spatial discretization can be avoided by semi-analytic methods [Nguyen et al., 1999; Nguyen, 2004; Fachinotti et al., 2011; Flint et al., 2018; Elsen et al., 2007]. In these methods, the temperature field is expressed as the convolution of the fundamental solution of the heat equation and the applied heat load. The convolution over space can typically be solved analytically, so that only numerical

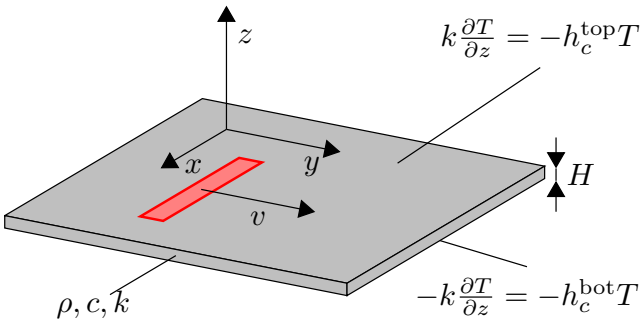

Figure 4.1. The considered infinite plate

evaluation of the convolution over time remains. This is still a computationally intensive operation when the solution is evaluated on a fine grid.

In this chapter, a novel semi-analytic approximation method to reduce the computational cost of 2-D transient moving load problems with constant coefficients is proposed. In this semi-analytic approximation, the heat conduction problem in two spatial dimensions is decoupled into three problems in one spatial dimension. This significantly reduces the computational cost, especially on fine grids. The proposed method is demonstrated by an example from precision engineering, more specifically for a wafer heating problem.

The remainder of this chapter is structured as follows. After the considered 2-D heat conduction problem has been introduced in Section 4.2, the semi-analytic approximation is introduced in Section 4.3. In Section 4.4, a physical interpretation of the constructed approximation is presented. The developed techniques are then applied to a wafer heating problem in Section 4.5. Finally, the conclusions are presented and the results are discussed in Section 4.6.

4.2 Problem formulation

Consider the thin infinite plate with thickness H [m] and constant material properties in Figure 4.1. Because the plate is thin, the temperature gradient along the thickness of the plate can be neglected and the temperature field $T_{2\text{D}} = T_{2\text{D}}(x, y, t)$ [K] with respect to a reference temperature T_0 is only a function of the in-plane Cartesian coordinates x and y. The heat losses to the surrounding media at the top and bottom of the plate are proportional to the temperature with constant heat transfer coefficients h_c^{top} and h_c^{bot} [W/m^{2}K], respectively. The temperature field $T_{2\text{D}}$ thus satisfies the following heat equation with constant coefficients, see e.g. [Hahn and Ozisik, 2012]

$$\rho c H \frac{\partial T_{2\text{D}}}{\partial t} = kH \left(\frac{\partial^2 T_{2\text{D}}}{\partial x^2} + \frac{\partial^2 T_{2\text{D}}}{\partial y^2} \right) - \left(h_c^{\text{top}} + h_c^{\text{bot}} \right) T_{2\text{D}} + Q, \tag{4.1}$$

where ρ [kg/m^3] is the mass density, c [J/kgK] the specific heat capacity, k [W/mK] the thermal conductivity, and Q [W/m^2] the applied heat load. Equation (4.1) is considered on the unbounded spatial domain $(x, y) \in \mathbb{R}^2$ with zero initial conditions $T_{2\mathrm{D}}(x, y, t = 0) = 0$.

The heat load Q is assumed to be of the form

$$Q(x, y, t) = X(x)Y(y - vt)\bar{Q}(t), \tag{4.2}$$

where $X(x) \geq 0$ [1/m] describes the shape of the applied heat load in the x-direction, $Y(y) \geq 0$ [1/m] describes the shape of the applied heat load in the y-direction, v [m/s] denotes the velocity of the moving load and $\bar{Q}(t) \geq 0$ [W] is the rate at which heat is applied at time t. Note that the uniform heat load applied in a rectangular area shown in Figure 4.1 can be written in this form by taking block functions for $X(x)$ and $Y(y)$. Such a heat load has been considered in laser hardening [Oh and Ki, 2017] and will also be considered in the lithography example in Section 4.5. Also the Gaussian heat distribution considered in many applications (see for example [Goldak et al., 1984; Prasad and Narayanan, 1996; Zhang et al., 2004; Irwin and Michaleris, 2015]) is of the form in (4.2). Observe that Q moves with a constant velocity v in positive y-direction.

Dividing (4.1) by ρcH yields

$$\frac{\partial T_{2\mathrm{D}}}{\partial t} = D\left(\frac{\partial^2 T_{2\mathrm{D}}}{\partial x^2} + \frac{\partial^2 T_{2\mathrm{D}}}{\partial y^2}\right) - hT_{2\mathrm{D}} + \Theta, \tag{4.3}$$

where $D = k/\rho c > 0$ [m^2/s] denotes the thermal diffusivity, $h = (h_c^{\mathrm{top}} + h_c^{\mathrm{bot}})/(\rho cH) \geq 0$ [1/s], and $\Theta = Q/(\rho cH)$ [K/s] can be written as

$$\Theta(x, y, t) = X(x)Y(y - vt)\bar{\Theta}(t), \tag{4.4}$$

where $\bar{\Theta}(t) = \bar{Q}(t)/(\rho cH)$ [Km^2/s].

The fundamental solution of (4.3) (i.e. the response of the homogeneous equation (4.3) with $\Theta \equiv 0$ resulting from the initial condition $T_{2\mathrm{D}}(x, y, t = 0) = T_0\delta(x)\delta(y)$, with $T_0 = 1$ [Km^2]) is given by [Evans, 2010]

$$T_0\Phi_{2\mathrm{D}}(x, y, t) = T_0 e^{-ht}\Phi(x, t)\Phi(y, t), \tag{4.5}$$

where $\Phi(x, t)$ denotes the fundamental solution of the heat equation in one spatial dimension

$$\Phi(x, t) = \frac{1}{\sqrt{4D\pi t}} \exp\left(\frac{-x^2}{4Dt}\right). \tag{4.6}$$

This can be checked by differentiating (4.5) to time and using that $\Phi(x, t)$ is the solution to the one-dimensional (1-D) heat equation (i.e. $\partial\Phi/\partial t = D\partial^2\Phi/\partial x^2$),

see also e.g. [Evans, 2010]. Since (4.3) is considered with zero initial conditions, Duhamel's principle [Evans, 2010] asserts that

$$T_{2\mathrm{D}}(x,y,t) = \int_0^t \int_{-\infty}^{+\infty} \int_{-\infty}^{+\infty} \Phi_{2\mathrm{D}}(x',y',\tau) \Theta(x-x',y-y',t-\tau)\,\mathrm{d}x'\,\mathrm{d}y'\,\mathrm{d}\tau. \quad (4.7)$$

Subsituting (4.4) and (4.5) in this equation, it follows that

$$T_{2\mathrm{D}}(x,y,t) = \int_0^t f(y,t,\tau)N(x,\tau)\,\mathrm{d}\tau, \quad (4.8)$$

where

$$f(y,t,\tau) = \int_{-\infty}^{+\infty} e^{-h\tau}\Phi(y',\tau)Y(y-y'-v(t-\tau))\bar{\Theta}(t-\tau)\,\mathrm{d}y', \quad (4.9)$$

$$N(x,\tau) = \int_{-\infty}^{+\infty} \Phi(x',\tau)X(x-x')\,\mathrm{d}x'. \quad (4.10)$$

4.3 Semi-analytic approximation

The semi-analytic approximation will now be constructed by simplifying the integral in (4.8). Note that the only factor in (4.8) that depends on x is $N(x,\tau)$. In the semi-analytic approximation, this factor will be moved outside the integral over τ.

To this end, $N(x,\tau)$ is approximated by a first-order Taylor series expansion around $\tau = t^*$, where t^* does not depend on τ and is not determined yet. This yields

$$N(x,\tau) = N(x,t^* + (\tau - t^*)) \approx N(x,t^*) + (\tau - t^*)\frac{\partial N}{\partial \tau}\bigg|_{(x,\tau)=(x,t^*)}. \quad (4.11)$$

Substituting this approximation back into (4.8), a semi-analytic approximation $\tilde{T}_{2\mathrm{D}}$ of the true temperature field $T_{2\mathrm{D}}$ is obtained as

$$\tilde{T}_{2\mathrm{D}}(x,y,t) = T_{1\mathrm{D}}(y,t)N(x,t^*) + \left(T_{1\mathrm{D}}^{(1)}(y,t) - t^* T_{1\mathrm{D}}(y,t)\right)\frac{\partial N}{\partial \tau}\bigg|_{(x,\tau)=(x,t^*)}, \quad (4.12)$$

where

$$T_{1\mathrm{D}}(y,t) = \int_0^t f(y,t,\tau)\,\mathrm{d}\tau, \quad (4.13)$$

$$T_{1\mathrm{D}}^{(1)}(y,t) = \int_0^t \tau f(y,t,\tau)\,\mathrm{d}\tau. \quad (4.14)$$

The error in the semi-analytic approximation $\tilde{T}_{2D}$ originates from the Taylor series approximation of $N(x,\tau)$ in (4.11), which can be expressed as, see e.g. [Abbott, 2015]

$$\frac{1}{2}(\tau - t^*)^2 \left.\frac{\partial^2 N}{\partial \tau^2}\right|_{(x,\tau)=(x,\tilde{t}^*)}. \tag{4.15}$$

where $\tilde{t}^*$ is an (unknown) point between t^* and τ. Assuming the difference between t^* and τ is small, $\tilde{t}^*$ can be approximated by t^*. The error in (4.15) can be approximated by the first higher-order term that is omitted in the Taylor expansion (4.11). Based on (4.15) with $\tilde{t}^*$ replaced by t^*, the error in the semi-analytic approximation is estimated as

$$R_{1D}(y,t,t^*) \left.\frac{\partial^2 N}{\partial \tau^2}\right|_{(x,\tau)=(x,t^*)}, \tag{4.16}$$

where

$$R_{1D}(y,t,t^*) = \frac{1}{2}\int_0^t (\tau - t^*)^2 f(y,t,\tau)\,\mathrm{d}\tau. \tag{4.17}$$

The expansion point t^* is chosen to minimize the estimated approximation error R_{1D}. To find the value of t^* that minimizes R_{1D}, note that

$$\frac{\partial R_{1D}}{\partial t^*} = -\int_0^t (\tau - t^*) f(y,t,\tau)\,\mathrm{d}\tau = -T_{1D}^{(1)}(y,t) + t^* T_{1D}(y,t), \tag{4.18}$$

where $T_{1D}^{(1)}$ and T_{1D} are as in (4.14) and (4.13), respectively. The expansion point t^* is now chosen such that $\partial R_{1D}/\partial t^* = 0$, i.e. as

$$t^* = t^*(y,t) = \frac{T_{1D}^{(1)}(y,t)}{T_{1D}(y,t)}. \tag{4.19}$$

Note that the choice of t^* in (4.19) cancels the second term on the Right Hand Side (RHS) of (4.12), so that the semi-analytic approximation $\tilde{T}_{2D}$ reduces to

$$\tilde{T}_{2D}(x,y,t) = T_{1D}(y,t) N(x, t^*(y,t)). \tag{4.20}$$

Furthermore, note that the RHS of (4.19) is not well-defined when $T_{1D}(y,t) = 0$. However, when $T_{1D}(y,t) = 0$ equation (4.20) shows that $\tilde{T}_{2D}(x,y,t) = 0$ for any the choice of t^*.

The critical point t^* in (4.19) indeed constitutes a minimum of R_{1D} when the second derivative $\partial^2 R_{1D}/\partial t^{*2}$ is positive. Using (4.17), it follows that $\partial^2 R_{1D}/\partial t^{*2} = T_{1D}(y,t)$. Since Y and $\bar{\Theta}$ are assumed to be nonnegative, (4.9) shows that f is nonnegative, so that (4.13) shows that $T_{1D}(y,t)$ is nonnegative. The choice for t^* in (4.19) indeed constitutes a minimum of R_{1D} unless $T_{1D}(y,t) = 0$, but, as discussed above, (4.20) shows that $\tilde{T}_{2D}(x,y,t) = 0$ in this case for any choice of t^*.

Furthermore, the definition of $T_{1D}^{(1)}$ in (4.14) shows that

$$0 \leq T_{1D}^{(1)}(y,t) \leq \int_0^t tf(y,t,\tau)\ \mathrm{d}\tau = tT_{1D}(y,t). \tag{4.21}$$

When $T_{1D}(y,t) > 0$, the above inequalities can be divided by $T_{1D}(y,t)$, which yields

$$0 \leq t^*(y,t) \leq t. \tag{4.22}$$

Since the integral expressions in (4.10), (4.13), and (4.14) can generally not be solved explicitly, it will be convenient to express $N(x,\tau)$, $T_{1D}(y,t)$, and $T_{1D}^{(1)}(y,t)$ as the solutions of Partial Differential Equations (PDEs) in one spatial dimension. Using that $\Phi(x,\tau)$ is the fundamental solution for the heat equation in one spatial dimension, it follows that $N(x,\tau)$ in (4.10) is in fact the solution to the initial value problem

$$\frac{\partial N}{\partial \tau} = D\frac{\partial^2 N}{\partial x^2}, \qquad N(x,0) = X(x), \tag{4.23}$$

and by looking back at (4.9) that T_{1D} in (4.13) is the solution to the PDE

$$\frac{\partial T_{1D}}{\partial t} = D\frac{\partial^2 T_{1D}}{\partial y^2} - hT_{1D} + Y(y-vt)\bar{\Theta}(t), \tag{4.24}$$

with zero initial conditions. To see how $T_{1D}^{(1)}(y,t)$ can be computed as the solution of a PDE, note that (4.14) can be rewritten as

$$T_{1D}^{(1)}(y,t) = tT_{1D}(y,t) - T_{1D}^{(1c)}(y,t), \tag{4.25}$$

where

$$T_{1D}^{(1c)}(y,t) = \int_0^t (t-\tau)f(y,t,\tau)\ \mathrm{d}\tau. \tag{4.26}$$

The integral in (4.26) can be interpreted as the solution to the PDE

$$\frac{\partial T_{1D}^{(1c)}}{\partial t} = D\frac{\partial^2 T_{1D}^{(1c)}}{\partial y^2} - hT_{1D}^{(1c)} + tY(y-vt)\bar{\Theta}(t), \tag{4.27}$$

with zero initial conditions.

The semi-analytic approximation $\tilde{T}_{2D}$ in (4.20) can thus be computed in the following steps

1. Discretize (4.23) to find $N(x,t)$.
2. Discretize (4.24) to find $T_{1D}(y,t)$.
3. Discretize (4.27) to find $T_{1D}^{(1c)}(y,t)$.

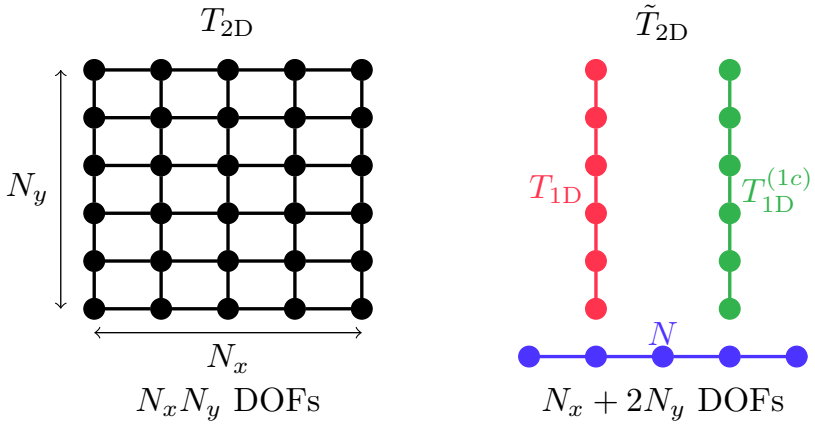

Figure 4.2. The number of DOFs in a standard 2-D FE solution and the number of DOFs in the semi-analytic approximation $\tilde{T}_{2D}$ in (4.20)

4. Compute $T_{1D}^{(1)}$ from (4.25).
5. Compute t^* from (4.19).
6. Compute $\tilde{T}_{2D}(x, y, t)$ from (4.20).

Note that this procedure requires to solve three PDEs in one spatial dimension ((4.23), (4.24), and (4.27)), whereas (4.3) is a PDE in two spatial dimensions. This means the procedure to compute $\tilde{T}_{2D}$ will be much more efficient than computing T_{2D} by discretizing (4.3). For example, on the rectangular grid in Figure 4.2 with N_x grid points in the x-direction and N_y gridpoints in the y-direction, the spatial discretization of (4.3) yields $N_x N_y$ Ordinary Differential Equations (ODEs) whereas the spatial discretization of (4.23), (4.24), and (4.27) only leads to $N_x + 2N_y$ ODEs.

In some cases, a closed form analytic expression for the solution for $N(x, \tau)$ can be obtained by computing the integral in (4.10) directly. A closed form analytic expression for $T_{1D}(y, t)$ and $T_{1D}^{(1)}(y, t)$ in (4.13) and (4.14) is impossible to obtain for most practical situations.

It is important to note that, at a certain level of accuracy, the truncation of the Taylor series in (4.11) introduces an error that cannot be reduced further by refining the 1-D mesh. To reduce this error, more terms in the Taylor series expansion (4.11) should be considered, which leads to higher-order approximations. Because the semi-analytic approximation $\tilde{T}_{2D}$ in (4.20) is based on the first-order Taylor series approximation in (4.11), $\tilde{T}_{2D}$ in (4.20) will be called the first-order semi-analytic approximation. The nth-order semi-analytic approximation follows by substitution of an nth-order Taylor series approximation for

$N(x,\tau)$ around $\tau = t^*$ in (4.8). In particular, the second-order semi-analytic approximation is found by adding (4.16) to the first-order semi-analytic approximation $\tilde{T}_{2\mathrm{D}}$ in (4.20). The computation of an n-th order ($n \geq 2$) semi-analytic approximation is addressed in Appendix B.1.

4.4 Physical properties and interpretation

The (first-order) semi-analytic approximation $\tilde{T}_{2\mathrm{D}}$ defined in the previous section is built from three functions: $T_{1\mathrm{D}}$, N, and t^*. These three functions have a clear physical interpretation in terms of the original problem.

For the physical interpretation, note that integrating $N(x,\tau)$ in (4.10) over x gives

$$\begin{aligned}\int_{-\infty}^{+\infty} N(x,\tau)\ \mathrm{d}x &= \int_{-\infty}^{+\infty}\int_{-\infty}^{+\infty} \Phi(x',\tau)X(x-x')\ \mathrm{d}x'\ \mathrm{d}x \\ &= \int_{-\infty}^{+\infty}\int_{-\infty}^{+\infty} \Phi(x-x'',\tau)X(x'')\ \mathrm{d}x\ \mathrm{d}x'', \end{aligned} \tag{4.28}$$

where the second identity follows after a change of variables $x'' = x - x'$ and changing the order of integration. Since the integral of $\Phi(x,\tau)$ from $x = -\infty$ to $x = +\infty$ equals 1, it follows that

$$\int_{-\infty}^{+\infty} N(x,\tau)\ \mathrm{d}x = \int_{-\infty}^{+\infty} X(x)\ \mathrm{d}x, \tag{4.29}$$

for all $\tau \geq 0$. Integrating the formula for $T_{2\mathrm{D}}$ in (4.8) over x and using (4.13) and (4.29) now yields

$$\int_{-\infty}^{+\infty} T_{2\mathrm{D}}(x,y,t)\ \mathrm{d}x = T_{1\mathrm{D}}(y,t)\int_{-\infty}^{+\infty} X(x)\ \mathrm{d}x. \tag{4.30}$$

Also, integrating (4.20) over x using (4.29) results in

$$\int_{-\infty}^{+\infty} \tilde{T}_{2\mathrm{D}}(x,y,t)\ \mathrm{d}x = T_{1\mathrm{D}}(y,t)\int_{-\infty}^{+\infty} X(x)\ \mathrm{d}x. \tag{4.31}$$

Since the RHS of (4.30) is equal to the RHS of (4.31), $T_{1\mathrm{D}}$ is chosen such that the internal energy of the semi-analytic approximation on lines in x-direction $\rho cH\int_{-\infty}^{+\infty}\tilde{T}_{2\mathrm{D}}\ \mathrm{d}x$ is matched with the internal energy of the exact solution along lines in the x-direction $\rho cH\int_{-\infty}^{+\infty}T_{2\mathrm{D}}\ \mathrm{d}x$. In particular, (4.29) shows that the shape functions $N(x,\tau)$ describing the dependence on x are normalized such that the integral over x is constant.

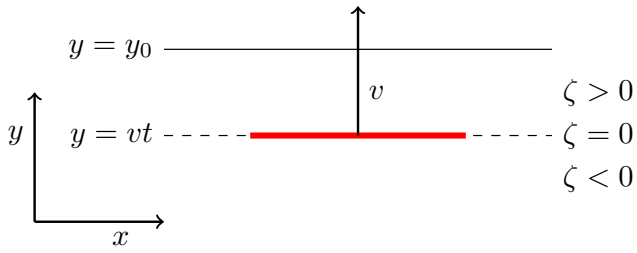

Figure 4.3. A typical line heat source

A physical interpretation of N and t^* can be found for the case where $Y(y - vt) = \delta(y - vt)$ is a Dirac delta and $\bar{\Theta}(t) \equiv 1$. In this case, the heat load is applied on a line in the x-direction (see Figure 4.3) and does not vary over time.

To find a physical interpretation for N, consider a line $y = y_0$ in the x-direction. As observed by [Goldak et al., 1984], the heat transport into the y-direction may be neglected when the velocity v is high. Looking back at the original problem (4.3), this means that the term $D\partial^2 T_{2\mathrm{D}}/\partial y^2$ can be neglected for v large. On a line $y = y_0$, the temperature profiles are expected to resemble the solution $N_{y_0}(x,t)$ of

$$\frac{\partial N_{y_0}}{\partial t} = D\frac{\partial^2 N_{y_0}}{\partial x^2} - hN_{y_0} + X(x)\delta(y_0 - vt). \tag{4.32}$$

For zero initial conditions at $t \to -\infty$, the solution to this equation is

$$N_{y_0}(x,t) = e^{h(y_0/v - t)} \begin{cases} 0 & \text{for } t < y_0/v \\ N(x, t - y_0/v) & \text{for } t \geq y_0/v, \end{cases} \tag{4.33}$$

where N is the solution of (4.23). The factor $e^{h(y_0/v-t)}$ does not depend on x, so that it does not change the shape profiles that are observed in the x-direction. The expected profiles in the x-direction are thus indeed snapshots from $N(x,\tau)$.

For the interpretation of $t^* = t^*(y,t)$, it will be convenient to introduce a coordinate frame fixed to the heat load defined by

$$(x, \zeta, t) = (x, y - vt, t). \tag{4.34}$$

Now observe that the semi-analytic approximation in (4.20) uses $N(x,t^*)$ as the profile in the x-direction. Furthermore, the expected profile in (4.33) is $N(x, t - y_0/v)$, so that it is expected that t^* approaches

$$t^*_{\mathrm{phys}} = t - y_0/v = -\zeta_0/v, \qquad (\zeta_0 < 0), \tag{4.35}$$

where $\zeta_0 = y_0 - vt$. The expression for t^*_{phys} in (4.35) in fact describes the time since the heat load has arrived at $y = y_0$. This can be seen from Figure 4.3:

Table 4.1. Considered parameter values

Symbol	Description	Value	Unit
Radius of the wafer	R	150	mm
Thermal diffusifity of silicon	D	91	mm^2/s
Wafer thickness	H	0.7	mm
Cooling rate to environment	h	1	1/s
Length of slit (x-direction)	L	26	mm
Width of slit (y-direction)	W	5	mm
Scan velocity	v	330	mm/s
Time to scan one field	t_1	0.115	s

since the heat load is located at $y = vt$ (because $Y(y-vt) = \delta(y-vt)$), the time the heat load arrives at y_0 is $t_0 = y_0/v$. At time t, the time since the heat load has arrived at $y = y_0$ is $t - t_0 = t - y_0/v$, which is precisely t^*_{phys}.

This interpretation is indeed closely related to the formula for t^* in (4.19). For $\bar{\Theta}(t) \equiv 1$ and $Y(y) = \delta(y)$, it easy to see from (4.9) that $f(y,t,\tau) = f(\zeta+vt,t,\tau)$ is only a function of ζ and τ. Using this observation, it is possible to compute

$$\lim_{t\to\infty} t^*(\zeta+vt,t) = \frac{\int_0^\infty \tau f(\zeta+vt,t,\tau)\ \mathrm{d}\tau}{\int_0^\infty f(\zeta+vt,t,\tau)\ \mathrm{d}\tau} = \frac{2D}{v^2+4Dh} + \frac{|\zeta|}{\sqrt{v^2+4Dh}}, \quad (4.36)$$

where the integrals have been computed directly in MAPLE. By expanding (4.36) in a first order Taylor expansion in $1/v$ around $1/v = 0$, it follows that the expression in (4.36) approaches $|\zeta|/|v|$ for $v \to \infty$. Since the choice of the line $y = y_0$ was arbitrary in the derivation of t^*_{phys}, y_0 in (4.35) may be replaced by y and it follows that $t^*_{\text{phys}} = -\zeta/v = |\zeta|/v$ for $\zeta < 0$. In case $Y(y-vt) = \delta(y-vt)$, $\bar{\Theta}(t) \equiv 1$, and v is large, t^* can thus be interpreted as the time since the heat load has arrived.

4.5 Application to a wafer heating problem

The method is applied to a wafer heating problem. The scanning of a single field of the wafer is considered. As described in Chapter 3 and [Veldman et al., 2018], the response for a single field can be used to obtain the response for the whole wafer.

In the considered problem, a uniform heat load is applied in a rectangular area (the slit) with length L in the x-direction and length W in y-direction which moves with a constant velocity v in the positive y-direction during the time interval $t \in [0, t_1]$, see Figure 4.4. The considered parameter values used to generate the results are given in Table 4.1.

The computed semi-analytic approximation $\tilde{T}_{2\text{D}}$ is compared to solutions $T_{2\text{D}}$ that result from a conventional 2-D FE analysis. The 2-D FE analysis

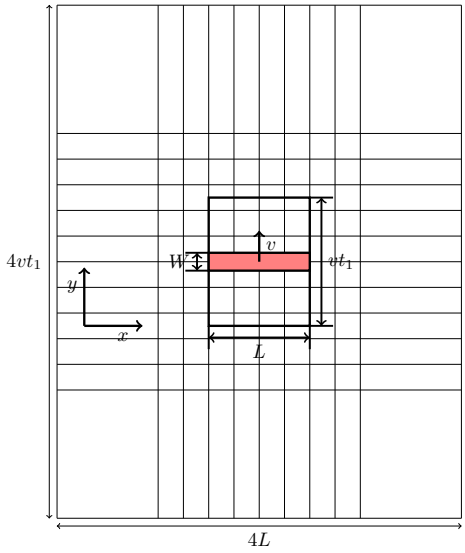

Figure 4.4. The scanning of one field on the wafer with the coarsest mesh that is considered.

uses rectangular 4-node bilinear quadrilateral elements. Around the area in which the heat load is applied, square elements with length L_e [m] are used and further away from the heat load the element size is increased to efficiently approximate the solution on the infinite domain. Starting from the coarsest mesh using $L_e = 6.4$ mm as shown in Figure 4.4, each element is subdivided into four smaller elements of equal size until the element size $L_e = 0.1$ mm is reached. For an FE simulation with $L_e = 0.1$ mm on the domain in Figure 4.4 with perfectly insulated edges, the temperature increase on the edges is below 0.33% of the maximal temperature that occurs during the simulation, indicating that solutions computed on this domain will closely resemble the infinite domain solutions. The heat load is applied between $t = 0$ and $t = t_1 = 0.115$ s and the time in the simulation runs from $t = 0$ to $t = 3$ s, so that also the passive cooling that occurs after the heat load has been applied is included in the simulation. The code for the spatial discretization is written in MATLAB, and the time integration is done using MATLAB's ODE solver ode15s with the default tolerances (a relative tolerance of 10^{-3} and an absolute tolerance of 10^{-6}).

The semi-analytic approximation $\tilde{T}_{2\mathrm{D}}$ is computed on the same grids as the FE solutions. The heat load in Figure 4.4 can be written in the form (4.4) by setting $X(x)$ equal to $1/L$ for $x \in [-L/2, L/2]$ and zero otherwise, $Y(\zeta)$ equal to $1/W$ for $\zeta \in [-W/2, W/2]$ and zero otherwise, and $\bar{Q}(t)$ equal to 1 [W] for $0 \leq t \leq t_1$ and zero afterwards. For the considered $X(x)$, a closed-form

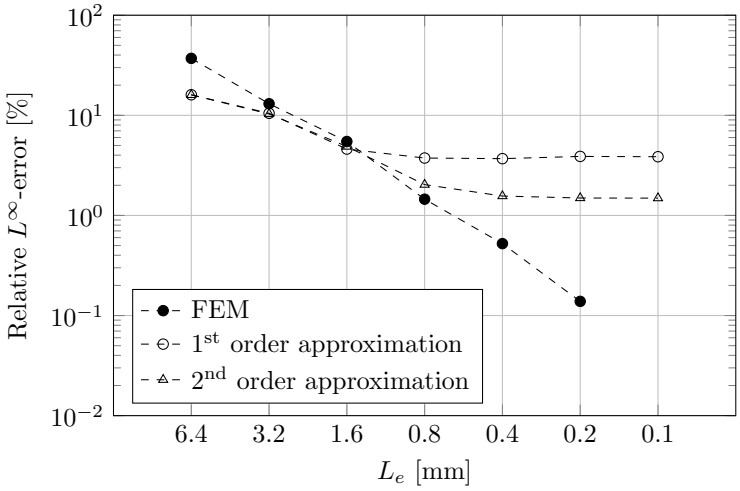

Figure 4.5. The relative L^∞-error in the temperature field for varying mesh sizes L_e in the FE solution and the first- and second-order semi-analytic approximation

analytic expression for $N(x, t^*)$ can be determined by solving the integral in (4.10) explicitly, which yields

$$N(x,t^*) = \frac{1}{2L}\left[\operatorname{erf}\left(\frac{x+L/2}{\sqrt{4Dt^*}}\right) - \operatorname{erf}\left(\frac{x-L/2}{\sqrt{4Dt^*}}\right)\right], \tag{4.37}$$

where erf denotes the error function. To compute $T_{1\mathrm{D}}(y,t)$ and $T_{1\mathrm{D}}^{(1c)}(y,t)$, (4.24) and (4.27) are descritized using the same grid in the y-direction as for the 2-D FE solution. The spatial discretization is programmed in MATLAB and uses 2-node linear elements and the temporal discretization is again done by MATLAB's ode15s with the default tolerances. It is important to note that for larger grid sizes the discretization introduces spurious oscillations, see [Zienkiewicz et al., 2014] in $T_{1\mathrm{D}}(y,t)$ and $T_{1\mathrm{D}}^{(1c)}(y,t)$, which can result in negative values of t^*. Since (4.37) is only defined for $t^* > 0$, we set $N(x,t^*) = N(x,0) = X(x)$ when negative values of t^* appear. Since negative values of t^* only appear when $T_{1\mathrm{D}}$ is small, (4.20) shows that this does not affect the semi-analytic approximation much.

Figure 4.5 shows the relative error in the temperature field for the FE solution and the first- and second-order semi-analytic approximation. The FE solution with $L_e = 0.1$ mm is used as reference. The relative error is computed by taking the maximum over space and time of the absolute value of the error, divided by the maximum of the reference solution over space and time. The error in FE solution decreases at a constant rate, but the error in the first-order semi-analytic approximation stops decreasing at $L_e = 1.6$ mm. At this point,

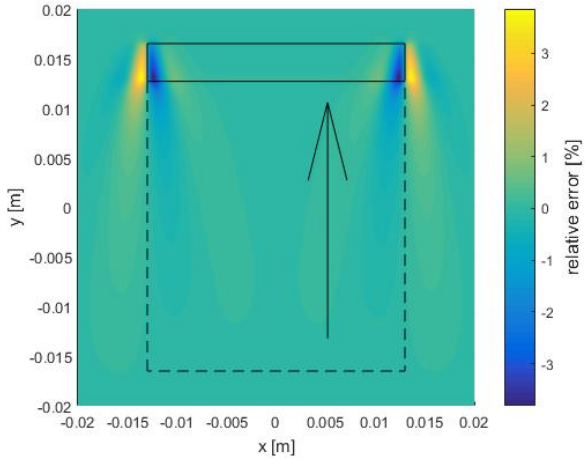

Figure 4.6. A snapshot of the error in the first-order semi-analytic approximation (computed for an element size of $L_e = 0.1$ mm) at the moment $t = t_{\mathrm{m}} = 0.1036$ s the maximal error occurs (the heat load is applied in the solid rectangle which scans the dashed rectangle in the direction of the arrow)

the error in the first-order semi-analytic approximation is no longer dominated by discretization errors but by the error introduced by the truncation of the Taylor series approximation in (4.11). This limits the accuracy of the first-order semi-analytic approximation to about 4%. For the second-order semi-analytic approximation, the error stops decreasing at $L_e = 0.4$ mm and the accuracy is limited to about 1.5%.

Figure 4.6 shows the snapshot of the error profile of the first-order semi-analytic approximation at the moment $t = t_{\mathrm{m}} = 0.1036$ s at which the maximal error is observed. The relative error in Figure 4.6 is computed by dividing the observed error by the maximal temperature observed during the simulation for the FE model with element size $L_e = 0.1$ mm. The maximal relative error is indeed below 4% and this error occurs near the left and right side of the field, so near $x = \pm L/2$. The location of the maximal error is in agreement with the leading term of the error in the first-order semi-analytic approximation in (4.16), which contains the factor $\partial^2 N/\partial\tau^2(x, t^*)$. Since $N(x, \tau)$ is the solution of (4.23), $\partial^2 N/\partial\tau^2(x, t^*)$ is largest near the discontinuities in the initial condition $N(x, 0) = X(x)$ at $x = \pm L/2$. Note that for smoother initial conditions $X(x)$, such as a Gaussian heat distribution, smaller errors as well as faster convergence may be expected when adding higher order terms.

Figure 4.5 shows that the second-order semi-analytic approximation, which is obtained by adding (4.16) to the first-order semi-analytic approximation, is more accurate than the first-order approximation. Since the coefficient $R_{1\mathrm{D}}(y, t, t^*)$ is

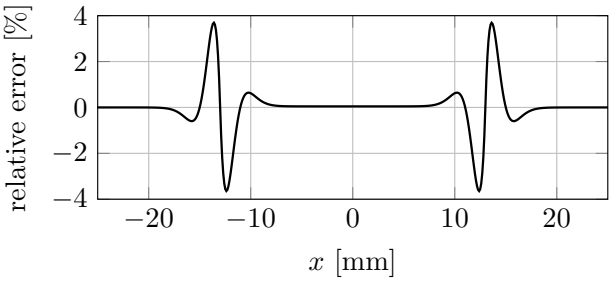

(a) Observed error profile $\tilde{T}_{2\mathrm{D}}(x, y_\mathrm{m}, t_\mathrm{m}) - T_{2\mathrm{D}}(x, y_\mathrm{m}, t_\mathrm{m})$

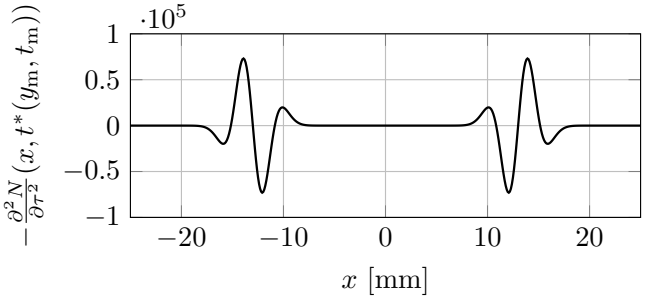

(b) Expected error profile $-\frac{\partial^2 N}{\partial \tau^2}(x, t^*(y_\mathrm{m}, t_\mathrm{m}))$

Figure 4.7. The error in the first-order semi-analytic approximation (computed for an element size of $L_e = 0.1$ mm) along the line $y = y_\mathrm{m} = 32$ mm at the moment $t = t_\mathrm{m} = 0.1036$ s compared to $-\frac{\partial^2 N}{\partial \tau^2}(x, t^*(y_\mathrm{m}, t_\mathrm{m}))$, which is the situation where the maximal error in the semi-analytic approximation is observed.

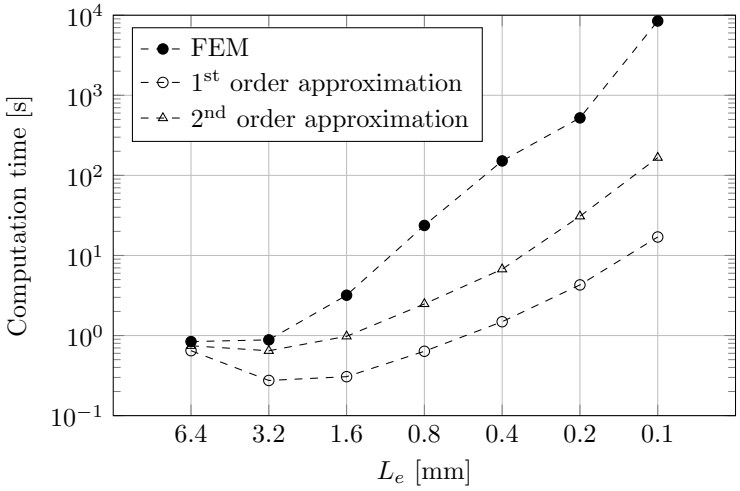

Figure 4.8. Computational times for the FE analysis and the first- and second-order semi-analytic approximation (under Windows 7, 3.3 GHz Intel Core i5 CPU, MATLAB 2016b)

nonnegative because of (4.17), the expected shape of the error profile in the x-direction is given by $-\partial^2 N/\partial\tau^2(x, t^*(y,t))$. Figure 4.7a now shows the observed error profile in the first-order semi-analytic approximation in the x-direction $\tilde{T}_{2\mathrm{D}}(x, y_\mathrm{m}, t_\mathrm{m}) - T_{2\mathrm{D}}(x, y_\mathrm{m}, t_\mathrm{m})$ and Figure 4.7b shows the expected error profile in the x-direction $-\partial^2 N/\partial\tau^2(x, t^*(y_\mathrm{m}, t_\mathrm{m}))$. The y-coordinate $y_\mathrm{m} = 32$ mm and time instant $t_\mathrm{m} = 0.1036$ s are chosen such that maximal error occurs at the line $y = y_\mathrm{m}$ at time $t = t_\mathrm{m}$. Indeed, the shape of the profiles in Figures 4.7a and 4.7b are very similar. This suggests that the expression in (4.16) gives a good indication of the observed error. Figure 4.5 confirms that for the second-order approximation that is found by adding the term $R_{1\mathrm{D}}\partial^2 N/\partial\tau^2$ in (4.16) to the first-order approximation, the relative error is reduced to 1.5%.

Figure 4.8 shows the CPU times needed to obtain the temperature field for the FE solution and the first- and second-order semi-analytic approximations. At $L_e = 1.6$ mm, the first-order semi-analytic approximation is computed almost 10 times faster than the FE solution, while a similar accuracy is obtained, see Figure 4.5. Computing the second-order semi-analytic approximation increases the computational cost because one additional PDE in one spatial dimension must be solved and because the time integration using MATLAB's ode15s now requires stricter tolerances (the absolute and relative tolerance were set to 10^{-8} for the second-order semi-analytic approximation). Nevertheless, at $L_e = 0.8$ mm the second-order semi-analytic approximation is still computed 10 times faster than the FE solution with a comparable accuracy, see Figure 4.5.

4.6 Conclusions and discussions

A semi-analytic approximation for the calculation of the 2-D temperature field resulting from a moving heat load has been introduced. The approximation decouples the problem in two spatial dimensions into three problems in one spatial dimension. Especially on fine meshes, this leads to a significant reduction in computational time compared to a conventional 2-D FE analysis. This reduction in computational time comes at the cost of an error that, for a certain level of accuracy, cannot be reduced further by refining the 1-D mesh, but can be reduced by computing higher order semi-analytic approximations, see Appendix B.1. In the presented wafer heating example, the first-order semi-analytic approximation reduces the time to compute the temperature field resulting from the scanning of a single field by a factor 10 compared to a standard FE approach with similar 4%-accuracy. For the second-order semi-analytic approximation this error is reduced to 1.5%. This approximation of the solution on the infinite domain can then be used to efficiently compute the solution resulting from the scanning of the whole wafer using the method from Chapter 3.

As stated before, the proposed method introduces an additional error that at a certain accuracy level cannot be decreased by refining the 1-D mesh size. However, the 4% error achieved for the first-order semi-analytic approximation in the wafer heating example is acceptable for two reasons: 1) the temperature field itself is not of interest, but only the displacements induced by it. For the considered example, the 4% error in the first-order semi-analytic approximation of the temperature field leads to a 0.4% error in the resulting displacements; 2) when the model is used in combination with a feedback control loop, the feedback controller will create some robustness to modeling errors.

For the considered example, the difference between the 4%-accuracy of the first-order semi-analytic approximation and the 1.5%-accuracy of the second-order semi-analytic approximation is relatively small. So, for the considered rectangular uniform shape of the heat load considering more terms in the Taylor series approximation (4.11) does not rapidly increase the accuracy of the semi-analytic approximation. On the other hand, for an element size of $L_e = 0.8$ mm, the second-order approximation is still computed 10 times faster than an FE solution with similar accuracy, so that higher-order approximations may be valuable. Moreover, for a smoother shape $X(x)$ of the heat load in the x-direction increasing the order of the semi-analytic approximation may lead to faster convergence.

In the derivation of the approximation, it was assumed that the heat load is of the form (4.2), with $X(x) \geq 0$, $Y(y) \geq 0$, and $\bar{Q}(t) \geq 0$. The assumption that $X(x)$, $Y(y)$, and $\bar{Q}(t)$ are nonnegative is not very restrictive. Consider for example the case where $\bar{Q}(t)$ does not satisfy this assumption. In that case it is

always possible to write $\bar{Q}(t)$ as the difference of two nonnegative functions

$$\bar{Q}(t) = \bar{Q}^+(t) - \bar{Q}^-(t), \tag{4.38}$$

where $\bar{Q}^+(t) = \bar{Q}(t)$ when $\bar{Q}(t) > 0$ and zero otherwise, and $\bar{Q}^-(t) = -\bar{Q}(t)$ when $\bar{Q}(t) < 0$ and zero otherwise. Since the functions $\bar{Q}^+(t)$ and $\bar{Q}^-(t)$ are nonnegative, the approximation can be computed when $\bar{Q}(t)$ in (4.1) is replaced by $\bar{Q}^+(t)$ and by $\bar{Q}^-(t)$. Since the PDE in (4.3) is linear, the approximation resulting from $\bar{Q}^-(t)$ may now be subtracted from the approximation resulting from $\bar{Q}^+(t)$ to find an approximation resulting from $\bar{Q}(t)$. A similar procedure can be applied when $X(x)$ or $Y(y)$ are not nonnegative.

Finally, it is worth mentioning that the method can be generalized to a 3-D spatial domain $(x, y, z) \in \mathbb{R}^3$. It is shown in Appendix B.2 that the problem can be decoupled into four 1-D problems, when the applied heat load can be written as

$$Q_{3\mathrm{D}}(x, y, z, t) = X(x)Y(y - vt)Z(z)\bar{Q}(t). \tag{4.39}$$

In this case, the potential reduction in computational cost is even larger than the reduction for the 2-D problem considered in this chapter.

Part III

Actuator placement for feedforward control

Chapter 5

Optimal thermal actuation for mitigation of heat-induced wafer deformation

5.1 Introduction

Photolithography is a crucial step in the production of Integrated Circuits (ICs). During the photolithography process a light source projects a pattern of electronic connections onto a silicon wafer coated with a photoresist. The pattern is not projected on the whole wafer at once, but only in a small area, called the slit, that moves over the surface of the wafer, see e.g. [Veldman et al., 2018], Chapter 2, or Part II. The light used to project the pattern causes a local temperature increase and thermal expansion of the wafer, which leads to a deteriorated imaging quality. With the critical dimensions of the projected pattern approaching the subnanometer range, this process has a significant impact on the quality of the produced ICs, see e.g. [Subramany et al., 2016; Aung et al., 2018; van den Hurk et al., 2018].

The deterioration of the imaging quality due to wafer heating can potentially be mitigated by moving thermal actuators that are placed above the wafer. The design of a thermal actuator layout is an important but nontrivial task which

This chapter is based on D. W. M. Veldman et al. (2019b). Optimal thermal actuation for mitigation of heat-induced wafer deformation. *To appear in IEEE Transactions on Control Systems Technology.* The main change is the addition of Section C.4, which was not included in the original paper, but the other sections of Appendix C have been restructured and extended as well. Related preliminary results are reported in D. W. M. Veldman et al. (2019a). 'Optimal actuator shape design with input and state constraints for a wafer heating application'. In: *Proceedings of the 2019 American Control Conference.* Philadelphia, PA, pages 3789–3794.

is critical for the performance of the resulting control system. One difficulty is that the designed thermal actuator layout should be able to reduce the wafer deformations in the slit below a certain level by using only a small amount of heating power. Furthermore, many types of thermal actuators can only heat or cool. Therefore, deciding which areas should be heated and which should be cooled is an important design decision.

The design of such a thermal actuator layout can be considered as an input selection problem which has been considered in many publications, see e.g. [Skogestad and Postlethwaite, 2007; van de Wal and de Jager, 2001]. Because there is a priori knowledge about the heat load generated by the projection light, methods that can use this information are most natural for this problem. The first of these methods have been proposed in [Al-Sulaiman and Zaman, 1994] and [Cao et al., 1996]. For every input set, both publications evaluate a quadratic cost function similar to the one used in the Linear Quadratic Tracking (LQT) problem, see e.g. [Naidu, 2002]. An advantage of this approach is that input constraints can be included.

The main problem with the approach in [Al-Sulaiman and Zaman, 1994] and [Cao et al., 1996] is that the physics of the problem is essentially governed by Partial Differential Equations (PDEs) which means that there is a very large number of possible actuator layouts, even after spatial discretization by, for example, the Finite Element (FE) method. Therefore, evaluating the cost function for every input set is computationally intractable. More efficient algorithms can be obtained by changing the problem formulation. An example of this are the results in [Stadler, 2009] who showed for (time-independent) elliptic PDEs that adding an L^1-control cost to the classical LQT cost promotes sparsity of the resulting optimal control, i.e. it results in a (time-independent) optimal control that is zero in large parts of the domain and thus gives a good indication of effective actuator locations. In [Herzog et al., 2012], this idea has been extended to the control of parabolic PDEs where an additional L^1-type cost promotes the directional sparsity of the resulting control, i.e. it results in controls that depend on space and time that are zero for all time in large parts of the domain. In [Kunisch et al., 2014], the problem formulation is further modified to enable the design of point actuators for parabolic PDEs. This framework was extended in [Boulanger and Trautmann, 2017] to design point actuators for the one-dimensional Korteweg-de Vries-Burgers equation.

A problem setting closely related to the results in [Stadler, 2009] and [Herzog et al., 2012] is considered in [Privat et al., 2017] and [Kalise et al., 2018]. In both papers, an optimal actuation restriction problem is studied, i.e. the question "if actuation can only be applied in a certain fraction of the considered spatial domain, actuation in which area of the domain is most effective?" is answered. In [Privat et al., 2017], an analytic solution for one-dimensional parabolic equations with probabilistic initial conditions is derived and in [Kalise et al., 2018], a gradient-based optimization algorithm is proposed and applied to

two-dimensional problems. It is worth mentioning that the approach in [Privat et al., 2017] can also be used to find an optimal shape for the actuation heat load. Here, in contrast to the optimal actuation restriction problem, actuation can be applied in the whole design domain but is required to have a fixed shape of which the intensity varies over time. However, the shapes obtained from the method in [Privat et al., 2017] are designed under probabilistic initial conditions, which means that the available information about the disturbance in the wafer heating problem cannot be used. It is worth mentioning that the optimization of a single-shape actuation heat can also be considered as a combined plant and control design problem, see e.g. [Fathy et al., 2001; Herber and Allison, 2019]. In this setting, the actuation heat load is viewed as part of the plant and only the intensity is considered as a control input.

None of the above mentioned PDE-oriented approaches addresses how the designed actuation heat load should be realized by physical actuators. In particular, the following difficulties arise when these approaches are applied to the wafer heating problem. First of all, most existing thermal actuators are not suitable to realize controls with high (directional) sparsity, i.e. controls that are concentrated near a few points in the spatial domain. This is even more problematic because most of these approaches allow the spatial shape of the control to vary over time inside the (small) regions where the control is concentrated. An actuator layout that can create such controls would thus require a high density of small thermal actuators in these regions, which is even harder to realize in reality. Secondly, there is the problem that thermal actuators can typically only heat or cool, which makes deciding where heaters and where coolers are placed an important aspect of the design of a thermal actuator layout. This problem is not addressed by the methods mentioned above. Thirdly, the relation between the weightings in the cost function and the achieved imaging quality is not easily determined. In practice, the designer needs to meet a certain performance, i.e. the deformation on the wafer surface needs to be below a certain tolerance. However, tuning the weights in the LQT cost function such that this goal is achieved is not straightforward and will require many iterative designs.

Because of the first difficulty, the design of controls with directional sparsity is not considered in this chapter. Instead, the focus is on the computation of the optimal actuation heat load that consists of a single shape which leads to controls that are distributed over larger areas in space and therefore easier to realize by thermal actuators. This problem formulation also has the advantage that, at least when the corresponding intensity does not change sign, the shape of the actuation heat load can give a good indication of where heaters and coolers should be placed. This approach therefore also presents a way to address the second difficulty. The third difficulty is addressed by formulating the required imaging quality as a constraint. This leads to a state-constrained optimization problem and, to the best of our knowledge, such problems have always been studied without state constraints. It should be noted that the presented approach

will not describe, just as the all other previously mentioned PDE-oriented approaches, how the designed actuation heat load should be realized by thermal actuators. However, for the considered wafer heating problem the shape of the actuation heat load computed by our approach gives a good indication about the choice and placement of actuators that could approximately realize this shape.

In this chapter, a method to compute the spatial shape and corresponding (scalar and time-dependent) intensity of the smallest actuation heat load preserving certain input and state constraints is presented. A gradient-based optimization algorithm is used to find the optimal shape and intensity simultaneously. The method is applied to a two-dimensional thermomechanical wafer heating model. The obtained shape of the actuation heat load clearly indicates where heaters and coolers should be placed and has a clear physical interpretation.

The remainder of this chapter is structured as follows. In Section 5.2, the wafer heating physics is described and the optimization problem for the actuation heat load is formulated. In Section 5.3, the finite element discretization and optimization procedure are discussed. In Section 5.4, the resulting actuation heat loads are presented and compared to free-shape solutions of the optimal control problem that are not required to consist of a single shape. Finally, in Section 5.5, the conclusions are formulated and discussed.

5.2 Modeling and problem formulation

5.2.1 Wafer heating model

The wafer is a thin silicon disk, typically with a radius of 300 mm and a thickness of 0.775 mm. When the wafer is exposed to the projection light, it is placed on a water-cooled supporting structure which is assumed to have a constant temperature T_0. Because the wafer is thin, the temperature variations along the thickness are negligible and the temperature field in the wafer can be considered to be a function of the in-plane Cartesian coordinates (x, y) and time t only. The temperature increase in the wafer T relative to the temperature of the supporting structure T_0 is the solution of the two-dimensional heat equation

$$\rho c H \frac{\partial T}{\partial t} = kH \left(\frac{\partial^2 T}{\partial x^2} + \frac{\partial^2 T}{\partial y^2} \right) - h_c T + Q, \tag{5.1}$$

where ρ [kg/m^3], c [J/kg/K], k [W/m/K], and H [m] are the mass density, specific heat capacity, thermal conductivity, and thickness of the wafer, respectively, h_c [W/m^2/K] is the thermal conductance between the wafer and the supporting structure, and $Q = Q(x, y, t)$ [W/m^2] is the heat load that results from the projecting light and from actuation, i.e.

$$Q = Q_{\text{exp}} + Q_{\text{act}}, \tag{5.2}$$

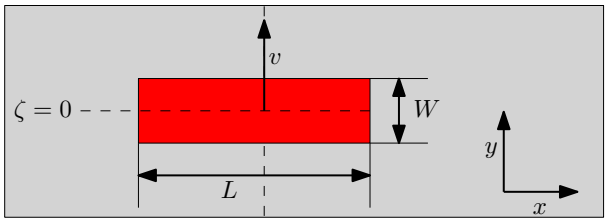

Figure 5.1. The heat load (red) that is applied to the wafer (gray)

where $Q_{\text{exp}} = Q_{\text{exp}}(x, y, t)$ is the heat load resulting from the light that projects the pattern of electronic connections on the wafer and $Q_{\text{act}} = Q_{\text{act}}(x, y, t)$ is the actuation heat load. Note that convective and radiative heat transfer are negligible compared to the heat conduction to the supporting structure. It is assumed that the wafer temperature is initially equal to the temperature of the supporting structure T_0, i.e. the initial condition is $T(x, y, 0) = 0$. The spatial domain $(x, y) \in \mathbb{R}^2$ is considered to be infinite. Note that this assumption limits our analysis to fields that are not close to the wafer edge. This assumption is valid for the majority of fields on the wafer, see e.g. Chapter 3.

The heat load Q_{exp} is induced by the light that projects the pattern of electronic connections on the wafer and has a power P_{exp} [W] which is uniformly applied over the slit $\Omega_{\text{slit}} \subset \mathbb{R}^2$ (the red area in Figure 5.1 with length L and width W). During the exposure of the wafer, the light source consecutively scans about 100 rectangular areas on the wafer, which are called fields. Here, the scanning of a single field is considered. During the time interval $t \in (0, t_e)$ in which a single field is scanned, the slit moves with a constant velocity v in the positive y-direction,

$$Q_{\text{exp}}(x, y, t) = B_{\text{exp}}(x, y - vt)u_{\text{exp}}(t), \tag{5.3}$$

where $B_{\text{exp}}(x, y - vt)$ [$1/\text{m}^2$] and $u_{\text{exp}}(t)$ [W] are the shape and intensity of the expose load, respectively. In particular, the shape $B_{\text{exp}}(x, y - vt)$ equals $1/(LW)$ when $x \in [-L/2, L/2]$ and $y - vt \in [-W/2, W/2]$ and zero otherwise and the intensity $u_{\text{exp}}(t) = P_{\text{exp}}$ is constant. The actuation heat load Q_{act} will be discussed in the next subsection.

Because the considered domain is infinite and the applied heat load is moving, it is convenient to consider a moving coordinate system $(x, \zeta, t) = (x, y - vt, t)$ in which the spatial shape B_{exp} is fixed. Let $T^{(y)}(x, y, t)$ and $Q^{(y)}(x, y, t)$ denote the temperature field and applied heat load expressed in (x, y, t)-coordinates as in (5.1). The temperature field $T^{(\zeta)}(x, \zeta, t)$ and applied heat load $Q^{(\zeta)}(x, \zeta, t)$ expressed in (x, ζ, t)-coordinates are then equal to $T^{(y)}(x, \zeta+vt, t)$ and $Q^{(y)}(x, \zeta+vt, t)$, respectively. It can be shown that $T(x, \zeta, t) = T^{(\zeta)}(x, \zeta, t)$ satisfies, see

e.g. [Hahn and Ozisik, 2012]

$$\rho c H \left(\frac{\partial T}{\partial t} - v \frac{\partial T}{\partial \zeta} \right) = kH \left(\frac{\partial^2 T}{\partial x^2} + \frac{\partial^2 T}{\partial \zeta^2} \right) - h_c T + Q, \tag{5.4}$$

with $Q(x, \zeta, t) = Q^{(\zeta)}(x, \zeta, t)$. In particular, the heat load induced by the expose load $Q^{(y)}_{\text{exp}}(x, y, t)$ in (5.3) becomes

$$Q^{(\zeta)}_{\text{exp}}(x, \zeta, t) = B_{\text{exp}}(x, \zeta) u_{\text{exp}}(t). \tag{5.5}$$

In the remainder of this chapter, only the (x, ζ, t)-coordinate system will be used and the used coordinate system will no longer be indicated, i.e. $T = T(x, \zeta, t) = T^{(\zeta)}(x, \zeta, t)$ and $Q = Q(x, \zeta, t) = Q^{(\zeta)}(x, \zeta, t)$. Note that the origin of (x, ζ)-coordinate system is at the center of the slit, see Figure 5.1.

The mechanical model used to predict the resulting in-plane displacement field is based on linear strain-displacement relations and the plane-stress relations for an isotropic material. It is assumed that inertia effects are negligible, which is a standard assumption in thermomechanical models [Fung and Tong, 2001]. The resulting model in ζ-coordinates takes the form

$$\frac{EH}{1-\nu^2} \left(\frac{\partial^2 d_x}{\partial x^2} + \frac{1-\nu}{2} \frac{\partial^2 d_x}{\partial \zeta^2} + \frac{1+\nu}{2} \frac{\partial^2 d_\zeta}{\partial x \partial \zeta} \right) - k_s d_x = \frac{\alpha E H}{1-\nu} \frac{\partial T}{\partial x}, \tag{5.6}$$

$$\frac{EH}{1-\nu^2} \left(\frac{\partial^2 d_\zeta}{\partial \zeta^2} + \frac{1-\nu}{2} \frac{\partial^2 d_\zeta}{\partial x^2} + \frac{1+\nu}{2} \frac{\partial^2 d_x}{\partial x \partial \zeta} \right) - k_s d_\zeta = \frac{\alpha E H}{1-\nu} \frac{\partial T}{\partial \zeta}, \tag{5.7}$$

where $d_x = d_x(x, \zeta, t)$ [m] and $d_\zeta = d_\zeta(x, \zeta, t)$ [m] are the displacement field components in x- and ζ-direction, respectively, E [N/m^2], ν [-], and α [1/K] are the Young's modulus, Poisson's ratio, and coefficient of thermal expansion of the wafer, respectively, and k_s [N/m^3] represents the shear stiffness of the supporting structure per unit area.

The applied actuation heat load should compensate the light-induced heat load Q_{exp} such that a sufficiently good imaging quality is attained. This is achieved when the deformation in the slit is below a certain threshold δ_{slit}. It is thus required that for all $(x, \zeta) \in \Omega_{\text{slit}}$ and all $0 \leq t \leq t_e$

$$d_x^2(x, \zeta, t) + d_\zeta^2(x, \zeta, t) \leq \delta_{\text{slit}}^2. \tag{5.8}$$

The applied actuation heat load should also prevent slip between the wafer and the supporting structure, which means that the displacement in the whole wafer surface should be below the threshold δ_{slip}. It is thus required that for all $(x, \zeta) \in \mathbb{R}^2$ and all $0 \leq t \leq t_e$

$$d_x^2(x, \zeta, t) + d_\zeta^2(x, \zeta, t) \leq \delta_{\text{slip}}^2. \tag{5.9}$$

It will be convenient to write (5.8) and (5.9) as one inequality (which should hold for all $(x, \zeta) \in \mathbb{R}^2$ and all $0 \leq t \leq t_e$)

$$d_x^2(x, \zeta, t) + d_\zeta^2(x, \zeta, t) \leq d_{\max}^2(x, \zeta), \tag{5.10}$$

where $d_{\max}(x,\zeta)$ is equal to $\min\{\delta_{\text{slit}},\delta_{\text{slip}}\}$ for $(x,\zeta)\in\Omega_{\text{slit}}$ and equal to δ_{slip} otherwise.

Finally, the constraint (5.10) should be achieved by the smallest possible actuation heat load. In particular, it is required that the actuation heat load has minimal (squared) L^2-norm

$$J_0 = \int_0^{t_e} \iint_{\mathbb{R}^2} Q_{\text{act}}^2(x,\zeta,t)\ \mathrm{d}x\ \mathrm{d}\zeta\ \mathrm{d}t. \tag{5.11}$$

In short, the cost functional J_0 in (5.11) should be minimized over the actuation heat loads $Q_{\text{act}}(x,\zeta,t)$ that result in a displacement field for which the constraint (5.10) is satisfied.

5.2.2 Actuation heat load

The heat load Q_{act} should be realized by a layout of thermal actuators. The case where thermal actuators are placed above the wafer is considered. Because of the current design of wafer scanners where the wafer is placed on a stage that moves underneath the expose light, see e.g. [Rice, 2014] or Chapter 1, it is most natural to assume that these actuators are fixed to the machine frame. This means that their absolute speed is zero and that their relative speed w.r.t. the wafer is the same as the relative speed of the expose load. To get insight in an effective placement of actuators, it is thus required that the actuation heat load has a fixed shape in the (x,ζ)-coordinate system that is moving w.r.t. the wafer, i.e.

$$Q_{\text{act}}(x,\zeta,t) = B(x,\zeta)u(t), \tag{5.12}$$

where $B(x,\zeta)$ [1/m^2] and $u(t)$ [W] are the shape and intensity of the actuation heat load, respectively. It is not possible to apply thermal actuation in the area where the pattern is currently projected because the required thermal actuators will block the projecting light source. Since the light source projects the pattern in the area $\Omega_{\text{slit}}\subset\mathbb{R}^2$, it is thus required that

$$B(x,\zeta) = 0, \qquad \text{for } (x,\zeta)\in\Omega_{\text{slit}}. \tag{5.13}$$

Note that this constraint prevents to have $Q_{\text{act}} = -Q_{\text{exp}}$, i.e. the situation where the actuation heat load cancels the expose load, which would lead to $d_x(x,\zeta,t) = d_\zeta(x,\zeta,t) = 0$. The results in Section 5.4 will demonstrate that there are values of δ_{slit} and δ_{slip} for which there is no actuation heat load such that (5.10) and (5.13) are satisfied. Furthermore, an important aspect of the design of a thermal actuator layout is that thermal actuators can typically only heat or cool. By requiring that the intensity $u(t)$ is nonnegative, i.e.

$$u(t) \geq 0, \tag{5.14}$$

it is clear that areas where the designed shape of the actuation heat load $B(x,\zeta)$ is positive should be heated and areas where $B(x,\zeta)$ is negative should be cooled.

Note that the representation $(B(x,\zeta),u(t))$ of $Q_{\text{act}}(x,\zeta,t)$ in (5.12) is clearly nonunique: if $(B_0(x,\zeta,t),u_0(t))$ is a representation satisfying (5.14), then the same actuation heat load $Q_{\text{act}}(x,\zeta,t) = B_0(x,\zeta)u_0(t)$ can be represented by $(\beta B_0(x,\zeta),u_0(t)/\beta)$ for any $\beta > 0$. This nonuniqueness can be removed by normalizing the shape of the actuation heat load $B(x,\zeta)$ such that it has unit L^1-norm, i.e.

$$\iint_{\mathbb{R}^2} |B(x,\zeta)| \, \mathrm{d}x \, \mathrm{d}\zeta = 1. \tag{5.15}$$

Note that this normalization is consistent with $B(x,\zeta)$ having the unit $[1/\mathrm{m}^2]$ and $u(t)$ having the unit [W]. Also note that this normalization and the constraint on the sign of $u(t)$ in (5.14) gives $u(t)$ the interpretation of the total applied actuation power, i.e.

$$u(t) = \iint_{\mathbb{R}^2} |Q_{\text{act}}(x,\zeta,t)| \, \mathrm{d}x \, \mathrm{d}\zeta. \tag{5.16}$$

It is now clear that the constraint on $u(t)$ in (5.14) and normalization of $B(x,\zeta)$ in (5.15) make the representation of a single-shape actuation heat load $B(x,\zeta)u(t)$ unique. Note that this (obviously) does not imply that the optimal single-shape actuation heat load will be unique. To simplify the optimization algorithm, the normalization (5.15) will not be enforced during the optimization process but is only applied afterwards to obtain results that are easier to interpret and compare.

Finding a solution to the obtained optimization problem is not trivial because of the nonlinear constraint on the resulting displacements in (5.10) and because of the combined optimization of the shape and intensity of the actuation heat load in (5.12). The first problem will be addressed by the two-step solution procedure described in the next subsection. The second problem will be addressed by the optimization algorithm in Section 5.3.

5.2.3 Two-step solution procedure

Because the nonlinear state constraint as in (5.10) leads to a complex (and potentially unsolvable) optimization problem, a two-step optimization procedure is proposed, in which two considerably simpler optimization problems that only involve linear input constraints need to be solved. In the first step, it is attempted to find an actuation heat load Q_{act} for which the constraint (5.10) is satisfied. Note that depending on the values of δ_{slit} and δ_{slip} such a solution might not exist and that it is not trivial to find such a solution. In the second step, the admissible solution found in the first step is used as a starting point for the minimization of the cost functional J_0 in (5.11) subject to the constraint (5.10).

Finding an admissible solution

To find an admissible solution, i.e. an actuation heat load that respects the constraint (5.10), the following penalty functional is considered

$$J_1 = \int_0^{t_e} \iint_{\mathbb{R}^2} \left[d_x^2(x,\zeta,t) + d_\zeta^2(x,\zeta,t) - d_{\max}^2(x,\zeta) \right]^+ \, \mathrm{d}x \, \mathrm{d}\zeta \, \mathrm{d}t, \tag{5.17}$$

where the function $[\,\cdot\,]^+ : \mathbb{R} \to \mathbb{R}$ is defined by

$$[a]^+ = \begin{cases} a & \text{when } a \geq 0, \\ 0 & \text{otherwise.} \end{cases} \tag{5.18}$$

Note that the integrand only contributes to the value of J_1 when $d_x^2(x,\zeta,t) + d_\zeta^2(x,\zeta,t) - d_{\max}^2(x,\zeta) > 0$, so when the maximally allowed displacement in (5.10) is exceeded. Also note that $J_1 \geq 0$ and that if $J_1 = 0$ then the maximally allowed displacement $d_{\max}(x,\zeta)$ is not exceeded. An admissible solution can thus be found by minimizing J_1.

Note that J_1 is convex (but not strictly convex) in the displacement field components d_x and d_ζ, and that by linearity of (5.4), (5.6)–(5.7) J_1 is also convex in the applied heat load Q_{act}. This implies that varying $B(x,\zeta)$ while keeping $u(t)$ fixed and varying $u(t)$ while keeping $B(x,\zeta)$ fixed cannot decrease J_1 further than the value of J_1 at a local minimum, see e.g. [Boyd and Vandenberghe, 2004]. However, the simultaneous minimization of J_1 over $B(x,\zeta)$ and $u(t)$ is nonconvex. It is therefore possible that an admissible solution exists even if a (local) minimum with $J_1 > 0$ is found.

Finding the optimal solution

In case an admissible actuation heat load $Q_{\text{act}}(x,\zeta,t) = B(x,\zeta)u(t)$ has been found, it has been established that the admissible set is nonempty. The problem that remains is finding the point in the admissible set for which the L^2-norm in (5.11) is minimal. Since a point in the admissible set has already been found, it is natural to use this as a starting point for our search. The nonlinear state constraint (5.10) is preserved during the iterations by the barrier function method, see e.g. [Nesterov and Nemirovskii, 1994]. The barrier functional is defined as $J_2 = \infty$ when the constraint (5.10) is not satisfied for any $(x,\zeta) \in \mathbb{R}^2$ and $0 \leq t \leq t_e$ and otherwise as

$$J_2 = \int_0^{t_e} \iint_{\mathbb{R}^2} \left[\left(\frac{d_{\max}^2(x,\zeta)}{d_{\max}^2(x,\zeta) - d_x^2(x,\zeta,t) - d_\zeta^2(x,\zeta,t)} \right)^p - 1 \right] \, \mathrm{d}x \, \mathrm{d}\zeta \, \mathrm{d}t, \tag{5.19}$$

where the power $p > 1$ can be tuned. The term '-1' assures that $J_2 = 0$ when $d_x(x,\zeta,t) = d_\zeta(x,\zeta,t) = 0$. The constraint (5.10) is preserved during iterations by minimizing

$$J_0 + wJ_2, \tag{5.20}$$

where $w > 0$ is a weight that can be tuned. The tuning of the power p and the weight w is discussed in Appendix C.1.

It follows that $J_0 + wJ_2$ is strictly convex in the actuation heat load Q_{act}. Minimizing $J_0 + wJ_2$ for a fixed shape of the actuation heat load $B(x, \zeta)$ yields therefore a unique optimal intensity $u(t)$ and minimizing $J_0 + wJ_2$ for a fixed intensity $u(t)$ yields a unique shape of the actuation heat load $B(x, \zeta)$, see Appendix C.2. Whether the optimal single-shape actuation heat load $B(x, \zeta)u(t)$ is unique has not been proven, but the numerical results in Section 5.4 suggest this may be the case.

5.3 Spatial discretization and optimization

5.3.1 Finite element method

The finite element method, see e.g. [Zienkiewicz et al., 2013], is used to solve the thermal model (5.4) and the thermomechanical model (5.6)–(5.7), which enables the computation of the cost functionals J_0, J_1, and J_2 in (5.11), (5.17), and (5.19), respectively. Note that the considered problem in Figure 5.1 is symmetric in $x = 0$. Therefore, only the domain $x \geq 0$ is considered and symmetric boundary conditions ($\partial T/\partial x = 0$) are applied at $x = 0$.

For the thermal model (5.4), the temperature field $T(x, \zeta, t)$ is expressed as a linear combination of FE shape functions as

$$T(x, \zeta, t) = \mathbf{N}(x, \zeta)\boldsymbol{\theta}(t), \tag{5.21}$$

where $\mathbf{N}(x, \zeta)$ is the (row) vector of (linear) finite element shape functions, and $\boldsymbol{\theta}(t)$ is the (column) vector of nodal temperatures. The actuation heat load Q_{act} of the form (5.12) is expressed as

$$Q_{\text{act}}(x, \zeta, t) = \mathbf{N}(x, \zeta)\mathbf{B}u(t), \tag{5.22}$$

where $\mathbf{B}$ is the (column) vector with the nodal values of the shape $B(x, \zeta)$ of the actuation heat load in (5.12). Note that the shape functions $\mathbf{N}(x, \zeta)$ describe the temperature field in a bounded domain. This step thus involves a truncation of the infinite domain $x \geq 0$ to a bounded domain Ω which should be chosen large enough to accurately approximate the solution on the infinite domain.

For the thermal FE model, all edges of the bounded domain Ω are perfectly insulated, i.e. $\partial T/\partial n = n_x \partial T/\partial x + n_y \partial T/\partial y = 0$ on the edge $\partial\Omega$, where $\mathbf{n} = [n_x, n_y]^\top$ is the normal to the edge. A Galerkin discretization of (5.4) with this boundary condition that also incorporates the constraint (5.13) takes the form

$$\mathbf{E}\dot{\boldsymbol{\theta}}(t) = \mathbf{A}\boldsymbol{\theta}(t) + \mathbf{B}_{\text{exp}}u_{\text{exp}}(t) + \mathbf{E}_{\mathbf{B}}\mathbf{B}u(t), \tag{5.23}$$

with initial condition $\boldsymbol{\theta}(0) = \mathbf{0}$ and

$$\mathbf{E}_0 = \iint_\Omega \mathbf{N}^\top \mathbf{N} \, \mathrm{d}x \, \mathrm{d}\zeta, \quad \mathbf{E} = \rho c H \mathbf{E}_0, \tag{5.24}$$

$$\mathbf{A} = \iint_\Omega \left(\rho c H v \mathbf{N}^\top \frac{\partial \mathbf{N}}{\partial \zeta} - h_c \mathbf{N}^\top \mathbf{N} - kH \left(\frac{\partial \mathbf{N}^\top}{\partial x} \frac{\partial \mathbf{N}}{\partial x} + \frac{\partial \mathbf{N}^\top}{\partial \zeta} \frac{\partial \mathbf{N}}{\partial \zeta} \right) \right) \mathrm{d}x \, \mathrm{d}\zeta, \tag{5.25}$$

$$\mathbf{B}_{\mathrm{exp}} = \iint_\Omega \mathbf{N}^\top B_{\mathrm{exp}} \, \mathrm{d}x \, \mathrm{d}\zeta, \tag{5.26}$$

$$\mathbf{E}_{\mathbf{B}} = \iint_{\Omega \setminus \Omega_{\mathrm{slit}}} \mathbf{N}^\top \mathbf{N} \, \mathrm{d}x \, \mathrm{d}\zeta, \tag{5.27}$$

where the dependence of $\mathbf{N}(x, \zeta)$ and $B_{\mathrm{exp}}(x, \zeta)$ on x and ζ has been dropped. Here, $\mathbf{E}$ and $\mathbf{A}$ are the heat capacity matrix and heat conduction matrices, respectively. Note that the constraint (5.13) is incorporated in $\mathbf{E}_{\mathbf{B}}$.

The mechanical FE model uses the same shape functions as the thermal FE model. The displacement field components $d_x(x, \zeta, t)$ and $d_\zeta(x, \zeta, t)$ are thus approximated as

$$d_x(x, \zeta, t) = \mathbf{N}(x, \zeta) \mathbf{d}_x(t), \quad d_\zeta(x, \zeta, t) = \mathbf{N}(x, \zeta) \mathbf{d}_\zeta(t), \tag{5.28}$$

where $\mathbf{d}_x(t)$ and $\mathbf{d}_\zeta(t)$ are the (column) vectors of nodal displacement field components in x- and ζ-direction, respectively. Application of the Galerkin method to (5.6)–(5.7) based on the expressions for $T(x, \zeta, t)$ in (5.21) and the expressions for $d_x(x, \zeta, t)$ and $d_\zeta(x, \zeta, t)$ in (5.28) (with free boundary conditions, i.e. no external force is applied at the edges) yields (see also Appendix C.3.1)

$$\mathbf{K}\mathbf{d}(t) = \mathbf{L}\boldsymbol{\theta}(t), \tag{5.29}$$

where

$$\mathbf{d}(t) = \begin{bmatrix} \mathbf{d}_x(t) \\ \mathbf{d}_\zeta(t) \end{bmatrix}, \qquad \mathbf{K} = \begin{bmatrix} \mathbf{K}_{xx} & \mathbf{K}_{x\zeta} \\ \mathbf{K}_{\zeta x} & \mathbf{K}_{\zeta\zeta} \end{bmatrix}, \qquad \mathbf{L} = \begin{bmatrix} \mathbf{L}_x \\ \mathbf{L}_\zeta \end{bmatrix}, \tag{5.30}$$

with

$$\mathbf{K}_{xx} = \iint_\Omega \left(\frac{EH}{1-\nu^2} \frac{\partial \mathbf{N}^\top}{\partial x} \frac{\partial \mathbf{N}}{\partial x} + \frac{EH}{2(1+\nu)} \frac{\partial \mathbf{N}^\top}{\partial \zeta} \frac{\partial \mathbf{N}}{\partial \zeta} + k_s \mathbf{N}^\top \mathbf{N} \right) \mathrm{d}x \, \mathrm{d}\zeta, \tag{5.31}$$

$$\mathbf{K}_{x\zeta} = \mathbf{K}_{\zeta x}^\top = \iint_\Omega \frac{EH}{1-\nu^2} \left(\nu \frac{\partial \mathbf{N}^\top}{\partial x} \frac{\partial \mathbf{N}}{\partial \zeta} + \frac{1-\nu}{2} \frac{\partial \mathbf{N}^\top}{\partial \zeta} \frac{\partial \mathbf{N}}{\partial x} \right) \mathrm{d}x \, \mathrm{d}\zeta, \tag{5.32}$$

$$\mathbf{K}_{\zeta\zeta} = \iint_\Omega \left(\frac{EH}{1-\nu^2} \frac{\partial \mathbf{N}^\top}{\partial \zeta} \frac{\partial \mathbf{N}}{\partial \zeta} + \frac{EH}{2(1+\nu)} \frac{\partial \mathbf{N}^\top}{\partial x} \frac{\partial \mathbf{N}}{\partial x} + k_s \mathbf{N}^\top \mathbf{N} \right) \mathrm{d}x \, \mathrm{d}\zeta, \tag{5.33}$$

$$\mathbf{L}_x = \frac{\alpha EH}{1-\nu} \iint_\Omega \frac{\partial \mathbf{N}^\top}{\partial x} \mathbf{N} \, \mathrm{d}x \, \mathrm{d}\zeta, \tag{5.34}$$

$$\mathbf{L}_\zeta = \frac{\alpha EH}{1-\nu} \iint_\Omega \frac{\partial \mathbf{N}^\top}{\partial \zeta} \mathbf{N} \, \mathrm{d}x \, \mathrm{d}\zeta. \tag{5.35}$$

Here, $\mathbf{K}$ and $\mathbf{L}$ denote the stiffness matrix and the thermal load matrix, respectively. Note that $\mathbf{K}$ is invertible for $k_s > 0$.

At the edge $x = 0$ a symmetric boundary condition is needed, which means that the displacement in x-direction is zero and the displacement in ζ-direction is free. In the FE model, this means that the entries of $\mathbf{d}_x(t)$ in (5.28) that correspond to nodes on the line $x = 0$ are zero. The mechanical Degrees of Freedom (DOFs) $\mathbf{d}(t)$ in (5.30) can thus be partitioned into free DOFs $\mathbf{d}_\mathrm{f}(t)$ and constrained DOFs $\mathbf{d}_\mathrm{c}(t)$, where the constrained DOFs are zero, i.e. $\mathbf{d}_\mathrm{c}(t) = \mathbf{0}$. It follows that there exists a Boolean matrix $\mathbf{S}$ such that

$$\mathbf{d}_\mathrm{f}(t) = \mathbf{S}\mathbf{d}(t), \qquad \mathbf{d}(t) = \mathbf{S}^\top \mathbf{d}_\mathrm{f}(t). \tag{5.36}$$

Inserting the second identity in (5.29) and multiplying the resulting equation by $\mathbf{S}$ yields an equation for the free DOFs

$$\mathbf{S}\mathbf{K}\mathbf{S}^\top \mathbf{d}_\mathrm{f}(t) = \mathbf{S}\mathbf{L}\boldsymbol{\theta}(t). \tag{5.37}$$

Solving this equation for $\mathbf{d}_\mathrm{f}(t)$ and inserting the result back into the second identity in (5.36) yields an expression for the nodal displacements in which the symmetric boundary condition is considered

$$\mathbf{d}(t) = \begin{bmatrix} \mathbf{d}_x(t) \\ \mathbf{d}_\zeta(t) \end{bmatrix} = \mathbf{S}^\top \left(\mathbf{S}\mathbf{K}\mathbf{S}^\top\right)^{-1} \mathbf{S}\mathbf{L}\boldsymbol{\theta}(t). \tag{5.38}$$

The discretization of the cost functional J_0 in (5.11) is made based on the expression for $Q_\mathrm{act}(x, \zeta, t)$ in (5.22), which yields

$$J_0 = 2 \int_0^{t_e} u(t) \mathbf{B}^\top \mathbf{E}_0 \mathbf{B} u(t) \, \mathrm{d}t, \tag{5.39}$$

with $\mathbf{E}_0$ as in (5.24). Note that the factor 2 is introduced because $\mathbf{E}_0$ only considers the integral over (a subset of) the right half plane $x \geq 0$. The non-quadratic cost functionals J_1 and J_2 are discretized by nodal interpolation. This means that a scalar nonlinear function $f(x, \zeta)$ on the domain $(x, \zeta) \in \mathbb{R}^2$ is approximated in terms of the FE shape functions $\mathbf{N}(x, \zeta)$ by $\mathbf{N}(x, \zeta)\mathbf{f}$, where $\mathbf{f}$ is a vector containing the nodal values of $f(x, \zeta)$ at the nodes of the FE mesh. The integral of $f(x, \zeta)$ over $(x, \zeta) \in \mathbb{R}^2$ is then approximated as

$$\begin{aligned} \iint_{\mathbb{R}^2} f(x, \zeta) \, \mathrm{d}x \, \mathrm{d}\zeta &\approx \iint_\Omega \mathbf{N}(x, \zeta)\mathbf{f} \, \mathrm{d}x \, \mathrm{d}\zeta \\ &= \iint_\Omega \mathbf{1}^\top \mathbf{N}^\top(x, \zeta)\mathbf{N}(x, \zeta)\mathbf{f} \, \mathrm{d}x \, \mathrm{d}\zeta = \mathbf{1}^\top \mathbf{E}_0 \mathbf{f}, \end{aligned} \tag{5.40}$$

where $\mathbf{1}$ is a column vector of ones. For the second identity it is assumed that

$$\mathbf{N}(x, \zeta)\mathbf{1} = 1, \tag{5.41}$$

for all $(x, \zeta) \in \Omega$. This assumption is satisfied for standard Lagrangian FE shape functions $\mathbf{N}(x, \zeta)$, see e.g. [Zienkiewicz et al., 2013]. The nonquadratic cost functionals J_1 and J_2 in (5.17) and (5.19) are thus discretized as

$$J_1 = 2 \int_0^{t_e} \mathbf{1}^\top \mathbf{E}_0 \left[\mathbf{d}_x^2(t) + \mathbf{d}_\zeta^2(t) - \mathbf{d}_{\max}^2 \right]^+ \, \mathrm{d}t \tag{5.42}$$

$$J_2 = 2 \int_0^{t_e} \mathbf{1}^\top \mathbf{E}_0 \left(\left(\frac{\mathbf{d}_{\max}^2}{\mathbf{d}_{\max}^2 - \mathbf{d}_x^2(t) - \mathbf{d}_\zeta^2(t)} \right)^p - \mathbf{1} \right) \mathrm{d}t \tag{5.43}$$

where the operations $[\,\cdot\,]^+$, $(\,\cdot\,)^2$, $[\,\cdot\,]^p$, $\cdot/\cdot$ are applied component-wise, and $\mathbf{d}_{\max}$ is a vector containing the values of $d_{\max}(x, \zeta)$ in the nodes of the FE model. Again, the factor 2 appears because $\mathbf{E}_0$ in (5.24) only considers the integral over (a subset of) the right half plane $x \geq 0$.

5.3.2 Sensitivity Analysis

As discussed in Section 5.2.3, two optimization problems need to be solved. In the first optimization problem, the cost functional is $J = J_1$ and in the second optimization problem the cost functional is $J = J_0 + wJ_2$. In this section, the computation of the gradients of these cost functionals w.r.t. the discretized shape of the actuation heat load $\mathbf{B}$ and the intensity $u(t)$ is discussed. These will be used in the gradient-based optimization procedure in Subsection 5.3.3.

The computation of the gradient w.r.t. the intensity $u(t)$ is based on the following well-known result. Consider a cost functional of the form

$$J = J(\mathbf{B}, u) = \int_0^{t_e} \left(\bar{f}(\boldsymbol{\theta}(t)) + g(\mathbf{B}, u(t)) \right) \, \mathrm{d}t, \tag{5.44}$$

where the state $\boldsymbol{\theta}(t)$ depends on $\mathbf{B}$ and $u(t)$ through (5.23). The gradient $\nabla_u J(\mathbf{B}, u)$ is defined by the property that for any variation $\tilde{u}(t)$ of $u(t)$, it holds that

$$\langle \nabla_u J(\mathbf{B}, u), \tilde{u} \rangle_u = \lim_{\varepsilon \to 0} \frac{J(\mathbf{B}, u + \varepsilon \tilde{u}) - J(\mathbf{B}, u)}{\varepsilon}, \tag{5.45}$$

where $\langle \,\cdot\,, \,\cdot\, \rangle_u$ is the inner product on the space of intensities

$$\langle u_1(t), u_2(t) \rangle_u = \int_0^{t_e} u_1(t) u_2(t) \, \mathrm{d}t. \tag{5.46}$$

The gradient $\nabla_u J(\mathbf{B}, u)$ can be computed based on the adjoint state $\boldsymbol{\varphi}(t)$, see e.g. [Naidu, 2002; Borzì and Schulz, 2012]

$$\left(\nabla_u J(\mathbf{B}, u) \right)(t) = \mathbf{B}^\top \mathbf{E}_{\mathbf{B}} \boldsymbol{\varphi}(t) + \frac{\partial g}{\partial u}(\mathbf{B}, u(t)), \tag{5.47}$$

where $\partial g/\partial u$ denotes the partial derivative of g w.r.t. its second argument and $\boldsymbol{\varphi}(t)$ is the solution of

$$-\mathbf{E}^\top \dot{\boldsymbol{\varphi}}(t) = \mathbf{A}^\top \boldsymbol{\varphi}(t) + \left(\frac{\partial \bar{f}}{\partial \boldsymbol{\theta}}(\boldsymbol{\theta}(t))\right)^\top, \qquad \boldsymbol{\varphi}(t_e) = \mathbf{0}. \tag{5.48}$$

The gradient $\nabla_u J(\mathbf{B}_0, u_0)$ can thus be computed in the following steps:

1) compute $\boldsymbol{\theta}_0(t)$ as the solution of (5.23) with $\mathbf{B} = \mathbf{B}_0$ and $u(t) = u_0(t)$ by integrating forward in time starting from the initial condition $\boldsymbol{\theta}(0) = \mathbf{0}$,

2) compute $\boldsymbol{\varphi}_0(t)$ from (5.48) with $\boldsymbol{\theta}(t) = \boldsymbol{\theta}_0(t)$, $\mathbf{B} = \mathbf{B}_0$, and $u(t) = u_0(t)$ by integrating backward in time starting from the final condition $\boldsymbol{\varphi}(t_e) = \mathbf{0}$,

3) compute $\nabla J(\mathbf{B_0}, u_0)$ from (5.47) with $\boldsymbol{\varphi}(t) = \boldsymbol{\varphi}_0(t)$, $\boldsymbol{\theta}(t) = \boldsymbol{\theta}_0(t)$, $\mathbf{B} = \mathbf{B}_0$, and $u(t) = u_0(t)$.

The cost functionals $J = J_1$ and $J = J_0 + wJ_2$ with J_0, J_1, and J_2 as in (5.39), (5.42)–(5.43) are written in the form

$$J = J(\mathbf{B}, u) = \int_0^{t_e} \left(f(\mathbf{d}(t)) + g(\mathbf{B}, u(t))\right)\, \mathrm{d}t, \tag{5.49}$$

where $\mathbf{d}(t)$ is the vector of nodal displacements resulting from $\mathbf{B}$ and $u(t)$, i.e. $\mathbf{d}(t)$ is computed by solving $\boldsymbol{\theta}(t)$ from (5.23) and then $\mathbf{d}(t)$ from (5.38). Note that (5.49) can be written in the form (5.44) by setting

$$\bar{f}(\boldsymbol{\theta}(t)) = f(\mathbf{S}^\top \left(\mathbf{S}\mathbf{K}\mathbf{S}^\top\right)^{-1} \mathbf{S}\mathbf{L}\boldsymbol{\theta}(t)). \tag{5.50}$$

In particular, it follows that

$$\frac{\partial \bar{f}}{\partial \boldsymbol{\theta}} = \frac{\partial f}{\partial \mathbf{d}} \frac{\partial \mathbf{d}}{\partial \boldsymbol{\theta}} = \frac{\partial f}{\partial \mathbf{d}} \mathbf{S}^\top \left(\mathbf{S}\mathbf{K}\mathbf{S}^\top\right)^{-1} \mathbf{S}\mathbf{L}. \tag{5.51}$$

Using (5.51), (5.48) can now be expressed in terms of the function f instead of $\bar{f}$ so that the gradient of the cost functional (5.49) can also be computed based on the adjoint state. Explicit expressions for f, g, $\partial f/\partial \mathbf{d}$, and $\partial g/\partial u$ when $J = J_1$ or $J = J_0 + wJ_2$ are given in Appendix C.3.2.

Similarly, the gradient $\nabla_{\mathbf{B}} J(\mathbf{B}, u)$ is defined by the property that for any variation $\tilde{\mathbf{B}}$ of $\mathbf{B}$, it holds that

$$\langle \nabla_{\mathbf{B}} J(\mathbf{B}, u), \tilde{\mathbf{B}} \rangle_B = \lim_{\varepsilon \to 0} \frac{J(\mathbf{B} + \varepsilon \tilde{\mathbf{B}}, u) - J(\mathbf{B}, u)}{\varepsilon}, \tag{5.52}$$

where $\langle \cdot\,, \cdot \rangle_B$ is the inner product on the space of actuation heat load shapes (which are parametrized by their nodal values according to (5.22)) defined by

$$\langle \mathbf{B}_1, \mathbf{B}_2 \rangle_B = \mathbf{B}_1^\top \mathbf{E}_0 \mathbf{B}_2. \tag{5.53}$$

In Appendix C.3.3 it is shown that the gradient of a cost functional J w.r.t. $\mathbf{B}$ of the form (5.44) can be expressed in terms of the adjoint state $\boldsymbol{\varphi}(t)$ in (5.48) as

$$\nabla_{\mathbf{B}} J(\mathbf{B}, u) = \mathbf{E}_0^{-1} \mathbf{E}_{\mathbf{B}} \int_0^{t_e} \boldsymbol{\varphi}(t) u(t) \, \mathrm{d}t + \mathbf{E}_0^{-1} \int_0^{t_e} \left(\frac{\partial g}{\partial \mathbf{B}}(\mathbf{B}, u(t)) \right)^\top \mathrm{d}t. \quad (5.54)$$

The procedure to compute $\nabla_{\mathbf{B}} J(\mathbf{B}, u)$ is similar to the procedure to compute $\nabla_u J(\mathbf{B}, u)$ described above. Using (5.51), this result can again be applied for $J = J_1$ and $J = J_0 + wJ_2$ which are of the form (5.49). Explicit formulas for $\partial g / \partial \mathbf{B}$ are given in Appendix C.3.2.

5.3.3 Optimization algorithm

With the actuation heat load that consists of a single shape as in (5.22), both the shape of the discretized actuation heat load $\mathbf{B}$ and the intensity $u(t)$ need to be optimized. Since J_1 and $J_0 + wJ_2$ are convex in u, minimizing $J(\mathbf{B}, u)$ over u for fixed $\mathbf{B}$ yields a unique minimal value of J, although the minimizer u is not necessarily unique, see e.g. [Boyd and Vandenberghe, 2004] or Appendix C.2. The function $\hat{J}(\mathbf{B}) = \min_u J(\mathbf{B}, u)$ is thus well defined. A possible approach is to minimize $\hat{J}(\mathbf{B})$ over $\mathbf{B}$. One can easily verify that $\hat{J}(\mathbf{B}) = \hat{J}(\beta \mathbf{B})$ for any $\beta > 0$. This scaling freedom can be removed by normalizing $\mathbf{B}$, e.g. using (5.15) or by requiring that $\|\mathbf{B}\|_B^2 = \langle \mathbf{B}, \mathbf{B} \rangle_B = 1$. In the latter case $\hat{J}(\mathbf{B})$ is in fact minimized over the Stiefel manifold, on which there are typically multiple local minima, see e.g. [Manton et al., 2003; Absil et al., 2008]. Another disadvantage of this approach is that every evaluation of $\hat{J}(\mathbf{B})$ requires the solution of an optimal control problem, which is costly.

We therefore use a different approach in which the shape $\mathbf{B}$ and intensity $u(t)$ of the actuation heat load are updated alternately. In this way it is prevented that a lot of time is spent on the computation of the optimal intensity $u(t)$ for a suboptimal shape of the actuation heat load $\mathbf{B}$, which typically happens when the minimization of $\hat{J}(\mathbf{B})$ is considered. The resulting algorithm takes the following form. Here, $\mathbf{B}^{(k)}$ and $u^{(k)}(t)$ denote the k-th iterate of $\mathbf{B}$ and $u(t)$, respectively, `max_iters` denotes the maximum number of iterations, 'UpdateB' and 'UpdateU' represent the update schemes for $\mathbf{B}$ and u, and 'Converged' represents the method that checks for convergence. The methods 'UpdateB' , 'UpdateU', and 'Converged' will be elaborated below.

Note that it is possible to choose the initial guess $\mathbf{B}^{(0)} = \mathbf{0}$ but that the initial guess $u^{(0)}$ must be nonzero because otherwise $\nabla_{\mathbf{B}} J(\mathbf{B}^{(0)}, u^{(0)}) = \mathbf{0}$, which leads to a problem in 'updateB' in line 4. Swapping lines 4 and 5 such that first u is updated and then $\mathbf{B}$ is updated leads to an algorithm in which the initial guess $u^{(0)}$ can be zero and $\mathbf{B}^{(0)}$ must be nonzero. However, this form is not presented here because it is easier to generate an initial guess for $u(t)$, which depends on one variable, than for $\mathbf{B}$, which represents a function depending on

Algorithm 5.1 Alternating update scheme

1: Initial guess $\mathbf{B}^{(0)}$ and $u^{(0)} \neq 0$
2: $k = 0$
3: **while** $k <$`max_iters` **do**
4: $\quad \mathbf{B}^{(k+1)} = \text{UpdateB}(\mathbf{B}^{(k)}, u^{(k)})$
5: $\quad u^{(k+1)} = \text{UpdateU}(\mathbf{B}^{(k+1)}, u^{(k)})$
6: $\quad$ **if** Converged($\mathbf{B}^{(k)}$, $\mathbf{B}^{(k+1)}$, $u^{(k)}$, $u^{(k+1)}$) **then**
7: $\quad\quad$ **return** $(\mathbf{B}^{(k+1)}, u^{(k+1)})$
8: $\quad$ **end if**
9: $\quad k = k + 1$
10: **end while**

the two spatial variables (x, ζ) and because the considered examples have shown good convergence starting from the initial guess $\mathbf{B}^{(0)} = \mathbf{0}$. It is recommended to use an initial guess $u^{(0)}$ that satisfies $u^{(0)}(t_e) = 0$ because $u(t_e) = 0$ must hold at the minimum of J.

The update procedure 'UpdateB' in line 4 of the algorithm updates the current iterate $\mathbf{B}^{(k)}$ in the direction of the gradient

$$\mathbf{B}^{(k+1)} = \mathbf{B}^{(k)} - h_{\mathbf{B}} \nabla_{\mathbf{B}} J(\mathbf{B}^{(k)}, u^{(k)}). \tag{5.55}$$

The stepsize $h_{\mathbf{B}} > 0$ is estimated based on a quadratic approximation of the cost function $J(\mathbf{B}^{(k+1)}, u^{(k)})$ around $h_{\mathbf{B}} = 0$

$$J(\mathbf{B}^{(k+1)}, u^{(k)}) \approx J(\mathbf{B}^{(k)}, u^{(k)}) + h_{\mathbf{B}} G_{\mathbf{B}}^{(k)} + \frac{1}{2} h_{\mathbf{B}}^2 H_{\mathbf{B}}^{(k)}, \tag{5.56}$$

with

$$G_{\mathbf{B}}^{(k)} = -\langle \nabla_{\mathbf{B}} J(\mathbf{B}^{(k)}, u^{(k)}), \nabla_{\mathbf{B}} J(\mathbf{B}^{(k)}, u^{(k)}) \rangle_B, \tag{5.57}$$

$$H_{\mathbf{B}}^{(k)} = \frac{\partial^2}{\partial h^2} \left[J(\mathbf{B}^{(k)} + h \nabla_{\mathbf{B}} J(\mathbf{B}^{(k)}, u^{(k)}), u^{(k)}) \right]_{h=0}. \tag{5.58}$$

The formula for $G_{\mathbf{B}}^{(k)}$ follows after taking $\tilde{\mathbf{B}} = -\nabla_{\mathbf{B}} J(\mathbf{B}^{(k)}, u^{(k)})$ in the definition of the gradient in (5.52). The computation of $H_{\mathbf{B}}^{(k)}$ is discussed in Appendix C.3.4. The stepsize $h_{\mathbf{B}}$ can now be estimated by minimizing the RHS of (5.56), which leads to $h_{\mathbf{B},\text{opt}} = -G_{\mathbf{B}}^{(k)} / H_{\mathbf{B}}^{(k)}$. Since the considered cost functions are not quadratic, the expansion in (5.56) is an approximation and there is no guarantee that this choice indeed leads to a decrease in the cost function J. If an increase is observed, the step size is halved until a decrease in J is observed. Note that this will eventually happen because (away from a critical point of J where $\nabla_{\mathbf{B}} J = 0$) $G_{\mathbf{B}}^{(k)} < 0$ and the linear term in (5.56) will dominate for h small enough.

The update described by 'UpdateU' in line 5 of the algorithm preserves the constraint (5.14) through the projected gradient method, see e.g. [Hinze et al., 2009]. The current iterate $u^{(k)}(t)$ is thus updated according to

$$u^{(k+1)}(t) = \Pi_u \left(u^{(k)} - h_u \nabla_u J(\mathbf{B}^{(k+1)}, u^{(k)}) \right)(t), \tag{5.59}$$

where $h_u > 0$ denotes the step size and Π_u denotes the projection onto the admissible set given by

$$\left(\Pi_u(u)\right)(t) = \begin{cases} 0 & \text{when } u(t) \leq 0, \\ u(t) & \text{otherwise.} \end{cases} \tag{5.60}$$

Note that $u^{(k+1)}$ does not depend linearly on h_u. For example, when $u^{(k)}(t_1) = 1$ and $(\nabla_u J)(t_1) = 1$ on a certain time instant $t = t_1$, then $u^{(k+1)}(t_1) = 1 - h_u$ for $0 \leq h_u \leq 1$ and $u^{(k+1)}(t_1) = 0$ for $h_u \geq 1$. Determining the step size h_u is thus more involved than determining the step size $h_{\mathbf{B}}$.

To estimate h_u, an approximation of $u^{(k+1)}(t)$ for small $h_u > 0$ will be used. Therefore, $\Pi\nabla_u J(\mathbf{B}^{(k+1)}, u^{(k)})$, the right derivative of $u^{(k+1)}(t)$ in (5.59) in $h_u = 0$, is considered

$$\left(\Pi\nabla_u J(\mathbf{B}^{(k+1)}, u^{(k)})\right)(t) := \lim_{h_u \downarrow 0} \frac{u^{(k+1)}(t) - u^{(k)}(t)}{h_u}. \tag{5.61}$$

The right derivative $\Pi\nabla_u(\mathbf{B}^{(k+1)}, u^{(k)})$ is sometimes called the projected gradient but is *not* equal to $\Pi_u(\nabla_u(\mathbf{B}^{(k+1)}, u^{(k)}))$, the projection of the gradient $\nabla_u J(\mathbf{B}^{(k+1)}, u^{(k)})$ on the admissible set. To find an explicit expression for $\Pi\nabla_u J(\mathbf{B}^{(k+1)}, u^{(k)})$, note that $u^{(k)}(t) - h_u \left(\nabla_u J\right)(t) > 0$ for $h_u > 0$ sufficiently small if $u^{(k)}(t) > 0$ or if $u^{(k)}(t) = 0$ and $\left(\nabla_u J\right)(t) < 0$. In these situations, the projection Π_u in (5.59) does not affect the update and $u^{(k+1)}(t) = u^{(k)}(t) - h_u \left(\nabla_u J\right)(t)$. In the remaining situation where $u^{(k)}(t) = 0$ and $\left(\nabla_u J\right)(t) \geq 0$, it holds that $u^{(k)}(t) - h_u \left(\nabla_u J\right)(t) \leq 0$ for all $h_u > 0$ so that $u^{(k+1)}(t) = u^{(k)}(t) = 0$ in this case. Inserting these results into (5.61) yields

$$\begin{aligned} &\left(\Pi\nabla_u J(\mathbf{B}^{(k+1)}, u^{(k)})\right)(t) = \\ &\begin{cases} 0 & \text{if } u^{(k)}(t) = 0 \text{ and } \nabla_u J(\mathbf{B}^{(k+1)}, u^{(k)})(t) \geq 0, \\ \nabla_u J(\mathbf{B}^{(k+1)}, u^{(k)})(t) & \text{otherwise.} \end{cases} \end{aligned} \tag{5.62}$$

The second-order approximation of $J(\mathbf{B}^{(k+1)}, u^{(k+1)})$ for positive h_u near $h_u = 0$ thus takes the form

$$J(\mathbf{B}^{(k+1)}, u^{(k+1)}) \approx J(\mathbf{B}^{(k+1)}, u^{(k)}) + h_u G_u^{(k)} + \frac{1}{2} h_u^2 H_u^{(k)}, \tag{5.63}$$

with

$$G_u^{(k)} = -\langle \nabla_u J(\mathbf{B}^{(k+1)}, u^{(k)}), \Pi \nabla_u J(\mathbf{B}^{(k+1)}, u^{(k)}) \rangle_u, \tag{5.64}$$

$$H_u^{(k)} = \frac{\partial^2}{\partial h^2} \left(J(\mathbf{B}^{(k+1)}, u^{(k)} + h \Pi \nabla_u J(\mathbf{B}^{(k+1)}, u^{(k)})) \right) \Big|_{h=0}, \tag{5.65}$$

where the expression for $G_u^{(k)}$ follows from the definition of $\nabla_u J(\mathbf{B}^{(k+1)}, u^{(k)})$ in (5.45) with $\tilde{u} = \Pi \nabla_u J(\mathbf{B}^{(k+1)}, u^{(k)})$. The computation of $H_u^{(k)}$ is further discussed in Appendix C.3.4. Similarly as for $h_{\mathbf{B}}$, the step size is estimated as $h_{u,\mathrm{opt}} = -G_u^{(k)}/H_u^{(k)}$. If this step size does lead to an increase in the cost function, the step size is halved until a decrease in J is observed. This process will terminate eventually because the linear term in (5.63) will dominate the higher-order terms and $G_u^{(k)} < 0$.

The criteria for convergence checked in line 6 of the algorithm are:

1) the relative change $\|\mathbf{B}^{(k+1)} - \mathbf{B}^{(k)}\|_B / \|\mathbf{B}^{(k)}\|_B$ is below `tol`,

2) the relative change $\|u^{(k+1)} - u^{(k)}\|_u / \|u^{(k)}\|_u$ is below `tol`,

3) the relative decrease of the cost functional $(J(\mathbf{B}^{(k)}, u^{(k)}) - J(\mathbf{B}^{(k+1)}, u^{(k+1)}))/J(\mathbf{B}^{(k)}, u^{(k)})$ is below `tol`.

Note that the same tolerance `tol` is used in all three conditions and that the norms $\|\cdot\|_B$ and $\|\cdot\|_u$ are induced by the inner products in (5.53) and (5.46), respectively.

Note that the shape of the actuation heat load $B(x, \zeta) = \mathbf{N}(x, \zeta)\mathbf{B}$ is not enforced to have unit L^1-norm during the update process. The normalization (5.15) is achieved by rescaling $\mathbf{B}$ and $u(t)$ after the algorithm has terminated.

5.4 Results

Recall that the considered situation in Figure 5.1 is symmetric in $x = 0$, so that only the domain $x \geq 0$ needs to be considered in the FE model. This infinite domain is truncated to $(x, \zeta) \in \Omega = [0, 4L] \times [-3vt_e, 3vt_e]$, which is chosen such that the temperature increase and deformation at the edges of the domain are negligible. The FE model uses linear quadrilateral elements and has 6360 nodes and 6188 elements. The mesh is shown in Figure 5.2. A rectangular grid is used with a mesh size of 2 mm in the x-direction and a mesh size of 0.7 mm in the ζ-direction near the area where the heat load is applied and a mesh size of 2 mm outside this area. The time interval $[0, t_e]$ is discretized using $N = 200$ equidistant time points. The time discretization scheme of [Apel and Flaig, 2012] is used, which means that the state equation (5.23) is discretized using the Crank-Nicolson scheme [Crank and Nicolson, 1947] and the adjoint state

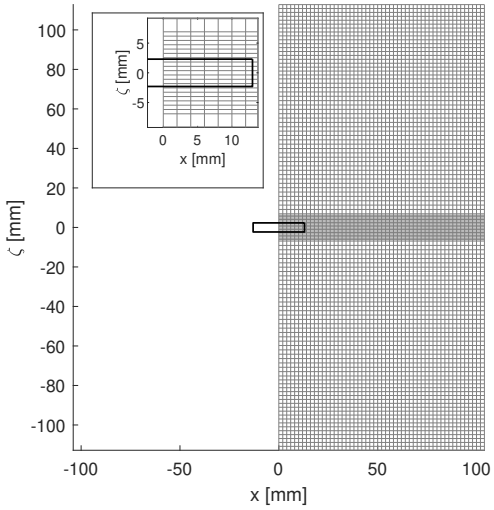

Figure 5.2. The used mesh (gray lines) with the slit area in which the heat load Q_{exp} is applied (black rectangle)

equation (5.48) in such a way that the gradients resulting from the discretization of (5.47) and (5.54) are the exact gradients of the discretized cost functional (this is not the case when the Crank-Nicolson scheme is also used for (5.48)). Details can be found in Appendix C.3.5. Frequently, linear systems involving the stiffness matrix $\mathbf{SKS}^\top$ and the matrix $\mathbf{E}/\tau - \mathbf{A}/2$, where τ is the grid spacing of the time grid, need to be solved. To speed up this process, these systems are solved using a precomputed Lower-Upper (LU) factorization.

The used parameter values are given in Table 5.1. Note that an actuation heat load will be designed that achieves a maximal deformation in the slit of $\delta_{\text{slit}} = 2$ nm, which is a reduction of a factor 2 compared to the maximal deformation of 4.1 nm that occurs without actuation. Also observe that $\delta_{\text{slip}} = 3.67$ nm is exceeded without actuation, which means actuation is needed to prevent slip. It should be noted that no admissible solution can be found when δ_{slit} or δ_{slip} are chosen too small. For example, for $\delta_{\text{slit}} = 0.5$ nm and $\delta_{\text{slip}} = 3.67$ nm, no admissible actuation heat load can be found.

5.4.1 Single-shape actuation heat load

Figures 5.3a, 5.4a, and 5.5a illustrate the design procedure described in the previous section. For ease of interpretation, the shape of the actuation heat load computed in the domain $x \geq 0$ is mirrored in $x = 0$ in these figures, although the domain $x < 0$ is not considered in the FE model. Starting from the initial

Table 5.1. Parameter values

Description	Symbol	Value	Unit
Mass density	ρ	2329	$\mathrm{kg/m^3}$
Specific heat capacity	c	705	J/kg/K
Thermal conductivity	k	149	W/K/m
Thermal conductance to surroundings	h_c	1500	$\mathrm{W/m^2/K}$
Young's modulus	E	167	GPa
Poisson's ratio	ν	0.3	-
Stiffness of the surroundings/unit area	k_s	$1.21 \cdot 10^{12}$	$\mathrm{N/m^3}$
Thickness	H	0.775	mm
Length of slit in x-direction	L	26	mm
Length of slit in y-direction	W	4.6	mm
Velocity of applied heat load	v	0.276	m/s
Applied heating power	P_{exp}	3.2	W
Length of considered time interval	t_e	0.136	s
Allowed deformation in the slit	δ_{slit}	2	nm
Allowed deformation on the wafer	δ_{slip}	3.67	nm
Power in cost function J_2	p	3.5	-
Weight	w	$2.1 \cdot 10^5$	$\mathrm{W^2/m^4}$
Tolerance	`tol`	10^{-3}	-

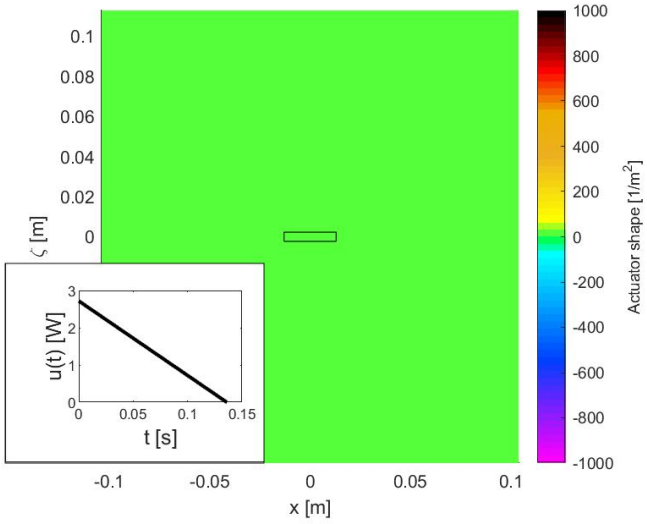

(a) Initial guess 1

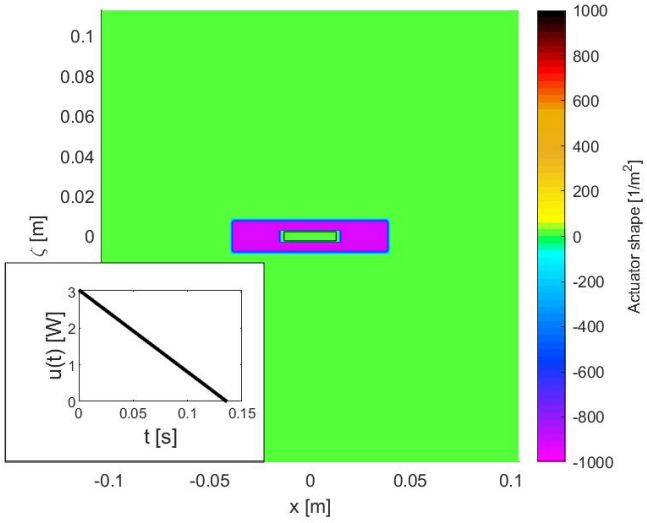

(b) Initial guess 2

Figure 5.3. The shapes $B(x, \zeta)$ and intensities $u(t)$ of the actuation heat load that are used as initial guess in the optimization. The black rectangle indicates Ω_{slit}.

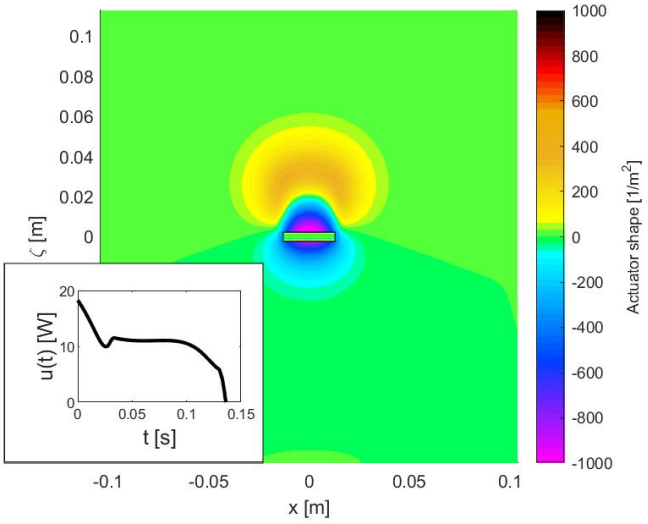

(a) Initial guess 1

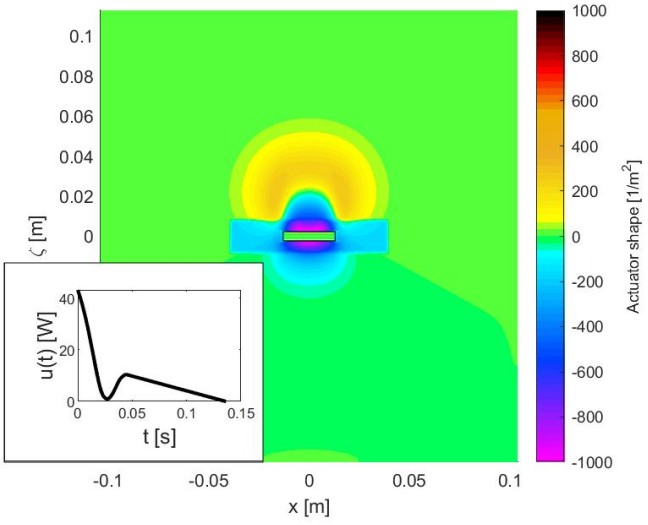

(b) Initial guess 2

Figure 5.4. The (admissible) shapes $B(x, \zeta)$ and intensities $u(t)$ of the actuation heat load found after minimizing J_1 starting from the two initial guesses in Figure 5.3. The black rectangle indicates Ω_{slit}.

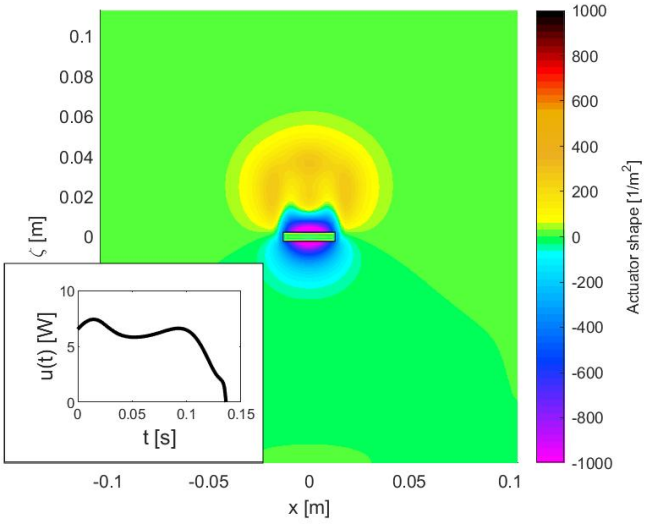

(a) Initial guess 1

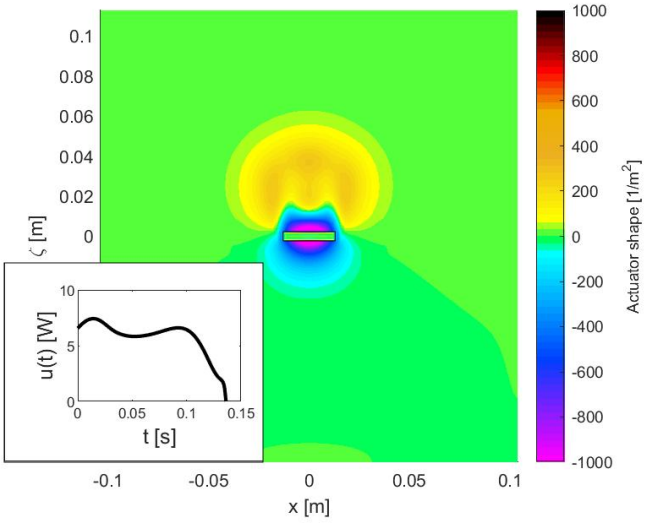

(b) Initial guess 2

Figure 5.5. The shapes $B(x, \zeta)$ and intensities $u(t)$ of the actuation heat load found after minimizing $J_0 + wJ_2$ starting from the two solutions in Figure 5.4. The black rectangle indicates Ω_{slit}.

guess in Figure 5.3a where the shape of the actuation heat load $B(x,\zeta) = 0$ and the intensity is chosen rather arbitrarily as $u(t) = t_e - t$ [W], minimizing J_1 in (5.17) leads to the admissible design in Figure 5.4a. This design is then used to initialize the optimization procedure for $J_0 + wJ_2$, which leads to the design in Figure 5.5a. Note that the normalization $\|B\|_{L^1} = 1$ is applied in Figures 5.3, 5.4, and 5.5 (except for Figure 5.3a where $B(x,\zeta) = 0$). The intensities $u(t)$ in Figures 5.4a and 5.5a clearly show that the second optimization step significantly reduces the applied heat. In particular, the value of $J_0 = 4963$ for the design in Figure 5.4a is reduced to $J_0 = 1434$ for the design in Figure 5.5a.

The designed shape of the optimal actuation heat load in Figure 5.5a can be understood as follows. Note that having $Q_{\text{act}} = -Q_{\text{exp}}$ would result in zero deformations because no net heat load is applied. However, the constraint (5.13) excludes this solution. The cooling around the slit in Figure 5.5a attempts to have some of this effect while respecting the constraint (5.13). A more surprising aspect of the shape in Figure 5.5a may be the heating applied in the area where $\zeta > 0$. To understand this, recall that the expose load moves in the positive ζ-direction, which means that during scanning the heat applied by the expose light is accumulating in the area where $\zeta < 0$. The thermal expansion due to this heating pushes the slit into the positive ζ-direction. The actuation heat load applied in the area where $\zeta > 0$ now creates thermal expansion in front of the slit, which pushes the slit back into the negative ζ-direction, thus reducing the total deformation in the slit.

Table 5.2 lists the values of $J_0 + wJ_2$, J_0 and

$$E_{\text{act}} = \int_0^{t_e} \iint_{\mathbb{R}^2} |Q_{\text{act}}(x,\zeta,t)| \, \mathrm{d}x \, \mathrm{d}\zeta \, \mathrm{d}t, \tag{5.66}$$

for the computed optimal actuation heat load found after minimizing $J_0 + wJ_2$. Note that E_{act} has the interpretation of the total applied actuation energy in [J]. Table 5.3 shows how many iterations (i.e. # updates of $\mathbf{B}$ + # updates of $u(t)$) are needed and the computational time that is required to compute the optimal actuation heat load. As can be seen, finding an admissible solution, i.e. finding an actuation heat load for which $J_1 = 0$, requires only a few iterations, whereas the minimization of $J_0 + wJ_2$ requires more. Note that the number of iterations needed for the minimization of J_1 will increase as the constraint (5.10) becomes more stringent.

Figures 5.3b, 5.4b, and 5.5b show the shapes $B(x,\zeta)$ and intensities $u(t)$ that are obtained starting from the initial intensity $u^{(0)}(t) = 20(t_e - t)$ and the initial shape $B^{(0)}(x,\zeta)$ is $-1/(8LW)$ for $(x,\zeta) \in [-3L/2, 3L/2] \times [-3W/2, 3W/2] \backslash \Omega_{\text{slit}}$ and zero otherwise, see Figure 5.3b. This initial guess is motivated by the idea that cooling around the slit is a quite effective method to reduce the deformation in the slit. The fact that the shapes and intensities of the actuation heat loads in Figure 5.4 are different illustrates that there are indeed many admissible solutions that satisfy the constraints (5.10) and (5.13). The particular solution

Table 5.2. Minima found after the optimization of the single-shape actuation heat load $Q_{\text{act}}(x, \zeta, t) = B(x, \zeta)u(t)$

	Initial guess 1 (Figure 5.5a)	Initial guess 2 (Figure 5.5b)	Cooler constraints (Figure 5.6a)	Heater constraints (Figure 5.6b)
$J_0 + wJ_2$	1607	1607	2335	6396
J_0	1434	1434	2145	5280
E_{act}	0.794	0.793	0.555	2.000

Table 5.3. Iterations and computational time required to find the single-shape actuation heat load $Q_{\text{act}}(x, \zeta, t) = B(x, \zeta)u(t)$

	minimizing of J_1		minimizing $J_0 + wJ_2$	
	# iterations	time [s]	# iterations	time [s]
Initial guess 1	3	4	133	350
Initial guess 2	4	7	203	541
Cooler constraints	5	12	223	700
Heater constraints	9	26	247	732

found after minimizing J_1 thus strongly depends on the initial guess that is used. Note that the optimal designs in Figure 5.5 are very similar, which suggests that the single-shape optimal actuation heat load may be unique. This is also indicated by the results in Table 5.2.

The algorithm from Section 5.3.3 can be extended such that constraints on the shape of the actuation heat load $B(x, \zeta)$ can be incorporated. The updates for $B(x, \zeta)$ are then also computed using the projected gradient method, similarly as the updates of $u(t)$ outlined in Section 5.3.3. This enables the design of an actuation heat load that can only cool (i.e. $B(x, \zeta) \leq 0$) or heat (i.e. $B(x, \zeta) \geq 0$). The optimal designs computed with these additional constraints are shown in Figure 5.6. The initial guess in Figure 5.3a was also used as starting point for these results. The actuation heat load in Figure 5.6a seems to aim at counteracting the heat load induced by the expose light, i.e. it attempts to approximate the situation $Q_{\text{act}} = -Q_{\text{exp}}$ as well as possible. It is remarkable to see that the heating in Figure 5.6b is applied all around the slit (in particular also for $\zeta < 0$) but not in the direct neighborhood of the slit. Such heating leads to thermal expansion of the material around the slit and compression of the material inside the slit and can thus counteract the thermal expansion due to the expose light inside the slit. Table 5.2 indicates that the minimal values of $J_0 + wJ_2$ and J_0 obtained with these additional constraints are indeed higher than the minimal value for the designs obtained without these constraints. Note that the actuation heat load with cooler constraints has a lower L^1-norm than

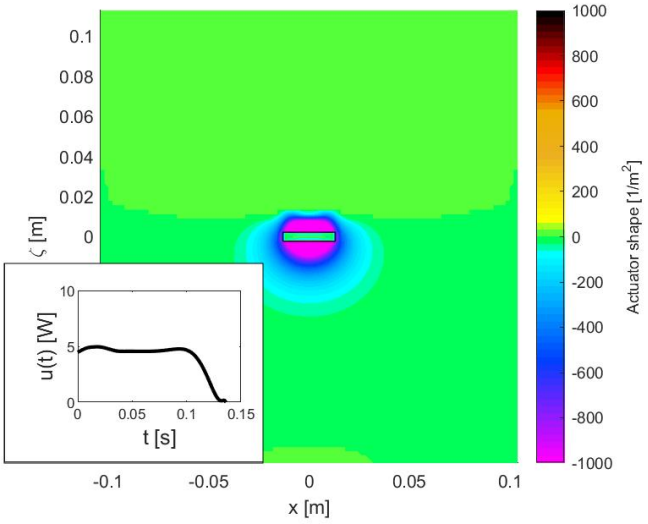

(a) Cooler constraints

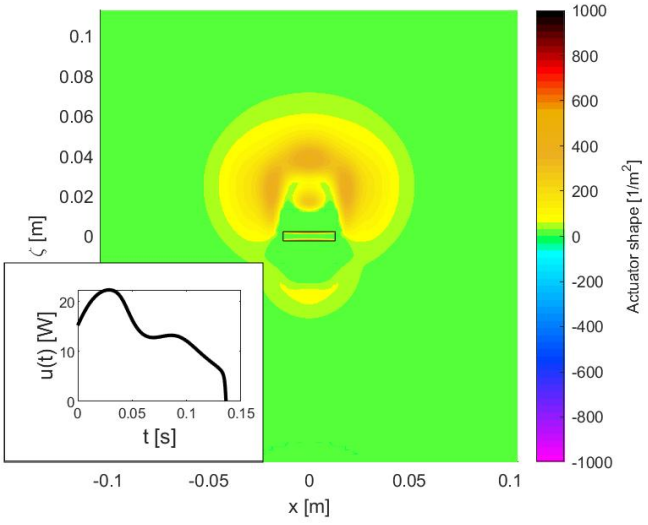

(b) Heater constraints

Figure 5.6. The optimal shapes $B(x, \zeta)$ and intensities $u(t)$ computed with cooler constraints $B(x, \zeta) \leq 0$ and $u(t) \geq 0$ and with heater constraints $B(x, \zeta) \geq 0$ and $u(t) \geq 0$.

the unconstrained actuation heat load. This reflects that the shape $B(x,\zeta)$ designed with cooler constraints is concentrated in a smaller area than the other designs which leads to a smaller L^1-norm, as was already observed in [Stadler, 2009; Herzog et al., 2012].

5.4.2 Comparison to free-shape optimal controls

The obtained single-shape actuation heat loads of the form (5.12) will be compared to a free-shape actuation heat load

$$Q_{\text{act}}(x,\zeta,t) = U(x,\zeta,t). \tag{5.67}$$

Similar to the constraint (5.13) for the single-shape actuation heat load, it is required that no heat can be applied inside the area Ω_{slit} where the light source projects the pattern, i.e.

$$U(x,\zeta,t) = 0, \qquad \text{for } (x,\zeta) \in \Omega_{\text{slit}},\ 0 \le t \le t_e. \tag{5.68}$$

The actuation heat load in (5.67) leads to an optimal control problem with a strictly convex cost functional J_0, a convex state constraint (5.10), and a convex input constraint (5.68). For this problem it can be shown that if the admissible set is nonempty, the solution to this problem is unique, see Appendix C.2. This problem is solved similarly as for the single-shape actuation heat load. First the cost functional J_1 in (5.17) is minimized to find an admissible solution which is used as starting point for the minimization of $J_0 + wJ_2$. The main difference is that now the actuation heat load in (5.67) is used to compute the temperature field in (5.4) and cost functional J_0 in (5.11). The minimization is again implemented using the projected gradient method, see e.g. [Hinze et al., 2009; Borzì and Schulz, 2012], which enables the preservation of the constraint (5.68) throughout the iterations. The gradient is computed from (5.47) based on the adjoint state. The step size is controlled based on Hessian information, similarly as for the single-shape actuation heat load in Subsection 5.3.3.

The free-shape optimal controls have been computed for the same four cases that have been considered for the single-shape actuation heat load in the previous subsection. In particular, the controls have been computed starting from two different initial guesses ($U^{(0)}(x,\zeta,t) = 0$ and $U^{(0)}(x,\zeta,t) = B(x,\zeta)u(t)$ with $B(x,\zeta)$ and $u(t)$ as in Figure 5.3b), with cooler constraints ($U(x,\zeta,t) \le 0$), and with heater constraints ($U(x,\zeta,t) \ge 0$). Naturally, the obtained minimal values of $J_0 + wJ_2$ for the free-shape actuation heat load in Table 5.4 are lower than the values obtained for the single-shape actuation heat load in Table 5.2. The number of iterations and times required for the computation of the free-shape optimal controls are given in Table 5.5.

To give an impression of the computed controls, a Proper Orthogonal Decomposition (POD), see e.g. [Pinnau, 2008], of the optimal control $U(x,\zeta,t)$ is

Table 5.4. Minima found after the optimization of the free-shape optimal control $Q_{\mathrm{act}}(x,\zeta,t) = U(x,\zeta,t)$

	Initial guess 1 (Figure 5.7a)	Initial guess 2 (Figure 5.7b)	Cooler constraints (Figure 5.8a)	Heater constraints (Figure 5.8b)
$J_0 + wJ_2$	1405	1405	2279	4617
J_0	1203	1204	2057	3676
E_{act}	0.687	0.686	0.555	1.610

Table 5.5. Iterations and computational time required to find the free-shape optimal control $Q_{\mathrm{act}}(x,\zeta,t) = U(x,\zeta,t)$

	minimizing J_1		minimizing $J_0 + wJ_2$	
	# iterations	time [s]	# iterations	time [s]
Initial guess 1	4	9	57	159
Initial guess 2	6	12	60	161
Cooler constraints	7	25	100	375
Heater constraints	9	40	120	442

made (the POD was computed w.r.t. the $\langle\,\cdot\,,\,\cdot\,\rangle_B$-inner product from (5.53)). The first POD modes $B_{\mathrm{POD}}(x,\zeta)$ obtained for the four considered cases are shown in Figures 5.7 and 5.8. The inserts in these figures also show $u_{\mathrm{POD}}(t) = \langle U(x,\zeta,t), B_{\mathrm{POD}}(x,\zeta)\rangle_B$. Since the optimal control $U(x,\zeta,t)$ is unique, the controls $U(x,\zeta,t)$ obtained for the first two cases should be the same. Indeed, the first POD modes in Figures 5.7a and 5.7b cannot be distinguished. This demonstrates the accuracy of the used algorithm.

The obtained shapes of the actuation heat load in Figures 5.7 and 5.8 are similar to the obtained shapes in Figures 5.5 and 5.6 that were obtained by the optimization of the single shape actuation heat load. However, the intensities are clearly distinct. It is remarkable that the intensities $u_{\mathrm{POD}}(t)$ never change sign, i.e. they satisfy the constraint (5.14), and that the spatial shapes in Figures 5.8a and 5.8b also satisfy the input constraints $B(x,\zeta) \le 0$ and $B(x,\zeta) \ge 0$, respectively. This is not guaranteed by the POD method.

Note that $B_{\mathrm{POD}}(x,\zeta)u_{\mathrm{POD}}(t)$ is the best least-squares approximation of the free-shape optimal control $U(x,\zeta,t)$ that consists of a single shape. However, applying $Q_{\mathrm{act}}(x,\zeta,t) = B_{\mathrm{POD}}(x,\zeta)u_{\mathrm{POD}}(t)$ leads to a violation of the constraint (5.10) in all considered situations. This can be partially understood by considering the minimization of J_0 subject to the constraints (5.10) and (5.68), which yields a (unique) free-shape optimal control $U^*(x,\zeta,t)$. As the L^2-norm of the first POD mode of $U^*(x,\zeta,t)$ is smaller than the L^2-norm of $U^*(x,\zeta,t)$ itself (unless $U^*(x,\zeta,t)$ consists of a single spatial shape) and because J_0 is defined

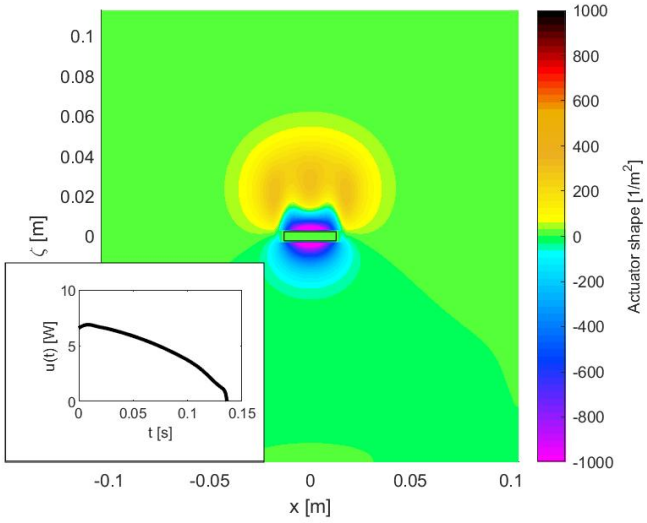

(a) Initial guess 1

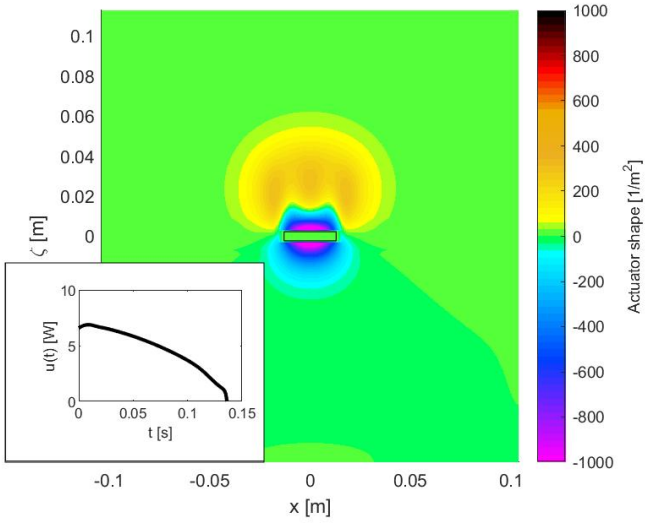

(b) Initial guess 2

Figure 5.7. The first POD mode of the actuation heat load $U(x, \zeta, t)$ computed starting from the initial guess $U^{(0)}(x, \zeta, t) = 0$ (initial guess 1) and starting from the initial guess $U^{(0)}(x, \zeta, t) = B(x, \zeta)u(t)$ with $B(x, \zeta)$ and $u(t)$ as in Figure 5.3b (initial guess 2).

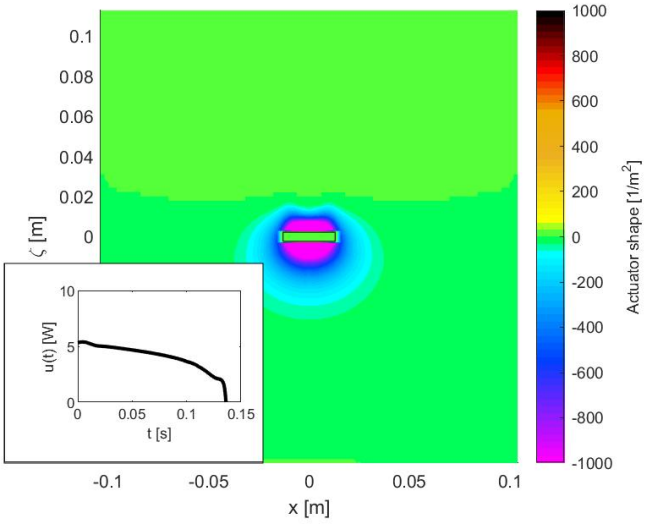

(a) Cooler constraints

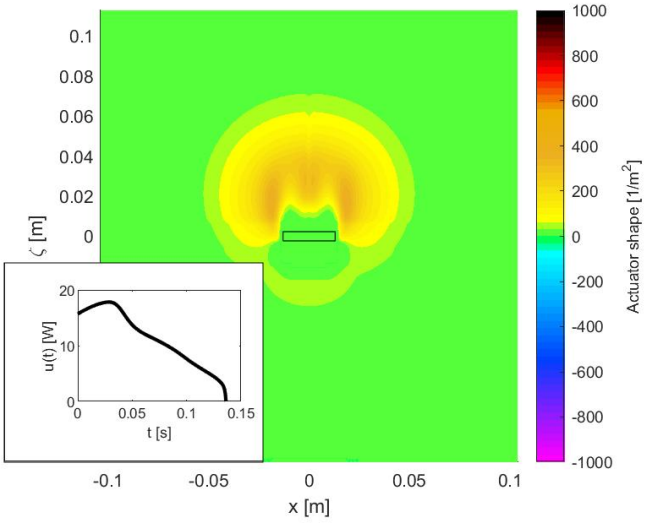

(b) Heater constraints

Figure 5.8. The first POD mode of the actuation heat load $U(x, \zeta, t)$ computed with cooler constraints $B(x, \zeta) \geq 0$ and $u(t) \leq 0$ and with heater constraints $B(x, \zeta) \geq 0$ and $u(t) \geq 0$.

as the squared L^2-norm of $U^*(x,\zeta,t)$ in (5.11), it follows that applying the first POD mode will always lead to a violation of the constraint (5.10). If the weight w is small enough, the minimization of $J_0 + wJ_2$ resembles the minimization of J_0 subject to the constraint (5.10). It therefore seems reasonable to expect a similar result for the minimization of $J_0 + wJ_2$ considered in this section.

The computed POD shapes offer a partial explanation for the observed uniqueness of the single-shape actuation heat load $B(x,\zeta)u(t)$ in Section 5.4.1. Inspection of the numerical results shows that the singular value corresponding to the first POD mode is more than 3 times larger than the second singular value for all 4 considered cases. This indicates that there is a single shape most important in $U(x,\zeta,t)$. It can therefore be expected that the single-shape actuation heat load will have a shape similar to the dominant shape in $U(x,\zeta,t)$.

Note that Table 5.5 shows that the free-shape optimal controls $U(x,\zeta,t)$ are computed faster than the single-shape actuation heat loads. This suggests that the single-shape actuation heat load could be computed faster starting from the initialization $B_{\mathrm{POD}}(x,\zeta)u_{\mathrm{POD}}(t)$. However, it turns out that reduction in computational cost achieved by the better initialization does not outweigh the computational cost to obtain the free-shape optimal control $U(x,\zeta,t)$ required to compute $B_{\mathrm{POD}}(x,\zeta)u_{\mathrm{POD}}(t)$.

5.5 Conclusions and discussions

An approach to compute the shape and intensity of the smallest actuation heat load that sufficiently mitigates wafer deformation has been proposed. The method consists of two steps. The first step is a search for an actuation heat load that sufficiently reduces the wafer deformations. In the second step, the actuation effort is minimized while keeping the wafer deformation sufficiently small. The method has been used to design an optimal single-shape actuation heat load in a 2-D wafer heating model for the scanning of a single field.

It has been shown that different initializations of the optimization algorithm converge to the same single-shape actuation heat load. This suggests that the optimal single-shape actuation heat load may be unique. However, this claim has not been proven. This claim is supported by the computed free-shape actuation heat loads, of which the (typically unique) first POD mode resembles the obtained single-shape actuation heat loads.

The proposed method to design a single-shape actuation heat load has great flexibility and can be applied to many variations of the problem. For example, it has been demonstrated that additional input constraints requiring that the applied actuation heat load can only heat or cool can be included easily in the design. Three other relevant modifications are presented in Appendix C.4. In the first modification, the possibility to adapt the rigid body modes of the wafer and mirrors is considered in the design of the actuation heat load. The second

modification considers the scanning of multiple fields and the third modification considers the scanning of a field near the wafer edge.

A time consuming step in the algorithm is solving the Ordinary Differential Equations (ODEs) for the temperature field. The cost of these computations can potentially be reduced by applying Model Order Reduction (MOR) techniques. Especially because the actuation heat load consists of a single shape, such techniques show great potential to reduce the computational cost. In particular, such MOR techniques might enable to compute the single-shape actuation heat load faster than the free-shape optimal control and might enable the application of the method to much larger FE models, which are typically needed for more complex patterns of the projection light and three-dimensional wafer clamp models.

Another interesting problem is the design of an actuation heat load that consists of multiple shapes, e.g. an actuation heat load of of the form

$$Q_{\mathrm{act}}(x, \zeta, t) = B_1(x, \zeta)u_1(t) + B_2(x, \zeta)u_2(t). \tag{5.69}$$

However, such an extension comes with several additional problems and will be investigated further in the next chapter.

Chapter 6

Optimal thermal actuation for mirror temperature control

6.1 Introduction

The latest generation wafer scanners uses Extreme Ultraviolet (EUV) light to project a pattern of electronic connections onto a silicon wafer. Because EUV light is absorbed strongly by almost all materials, the projection takes place in a near vacuum chamber and a sequence of mirrors, instead of the glass lenses, are used to focus the projection light. The mirrors consist of multiple layers of molybdenum and silicon (each a few nanometers thick) and have an extremely low surface roughness (below a tenth of a nanometer), see [Levinson, 2010; Zeiss, 2020]. Despite this advanced design, the mirrors still only have a moderate reflectance of 60-70 % [Levinson, 2010], meaning that about 30% of the incoming EUV light is absorbed by each mirror. This absorption leads to a significant temperature increase (which can exceed 10 Kelvin), and the resulting thermal expansion of the mirror significantly affects the imaging quality.

As indicated in [Bittner et al., 2012], Infrared (IR) light sources could be used to control the temperature and thermal expansion of the mirrors. As the IR wavelength is much longer than the EUV wavelength, this actuation can be applied directly to the optical surfaces of the mirrors without affecting the pattern that is created on the wafer by the EUV light. The most natural way to apply the IR heating to the mirror is by shining an IR laser trough a lens that distributes the IR light over the mirror surface. The heat load applied by one IR laser thus has a fixed spatial shape of which the intensity could be varied over time (by varying the power of the IR laser). There could be multiple IR laser sources, but their number will be limited. This means that the heat load applied

to the mirror would be a combination of a small number of spatial shapes with time-varying intensities.

The spatial shapes of the IR actuation heat load are crucial for the achievable performance. However, designing effective spatial shapes is not straightforward because the latest-generation wafer scanners contain a flexible illumination system, see e.g. [Lowisch et al., 2013; Bilski et al., 2019]. Such a system enables the use of a very large number of illumination settings which can be used to improve the imaging quality for the particular pattern of electronic connections that is projected. Because each illumination setting leads to a different distribution of EUV light over some of the mirrors (although not on the reticle and the wafer), the selected spatial shapes of the IR actuation heat load should be able to counteract a wide variety of potential EUV disturbance heat loads.

Determining the spatial shapes of the actuation IR heat load can thus be considered as an input selection problem, which has been considered in many publications, see e.g. [van de Wal and de Jager, 2001] for an overview. Because thermal expansion of the mirror is governed by Partial Differential Equations (PDEs) and because there is a priori knowledge about the disturbances available, PDE-oriented input selection approaches that can take into account this a priori knowledge are most natural. Several of these approaches have been developed [Stadler, 2009; Herzog et al., 2012; Kunisch et al., 2014; Boulanger and Trautmann, 2017], but none of these approaches can consider constraints on the resulting temperature increase as will be considered in this chapter.

Just as in Chapter 5 and in the other PDE-oriented approaches mentioned above, the optimal shapes of the IR actuation heat load will be determined as the solution of an optimization problem. The optimization of both the spatial shapes of the IR actuation heat load and their corresponding intensities comes with two important challenges.

First of all, there is the problem that the set of actuation heat loads that consist of a fixed number of spatial shapes is not convex. This means that a cost functional on the set of actuation heat loads consisting of a fixed number of spatial shapes will have multiple local minima, even if the cost functional is convex in each individual actuation heat load. In particular, a found local minimum does not need to be the global minimum, and the global minimum does not need to be unique. This problem is well known in the optimization literature and is closely related to the optimization over matrix manifolds [Edelman et al., 1999; Absil et al., 2008; Wen and Yin, 2013], the theory for biconvex optimization problems [Floudas and Visweswaran, 1990; Gorski et al., 2007], and weighted and constrained low-rank approximations [Manton et al., 2003; Markovsky and van Huffel, 2007].

Secondly, there is the problem that an actuation heat load generated by a limited set of spatial shapes can typically also be generated by a different set of spatial shapes. So even if the global minimum has been found, it is typically not clear which spatial shapes should be used. This problem will be

discussed further in Subsection 6.2.2. As the applied IR actuation heat load is nonnegative (it can only heat and not cool), this problem is closely related to the existence and uniqueness of nonnegative matrix factorizations [Cohen and Rothblum, 1993; Lee and Seung, 1999; Lee and Seung, 2001; Laurberg et al., 2008]. This theory provides certain conditions under which the shapes used to generate the actuation heat load are unique.

To some extent, these challenges were also encountered during the design of an actuation heat load consisting of a single spatial shape in Chapter 5. However, they are much more problematic for the design of a heat load consisting of multiple spatial shapes. For example, the optimization algorithm in Chapter 5 converged to the same single shape actuation heat load for various initializations, but the results in this chapter demonstrate that this is no longer the case for actuation heat loads consisting of multiple spatial shapes. Furthermore, the representation of a single shape actuation heat load can be made unique choosing a certain normalization of the spatial-shape (or intensity), see Chapter 5. This is typically no longer the case when multiple spatial shapes are considered.

This chapter contains a method for the optimization of an (IR) actuation heat load consisting of a limited number of spatial shapes that can effectively keep the steady-state temperature resulting from a large number of (EUV) disturbance heat loads sufficiently close to a desired temperature. The method is applied to a large-scale FE model of a mirror in a next-generation wafer scanner. The obtained spatial shapes give an indication of an effective IR heater layout for the control of mirror heating in next-generation wafer scanners.

As it takes approximately 30 hours for the mirror to reach the steady-state temperature, transient temperature fields are common practice during exposure. In particular, wafers are processed in groups of 25 that are called *lots* and customers of ASML have the possibility to change the illumination pattern after each lot of wafers that has been processed, which takes about 9 minutes (assuming a throughput of 170 wafers per hour). However, as changing the machine settings takes time, the illumination pattern will typically remain the same for longer periods of time. Because the sequence in which the illumination patterns will be used by the customer is not known to ASML, the actuation heat load shapes and intensities will be designed only based on steady-state temperature fields in this chapter. Even with this simplification, finding the optimal spatial shapes to generate the actuation heat load remains a challenging problem.

The remainder of this chapter is structured as follows. Section 6.2 contains the problem description, which consists of a description of the physical model of the mirror and the formulation of the optimization problem for the actuation heat load. Section 6.3 describes the procedure to find the optimal spatial shapes and corresponding intensities of the actuation heat load. This procedure consists of a spatial discretization by the FE method and a gradient-based optimization algorithm. The results obtained by this approach are reported in Section 6.4. Finally, Section 6.5 contains the conclusions and discussions.

6.2 Problem formulation

6.2.1 Physical model

A schematic overview of the considered mirror model is shown in Figure 6.1. The mirror occupies a box-shaped domain $\Omega \subset \mathbb{R}^3$ aligned with the indicated Cartesian coordinate system (x, y, z). The origin of the coordinate system is chosen at the center of the top surface of the mirror. The domain Ω has length L in the x-direction, width W in the y-direction, and height H in the z-direction. The mirror is cooled through the boundary of the spatial domain $\partial\Omega \subset \mathbb{R}^3$, which is partitioned into the top surface $\partial\Omega_{\text{top}}$ and the other surfaces $\partial\Omega^c_{\text{top}} = \partial\Omega \backslash \partial\Omega_{\text{top}}$. Note that the top surface $\partial\Omega_{\text{top}}$ is located at $z = 0$ which means that $\partial\Omega_{\text{top}} = A_{\text{top}} \times \{0\}$, where $A_{\text{top}} = [-L/2, L/2] \times [-W/2, W/2] \subset \mathbb{R}^2$. The elliptical area (light gray) inside which the EUV light (purple) is projected is called the Optical Footprint (OFP) and is denoted by $\partial\Omega_{\text{OFP}} = A_{\text{OFP}} \times \{0\} \subset \partial\Omega_{\text{top}}$. The actuation heat load (red) can be applied on the whole top surface A_{top}. The mirror is made of ULE and the used parameter values are given in Table 6.1.

The $n = 17$ EUV heat loads $Q_{\text{EUV},j}(x, y)$ (with $1 \leq j \leq n$) that are applied to the top surface of the mirror $\partial\Omega_{\text{top}} = A_{\text{top}} \times \{0\}$ are shown in Figures 6.2 and 6.3. As the material properties are constant, the steady-state temperature increase $T_j = T_j(x, y, z)$ (relative to the reference temperature $T_0 = 22$ °C) resulting from the j-th EUV heat load $Q_{\text{EUV},j}$ and the j-th actuation heat load $Q_{\text{act},j}$ satisfies the PDE (again with $1 \leq j \leq n$)

$$\nabla^2 T_j = 0, \qquad \text{on } \Omega, \tag{6.1}$$

with Boundary Conditions (BCs)

$$k\nabla T_j \cdot \mathbf{n} = -h_{\text{top}} T_j + Q_{\text{EUV},j} + Q_{\text{act},j}, \qquad \text{on } \partial\Omega_{\text{top}}, \tag{6.2}$$

$$k\nabla T_j \cdot \mathbf{n} = -h^c_{\text{top}} T_j, \qquad \text{on } \partial\Omega^c_{\text{top}}, \tag{6.3}$$

where ∇ and ∇^2 denote the gradient and Laplacian operators, $\mathbf{n}$ is the outward pointing normal, k denotes the thermal conductivity, and h_{top} and h^c_{top} denote the convection coefficients on $\partial\Omega_{\text{top}}$ and $\partial\Omega^c_{\text{top}}$, respectively. Note that the convection coefficient on $\partial\Omega^c_{\text{top}}$ is higher than on $\partial\Omega_{\text{top}}$, i.e. $h_{\text{top}} < h^c_{\text{top}}$, because these surfaces are close to the water-cooled supporting structure.

The actuation heat loads $\{Q_{\text{act},j}(x, y)\}_{1 \leq j \leq n}$ are induced by IR laser beams that are distributed over the top surface of the mirror A_{top} by a lens, see Figure 6.1. The heat load resulting from the i-th IR laser thus has a fixed spatial shape $B_i(x, y)$. The intensity $u_{i,j}$ with which the i-th spatial shape is applied in the j-th EUV load case can be varied by changing the power generated by the i-th IR laser and can thus be different in each load case j. Note that m, the number of spatial shapes in the actuation heat load, will typically be much smaller than

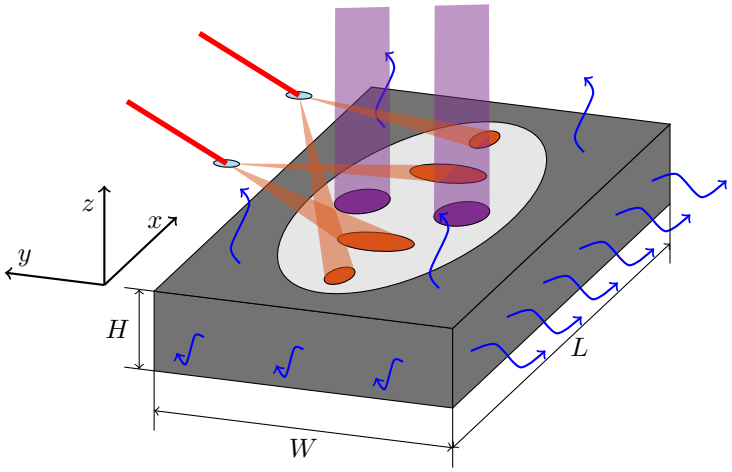

Figure 6.1. Schematic overview of the considered mirror model. The mirror (gray) heats up and expands due to the EUV disturbance heat loads (purple) that are applied in the Optical Footprint (OFP, light gray) and the IR actuation heat loads (red) that can be applied to the top surface. The spatial shapes of the actuation heat load are generated by breaking IR light through lenses (light blue). Convection to the environment (blue arrows) reduces the temperature of the mirror.

Table 6.1. Parameter values used in the physical model

Description	Symbol	Value	Unit
Length	L	685	mm
Width	W	310	mm
Height	H	167	mm
Thermal conductivity	k	1.31	W/m/K
Convection coefficient top	h_{top}	1	$\text{W/m}^2\text{/K}$
Convection coefficient sides	h_{sides}	3	$\text{W/m}^2\text{/K}$

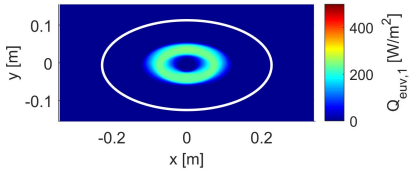

(a) $Q_{\mathrm{EUV},1}(x,y)$, $P_{\mathrm{EUV},1} = 3.25$ W

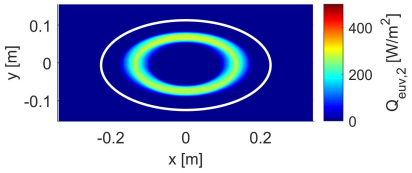

(b) $Q_{\mathrm{EUV},2}(x,y)$, $P_{\mathrm{EUV},2} = 5.57$ W

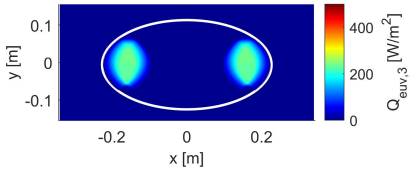

(c) $Q_{\mathrm{EUV},3}(x,y)$, $P_{\mathrm{EUV},3} = 3.64$ W

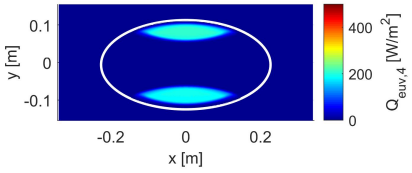

(d) $Q_{\mathrm{EUV},4}(x,y)$, $P_{\mathrm{EUV},4} = 3.01$ W

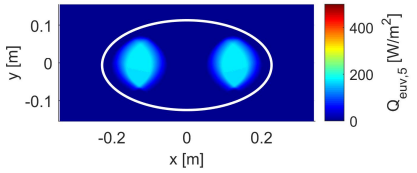

(e) $Q_{\mathrm{EUV},5}(x,y)$, $P_{\mathrm{EUV},5} = 3.70$ W

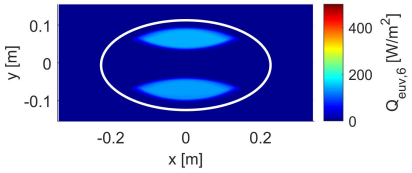

(f) $Q_{\mathrm{EUV},6}(x,y)$, $P_{\mathrm{EUV},6} = 2.94$ W

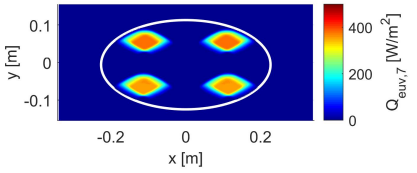

(g) $Q_{\mathrm{EUV},7}(x,y)$, $P_{\mathrm{EUV},7} = 5.87$ W

Figure 6.2. The first seven EUV heat loads $Q_{\mathrm{EUV},j}(x,y)$ $(1 \leq j \leq 7)$ with their respective heating power $P_{\mathrm{EUV},j}$. The white ellipse indicates the OFP.

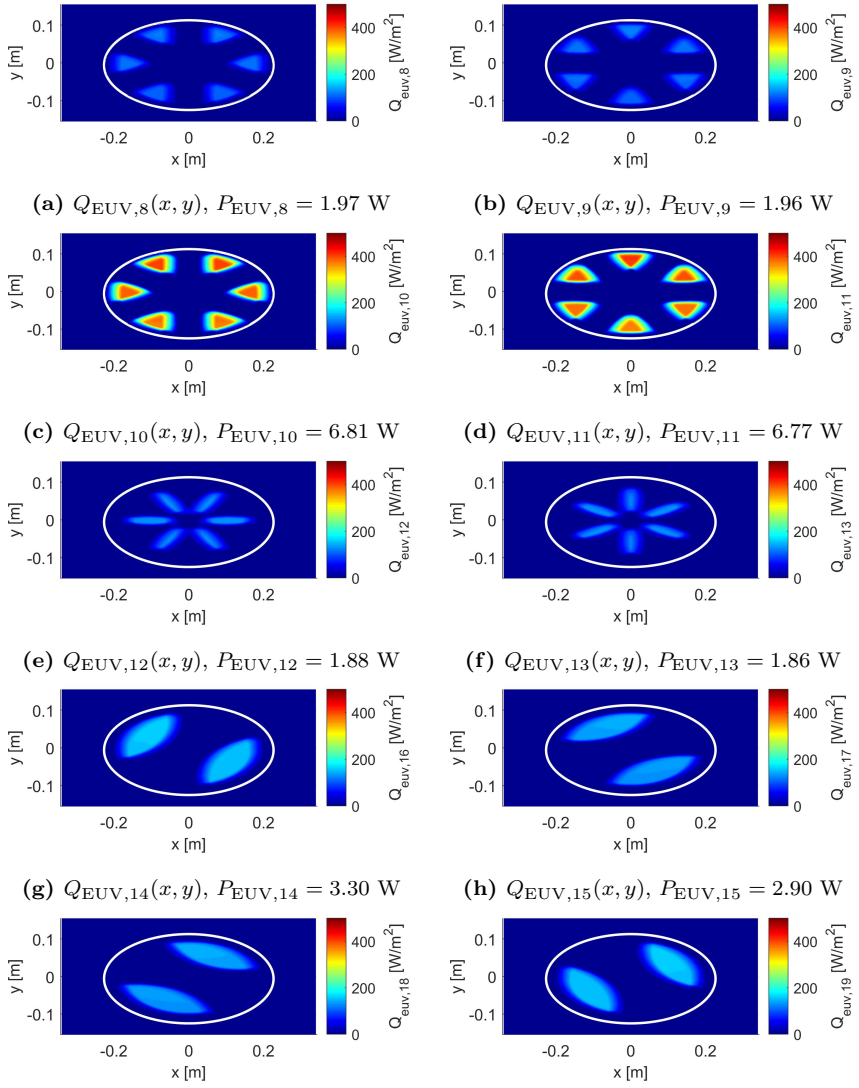

(a) $Q_{\mathrm{EUV},8}(x,y)$, $P_{\mathrm{EUV},8} = 1.97$ W **(b)** $Q_{\mathrm{EUV},9}(x,y)$, $P_{\mathrm{EUV},9} = 1.96$ W

(c) $Q_{\mathrm{EUV},10}(x,y)$, $P_{\mathrm{EUV},10} = 6.81$ W **(d)** $Q_{\mathrm{EUV},11}(x,y)$, $P_{\mathrm{EUV},11} = 6.77$ W

(e) $Q_{\mathrm{EUV},12}(x,y)$, $P_{\mathrm{EUV},12} = 1.88$ W **(f)** $Q_{\mathrm{EUV},13}(x,y)$, $P_{\mathrm{EUV},13} = 1.86$ W

(g) $Q_{\mathrm{EUV},14}(x,y)$, $P_{\mathrm{EUV},14} = 3.30$ W **(h)** $Q_{\mathrm{EUV},15}(x,y)$, $P_{\mathrm{EUV},15} = 2.90$ W

(i) $Q_{\mathrm{EUV},16}(x,y)$, $P_{\mathrm{EUV},16} = 2.90$ W **(j)** $Q_{\mathrm{EUV},17}(x,y)$, $P_{\mathrm{EUV},17} = 3.30$ W

Figure 6.3. The last ten EUV heat loads $Q_{\mathrm{EUV},j}(x,y)$ $(8 \leq j \leq 17)$ with their respective heating power $P_{\mathrm{EUV},j}$. The white ellipse indicates the OFP.

n, the number of load cases. The n actuation heat loads $Q_{\text{act},j}(x,y)$ are thus created with only m spatial shapes $B_i(x,y)$, i.e.

$$Q_{\text{act},j}(x,y) = \sum_{i=1}^{m} B_i(x,y)u_{i,j}, \qquad 1 \leq j \leq n, (x,y) \in A_{\text{top}}. \tag{6.4}$$

Note that that, in contrast to Chapter 5, the intensities $u_{i,j}$ are not time-dependent because only steady-state temperature fields will be considered. Because each IR laser can only heat and not cool

$$B_i(x,y) \geq 0, \qquad u_{i,j} \geq 0, \qquad 1 \leq i \leq m, 1 \leq j \leq n, (x,y) \in A_{\text{top}}. \tag{6.5}$$

The representation of the heat loads $\{Q_{\text{act},j}(x,y)\}_{1\leq j\leq n}$ in terms of multiple spatial shapes $\{B_i(x,y)\}_{1\leq i\leq m}$ is significantly more involved than the representation of an actuation heat load consisting of a single spatial shape as considered in Chapter 5. This problem will be discussed further in Subsection 6.2.2.

The actuation heat loads $\{Q_{\text{act},j}(x,y)\}_{1\leq j\leq n}$ are introduced to improve the imaging quality of the wafer scanner. Because variations in the temperature of the OFP typically lead to unflatness of the OFP, the actuation heat loads $\{Q_{\text{act},j}(x,y)\}_{1\leq j\leq n}$ are required to keep the temperature in the OFP sufficiently close to a desired temperature T^* in all considered load cases, i.e.

$$|T_j(x,y,0) - T^*| \leq \delta, \qquad 1 \leq j \leq n, (x,y) \in A_{\text{OFP}}, \tag{6.6}$$

where δ denotes the maximally allowed deviation from T^*. Note, however, that it is hard to relate the maximally allowed deviation δ to the achieved imaging quality. Determining the achieved imaging quality requires a very complex physical model which should not only take into account the nonlinear relation between temperature and deformation (the thermal strain is a quadratic function of temperature for ULE, see Chapter 2), but also the propagation of optical errors through the next mirrors in the projection system, see [Merks, 2015; Habets et al., 2016]. Because of these difficulties, the simpler constraint (6.6) will be used in this chapter. Although this constraint is thus not completely representative for the achieved optical performance, it is representative for the current state of the art at ASML and Zeiss, who still use thermal performance variables in their specifications.

A part of the IR light received by the mirror will be reflected and may cause heating of other components in the wafer scanner. It is therefore desirable to keep the actuation heat loads as small as possible, i.e. to minimize

$$\mathcal{J}_0 = \sum_{j=1}^{n} \iint_{A_{\text{top}}} Q_{\text{act},j}^2(x,y)\ \mathrm{d}x\ \mathrm{d}y. \tag{6.7}$$

Summarizing, the optimal spatial shapes $\{B_i(x,y)\}_{1\leq i\leq m}$ and corresponding intensities $\{u_{i,j}\}_{1\leq i\leq m, 1\leq j\leq n}$ will thus be determined by minimizing the cost

function $\mathcal{J}_0$ in (6.7) over all sets of actuation heat loads of the form (6.4) subject to the inequality constraints (6.5) and (6.6) and the equality constraints of the physical model (6.1)–(6.3).

Because $\mathcal{J}_0$ is strictly convex in the applied actuation heat load $Q_{\mathrm{act},j}$ and because the constraint (6.6) is convex in $T_j(x,y,z)$ and thus also in $Q_{\mathrm{act},j}$, the minimization of $\mathcal{J}_0$ over the intensities $u_{i,j}$ for fixed spatial shapes $B_i(x,y)$ yields a unique minimizer when the shapes $B_i(x,y)$ are linearly independent. Similarly, the minimization of $\mathcal{J}_0$ over the spatial shapes $B_i(x,y)$ for fixed intensities $u_{i,j}$ yields a unique minimizer when the matrix of the intensities $(u_{i,j})_{i,j}$ has full rank. Note, however, that the simultaneous minimization of $\mathcal{J}_0$ over both the intensities $u_{i,j}$ and the spatial shapes $B_i(x,y)$ is not convex and that the uniqueness of the optimal actuation heat loads $Q_{\mathrm{act},j}(x,y)$ of the form (6.4) is thus not guaranteed. Apart from the uniqueness of the optimal actuation heat loads $Q_{\mathrm{act},j}(x,y)$, the uniqueness of the spatial shapes $B_i(x,y)$ and intensities $u_{i,j}$ that represent the actuation heat loads $Q_{\mathrm{act},j}(x,y)$ is also not guaranteed. This problem will be discussed in the following subsection.

6.2.2 Representation of the actuation heat load

The representation of a set of actuation heat loads of the form (6.4) satisfying the constraints (6.5) is significantly more involved for multiple spatial shapes $m > 1$ than for $m = 1$ spatial shape, as was considered in Chapter 5. The major difficulties will be discussed in this subsection. To this end, it will be convenient to rewrite the j-th actuation heat load $Q_{\mathrm{act},j}(x,y)$ in (6.4) as

$$Q_{\mathrm{act},j}(x,y) = \begin{bmatrix} B_1(x,y) & B_2(x,y) & \cdots & B_m(x,y) \end{bmatrix} \begin{bmatrix} u_{1,j} \\ u_{2,j} \\ \vdots \\ u_{m,j} \end{bmatrix} =: \mathcal{B}(x,y)\mathbf{u}_j, \quad (6.8)$$

and to introduce the (row)vector of actuation heat loads

$$\begin{aligned} \mathcal{Q}_{\mathrm{act}}(x,y) &:= \begin{bmatrix} Q_{\mathrm{act},1}(x,y) & Q_{\mathrm{act},2}(x,y) & \cdots & Q_{\mathrm{act},n}(x,y) \end{bmatrix} \\ &= \mathcal{B}(x,y) \begin{bmatrix} \mathbf{u_1} & \mathbf{u}_2 & \cdots & \mathbf{u}_n \end{bmatrix} =: \mathcal{B}(x,y)\mathbf{U}. \end{aligned} \quad (6.9)$$

Note that the matrix $\mathbf{U}$ now contains the intensities $\{u_{i,j}\}_{1\le i\le m, 1\le j\le n}$, i.e.

$$\mathbf{U} = \begin{bmatrix} u_{1,1} & u_{1,2} & \cdots & u_{1,n} \\ u_{2,1} & u_{2,2} & \cdots & u_{2,n} \\ \vdots & \vdots & & \vdots \\ u_{m,1} & u_{m,2} & \cdots & u_{m,n} \end{bmatrix}. \quad (6.10)$$

The required number of spatial shapes

A set of nonnegative actuation heat loads $\{Q_{\mathrm{act},j}(x,y)\}_{1\le j\le n}$ can be generated by a single nonnegative spatial shape $B(x,y)$ and nonnegative intensities $\{\mathbf{u}_j\}_{1\le j\le n}$ precisely when $\dim(\mathrm{span}\{Q_{\mathrm{act},j}(x,y)\}_{1\le j\le n}) = 1$. A similar result can be obtained when $\dim(\mathrm{span}\{Q_{\mathrm{act},j}(x,y)\}_{1\le j\le n}) = 2$.

Lemma 6.1. *Let* $\{Q_{\mathrm{act},j}(x,y)\}_{1\le j\le n}$ *be a set of* nonnegative *actuation heat loads. If* $\dim(\mathrm{span}\{Q_{\mathrm{act},j}(x,y)\}_{1\le j\le n}) \le 2$*, then the* n *actuation heat loads can be represented in the form* (6.4) *using* $m := \dim(\mathrm{span}\{Q_{\mathrm{act},j}(x,y)\}_{1\le j\le n})$ nonnegative *spatial shapes* $B_i(x,y)$ *and* $m \times n$ nonnegative *intensities* $u_{i,j}$*.*

Proof. See [Thomas, 1974] or Theorem 4.1 in [Cohen and Rothblum, 1993]. □

However, a similar result does not hold when $\dim(\mathrm{span}\{Q_{\mathrm{act},j}(x,y)\}_{1\le j\le n}) \ge 3$, as the following example demonstrates.

Example 6.2. *Let* S_1*,* S_2*,* S_3*, and* S_4 *be nonempty disjoint subsets of* $\partial\Omega_{\mathrm{top}}$ *and let* $\chi_S(x,y)$ *denote the characteristic function of a set* S*, i.e.* $\chi_S(x,y) = 1$ *if* $(x,y) \in S$ *and* $\chi_S(x,y) = 0$ *otherwise. Consider the following set of nonnegative actuation heat loads*

$$\underbrace{\begin{bmatrix} Q_{\mathrm{act},1}(x,y) \\ Q_{\mathrm{act},2}(x,y) \\ Q_{\mathrm{act},3}(x,y) \\ Q_{\mathrm{act},4}(x,y) \end{bmatrix}^{\top}}_{\mathcal{Q}_{\mathrm{act}}(x,y)} = \underbrace{\begin{bmatrix} \chi_{S_1}(x,y) \\ \chi_{S_2}(x,y) \\ \chi_{S_3}(x,y) \\ \chi_{S_4}(x,y) \end{bmatrix}^{\top}}_{\chi(x,y)} \underbrace{\begin{bmatrix} 1 & 1 & 0 & 0 \\ 1 & 0 & 1 & 0 \\ 0 & 1 & 0 & 1 \\ 0 & 0 & 1 & 1 \end{bmatrix}}_{\mathbf{A}_4}. \tag{6.11}$$

It is clear that $\dim(\mathrm{span}\{Q_{\mathrm{act},j}(x,y)\}_{1\le j\le 4}) = 3$ *because the rank of matrix* $\mathbf{A}_4$ *is* 3*. However, these* 4 *actuation heat loads cannot be generated by less than* 4 nonnegative *spatial shapes and* 4×4 nonnegative *intensities because* $\mathbf{A}_4$ *has* nonnegative rank 4*, see e.g. [Thomas, 1974; Cohen and Rothblum, 1993].*

It is thus not straightforward to determine how many spatial shapes are needed to generate a given set of actuation heat loads.

The uniqueness of the spatial shapes

Even if it is known that m spatial shapes are needed to generate a set of actuation heat loads $\{Q_{\mathrm{act},j}\}_{1\le j\le n}$ as in (6.5), the problem remains whether spatial shapes $\{B_i(x,y)\}_{1\le i\le m}$ and intensities $\{\mathbf{u}_j\}_{1\le j\le n}$ are unique.

With the notation from (6.9), it is easy to see that the sets of spatial shapes $\{B_i(x,y)\}_{1\le i\le m}$ and intensities $\{u_{i,j}\}_{1\le i\le m, 1\le j\le n}$ that represent a set of an actuation heat loads $\{Q_{\mathrm{act},j}\}_{1\le j\le n}$ are typically not unique because

$$\mathcal{Q}_{\mathrm{act}}(x,y) = \mathcal{B}(x,y)\mathbf{U} = (\mathcal{B}(x,y)\mathbf{M})\left(\mathbf{M}^{-1}\mathbf{U}\right), \tag{6.12}$$

for any $m \times m$ invertible matrix $\mathbf{M}$. The same set of actuation heat loads is thus generated by the spatial shapes $\mathcal{B}(x,y)$ and intensities $\mathbf{U}$ and by the spatial shapes $\mathcal{B}(x,y)\mathbf{M}$ and intensities $\mathbf{M}^{-1}\mathbf{U}$.

Remark 6.3. *It is important to note that not all representations for a set of actuation heat loads $\{Q_{\text{act},j}\}_{1\leq j\leq n}$ can be obtained through an invertible matrix $\mathbf{M}$, as the following example demonstrates. Consider the vector of actuation heat loads $\mathbf{Q}_{\text{act}}(x,y) = \chi(x,y)\mathbf{A}_4$ from Example 6.2 in* (6.11)*. Then*

$$\mathbf{Q}_{\text{act}}(x,y) = \underbrace{\chi(x,y)\mathbf{A}_4}_{\mathcal{B}(x,y)}\underbrace{\mathbf{I}_4}_{\mathbf{U}} = \underbrace{\chi(x,y)\mathbf{I}_4}_{\tilde{\mathcal{B}}(x,y)}\underbrace{\mathbf{A}_4}_{\tilde{\mathbf{U}}}, \tag{6.13}$$

where $\mathbf{I}_4$ denotes the 4×4 identity matrix. Since the rank of $\mathbf{U} = \mathbf{I}_4$ is 4 and the rank of $\tilde{\mathbf{U}} = \mathbf{A}_4$ is 3, it is clear that there is no invertible matrix $\mathbf{M}$ such that $\mathbf{U} = \mathbf{M}^{-1}\tilde{\mathbf{U}}$. In other words, the two representations $(\mathcal{B}(x,y), \mathbf{U})$ and $(\tilde{\mathcal{B}}(x,y), \tilde{\mathbf{U}})$ in (6.13) *are not linked through an invertible matrix $\mathbf{M}$. Note however that two representations $(\mathcal{B}(x,y), \mathbf{U})$ and $(\tilde{\mathcal{B}}(x,y), \tilde{\mathbf{U}})$ can always be linked trough an invertible matrix $\mathbf{M}$ if the ranks of $\mathbf{U}$ and $\tilde{\mathbf{U}}$ are equal.*

The constraints (6.5) limit the freedom in the choice of the matrix $\mathbf{M}$ because the transformed shapes $\mathcal{B}(x,y)\mathbf{M}$ and intensities $\mathbf{M}^{-1}\mathbf{U}$ are not necessarily nonnegative if the original shapes $\mathcal{B}(x,y)$ and intensities $\mathbf{U}$ are nonnegative. However, if both $\mathbf{M}$ and $\mathbf{M}^{-1}$ only have nonnegative elements, it is clear that transforming a pair $(\mathcal{B}(x,y), \mathbf{U})$ that satisfies the constraints (6.5) also leads to a pair $(\mathcal{B}(x,y)\mathbf{M}, \mathbf{M}^{-1}\mathbf{U})$ that satisfies the constraints (6.5).

The following result shows that there is only a very limited class of matrices $\mathbf{M}$ for which both $\mathbf{M}$ and $\mathbf{M}^{-1}$ have nonnegative elements.

Lemma 6.4. *Any invertible matrix $\mathbf{M}$ for which both $\mathbf{M}$ and $\mathbf{M}^{-1}$ have only nonnegative elements is of the form $\mathbf{M} = \mathbf{DP}$, where $\mathbf{D}$ is a diagonal matrix with nonnegative elements and $\mathbf{P}$ is a permutation matrix.*

The proof of Lemma 6.4 can be found in Appendix D.1.

The constraints (6.5) can thus never eliminate the possibility to transform the shapes and intensities by a matrix $\mathbf{M}$ of the form $\mathbf{M} = \mathbf{DP}$. This remaining freedom is not problematic for the considered design problem as the permutation matrix $\mathbf{P}$ only represents a different numbering of the spatial shapes and the diagonal matrix $\mathbf{D}$ only represents a rescaling of the spatial shapes. This clearly does not influence the design of the lenses that project the IR light onto the mirror as displayed in Figure 6.1.

Note that the freedom in the matrix $\mathbf{D}$ can be used to rescale every spatial shape such that it has unit L^1-norm, i.e. to assure that

$$\iint_{A_{\text{top}}} B_i(x,y)\ \mathrm{d}x\ \mathrm{d}y = 1. \tag{6.14}$$

Note that this makes the unit of $B_i(x, y)$ [1/m^2]. Because the unit of $Q_{\mathrm{act},j}(x, y)$ is [W/m^2], the intensities $u_{i,j}$ thus get the unit [W]. In particular, the 1-norm of the intensity vector $\mathbf{u}_j$ now gets the interpretation of applied actuation power

$$\|\mathbf{u}_j\|_1 = \sum_{i=1}^{m} u_{i,j} = \iint_{A_{\mathrm{top}}} Q_{\mathrm{act},j}(x, y)\ \mathrm{d}x\ \mathrm{d}y. \tag{6.15}$$

The following result gives sufficient conditions under which the only matrices $\mathbf{M}$ that respect the constraints (6.5) are of the form $\mathbf{M} = \mathbf{DP}$.

Lemma 6.5. *Let $(\mathcal{B}(x, y), \mathbf{U})$ be a representation of a set actuation heat loads as in* (6.9) *that satisfies the constraints* (6.5) *and let $\mathbf{e}_i$ denote the i-th standard basis vector in $\mathbb{R}^m$. If there exist for every $1 \leq i \leq m$ a point $(x_i, y_i) \in A_{\mathrm{top}}$ and an index $1 \leq j_i \leq n$ such that*

$$\mathcal{B}(x_i, y_i) = c_i \mathbf{e}_i^\top, \qquad \mathbf{u}_{j_i} = d_i \mathbf{e}_i, \tag{6.16}$$

for some $c_i, d_i > 0$, then the only invertible matrices $\mathbf{M}$ for which $\mathcal{B}(x, y)\mathbf{M}$ and $\mathbf{M}^{-1}\mathbf{U}$ satisfy the constraints (6.5) *are of the form $\mathbf{M} = \mathbf{DP}$, where $\mathbf{D}$ is a diagonal matrix with nonnegative elements and $\mathbf{P}$ is a permutation matrix.*

The proof of Lemma 6.5 can be found in Appendix D.1.

Slightly weaker conditions can be found in literature, see e.g. [Donoho and Stodden, 2004; Laurberg et al., 2008]. However, these conditions are almost never satisfied in practice and there is almost always more freedom remaining in the choice of the matrix $\mathbf{M}$. To see why this is the case, consider for simplicity the case where there are only $m = 2$ spatial shapes and note that for any $\beta > 0$

$$\mathbf{M} = \begin{bmatrix} 1 & 0 \\ -\beta & 1 \end{bmatrix}, \qquad \Leftrightarrow \qquad \mathbf{M}^{-1} = \begin{bmatrix} 1 & 0 \\ \beta & 1 \end{bmatrix}. \tag{6.17}$$

Now observe that the first entry of $\mathcal{B}(x, y)\mathbf{M}$, with $\mathbf{M}$ as in (6.17), is equal to $B_1(x, y) - \beta B_2(x, y)$ and that the second entry is $B_2(x, y)$. Because the matrix $\mathbf{M}^{-1}$ in (6.17) has only nonnegative entries, $\mathcal{B}(x, y)\mathbf{M}$ and $\mathbf{M}^{-1}\mathbf{U}$ will satisfy the constraints (6.5) if $\mathcal{B}(x, y)$ and $\mathbf{U}$ satisfy the constraints (6.5) and if $B_1(x, y) - \beta B_2(x, y)$ is nonnegative. As the matrix $\mathbf{M}$ in (6.17) is clearly not of the form $\mathbf{M} = \mathbf{DP}$, it is clear that the representation of the actuation heat load is not unique if it is possible to subtract a positive multiple of one spatial shape from another spatial shape without violating the constraints (6.5). A similar argument shows that the representation of the actuation heat load is also not unique if it possible to subtract a positive multiple of a row of $\mathbf{U}$ from another row of $\mathbf{U}$ without violating the constraints (6.5).

The above argument can be formalized and generalized for heat loads consisting of more than $m = 2$ spatial shapes using the following definition and lemma based on [Laurberg et al., 2008].

Definition 6.6. *A set of spatial shapes* $\{B_i(x,y)\}_{1\leq i\leq m}$ *is called* boundary close *if there do not exist indices* $1 \leq i_1, i_2 \leq m$, $i_1 \neq i_2$ *such that* $B_{i_1}(x,y) - \beta B_{i_2}(x,y) \geq 0$ *for some* $\beta > 0$ *and all* $(x,y) \in A_{\text{top}}$. *Similarly, the rows of the matrix* $\mathbf{U}$ *are called* boundary close *if there do not exist indices* $1 \leq i_1, i_2 \leq m$, $i_1 \neq i_2$ *such that* $u_{i_1,j} - \beta u_{i_2,j} > 0$ *for some* $\beta > 0$ *and all* $1 \leq j \leq n$.

Lemma 6.7. *Consider a representation* $(\mathcal{B}(x,y), \mathbf{U})$ *of a set of actuation heat loads that satisfies the constraint* (6.5). *If either the entries of* $\mathcal{B}(x,y)$ *or the rows of* $\mathbf{U}$ *are not boundary close, then there exists a matrix* $\mathbf{M}$ *that is not of the form* $\mathbf{M} = \mathbf{DP}$ *such that the entries of* $\mathcal{B}(x,y)\mathbf{M}$ *and* $\mathbf{M}^{-1}\mathbf{U}$ *are nonnegative.*

The proof of Lemma 6.7 can be found in Appendix D.1.

Note that the entries of $\mathcal{B}(x,y)$ and the rows of $\mathbf{U}$ are always boundary close when $m = 1$, as it is then not possible to find two distinct indices i_1 and i_2. For $m > 1$, it is always possible to make either the entries of $\mathcal{B}(x,y)$ or the rows of $\mathbf{U}$ boundary close by subtracting positive multiples of entries of $\mathcal{B}(x,y)$ or rows of $\mathbf{U}$ until this is no longer possible. However, as this corresponds to adding positive multiples of rows of $\mathbf{U}$ or entries of $\mathcal{B}(x,y)$, the other variable will then not be boundary close.

Also note that if the entries of $\mathcal{B}(x,y)$ and the rows of $\mathbf{U}$ are boundary close, it is not guaranteed that the conditions of Lemma 6.5 are satisfied and that there can be situations in which Lemmas 6.5 and 6.7 do not say whether a representation is unique or not.

6.3 Solution procedure

This section contains the procedure used to find a solution to the optimization problem posed in Section 6.2 and consists of four subsections. Subsection 6.3.1 contains the general solution approach, which is similar to the one used in Chapter 5. The spatial discretization by the FE method is described in Subsection 6.3.2. Subsection 6.3.3 contains the gradients of the discretized problem which are used in the optimization algorithm outlined in Subsection 6.3.4.

6.3.1 Two-step approach

Because finding a set of actuation heat loads $\{Q_{\text{act},j}(x,y)\}_{1\leq j\leq n}$ of the form (6.4) that satisfy the constraints (6.5) and (6.6) is not straightforward, a two-step solution approach similar to the one in Chapter 5 will be used. The first step is a search for an admissible solution that satisfies the constraints (6.5) and (6.6) in which the cost functional $\mathcal{J}_0$ in (6.7) is disregarded. The found admissible solution is then used to initialize the minimization of the cost functional $\mathcal{J}_0$ in the second step. A barrier function is used to preserve the steady-state temperature constraints in this step.

An admissible solution that satisfies the constraints (6.6) is found by minimizing the following penalty functional

$$\mathcal{J}_1 = \sum_{j=1}^{n} \iint_{A_{\text{top}}} \left[(T_j(x,y,0) - T^*)^2 - \delta^2 \right]^+ \, \mathrm{d}x \, \mathrm{d}y, \tag{6.18}$$

where the function $[\,\cdot\,]^+$ is given by

$$[a]^+ = \begin{cases} a & \text{when } a \geq 0, \\ 0 & \text{when } a < 0. \end{cases} \tag{6.19}$$

Note that the integrand is zero precisely when the deviation of $T_j(x,y,0)$ from the desired temperature T^* is equal to or below the maximally allowed deviation δ, so that $\mathcal{J}_1$ is zero precisely when the constraint (6.6) is satisfied. Also note that the constraint (6.6) has been squared to make $\mathcal{J}_1$ differentiable. Because $\mathcal{J}_1$ is convex in $T_j(x,y,z)$ it is also convex in the applied actuation heat load $Q_{\text{act},j}(x,y)$. This implies that any local minimum found during the optimization of $\mathbf{U}$ for $\mathcal{B}(x,y)$ fixed or during the optimization of $\mathcal{B}(x,y)$ with $\mathbf{U}$ fixed is a global minimum. In particular, a local minimum with $\mathcal{J}_1 > 0$ found with $\mathcal{B}(x,y)$ fixed implies that no admissible $\mathbf{U}$ exists for the considered $\mathcal{B}(x,y)$ and vice versa. However, the minimization over both $\mathcal{B}(x,y)$ and $\mathbf{U}$ is not convex so that it is still possible that an admissible solution exists if a local minimum with $\mathcal{J}_1 > 0$ is found.

The constraints (6.6) are preserved in the second step by minimizing

$$\mathcal{J}_0 + w\mathcal{J}_2, \tag{6.20}$$

where $\mathcal{J}_0$ is given by (6.7), $w > 0$ denotes a weight, and the penalty function $\mathcal{J}_2$ is infinite when the constraint (6.6) is not satisfied and otherwise defined as

$$\mathcal{J}_2 = \sum_{j=1}^{n} \iint_{A_{\text{OFP}}} \left(\left(\frac{\delta^2}{\delta^2 - (T_j(x,y,0) - T^*)^2} \right)^p - 1 \right) \, \mathrm{d}x \, \mathrm{d}y, \tag{6.21}$$

with $p > 1$ a power that can be tuned. The choice of the weight w and the power p are further discussed in Appendix D.2. Note that the term '-1' in (6.21) assures that $\mathcal{J}_2 = 0$ when $T_j(x,y,0) = T^*$ for all $(x,y) \in A_{\text{top}}$ and $1 \leq j \leq n$. Because $\mathcal{J}_0 + w\mathcal{J}_2$ is strictly convex in the applied actuation heat load $Q_{\text{act},j}$, the minimization of $\mathcal{J}_0$ over the intensities $\mathbf{U}$ for fixed spatial shapes $\mathcal{B}(x,y)$ yields a unique minimizer if the spatial shapes $B_i(x,y)$ are linearly independent. Similarly, the minimization of $\mathcal{J}_0 + w\mathcal{J}_2$ over the spatial shapes $\mathcal{B}(x,y)$ for fixed intensities $\mathbf{U}$ yields a unique minimizer if $\mathbf{U}$ has full rank. However, the minimization of $\mathcal{J}_0 + w\mathcal{J}_2$ over $\mathcal{B}(x,y)$ and $\mathbf{U}$ simultaneously is not convex, and the uniqueness of the found actuation heat loads $\mathcal{B}(x,y)\mathbf{U}$ is thus not guaranteed.

6.3.2 Spatial discretization

So far, the optimization problem has been formulated on a continuous spatial domain. This section describes the spatial discretization of the problem by the FE method.

The spatial discretization is based on a set of linear Lagrangian FE shape functions, which are stored in a row vector $\mathbf{N} : \Omega \to \mathbb{R}^{1\times N}$. As only a small number $N_{\text{top}} \ll N$ shape functions will be nonzero at the top surface $\partial\Omega_{\text{top}}$, it will be useful to introduce a matrix $\mathbf{C}_{\text{top}} \in \{0,1\}^{N_{\text{top}}\times N}$ such that $\mathbf{N}(x,y,z)\mathbf{C}_{\text{top}}^\top$ is the (row)vector of the N_{top} shape functions that are nonzero on $\partial\Omega_{\text{top}}$. The actuation heat loads $Q_{\text{act},j} : A_{\text{top}} \to \mathbb{R}$ of the form (6.8) are only applied to the top surface $\partial\Omega_{\text{top}} = A_{\text{top}} \times \{0\}$ and are therefore approximated by

$$Q_{\text{act},j}(x,y) = \mathbf{N}(x,y,0)\mathbf{C}_{\text{top}}^\top \mathbf{q}_{\text{act},j}, \qquad \mathbf{q}_{\text{act},j} = \mathbf{B}\mathbf{u}_j, \tag{6.22}$$

where $\mathbf{q}_{\text{act},j} \in \mathbb{R}^{N_{\text{top}}}$ denotes the vector of nodal values of $Q_{\text{act},j}(x,y)$ and the rows of the matrix $\mathbf{B} \in \mathbb{R}^{N_{\text{top}}\times m}$ contain the nodal values of $\mathcal{B}(x,y)$.

Physical model

To discretize the mirror model (6.1)–(6.3), first the weak form of (6.1) is derived by requiring that

$$k \iiint_\Omega f\nabla^2 T_j \,\mathrm{d}V = 0, \tag{6.23}$$

for any test function $f = f(x,y,z)$. The introduction of the thermal conductivity k will be convenient in the derivations below. One of Green's identities now asserts that

$$k \iiint_\Omega f\nabla^2 T_j \,\mathrm{d}V = -k \iiint_\Omega \nabla f \cdot \nabla T_j \,\mathrm{d}V + k \iint_{\partial\Omega} f\nabla T_j \cdot \mathbf{n} \,\mathrm{d}S, \tag{6.24}$$

where $\mathbf{n}$ denotes the outward pointing normal to the surface $\partial\Omega$. Inserting this result into (6.23) and using the boundary conditions (6.2) and (6.3) yields

$$\begin{aligned} -k \iiint_\Omega \nabla f \cdot \nabla T_j \,\mathrm{d}V - h_{\text{top}}^c \iint_{\partial\Omega_{\text{top}}^c} fT_j \,\mathrm{d}S - h_{\text{top}} \iint_{\partial\Omega_{\text{top}}} fT_j \,\mathrm{d}S \\ + \iint_{\partial\Omega_{\text{top}}} fQ_{\text{EUV},j} \,\mathrm{d}S + \iint_{\partial\Omega_{\text{top}}} fQ_{\text{act},j} \,\mathrm{d}S = 0. \end{aligned} \tag{6.25}$$

The FE model is now based on the approximations (6.22) and the Galerkin projections

$$T_j(x,y,z) = \mathbf{N}(x,y,z)\boldsymbol{\theta}_j, \qquad f(x,y,z) = \mathbf{f}^\top \mathbf{N}^\top(x,y,z), \tag{6.26}$$

where $\boldsymbol{\theta}_j \in \mathbb{R}^N$ and $\mathbf{f} \in \mathbb{R}^N$ contain the nodal values of $T_j(x,y,z)$ and $f(x,y,z)$, respectively. Inserting these approximations into (6.25) and requiring that the

resulting equation should hold for all nodal values of the test function $\mathbf{f}$ results in the thermal FE model

$$\mathbf{A}\boldsymbol{\theta}_j = \mathbf{q}_{\mathrm{EUV},j} + \mathbf{E_B}\mathbf{q}_{\mathrm{act},j}, \qquad \mathbf{q}_{\mathrm{act},j} = \mathbf{B}\mathbf{u}_j, \tag{6.27}$$

where

$$\begin{aligned}\mathbf{A} = k \iiint_{\Omega} (\nabla\mathbf{N})^\top \nabla\mathbf{N} \,\mathrm{d}V \\ + h^c_{\mathrm{top}} \iint_{\partial\Omega^c_{\mathrm{top}}} \mathbf{N}^\top\mathbf{N} \,\mathrm{d}S + h_{\mathrm{top}} \iint_{\partial\Omega_{\mathrm{top}}} \mathbf{N}^\top\mathbf{N} \,\mathrm{d}S,\end{aligned} \tag{6.28}$$

$$\mathbf{q}_{\mathrm{EUV},j} = \iint_{\partial\Omega_{\mathrm{top}}} \mathbf{N}^\top Q_{\mathrm{EUV},j} \,\mathrm{d}S, \qquad \mathbf{E_B} = \iint_{\partial\Omega_{\mathrm{top}}} \mathbf{N}^\top\mathbf{N}\mathbf{C}^\top_{\mathrm{top}} \,\mathrm{d}S. \tag{6.29}$$

Note that $\mathbf{A} \in \mathbb{R}^{N\times N}$ is square but that $\mathbf{E_B} \in \mathbb{R}^{N\times N_{\mathrm{top}}}$ is not. As only the temperature at the top surface $\partial\Omega_{\mathrm{top}}$ is of interest, (6.27) is rewritten as

$$\boldsymbol{\theta}_{\mathrm{top},j} = \boldsymbol{\theta}_{\mathrm{EUV},j} + \boldsymbol{\Gamma}\mathbf{q}_{\mathrm{act},j}, \qquad \mathbf{q}_{\mathrm{act},j} = \mathbf{B}\mathbf{u}_j, \tag{6.30}$$

where

$$\boldsymbol{\theta}_{\mathrm{top},j} = \mathbf{C}_{\mathrm{top}}\boldsymbol{\theta}_j, \qquad \boldsymbol{\theta}_{\mathrm{EUV},j} = \mathbf{C}_{\mathrm{top}}\mathbf{A}^{-1}\mathbf{q}_{\mathrm{EUV},j}, \qquad \boldsymbol{\Gamma} = \mathbf{C}_{\mathrm{top}}\mathbf{A}^{-1}\mathbf{E_B}. \tag{6.31}$$

As $N_{\mathrm{top}} \ll N$, it is most efficient to precompute $\boldsymbol{\theta}_{\mathrm{EUV},j}$ and $\boldsymbol{\Gamma}$ before the optimization process. The remaining computational cost to obtain $\boldsymbol{\theta}_{\mathrm{top},j}$ at every iteration from (6.30) is then very small.

Cost functionals

The discretization of the cost functional $\mathcal{J}_0$ is obtained directly by substitution of (6.22) into (6.7)

$$J_0 = \sum_{j=1}^{n} \mathbf{q}^\top_{\mathrm{act},j}\mathbf{E}_0\mathbf{q}_{\mathrm{act},j} = \sum_{j=1}^{n} \mathbf{u}_j^\top\mathbf{B}^\top\mathbf{E}_0\mathbf{B}\mathbf{u}_j, \tag{6.32}$$

where

$$\mathbf{E}_0 = \iint_{\partial\Omega_{\mathrm{top}}} \mathbf{C}_{\mathrm{top}}\mathbf{N}^\top\mathbf{N}\mathbf{C}^\top_{\mathrm{top}} \,\mathrm{d}S = \mathbf{C}_{\mathrm{top}}\mathbf{E_B}, \tag{6.33}$$

with $\mathbf{E_B}$ as in (6.29). The cost functionals $\mathcal{J}_1$ and $\mathcal{J}_2$ are discretized by nodal interpolation. In this procedure, a function $f(x, y)$ on A_{top} is approximated by $\mathbf{N}(x, y, 0)\mathbf{C}^\top_{\mathrm{top}}\mathbf{f}$, where $\mathbf{f}$ is a vector containing the nodal values of $f(x, y)$ on A_{top}. The integral of $f(x, y)$ over A_{OFP} is then approximated by

$$\iint_{A_{\mathrm{OFP}}} f(x, y) \,\mathrm{d}x \,\mathrm{d}y \approx \iint_{\partial\Omega_{\mathrm{OFP}}} \mathbf{N}\mathbf{C}^\top_{\mathrm{top}}\mathbf{f} \,\mathrm{d}S = \mathbf{w}^\top_{\mathrm{OFP}}\mathbf{f}, \tag{6.34}$$

where

$$\mathbf{w}_{\mathrm{OFP}} = \iint_{\partial\Omega_{\mathrm{OFP}}} \mathbf{C}_{\mathrm{top}}\mathbf{N}^{\top}\,\mathrm{d}S. \tag{6.35}$$

Discretization of the cost functionals $\mathcal{J}_1$ and $\mathcal{J}_2$ in (6.18) and (6.21) by this method now yields

$$J_1 = \mathbf{w}_{\mathrm{OFP}}^{\top}\left[(\boldsymbol{\theta}_{\mathrm{top},j} - T^*\mathbf{1})^2 - \delta^2\mathbf{1}\right]^+, \tag{6.36}$$

$$J_2 = \mathbf{w}_{\mathrm{OFP}}^{\top}\left(\left(\frac{\delta^2\mathbf{1}}{\delta^2\mathbf{1} - (\boldsymbol{\theta}_{\mathrm{top},j} - T^*\mathbf{1})^2}\right)^p - \mathbf{1}\right), \tag{6.37}$$

where $\mathbf{1}$ denotes a (column) vector with ones of length N_{top} and the operations $[\,\cdot\,]^+$, $(\,\cdot\,)^2$, $\cdot\,/\,\cdot$, and $(\,\cdot\,)^p$ are applied componentwise.

6.3.3 Sensitivity analysis

The cost functionals $J = J_1$ and $J = J_0 + wJ_2$ with J_0, J_1, and J_2 as in (6.32), (6.36), and (6.37), respectively, will be updated by a gradient-based optimization algorithm. This requires the computation of the gradients $\nabla_{\mathbf{B}}J$ and $\nabla_{\mathbf{U}}J$ of a cost function $J = J(\mathbf{B},\mathbf{U})$ w.r.t. $\mathbf{B}$ and $\mathbf{U}$. These are defined by the property that for any variations $\tilde{\mathbf{B}}$ and $\tilde{\mathbf{U}}$

$$\left\langle \nabla_{\mathbf{B}}J(\mathbf{B},\mathbf{U}), \tilde{\mathbf{B}} \right\rangle_B = \lim_{h\to 0} \frac{J(\mathbf{B}+h\tilde{\mathbf{B}},\mathbf{U}) - J(\mathbf{B},\mathbf{U})}{h}, \tag{6.38}$$

$$\left\langle \nabla_{\mathbf{U}}J(\mathbf{B},\mathbf{U}), \tilde{\mathbf{U}} \right\rangle_U = \lim_{h\to 0} \frac{J(\mathbf{B},\mathbf{U}+h\tilde{\mathbf{U}}) - J(\mathbf{B},\mathbf{U})}{h}, \tag{6.39}$$

where $\langle\,\cdot\,,\,\cdot\,\rangle_B$ and $\langle\,\cdot\,,\,\cdot\,\rangle_U$ denote the inner products on the spaces of shape and intensity matrices defined by

$$\langle\hat{\mathbf{B}},\check{\mathbf{B}}\rangle_B = \mathrm{trace}\left(\hat{\mathbf{B}}^{\top}\mathbf{E}_0\check{\mathbf{B}}\right), \qquad \langle\hat{\mathbf{U}},\check{\mathbf{U}}\rangle_U = \mathrm{trace}\left(\hat{\mathbf{U}}^{\top}\check{\mathbf{U}}\right), \tag{6.40}$$

with $\mathbf{E}_0$ as in (6.33). Note that the gradients $\nabla_{\mathbf{B}}J$ and $\nabla_{\mathbf{U}}J$ thus depend on the used inner products.

To compute the gradients it is useful to observe that by eliminating $\boldsymbol{\theta}_{\mathrm{top},j}$ from (6.36) and (6.37) using (6.30), the cost functionals $J = J_1$ and $J = J_0 + wJ_2$ can be written in the form

$$J = \sum_{j=1}^{n} f_j(\mathbf{q}_{\mathrm{act},j}) = \sum_{j=1}^{n} f_j(\mathbf{B}\mathbf{u}_j), \tag{6.41}$$

for certain functions $f_j : \mathbb{R}^{N_{\mathrm{top}}} \to \mathbb{R}$. In Appendix D.3, it is shown that the gradients w.r.t. $\mathbf{B}$ and $\mathbf{U}$ of a cost functional of the form (6.41) are

$$\nabla_{\mathbf{B}}J(\mathbf{B},\mathbf{U}) = \mathbf{E}_0^{-1}\mathbf{G}^{\top}(\mathbf{B},\mathbf{U})\mathbf{U}^{\top}, \qquad \nabla_{\mathbf{U}}J(\mathbf{B},\mathbf{U}) = \mathbf{B}^{\top}\mathbf{G}^{\top}(\mathbf{B},\mathbf{U}), \tag{6.42}$$

where $\mathbf{G}(\mathbf{B},\mathbf{U})$ is the $n \times N_{\text{top}}$-matrix

$$\mathbf{G}(\mathbf{B},\mathbf{U}) = \begin{bmatrix} \frac{\partial f_1}{\partial \mathbf{q}_{\text{act},1}}(\mathbf{B}\mathbf{u}_1) \\ \frac{\partial f_2}{\partial \mathbf{q}_{\text{act},2}}(\mathbf{B}\mathbf{u}_2) \\ \vdots \\ \frac{\partial f_n}{\partial \mathbf{q}_{\text{act},n}}(\mathbf{B}\mathbf{u}_n) \end{bmatrix}. \tag{6.43}$$

Explicit formulas for the functions $f_j(\mathbf{q}_{\text{act},j})$ and their derivatives can be found in Appendix D.3 as well.

6.3.4 Optimization algorithm

Algorithm 6.1 shows the main steps of the used optimization algorithm.

Algorithm 6.1 Main steps in the optimization procedure

1: Choose some initial guess $\underline{\mathbf{B}}_{\text{init}} \in \mathbb{R}_+^{N_{\text{top}} \times n}$ and set $\underline{\mathbf{U}} = \mathbf{I}_n$.
2: Minimize J_1 over $\underline{\mathbf{B}}$ starting from $\underline{\mathbf{B}} = \underline{\mathbf{B}}_{\text{init}}$ to find an admissible $\underline{\mathbf{B}}_{\text{adm}}$.
3: Minimize $J_0 + wJ_2$ over $\underline{\mathbf{B}}$ starting from $\underline{\mathbf{B}} = \underline{\mathbf{B}}_{\text{adm}}$ to find the optimal $\underline{\mathbf{B}}_{\text{opt}}$.
4: Compute $\mathbf{B}_{\text{init}} \in \mathbb{R}_+^{N_{\text{top}} \times m}$ and $\mathbf{U}_{\text{init}} \in \mathbb{R}_+^{m \times n}$ as an m-th order nonnegative matrix factorization of $\underline{\mathbf{B}}_{\text{opt}}$.
5: Minimize J_1 over $\mathbf{B}$ and $\mathbf{U}$ starting from $\mathbf{B} = \mathbf{B}_{\text{init}}$ and $\mathbf{U} = \mathbf{U}_{\text{init}}$ to find admissible $\mathbf{B}_{\text{adm}}$ and $\mathbf{U}_{\text{adm}}$.
6: Minimize $J_0 + wJ_2$ over $\mathbf{B}$ and $\mathbf{U}$ starting from $\mathbf{B} = \mathbf{B}_{\text{adm}}$ and $\mathbf{U} = \mathbf{U}_{\text{adm}}$ to find (locally) optimal $\mathbf{B}_{\text{opt}}$ and $\mathbf{U}_{\text{opt}}$.

The main idea behind Algorithm 6.1 is the following. As the optimization of an m-shape actuation heat load (with $m < n$) together with the corresponding intensities is nonconvex, finding a good initialization is important. This initialization is found by noting that the problem with n spatial shapes $\underline{\mathbf{B}} \in \mathbb{R}^{N_{\text{top}} \times n}$ and $\mathbf{U}$ fixed to $\underline{\mathbf{U}} = \mathbf{I}_n$ is convex and thus has a unique solution. This unique solution is computed in lines 1 to 3 of Algorithm 6.1. This solution is then used to initialize the optimization of the m-shape actuation heat load in lines 4 to 6.

The steps in Algorithm 6.1 are now considered in more detail. As $J_0 + wJ_2$ is strictly convex in $\underline{\mathbf{B}}$, the choice of the initial guess $\underline{\mathbf{B}}_{\text{init}}$ in line 1 will not influence the found $\underline{\mathbf{B}}_{\text{opt}}$ in line 3. Naturally, $\underline{\mathbf{B}}_{\text{init}}$ will influence the time required to solve the optimization problem in lines 2 and 3. The minimization of $J_0 + wJ_2$ in line 3 needs to be started from an admissible solution $(\underline{\mathbf{B}}_{\text{adm}}, \underline{\mathbf{U}}_{\text{adm}})$, which is found by minimizing J_1 in line 2. The optimization problems in lines 2 and 3 are solved using a gradient based algorithm that will be discussed later. In line 4, the most dominant spatial shapes and their corresponding intensities in $\underline{\mathbf{B}}_{\text{opt}}$ are found by computing a Nonnegative Matrix Factorization (NMF) of $\underline{\mathbf{B}}$. The NMF is computed using the `nnmf` function in MATLAB (version

2019a) in which the algorithms from [Berry et al., 2007] are implemented. It is important to note that `nnmf` uses a random initialization and that each call to `nnmf` therefore leads to a different initialization $\mathbf{B}_{\text{init}}$ and $\mathbf{U}_{\text{init}}$. However, the initializations $\mathbf{B}_{\text{init}}$ and $\mathbf{U}_{\text{init}}$ found in this way lead to much better $\mathbf{B}_{\text{opt}}$ and $\mathbf{U}_{\text{opt}}$ than random initializations, see also [Nouwens, 2020]. The thus obtained shapes $\mathbf{B}_{\text{init}}$ and intensities $\mathbf{U}_{\text{init}}$ are then used as an initialization for a gradient-based optimization algorithm which will be discussed later. Similarly as in lines 2 and 3, the minimization of $J_0 + wJ_2$ over $\mathbf{B}$ and $\mathbf{U}$ in line 6 is initialized from an admissible solution $(\mathbf{B}_{\text{adm}}, \mathbf{U}_{\text{adm}})$ found by minimizing J_1 in line 5.

The optimization problems over both $\mathbf{B}$ and $\mathbf{U}$ in lines 5 and 6 of Algorithm 6.1 are solved by the alternating update scheme in Algorithm 6.2, which is similar to the algorithm used in Chapter 5.

Algorithm 6.2 Alternating update scheme

```
1: Input: initial guess B^(0) and U^(0).
2: Set k = 0.
3: while k <max_iters do
4:     B^(k+1) = UpdateB(B^(k), U^(k))
5:     U^(k+1) = UpdateU(B^(k+1), U^(k))
6:     if Converged(B^(k), B^(k+1), U^(k), U^(k+1)) then
7:         return (B^(k+1), U^(k+1))
8:     end if
9:     k = k + 1
10: end while
```

Here, `max_iters` denotes the maximal number of iterations. The methods 'UpdateB', 'UpdateU', and 'Converged' will be elaborated below. For the optimization problems in lines 2 and 3 of Algorithm 6.1 in which $\mathbf{U}$ is fixed the update of $\mathbf{U}$ in line 5 of Algorithm 6.2 can of course be replaced by $\mathbf{U}^{(k+1)} = \mathbf{U}^{(k)}$.

The procedures 'UpdateB' and 'UpdateU' are very similar and only 'UpdateB' will be discussed in detail. This procedure essentially consists of a single update from a projected-gradient algorithm, see e.g. [Hinze et al., 2009]. The update thus takes the form

$$\mathbf{B}^{(k+1)} = \Pi\left(\mathbf{B}^{(k)} - h_{\mathbf{B}} \nabla_{\mathbf{B}} J(\mathbf{B}^{(k)}, \mathbf{U}^{(k)})\right), \tag{6.44}$$

where $h_{\mathbf{B}} > 0$ denotes the step size and $\Pi : \mathbb{R}^{N_{\text{top}} \times m} \to \mathbb{R}_+^{N_{\text{top}} \times m}$ denotes the projection on the admissible set of matrices with nonnegative entries, which is given by (for $1 \leq \ell \leq N_{\text{top}}$ and $1 \leq i \leq m$)

$$(\Pi(\mathbf{X}))_{\ell i} = \begin{cases} \mathbf{X}_{\ell i} & \text{when } \mathbf{X}_{\ell i} \geq 0, \\ 0 & \text{when } \mathbf{X}_{\ell i} < 0. \end{cases} \tag{6.45}$$

To estimate the step size $h_{\mathbf{B}}$, first consider

$$\tilde{\mathbf{B}}^{(k)} := \lim_{h_{\mathbf{B}} \downarrow 0} \frac{\Pi\left(\mathbf{B}^{(k)} - h_{\mathbf{B}} \nabla_{\mathbf{B}} J(\mathbf{B}^{(k)}, \mathbf{U}^{(k)})\right) - \mathbf{B}^{(k)}}{h_{\mathbf{B}}} \tag{6.46}$$

Note that when $\mathbf{B}_{\ell i}^{(k)} > 0$ or when $\mathbf{B}_{\ell i}^{(k)} = 0$ and $\left(\nabla_{\mathbf{B}} J(\mathbf{B}^{(k)}, \mathbf{U}^{(k)})\right)_{\ell i} \leq 0$, the projection Π does not influence the ℓi-th entry and $\tilde{\mathbf{B}}_{\ell i}^{(k)} = \left(\nabla_{\mathbf{B}} J(\mathbf{B}^{(k)}, \mathbf{U}^{(k)})\right)_{\ell i}$. In the remaining situation $\mathbf{B}_{\ell i}^{(k)} = 0$ and $\left(\nabla_{\mathbf{B}} J(\mathbf{B}^{(k)}, \mathbf{U}^{(k)})\right)_{\ell i} > 0$, from which it is easy to see that $\tilde{\mathbf{B}}_{\ell i}^{(k)} = 0$. It thus follows that

$$\tilde{\mathbf{B}}_{\ell i}^{(k)} = \begin{cases} 0 & \text{if } \mathbf{B}_{\ell i}^{(k)} = 0 \text{ and } \left(\nabla_{\mathbf{B}} J(\mathbf{B}^{(k)}, \mathbf{U}^{(k)})\right)_{\ell i} > 0, \\ \left(\nabla_{\mathbf{B}} J(\mathbf{B}^{(k)}, \mathbf{U}^{(k)})\right)_{\ell i} & \text{otherwise.} \end{cases} \tag{6.47}$$

With this definition, it is now possible to construct the following quadratic cost functional J for positive $h_{\mathbf{B}}$ near $h_{\mathbf{B}} = 0$

$$J(\mathbf{B}^{(k+1)}, \mathbf{U}^{(k)}) \approx J(\mathbf{B}^{(k)}, \mathbf{U}^{(k)}) + h_{\mathbf{B}} G_{\mathbf{B}}^{(k)} + \frac{h_{\mathbf{B}}^2}{2} H_{\mathbf{B}}^{(k)}, \tag{6.48}$$

where

$$G_{\mathbf{B}}^{(k)} = -\left\langle \nabla J(\mathbf{B}^{(k)}, \mathbf{U}^{(k)}), \tilde{\mathbf{B}}^{(k)} \right\rangle_B, \tag{6.49}$$

$$H_{\mathbf{B}}^{(k)} = \frac{\partial^2}{\partial h_{\mathbf{B}}^2} \left(J(\mathbf{B}^{(k)} + h_{\mathbf{B}} \tilde{\mathbf{B}}^{(k)}, \mathbf{U}^{(k)}) \right) \Big|_{h_{\mathbf{B}}=0}. \tag{6.50}$$

The computation of $H_{\mathbf{B}}^{(k)}$ is further addressed in Appendix D.3. The step size $h_{\mathbf{B}}$ that minimizes the approximation (6.48) is $h_{\mathbf{B},\text{opt}} = -G_{\mathbf{B}}^{(k)} / H_{\mathbf{B}}^{(k)}$. Because (6.48) is an approximation, there is no guarantee that this step size actually leads to a decrease in J. If $h_{\mathbf{B}} = h_{\mathbf{B},\text{opt}}$ does not lead to a decrease, $h_{\mathbf{B}}$ is halved until a decrease in J is observed. Note that $G_{\mathbf{B}}^{(k)} \leq 0$ and that a decrease in J will be observed for $h_{\mathbf{B}}$ small enough if $G_{\mathbf{B}}^{(k)} < 0$.

The method 'Converged' in line 6 of Algorithm 6.2 checks two criteria:

1. The relative change in cost function is below a specified tolerance `tolJ`, i.e. $J(\mathbf{B}^{(k)}, \mathbf{U}^{(k)}) - J(\mathbf{B}^{(k+1)}, \mathbf{U}^{(k+1)}) < \texttt{tolJ} J(\mathbf{B}^{(k)}, \mathbf{U}^{(k)})$.

2. The relative change in the applied heat loads is below a specified tolerance `tolQ`, i.e. $\|\mathbf{B}^{(k+1)}\mathbf{U}^{(k+1)} - \mathbf{B}^{(k)}\mathbf{U}^{(k)}\|_B < \texttt{tolQ} \|\mathbf{B}^{(k)}\mathbf{U}^{(k)}\|_B$.

Here, $\| \cdot \|_B$ denotes the norm induced by the inner product $\langle \cdot , \cdot \rangle_B$ in (6.40).

6.4 Results

The volume $(x, y, z) \in [-L/2, L/2] \times [-W/2, W/2] \times [-H, 0]$ occupied by the mirror is discretized using 80 elements in the x-direction, 40 elements in the y-direction, and 16 elements in z-direction. With the used standard linear Lagrangian elements, this leads to a mesh with 51,200 elements and $N = 56,457$ nodes, of which there are $N_{\text{top}} = 3225$ in the top surface $\partial\Omega_{\text{top}}$. The FE matrices $\mathbf{C}_{\text{top}}$, $\mathbf{A}$, and $\mathbf{E}_{\mathbf{B}}$ and the 17 vectors $\mathbf{q}_{\text{EUV},j}$ in (6.28) and (6.29) are constructed using a MATLAB FE toolbox based on [de Best, 2015]. The computation of $\boldsymbol{\theta}_{\text{EUV},j}$ and $\boldsymbol{\Gamma}$ in (6.31) is sped up using a Lower-Upper (LU) decomposition of the matrix $\mathbf{A}$, but still takes about 8 minutes on a Windows 10, Intel Core i7, 8 GB RAM laptop that has been used to generate all results in this section.

The parameter values for the optimization problem are given in Table 6.2. Recall that the parameter values for the physical model are given in Table 6.1. Note that the value of $\delta = 3.5$ K might seem quite large but is in fact the smallest value for which an admissible solution consisting of only $m = 1$ spatial shape could be found. It is also quite close to the smallest value of $\delta = 3.2$ K for which an admissible solution consisting of $m = 17$ spatial shapes could be found. The values of δ for which an admissible solution can be found strongly depends on the chosen desired temperature T^*; the higher T^* the larger the range of δ's for which an admissible solution can be found. The selected value of T^* is based on a typical value of the zero-crossing temperature of ULE.

Following the first 3 lines in Algorithm 6.1, the optimal actuation heat load is first computed for the case $m = n = 17$, i.e. the case where the number of spatial shapes in the actuation heat load is equal to the number of EUV heat loads. For the physical interpretation it is useful to recall that the columns $\underline{\mathbf{B}}_{\text{opt},i}$ (with $1 \leq i \leq 17$) of $\underline{\mathbf{B}}_{\text{opt}}$ correspond to the spatial shapes

$$\underline{B}_{\text{opt},i}(x, y) = \mathbf{N}_{\text{top}}(x, y, 0)\mathbf{C}_{\text{top}}\underline{\mathbf{B}}_{\text{opt},i}. \tag{6.51}$$

The first 7 of the obtained spatial shapes $\underline{B}_{\text{opt},i}(x, y)$ are displayed in Figure 6.4. Note that the shapes have been normalized to have unit L^1-norm as in (6.14), which means that their corresponding intensities are the applied actuation powers $P_{\text{act},i}$. Note that many of the shapes in Figure 6.4 are significantly different, although the shapes $B_2(x, y)$, $B_4(x, y)$, and $B_6(x, y)$ in Figures 6.4b, 6.4d, and 6.4f show some resemblance. It is therefore not clear from these results what the most effective spatial shapes are.

The most effective spatial shapes are found in lines 4 to 6 of Algorithm 6.1. The obtained spatial shapes $\{B_i(x, y)\}_{1 \leq i \leq m}$ and intensities $u_{i,j}$ for $m = 1, 2, 3, 4$ and $n = 17$ are shown in Figures 6.5 to 6.8. Note that the spatial shapes $B_i(x, y)$ have been made boundary close (see Definition 6.6) such that they clearly show the different spatial shapes and are again scaled such that they have unit L_1-norm as in (6.14), which means that the intensities $u_{i,j}$ have unit Watt and can

Table 6.2. Parameter values used in the optimization problem

Description	Symbol	Value	Unit
Desired temperature increase	T^*	13	K
Maximally allowed deviation	δ	3.5	K
Power for barrier function	p	3.5	–
Weight for barrier function	w	48	$\mathrm{W}^2/\mathrm{m}^2$
Tolerance in convergence check	`tolJ`	10^{-5}	-
Tolerance in convergence check	`tolQ`	10^{-3}	-

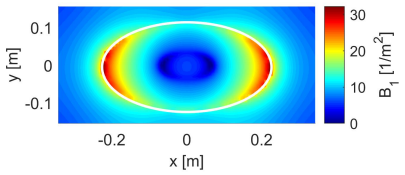

(a) $\underline{B}_{\mathrm{opt},1}(x,y)$, $P_{\mathrm{act},1} = 3.44$ W

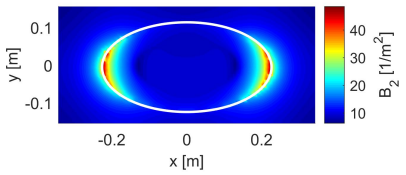

(b) $\underline{B}_{\mathrm{opt},2}(x,y)$, $P_{\mathrm{act},2} = 2.38$ W

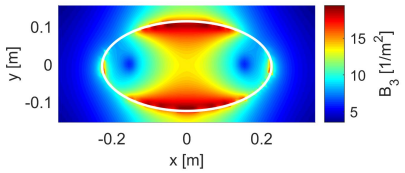

(c) $\underline{B}_{\mathrm{opt},3}(x,y)$, $P_{\mathrm{act},3} = 3.73$ W

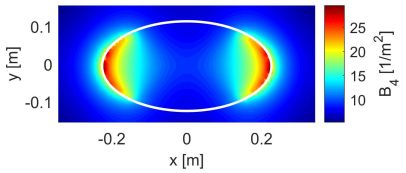

(d) $\underline{B}_{\mathrm{opt},4}(x,y)$, $P_{\mathrm{act},4} = 3.81$ W

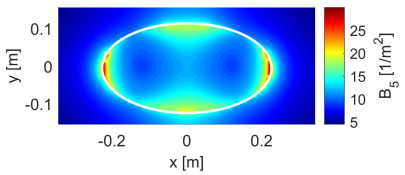

(e) $\underline{B}_{\mathrm{opt},5}(x,y)$, $P_{\mathrm{act},5} = 3.51$ W

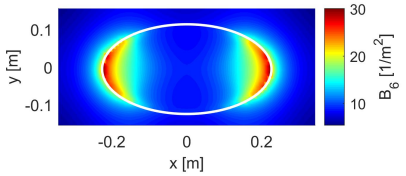

(f) $\underline{B}_{\mathrm{opt},6}(x,y)$, $P_{\mathrm{act},6} = 3.75$ W

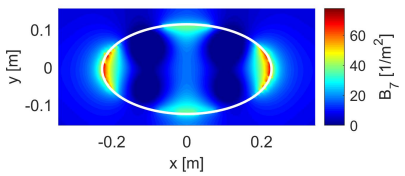

(g) $\underline{B}_{\mathrm{opt},7}(x,y)$, $P_{\mathrm{act},7} = 1.96$ W

Figure 6.4. The first seven shapes of the actuation heat load $\underline{B}_{\mathrm{opt},j}(x,y)$ with their intensities $P_{\mathrm{act},j}$ $(1 \leq j \leq 7)$ designed to counteract the $n = 17$ EUV heat loads $Q_{\mathrm{EUV},j}(x,y)$ in Figure 6.2. The white ellipse indicates the OFP.

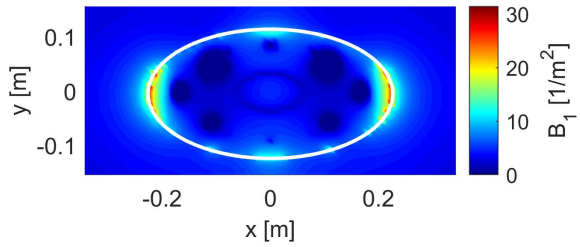

(a) Spatial shape $B_1(x, y)$

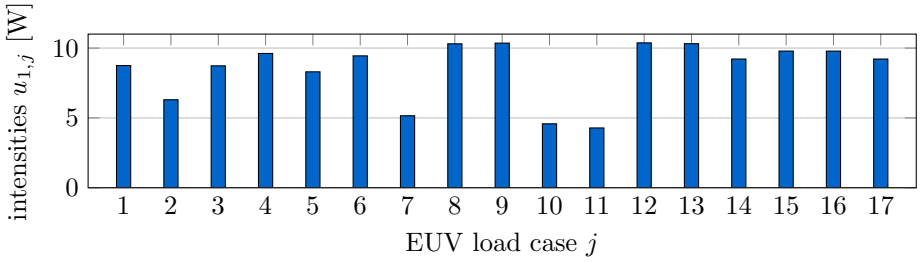

(b) Intensities $u_{1,j}$

Figure 6.5. Spatial shape $B(x, y)$ and intensities $u_j = u_{1,j}$ found for $m = 1$ and $n = 17$

be interpreted as the amount of heating power with which shape i is applied in EUV load case j.

The only spatial shape $B_1(x, y)$ obtained for $m = 1$ and $n = 17$ is shown in Figure 6.5a. This shape is heating up the edges of the OFP because these are closest to the sides of the mirror which are cooled through the convective boundary condition. Furthermore, the areas where the heat loads $Q_{\mathrm{EUV},1}(x, y)$ and $Q_{\mathrm{EUV},7}(x, y)$ in Figures 6.2a and 6.2g on page 170 are high can be recognized in the areas where $B_1(x, y)$ in Figure 6.5a is zero. This suggests that load cases $i = 1$ and $i = 7$ are among the most critical ones. It is also worth noting that the power of the actuation heat loads is the smallest for the load cases $j = 2, 7, 10, 11$, which are precisely the load cases in which the power applied by the EUV light is the largest, see Figures 6.2 and 6.3 on pages 170 and 171.

The spatial shapes $B_1(x, y)$ and $B_2(x, y)$ obtained for $m = 2$ and $n = 17$ are shown in Figures 6.6a and 6.6b. The area in which $B_1(x, y)$ is zero again resembles the area in which $Q_{\mathrm{EUV},7}(x, y)$ in Figure 6.2g is applied, which is also reflected in the fact that $u_{2,7} = 0$ W, see Figure 6.6c. The second spatial shape $B_2(x, y)$ is mainly applied in the areas where $B_1(x, y)$ is zero, and can thus be used to flatten the temperature field for the other load cases. Note that $u_{1,j} > 0$ for all $1 \leq j \leq n$, which means a positive multiple of the second row $u_{2,j}$ can be

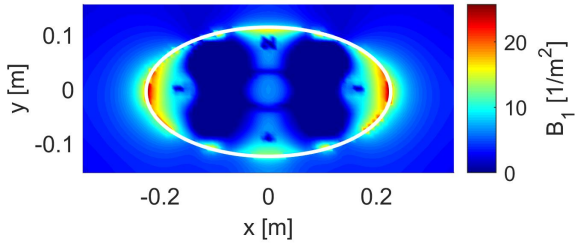

(a) Spatial shape $B_1(x, y)$

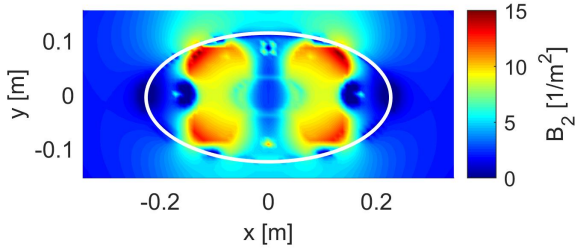

(b) Spatial shape $B_2(x, y)$

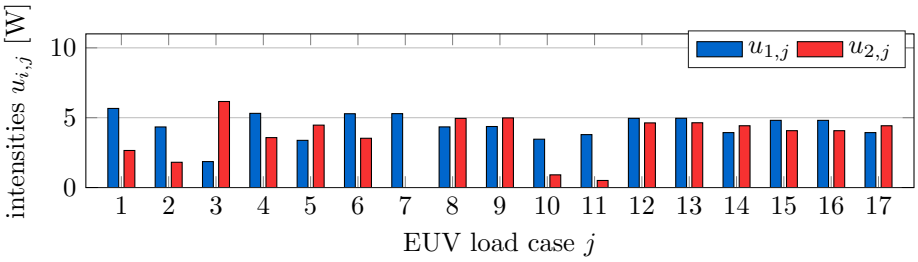

(c) Intensities $u_{i,j}$

Figure 6.6. Spatial shapes $B_i(x, y)$ and intensities $u_{i,j}$ found for $m = 2$ and $n = 17$

subtracted from the first row $u_{1,j}$. The rows of $\mathbf{U}$ are thus not boundary close (see Definition 6.6) and Lemma 6.7 shows that the found optimal actuation heat loads $Q_{\mathrm{act},j}(x,y)$ can also be generated by different spatial shapes. Furthermore, it is worth noting that the total applied actuation power $u_{1,j}+u_{2,j}$ in the j-th load case for $m=2$ (see Figure 6.6c) is slightly smaller than the actuation power $u_{1,j}$ applied with $m=1$ spatial shape (see Figure 6.5b).

The spatial shapes found for $m=3$ and $m=4$ and $n=17$ in Figures 6.7 and 6.8 are even harder to interpret. However, in both cases there is again one spatial shape that is zero in the area where $Q_{\mathrm{EUV},7}(x,y)$ is applied ($B_3(x,y)$ in Figure 6.7c and $B_2(x,y)$ in Figure 6.8b), which are also (almost) the only shape that is applied in the seventh load case (see Figures 6.7d and 6.8e).

Recall from Algorithm 6.1 that the results in Figures 6.5 to 6.8 have been computed starting from an NMF of the optimal shapes $\underline{\mathbf{B}}_{\mathrm{opt}}$ and that the obtained NMF depends on a random initialization. For $m=1$ and $m=2$, the randomness in the initialization hardly influences the obtained shapes $B_i(x,y)$ and intensities $u_{i,j}$. However, for $m\geq 3$ the obtained shapes and intensities differ significantly. Starting the second half of the optimization procedure (lines 5 and 6 in Algorithm 6.1) from a different NMF $\mathbf{B}_{\mathrm{init}}\mathbf{U}_{\mathrm{init}}$ can lead to very different spatial shapes $\mathbf{B}_{\mathrm{opt}}$ and intensities $\mathbf{U}_{\mathrm{opt}}$. This is illustrated by the optimal shapes and intensities in Figure 6.9 which have been obtained from a different NMF than the optimal shapes and intensities in Figure 6.7. The two sets of spatial shapes in Figures 6.7 and 6.9 are significantly different. However, the values of $\mathcal{J}_0+w\mathcal{J}_2=6372$ and $\mathcal{J}_0=5845$ found for the shapes and intensities in Figure 6.7 are quite close to the values of $\mathcal{J}_0+w\mathcal{J}_2=6385$ and $\mathcal{J}_0=5837$ found for the shapes and intensities in Figure 6.9

To study the influence of this random element in the NMF further, the optimal m-shape actuation heat loads have been computed starting from $N_s=30$ different NMFs for $m=1,2,3,4$. The results are summarized in Tables 6.3 and 6.4. The numbers between round brackets in Tables 6.3 and 6.4 denote the standard deviation in the considered quantities over the $N_s=30$ considered NMFs. In Table 6.4, $\bar{P}_{\mathrm{act}}$ denotes the applied actuation power averaged over the $n=17$ load cases.

The results in Table 6.3 show that the NMF significantly influences the number of iterations and computational time. This effect is especially strong when $m=1$ and $m=2$, which are the cases where finding an admissible solution is most difficult. For $m=1$, an admissible solution could not be found starting from 15 of the 30 considered NMFs. The data in Tables 6.3 and 6.4 for $m=1$ therefore only considers the 15 of the 30 NMFs for which an admissible solution could be found. For $m=2$, the standard deviation of the number of iterations and computational time for the minimization of $\mathcal{J}_1$ exceeds the mean, which indicates a strong influence of the NMF $\mathbf{B}_{\mathrm{init}}\mathbf{U}_{\mathrm{init}}$. Note that for $m=3$ and $m=4$, the admissible set seems to be much larger and the minimization of $\mathcal{J}_1$ requires only a few iterations and not so much time.

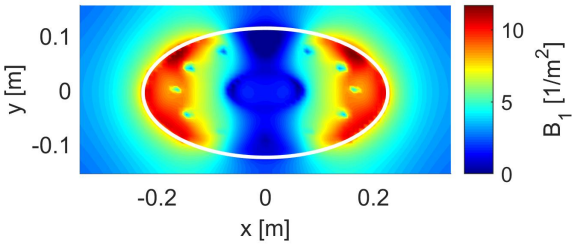

(a) Spatial shape $B_1(x, y)$

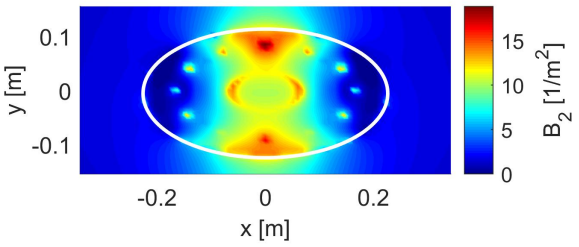

(b) Spatial shape $B_2(x, y)$

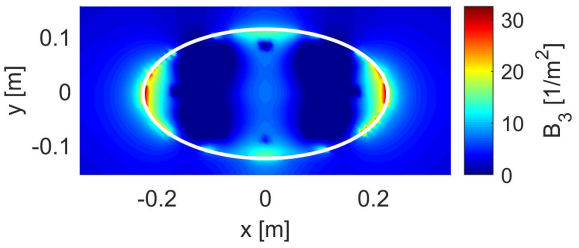

(c) Spatial shape $B_3(x, y)$

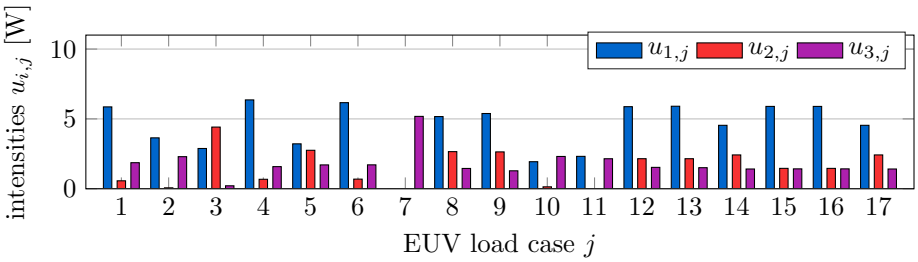

(d) Intensities $u_{i,j}$

Figure 6.7. Spatial shapes $B_i(x, y)$ and intensities $u_{i,j}$ found for $m = 3$ and $n = 17$

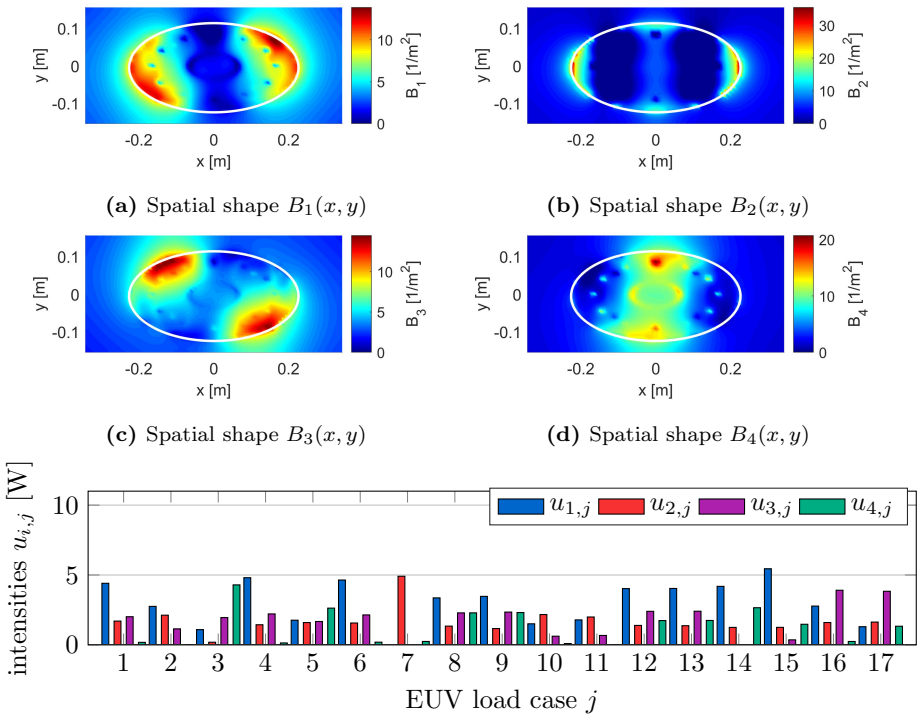

(a) Spatial shape $B_1(x, y)$

(b) Spatial shape $B_2(x, y)$

(c) Spatial shape $B_3(x, y)$

(d) Spatial shape $B_4(x, y)$

(e) Intensities $u_{i,j}$

Figure 6.8. Spatial shapes $B_i(x, y)$ and intensities $u_{i,j}$ found for $m = 4$ and $n = 17$

Table 6.3. Mean and standard deviation (between round brackets) in the number of iterations and the computational time to obtain the optimal actuation heat loads consisting of m spatial shapes initialized from 30 different NMFs.

	Minimizing $\mathcal{J}_1$				Minimizing $\mathcal{J}_0 + w\mathcal{J}_2$			
m	# iterations		time [s]		# iterations		time [s]	
1	158	(37)	41	(13)	415	(38)	44	(4)
2	61	(75)	18	(32)	864	(80)	101	(10)
3	6	(2)	2	(1)	334	(64)	46	(9)
4	6	(3)	2	(1)	297	(60)	41	(8)
17	20	(–)	14	(–)	210	(–)	75	(–)

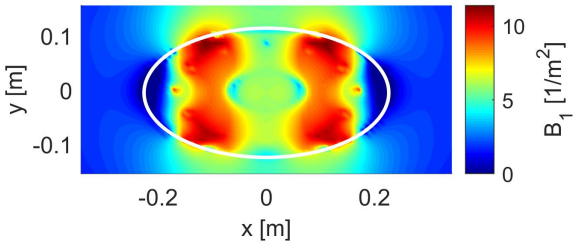

(a) Spatial shape $B_1(x, y)$

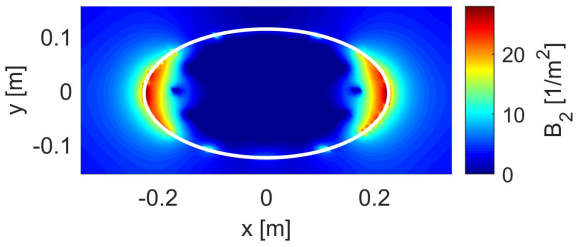

(b) Spatial shape $B_2(x, y)$

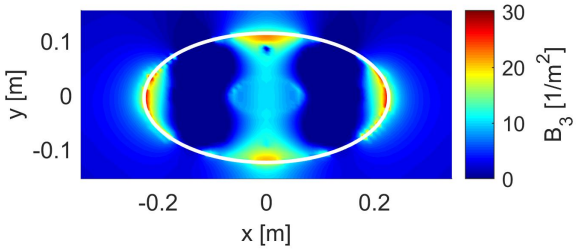

(c) Spatial shape $B_3(x, y)$

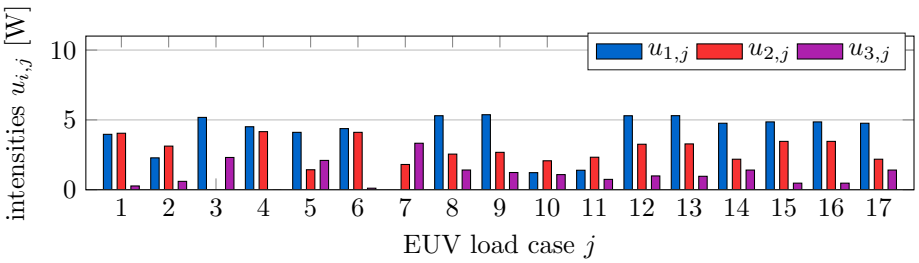

(d) Intensities $u_{i,j}$

Figure 6.9. Spatial shapes $B_i(x, y)$ and intensities $u_{i,j}$ found for $m = 3$ and $n = 17$, using a different NMF than in Figure 6.7

Table 6.4. Mean and standard deviation (in brackets) of the optimal actuation heat loads consisting of m spatial shapes initialized from 30 different NMFs.

m	$\mathcal{J}_0 + w\mathcal{J}_2$		$\mathcal{J}_0$		$\bar{P}_{\text{act}}$ [W]	
1	10,204	(3.1)	8,604	(3.4)	8.50	(0.004)
2	6,852	(2.1)	6,076	(1.6)	7.90	(0.003)
3	6,377	(7.3)	5,840	(3.3)	7.81	(0.006)
4	6,315	(5.7)	5,779	(12)	7.74	(0.013)
17	6,172	(–)	5,729	(–)	7.71	(–)

The results in Table 6.4 are in agreement with the earlier observation that the minimal values of the cost functions $\mathcal{J}_0+w\mathcal{J}_2$ and $\mathcal{J}_0$ obtained from different NMFs are very similar, although the obtained spatial shapes $B_i(x, y)$ and intensities $u_{i,j}$ can be very different. Indeed, the standard deviations (given between round brackets) in $\mathcal{J}_0 + w\mathcal{J}_2$, $\mathcal{J}_0$, and $\bar{P}_{\text{act}}$ are small compared to their mean values. Note that it is natural that the obtained minimal values of $\mathcal{J}_0 + w\mathcal{J}_2$, $\mathcal{J}_0$, and $\bar{P}_{\text{act}}$ decrease as the number of actuation heat load shapes m increases, because more spatial shapes allow more design freedom.

6.5 Conclusions and discussions

In this chapter, the temperature control of a mirror in a projection system for EUV lithography has been considered. Because the projection system has a large number of potential illumination settings, a thermal actuator layout should be able to control the steady-state mirror temperature resulting from a large number of potential disturbance heat loads. In order to aid the design of such a thermal actuator layout, an approach to compute the optimal actuation heat loads that consist of much less spatial shapes than the disturbance heat loads has been proposed. The computed actuation heat load is able to keep the steady-state mirror temperatures sufficiently close to a desired temperature in all considered load cases. The method has been applied to a 3-D mirror model to design actuation heat loads consisting of $m = 1, 2, 3$, and 4 spatial shapes that counteract $n = 17$ disturbances. The proposed approach provides useful insights for the design of a thermal actuation layout for mirror heating.

The proposed optimization algorithm consists of two stages. In the first stage, the number of spatial shapes of the actuation heat load is not limited which leads to a convex problem with a unique solution. The optimization in the second stage is initialized from an nonnegative matrix factorization of the actuation heat loads found in the first stage. Alternating updates of the spatial shapes and intensities are used to find the optimal actuation heat loads consisting of a limited number of spatial shapes. The proposed algorithm seems to converge to the same set of actuation heat loads, but the representation in terms of

spatial shapes and intensities differs depending on the found nonnegative matrix factorization which depends on a random initialization. For the considered FE model with about 50,000 nodes, the bulk of the computational time (about 8 minutes) is consumed in the computation of the mapping from the nodal top surface heat loads to the nodal top surface temperatures. The remaining cost for the optimization is smaller (typically about 2 or 3 minutes).

In contrast to the situation in Chapter 5 where an actuation heat load consisting of only $m = 1$ spatial shapes was considered, the representation of actuation heat loads consisting of $m > 1$ spatial shapes and intensities is typically not unique, see Subsection 6.2.2. For the set of load cases considered in this chapter, the proposed method always seems to converge to a set of m spatial shapes and intensities with (approximately) minimal cost. However, there are typically many sets of m spatial shapes that lead to (approximately) the same cost. As the spatial shapes used to create the set of actuation heat loads give a good indication of the effective thermal actuator layout, the choice of these spatial shapes is an important topic for future research.

In this chapter, the spatial shapes have been designed based on steady-state temperature constraints. However, the optical performance of the lithography system will also depend on the transient response and is not determined by the temperature field directly but by the propagation of the optical error resulting from the heat-induced deformations in the OFP. Such extensions seem to be necessary for a better understanding of the mirror heating problem but come with several additional problems. For example, the size of the considered FE model indicates that a transient analysis requires a reduction of the model complexity, for example by model order reduction, see e.g. [Antoulas, 2005], or by semi-analytic techniques, see e.g. Chapter 4. When considering deformation in the OFP or even the resulting optical errors, the biconvex nature of the discussed problem is lost due to the quadratic relation between temperature and deformations. Reliably finding a local minimum with an acceptable performance therefore becomes very challenging for such problems.

Part IV

Sensor placement for feedback control

Chapter 7

Sensor and actuator placement for proportional feedback control in advection-diffusion equations

7.1 Introduction

The placement of sensors and actuators is an important aspect of control system design for which many techniques have been developed, see e.g. [van de Wal and de Jager, 2001]. The simplest approach to this problem is to choose a controller design method and evaluate the resulting closed-loop performance for a large number of sensor and/or actuator locations. However, such an approach is computationally demanding when there are a large number of potential sensor and/or actuator locations. This is typically the case when the problem is governed by Partial Differential Equations (PDEs).

Several publications have considered the sensor and/or actuator placement problem for parabolic PDEs such as the heat equation. For example, a strategy for sensor placement based on the kernel representation of feedback operators in infinite-dimensional linear quadratic estimation problems is proposed in [Burns and Rubio, 1997]. More recent extensions of these ideas can be found in [Burns and Rautenberg, 2015a; Burns and Rautenberg, 2015b]. Another approach proposed in [Armaou and Demetriou, 2006] used modal observability and controllability measures to determine optimal sensor and actuator locations in parabolic

This chapter is based on D. W. M. Veldman et al. (2020a). 'Sensor and actuator placement for proportional feedback control in advection-diffusion equations'. *IEEE Control Systems Letters*, volume 4, number 1, pages 193–198. The main additions to the original paper are Definition 7.1, the structuring of Sections 7.2 and 7.3 into subsections, and Appendix E.

PDEs. In the approach proposed in [Vaidya et al., 2012], the optimal area for sensing or actuation in advective PDEs is determined by maximizing the support of the observability or controllability Gramian, respectively. The idea to determine the optimal area for sensing was also considered in [Privat et al., 2015], who proposed a method to determine the optimal area for sensing by optimizing observability in a stochastic setting. A similar idea can be used to determine the optimal area for actuation [Privat et al., 2017].

These approaches do not explicitly address the design of the resulting feedback controller (and/or observer). This is an important aspect of the control system design which may affect the found optimal sensor and actuator locations. Such combined actuator location and controller optimization problems have been considered in [Chen and Rowley, 2011; Morris, 2011; Darivandi et al., 2013; Kasinathan and Morris, 2013]. The dual problem in which the variance of the estimation error is minimized over sensor locations and observers has also been addressed in [Burns and Rautenberg, 2015a; Burns and Rautenberg, 2015b] and [Zhang and Morris, 2018]. An additional problem is that practical implementation requires that the order of the controller (and/or observer) is sufficiently low. This seems to be a largely open problem, for which some potential solutions have been proposed in [Demetriou, 2005; Demetriou, 2017].

In many of the approaches that address the design of a feedback controller (and/or observer), the optimal sensor and/or actuator locations are determined by searching through a discrete set of potential sensor and/or actuation locations, see e.g. [Demetriou, 2005; Darivandi et al., 2013; Zhang and Morris, 2018]. Such an approach does not seem to use the connection to the underlying PDE fully.

In this chapter, the placement of a single sensor and/or a single actuator in advection-diffusion equations with proportional feedback control is addressed. The problem is considered on one-dimensional (1-D) and two-dimensional (2-D) infinite spatial domains. Based on analytic expressions for the transfer functions, geometric rules that characterize the optimal sensor and actuator locations for high-gain and low-gain feedback are derived. Numerical experiments indicate that the derived rules accurately predict all (locally) optimal actuator and/or sensor locations.

The remainder of this chapter is structured as follows. In Section 7.2, the analysis and numerical results for the 1-D spatial domain are presented. In Section 7.3, the 2-D spatial domain is considered. In Section 7.4, the conclusions are formulated and future work is discussed.

7.2 One-dimensional spatial domain

Consider the following PDE with constant coefficients on the 1-D spatial domain $x \in \mathbb{R}$

$$\frac{\partial T}{\partial t} = v\frac{\partial T}{\partial x} + D\frac{\partial^2 T}{\partial x^2} - hT + \frac{1}{c}\delta(x - x_u)u(t) + \frac{1}{c}\delta(x - x_w)w(t), \tag{7.1}$$

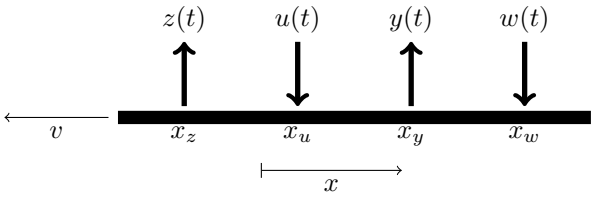

Figure 7.1. The 1-D spatial domain with the locations x_y, x_u, x_w, and x_z of the sensor, actuator, disturbance, and performance variable, respectively.

$$y(t) = T(x_y, t), \qquad z(t) = T(x_z, t), \tag{7.2}$$

with initial condition $T(x, 0) = 0$. Here, $\delta(x)$ denotes the Dirac delta. This PDE can be used to model the temperature $T = T(x, t)$ [K] in a medium with heat capacity $c > 0$ [J/K/m], thermal diffusivity $D > 0$ [m^2/s], cooling rate to the environment $h > 0$ [1/s], and advective transport with velocity $v \geq 0$ [m/s].

The problem is to find the locations $x = x_u$ [m] of the control input $u(t)$ [W] and $x = x_y$ [m] of the measured output $y(t)$ [K] for which there exists a proportional feedback controller that minimizes the influence of the disturbance $w(t)$ [W] entering at $x = x_w$ [m] on the performance variable $z(t)$ [K] at $x = x_z$ [m]. The considered situation is illustrated in Figure 7.1.

In Appendix E.1.1, it is shown that the input-output relations of the system (7.1)–(7.2) are defined by irrational transfer functions

$$\begin{aligned} \begin{bmatrix} Z(s) \\ Y(s) \end{bmatrix} &= \begin{bmatrix} G_{zw}(s) & G_{zu}(s) \\ G_{yw}(s) & G_{yu}(s) \end{bmatrix} \begin{bmatrix} W(s) \\ U(s) \end{bmatrix} \\ &= \begin{bmatrix} G(s, x_z - x_w) & G(s, x_z - x_u) \\ G(s, x_y - x_w) & G(s, x_y - x_u) \end{bmatrix} \begin{bmatrix} W(s) \\ U(s) \end{bmatrix}, \end{aligned} \tag{7.3}$$

where $Z(s)$, $Y(s)$, $W(s)$, and $U(s)$ denote the Laplace transforms of $z(t)$, $y(t)$, $w(t)$, and $u(t)$, respectively, and

$$G(s, x) = \frac{1}{c} \frac{e^{-xv/2D}}{\sqrt{v^2 + 4D(s+h)}} e^{-|x|\sqrt{v^2+4D(s+h)}/2D}. \tag{7.4}$$

When considering irrational transfer functions, it is important to recall the following definition of $\mathcal{H}_\infty$, see e.g. Appendix A.6.3 of [Curtain and Zwart, 1995].

Definition 7.1. *The open right half of the complex plane* $\{s \in \mathbb{C} \mid \operatorname{Re}(s) > 0\}$ *is denoted by* $\mathbb{C}^+$. *The Hardy space* $\mathcal{H}_\infty$ *consists of all holomorphic functions* $\mathbb{C}^+ \to \mathbb{C}$ *that are bounded on* $\mathbb{C}^+$, *i.e.*

$$\mathcal{H}_\infty := \left\{ G : \mathbb{C}^+ \to \mathbb{C} \;\middle|\; G \text{ is holomorphic and } \sup_{s \in \mathbb{C}^+} |G(s)| < \infty \right\}. \tag{7.5}$$

The norm on $\mathcal{H}_\infty$ is denoted by

$$\|G\|_\infty := \sup_{s\in\mathbb{C}^+} |G(s)|. \tag{7.6}$$

Transfer functions of the form (7.4) are elements of $\mathcal{H}_\infty$ and it is not hard to show that $\|G(\cdot,x)\|_\infty = G(0,x)$ for a transfer function $G(s,x)$ of the form (7.4).

Remark 7.2. *The $\mathcal{H}_\infty$-norm of $G(s,x)$ in (7.4) is bounded by*

$$\|G(\cdot,x)\|_\infty = G(0,x) \le \frac{e^{-(xv+|xv|)/2D}}{c\sqrt{v^2+4Dh}}. \tag{7.7}$$

Therefore, the advection-dominated control problem (i.e. $|(x_z-x_w)v| \gg 2D$) is only relevant when x_z lies downstream of x_w (i.e. $(x_z-x_w)v<0$). Otherwise, the bound on the $\mathcal{H}_\infty$-norm in (7.7) shows that $\|G_{zw}\|_\infty \approx 0$ which means that control is not necessary.

Under proportional control $u(t) = -Py(t)$, the closed loop transfer function from $W(s)$ to $Z(s)$ is given by

$$M(s) := G_{zw}(s) - \frac{G_{zu}(s)PG_{yw}(s)}{1+PG_{yu}(s)}. \tag{7.8}$$

The objective is to a find a sensor location x_y and/or an actuator location x_u for which there exists a (stabilizing) feedback gain P that makes $\|M\|_\infty$ as small as possible.

Note that for high-gain feedback ($|PG_{yu}(s)| \gg 1$)

$$M(s) \approx M_{\mathrm{HG}}(s) := G_{zw}(s) - \frac{G_{zu}(s)G_{yw}(s)}{G_{yu}(s)}, \tag{7.9}$$

and that for low-gain feedback ($|PG_{yu}(s)| \ll 1$)

$$M(s) \approx M_{\mathrm{LG}}(s) := G_{zw}(s) - G_{zu}(s)PG_{yw}(s). \tag{7.10}$$

The following two lemmas describe which choices of sensor and actuator locations make $M_{\mathrm{HG}}(s)$ and $M_{\mathrm{LG}}(s)$ small.

Lemma 7.3. *Consider the transfer functions in (7.3)–(7.4). The high-gain feedback approximation $M_{\mathrm{HG}}(s)$ in (7.9) is zero for all s precisely when*

$$|x_z-x_u| + |x_y-x_w| = |x_y-x_u| + |x_z-x_w|. \tag{7.11}$$

Proof. Using (7.3)–(7.4), $G_{zu}(s)G_{yw}(s)/G_{yu}(s)$ can be rewritten as

$$\frac{1}{c}\frac{e^{-(x_z-x_w)v/2D}}{\sqrt{v^2+4D(s+h)}} e^{-(|x_z-x_u|+|x_y-x_w|-|x_y-x_u|)\sqrt{v^2+4D(s+h)}/2D}. \tag{7.12}$$

To obtain $M_{\mathrm{HG}}(s) \equiv 0$ in (7.9), this expression should be equal to $G_{zw}(s)$. This is the case when the second exponential factor in (7.12) is equal to the second exponential factor of $G_{zw}(s)$. These are equal precisely when (7.11) holds. □

It is not possible to achieve $M_{\mathrm{LG}}(s) = 0$ for all s. Since the magnitude of $G(s,x)$ is maximal for $s = 0$ (see also Remark 7.2), it is most important to make $M_{\mathrm{LG}}(s)$ small near $s = 0$. Locations where this is the case are characterized by the following result. Here, $'$ denotes the derivative w.r.t. s.

Lemma 7.4. *Consider the transfer functions in* (7.3)–(7.4). *There exists a* $P > 0$ *such that* $M_{\mathrm{LG}}(s)$ *in* (7.10) *satisfies* $M_{\mathrm{LG}}(0) = M'_{\mathrm{LG}}(0) = 0$ *precisely when*

$$|x_z - x_u| + |x_y - x_w| = |x_z - x_w| - \frac{2D}{\sqrt{v^2 + 4Dh}}. \tag{7.13}$$

Proof. Since $G(0,x)$ in (7.4) is positive, it is clear that

$$P = \frac{G_{zw}(0)}{G_{zu}(0)G_{yw}(0)}, \tag{7.14}$$

is positive and that this choice for P makes $M_{\mathrm{LG}}(0)$ in (7.10) zero. To compute $M'_{\mathrm{LG}}(0)$, note that for a transfer function $G(s,x)$ of the form (7.4)

$$\frac{\partial G}{\partial s}(s,x) = -\left(\frac{2D}{\sqrt{v^2 + 4D(h+s)}} + |x|\right)\frac{G(s,x)}{\sqrt{v^2 + 4D(h+s)}}. \tag{7.15}$$

Using (7.10) and the choice of P in (7.14) it now follows that

$$\begin{aligned} M'_{\mathrm{LG}}(0) &= G'_{zw}(0) - G'_{zu}(0)PG_{yw}(0) - G_{zu}(0)PG'_{yw}(0) \\ &= G'_{zw}(0) - G_{zw}(0)\left(\frac{G'_{zu}(0)}{G_{zu}(0)} + \frac{G'_{yw}(0)}{G_{yw}(0)}\right) \\ &= \frac{G_{zw}(0)}{\sqrt{v^2 + 4Dh}}\left(\frac{2D}{\sqrt{v^2 + 4Dh}} + |x_z - x_u| + |x_y - x_w| - |x_z - x_w|\right). \end{aligned} \tag{7.16}$$

This expression is zero precisely when (7.13) holds. □

It is important to note that Lemmas 7.3 and 7.4 consider approximations of the closed-loop transfer function $M(s)$ based on the assumption $|PG_{yu}(s)| \gg 1$ or $|PG_{yu}(s)| \ll 1$, respectively. Whether these assumptions can be realized is not obvious. In particular, the high-gain feedback assumption $|PG_{yu}(s)| \gg 1$ typically leads to instability. In view of Remark 7.2, the low-gain assumption is satisfied for all $s \in \mathbb{C}^+$ when $PG_{yu}(0) \ll 1$, but it is uncertain if the P selected in Lemma 7.4 indeed satisfies this condition.

7.2.1 Collocated control

The following result demonstrates that the high-gain feedback is effective and stabilizing for a particular collocated sensor and actuator placement.

Lemma 7.5. *Consider* (7.1)–(7.2) *and let* x_z, x_w *be fixed. If* $x_y = x_u$*, the proportional feedback controller* $u(t) = -Py(t)$ *is stabilizing for all* $P > 0$*. Furthermore, if* $x_y = x_u$ *is chosen between* x_z *and* x_w *there exists a* $P > 0$ *such that* $\|M\|_\infty < \varepsilon$ *for any* $\varepsilon > 0$*.*

Proof. Consider (7.1)–(7.2) with $w(t) = 0$ and $x_y = x_u$. Then the storage function $V(t) = \frac{1}{2}\int_{-\infty}^{+\infty} T^2(x,t)\,\mathrm{d}x$ has time derivative

$$\begin{aligned}
\dot{V}(t) &= \int_{-\infty}^{+\infty} T(x,t)\frac{\partial T}{\partial t}(x,t)\,\mathrm{d}x \\
&= v\int_{-\infty}^{+\infty} T(x,t)\frac{\partial T}{\partial x}(x,t)\,\mathrm{d}x + D\int_{-\infty}^{+\infty} T(x,t)\frac{\partial^2 T}{\partial x^2}(x,t)\,\mathrm{d}x \\
&\quad - h\int_{-\infty}^{+\infty} T^2(x,t)\,\mathrm{d}x + \frac{1}{c}\int_{-\infty}^{+\infty} T(x,t)\delta(x-x_u)u(t)\,\mathrm{d}t \\
&= v\,\frac{1}{2}T^2(x,t)\Big|_{x=-\infty}^{+\infty} + DT(x,t)\frac{\partial T}{\partial x}(x,t)\Big|_{x=-\infty}^{+\infty} \\
&\quad - D\int_{-\infty}^{\infty}\left(\frac{\partial T}{\partial x}(x,t)\right)^2\,\mathrm{d}x - h\int_{-\infty}^{+\infty} T^2(x,t)\,\mathrm{d}x + \frac{1}{c}T(x_u,t)u(t) \\
&\le \frac{1}{c}T(x_u,t)u(t) = \frac{1}{c}T(x_y,t)u(t) = \frac{-P}{c}y^2(t). \qquad (7.17)
\end{aligned}$$

Here, the second identity follows from the expression for $\partial T/\partial t$ in (7.1), the third identity after finding a primitive function for the first term and using integration by parts for the second term, the inequality because $T(x,t) \to 0$ for $x \to \pm\infty$, the fourth identity because $x_y = x_u$, and the last identity because $y(t) = T(x_y,t)$ and $u(t) = -Py(t)$. The closed loop is thus stable for all $P > 0$ if $x_y = x_u$.

Now note that for $P \to \infty$, $M(s) \to M_{\mathrm{HG}}(s)$ and that Lemma 7.3 asserts that $M_{\mathrm{HG}}(s) \equiv 0$ if (7.11) holds. For $x_y = x_u$, (7.11) reduces to $|x_z - x_u| + |x_u - x_w| = |x_z - x_w|$. This equation is satisfied precisely when x_u is between x_z and x_w. □

Remark 7.6. *Similarly as in [Morris, 1998], it is shown in Appendix E.2 that if all stabilizing (dynamic) controllers are considered,* $\|M\|_\infty$ *can be made arbitrarily small for all choices of* x_y *and* x_u*.*

Lemma 7.7. *When* $x_y \neq x_u$*, the feedback* $u(t) = -Py(t)$ *will always be destabilizing for* P *sufficiently large.*

Proof. In view of the Nyquist stability conditions [Skogestad and Postlethwaite, 2007], it suffices to show that $PG_{yu}(i\omega)$ will encircle the point '-1' for P sufficiently large when $x_y \neq x_u$. Because $\sqrt{v^2 + 4D(i\omega + h)}/2D \to \sqrt{4Di\omega}/2D = \sqrt{\omega/2D}(1+i)$ for $\omega \to \infty$, the argument of the second exponential factor in (7.4) approaches $-|x_y - x_u|\sqrt{\omega/2D} \mod 2\pi$ for $\omega \to \infty$. As the argument of

$1/\sqrt{v^2+4D(i\omega+h)}$ is in the interval $[-\pi/4, \pi/4]$, there are (in fact infinitely many) values of ω_- for which $\angle G_{yu}(i\omega_-) = \pi$. Picking one of these values ω_- and choosing P larger than $-1/G_{yu}(i\omega_-)$ will lead to at least one encirclement of the point '-1'. □

Remark 7.8. *Note that the result in Lemma 7.5 applies to any x_w and x_z chosen on opposite sides of $x_y = x_u$. A consequence of Lemma 7.5 is therefore that when the area in which the disturbance(s) are applied lies on the opposite side of $x_y = x_u$ as the area in which the performance variable(s) are measured, the influence of the disturbances on the performance variables can be made arbitrarily small by a stabilizing proportional feedback controller.*

7.2.2 Noncollocated control

Lemma 7.5 addresses a particularly effective sensor and actuator placement, which might not always be possible to achieve. Therefore, it is now assumed that the location of the actuator x_u is already fixed, i.e. for given x_z, x_w, and x_u, the goal is to find the optimal x_y for high-gain and low-gain proportional feedback control.

The optimal choice of x_y for *high-gain proportional feedback* depends on the ordering of x_z, x_w, and x_u. The six possible orderings of x_z, x_w, and x_u can be considered in three pairs:

- If x_u is between x_z and x_w (i.e. $x_z < x_u < x_w$ or $x_w < x_u < x_z$), Lemma 7.5 shows that the optimal choice for x_y is $x_y = x_u$.
- If x_z is between x_u and x_w (i.e. $x_u < x_z < x_w$ or $x_w < x_z < x_u$), it can be verified that (7.11) only holds when $x_y = x_z$.
- If x_w is between x_z and x_u (i.e. $x_z < x_w < x_u$ or $x_u < x_w < x_z$), it can be shown that (7.11) holds for all x_y that are on the same side of x_w as x_z. Because a greater distance $|x_y - x_u|$ limits the range of stabilizing gains P, the optimal choice for x_y is $x_y = x_w$ in this case.

The optimal sensor location x_y for high-gain feedback is thus the location x_z, x_w, or x_u that is between the other two.

The optimal choice of x_y for *low-gain proportional feedback* follows from (7.13), which typically gives two possible choices of x_y at equal distance of x_w. Note, however, that if $|x_z - x_w| < |x_z - x_u|$, (7.13) cannot be satisfied for any x_y. Furthermore, these potential optimal locations x_y are only good choices if the low-gain feedback assumption $|PG_{yu}(s)| \ll 1$ is satisfied. To check this, note that for the value of P in (7.14), $\|PG_{yu}\|_\infty$ is equal to

$$e^{(|x_z-x_u|+|x_y-x_w|-|x_z-x_w|-|x_y-x_u|)\sqrt{v^2+4Dh}/2D}. \tag{7.18}$$

For each of the two potential low-gain feedback locations, it should be checked whether this number is small.

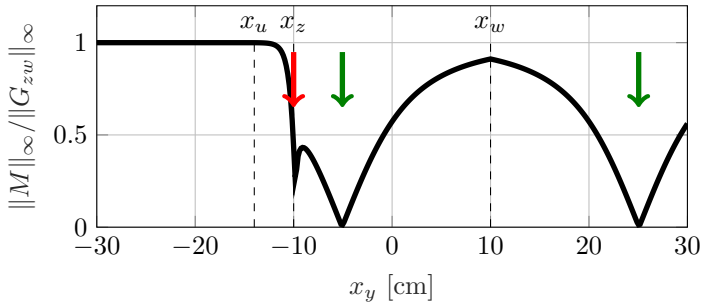

(a) $x_u = -14$ cm, $x_z = -10$ cm, $x_w = 10$ cm

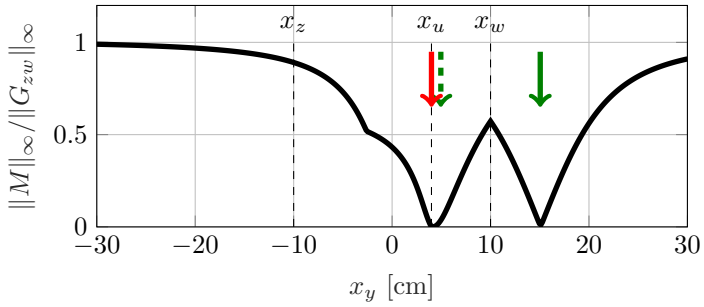

(b) $x_z = -10$ cm, $x_u = 4$ cm, $x_w = 10$ cm

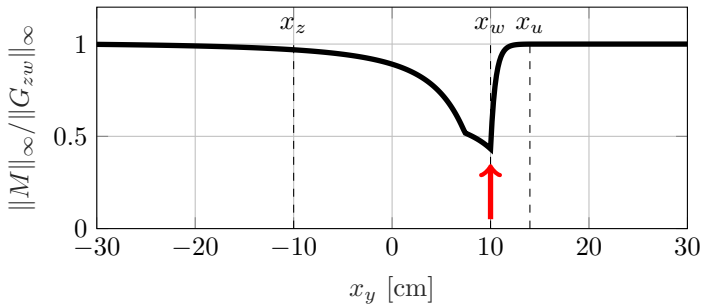

(c) $x_z = -10$ cm, $x_w = 10$ cm, $x_u = 14$ cm

Figure 7.2. The improvement in closed-loop performance $\|M\|_\infty$ relative to the open-loop performance $\|G_{zw}\|_\infty$ for varying sensor location x_y in the diffusion-dominated problem. The red arrows indicate locations where (7.11) is satisfied and the green arrows indicate locations where (7.13) is satisfied.

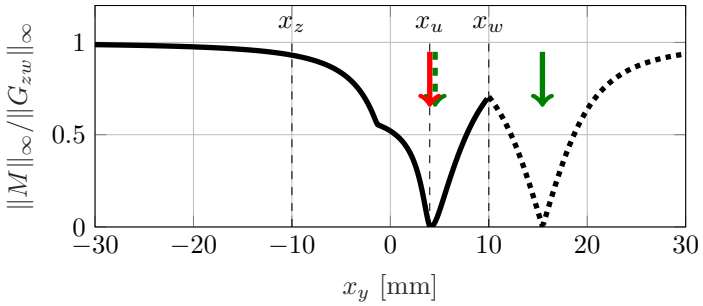

(a) $x_z = -10$ mm, $x_u = 4$ mm, $x_w = 10$ mm

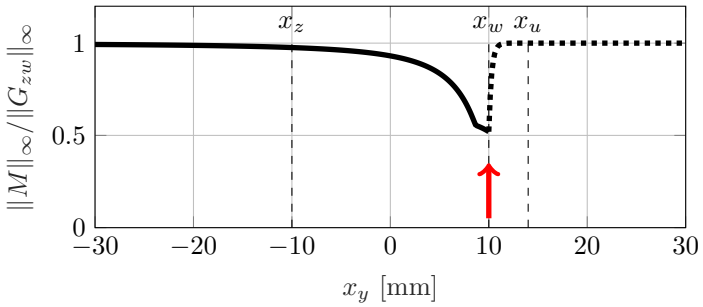

(b) $x_z = -10$ mm, $x_w = 10$ mm, $x_u = 14$ mm

Figure 7.3. The improvement in closed-loop performance $\|M\|_\infty$ relative to the open-loop performance $\|G_{zw}\|_\infty$ for varying sensor location x_y in the advection-dominated problem The red arrows indicate locations where (7.11) is satisfied and the green arrows indicate locations where (7.13) is satisfied.

7.2.3 Numerical results

The method to determine the optimal sensor locations is illustrated by designing the optimal proportional feedback controller for a range of sensor locations x_y while keeping the locations x_z, x_w, x_u fixed. The controller was designed as follows. First, the transfer function $G_{yw}(s)$ is evaluated on a grid of 4,000 frequency points $s = i\omega_k$ logarithmically distributed between $2\pi{\cdot}10^{-2}$ and $2\pi{\cdot}10^{6}$ [rad/s]. Similarly as in a loop-shaping controller design approach [Skogestad and Postlethwaite, 2007], the maximal allowable gain $P_{\max}$ for which the modulus margin is 0.5 is found by solving $\min_k |1 + PG_{yu}(i\omega_k)| = 0.5$ with `fzero` in MATLAB (version R2017b). The gain $P \in [0, P_{\max}]$ that minimizes the closed-loop performance $\|M\|_\infty$ is then determined by minimizing $\max_k |M(i\omega_k)|$ over P using `fminbnd`.

Figure 7.2 shows the closed-loop performance $\|M\|_\infty$ that can be obtained for

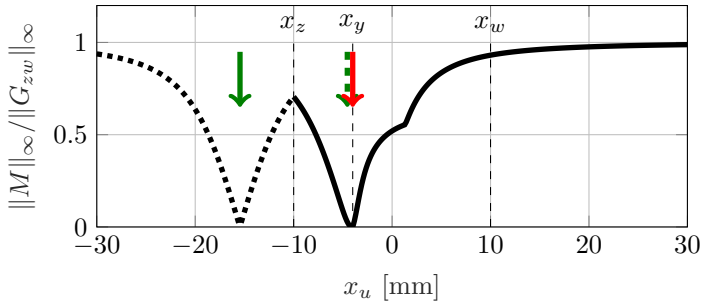

(a) $x_z = -10$ mm, $x_y = -4$ mm, $x_w = 10$ mm

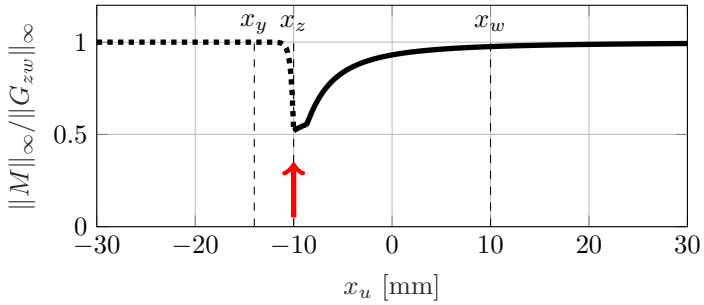

(b) $x_y = -14$ mm, $x_z = -10$ mm, $x_w = 10$ mm

Figure 7.4. The improvement in closed-loop performance $\|M\|_\infty$ relative to the open-loop performance $\|G_{zw}\|_\infty$ for varying actuator location x_u in the advection-dominated problem The red arrows indicate locations where (7.11) is satisfied and the green arrows indicate locations where (7.13) is satisfied.

the controller designed at each of the sensor locations for a diffusion-dominated problem with $v = 0$. Note that $\|M\|_\infty$ is normalized w.r.t. open-loop performance $\|G_{zw}\|_\infty$. The used parameter values are $c = 33$ [J/K/m], $v = 0$ [m/s], $D = 91 \cdot 10^{-6}$ [m^2/s], and $h = 1$ [1/s]. These are based on the wafer heating case study considered in Chapters 2–5. The locations x_z, x_w, and x_u are chosen rather arbitrarily. The red arrows indicate the predicted optimal locations for high-gain feedback, the green arrows indicate the predicted locations for low-gain feedback. A dashed green arrow indicates that (7.18) is larger than 0.1, i.e. that the low-gain feedback assumption is not satisfied. The three subfigures represent the three possible orderings of x_z, x_w, and x_u. The locations of the observed local minima are all very close to the predicted optimal locations. Note that Figure 7.2c represents the situation where $|x_z - x_w| < |x_z - x_u|$ for which (7.13) does not provide potential optimal locations for low-gain feedback.

Figure 7.3 represents the advection-dominated case (see Remark 7.2) where v is set to 0.33 [m/s] and the other parameters are the same as in Figure 7.2. Again a very good match is obtained between the observed local minima and the potential optimal sensor locations. It is important to note that the characteristic length $2D/v = 0.55$ mm is very small in this situation. Remark 7.2 thus shows that only situations where $x_z \leq x_w$ are of practical interest because $\|G_{zw}\|_\infty$ is negligible otherwise. Similar reasoning shows that $\|G_{zu}\|_\infty$ is negligible when $x_u < x_z < x_w$, which means that $z(t)$ is hardly affected by the control input. This situation is therefore not of practical interest either. The two remaining orderings of x_z, x_w, and x_u are considered in the Figure 7.3. Locations where $x_y > x_w$ are indicated by black dotted lines, because $\|G_{yw}\|_\infty$ is negligible there.

Figure 7.4 demonstrates that similar techniques can be used to determine the optimal actuator location x_u for a fixed sensor location x_y. The parameter values in Figure 7.4 are the same as in Figure 7.3. The figure clearly indicates that the roles of x_y and x_z are interchanged with the roles of x_u and x_w.

7.3 Two-dimensional spatial domain

Now consider the following parabolic PDE with constant coefficients on the 2-D infinite spatial domain $\mathbf{x} = (x_1, x_2) \in \mathbb{R}^2$

$$\frac{\partial T}{\partial t} = v\frac{\partial T}{\partial x_1} + D\frac{\partial^2 T}{\partial x_1^2} + D\frac{\partial^2 T}{\partial x_2^2} - hT + \frac{1}{c_2}\delta(\mathbf{x} - \mathbf{x}_u)u(t) + \frac{1}{c_2}\delta(\mathbf{x} - \mathbf{x}_w)w(t), \quad (7.19)$$

$$y(t) = T(\mathbf{x}_y, t), \qquad z(t) = T(\mathbf{x}_z, t), \quad (7.20)$$

with initial condition $T(x_1, x_2, 0) = 0$. Here, $\delta(x)$ denotes the Dirac delta. Similarly as before, this PDE can be used to model the temperature field $T = T(x_1, x_2, t)$ [K] in a medium with heat capacity c_2 [J/K/m^2], thermal diffusivity D [m^2/s], cooling rate h [1/s], and advective transport with velocity $v \geq 0$ [m/s]. Without loss of generality, it can be assumed that the velocity is in the x_1-direction. The input and output locations $\mathbf{x}_u = (x_{1,u}, x_{2,u})$, $\mathbf{x}_w = (x_{1,w}, x_{2,w})$, $\mathbf{x}_y = (x_{1,y}, x_{2,y})$, and $\mathbf{x}_z = (x_{1,z}, x_{2,z})$ now consist of two components. The considered situation is shown in Figure 7.5.

It is shown in Appendix E.1.2 that the input-output relations of the system (7.19)–(7.20) are defined by irrational transfer functions

$$\begin{bmatrix} Z(s) \\ Y(s) \end{bmatrix} = \begin{bmatrix} G_{zw}(s) & G_{zu}(s) \\ G_{yw}(s) & G_{yu}(s) \end{bmatrix} \begin{bmatrix} W(s) \\ U(s) \end{bmatrix} = \begin{bmatrix} G(s, \mathbf{x}_z - \mathbf{x}_w) & G(s, \mathbf{x}_z - \mathbf{x}_u) \\ G(s, \mathbf{x}_y - \mathbf{x}_w) & G(s, \mathbf{x}_y - \mathbf{x}_u) \end{bmatrix} \begin{bmatrix} W(s) \\ U(s) \end{bmatrix}, \quad (7.21)$$

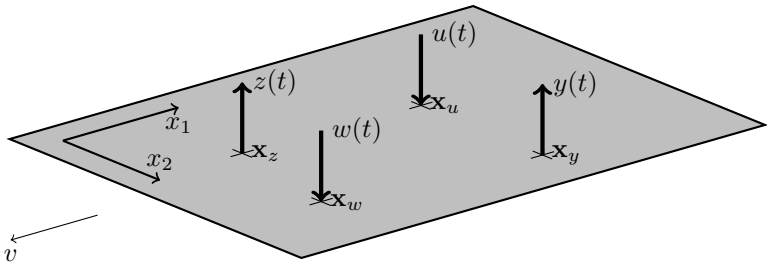

Figure 7.5. The 2-D spatial domain with the locations $\mathbf{x}_y$, $\mathbf{x}_u$, $\mathbf{x}_w$, and $\mathbf{x}_z$ of the sensor, actuator, disturbance, and performance variable, respectively

with

$$G(s,\mathbf{x}) = \frac{e^{-x_1 v/2D}}{2\pi c_2 D} K_0\left(\sqrt{v^2+4D(h+s)}\|\mathbf{x}\|/(2D)\right), \tag{7.22}$$

where $K_0(\zeta)$ denotes the modified Bessel function of the second kind of order zero and $\|\mathbf{x}\| := \sqrt{x_1^2+x_2^2}$ is the Euclidean norm.

Similarly as on the 1-D spatial domain, conditions for which the high-gain feedback approximation $M_{\mathrm{HG}}(s)$ is zero for all s can be determined.

Lemma 7.9. *Consider the transfer functions in* (7.21)–(7.22)*. The high-gain feedback approximation* $M_{\mathrm{HG}}(s)$ *in* (7.9) *is zero when either*

$$\|\mathbf{x}_y-\mathbf{x}_u\| = \|\mathbf{x}_y-\mathbf{x}_w\| \ \wedge\ \|\mathbf{x}_z-\mathbf{x}_u\| = \|\mathbf{x}_z-\mathbf{x}_w\|, \tag{7.23}$$

or

$$\|\mathbf{x}_y-\mathbf{x}_u\| = \|\mathbf{x}_z-\mathbf{x}_u\| \ \wedge\ \|\mathbf{x}_y-\mathbf{x}_w\| = \|\mathbf{x}_z-\mathbf{x}_w\|. \tag{7.24}$$

Proof. Note that if (7.23) holds, it follows that $G_{yu}(s) = G_{yw}(s)$ and that $G_{zu}(s) = G_{zw}(s)$, so that (7.9) shows that $M_{\mathrm{HG}}(s) = 0$. Similarly, (7.24) implies that $G_{yu}(s) = G_{zu}(s)$ and that $G_{yw}(s) = G_{zw}(s)$, so that $M_{\mathrm{HG}}(s) = 0$. □

To study the low-gain feedback approximation, the following asymptotic expansion of $K_0(\zeta)$ for $|\zeta| \to \infty$ will be used

$$K_0(\zeta) \approx \sqrt{\frac{\pi}{2\zeta}} e^{-\zeta}. \tag{7.25}$$

In particular, it can be shown that, see e.g. Chapter V in [Gray and Mathews, 1952],

$$\left| K_0(\zeta) - \sqrt{\frac{\pi}{2\zeta}} e^{-\zeta} \right| \le \frac{1}{8|\zeta|} \left| \sqrt{\frac{\pi}{2\zeta}} e^{-\zeta} \right|, \tag{7.26}$$

for $\zeta \in \mathbb{C}$ with $\mathrm{Re}(\zeta) \geq 0$. The relative error in the approximation will therefore be small for $|\zeta|$ large enough. Using (7.25), $G(s, \mathbf{x})$ in (7.22) is approximated by

$$\tilde{G}(s, \mathbf{x}) = \frac{e^{-x_1 v/2D} e^{-\sqrt{v^2+4D(h+s)}\|\mathbf{x}\|/2D}}{c_2 \sqrt{2\pi D \|\mathbf{x}\|} \sqrt[4]{v^2 + 4D(h+s)}}. \tag{7.27}$$

Now (7.21) can be approximated by

$$\begin{aligned} \begin{bmatrix} \tilde{Z}(s) \\ \tilde{Y}(s) \end{bmatrix} &= \begin{bmatrix} \tilde{G}_{zw}(s) & \tilde{G}_{zu}(s) \\ \tilde{G}_{yw}(s) & \tilde{G}_{yu}(s) \end{bmatrix} \begin{bmatrix} W(s) \\ U(s) \end{bmatrix} \\ &= \begin{bmatrix} \tilde{G}(s, \mathbf{x}_z - \mathbf{x}_w) & \tilde{G}(s, \mathbf{x}_z - \mathbf{x}_u) \\ \tilde{G}(s, \mathbf{x}_y - \mathbf{x}_w) & \tilde{G}(s, \mathbf{x}_y - \mathbf{x}_u) \end{bmatrix} \begin{bmatrix} W(s) \\ U(s) \end{bmatrix}, \end{aligned} \tag{7.28}$$

where $\tilde{Z}(s)$ and $\tilde{Y}(s)$ are good approximations of $Z(s)$ and $Y(s)$ when the error in the approximation (7.25) is small, i.e. when the factor $1/(8|\zeta|)$ in (7.26) is small. This is the case for all $s \in \mathbb{C}^+$ when $4\sqrt{v^2 + 4Dh}\|\mathbf{x}\|/D \gg 1$.

The transfer functions in (7.27)–(7.28) can be used to find conditions under which $M_{\mathrm{LG}}(s)$ is small.

Lemma 7.10. *Consider the transfer functions in* (7.27)–(7.28)*. There exists a* $P > 0$ *such that* $M_{\mathrm{LG}}(s)$ *in* (7.10) *satisfies* $M_{\mathrm{LG}}(0) = M'_{\mathrm{LG}}(0) = 0$ *precisely when*

$$\|\mathbf{x}_z - \mathbf{x}_u\| + \|\mathbf{x}_y - \mathbf{x}_w\| = \|\mathbf{x}_z - \mathbf{x}_w\| - \frac{D}{\sqrt{v^2 + 4Dh}}. \tag{7.29}$$

Proof. Apart from the observation that now

$$\tilde{G}'(s, \mathbf{x}) = -\left(\frac{D}{\sqrt{v^2 + 4D(h+s)}} + \|\mathbf{x}\| \right) \frac{\tilde{G}(s, \mathbf{x})}{\sqrt{v^2 + 4D(h+s)}}, \tag{7.30}$$

the proof is analogous to the proof of Lemma 7.4. □

7.3.1 Numerical results

The effectiveness of the proposed approach is illustrated by the numerical results in Figure 7.6. These figures show the minimal value of $\|M\|_\infty$, that can be obtained for a proportional feedback controller with a modulus margin of at least 0.5, as a function of the sensor location $\mathbf{x}_y = (x_{1,y}, x_{2,y})$, where $\mathbf{x}_z$, $\mathbf{x}_w$, and $\mathbf{x}_y$ are chosen rather arbitrarily. The color scale indicates the logarithm of the reduction in closed-loop performance $\|M\|_\infty$ relative to the open-loop performance $\|G_{zw}\|_\infty$. The parameter values are $c_2 = 1150$ [J/K/m^2], $v = 0.33$ [m/s], $D = 91 \cdot 10^{-6}$ [m^2/s], and $h = 1$ [1/s].

Figure 7.6a shows that the sensor locations where $\|M\|_\infty$ is minimal are accurately predicted by the red dashed circle around $\mathbf{x}_w$ described by (7.29). Note

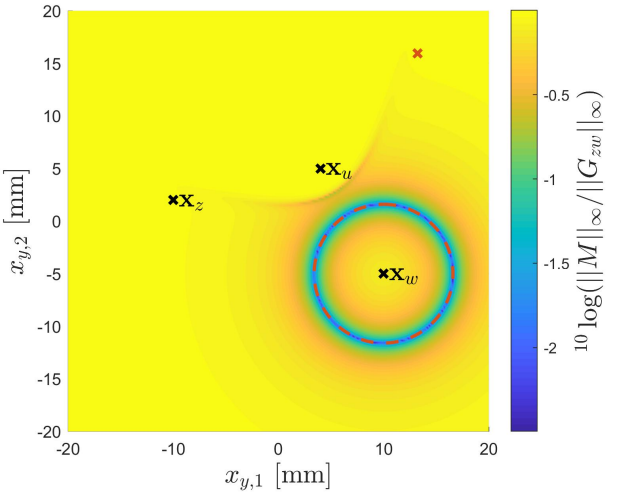

(a) $\mathbf{x}_z = (-10, 2)$ mm, $\mathbf{x}_u = (5, 5)$ mm, $\mathbf{x}_w = (10, -5)$ mm

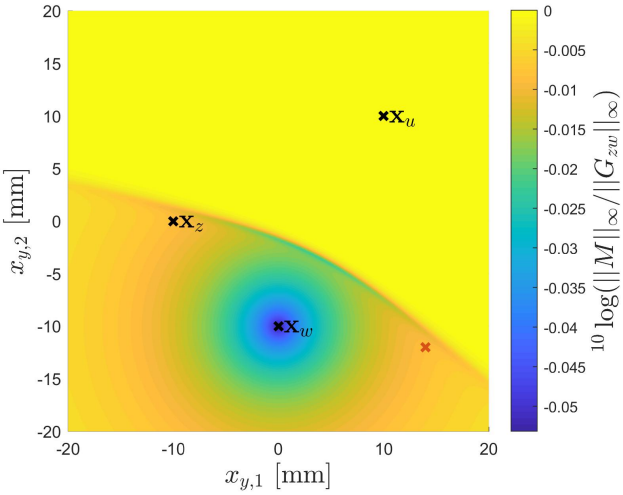

(b) $\mathbf{x}_z = (-10, 0)$ mm, $\mathbf{x}_u = (10, 10)$ mm, $\mathbf{x}_w = (-10, 0)$ mm

Figure 7.6. The improvement in closed-loop performance $\|M\|_\infty$ relative to the open-loop performance $\|G_{zw}\|_\infty$ for varying sensor location $\mathbf{x}_y = (x_{y,1}, x_{y,2})$ for two choices of $\mathbf{x}_z$, $\mathbf{x}_u$, and $\mathbf{x}_w$. Condition (7.24) is satisfied at $\mathbf{x}_y = \mathbf{x}_z$ and at the red cross and condition (7.29) at the dashed red line. Note that the color scale is logarithmic.

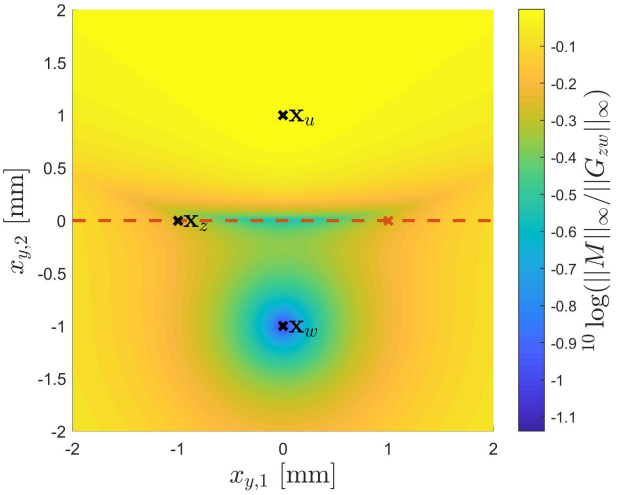

Figure 7.7. The improvement in closed-loop performance $\|M\|_\infty$ relative to the open-loop performance $\|G_{zw}\|_\infty$ for varying sensor location $\mathbf{x}_y = (x_{y,1}, x_{y,2})$ for $\mathbf{x}_z = (-1, 0)$ mm, $\mathbf{x}_u = (0, 1)$ mm, $\mathbf{x}_w = (0, -1)$ mm. Condition (7.24) is satisfied at $\mathbf{x}_y = \mathbf{x}_z$ and at the red cross and condition (7.23) at the dashed red line. Note that the color scale is logarithmic.

that $\|G_{yw}\|_\infty$ is negligible when $x_{1,y} > x_{1,w}$ because the problem is advection-dominated. Because $\|\mathbf{x}_z - \mathbf{x}_u\| \neq \|\mathbf{x}_z - \mathbf{x}_w\|$, (7.23) does not apply. Condition (7.24) applies when $\mathbf{x}_y = \mathbf{x}_z$ and in the location indicated by the red cross. No significant decrease in $\|M\|_\infty$ is visible at these locations, because the high-gain feedback assumption $|PG_{yu}(s)| \gg 1$ cannot be achieved.

Figure 7.6b shows a situation where $\|\mathbf{x}_z - \mathbf{x}_w\| < \|\mathbf{x}_z - \mathbf{x}_u\|$. In this case, there are no solutions that satisfy (7.29). The optimal sensor location is now $\mathbf{x}_y = \mathbf{x}_w$. This is the location for which the 'mismatch' in (7.29) is as small as possible. Note that the reduction in $\|M\|_\infty$ is significantly smaller than in Figure 7.6a. Just as in Figure 7.6a, condition (7.23) cannot be satisfied and no significant decrease in $\|M\|_\infty$ is observed at the locations where (7.24) is satisfied, again because the high-gain feedback assumption cannot be achieved.

Figure 7.7 shows again a situation where $\|\mathbf{x}_z - \mathbf{x}_w\| < \|\mathbf{x}_z - \mathbf{x}_u\|$ for which (7.29) cannot be satisfied. The global minimum is again at $\mathbf{x}_y = \mathbf{x}_w$. Furthermore, $\|\mathbf{x}_z - \mathbf{x}_w\| = \|\mathbf{x}_z - \mathbf{x}_u\|$ so that (7.23) is satisfied on the line $x_{y,2} = 0$. Indeed, $\|M\|_\infty$ decreases on this line, especially at locations $\mathbf{x}_y$ near $\mathbf{x}_u$ at which the high-gain feedback assumption $|PG_{yu}(s)| \gg 1$ can be approximated better.

7.4 Conclusions and discussions

A proportional-feedback control-system-design problem for advection-diffusion equations on 1-D and 2-D spatial domains with constant coefficients has been studied. Simple geometric rules have been derived describing the sensor and actuator locations for which high-gain and low-gain proportional feedback control can best reduce the influence of a disturbance applied at a given point. The derivation is based on high-gain and low-gain approximations of the analytic expression for the closed-loop transfer function. Numerical experiments indicate that the rules predict all locally optimal locations.

On the 1-D spatial domain, there are either one, two, or three locally optimal sensor or actuator locations depending on the ordering of the other input and output locations. The three possible orderings of the other input and output locations are shown in Figure 7.2. The optimal locations are accurately predicted by the conditions based on the high-gain and low-gain feedback approximations in Lemma 7.3 and 7.4. On the 2-D spatial domain, the locally optimal sensor locations are mainly characterized by the conditions based on the low-gain feedback approximation in Lemma 7.10. As the transfer function for collocated input-output locations is not well-defined for the 2-D spatial domain, the conditions based on the high-gain feedback approximation in Lemma 7.9 are less important.

For the wafer heating problem considered in Chapters 2–5, it would be interesting to extend the results to thermomechanical systems in which the performance variable $z(t)$ does not represent the temperature, but the displacement. Some first results in this direction are presented in Appendix E.3. Furthermore, extensions to spatially distributed inputs, noisy measurements, and dynamic feedback controllers are interesting topics for future research.

Part V

Closing

Chapter 8

Conclusions and recommendations

8.1 Conclusions

Thermomechanical effects are a determining factor for the performance of many high-precision systems, such as machine tools [Ramesh et al., 2000], electron microscopes [Evers et al., 2019a], and the wafer scanners considered in this thesis. With the heat loads acting on these machines increasing and the required positioning accuracy approaching the subnanometer range, modeling and control of thermomechanical effects is essential for the development of the current and next generation wafer scanners.

As discussed in Section 1.3, the modeling and control of the next-generation wafer scanners comes with several challenges, such as fast moving heat sources acting on slow thermal systems, nonlinear material behavior, unmeasurable performance variables, and limited actuation and sensing possibilities in both the thermal and the mechanical domain. The objective of this thesis has therefore been to develop effective and efficient methods for the modeling and control of thermomechanical systems.

The methods developed in this thesis are organized in three groups, which are represented by the three main contributions listed in Section 1.4 and by Parts II, III, and IV. The first contribution of this thesis has been presented in Part II which contains methods for the efficient simulation of wafer heating. This is a challenging problem due to the fast moving source that follows a complicated path. Part III contains the second contribution of this thesis which consists of methods for the computation of the optimal actuation heat load created using a limited number of spatial shapes. The obtained spatial shapes aid the design of

an actuator layout for feedforward control. The third contribution is presented in Part IV and constitutes simple guidelines for the placement of point sensors (and actuators) for feedback control of thermal systems. These guidelines also provide insight in the sensor (and actuator) placement in thermomechanical systems.

All the methods in this thesis have in common that they respect the spatially distributed nature of the considered problems since all methods use Partial Differential Equations (PDEs) as models. If necessary at all, spatial discretization is only applied at the final stage at which solutions need to be approximated numerically. This means that the developed methods keep a close connection to the underlying physics and are largely independent of the chosen discretization.

The contributions of this thesis are now elaborated further.

8.1.1 Simulation of moving heat source problems

Part II contains methods for the efficient and accurate simulation of thermal and thermomechanical systems with moving heat sources.

Chapter 3 contains a generalization of the method of images. The classical method of images dates back to the nineteenth century and relates temperature fields on the unbounded spatial domain $\mathbb{R}^2$ to temperature fields on box-shaped subdomains $\Omega \subset \mathbb{R}^2$. The results in Chapter 3 generalize the method of images to circular subdomains Ω and heat-induced deformations using a kernel representation. Because, on $\mathbb{R}^2$, the temperature and displacement fields resulting from multiple passings of the heat load can be easily obtained from the temperature and displacement fields resulting from a single passing, the theory developed in Chapter 3 enables the efficient simulation of the thermomechanical response resulting from many passings of a heat load on circular spatial domains Ω. When the number of passings of the heat load is large, as in the wafer heating application, this approach leads to a significant reduction in computational cost.

In Chapter 4, a semi-analytic approximation method for the temperature field resulting from a moving heat source is presented. The simulation of fast moving heat source problems requires a fine spatial and temporal grid which often comes with significant computational cost. The method developed in Chapter 4 reduces this computational cost by approximating the solution of a heat conduction problem on $\mathbb{R}^2$ in terms of the solutions of three heat conduction problems on $\mathbb{R}$. As the number of Degrees of Freedom (DOFs) in a simulation on a one-dimensional (1-D) spatial domain is typically much smaller than the number of DOFs in a simulation on a two-dimensional (2-D) spatial domain, this method leads to a significant reduction in computational cost. For the considered wafer heating application, the approximation with a 4%-error is computed 10 times faster than a standard FE solution with similar accuracy.

Although the methods in Part II were mainly developed with the wafer heating application in mind, they might also be applicable to moving heat source problems in a variety of other applications. In particular, the repetitive nature of the heat load that is exploited in Chapter 3 also occurs in laser hardening [Ko-

manduri and Hou, 2001] and additive manufacturing [Schwalbach et al., 2019], although the physical parameters can generally not be considered constant in these applications. Regarding Chapter 4, it is worth mentioning that analytic and semi-analytic modeling of the temperature response resulting from moving heat sources has been considered in various applications such as welding [Rosenthal, 1946; Nguyen et al., 1999; Nguyen, 2004; Fachinotti et al., 2011; Flint et al., 2018], metal cutting [Bunting and Cornfield, 1975; Nemchinsky, 2016], and laser hardening [Komanduri and Hou, 2001], although it is again questionable whether the physical parameters can be considered constant in these applications. The method proposed in Chapter 4 could be used to simplify the (semi-)analytic expressions for the temperature field in these publications, but it remains to be seen whether the error in the approximation is acceptable.

8.1.2 Feedforward control

Part III contains methods to compute the optimal actuation heat load created by a limited number of spatial shapes for the rejection of known thermal disturbances.

Chapter 5 considers the computation of the smallest single-shape actuation heat load that achieves certain constraints on the heat-induced wafer deformation. The proposed method consists of two stages. The first stage is the search for an admissible solution that satisfies the wafer deformation constraints and the second stage reduces the applied actuation heat load while still preserving the wafer deformation constraints. Both stages are formulated as optimization problems which are solved by a gradient-based optimization algorithm that updates the spatial shape and the corresponding time-dependent intensity of the actuation heat load alternately. The obtained spatial shape has a clear physical interpretation and gives a good idea about an effective thermal actuator layout for the control of heat-induced wafer deformation.

In Chapter 6, the thermal control of a mirror in the projection system of a wafer scanner is considered. Because the wafer scanner can be used with a large number of illumination settings, the projection light can create a large number of different heat loads on some of the mirrors. This makes designing an effective thermal actuator layout for these mirrors challenging. To aid such a design, Chapter 6 provides a method to compute a set of thermal actuation heat loads that can be created using a low number of spatial shapes. For each of the potential heat loads induced by the projection light, the corresponding designed actuation heat load achieves certain steady-state temperature constraints. The set of actuation heat loads is computed by a similar algorithm as in Chapter 5. Chapter 6 demonstrates that designing an actuation heat load consisting of multiple spatial shapes is more complex than the design of a single-shape actuation heat load and that the obtained spatial shapes are harder to interpret.

The results in Chapters 5 and 6 are closely related to PDE-constrained optimization [Stadler, 2009; Hinze et al., 2009; Herzog et al., 2012; Kunisch et al.,

2014; Boulanger and Trautmann, 2017], but extend the existing methods in two ways. First of all, none of these existing methods considers the optimization of the spatial shape of the actuation heat load; typically the area in which actuation can be applied is optimized. Secondly, existing methods only consider input constraints, i.e. constraints on the applied heat load, but not the state constraints, i.e. constraints on the temperature or heat-induced deformations, as we considered in Part III. The presented extensions might therefore be useful for a variety of applications other than the considered problems.

8.1.3 Feedback control

The effective sensor (and actuator) placement for feedback control of thermal systems is addressed in Part IV, which consists only of Chapter 7.

Chapter 7 considers sensor and actuator placement in advection-diffusion equations. The problem is studied in a generalized plant setting, see e.g. [Skogestad and Postlethwaite, 2007]. The disturbance and control inputs are point heat loads and the measured and performance outputs are temperatures at a point. The location of the sensor (or actuator) that minimizes the $\mathcal{H}_\infty$-norm of the transfer function from the disturbance to the performance variable is determined for given locations of the disturbance, the actuator (or sensor), and the performance variable. Using analytical expressions of the irrational transfer functions and high-gain and low-gain approximations of the closed-loop transfer function, simple guidelines for the optimal placement of thermal actuators and sensors in advection-diffusion equations are found. Numerical results demonstrate that these guidelines accurately predict the optimal locations.

The results in Chapter 7 are related to the combined sensor and/or actuator location and controller optimization for infinite-dimensional systems, which have been considered in several publications. In only very few of these the order of the controller is limited, see e.g. [Demetriou, 2005; Demetriou, 2017]. For the problem considered in Chapter 7, limiting the order of the controller is essential because all sensor and actuator placements lead to the same cost if the order of the controller is not limited. This demonstrates that it can be essential to limit the order of the controller in sensor and/or actuator placement problems.

Summarizing, this thesis contains several novel results related to the modeling and control of thermomechanical systems. Motivated by the many challenges appearing in the thermomechanical control of next-generation wafer scanners, methods for the efficient simulation of moving heat loads, the computation of a feedforward heat load consisting of a limited number of optimal spatial shapes, and the optimal placement of point sensors and actuators in thermal feedback control systems have been developed. Although the results in this thesis have been applied only to problems related to Extreme Ultraviolet (EUV) lithography, they are potentially relevant for many other applications.

8.2 Recommendations

There remain still many challenges in the modeling, analysis, and control of thermomechanical systems. Some recommendations for future research related to the work discussed in this thesis are as follows.

Integration of Model Order Reduction (MOR) techniques

As the thermomechanical systems considered in this thesis are governed by PDEs, spatial discretization typically leads to large systems of Ordinary Differential Equations (ODEs) that can be time consuming to solve. The computational cost of these operations can be reduced using MOR techniques. Due to the large scale of the considered systems, it can be difficult to compute the eigenvalues or singular values required for a modal analysis or methods like balanced truncation. Therefore, Krylov subspace methods, see e.g. [Antoulas, 2005], which only require the solution of (large-scale) linear systems seem most suitable.

This recommendation applies in particular to Chapters 3, 5, and 6. After a suitable coordinate transformation, the simulation for a single field on the wafer required in Chapter 3 can be viewed as the response of a single-input Linear Time-Invariant (LTI) system. The results for a representative 1-D problem in [van der Heijden, 2018] show that Krylov subspace methods are very effective for this problem. MOR techniques also seem particularly suitable for an actuation heat load that has a fixed shape as in Chapter 5 and are even necessary to extend the results in Chapter 6 to transient responses.

Opto-thermo-mechanical modelling and control

The performance of a lithography system is in the end determined by the quality of the pattern projected on the wafer, which is a result of thermomechanics and optics. Considering the whole optical chain instead of individual components is important as a large part of the errors introduced at one component can often be compensated most effectively by another component. There has been some research in this direction, see e.g. [Saathof, 2013; Merks, 2015; Habets et al., 2016]. In this thesis, Appendix C.4.1 and the example at the end of Section 3.5 also point in this direction. With the ever increasing performance requirements, modeling and control of the opto-thermo-mechanics in the whole optical chain will become more and more important.

Feedforward control for repetitive disturbances

In Chapter 5, an optimal actuation heat load consisting of a single spatial shape has been computed for the scanning of a single field on the wafer. However, such an actuation heat load should eventually be computed for a whole expose pattern consisting of about 100 fields. Some first steps in this direction have been taken in Appendix C.4.2 where the scanning of 4 fields has been considered. To

extend this to about 100 fields, the combination of the method from Chapter 5 with the field-by-field approach from Chapter 3 seems a promising direction to explore.

Nonlinear thermal expansion characteristics

In Chapter 6, thermal control of an EUV mirror was considered. EUV mirrors are made of Ultra Low Expansion glass (ULE), which has a nonlinear thermal expansion characteristic. As this nonlinear material behavior results in a strongly nonconvex optimization problem with many local minima, it is not trivial to extend the temperature-based method from Chapter 6 to deformation-based control. However, if such an extension could be obtained, it would provide insights that could be very valuable for the design of a thermal actuation layout for such a mirror.

Sensor and actuator placement for feedback control

In this thesis, actuator and sensor placement for feedback control has only been considered for a single actuator and a single sensor in Chapter 7. Methods for the placement of multiple actuators and/or sensors are of course required in many situations and there are several publications on this topic, see e.g. [van de Wal and de Jager, 2001]. Most of these methods search through a grid of potential actuator and/or sensor locations and do not seem to exploit the structure of the underlying PDE fully. Methods that do not use a grid of potential locations, such as the one presented in [Kasinathan and Morris, 2013], are relatively scarce but seem more natural (and therefore potentially more effective) for problems governed by PDEs.

Furthermore, the results from Chapter 7 illustrate that limiting the order of the controller influences the optimal locations (see also Subsection 8.1.3). The placement of sensors and/or actuators in combination with a constrained-order feedback controller is a very challenging problem, see e.g. [Merks, 2019], which deserves further investigation.

The combination of feedforward and feedback control

Feedforward control is often very effective when an accurate plant model is available but is not robust against unmodeled disturbances and plant dynamics. Feedback control can create robustness against unmodeled disturbances and plant dynamics but is not as effective as feedforward control for the rejection of known disturbances. Control systems therefore typically use a combination of feedback and feedforward control. The design of a (thermal) actuator layout should thus eventually be based on such a combination of feedforward and feedback control. This is a very challenging and relevant problem that has not received much attention in the literature but deserves further investigation.

Part VI

Appendices

Appendix A

Appendices to Chapter 3

A.1 An analytic expression for the kernel on the circular domain

In this appendix, a closed-form analytic expression for the kernel $W_{D,\gamma}$ satisfying the PDE (3.76) and the boundary conditions (3.81) and (3.82) in which the Dirac delta is replaced by $\delta_\gamma(r - R, \hat{\theta})$ in (3.83) will be derived.

To this end, $W_{D,\gamma}(r, \hat{\theta}, r')$ is written as a linear combination of the eigenfunctions of the Laplacian on the disk $D = \{(r, \hat{\theta}) \mid r \leq R\}$ that satisfy the Neumann boundary condition (3.82). These eigenfunctions $w(r, \hat{\theta})$ are thus solutions to the eigenvalue problem

$$\frac{1}{r}\frac{\partial}{\partial r}\left(r\frac{\partial w}{\partial r}(r, \hat{\theta})\right) + \frac{1}{r^2}\frac{\partial^2 w}{\partial \hat{\theta}^2}(r, \hat{\theta}) = \lambda w(r, \hat{\theta}), \qquad \frac{\partial w}{\partial r}(R, \hat{\theta}) = 0, \tag{A.1}$$

where λ denotes the eigenvalue corresponding to the eigenfunction $w(r, \hat{\theta})$. All solutions to the eigenvalue problem (A.1) can be found using the following separation of variables, see e.g. [Gray and Mathews, 1952]

$$w(r, \hat{\theta}) = f(r)\Theta(\hat{\theta}). \tag{A.2}$$

Inserting this expression for $w(r, \hat{\theta})$ in the first equation in (A.1) and dividing by $f(r)\Theta(\hat{\theta})/r^2$ shows that

$$\frac{\frac{\partial^2 \Theta}{\partial \hat{\theta}^2}(\hat{\theta})}{\Theta(\hat{\theta})} = r^2\lambda - \frac{r}{f(r)}\frac{\partial}{\partial r}\left(r\frac{\partial f}{\partial r}(r)\right) = \mu, \tag{A.3}$$

where μ is a constant that does not depend on $\hat{\theta}$ or r. Since the LHS of (A.3) is equal to μ and because the eigenfunction $w(r,\hat{\theta})$ in (A.2) should be periodic in $\hat{\theta}$, it follows that $\Theta(\hat{\theta})$ should be a solution of

$$\frac{\partial^2\Theta}{\partial\hat{\theta}^2}(\hat{\theta}) = \mu\Theta(\hat{\theta}), \qquad \Theta(0) = \Theta(2\pi), \frac{\partial\Theta}{\partial\hat{\theta}}(0) = \frac{\partial\Theta}{\partial\hat{\theta}}(2\pi). \tag{A.4}$$

The only solutions of (A.4) are

$$\Theta(\hat{\theta}) = \Theta_1\cos(n\hat{\theta}) + \Theta_2\sin(n\hat{\theta}), \tag{A.5}$$

for some constants $\Theta_1, \Theta_2 \in \mathbb{R}$ and $n \in \mathbb{Z}_{\geq 0}$. Note the solution in (A.5) corresponds to $\mu = -n^2$.

Now considering the second identity in (A.3) and the boundary condition for $w(r,\hat{\theta})$ in (A.1) with $\mu = -n^2$, it follows that the function $f(r)$ should satisfy

$$r\frac{\partial}{\partial r}\left(r\frac{\partial f}{\partial r}(r)\right) + \left(n^2 - \lambda r^2\right) f(r) = 0, \qquad \frac{\partial f}{\partial r}(R) = 0. \tag{A.6}$$

The ODE in (A.6) is known as Bessel's equation and its two independent solutions are known as the Bessel functions of order n of the first and second kind, see e.g. [Gray and Mathews, 1952]. The solution of the ODE in (A.6) can thus be expressed as

$$f(r) = F_1 J_n(\sqrt{-\lambda}r) + F_2 Y_n(\sqrt{-\lambda}r), \tag{A.7}$$

where $J_n(r)$ and $Y_n(r)$ are the Bessel functions of order n of the first and second kind, respectively, and $F_1, F_2 \in \mathbb{R}$ are constants. Since $f(r)$ should be bounded at $r = 0$ and $Y_n(r)$ grows unbounded for $r \to 0$, it follows that $F_2 = 0$. The boundary condition for $f(r)$ in (A.6) now implies that $\sqrt{-\lambda} = \beta_{n,m}/R$, where $\beta_{n,m}$ is the m-th ($m \geq 1$) root of $\partial J_n/\partial r(r) = 0$. In particular, note that rewriting $\sqrt{-\lambda} = \beta_{n,m}/R$ shows that the eigenvalues are

$$\lambda_{n,m} = -\frac{\beta_{n,m}^2}{R^2}. \tag{A.8}$$

There are infinitely many roots of $\partial J_n/\partial r = 0$ that are all located on the positive real axis except the first root of $\partial J_0/\partial r = 0$ which is $\beta_{0,1} = 0$ [Watson, 1966]. Note that $\beta_{0,1}$ corresponds the constant eigenfunction (this follows from (A.7) which shows that to $f(r) = F_1$ because $J_0(0) = 1$ and from (A.5) which shows that $\Theta(\hat{\theta}) = \Theta_1$ because $n = 0$). The eigenfunctions of (A.1) are thus

$$w_{n,m}(r,\hat{\theta}) = J_n\left(\beta_{n,m}r/R\right)\cos(n\hat{\theta}), \qquad n \geq 0, m \geq 1, \tag{A.9}$$

$$\tilde{w}_{n,m}(r,\hat{\theta}) = J_n\left(\beta_{n,m}r/R\right)\sin(n\hat{\theta}), \qquad n \geq 1, m \geq 1. \tag{A.10}$$

At any 'time instant' r', the kernel $W_{D,\gamma}(r,\hat{\theta},r')$ satisfying the boundary condition (3.82) may thus be written as

$$W_{D,\gamma}(r,\hat{\theta},r') = \sum_{n=0}^{\infty}\sum_{m=1}^{\infty} a_{n,m}(r')w_{n,m}(r,\hat{\theta}) + \sum_{n=1}^{\infty}\sum_{m=1}^{\infty} \tilde{a}_{n,m}(r')\tilde{w}_{n,m}(r,\hat{\theta}), \tag{A.11}$$

where the coefficients $a_{0,0}(r')$, $a_{n,m}(r')$, and $\tilde{a}_{n,m}(r')$ still need to be determined.

A set of ODEs for the coefficients $a_{0,0}(r')$, $a_{n,m}(r')$, and $\tilde{a}_{n,m}(r')$ can be obtained through a Galerkin discretization of (3.76). Using that $w_{0,0}(r,\hat{\theta})$, $w_{n,m}(r,\hat{\theta})$, and $w_{n,m}(r,\hat{\theta})$ are eigenfunctions of the Laplacian and the their eigenvalues are given by (A.8), it follows that inserting the expression for $W_{D,\gamma}(r,\hat{\theta},r')$ in (A.11) into the RHS of (3.76) yields

$$\begin{aligned}\nabla^2 W_{D,\gamma}(r,\hat{\theta},r') = &\sum_{n=0}^{\infty}\sum_{m=1}^{\infty} \frac{-\beta_{n,m}^2}{R^2} a_{n,m}(r')w_{n,m}(r,\hat{\theta}) \\ &+ \sum_{n=1}^{\infty}\sum_{m=1}^{\infty} \frac{-\beta_{n,m}^2}{R^2}\tilde{a}_{n,m}(r')\tilde{w}_{n,m}(r,\hat{\theta}).\end{aligned} \tag{A.12}$$

Using that the eigenfunctions $w_{0,0}(r,\hat{\theta})$, $w_{n,m}(r,\hat{\theta})$, and $\tilde{w}_{n,m}(r,\hat{\theta})$ are mutually orthogonal w.r.t. the inner product

$$\langle f,g\rangle = \int_0^R \int_0^{2\pi} f(r,\hat{\theta})g(r,\hat{\theta})r \,\mathrm{d}\hat{\theta}\,\mathrm{d}r, \tag{A.13}$$

it now follows that inserting the expansion (A.11) into (3.76) and taking the inner product with the shape function $w_{n,m}(r,\hat{\theta})$ leads to the following ODE

$$\frac{1}{r'}\frac{\partial}{\partial r'}\left(r'\frac{\partial a_{n,m}}{\partial r'}(r')\right) - \frac{n^2}{r'^2}a_{n,m}(r') = \frac{-\beta_{n,m}^2}{R^2}a_{n,m}(r'), \tag{A.14}$$

where the factor $\langle w_{n,m}, w_{n,m}\rangle$ has been omitted. Similarly, inserting (A.11) into (3.76) and projecting on $\tilde{w}_{n,m}(r,\hat{\theta})$ yields

$$\frac{1}{r'}\frac{\partial}{\partial r'}\left(r'\frac{\partial \tilde{a}_{n,m}}{\partial r'}(r')\right) - \frac{n^2}{r'^2}\tilde{a}_{n,m}(r') = \frac{-\beta_{n,m}^2}{R^2}\tilde{a}_{n,m}(r'), \tag{A.15}$$

where now the factor $\langle \tilde{w}_{n,m}, \tilde{w}_{n,m}\rangle$ has been omitted. Note that (A.14) and (A.15) are of the same form as the ODE for $f(r)$ in (A.6). When $(n,m) = (0,1)$, $\beta_{n,m} = 0$ and the solution of (A.14) is

$$a_{0,1}(r') = A_{0,1} + B_{0,1}\log(r'/R), \tag{A.16}$$

for some constants $A_{0,1}$ and $B_{0,1}$. In all other situations where $\beta_{n,m} > 0$, the solutions of (A.14)–(A.15) are

$$a_{n,m}(r') = A_{n,m} J_n(\beta_{n,m} r'/R) + B_{n,m} Y_n(\beta_{n,m} r'/R), \tag{A.17}$$

$$\tilde{a}_{n,m}(r') = \tilde{A}_{n,m} J_n(\beta_{n,m} r'/R) + \tilde{B}_{n,m} Y_n(\beta_{n,m} r'/R), \tag{A.18}$$

for some constants $A_{n,m}$, $B_{n,m}$, $\tilde{A}_{n,m}$, and $\tilde{B}_{n,m}$.

The constants $A_{n,m}$, $B_{n,m}$, $\tilde{A}_{n,m}$, and $\tilde{B}_{n,m}$ are determined based on the 'initial conditions' (3.81). Since the eigenfunctions $w_{n,m}(r,\hat{\theta})$ and $\tilde{w}_{n,m}(r,\hat{\theta})$ are linearly independent, it follows that the second condition in (3.81) implies that

$$\frac{\partial a_{n,m}}{\partial r'}(R) = 0, \qquad \frac{\partial \tilde{a}_{n,m}}{\partial r'}(R) = 0. \tag{A.19}$$

Inserting the expressions for $a_{n,m}(r')$ and $\tilde{a}_{n,m}(r')$ in (A.16)–(A.18) into (A.19) and using that $\beta_{n,m}$ is a zero of $\partial J_n/\partial r$, it follows that

$$B_{n,m} = 0, \qquad \tilde{B}_{n,m} = 0. \tag{A.20}$$

The constants $A_{n,m}$ and $\tilde{A}_{n,m}$ follow from the values of $a_{n,m}(R)$ and $\tilde{a}_{n,m}(R)$ that are determined such that $W_{D,\gamma}$ in (A.11) to satisfy the first condition in (3.81) in which the Dirac delta is replaced by $\delta_\gamma(r-R,\hat{\theta})$ in (3.83). The required values of $a_{0,0}(R)$, $a_{n,m}(R)$, and $\tilde{a}_{n,m}(R)$ follow from

$$a_{n,m}(R)\langle w_{n,m}, w_{n,m}\rangle = \langle W_{D,\gamma}(\cdot,\cdot,R), w_{n,m}\rangle = \langle \delta_\gamma(r-R,\hat{\theta}), w_{n,m}\rangle, \tag{A.21}$$

$$\tilde{a}_{n,m}(R)\langle \tilde{w}_{n,m}, \tilde{w}_{n,m}\rangle = \langle W_{D,\gamma}(\cdot,\cdot,R), \tilde{w}_{n,m}\rangle = \langle \delta_\gamma(r-R,\hat{\theta}), \tilde{w}_{n,m}\rangle, \tag{A.22}$$

where the first identities in these two equations follow from the expansion of $W_{D,\gamma}(r,\hat{\theta},r')$ in (A.11) and because the eigenfunctions are mutually orthogonal and the second identities follow from the first condition in (3.81) in which the Dirac delta is replaced by $\delta_\gamma(r-R,\hat{\theta})$ in (3.83). Using the expressions for $a_{n,m}(r')$ and $\tilde{a}_{n,m}(r')$ in (A.17) and (A.18) with $B_{n,m} = 0$ and $\tilde{B}_{n,m} = 0$ now shows that

$$A_{n,m} = \frac{\langle \delta_\gamma(r-R,\hat{\theta}), w_{n,m}\rangle}{J_n(\beta_{n,m})\langle w_{n,m}, w_{n,m}\rangle}, \qquad \tilde{A}_{n,m} = 0, \tag{A.23}$$

where the second identity in (A.22) follows because the functions $\tilde{w}_{n,m}(r,\hat{\theta})$ are anti-symmetric around $\hat{\theta} = 0$ and $\delta_\gamma(r-R,\hat{\theta})$ in (3.83) is symmetric around $\hat{\theta}$ which implies that $\langle \delta_\gamma(r-R,\hat{\theta}), \tilde{w}_{n,m}\rangle = 0$.

Because $\tilde{A}_{n,m} = 0$ and $\tilde{B}_{n,m} = 0$, it follows from (A.18) that $\tilde{a}_{n,m}(r') \equiv 0$, so that inserting (A.17) with $B_{n,m} = 0$ into (A.11) indeed yields an expression for $W_{D,\gamma}$ of the form (3.84).

To find explicit expressions for $A_{n,m}$, note that $w_{0,1}(r,\hat{\theta}) \equiv 1$ so that

$$\langle w_{0,1}, w_{0,1} \rangle = \int_0^{2\pi} \int_0^R r \, \mathrm{d}r \, \mathrm{d}\hat{\theta} = \pi R^2, \tag{A.24}$$

and that the known formulas for the integration of Bessel functions, see e.g. [Gray and Mathews, 1952] show that for $(n,m) \neq (0,1)$

$$\langle w_{n,m}, w_{n,m} \rangle = \pi R^2 \frac{\epsilon_n}{2} J_n^2(\beta_{n,m}) \left[1 - \frac{n^2}{\beta_{n,m}^2} \right], \tag{A.25}$$

where $\epsilon_n = 2$ when $n = 0$ and $\epsilon_n = 1$ for $n \neq 0$. Because $\delta_\gamma(r - R, \hat{\theta}) \to \frac{1}{R}\delta(r-R)\delta(\hat{\theta})$ for $\gamma \to 0$, it follows that

$$\langle \delta_0(r - R, \hat{\theta}), w_{n,m} \rangle = w_{n,m}(R, 0) = J_n(\beta_{n,m}). \tag{A.26}$$

Inserting this expression and (A.24) into (A.23) using that $J_0(0) = 1$ now yields (3.85) and inserting this expression and (A.25) into (A.23) yields (3.86).

For $\gamma > 0$, the expression for $\delta_\gamma(r - R, \hat{\theta})$ in (3.83) and the expression for $w_{n,m}(r,\hat{\theta})$ in (A.9) show that for $(n,m) = (0,1)$

$$\langle \delta_\gamma(r - R, \hat{\theta}), w_{0,1} \rangle = 1 - \frac{\gamma}{2} \left(1 - \frac{4}{\pi^2} \right), \tag{A.27}$$

and that for all other values of n and m

$$\langle \delta_\gamma(r - R, \hat{\theta}), w_{n,m} \rangle = C_{n,m} D_{n,m}, \tag{A.28}$$

where

$$C_{n,m} = \frac{1}{\gamma R^2} \int_{(1-\gamma)R}^{R} J_n \left(\frac{\beta_{n,m} r}{R} \right) \left(1 + \cos\left(\frac{\pi(r-R)}{\gamma R} \right) \right) r \, \mathrm{d}r, \tag{A.29}$$

$$D_{n,m} = \frac{1}{2\gamma} \int_{-\gamma}^{\gamma} \cos(n\hat{\theta}) \left(1 + \cos\left(\frac{\pi\hat{\theta}}{\gamma} \right) \right) \mathrm{d}\hat{\theta} = \frac{\sin(n\gamma)}{n\gamma(1 - \frac{n^2\gamma^2}{\pi^2})}. \tag{A.30}$$

The expressions for $\langle \delta_\gamma(r - R, \hat{\theta}), w_{0,0} \rangle$ and $D_{n,m}$ have been obtained using MAPLE. The coefficients $C_{n,m}$ are approximated numerically by a trapezoid quadrature rule.

A.2 Computation of the edge correction for the circular domain

In this appendix, details regarding the computation of the correction $\mathbf{d}_{D,\text{appr}}^{(BC)}$ for the circular domain with stress-free boundary conditions are given.

Recall that $\mathbf{d}_{D,\text{appr}}^{(BC)}$ is defined as the solution of (3.3) and (3.5) with $T_\Omega \equiv 0$ such that the stresses $\sigma_{D,\text{appr},rr}$ and $\sigma_{D,\text{appr},\theta\theta}$ resulting from the displacement field $\mathbf{d}_{D,\text{appr}} = \mathbf{d}_{D,\text{appr}}^{(T)} + \mathbf{d}_{D,\text{appr}}^{(BC)}$ as in (3.40) and (3.41) are zero on the edge $r = R$. Note that inserting (3.104) into (3.40) shows that the stress component $\sigma_{D,\text{appr},rr}^{(T)}$ resulting from $\mathbf{d}_{D,\text{appr}}^{(T)}$ is given by

$$\begin{aligned}\sigma_{D,\text{appr},rr}^{(T)}(r,\theta,t) = \frac{E}{1-\nu^2}\Bigg(&\frac{\partial d_{D,\infty,r}}{\partial r}(r,\theta,t) + \frac{\partial d_{D,\infty,r}}{\partial r}(2R-r,\theta,t)\\ &+ \nu\frac{d_{D,\infty,r}(r,\theta,t) - d_{D,\infty,r}(2R-r,\theta,t)}{r}\\ &+ \nu\frac{1}{r}\frac{\partial d_{D,\infty,\theta}}{\partial\theta}(r,\theta,t) + \nu\frac{2R-r}{r^2}\frac{\partial d_{D,\infty,\theta}}{\partial\theta}(2R-r,\theta,t)\\ &- (1+\nu)\alpha\left(T_{D,\infty}(r,\theta,t) + T_{D,\infty}(2R-r,\theta,t)\right)\Bigg). \end{aligned} \tag{A.31}$$

Evaluating this expression in $r = R$ shows that

$$\begin{aligned}&\sigma_{D,\text{appr},rr}^{(T)}(R,\theta,t) = \\ &\frac{2E}{1-\nu^2}\left(\frac{\partial d_{D,\infty,r}}{\partial r}(R,\theta,t) + \frac{\nu}{R}\frac{\partial d_{D,\infty,\theta}}{\partial\theta}(R,\theta,t) - (1+\nu)\alpha T_{D,\infty}(R,\theta,t)\right).\end{aligned} \tag{A.32}$$

Similarly, inserting the expression for $\mathbf{d}_{D,\text{appr}}$ in (3.104) into the expression for $\sigma_{r\theta}$ in (3.41), it follows that

$$\begin{aligned}\sigma_{D,\text{appr},r\theta}^{(T)}(r,\theta,t) = \frac{E}{2(1+\nu)}\Bigg[&\frac{1}{r}\left(\frac{\partial d_{D,\infty,r}}{\partial\theta}(r,\theta,t) - \frac{\partial d_{D,\infty,r}}{\partial\theta}(2R-r,\theta,t)\right)\\ &- \frac{1}{r}\left(d_{D,\infty,\theta}(r,\theta,t) + d_{D,\infty,\theta}(2R-r,\theta,t)\right) +\\ &\frac{\partial d_{D,\infty,\theta}}{\partial r}(r,\theta,t) - \frac{2R}{r^2}d_{D,\infty,\theta}(2R-r,\theta,t) - \frac{2R-r}{r}\frac{\partial d_{D,\infty,\theta}}{\partial r}(2R-r,\theta,t)\Bigg].\end{aligned} \tag{A.33}$$

Evaluating this expression in $r = R$ shows that

$$\sigma_{D,\text{appr},r\theta}^{(T)}(R,\theta,t) = \frac{-2E}{(1+\nu)R}d_{D,\infty,\theta}(R,\theta,t). \tag{A.34}$$

In order for $\mathbf{d}_{D,\text{appr}} = \mathbf{d}_{D,\text{appr}}^{(T)} + \mathbf{d}_{D,\text{appr}}^{(BC)}$ to satisfy the stress-free boundary conditions in (3.39), it thus follows that $\mathbf{d}_{D,\text{appr}}^{(BC)}$ should satisfy the boundary

conditions

$$\sigma^{(BC)}_{D,\mathrm{appr},rr} = \frac{-2E}{1-\nu^2}\left(\frac{\partial d_{D,\infty,r}}{\partial r} + \frac{\nu}{R}\frac{\partial d_{D,\infty,\theta}}{\partial \theta} - (1+\nu)\alpha T_{D,\infty}\right), \tag{A.35}$$

$$\sigma^{(BC)}_{D,\mathrm{appr},r\theta} = \frac{2E}{(1+\nu)R} d_{D,\infty,\theta}, \tag{A.36}$$

on the edge $r = R$. Since $\mathbf{d}_{D,\infty}$ is computed in Cartesian coordinates, these boundary conditions still need to be rewritten in terms of the Cartesian components $d_{D,\infty,x}(x,y,t)$ and $d_{D,\infty,y}(x,y,t)$. An expression for $d_{D,\infty,\theta}$ in terms of $d_{D,\infty,x}(x,y,t)$ and $d_{D,\infty,y}(x,y,t)$ directly follows from the second line of (3.37). To find an expression for $\partial d_{D,\infty,r}/\partial r$, note that the chain rule and (3.36) show that

$$\frac{\partial d_{D,\infty,x}}{\partial r} = \frac{\partial d_{D,\infty,x}}{\partial x}\frac{\partial x}{\partial r} + \frac{\partial d_{D,\infty,x}}{\partial y}\frac{\partial y}{\partial r} = \frac{\partial d_{D,\infty,x}}{\partial x}\cos(\theta) + \frac{\partial d_{D,\infty,x}}{\partial y}\sin(\theta). \tag{A.37}$$

A similar expression holds when $d_{D,\infty,x}$ is replaced by $d_{D,\infty,y}$. Using the first line of (3.37), it now follows that

$$\begin{aligned}
\frac{\partial d_{D,\infty,r}}{\partial r} &= \frac{\partial}{\partial r}\left(\cos(\theta) d_{D,\infty,x} + \sin(\theta) d_{D,\infty,y}\right) \\
&= \cos(\theta)\frac{\partial d_{D,\infty,x}}{\partial r} + \sin(\theta)\frac{\partial d_{D,\infty,y}}{\partial r} \\
&= \cos^2(\theta)\frac{\partial d_{D,\infty,x}}{\partial x} + \sin^2(\theta)\frac{\partial d_{D,\infty,y}}{\partial y} \\
&\qquad + \cos(\theta)\sin(\theta)\left(\frac{\partial d_{D,\infty,x}}{\partial y} + \frac{\partial d_{D,\infty,y}}{\partial x}\right).
\end{aligned} \tag{A.38}$$

For $\partial d_{D,\infty,\theta}/\partial\theta$ a similar procedure is used. So first the chain rule and (3.36) are used to find

$$\frac{\partial d_{D,\infty,x}}{\partial \theta} = \frac{\partial d_{D,\infty,x}}{\partial x}\frac{\partial x}{\partial \theta} + \frac{\partial d_{D,\infty,x}}{\partial y}\frac{\partial y}{\partial \theta} = -\frac{\partial d_{D,\infty,x}}{\partial x} r\sin(\theta) + \frac{\partial d_{D,\infty,x}}{\partial y} r\cos(\theta). \tag{A.39}$$

Again, a similar expression holds when $d_{D,\infty,x}$ is replaced by $d_{D,\infty,y}$. Now the second line of (3.37) now shows that

$$\begin{aligned}
\frac{\partial d_{D,\infty,r}}{\partial \theta} &= \frac{\partial}{\partial \theta}\left(-\sin(\theta) d_{D,\infty,x} + \cos(\theta) d_{D,\infty,y}\right) \\
&= -\cos(\theta) d_{D,\infty,x} - \sin(\theta) d_{D,\infty,y} - \sin(\theta)\frac{\partial d_{D,\infty,x}}{\partial \theta} + \cos(\theta)\frac{\partial d_{D,\infty,y}}{\partial \theta} \\
&= -\cos(\theta) d_{D,\infty,x} - \sin(\theta) d_{D,\infty,y} + r\sin^2(\theta)\frac{\partial d_{D,\infty,x}}{\partial x} \\
&\quad + r\cos^2(\theta)\frac{\partial d_{D,\infty,y}}{\partial y} - r\cos(\theta)\sin(\theta)\left(\frac{\partial d_{D,\infty,x}}{\partial y} + \frac{\partial d_{D,\infty,y}}{\partial x}\right).
\end{aligned} \tag{A.40}$$

Using the expression for $d_{D,\infty,\theta}$ that follows from the second line of (3.37) and (A.38) and (A.40), the boundary conditions (A.35) and (A.36) can be expressed completely in terms of the Cartesian components of $\mathbf{d}_{D,\infty}$.

The computation of $\mathbf{d}^{(BC)}_{D,\text{appr}}$ in cylindrical coordinates with boundary conditions (A.35) and (A.36) is now a standard plane stress elasticity problem. Details regarding the construction of the finite element formulation of this problem can be found in many textbooks such as [Zienkiewicz et al., 2013].

Appendix B

Appendices to Chapter 4

B.1 Higher-order approximations

The accuracy of the approximation can be increased by considering higher-order terms in the Taylor series approximation of $N(x,\tau)$ in (4.11). So instead of the first-order expansion in (4.11), we consider an n-th order Taylor series expansion ($n \geq 2$)

$$N(x,\tau) \approx \sum_{k=0}^{n} \frac{(\tau - t^*)^k}{k!} \left.\frac{\partial^k N}{\partial \tau^k}\right|_{(x,\tau)=(x,t^*)}. \tag{B.1}$$

Subsitution of this expansion in (4.8) leads to an approximation

$$\tilde{T}_{2\mathrm{D}}^{(n)}(x,y,t) = \sum_{k=0}^{n} A_{1\mathrm{D}}^{(k)}(y,t,t^*) \left.\frac{1}{k!}\frac{\partial^k N}{\partial \tau^k}\right|_{(x,\tau)=(x,t^*)}, \tag{B.2}$$

where

$$A_{1\mathrm{D}}^{(k)}(y,t,t^*) = \int_0^t (\tau - t^*)^k f(y,t,\tau)\ \mathrm{d}\tau. \tag{B.3}$$

Note that derivatives of $N(x,\tau)$ w.r.t. τ up to order n are needed. When an analytic expression for $N(x,\tau)$ can be obtained, these can be determined easily. However, when no analytic expression for $N(x,\tau)$ is available, obtaining these derivatives may be difficult. To illustrate the problem, note that (4.23) shows that $\frac{\partial N}{\partial \tau} = D\frac{\partial^2 N}{\partial x^2}$ so that the initial condition in (4.23) now gives that

$$\left.\frac{\partial N}{\partial \tau}\right|_{\tau=0} = D\frac{\partial^2 X}{\partial x^2}. \tag{B.4}$$

However, the blockfunction $X(x)$ considered in the example is clearly not twice differentiable, so that the RHS in the equation above is not well defined. In particular, we see that $\frac{\partial N}{\partial \tau}$ will behave wildly near $\tau = 0$, meaning that it is difficult to construct a numerical approximation of $\frac{\partial N}{\partial \tau}$ near $\tau = 0$. This becomes even more problematic for higher order derivatives.

The definition of $t^*(y,t)$ in (4.19) is not changed for the higher-order approximations, meaning in particular that $A_{1\mathrm{D}}^{(1)}(y,t,t^*) = 0$. To see how we can compute the coefficients $A_{1\mathrm{D}}^{(k)}(y,t,t^*)$, we make a binomial expansion of the factor $(\tau - t^*)^k$ to obtain

$$\begin{aligned} A_{1\mathrm{D}}^{(k)}(y,t,t^*) &= \int_0^t (\tau - t + t - t^*)^k f(y,t,\tau)\ \mathrm{d}\tau \\ &= \sum_{p=0}^{k} \binom{k}{p} (t-t^*)^{k-p} (-1)^p T_{1\mathrm{D}}^{(p,c)}(y,t), \end{aligned} \tag{B.5}$$

where

$$T_{1\mathrm{D}}^{(p,c)}(y,t) = \int_0^t (t-\tau)^p f(y,t,\tau)\ \mathrm{d}\tau. \tag{B.6}$$

Now we recognize $T_{1\mathrm{D}}^{(p,c)}(y,t)$ as the solution to the one-dimensional PDE

$$\frac{\partial T_{1\mathrm{D}}^{(p,c)}}{\partial t} = D\frac{\partial^2 T_{1\mathrm{D}}^{(p,c)}}{\partial y^2} - hT_{1\mathrm{D}}^{(p,c)} + t^p Y(y - vt)\bar{\Theta}(t), \tag{B.7}$$

with zero initial conditions. Now the procedure to compute the n-th order approximation $\tilde{T}_{2\mathrm{D}}^{(n)}$ is as follows:

1. Determine a closed form analytic expression for $N(x,t)$ by solving (4.10) directly and compute the first n derivatives w.r.t. τ of this expression.
2. Discretize the PDE in one spatial dimension in (B.7) for $p = 0, 1, \ldots, n$. to find $T_{1\mathrm{D}}^{(p,c)}(y,t)$.
3. Compute $t^*(y,t)$ from (4.19)
   (note that $T_{1\mathrm{D}} = T_{1\mathrm{D}}^{(0,c)}$ and $T_{1\mathrm{D}}^{(1)} = tT_{1\mathrm{D}}^{(0,c)} - T_{1\mathrm{D}}^{(1,c)}$).
4. Compute $A_{1\mathrm{D}}^{(k)}(y,t,t^*)$ from (B.5) for $k = 0, 2, 3, \ldots, n$.
5. Compute $\tilde{T}_{2\mathrm{D}}^{(n)}(x,y,t)$ from (B.2).

Note that, depending on the shape of the applied heat load in the x-direction $X(x)$, it is not always possible to find a closed-form expression for the integral in (4.10) required in step 1. If this is not the case, it is not clear how the first n derivatives of $N(x,\tau)$ w.r.t. τ can be obtained and the procedure above cannot be applied. Furthermore, observe that the main computational cost of this procedure is due to step 2, where $n+1$ PDEs in one spatial dimension need to be solved.

B.2 Three-dimensional spatial domain

Consider the following the heat conduction problem in three spatial dimensions with a moving heat load

$$\rho c \frac{\partial T_{3\mathrm{D}}}{\partial t} = k \left(\frac{\partial^2 T_{3\mathrm{D}}}{\partial x^2} + \frac{\partial^2 T_{3\mathrm{D}}}{\partial y^2} + \frac{\partial^2 T_{3\mathrm{D}}}{\partial z^2} \right) + Q_{3\mathrm{D}}, \tag{B.8}$$

where $T_{3\mathrm{D}}(x, y, z, t)$ denotes the temperature field, ρ, c, and k are the density, specific heat capacity, and thermal conductivity, respectively, and $Q_{3\mathrm{D}}$ is the applied heat load that is assumed to be of the form (4.39). Note that a completely unbounded spatial domain $(x, y, z) \in \mathbb{R}^3$ is considered here. This situation is not encountered in many applications, but the method of images can be used to convert this solution to spatial domains with boundaries (see Chapter 3), for example the half space $z \leq 0$ or box-shaped domains that are often of interest in welding problems, see e.g. [Flint et al., 2018]. Also note that it is not natural to model the cooling to the environment as in (4.1), since such cooling will typically occur through boundary conditions in a 3-D problem.

Similarly as for the 2D problem, it is convenient to divide (B.8) by ρc which leads to

$$\frac{\partial T_{3\mathrm{D}}}{\partial t} = D \left(\frac{\partial^2 T_{3\mathrm{D}}}{\partial x^2} + \frac{\partial^2 T_{3\mathrm{D}}}{\partial y^2} + \frac{\partial^2 T_{3\mathrm{D}}}{\partial z^2} \right) + \Theta_{3\mathrm{D}}, \tag{B.9}$$

where

$$\Theta_{3\mathrm{D}}(x, y, z, t) = X(x) Y(y - vt) Z(z) \bar{\Theta}(t), \tag{B.10}$$

with $\bar{\Theta}(t) = \bar{Q}(t)/\rho c$. The fundamental solution for (B.9) is

$$\Phi_{3\mathrm{D}}(x, y, z, t) = \Phi(x, t) \Phi(y, t) \Phi(z, t), \tag{B.11}$$

where $\Phi(x, t)$ is given by (4.6).

The solution to the 3-D problem is given by the convolution of the fundamental solution in (B.11) and the applied heat load in (B.10), so that

$$T_{3\mathrm{D}}(x, y, z, t) = \int_0^t f(y, t, \tau) N(x, z, \tau) \, \mathrm{d}\tau, \tag{B.12}$$

where

$$f(y, t, \tau) = \int_{-\infty}^{+\infty} \Phi(y', \tau) Y(y - y' - v(t - \tau)) \bar{\Theta}(t - \tau) \, \mathrm{d}y', \tag{B.13}$$

$$N(x, z, \tau) = \int_{-\infty}^{+\infty} \int_{-\infty}^{+\infty} \Phi(x', \tau) \Phi(z', \tau) X(x - x') Z(z - z') \, \mathrm{d}x' \, \mathrm{d}z'. \tag{B.14}$$

Similarly as before, $N(x, z, \tau)$ is approximated by a Taylor series around $\tau = t^*$

$$N(x, z, \tau) \approx N(x, z, t^*) + (\tau - t^*) \frac{\partial N}{\partial \tau} \bigg|_{(x,z,\tau)=(x,z,t^*)}. \tag{B.15}$$

Substitution of the approximation (B.15) in (B.12) leads to the approximation

$$\tilde{T}_{3\mathrm{D}}(x,y,z,t) = T_{1\mathrm{D}}(y,t)N(x,z,t^*(y,t)), \tag{B.16}$$

when the expansion point t^* is chosen as

$$t^*(y,t) = \frac{T_{1\mathrm{D}}^{(1)}(y,t)}{T_{1\mathrm{D}}(y,t)}, \tag{B.17}$$

with

$$T_{1\mathrm{D}}(y,t) = \int_0^t f(y,t,\tau)\ \mathrm{d}\tau, \tag{B.18}$$

$$T_{1\mathrm{D}}^{(1)}(y,t) = \int_0^t \tau f(y,t,\tau)\ \mathrm{d}\tau. \tag{B.19}$$

Because the function $f(y,t,\tau)$ for the 3-D problem in (B.13) is of the same form as the function $f(y,t,\tau)$ for the 2-D problem in (4.9), it is easy to see that $T_{1\mathrm{D}}(y,t)$ and $T_{1\mathrm{D}}^{(1)}(y,t)$ for the 3-D problem can be computed in the same way as for the 2-D problem, i.e. by solving the PDEs

$$\frac{\partial T_{1\mathrm{D}}}{\partial t} = D\frac{\partial^2 T_{1\mathrm{D}}}{\partial y^2} + Y(y-vt)\bar{\Theta}(t), \tag{B.20}$$

$$\frac{\partial T_{1\mathrm{D}}^{(1c)}}{\partial t} = D\frac{\partial^2 T_{1\mathrm{D}}^{(1c)}}{\partial y^2} + tY(y-vt)\bar{\Theta}(t), \tag{B.21}$$

and using (4.25).

To compute $N(x,z,\tau)$, note that (B.14) can be rewritten as

$$N(x,z,\tau) = N_x(x,\tau)N_z(z,\tau), \tag{B.22}$$

where

$$N_x(x,\tau) = \int_{-\infty}^{+\infty} \Phi(x',\tau)X(x-x')\ \mathrm{d}x', \tag{B.23}$$

$$N_z(z,\tau) = \int_{-\infty}^{+\infty} \Phi(z',\tau)Z(z-z')\ \mathrm{d}z'. \tag{B.24}$$

The functions N_x and N_z are now easily recognized as the solutions of the initial value problems

$$\frac{\partial N_x}{\partial \tau} = D\frac{\partial^2 N_x}{\partial x^2}, \qquad N_x(x,0) = X(x), \tag{B.25}$$

$$\frac{\partial N_z}{\partial \tau} = D\frac{\partial^2 N_z}{\partial z^2}, \qquad N_z(z,0) = Z(z). \tag{B.26}$$

Appendix C

Appendices to Chapter 5

C.1 Parameters in the barrier function J_2

In this appendix, feasible values for the power p and the weight w appearing in the cost functional $J_0 + wJ_2$ (with J_0 as in (5.11) and J_2 as in (5.19)) will be determined.

The power p should be chosen such that J_2 increases 'fast enough' near the edge of the admissible set. In particular, it is desired that the integrand is approximately zero at points (x, ζ, t) for which there is enough margin in (5.10) and that the integrand is large for points (x, ζ, t) where the margin in (5.10) is small. This idea can be translated into the requirement that the integrand in (5.19) for points (x, ζ, t) at which

$$d_{\max}(x,\zeta) - \sqrt{d_x^2(x,\zeta,t) + d_\zeta^2(x,\zeta,t)} < \varepsilon_1 d_{\max}(x,\zeta), \tag{C.1}$$

is at least $M \gg 1$ times larger than the value of the integrand in (5.19) for points (x, ζ, t) at which

$$d_{\max}(x,\zeta) - \sqrt{d_x^2(x,\zeta,t) + d_\zeta^2(x,\zeta,t)} > \varepsilon_2 d_{\max}(x,\zeta), \tag{C.2}$$

where $0 < \varepsilon_1 < \varepsilon_2 < 1$. Parameters ε_1 and ε_2 are used to quantify a 'small' and 'large enough' margin relative to maximally allowed displacement at that point. Note that equations (C.1) and (C.2) are equivalent to

$$\frac{d_x^2 + d_\zeta^2}{d_{\max}^2} > (1-\varepsilon_1)^2, \qquad \frac{d_x^2 + d_\zeta^2}{d_{\max}^2} < (1-\varepsilon_2)^2, \tag{C.3}$$

respectively, where the dependence on x, ζ, and t has been dropped. Note that the integrand in (5.19) can be rewritten as

$$-1+\left(\frac{d_{\max}^2}{d_{\max}^2-d_x^2-d_\zeta^2}\right)^p=\left(1-\frac{d_x^2+d_\zeta^2}{d_{\max}^2}\right)^{-p}-1. \tag{C.4}$$

Since this function is monotonically increasing in $d_x^2+d_\zeta^2$, the requirement on p translates to

$$\left(1-(1-\varepsilon_1)^2\right)^{-p}-1>M\left(\left(1-(1-\varepsilon_2)^2\right)^{-p}-1\right). \tag{C.5}$$

Using that $M>1$, it is easy to see that this equation is satisfied when

$$\left(1-(1-\varepsilon_1)^2\right)^{-p}>M\left(1-(1-\varepsilon_2)^2\right)^{-p}. \tag{C.6}$$

Some straightforward algebra now shows that this condition is equivalent to

$$p>\frac{\log(M)}{\log(2\varepsilon_2-\varepsilon_2^2)-\log(2\varepsilon_1-\varepsilon_1^2)}. \tag{C.7}$$

For the example in Section 5.4, the power p is determined based on the requirement that points for which the margin in (5.10) is below 0.1 nm contribute 1000 times more to the value of J_2 than points for which there is more than 1 nm margin in (5.10). Using that $\min_{x,\zeta} d_{\max}(x,\zeta)=2$ nm, this translates to $M=1000$, $\varepsilon_1=0.05$, and $\varepsilon_2=0.5$, for which (C.7) becomes $p>3.3858$. Indeed, this lower bound is slightly below the value of $p=3.5$ used in the examples in Section 5.4.

The weight w should be chosen such that the barrier function J_2 starts to dominate the value of cost functional J_0+wJ_2 when the margin in (5.10) becomes 'small' (as in (C.1)). To find the value of w that realizes this, typical magnitudes of the integrands in (5.11) and (5.19) are needed. It is reasonable to expect that the applied actuator heat load Q_{act} will be of similar magnitude as the heat load induced by the projecting light Q_{exp}. Recall that Q_{exp} has a power P_{exp} that is uniformly distributed over the area $L\times W$ (see Figure 5.1), so that Q_{exp} has a typical magnitude of P_{exp}/LW. The magnitude of the integrand in (5.11) is thus estimated as $(P_{\text{exp}}/LW)^2$. When the margin in (5.10) becomes 'small' as in (C.1) the typical magnitude of the integrand in (5.19) is $(1-(1-\varepsilon_1)^2)^{-p}-1$. The weight w should thus be chosen such that

$$\left(\frac{P_{\text{exp}}}{LW}\right)^2\approx w\left((1-(1-\varepsilon_1)^2)^{-p}-1\right). \tag{C.8}$$

For the considered parameter values this yields $w=2.1\cdot 10^5$, which is the value of w used in Section 5.4.

C.2 Uniqueness of the minimizer

In this appendix, the following general optimization problem will be considered

$$\min_{v \in V} J(v), \tag{C.9}$$

for a subset $V \subseteq H$ of a Hilbert space H with inner product $\langle \cdot, \cdot \rangle$ and norm $\| \cdot \|$ and a functional $J : V \to \mathbb{R}$. Some results regarding the uniqueness of the minimizer of such problems will be summarized which are then applied to the functionals J_0, J_1, and J_2 considered in Chapter 5.

The uniqueness of the minimizer relies on the convexity of the subset V and the (strict) convexity of the functional J. Convex subsets of $V \subseteq H$ and functionals J are defined as follows, see also Definition 10.14 in [Minoux, 1986].

Definition C.1. *A subset $V \subseteq H$ is called convex if for all $v_0, v_1 \in V$ and $\theta \in [0, 1]$ also*

$$(1 - \theta)v_0 + \theta v_1 \in V. \tag{C.10}$$

A functional $J : V \to \mathbb{R}$ is α-convex if there exists an $\alpha \geq 0$ such that for all $v_0, v_1 \in V$ and $\theta \in [0, 1]$

$$J((1 - \theta)v_0 + \theta v_1) \leq (1 - \theta)J(v_0) + \theta J(v_1) - \frac{\alpha}{2}\theta(1 - \theta)\|v_0 - v_1\|^2. \tag{C.11}$$

A 0-convex functional is also called convex.

Note that the intersection of two convex sets is convex and that any α-convex functional is convex. Furthermore, this definition also implies that $J + I$ is $(\alpha + \beta)$-convex if $J : V \to \mathbb{R}$ is α-convex and $I : V \to \mathbb{R}$ is β-convex. The uniqueness of the minimizer follows almost directly from this definition.

Lemma C.2. *Suppose V is convex and $J : V \to \mathbb{R}$ is α-convex for some $\alpha > 0$. If there exists a minimizer v_0 of* (C.9)*, then v_0 is the only minimizer of* (C.9)*.*

Proof. Since v_0 is a minimizer of (C.9), $J(v_0) = \min_{v \in V} J(v)$. For any point $v_1 \in V$ for which $J(v_1) = \min_{v \in V} J(v)$, (C.11) with $\theta = 1/2$ now shows that

$$J((v_0 + v_1)/2) \leq \min_{v \in V} J(v) - \frac{\alpha}{8}\|v_0 - v_1\|^2. \tag{C.12}$$

Since V is convex, $(v_0 + v_1)/2 \in V$ and $\min_{v \in V} J(v) \leq J((v_0 + v_1)/2)$ by definition of the infimum. It must thus hold that $\|v_0 - v_1\| = 0$, i.e. that $v_1 = v_0$, so the minimizer v_0 is unique. □

Note that (C.12) does not show that $v_1 = v_0$ when $\alpha = 0$. The 0-convexity of J is thus not sufficient to guarantee the uniqueness of the minimizer. However, (C.11) does show that the set in which a convex functional J assumes its minimal value is convex.

This result can now be applied to several optimization problems relevant to Chapter 5. First, consider the case where $B(x,\zeta)$ is fixed and only $u(t)$ is optimized. Because $T(x,\zeta,t)$, $d_x(x,\zeta,t)$, and $d_\zeta(x,\zeta,t)$ then depend linearly on $u(t)$ and because the constraint (5.10) is convex in $d_x(x,\zeta,t)$ and $d_\zeta(x,\zeta,t)$, the constraints (5.10) is convex in $u(t)$. The constraint (5.14) is also clearly convex in $u(t)$, so the set of admissible inputs $u(t)$ is convex. The minimization of J_0 over this set now yields a unique minimizer if convexity of J_0 in (5.11) is α-convex for some $\alpha > 0$. To see that this is the case, note that $J_0(u) = \|B\|_B^2\|u\|_u^2$, where $\|\cdot\|_B$ and $\|\cdot\|_u$ denote the norms induced by the L^2-inner products $\langle\cdot,\cdot\rangle_B$ and $\langle\cdot,\cdot\rangle_u$ on $\mathbb{R}^2$ and $(0,t_e)$, and therefore that

$$J_0((1-\theta)u_0+\theta u_1) = \|B\|_B^2\left((1-\theta)^2\|u_0\|_u^2+\theta^2\|u_1\|_u^2+2\theta(1-\theta)\langle u_0,u_1\rangle_u\right). \tag{C.13}$$

To eliminate $\langle u_0,u_1\rangle_u$, note that $\|u_0-u_1\|_u = \|u_0\|_u^2+\|u_1\|_u^2-2\langle u_0,u_1\rangle_u$. Using this expression to eliminate $2\langle u_0,u_1\rangle_u$ on the RHS of (C.13) yields

$$\begin{aligned}
&J_0((1-\theta)u_0+\theta u_1)\\
&= \|B\|_B^2\left((1-\theta)^2\|u_0\|_u^2+\theta^2\|u_1\|_u^2+\theta(1-\theta)(\|u_0\|_u^2+\|u_1\|_u^2-\|u_0-u_1\|_u^2)\right)\\
&= \|B\|_B^2\left((1-\theta)\|u_0\|_u^2+\theta\|u_1\|_u^2-\theta(1-\theta)\|u_0-u_1\|_u^2\right),
\end{aligned} \tag{C.14}$$

which shows that J_0 is $2\|B\|_B^2$-convex in $u(t)$. So as long as $B \neq 0$, minimizing J_0 over $u(t)$ for $B(x,\zeta)$ fixed subject to (5.10) and (5.14) yields a unique minimizer. In a similar fashion, it can be shown that J_0 is $2\|u\|_u^2$-convex in $B(x,\zeta)$, and thus that minimizing J_0 over $B(x,\zeta)$ for $u \neq 0$ fixed subject to (5.10) and (5.13) yields a unique minimizer. Note that similar arguments apply after spatial and/or temporal discretization, as long as the discretization preserves the convexity of the cost function and the constraints.

When considering free-shape optimal controls $U(x,\zeta,t)$, a similar computation shows that J_0 is 2-convex in $U(x,\zeta,t)$. Minimizing J_0 over $U(x,\zeta,t)$ subject to (5.10) and (5.68) thus also yields a unique minimizer.

Similar results apply to the minimization of $J_0 + wJ_2$. To see how, note that because $T(x,\zeta,t)$, $d_x(x,\zeta,t)$, and $d_\zeta(x,\zeta,t)$ depend linearly on the applied actuation heat load, the (0-)convexity of J_2 in $d_x(x,\zeta,t)$ and $d_\zeta(x,\zeta,t)$ implies that J_2 is (0-)convex in the applied actuation heat load. It thus follows that J_2 is convex in $u(t)$ for $B(x,\zeta)$ fixed, convex in $B(x,\zeta)$ for $u(t)$ fixed, and convex in $U(x,\zeta,t)$. Therefore, $J_0 + wJ_2$ is still $2\|B\|_B^2$-convex in $u(t)$ for $B(x,\zeta)$ fixed, $2\|u\|_u^2$-convex in $B(x,\zeta)$ for $u(t)$ fixed, and 2-convex in $U(x,\zeta,t)$. The uniqueness of the minimizer is thus also guaranteed in these cases.

Note that this appendix only addresses the uniqueness of the minimizer and assumes the existence of the minimizer. The existence of the minimizer is easy to proof for a finite-dimensional problems: it for example suffices to show that the cost functional is continuous and the admissible set is bounded and closed (compact). For infinite-dimensional problems, showing the existence of the minimizer is harder but several results are available, see e.g. [Edalatzadeh, 2019].

C.3 Numerical implementation

C.3.1 FE discretization of the mechanical model

To find the FE matrices of the mechanical model in (5.29)–(5.35), observe that the mechanical model in (5.6) and (5.7) can also be written as

$$\frac{\partial \sigma_{xx}}{\partial x} + \frac{\partial \sigma_{x\zeta}}{\partial \zeta} - k_s d_x = 0, \qquad \frac{\partial \sigma_{\zeta\zeta}}{\partial \zeta} + \frac{\partial \sigma_{x\zeta}}{\partial x} - k_s d_\zeta = 0, \tag{C.15}$$

where the stress components σ_{xx}, σ_{xy}, and $\sigma_{\zeta\zeta}$ are given by

$$\sigma_{xx} = \frac{EH}{1-\nu^2}\left(\frac{\partial d_x}{\partial x} + \nu\frac{\partial d_\zeta}{\partial \zeta} - (1+\nu)\alpha T\right), \tag{C.16}$$

$$\sigma_{x\zeta} = \frac{EH}{2(1+\nu)}\left(\frac{\partial d_x}{\partial \zeta} + \frac{\partial d_\zeta}{\partial x}\right), \tag{C.17}$$

$$\sigma_{\zeta\zeta} = \frac{EH}{1-\nu^2}\left(\frac{\partial d_\zeta}{\partial \zeta} + \nu\frac{\partial d_x}{\partial x} - (1+\nu)\alpha T\right). \tag{C.18}$$

To obtain the weak form, note that (C.15) can be rewritten as

$$\nabla \cdot \begin{bmatrix}\sigma_{xx}\\ \sigma_{x\zeta}\end{bmatrix} = k_s d_x, \qquad \nabla \cdot \begin{bmatrix}\sigma_{x\zeta}\\ \sigma_{\zeta\zeta}\end{bmatrix} = k_s d_\zeta, \tag{C.19}$$

where $\nabla\cdot$ denotes the divergence operator. Multiplying these equations by test functions $f_x(x,\zeta)$ and $f_\zeta(x,\zeta)$ and integrating over $(x,\zeta) \in \Omega \subset \mathbb{R}^2$, the divergence theorem now shows that

$$\begin{aligned} k_s \iint_\Omega (f_x d_x + f_\zeta d_\zeta)\ \mathrm{d}x\ \mathrm{d}\zeta = \iint_\Omega \left(f_x \nabla \cdot \begin{bmatrix}\sigma_{xx}\\ \sigma_{x\zeta}\end{bmatrix} + f_\zeta \nabla \cdot \begin{bmatrix}\sigma_{x\zeta}\\ \sigma_{\zeta\zeta}\end{bmatrix}\right)\ \mathrm{d}x\ \mathrm{d}\zeta = \\ -\iint_\Omega \left(\nabla f_x \cdot \begin{bmatrix}\sigma_{xx}\\ \sigma_{x\zeta}\end{bmatrix} + \nabla f_\zeta \cdot \begin{bmatrix}\sigma_{x\zeta}\\ \sigma_{\zeta\zeta}\end{bmatrix}\right)\ \mathrm{d}x\ \mathrm{d}\zeta + \int_{\partial\Omega} \left(f_x \begin{bmatrix}\sigma_{xx}\\ \sigma_{x\zeta}\end{bmatrix} + f_\zeta \begin{bmatrix}\sigma_{x\zeta}\\ \sigma_{\zeta\zeta}\end{bmatrix}\right)\cdot \mathbf{n}\ \mathrm{d}\ell, \end{aligned} \tag{C.20}$$

where ∇ denotes the gradient and $\mathbf{n}$ is the outward pointing normal to the edge $\partial\Omega$. For stress-free boundary conditions, the integral over $\partial\Omega$ vanishes so that

$$\iint_\Omega \left(\nabla f_x \cdot \begin{bmatrix}\sigma_{xx}\\ \sigma_{x\zeta}\end{bmatrix} + \nabla f_\zeta \cdot \begin{bmatrix}\sigma_{x\zeta}\\ \sigma_{\zeta\zeta}\end{bmatrix}\right)\ \mathrm{d}x\ \mathrm{d}\zeta + k_s \iint_\Omega (f_x d_x + f_\zeta d_\zeta)\ \mathrm{d}x\ \mathrm{d}\zeta = 0. \tag{C.21}$$

Writing the gradients of f_x and f_ζ explicitly in terms of derivatives w.r.t. x and ζ thus yields

$$\begin{aligned} \iint_\Omega \left(\frac{\partial f_x}{\partial x}\sigma_{xx} + \frac{\partial f_x}{\partial \zeta}\sigma_{x\zeta} + f_x k_s d_x\right)\ \mathrm{d}x\ \mathrm{d}\zeta + \\ \iint_\Omega \left(\frac{\partial f_\zeta}{\partial x}\sigma_{x\zeta} + \frac{\partial f_\zeta}{\partial \zeta}\sigma_{\zeta\zeta} + f_\zeta k_s d_\zeta\right)\ \mathrm{d}x\ \mathrm{d}\zeta = 0. \end{aligned} \tag{C.22}$$

The test functions $f_x(x,\zeta)$ and $f_\zeta(x,\zeta)$ are now approximated in terms of the same FE shape functions $\mathbf{N}(x,\zeta)$ that were used for the temperature and displacement fields

$$f_x(x,\zeta) = \mathbf{f}_x^\top \mathbf{N}^\top(x,\zeta), \qquad f_\zeta(x,\zeta) = \mathbf{f}_\zeta^\top \mathbf{N}^\top(x,\zeta), \tag{C.23}$$

where $\mathbf{f}_x$ and $\mathbf{f}_\zeta$ denote the vectors of nodal values of the test functions. Inserting expressions for the stress components (C.16)–(C.18), the approximations for $T(x,\zeta,t)$, $d_x(x,\zeta,t)$, and $d_\zeta(x,\zeta,t)$ from (5.21) and (5.28), and the approximations for the test functions $f_x(x,\zeta)$ and $f_\zeta(x,\zeta)$ from (C.23) into (C.22), it follows that

$$\begin{bmatrix}\mathbf{f}_x\\ \mathbf{f}_\zeta\end{bmatrix}^\top \begin{bmatrix}\mathbf{K}_{xx} & \mathbf{K}_{x\zeta}\\ \mathbf{K}_{\zeta x} & \mathbf{K}_{\zeta\zeta}\end{bmatrix} \begin{bmatrix}\mathbf{d}_x(t)\\ \mathbf{d}_\zeta(t)\end{bmatrix} - \begin{bmatrix}\mathbf{f}_x\\ \mathbf{f}_\zeta\end{bmatrix}^\top \begin{bmatrix}\mathbf{L}_x\\ \mathbf{L}_\zeta\end{bmatrix} \boldsymbol{\theta}(t) = 0, \tag{C.24}$$

with $\mathbf{K}_{xx}$, $\mathbf{K}_{x\zeta}$, $\mathbf{K}_{\zeta x}$, $\mathbf{K}_{\zeta\zeta}$, $\mathbf{L}_x$, and $\mathbf{L}_\zeta$ as in (5.31)–(5.35). As this equation must hold for all $\mathbf{f}_x$ and $\mathbf{f}_\zeta$, (5.29) now follows with the definitions in (5.30)–(5.35).

C.3.2 Explicit expressions for the derivatives of f and g

The cost functional $J = J_1$ with J_1 as in (5.42) can be written in the form (5.49) by setting

$$f(\mathbf{d}(t)) = 2\mathbf{1}^\top \mathbf{E}_0 \left[\mathbf{d}_x^2(t) + \mathbf{d}_\zeta^2(t) - \mathbf{d}_{\max}^2\right]^+, \tag{C.25}$$

and $g(\mathbf{B}, u(t)) = 0$. The derivative of f w.r.t. $\mathbf{d} = [\mathbf{d}_x^\top, \mathbf{d}_\zeta^\top]^\top$ is

$$\frac{\partial f}{\partial \mathbf{d}}(\mathbf{d}(t)) = 4 \begin{bmatrix}\mathbf{d}_x(t) \circ \mathbf{1}^+(t) \circ \mathbf{E}_0\mathbf{1}\\ \mathbf{d}_\zeta(t) \circ \mathbf{1}^+(t) \circ \mathbf{E}_0\mathbf{1}\end{bmatrix}^\top, \tag{C.26}$$

where $\circ$ denotes the component-wise (Hadamard) product of vectors and the i-th component of $\mathbf{1}^+(t)$ is

$$\mathbf{1}_i^+(t) = \begin{cases} 1 & \text{when } \mathbf{d}_{x,i}^2(t) + \mathbf{d}_{\zeta,i}^2(t) - \mathbf{d}_{\max,i}^2 \geq 0,\\ 0 & \text{otherwise.}\end{cases} \tag{C.27}$$

where $\mathbf{d}_{x,i}(t)$, $\mathbf{d}_{\zeta,i}(t)$, and $\mathbf{d}_{\max,i}(t)$ are the i-th components of $\mathbf{d}_x(t)$, $\mathbf{d}_\zeta(t)$, and $\mathbf{d}_{\max}(t)$, respectively.

Differentiating (C.26) again to $\mathbf{d}$ yields the Hessian

$$\frac{\partial^2 f}{\partial \mathbf{d}^2}(\mathbf{d}(t)) = 4 \begin{bmatrix}\operatorname{diag}(\mathbf{1}^+(t) \circ \mathbf{E}_0\mathbf{1}) & 0\\ 0 & \operatorname{diag}(\mathbf{1}^+(t) \circ \mathbf{E}_0\mathbf{1})\end{bmatrix}, \tag{C.28}$$

where $\operatorname{diag}(\mathbf{v})$ denotes a matrix with the components of the vector $\mathbf{v}$ on the diagonal.

The cost functional $J = J_0 + wJ_2$ with J_0 and J_2 as in (5.39) and (5.43) can be written in the form (5.49) by setting

$$f(\mathbf{d}(t)) = 2w\mathbf{1}^\top \mathbf{E}_0 \left(\left(\frac{\mathbf{d}_{\max}^2}{\mathbf{d}_{\max}^2 - \mathbf{d}_x^2(t) - \mathbf{d}_\zeta^2(t)} \right)^p - \mathbf{1} \right), \tag{C.29}$$

$$g(\mathbf{B}, u(t)) = 2u^\top(t)\mathbf{B}^\top \mathbf{E}_0 \mathbf{B} u(t). \tag{C.30}$$

The derivative of f w.r.t. $\mathbf{d} = [\mathbf{d}_x^\top, \mathbf{d}_\zeta^\top]^\top$ is

$$\frac{\partial f}{\partial \mathbf{d}}(\mathbf{d}(t)) = 4w \begin{bmatrix} \mathbf{d}_x(t) \circ \mathbf{a}(t) \circ \mathbf{E}_0\mathbf{1} \\ \mathbf{d}_\zeta(t) \circ \mathbf{a}(t) \circ \mathbf{E}_0\mathbf{1} \end{bmatrix}^\top, \tag{C.31}$$

with

$$\mathbf{a}(t) = p \left(\frac{\mathbf{d}_{\max}^2}{\mathbf{d}_{\max}^2 - \mathbf{d}_x^2(t) - \mathbf{d}_\zeta^2(t)} \right)^{p+1} \circ \frac{\mathbf{1}}{\mathbf{d}_{\max}^2}, \tag{C.32}$$

where $\circ$ again denotes the component-wise Hadamard product of vectors and the operations $\cdot \,/\, \cdot$, $(\,\cdot\,)^2$ and $(\,\cdot\,)^p$ are again applied component-wise.

To obtain the Hessian of f note that

$$\frac{\partial^2 f}{\partial \mathbf{d}^2}(\mathbf{d}(t)) = \begin{bmatrix} \frac{\partial^2 f}{\partial \mathbf{d}_x^2}(\mathbf{d}(t)) & \frac{\partial^2 f}{\partial \mathbf{d}_x \partial \mathbf{d}_\zeta}(\mathbf{d}(t)) \\ \frac{\partial^2 f}{\partial \mathbf{d}_x \partial \mathbf{d}_\zeta}(\mathbf{d}(t)) & \frac{\partial^2 f}{\partial \mathbf{d}_\zeta^2}(\mathbf{d}(t)) \end{bmatrix}. \tag{C.33}$$

By differentiating the top part of (C.31) w.r.t. $\mathbf{d}_x$, we see that $\partial^2 f / \partial \mathbf{d}_x^2$ is a diagonal matrix with diagonal equal to

$$4w \left(\mathbf{a}(t) + 2(p+1)\mathbf{a}(t) \circ \frac{\mathbf{d}_x^2(t)}{\mathbf{b}(t)} \right) \circ \mathbf{E}_0\mathbf{1}, \tag{C.34}$$

where $\mathbf{b}(t) = \mathbf{d}_{\max}^2 - \mathbf{d}_x^2(t) - \mathbf{d}_\zeta^2(t)$. Similarly, the diagonal entries of $\partial^2 f / \partial \mathbf{d}_x \partial \mathbf{d}_\zeta$ and $\partial^2 f / \partial \mathbf{d}_\zeta^2$ are

$$4w \left(2(p+1)\mathbf{a}(t) \circ \frac{\mathbf{d}_x(t) \circ \mathbf{d}_\zeta(t)}{\mathbf{b}(t)} \right) \circ \mathbf{E}_0\mathbf{1}, \tag{C.35}$$

$$4w \left(\mathbf{a}(t) + 2(p+1)\mathbf{a}(t) \circ \frac{\mathbf{d}_\zeta^2(t)}{\mathbf{b}(t)} \right) \circ \mathbf{E}_0\mathbf{1}. \tag{C.36}$$

The derivatives and Hessians of the g in (C.30) in the point $(\mathbf{B}, u(t))$ are

$$\frac{\partial g}{\partial \mathbf{B}} = 4u^2(t)\mathbf{B}^\top \mathbf{E}_0, \qquad \frac{\partial^2 g}{\partial \mathbf{B}^2} = 4u^2(t)\mathbf{E}_0, \tag{C.37}$$

$$\frac{\partial g}{\partial u} = 4u(t)\mathbf{B}^\top \mathbf{E}_0 \mathbf{B}, \qquad \frac{\partial^2 g}{\partial u^2} = 4\mathbf{B}^\top \mathbf{E}_0 \mathbf{B}. \tag{C.38}$$

C.3.3 The gradient w.r.t. B

To derive the formula (5.54) for the gradient $\nabla_{\mathbf{B}} J(\mathbf{B}, u)$ of the cost functional J in (5.44), consider a perturbation $\tilde{\mathbf{B}}$ of $\mathbf{B}$. From (5.23), it follows that changing $\mathbf{B}$ to $\mathbf{B} + \tilde{\mathbf{B}}$ changes the state $\boldsymbol{\theta}(t)$ to $\boldsymbol{\theta}(t) + \tilde{\boldsymbol{\theta}}(t)$, where $\tilde{\boldsymbol{\theta}}(t)$ is the solution of

$$\mathbf{E}\dot{\tilde{\boldsymbol{\theta}}}(t) = \mathbf{A}\tilde{\boldsymbol{\theta}}(t) + \mathbf{E}_{\mathbf{B}}\tilde{\mathbf{B}}u(t), \qquad \tilde{\boldsymbol{\theta}}(0) = \mathbf{0}. \tag{C.39}$$

Using the definition of the gradient (5.52) and the form of the cost function (5.44), it follows that

$$\begin{aligned}
\langle \nabla_{\mathbf{B}} J(\mathbf{B}, u), \tilde{\mathbf{B}} \rangle_B &= \lim_{\varepsilon \to 0} \frac{J(\mathbf{B} + \varepsilon\tilde{\mathbf{B}}, u) - J(\mathbf{B}, u)}{\varepsilon} \\
&= \lim_{\varepsilon \to 0} \int_0^{t_e} \frac{\bar{f}(\boldsymbol{\theta}(t) + \varepsilon\tilde{\boldsymbol{\theta}}(t)) - \bar{f}(\boldsymbol{\theta}(t))}{\varepsilon}\, \mathrm{d}t \\
&\qquad + \int_0^{t_e} \frac{g(\mathbf{B} + \varepsilon\tilde{\mathbf{B}}, u(t)) - g(\mathbf{B}, u(t))}{\varepsilon}\, \mathrm{d}t \\
&= \int_0^{t_e} \left(\frac{\partial \bar{f}}{\partial \boldsymbol{\theta}}(\boldsymbol{\theta}(t))\tilde{\boldsymbol{\theta}}(t) + \frac{\partial g}{\partial \mathbf{B}}(\mathbf{B}, u(t))\tilde{\mathbf{B}} \right) \mathrm{d}t.
\end{aligned} \tag{C.40}$$

With $\boldsymbol{\varphi}(t)$ the adjoint state as in (5.48), it follows that

$$\begin{aligned}
0 = {} & \boldsymbol{\varphi}^\top(t)\mathbf{E}\tilde{\boldsymbol{\theta}}(t)\Big|_{t=0}^{t_e} \\
&= \int_0^{t_e} \left(\dot{\boldsymbol{\varphi}}^\top(t)\mathbf{E}\tilde{\boldsymbol{\theta}}(t) + \boldsymbol{\varphi}^\top(t)\mathbf{E}\dot{\tilde{\boldsymbol{\theta}}}(t) \right) \mathrm{d}t \\
&= -\int_0^{t_e} \frac{\partial \bar{f}}{\partial \boldsymbol{\theta}}(\boldsymbol{\theta}(t))\tilde{\boldsymbol{\theta}}(t)\, \mathrm{d}t + \int_0^{t_e} \boldsymbol{\varphi}^\top(t)\mathbf{E}_{\mathbf{B}}\tilde{\mathbf{B}}u(t)\, \mathrm{d}t,
\end{aligned} \tag{C.41}$$

where the last identity follows after substitution of (5.48) and (C.39) for $\mathbf{E}^\top\dot{\boldsymbol{\varphi}}(t)$ and $\mathbf{E}\dot{\tilde{\boldsymbol{\theta}}}(t)$, respectively. Using (C.41) to replace the first term in (C.40), it follows

$$\begin{aligned}
\langle \nabla_{\mathbf{B}} J(\mathbf{B}, u), \tilde{\mathbf{B}} \rangle_B &= \int_0^{t_e} \left(\boldsymbol{\varphi}^\top(t)\mathbf{E}_{\mathbf{B}}\tilde{\mathbf{B}}u(t) + \frac{\partial g}{\partial \mathbf{B}}(\mathbf{B}, u(t))\tilde{\mathbf{B}} \right) \mathrm{d}t \\
&= \left\langle \mathbf{E}_0^{-1} \int_0^{t_e} \left[\mathbf{E}_{\mathbf{B}}\boldsymbol{\varphi}(t)u(t) + \left[\frac{\partial g}{\partial \mathbf{B}}(\mathbf{B}, u(t)) \right]^\top \right] \mathrm{d}t, \tilde{\mathbf{B}} \right\rangle_B,
\end{aligned} \tag{C.42}$$

where the last identity follows because $u(t)$ is scalar and from the definition of the inner product $\langle \cdot\,, \cdot \rangle_B$ in (5.53).

Since (C.42) holds for all perturbations $\tilde{\mathbf{B}}$, (5.54) follows.

C.3.4 Computation of the Hessians

To compute $H_{\mathbf{B}}$, the second derivative of the function $h \mapsto J(\mathbf{B} + h\tilde{\mathbf{B}}, u)$ is computed as

$$\begin{aligned} H_{\mathbf{B}} &= \frac{\partial^2}{\partial h^2}\left(J(\mathbf{B}+h\tilde{\mathbf{B}},u)\right)\Big|_{h=0} \\ &= \frac{\partial^2}{\partial h^2}\int_0^{t_e}\left(\bar{f}(\boldsymbol{\theta}(t)+h\tilde{\boldsymbol{\theta}}(t))+g(\mathbf{B}+h\tilde{\mathbf{B}},u(t))\right)\,\mathrm{d}t\Big|_{h=0} \\ &= \int_0^{t_e}\left(\tilde{\boldsymbol{\theta}}^\top(t)\frac{\partial^2\bar{f}}{\partial\boldsymbol{\theta}^2}(\boldsymbol{\theta}(t))\tilde{\boldsymbol{\theta}}(t)+\tilde{\mathbf{B}}^\top\frac{\partial^2 g}{\partial\mathbf{B}^2}(\mathbf{B},u(t))\tilde{\mathbf{B}}\right)\,\mathrm{d}t. \end{aligned} \tag{C.43}$$

where $\tilde{\boldsymbol{\theta}}(t)$ is the solution of (C.39), i.e. $\tilde{\boldsymbol{\theta}}(t)$ is the change in state due to the perturbation $\tilde{\mathbf{B}}$. The Hessian $H_{\mathbf{B}}$ in the point $(\mathbf{B}_0, u_0)$ for the direction $\tilde{\mathbf{B}}$ can thus be computed in the following steps:

1) compute $\boldsymbol{\theta}_0(t)$ as the solution of (5.23) with $\mathbf{B} = \mathbf{B}_0$ and $u(t) = u_0(t)$ by integrating forward in time starting from the initial condition $\boldsymbol{\theta}(0) = \mathbf{0}$,
2) compute $\tilde{\boldsymbol{\theta}}_0(t)$ from (C.39) with $u(t) = u_0(t)$,
3) evaluate the integral in (C.43) with $\mathbf{B} = \mathbf{B}_0$, $u(t) = u_0(t)$, $\boldsymbol{\theta}(t) = \boldsymbol{\theta}_0(t)$, and $\tilde{\boldsymbol{\theta}}(t) = \tilde{\boldsymbol{\theta}}_0(t)$.

To compute $H_{\mathbf{B}}$ for a cost functional of the form (5.49), observe that it follows from (5.50) that

$$\frac{\partial^2\bar{f}}{\partial\boldsymbol{\theta}^2}(\boldsymbol{\theta}(t)) = \mathbf{M}^\top\frac{\partial^2 f}{\partial\mathbf{d}^2}(\boldsymbol{\theta}(t))\mathbf{M}, \tag{C.44}$$

where $\mathbf{M} = \mathbf{S}^\top\left(\mathbf{S}\mathbf{K}\mathbf{S}^\top\right)^{-1}\mathbf{S}\mathbf{L}$. Explicit expressions for $\partial^2 f/\partial\mathbf{d}^2$ are given in Appendix C.3.2.

The Hessian of a cost function J of the form (5.44) in the direction $\hat{u}(t)$ is

$$\begin{aligned} H_u &= \frac{\partial^2}{\partial h^2}\left(J(\mathbf{B},u+h\hat{u})\right)\Big|_{h=0} \\ &= \int_0^{t_e}\left(\hat{\boldsymbol{\theta}}^\top(t)\frac{\partial^2\bar{f}}{\partial\boldsymbol{\theta}^2}(\boldsymbol{\theta}(t))\hat{\boldsymbol{\theta}}(t)+\hat{u}^2(t)\frac{\partial^2 g}{\partial u^2}(\mathbf{B},u(t))\right)\,\mathrm{d}t, \end{aligned} \tag{C.45}$$

where $\hat{\boldsymbol{\theta}}(t)$ is the change in state due to the perturbation $\hat{u}(t)$, i.e. $\hat{\boldsymbol{\theta}}(t)$ is the solution of

$$\mathbf{E}\dot{\hat{\boldsymbol{\theta}}}(t) = \mathbf{A}\hat{\boldsymbol{\theta}}(t) + \mathbf{E}_{\mathbf{B}}\mathbf{B}\hat{u}(t), \qquad \hat{\boldsymbol{\theta}}(0) = \mathbf{0}. \tag{C.46}$$

The Hessian H_u in the point $(\mathbf{B}_0, u_0)$ for the direction $\tilde{u}(t)$ can thus be computed in the following steps:

1) compute $\boldsymbol{\theta}_0(t)$ as the solution of (5.23) with $\mathbf{B} = \mathbf{B}_0$ and $u(t) = u_0(t)$ by integrating forward in time starting from the initial condition $\boldsymbol{\theta}(0) = \mathbf{0}$,

2) compute $\hat{\boldsymbol{\theta}}_0(t)$ from (C.46) with $\mathbf{B} = \mathbf{B}_0$,

3) evaluate the integral in (C.45) with $\mathbf{B} = \mathbf{B}_0$, $u(t) = u_0(t)$, $\boldsymbol{\theta}(t) = \boldsymbol{\theta}_0(t)$, and $\hat{\boldsymbol{\theta}}(t) = \hat{\boldsymbol{\theta}}_0(t)$.

C.3.5 Time Discretization

This subsection summarizes the time discretization of the cost functional (5.44), state equation (5.23), adjoint state equation (5.48), and the gradients (5.47) and (5.54) following the method in [Apel and Flaig, 2012] that leads to discretely consistent gradients. In other words, the results obtained after discretizing the continuous-time gradients in (5.47) and (5.54) by this scheme are equal to the expressions obtained by directly computing the gradients of the (time-)discretized cost functionals.

Consider a uniform grid of $N+1$ grid points $t_k = k\tau$ for $k = 0, 1, \ldots, N$ where $\tau = t_e/N$. The state equation (5.23) is discretized with the Crank-Nicolson method [Crank and Nicolson, 1947], which leads to

$$\mathbf{E}\frac{\boldsymbol{\theta}_{k+1} - \boldsymbol{\theta}_k}{\tau} = \mathbf{A}\frac{\boldsymbol{\theta}_{k+1} + \boldsymbol{\theta}_k}{2} + \mathbf{B}_{\exp} u_{\exp,k+1/2} + \mathbf{E}_{\mathbf{B}}\mathbf{B} u_{k+1/2}, \quad \boldsymbol{\theta}_0 = \mathbf{0}, \tag{C.47}$$

where the state vector is sampled in the grid point t_k as $\boldsymbol{\theta}_k = \boldsymbol{\theta}(t_k)$, and the mean values of the input appear naturally as $u_{\exp,k+1/2} = (u_{\exp}(t_k) + u_{\exp}(t_{k+1}))/2$, and $u_{k+1/2} = (u(t_k) + u(t_{k+1}))/2$. The cost functional (5.44) is discretized using the trapezoid rule for the state-dependent part and the midpoint rule for the part dependent on $\mathbf{B}$ and $u(t)$

$$J^\tau = \tau \sum_{k=0}^{N-1} \left[\frac{\bar{f}(\boldsymbol{\theta}_{k+1}) + \bar{f}(\boldsymbol{\theta}_k)}{2} + g(\mathbf{B}, u_{k+1/2}) \right]. \tag{C.48}$$

To find an expression of the discretely consistent gradient, the Lagrangian for the discretized problem is formed as

$$\begin{aligned} \mathcal{L}^\tau = \tau \sum_{k=0}^{N-1} \left[\frac{\bar{f}(\boldsymbol{\theta}_{k+1}) + \bar{f}(\boldsymbol{\theta}_k)}{2} + g(\mathbf{B}, u_{k+1/2}) \right] - \boldsymbol{\varphi}_0^\top \mathbf{E}\boldsymbol{\theta}_0 + \\ \tau \sum_{k=0}^{N-1} \boldsymbol{\varphi}_{k+1/2}^\top \left[\mathbf{A}\frac{\boldsymbol{\theta}_{k+1} + \boldsymbol{\theta}_k}{2} + \mathbf{B}_{\exp} u_{\exp,k+1/2} + \mathbf{E}_{\mathbf{B}}\mathbf{B} u_{k+1/2} - \mathbf{E}\frac{\boldsymbol{\theta}_{k+1} - \boldsymbol{\theta}_k}{\tau} \right], \end{aligned} \tag{C.49}$$

where $\boldsymbol{\varphi}_0$ and $\boldsymbol{\varphi}_{k+1/2}$ are the (discretized) Lagrange multipliers.

Note that derivatives of $\mathcal{L}^\tau$ in (C.49) w.r.t. $\boldsymbol{\varphi}_0$ and $\boldsymbol{\varphi}_{k+1/2}$ are zero precisely when (C.47) holds. Requiring that the derivatives of $\mathcal{L}^\tau$ w.r.t. $\boldsymbol{\theta}_k$ are zero yields

equations for the adjoint state variables $\boldsymbol{\varphi}_{k+1/2}$ and $\boldsymbol{\varphi}_0$. For $k = N$, the obtained equation is

$$\mathbf{0}^\top = \frac{\partial \mathcal{L}^\tau}{\partial \boldsymbol{\theta}_N} = \frac{\tau}{2}\frac{\partial \bar{f}}{\partial \boldsymbol{\theta}}(\boldsymbol{\theta}_N) + \frac{\tau}{2}\boldsymbol{\varphi}_{N-1/2}^\top \mathbf{A} - \boldsymbol{\varphi}_{N-1/2}^\top \mathbf{E}. \tag{C.50}$$

Note that $\boldsymbol{\varphi}_{N-1/2}$ can be solved from this equation. Requiring that the derivatives of $\mathcal{L}^\tau$ w.r.t. $\boldsymbol{\theta}_k$ are zero for $0 < k < N$, it follows that

$$\mathbf{0}^\top = \frac{\partial \mathcal{L}^\tau}{\partial \boldsymbol{\theta}_k} = \tau\frac{\partial \bar{f}}{\partial \boldsymbol{\theta}}(\boldsymbol{\theta}_k) + \frac{\tau}{2}(\boldsymbol{\varphi}_{k-1/2} + \boldsymbol{\varphi}_{k+1/2})^\top \mathbf{A} - (\boldsymbol{\varphi}_{k-1/2} - \boldsymbol{\varphi}_{k+1/2})^\top \mathbf{E}. \tag{C.51}$$

Note that this is an equation from which $\boldsymbol{\varphi}_{k-1/2}$ can be solved using $\boldsymbol{\varphi}_{k+1/2}$. Setting the derivative of $\mathcal{L}^\tau$ w.r.t. $\boldsymbol{\theta}_k$ to zero for $k = 0$, it follows that

$$\mathbf{0}^\top = \frac{\partial \mathcal{L}^\tau}{\partial \boldsymbol{\theta}_0} = \frac{\tau}{2}\frac{\partial \bar{f}}{\partial \boldsymbol{\theta}}(\boldsymbol{\theta}_0) + \frac{\tau}{2}\boldsymbol{\varphi}_{1/2}^\top \mathbf{A} - (\boldsymbol{\varphi}_0 - \boldsymbol{\varphi}_{1/2})^\top \mathbf{E}. \tag{C.52}$$

Note that $\boldsymbol{\varphi}_0$ can be determined from this equation. However, it turns out that $\boldsymbol{\varphi}_0$ does not appear in the expressions for the gradients below, so that this equation does not need to be considered further. Taking the transpose and rearranging (C.50) and (C.51), it follows that the discretized adjoint state variables $\boldsymbol{\varphi}_{k+1/2}$ $(k = 0, 1, 2, \ldots N-1)$ can be computed starting from the solution of

$$\mathbf{E}^\top \frac{\boldsymbol{\varphi}_{N-1/2}}{\tau} = \mathbf{A}^\top \frac{\boldsymbol{\varphi}_{N-1/2}}{2} + \frac{1}{2}\left(\frac{\partial \bar{f}}{\partial \boldsymbol{\theta}}(\boldsymbol{\theta}_N)\right)^\top, \tag{C.53}$$

after which $\boldsymbol{\varphi}_{k-1/2}$ $(k = N-1, \ldots, 2, 1)$ can be solved iteratively from

$$\mathbf{E}^\top \frac{\boldsymbol{\varphi}_{k-1/2} - \boldsymbol{\varphi}_{k+1/2}}{\tau} = \mathbf{A}^\top \frac{\boldsymbol{\varphi}_{k-1/2} + \boldsymbol{\varphi}_{k+1/2}}{2} + \left(\frac{\partial \bar{f}}{\partial \boldsymbol{\theta}}(\boldsymbol{\theta}_k)\right)^\top. \tag{C.54}$$

Note that these equations indeed resemble a time-discretization of the equation for the adjoint state in continuous time in (5.48), but not the discretization of (5.48) that would be obtained based on the Crank-Nicolson scheme.

The *total* derivative of J^τ w.r.t. $u_{k+1/2}$ or $\mathbf{B}$ (i.e. the derivative in which the states $\boldsymbol{\theta}_k$ are considered as a function of $u_{k+1/2}$ and $\mathbf{B}$) can be found using the *partial* derivative of $\mathcal{L}^\tau$ w.r.t. $u_{k+1/2}$ or $\mathbf{B}$. To see how, note that if (C.47) holds (i.e. if $\partial \mathcal{L}^\tau / \partial \boldsymbol{\varphi}_{k+1/2} = 0$ and $\partial \mathcal{L}^\tau / \partial \boldsymbol{\varphi}_0 = 0$), it follows from (C.48) and (C.49) that $J^\tau = \mathcal{L}^\tau$. In particular, when (C.47) holds, the total derivative of $\mathcal{L}^\tau$ (w.r.t. $u_{k+1/2}$ or $\mathbf{B}$) is thus equal to the total derivative of J^τ (w.r.t. $u_{k+1/2}$ or $\mathbf{B}$). When $\partial \mathcal{L}^\tau / \partial \boldsymbol{\theta}_k = 0$, $\partial \mathcal{L}^\tau / \partial \boldsymbol{\varphi}_{k+1/2} = 0$, and $\partial \mathcal{L}^\tau / \partial \boldsymbol{\varphi}_0 = 0$, the total derivative of $\mathcal{L}^\tau$ w.r.t. $u_{k+1/2}$ or $\mathbf{B}$ reduces to the partial derivative of $\mathcal{L}^\tau$ w.r.t. $u_{k+1/2}$ or $\mathbf{B}$, respectively. The derivation above has demonstrated that (C.53) and (C.54) hold precisely when $\partial \mathcal{L}^\tau / \partial \boldsymbol{\theta}_k = 0$. It thus follows that

$$\frac{\mathrm{d}J^\tau}{\mathrm{d}u_{k+1/2}} = \frac{\partial \mathcal{L}^\tau}{\partial u_{k+1/2}}, \qquad \frac{\mathrm{d}J^\tau}{\mathrm{d}\mathbf{B}} = \frac{\partial \mathcal{L}^\tau}{\partial \mathbf{B}}, \tag{C.55}$$

when (C.47), (C.53), and (C.54) hold. Taking the partial derivatives of $\mathcal{L}^\tau$ in (C.49) now shows that

$$\frac{\mathrm{d}J^\tau}{\mathrm{d}u_{k+1/2}} = \frac{\partial \mathcal{L}^\tau}{\partial u_{k+1/2}} = \tau \frac{\partial g}{\partial u}(\mathbf{B}, u_{k+1/2}) + \tau \boldsymbol{\varphi}_{k+1/2}^\top \mathbf{E}_{\mathbf{B}} \mathbf{B}, \tag{C.56}$$

$$\frac{\mathrm{d}J^\tau}{\mathrm{d}\mathbf{B}} = \frac{\partial \mathcal{L}^\tau}{\partial \mathbf{B}} = \tau \sum_{k=0}^{N-1} \frac{\partial g}{\partial \mathbf{B}}(\mathbf{B}, u_{k+1/2}) + \tau \sum_{k=0}^{N-1} \boldsymbol{\varphi}_{k+1/2}^\top \mathbf{E}_{\mathbf{B}} u_{k+1/2}. \tag{C.57}$$

The gradients of J^τ w.r.t. to $u_{k+1/2}$ and $\mathbf{B}$ w.r.t. the (discretized) inner products $\tau \sum_{k=0}^{N-1} u_{k+1/2}^{(1)} u_{k+1/2}^{(2)}$ and $\mathbf{B}_1^\top \mathbf{E}_0 \mathbf{B}_2$ follow from these expressions as

$$(\nabla_u J^\tau)_{k+1/2} = \frac{1}{\tau} \left(\frac{\mathrm{d}J^\tau}{\mathrm{d}u_{k+1/2}} \right)^\top = \mathbf{B}^\top \mathbf{E}_{\mathbf{B}} \boldsymbol{\varphi}_{k+1/2} + \frac{\partial g}{\partial u}(\mathbf{B}, u_{k+1/2}), \tag{C.58}$$

$$\nabla_{\mathbf{B}} J^\tau = \mathbf{E}_0^{-1} \left(\frac{\mathrm{d}J^\tau}{\mathrm{d}\mathbf{B}} \right)^\top = \tau \mathbf{E}_0^{-1} \sum_{k=0}^{N-1} \left[\mathbf{E}_{\mathbf{B}} \boldsymbol{\varphi}_{k+1/2} u_{k+1/2} + \frac{\partial g}{\partial \mathbf{B}}(\mathbf{B}, u_{k+1/2}) \right]. \tag{C.59}$$

C.4 Three modifications of the design problem

This appendix considers three modifications of the design problem considered in Chapter 5 that are more representative for the wafer heating problem. Recall that the scanning of a single field far from the edge of the wafer was considered in Chapter 5. This problem is modified in this appendix in the following ways:

1) Certain correctable shapes that result from adjustments in the positioning of the wafer stage and the mirrors will be included in the design of the optimal single-shape actuation heat load.

2) Instead of a single field, multiple fields will be considered.

3) Instead of a field far from the edge of the wafer, a single field near the edge of the wafer will be considered.

C.4.1 Including correctables

This subsection considers the combination of the optimal actuation heat load design with an error correction scheme. In the schematic representation in Figure 1.8b, this means that the gray arrow is considered in this appendix as well.

When an error correction scheme is applied, the quality of the lithographic process is not directly determined by the deformation of the wafer, but by the imaging error that remains after corrections in the rigid-body modes of the wafer stage and the mirrors have been applied. Such corrections can lead to

more than 10 distinct spatial shapes that can be used to correct the projected pattern [Merks, 2015]. The imaging quality is thus not directly determined by the displacement field components $d_x(x,\zeta,t)$ and $d_\zeta(x,\zeta,t)$ resulting from (5.4) and (5.6)–(5.7), but by

$$\begin{bmatrix} d_{c,x}(x,\zeta,t) \\ d_{c,\zeta}(x,\zeta,t) \end{bmatrix} = \begin{bmatrix} d_x(x,\zeta,t) \\ d_\zeta(x,\zeta,t) \end{bmatrix} - \begin{bmatrix} \mathbf{N}_{c,x}(x,\zeta) \\ \mathbf{N}_{c,\zeta}(x,\zeta) \end{bmatrix} \mathbf{c}(t), \qquad (x,\zeta) \in \Omega_{\text{slit}}, \tag{C.60}$$

where $d_{c,x}(x,\zeta,t)$ and $d_{c,\zeta}(x,\zeta,t)$ are the x- and ζ-components of the corrected displacement field, respectively, $\mathbf{N}_{c,x}(x,\zeta), \mathbf{N}_{c,\zeta}(x,\zeta) : \Omega_{\text{slit}} \to \mathbb{R}^{1\times c}$ are (row) vectors containing the x- and ζ-components of the c spatial shapes of the corrections, and $\mathbf{c}(t) : [0,t_e] \to \mathbb{R}^c$ is the (column) vector containing the intensity of each correction.

Note, however, that these correctable shapes influence the projection of the pattern onto the wafer but that they cannot be used to prevent slip between the wafer and its supporting structure. The constraints on the wafer deformation are thus

$$d_{c,x}^2(x,\zeta,t) + d_{c,\zeta}^2(x,\zeta,t) \leq \delta_{\text{slit}}^2, \qquad (x,\zeta) \in \Omega_{\text{slit}}, t \in [0,t_e], \tag{C.61}$$

$$d_x^2(x,\zeta,t) + d_\zeta^2(x,\zeta,t) \leq \delta_{\text{slip}}^2, \qquad (x,\zeta) \in \mathbb{R}^2, t \in [0,t_e]. \tag{C.62}$$

The optimization problem is now thus to minimize J_0 in (5.11) subject to the inequality constraints, (5.14), (C.61), and (C.62), the equality constraints (5.13), (5.12), and (C.60), and the physical model (5.4) and (5.6)–(5.7). After considering the equality constraints and the physical model, this can be written as an optimization problem in $B(x,\zeta)$, $u(t)$, and $\mathbf{c}(t)$.

A similar approach as in Subsection 5.2.3 is used, but an admissible solution satisfying (C.61) and (C.62) is now found by minimizing

$$\begin{aligned} J_1 = &\int_0^{t_e} \iint_{\mathbb{R}^2} \left[d_x^2(x,\zeta,t) + d_\zeta^2(x,\zeta,t) - \delta_{\text{slip}}^2\right]^+ \,\mathrm{d}x\,\mathrm{d}\zeta\,\mathrm{d}t \\ &+ \int_0^{t_e} \iint_{\Omega_{\text{slit}}} \left[d_{c,x}^2(x,\zeta,t) + d_{c,\zeta}^2(x,\zeta,t) - \delta_{\text{slit}}^2\right]^+ \,\mathrm{d}x\,\mathrm{d}\zeta\,\mathrm{d}t, \end{aligned} \tag{C.63}$$

and the barrier function is now defined as

$$\begin{aligned} J_2 = &\int_0^{t_e} \iint_{\mathbb{R}^2} \left(\left(\frac{\delta_{\text{slip}}^2}{\delta_{\text{slip}}^2 - d_x^2(x,\zeta,t) - d_\zeta^2(x,\zeta,t)} \right)^p - 1 \right) \,\mathrm{d}x\,\mathrm{d}\zeta\,\mathrm{d}t + \\ &\int_0^{t_e} \iint_{\Omega_{\text{slit}}} \left(\left(\frac{\delta_{\text{slit}}^2}{\delta_{\text{slit}}^2 - d_{c,x}^2(x,\zeta,t) - d_{c,\zeta}^2(x,\zeta,t)} \right)^p - 1 \right) \,\mathrm{d}x\,\mathrm{d}\zeta\,\mathrm{d}t. \end{aligned} \tag{C.64}$$

The FE element method is again used to approximate the solutions of the PDEs (5.4) and (5.6)–(5.7). Discretization of (C.63) and (C.64) by nodal interpolation

yields

$$J_1 = 2\int_0^{t_e} \mathbf{1}^\top \mathbf{E}_0 \left[\mathbf{d}_x^2(t) + \mathbf{d}_\zeta^2(t) - \delta_{\text{slip}}^2 \mathbf{1}\right]^+ \,\mathrm{d}t + 2\int_0^{t_e} \mathbf{1}^\top \mathbf{E}_{\text{slit}} \left[\mathbf{d}_{c,x}^2(t) + \mathbf{d}_{c,\zeta}^2(t) - \delta_{\text{slit}}^2 \mathbf{1}\right]^+ \,\mathrm{d}t, \quad \text{(C.65)}$$

$$J_2 = 2\int_0^{t_e} \mathbf{1}^\top \mathbf{E}_0 \left(\left(\frac{\delta_{\text{slip}}^2 \mathbf{1}}{\delta_{\text{slip}}^2 \mathbf{1} - \mathbf{d}_x^2(t) - \mathbf{d}_\zeta^2(t)}\right)^p - \mathbf{1}\right) \,\mathrm{d}t + 2\int_0^{t_e} \mathbf{1}^\top \mathbf{E}_{\text{slit}} \left(\left(\frac{\delta_{\text{slit}}^2 \mathbf{1}}{\delta_{\text{slit}}^2 \mathbf{1} - \mathbf{d}_{c,x}^2(t) - \mathbf{d}_{c,\zeta}^2(t)}\right)^p - \mathbf{1}\right) \,\mathrm{d}t, \quad \text{(C.66)}$$

where $\mathbf{E}_{\text{slit}} = \mathbf{E}_0 - \mathbf{E}_\mathbf{B}$ with $\mathbf{E}_0$ and $\mathbf{E}_\mathbf{B}$ as in (5.24) and (5.27), respectively, and

$$\mathbf{d}_{c,x}(t) = \mathbf{d}_x(t) - \mathbf{C}_x \mathbf{c}(t), \qquad \mathbf{d}_{c,\zeta}(t) = \mathbf{d}_\zeta(t) - \mathbf{C}_\zeta \mathbf{c}(t), \quad \text{(C.67)}$$

where $\mathbf{d}_x(t)$ and $\mathbf{d}_\zeta(t)$ are the nodal displacement field components, $\mathbf{d}_{c,x}(t)$ and $\mathbf{d}_{c,\zeta}(t)$ are the corrected nodal displacement field components, and $\mathbf{C}_x$ and $\mathbf{C}_\zeta$ are matrices containing the nodal values of the correctable shapes $\mathbf{N}_{c,x}$ and $\mathbf{N}_{c,\zeta}$, respectively. Note that entries of $\mathbf{C}_x$ and $\mathbf{C}_\zeta$ corresponding to nodes in elements that do not overlap with Ω_{slit} can be set to zero and that the operations $(\cdot)^2$, $[\cdot]^+$, $\cdot/\cdot$, $(\cdot)^p$ on vectors in (C.65) and (C.66) should be interpreted component-wise.

The optimization over $\mathbf{B}$, $u(t)$, and $\mathbf{c}(t)$ is implemented by modifying the algorithm from Subsection 5.3.3. The main difference is that after the updates for $\mathbf{B}$ and $u(t)$ also an update for $\mathbf{c}(t)$ is applied. The updates for $\mathbf{B}$ and $u(t)$ are computed similarly as before. Because J_1 and J_2 in (C.65) and (C.66) are very similar to J_1 and J_2 in (5.42) and (5.43), explicit formulas for the gradients $\nabla_u J$ and $\nabla_\mathbf{B} J$ and Hessians H_u and $H_\mathbf{B}$ will be omitted here. For the gradient $\nabla_\mathbf{c} J$ w.r.t. the corrections $\mathbf{c}(t)$, note that for a cost functional of the form $J = \int_0^{t_e} F(\mathbf{c}(t), t)\,\mathrm{d}t$, the definition of the gradient $\nabla_\mathbf{c}$ implies that for every perturbation $\tilde{\mathbf{c}}(t)$ of $\mathbf{c}(t)$

$$\langle \nabla_\mathbf{c} J(\mathbf{c}), \tilde{\mathbf{c}} \rangle_\mathbf{c} = \lim_{\varepsilon \to 0} \frac{J(\mathbf{c} + \varepsilon\tilde{\mathbf{c}}) - J(\mathbf{c})}{\varepsilon} = \int_0^{t_e} \frac{\partial F}{\partial \mathbf{c}}(\mathbf{c}(t), t)\tilde{\mathbf{c}}(t)\,\mathrm{d}t. \quad \text{(C.68)}$$

Choosing $\langle \cdot, \cdot \rangle_\mathbf{c}$ as the standard L^2-inner product thus shows that

$$\left(\nabla_\mathbf{c} J(\mathbf{c})\right)(t) = \left(\frac{\partial F}{\partial \mathbf{c}}(\mathbf{c}(t), t)\right)^\top. \quad \text{(C.69)}$$

For $\mathbf{B}$ and $u(t)$ fixed, J_1 and J_2 in (C.65) and (C.66) are written in the form $J = \int_0^{t_e} f(\mathbf{d}_c(t))\,\mathrm{d}t$, where $\mathbf{d}_c(t) = [\mathbf{d}_{c,x}(t), \mathbf{d}_{c,\zeta}(t)]^\top$. Using (C.69) and (C.67),

it now follows that

$$\begin{aligned}\nabla_{\mathbf{c}} J &= \left(\frac{\partial f}{\partial \mathbf{d}_{c,x}} \frac{\partial \mathbf{d}_{c,x}}{\partial \mathbf{c}} + \frac{\partial f}{\partial \mathbf{d}_{c,\zeta}} \frac{\partial \mathbf{d}_{c,\zeta}}{\partial \mathbf{c}} \right)^\top \\ &= -\mathbf{C}_x^\top \left(\frac{\partial f}{\partial \mathbf{d}_{c,x}}(\mathbf{d}_c(t)) \right)^\top - \mathbf{C}_\zeta^\top \left(\frac{\partial f}{\partial \mathbf{d}_{c,\zeta}}(\mathbf{d}_c(t)) \right)^\top . \end{aligned} \tag{C.70}$$

As the functions $f(\mathbf{d}_{\mathbf{c}}(t))$ that appear when J_1 and J_2 in (C.65) and (C.66) are written in the form $J = \int_0^{t_e} f(\mathbf{d}_c(t))\ \mathrm{d}t$ are of a form very similar to (C.25) and (C.29), the derivatives of f w.r.t. to $\mathbf{d}_{c,x}$ and $\mathbf{d}_{c,\zeta}$ are easily determined using the expressions in (C.26) and (C.31). To determine the stepsize in a certain update direction $\tilde{\mathbf{c}}(t)$, also $H_{\mathbf{c}}$, the second derivative of $h \mapsto J(\mathbf{c} + h\tilde{\mathbf{c}})$ is needed. For a cost functional of the form $J = \int_0^{t_e} F(\mathbf{c}(t), t)\ \mathrm{d}t$, it follows that

$$H_{\mathbf{c}} = \frac{\partial^2}{\partial h^2} \int_0^{t_e} F(\mathbf{c}(t) + h\tilde{\mathbf{c}}(t), t)\ \mathrm{d}t = \int_0^{t_e} \tilde{\mathbf{c}}^\top(t) \frac{\partial^2 F}{\partial \mathbf{c}^2}(\mathbf{c}(t), t) \tilde{\mathbf{c}}(t)\ \mathrm{d}t. \tag{C.71}$$

For a functional of the form $J = \int_0^{t_e} f(\mathbf{d}_c(t))\ \mathrm{d}t$ that only implicitly depends on $\mathbf{c}(t)$ through $\mathbf{d}_c(t)$, $H_{\mathbf{c}}$ can be obtained by substituting

$$\frac{\partial^2 F}{\partial \mathbf{c}^2}(\mathbf{c}(t), t) = \begin{bmatrix} \mathbf{C}_x \\ \mathbf{C}_\zeta \end{bmatrix}^\top \frac{\partial^2 f}{\partial \mathbf{d}_c^2}(\mathbf{d}_c(t)) \begin{bmatrix} \mathbf{C}_x \\ \mathbf{C}_\zeta \end{bmatrix}. \tag{C.72}$$

For J_1 and J_2 as in (C.65) and (C.66), expressions for $\partial^2 f / \partial \mathbf{d}_c^2$ follow easily using (C.28) and (C.33)–(C.36). Note that $\nabla_{\mathbf{c}} J$ and $H_{\mathbf{c}}$ can be computed with the adjoint state $\boldsymbol{\varphi}(t)$, which means that updating $\mathbf{c}(t)$ requires significantly less computational time than updating $\mathbf{B}$ or $u(t)$.

The resulting algorithm has been used to design a single-shape actuation heat load $B(x, \zeta)u(t)$ together with $c = 1$ or $c = 2$ correctable shapes. For the design with $c = 1$ correctable shape, only the translation in ζ-direction is considered, i.e. $C_x(x, \zeta) = 0$ and $C_\zeta(x, \zeta) = 1$. For the design with $c = 2$ correctable shapes, the translation in ζ-direction and a zoom in/zoom out correction are considered, i.e. $C_x(x, \zeta) = [0, x/\gamma]$ and $C_\zeta(x, \zeta) = [1, \zeta/\gamma]$ with $\gamma = \max_{(x,\zeta) \in \Omega_{\text{slit}}} \sqrt{x^2 + \zeta^2}$. Note that corrections in the translation in x-direction and in the rotation in the (x, ζ)-plane are not considered because their contribution will be zero due to symmetry of the problem in the line $x = 0$.

The optimal actuation heat load shapes $B(x, \zeta)$, the intensity of the applied actuation heat load $u(t)$, and the corrections $\mathbf{c}(t)$ for the two design problems are shown in Figure C.1. The considered parameters and the mesh are the same as in Section 5.4. The shapes of the actuation heat loads in Figure C.1 are clearly different from the shape designed without correctable shapes in Figure 5.5. In particular, there is less heating in front of the slit in Figure C.1a than in Figure 5.5, because a significant shift in ζ-direction of almost 2 nm is applied.

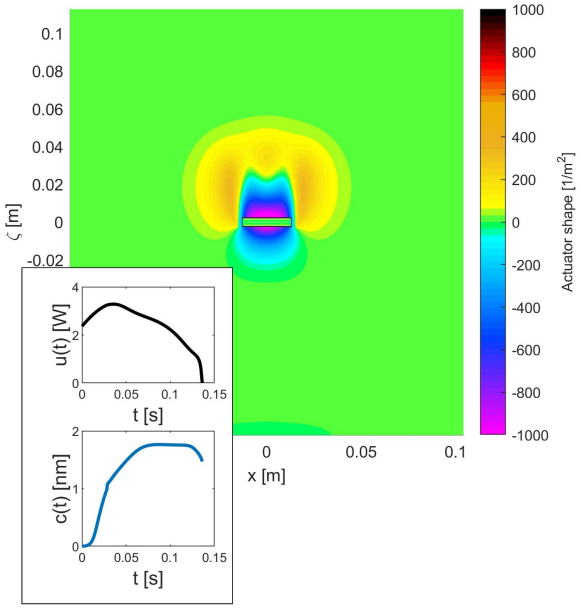

(a) 1 correctable shape

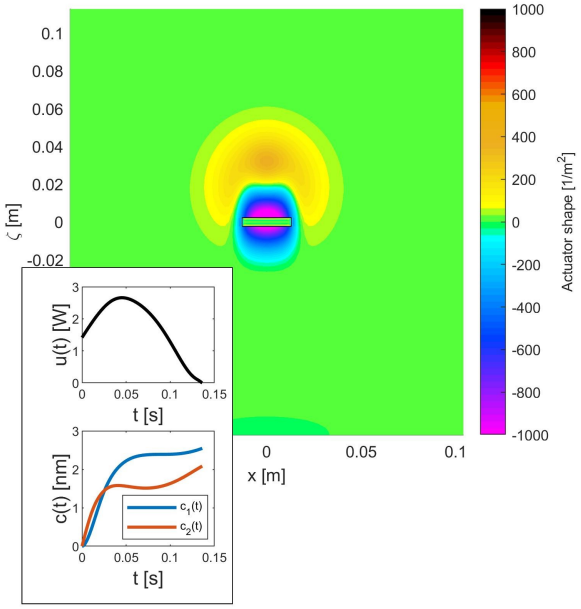

(b) 2 correctable shapes

Figure C.1. The designs obtained with $c = 1$ and $c = 2$ correctable shapes

Table C.1. Minima found after the optimization of the single-shape actuation heat load $B(x,\zeta)u(t)s$ and the corrections $\mathbf{c}(t)$

	$c=1$, initial guess 1	$c=1$, initial guess 2	$c=2$, initial guess 1	$c=2$, initial guess 2
$J_0 + wJ_2$	437	437	324	324
J_0	293	293	171	171
E_{act}	0.342	0.340	0.238	0.238

Table C.2. Iterations and times required for the optimization of the single-shape actuation heat load $B(x,\zeta)u(t)s$ and the corrections $\mathbf{c}(t)$

	minimizing J_1		minimizing $J_0 + wJ_2$	
	# iterations	time [s]	# iterations	time [s]
$c=1$, initial guess 1	6	10	504	1164
$c=1$, initial guess 2	5	13	357	821
$c=2$, initial guess 1	6	10	180	410
$c=2$, initial guess 2	3	6	186	435

The heating in Figure C.1a is mainly applied on the left and right side of the slit, which reduces the expansion in the x-direction. When also considering the zoom in/zoom out correction, the design in Figure C.1b is obtained. Because the expansion in the x-direction can be compensated (partially) by the zoom in/zoom out correction, the significant heating on the left and right side of the slit from Figure C.1a is no longer visible in this figure.

Some relevant data regarding the found minima is presented in Table C.1. This table clearly demonstrates that considering additional correctable shapes can significantly reduce the applied actuation heat load. In particular, compared to the designs with correctable shapes in Table 5.2, J_0 is reduced by almost a factor 4 and the applied heat E_{act} by more than a factor 2. To investigate the possible uniqueness of the minimizer, $B(x,\zeta)$, $u(t)$, and $\mathbf{c}(t)$ have been optimized starting from the initial guess in Figure 5.3a (initial guess 1) and from the initial guess in Figure 5.3b (initial guess 2). Table C.1 clearly shows that the same minimum is found for both initializations. This could also be verified graphically. As expected, Table C.2 shows that the number of iterations (# iterations for $\mathbf{B}$ + # iterations for $u(t)$ + # iterations for $\mathbf{c}(t)$) and the computational times are influenced by the initial guess.

C.4.2 The scanning of multiple fields

This subsection considers the design of an optimal actuation heat load for the scanning of multiple fields. The actuation heat load Q_{act} is still designed in a coordinate frame fixed to the slit. However, for the scanning of multiple fields, the definition of the coordinate system $(x, \zeta, t) = (x, y - vt, t)$ fixed to Q_{exp} used in Chapter 5 needs to be modified to

$$(\eta, \zeta, t) = (x - x_{\text{slit}}(t), y - y_{\text{slit}}(t), t), \tag{C.73}$$

where $(x_{\text{slit}}(t), y_{\text{slit}}(t))$ denotes the location of the center of the slit at time t (in the (x, y)-coordinate frame fixed to the wafer). The position of the center of the slit is a piece-wise affine function of the form (see also e.g. Figure 1.7)

$$\begin{bmatrix} x_{\text{slit}}(t) \\ y_{\text{slit}}(t) \end{bmatrix} = \begin{bmatrix} x_{\text{field},i} \\ y_{\text{field},i} + (-1)^{i-1} v(t - t_{\text{field}}/2 - (i-1)t_{\text{field}}) \end{bmatrix}, \tag{C.74}$$

for $t \in [(i-1)t_{\text{field}}, it_{\text{field}})$ with $i \in \mathbb{N}$ and $t_{\text{field}} = 0.136$ s is the time required to scan one field. Here, $(x_{\text{field},i}, y_{\text{field},i})$ is the location of the center of the i-th field and v is the velocity with which a field is scanned. Note that the direction in which a field is scanned alternates (due to the alternating scanning directions for the reticle, see Chapter 1) and that $x_{\text{slit}}(t)$ and $y_{\text{slit}}(t)$ will typically jump at the times $t = it_{\text{field}}$.

Using (C.74), the thermal model (5.1) is reformulated in (η, ζ)-coordinates (and for $t \in ((i-1)t_{\text{field}}, it_{\text{field}})$) as

$$\rho c H \left(\frac{\partial T}{\partial t} + (-1)^i v \frac{\partial T}{\partial \zeta} \right) = kH \left(\frac{\partial^2 T}{\partial \eta^2} + \frac{\partial^2 T}{\partial \zeta^2} \right) - h_c T + Q, \tag{C.75}$$

where the temperature field $T = T(\eta, \zeta, t)$ and the applied heat load $Q = Q(\eta, \zeta, t)$ are now expressed in (η, ζ)-coordinates and all other parameters are the same as in (5.1). Note that both the heat induced by the projection light and the single-shape actuation heat load have a fixed shape in the (η, ζ)-coordinate frame, i.e.

$$Q(\eta, \zeta, t) = B_{\text{exp}}(\eta, \zeta)\bar{u}_{\text{exp}} + B(\eta, \zeta)u(t). \tag{C.76}$$

To account for the jumps in the slit position at the times $t = it_{\text{field}}$, define

$$\begin{bmatrix} \Delta x_i \\ \Delta y_i \end{bmatrix} := \lim_{t \downarrow it_{\text{field}}} \begin{bmatrix} x_{\text{slit}}(t) \\ y_{\text{slit}}(t) \end{bmatrix} - \lim_{t \uparrow it_{\text{field}}} \begin{bmatrix} x_{\text{slit}}(t) \\ y_{\text{slit}}(t) \end{bmatrix}. \tag{C.77}$$

Because the temperature field in (x, y)-coordinates is a continuous function of time, the temperature field in (η, ζ)-coordinates jumps at $t = it_{\text{field}}$ as

$$\lim_{t \downarrow it_{\text{field}}} T(\eta, \zeta, t) = \lim_{t \uparrow it_{\text{field}}} T(\eta + \Delta x_i, \zeta + \Delta y_i, t). \tag{C.78}$$

These jumps in the temperature field of course lead to jumps the displacement field in (η, ζ)-coordinates as well. Note that (C.75) and (C.78) form an (infinite-dimensional) jump-flow system, see e.g. [Goebel et al., 2009].

The remainder of the optimization requires hardly any modifications compared to Section 5.2. The mechanical model in (η, ζ)-coordinates remains essentially of the same form as (5.6)-(5.7), only the derivatives w.r.t. x are replaced by derivatives w.r.t. η. The constraints (5.10), (5.13), and (5.14) and the cost functions J_0, J_1, and J_1 in (5.11), (5.17), and (5.19) are also easily reformulated in (η, ζ)-coordinates, essentially by replacing x by η. Also note that the length of the considered time interval t_e is now of course not t_{field} but $t_e = N_{\text{f}} t_{\text{field}}$, where N_{f} is the number of fields that are being scanned.

The spatial discretization is obtained based on a set of shape functions $\mathbf{N}(\eta, \zeta)$, which leads to a truncation of the unbounded spatial domain $(\eta, \zeta) \in \mathbb{R}^2$ to a bounded domain $(\eta, \zeta) \in \Omega$. In particular, a Galerkin discretization of (C.75) and (C.76) based on the approximation $T(\eta, \zeta, t) \approx \mathbf{N}(\eta, \zeta)\boldsymbol{\theta}(t)$ yields

$$\mathbf{E}\dot{\boldsymbol{\theta}}(t) = \mathbf{A}_i \boldsymbol{\theta}(t) + \mathbf{B}_{\text{exp}} \bar{u}_{\text{exp}} + \mathbf{B} u(t), \tag{C.79}$$

where $\mathbf{A}_i$ is equal to $\mathbf{A}_+$ if i is odd and equal to $\mathbf{A}_-$ if i is even and

$$\mathbf{A}_\pm = \iint_\Omega \left(\pm \rho c H v \mathbf{N}^\top \frac{\partial \mathbf{N}}{\partial \zeta} - h_c \mathbf{N}^\top \mathbf{N} - kH \left(\frac{\partial \mathbf{N}^\top}{\partial \eta} \frac{\partial \mathbf{N}}{\partial \eta} + \frac{\partial \mathbf{N}^\top}{\partial \zeta} \frac{\partial \mathbf{N}}{\partial \zeta} \right) \right) \mathrm{d}\eta \, \mathrm{d}\zeta. \tag{C.80}$$

All other matrices are defined similarly as in Section 5.3.1. In particular, $\boldsymbol{\theta}(t)$ and $\mathbf{B}$ are the nodal values of the temperature field $T(\eta, \zeta, t)$ and the shape of applied actuation heat load $B(\eta, \zeta)$. Discretization of the jump equation (C.78) leads to

$$\lim_{t \downarrow i t_{\text{field}}} \boldsymbol{\theta}(t) = \lim_{t \uparrow i t_{\text{field}}} \mathbf{S}_i \boldsymbol{\theta}(t). \tag{C.81}$$

where the matrix $\mathbf{S}_i$ represents the shift along $(-\Delta x_i, -\Delta y_i)$. The discretization of the mechanical model and the cost functions is completely analogous to Section 5.3.1.

Because of these jumps, the temporal discretization requires some care. Each time interval $[(i-1)t_{\text{field}}, i t_{\text{field}}]$ is discretized using $N+1$ grid points $t_{i,k} = k\tau + (i-1)t_{\text{field}}$ with $\tau = t_{\text{field}}/N$, $0 \le k \le N$, and $1 \le i \le N_{\text{f}}$. On each time interval, the system of ODEs (C.79) is discretized using the Crank-Nicolson scheme, just as in Appendix C.3.5. With the notation $\boldsymbol{\theta}_{i,k} = \boldsymbol{\theta}(t_{i,k})$, the jump condition (C.81) becomes

$$\boldsymbol{\theta}_{i+1,0} = \mathbf{S}_i \boldsymbol{\theta}_{i,N}, \qquad 1 \le i \le N_{\text{f}} - 1. \tag{C.82}$$

Similarly as in Appendix C.3.5, discretely consistent gradients are derived based

on the Lagrangian for the discretized problem

$$\mathcal{L}^\tau = \tau \sum_{i=1}^{N_\mathrm{f}} \sum_{k=0}^{N-1} \left[\frac{\bar{f}(\boldsymbol{\theta}_{i,k+1}) + \bar{f}(\boldsymbol{\theta}_{i,k})}{2} + g(\mathbf{B}, u_{i,k+1/2}) \right] + \boldsymbol{\varphi}_{0,0}^\top \mathbf{E} \boldsymbol{\theta}_{1,0}$$
$$\tau \sum_{i=1}^{N_\mathrm{f}} \sum_{k=0}^{N-1} \boldsymbol{\varphi}_{i,k+1/2}^\top \left[\mathbf{A}_i \frac{\boldsymbol{\theta}_{i,k+1} + \boldsymbol{\theta}_{i,k}}{2} + \mathbf{Q}_{i,k+1/2} - \mathbf{E} \frac{\boldsymbol{\theta}_{i,k+1} - \boldsymbol{\theta}_{i,k}}{\tau} \right]$$
$$+ \sum_{i=1}^{N_\mathrm{f}-1} \boldsymbol{\varphi}_{i,0}^\top \left[\boldsymbol{\theta}_{i+1,0} - \mathbf{S}_i \boldsymbol{\theta}_{i,N} \right], \quad \text{(C.83)}$$

with $\mathbf{Q}_{i,k+1/2} = \mathbf{B}_\mathrm{exp} u_{\mathrm{exp},i,k+1/2} + \mathbf{E}_\mathbf{B} \mathbf{B} u_{i,k+1/2}$.

The adjoint state variables $\boldsymbol{\varphi}_{i,k+1/2}$ and $\boldsymbol{\varphi}_{i,0}$ can again be determined by setting the partial derivatives of $\mathcal{L}^\tau$ w.r.t. $\boldsymbol{\theta}_{i,k}$ to zero. The general procedure is as follows. First, $\boldsymbol{\varphi}_{N_\mathrm{f},N-1/2}$ can be determined from $\partial \mathcal{L}^\tau / \partial \boldsymbol{\theta}_{N_\mathrm{f},N} = 0$, which leads to an equation similar to (C.53). Once $\boldsymbol{\varphi}_{i,N-1/2}$ is known, the conditions $\partial \mathcal{L}^\tau / \partial \boldsymbol{\theta}_{i,k} = 0$ (with $k = N-1, \ldots, 1$) lead to equations similar to (C.54) from which $\boldsymbol{\varphi}_{i,N-3/2}$ up to $\boldsymbol{\varphi}_{i,1/2}$ can be determined. Next, $\boldsymbol{\varphi}_{i,0}$ and $\boldsymbol{\varphi}_{i-1,N-1/2}$ are determined from the equations $\partial \mathcal{L}^\tau / \partial \boldsymbol{\theta}_{i,0} = 0$ and $\partial \mathcal{L}^\tau / \partial \boldsymbol{\theta}_{i-1,N} = 0$, which read (for $2 \leq i \leq N_\mathrm{f} - 1$)

$$\frac{\partial \mathcal{L}^\tau}{\partial \boldsymbol{\theta}_{i,0}} = \frac{\tau}{2} \frac{\partial \bar{f}}{\partial \boldsymbol{\theta}}(\boldsymbol{\theta}_{i,0}) + \tau \boldsymbol{\varphi}_{i,1/2}^\top \left(\frac{\mathbf{A}_i}{2} + \frac{\mathbf{E}}{\tau} \right) + \boldsymbol{\varphi}_{i-1,0}^\top = 0, \quad \text{(C.84)}$$

$$\frac{\partial \mathcal{L}^\tau}{\partial \boldsymbol{\theta}_{i-1,N}} = \frac{\tau}{2} \frac{\partial \bar{f}}{\partial \boldsymbol{\theta}}(\boldsymbol{\theta}_{i-1,N}) + \tau \boldsymbol{\varphi}_{i-1,N-1/2}^\top \left(\frac{\mathbf{A}_{i-1}}{2} - \frac{\mathbf{E}}{\tau} \right) - \boldsymbol{\varphi}_{i-1,0}^\top \mathbf{S}_{i-1} = 0. \quad \text{(C.85)}$$

Equation (C.84) and the found $\boldsymbol{\varphi}_{i,1/2}$ thus enable to find $\boldsymbol{\varphi}_{i-1,0}$, from which $\boldsymbol{\varphi}_{i-1,N-1/2}$ can be determined using (C.85). Conditions $\partial \mathcal{L}^\tau / \partial \boldsymbol{\theta}_{i-1,k} = 0$ (with $k = N-1, \ldots, 1$) now again lead to equations similar to (C.54) from which $\boldsymbol{\varphi}_{i-1,N-3/2}$ up to $\boldsymbol{\varphi}_{i-1,1/2}$ can be determined and the procedure can be repeated.

Expressions for the gradients $\nabla_u J$ and $\nabla_\mathbf{B} J$ are now be found based on the partial derivatives of the Lagrangian $\mathcal{L}^\tau$ in (C.83) w.r.t. $u_{i,k}$ and $\mathbf{B}$, similarly as in Appendix C.3.5. The found expressions in terms of the adjoint state variables $\boldsymbol{\varphi}_{i,k}$ are very similar to (C.58) and (C.59).

The method has been applied to the two scanning patterns in Figure C.2. Note that for the pattern in Figure C.2a, $\Delta x_i = L_\mathrm{field}$ and $\Delta y_i = 0$ ($i = 1, 2, 3$), where $L_\mathrm{field} = 26$ mm is the length of a field in the x-direction and for the pattern in Figure C.2b, $\Delta x_1 = L_\mathrm{field}$, $\Delta x_2 = 0$, $\Delta x_3 = -L_\mathrm{field}$ and $\Delta y_1 = \Delta y_3 = 0$ and $\Delta y_2 = W_\mathrm{field}$, where $W_\mathrm{field} = 33$ mm is the length of a field in the y-direction. The other parameter values are the same as in Table 5.1.

The obtained optimal actuation heat load shapes $B(\eta, \zeta)$ and intensities $u(t)$ are shown in Figures C.3 and C.4. Note that the problem is no longer symmetric

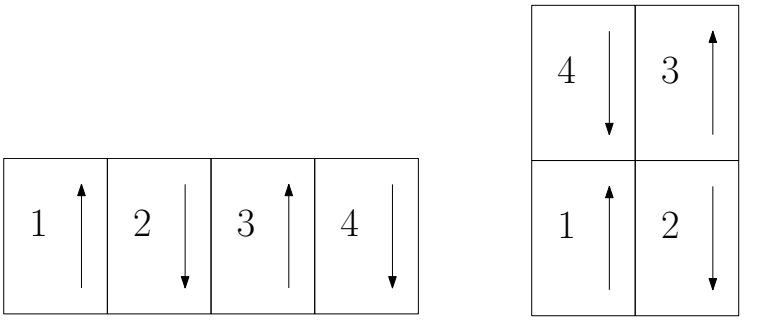

(a) Scanning pattern (SP) 1 **(b)** Scanning pattern (SP) 2

Figure C.2. The two considered scanning patterns. The rectangles and arrows indicate the fields with their scanning directions and the numbers indicate the order in which fields are scanned.

Table C.3. Minima found after the optimization of the single-shape actuation heat load $B(\eta,\zeta)u(t)s$ for the two scanning patterns (SPs) in Figure C.2, each starting from two initial guesses (IGs).

	SP 1, IG 1	SP 1, IG 2	SP 2, IG 1	SP 2, IG 2
$J_0 + wJ_2$	9164	9167	8483	8485
J_0	8271	8277	7683	7680
E_{act}	4.058	4.020	3.811	3.797

in $\eta = 0$, which means that the whole spatial domain in the figures is discretized, and that the spatial grids used for scanning patterns 1 and 2 cover different parts of the (η,ζ)-space. Both meshes contain about 20,000 nodes. Just as in Section 5.4, $N = 200$ time points are used for the time interval during which one field is scanned. Observe that the obtained actuation heat load shapes both cool the area around the slit, but that the location in which the heating is applied are different for both expose patterns and hard to interpret. Also note that the intensities $u(t)$ in Figures C.3 and C.4 are discontinuous at the jump times and larger than the intensity obtained when considering a single field in Figure 5.5a.

Table C.3 shows some properties of the found minima. The minimal values of $J_0 + wJ_2$, J_0, and E_{act} are all significantly larger than the values for a single field in Table 5.2. This is natural to expect because the considered time window is four times larger and because the temperature increase due to the scanning of previous fields makes it harder to satisfy the deformation constraint. Again two initial guesses have been considered which lead to almost identical minimizers. For initial guess 1, $B(\eta,\zeta) = 0$ and, for each time interval $[(i-1)t_{\text{field}}, it_{\text{field}})$, $u(t)$ is the same as in Figure 5.3a. For initial guess 2, $B(\eta,\zeta)$ has the same shape as $B(x,\zeta)$ in Figure 5.3b and $u(t)$ is the same as for initial guess 1.

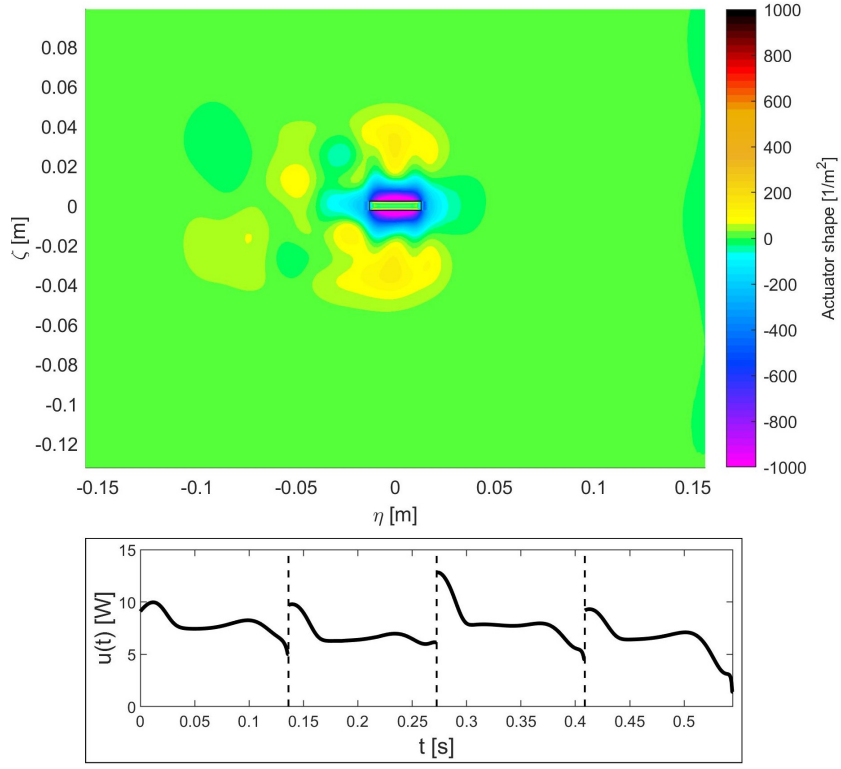

Figure C.3. The shape $B(\eta, \zeta)$ and the intensity $u(t)$ designed for scanning pattern 1. The black rectangle in the top graph indicates the slit and the dashed lines in the bottom graph indicate the jumps to the next field.

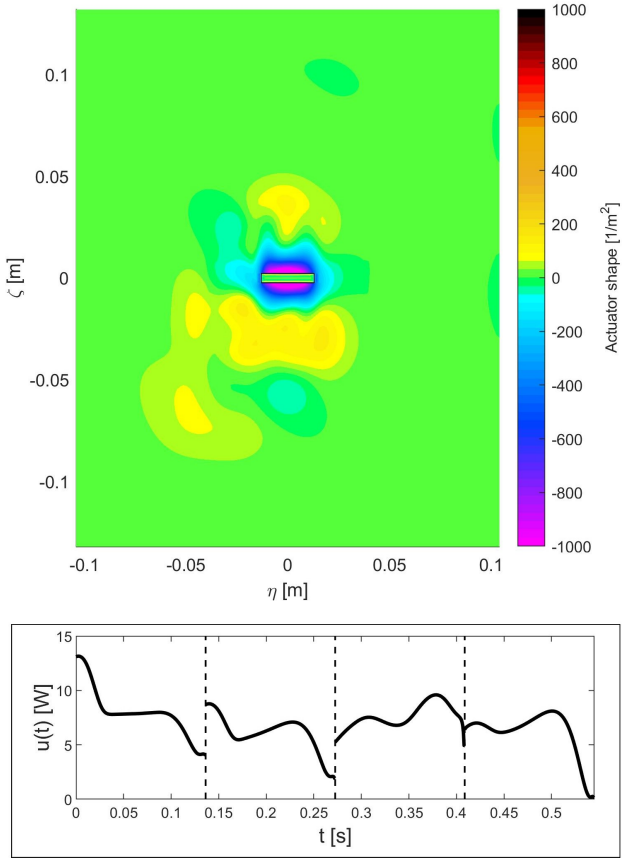

Figure C.4. The shape $B(\eta, \zeta)$ and the intensity $u(t)$ designed for scanning pattern 2. The black rectangle in the top graph indicates the slit and the dashed lines in the bottom graph indicate the jumps to the next field.

Table C.4. Iterations and computational times required for the optimization of the single-shape actuation heat load $B(\eta,\zeta)u(t)s$ for the two scanning patterns (SPs) in Figure C.2, each starting from two initial guesses (IGs).

	minimizing J_1		minimizing $J_0 + wJ_2$	
	# iterations	time [s]	# iterations	time [s]
SP 1, IG 1	12	573	162	7923
SP 1, IG 2	14	737	156	7598
SP 2, IG 1	8	382	154	7598
SP 2, IG 2	7	336	246	11757

The required number of iterations and computational times are given in Table C.4. Note that finding a feasible solution requires a few more iterations than for the scanning of a single field, but that minimizing $J_0 + wJ_2$ requires a similar amount of iterations as for the single field, see Table 5.3. Also note that the computational time per iteration is significantly longer than for a single field because there are significantly more points in the spatial and temporal grids.

C.4.3 Fields near the edge of the wafer

The third modification considers the scanning of fields near the edge of the wafer. The scanning of these fields will typically lead to larger heat-induced deformation because the in-plane stiffness of the wafer is lower near the edge.

Because the position of the wafer edge is fixed in the (x,y)-coordinate system, it is most convenient to compute the temperature and displacement fields in (x,y)-coordinates. However, the thermal actuators are still moving together with the expose light, which means that the shape of the actuation heat load is fixed in the moving (x,ζ)-coordinate system. The computation of the optimal actuation heat load thus requires two sets of shape functions: one for the (x,y)-coordinates and one for the (x,ζ)-coordinates. This leads to the following approximations

$$T(x,y,t) = \mathbf{N}^y(x,y)\boldsymbol{\theta}(t), \qquad B(x,\zeta) = \mathbf{N}^\zeta(x,\zeta)\mathbf{B}, \tag{C.86}$$

$$d_x(x,y,t) = \mathbf{N}^y(x,y)\mathbf{d}_x(t), \qquad d_y(x,y,t) = \mathbf{N}^y(x,y)\mathbf{d}_y(t), \tag{C.87}$$

where $\mathbf{N}^y(x,y)$ and $\mathbf{N}^\zeta(x,\zeta)$ denote (row-vectors) of FE shape functions, and $\boldsymbol{\theta}(t)$, $\mathbf{B}$, $\mathbf{d}_x(t)$, and $\mathbf{d}_x(t)$, denote the nodal values of the temperature field $T(x,y,t)$, the shape of the actuation heat load $B(x,\zeta)$, and the x- and y-components of the displacement field $d_x(x,y,t)$ and $d_y(x,y,t)$, respectively. A Galerkin discretization of (5.1) based on (C.86) (using (5.3) and (5.12) and considering the constraint (5.13)) now takes the form

$$\mathbf{E}\dot{\boldsymbol{\theta}}(t) = \mathbf{A}\boldsymbol{\theta}(t) + \mathbf{B}_{\text{exp}}(t)u_{\text{exp}}(t) + \mathbf{E}_{\mathbf{B}}(t)\mathbf{B}u(t), \tag{C.88}$$

with

$$\mathbf{A} = -\iint_\Omega kH\left(\frac{\partial \mathbf{N}^{y\top}}{\partial x}\frac{\partial \mathbf{N}^{y}}{\partial x} + \frac{\partial \mathbf{N}^{y\top}}{\partial y}\frac{\partial \mathbf{N}^{y}}{\partial y} + h_c \mathbf{N}^{y\top}\mathbf{N}^{y}\right)\,\mathrm{d}x\,\mathrm{d}y, \tag{C.89}$$

$$\mathbf{E} = \rho c H \iint_\Omega \mathbf{N}^{y\top}(x,y)\mathbf{N}^{y}(x,y)\,\mathrm{d}x\,\mathrm{d}y, \tag{C.90}$$

$$\mathbf{B}_{\mathrm{exp}}(t) = \iint_\Omega \mathbf{N}^{y\top}(x,y) B_{\mathrm{exp}}(x, y-vt)\,\mathrm{d}x\,\mathrm{d}y, \tag{C.91}$$

$$\mathbf{E}_{\mathbf{B}}(t) = \iint_{\Omega\setminus\Omega_{\mathrm{slit}}(t)} \mathbf{N}^{y\top}(x,y)\mathbf{N}^{\zeta}(x,y-vt)\,\mathrm{d}x\,\mathrm{d}y, \tag{C.92}$$

where $(x,y) \in \Omega \subset \mathbb{R}^2$ denotes the spatial domain, $(x,y) \in \Omega_{\mathrm{slit}}(t) \subset \mathbb{R}^2$ denotes the slit, and the dependence of $\mathbf{N}^y$ on (x,y) has been omitted in the expression for $\mathbf{A}$. Note that the computation of $\mathbf{E}_{\mathbf{B}}(t)$ is rather cumbersome because it requires the projection of every $\mathbf{N}^{\zeta}$-shape function onto the set of $\mathbf{N}^{y}$-shape functions. This computation is somewhat simplified by the nodal approximation

$$\mathbf{N}^{\zeta}(x, y-vt) \approx \mathbf{N}^{y}(x,y)\mathbf{S}_{\zeta\to y}(t), \tag{C.93}$$

where $\mathbf{S}_{\zeta\to y}(t)$ interpolates the $\mathbf{N}^{\zeta}$-shape functions in the nodes of the $\mathbf{N}^{y}$-grid, i.e. for every node (x_i, y_i) in the $\mathbf{N}^{y}$-grid that falls inside the domain currently covered by the $\mathbf{N}^{\zeta}$-shape functions, (C.93) holds exactly and for nodes (x_i, y_i) outside this domain $\mathbf{N}^{y}(x_i,y_i)\mathbf{S}_{\zeta\to y}(t) = \mathbf{0}$. Inserting (C.93) into (C.92) yields the approximation

$$\tilde{\mathbf{E}}_{\mathbf{B}}(t) = \mathbf{E}_{\mathbf{B}0}(t)\mathbf{S}_{\zeta\to y}(t), \qquad \mathbf{E}_{\mathbf{B}0}(t) = \iint_{\Omega\setminus\Omega_{\mathrm{slit}}(t)} \mathbf{N}^{y\top}\mathbf{N}^{y}\,\mathrm{d}x\,\mathrm{d}y. \tag{C.94}$$

The mechanical model in (x,y)-coordinates is similar to the model in (x,ζ)-coordinates in (5.6) and (5.7), only ζ is replaced by y. The stiffness matrix $\mathbf{K}$ and thermal load matrix $\mathbf{L}$ can thus be obtained similarly as in Subsection 5.3.1 using the approximations (C.87).

The discretization of the cost functionals J_0, J_1, and J_2 can be done similarly as in Subsection 5.3.1. The formulas (5.39), (5.42), and (5.43) are still valid, only the matrix $\mathbf{E}_0$ is now defined as

$$\mathbf{E}_0 = \iint_\Omega \mathbf{N}^{y\top}\mathbf{N}^{y}\,\mathrm{d}x\,\mathrm{d}y, \tag{C.95}$$

$\mathbf{d}_{\zeta}(t)$ should be replaced by $\mathbf{d}_{y}(t)$, and the vector containing the nodal values of the maximally allowed displacement $\mathbf{d}_{\max}$ is now time-dependent due to the time dependence of $\Omega_{\mathrm{slit}}(t)$ in (x,y)-coordinates. The computation of the gradients $\nabla_u J$ and $\nabla_{\mathbf{B}} J$ in Subsection 5.3.2 is not significantly influenced by the time-dependence of the matrices. Note however that the natural inner product on

the space of the heat load shapes $\mathbf{B}$ is now given by

$$\langle \mathbf{B}^1, \mathbf{B}^2 \rangle_B = \mathbf{B}^{1\top} \mathbf{E}_0^\zeta \mathbf{B}^2, \qquad \mathbf{E}_0^\zeta = \iint_{\Omega^\zeta} \mathbf{N}^{\zeta\top} \mathbf{N}^\zeta \, \mathrm{d}x \, \mathrm{d}\zeta, \tag{C.96}$$

where Ω^ζ denotes the domain covered by the $\mathbf{N}^\zeta$-shape functions.

The time discretization of (C.88) on uniform grid $t_k = k\tau$ is done by a slight modification of the Crank-Nicolson scheme, which yields

$$\mathbf{E} \frac{\boldsymbol{\theta}_{k+1} - \boldsymbol{\theta}_k}{\tau} = \mathbf{A} \frac{\boldsymbol{\theta}_{k+1} - \boldsymbol{\theta}_k}{2} + \mathbf{B}_{\mathrm{exp},k+1/2} u_{\mathrm{exp},k+1/2} + \tilde{\mathbf{E}}_{\mathbf{B},k+1/2} \mathbf{B} u_{k+1/2}, \tag{C.97}$$

where the matrix $\mathbf{E}_\mathbf{B}(t)$ was replaced by the approximation $\tilde{\mathbf{E}}_\mathbf{B}(t)$ in (C.94), the subscripts k and $k+1/2$ indicate the samples at $t = t_k$ and $t = t_{k+1/2} = (t_{k+1} + t_k)/2$, and the modification of the Crank-Nicolson scheme is the result of the approximations

$$\frac{\mathbf{B}_{\mathrm{exp},k+1} u_{\mathrm{exp},k+1} + \mathbf{B}_{\mathrm{exp},k} u_{\mathrm{exp},k}}{2} \approx \mathbf{B}_{\mathrm{exp},k+1/2} u_{\mathrm{exp},k+1/2}, \tag{C.98}$$

$$\frac{\tilde{\mathbf{E}}_{\mathbf{B},k+1} \mathbf{B} u_{k+1} + \tilde{\mathbf{E}}_{\mathbf{B},k} \mathbf{B} u_k}{2} \approx \tilde{\mathbf{E}}_{\mathbf{B},k+1/2} \mathbf{B} u_{k+1/2}. \tag{C.99}$$

Note that this modification of the Crank-Nicolson scheme enables the use of the intermediate inputs $u_{k+1/2}$ as design variables, which is not possible when using the LHSs of (C.98) and (C.99). The intermediate values $u_{k+1/2}$ were also used in Appendix C.3.5. The temporal discretization and the resulting formulas for the gradients are thus very similar to the ones in that appendix.

The resulting algorithm is now applied to design the optimal actuation heat load for two fields in the expose pattern in Figure 1.7 near the edge of the wafer. In particular, Field 1 (the field on the left on the bottom row) and Field 32 (the field on the left of the fourth row from the bottom) are considered. The two grids used to construct the linear Lagrangian FE shape functions $\mathbf{N}^y(x, y)$ are shown in Figure C.5. These grids contain 9320 and 8885 nodes, respectively. The grids for the $\mathbf{N}^\zeta$-shape functions are similar but are not truncated near the edge of the wafer. These grids contain 16748 nodes for both considered fields.

The obtained optimal shapes $B(x, \zeta)$ and intensities $u(t)$ are shown in Figure C.6, which were generated for the same parameter values that were used in Section 5.4. Note that the shape obtained for Field 1 resembles the optimal shape for a field far from the edge of the wafer, see Figure 5.5a and that the shape is only slightly asymmetrical in the line $x = 0$. For field 32, the optimal actuation heat load shape is clearly asymmetrical.

Table C.5 shows some characteristics of the found minima. It is remarkable to see that the values J_0, $J_0 + wJ_2$, and E_{act} found for the scanning of Field 1 are smaller than for a field far away from the edge of the wafer, see Table 5.2. The reduced in-plane stiffness thus actually reduces the heat-induced deformation in

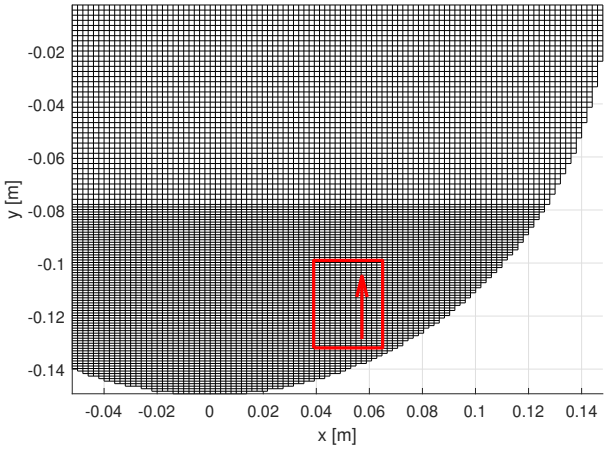

(a) Field 1

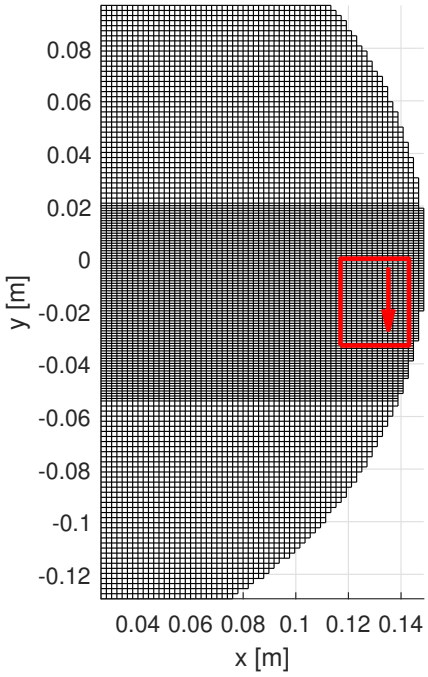

(b) Field 32

Figure C.5. Grids used to generate the shape functions $\mathbf{N}^y(x, y)$ for the two considered fields. The red rectangle and red arrow indicate the location and scanning direction of the considered field.

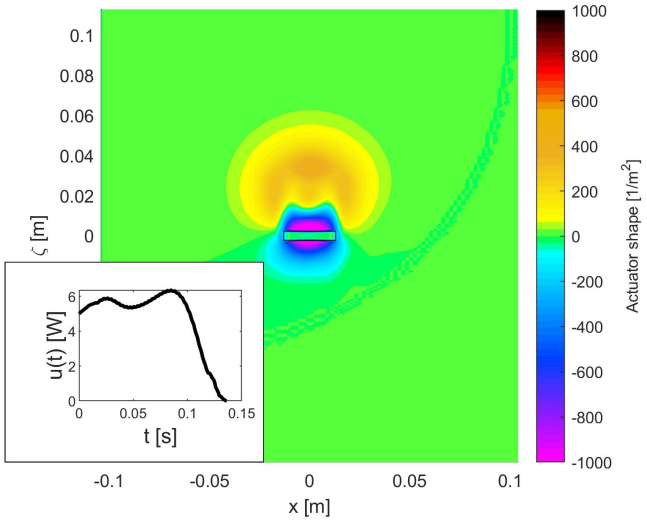

(a) Field 1

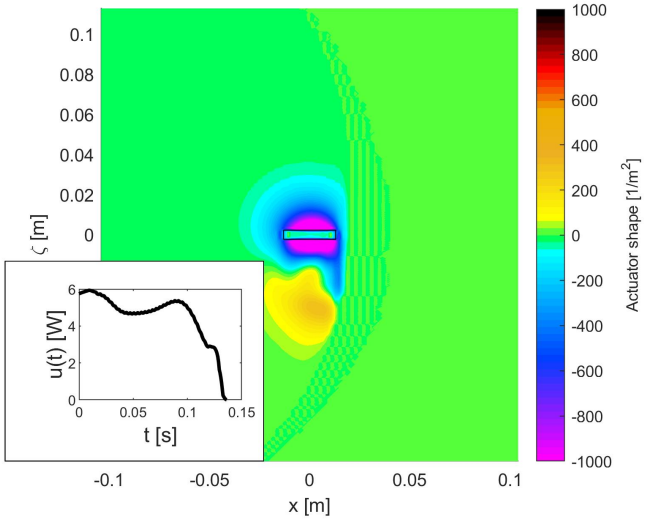

(b) Field 32

Figure C.6. The obtained optimal actuator shapes $B(x, \zeta)$ and intensities $u(t)$ for the scanning of two fields near the edge of the wafer. The black rectangle indicates the location of the slit.

Table C.5. Minima found after the optimization of the single-shape actuation heat load $B(\eta, \zeta)u(t)s$ for two fields near the edge of the wafer

	Field 1	Field 32
$J_0 + wJ_2$	1368	1979
J_0	1206	1823
E_{act}	0.652	0.628

Table C.6. Iterations and computational times required for the optimization of the single-shape actuation heat load $B(\eta, \zeta)u(t)s$ for two fields near the edge of the wafer

	minimizing J_1		minimizing $J_0 + wJ_2$	
	# iterations	time [s]	# iterations	time [s]
Field 1	5	317	160	10167
Field 32	6	386	158	9510

Field 1. This can be understood as follows. Since the heat load is moving away from the wafer edge, the temperature increase due to Q_{exp} occurs between the slit and the wafer edge. Because the in-plane stiffness near the wafer edge is lower, this temperature increase pushes the slit less in the positive y-direction than on the unbounded spatial domain. Note, however, that if the scanning direction would be reversed, i.e. if the heat load Q_{exp} moves towards the edge, the occurring heat-induced deformations would actually increase due to the reduced in-plane stiffness near the edge of the wafer. The values of J_0 and $J_0 + wJ_2$ for Field 32 in Table C.5 are actually higher than for a field away from the wafer edge, see Table 5.2. This indicates that in this case the reduced in-plane stiffness near the wafer edge indeed results in larger heat-induced deformations which are harder to control. Note, however, that E_{act} for Field 32 is smaller than for a field away from the wafer edge. The reason for this seems to be that the actuation heat load in Figure C.6b is concentrated in a smaller area than the heat load in Figure 5.5a which results in a smaller L^1-norm, see e.g. [Stadler, 2009; Herzog et al., 2012].

Table C.6 shows the number of iterations and times required to obtain the found minima. Note that the number of required iterations is again similar as in Table 5.3, but that the computational cost for each iteration is significantly higher. The main reason for this difference is that the matrices $\mathbf{E}_{\mathbf{B}0}(t)$ and $\mathbf{S}_{\zeta \to y}(t)$ in (C.94) need to be constructed at every time instant. Especially the construction of the interpolation matrix $\mathbf{S}_{\zeta \to y}(t)$ is time consuming.

Appendix D

Appendices to Chapter 6

D.1 Proofs regarding the representation of the actuation heat load

In this appendix, the proofs of Lemmas 6.4, 6.5, and 6.7 are given.

Proof of Lemma 6.4. Let $\mathbf{M}$ be an invertible matrix such that both $\mathbf{M}$ and $\mathbf{M}^{-1}$ have only nonnegative entries and consider the i-th row of $\mathbf{M}$. Since $\mathbf{M}$ is nonsingular, this row contains at least one nonzero element $\mathbf{M}_{ik}$. As $\mathbf{M}\mathbf{M}^{-1} = \mathbf{I}$, the off-diagonal elements in the i-th row of $\mathbf{M}\mathbf{M}^{-1}$ must be zero, i.e. for all $\ell \neq i$

$$0 = \left(\mathbf{M}\mathbf{M}^{-1}\right)_{i\ell} = \sum_{r=1}^{m} \mathbf{M}_{ir}\mathbf{M}^{-1}_{r\ell} \geq \mathbf{M}_{ik}\mathbf{M}^{-1}_{k\ell}. \tag{D.1}$$

Since $\mathbf{M}_{ik} > 0$ it follows that $\mathbf{M}^{-1}_{k\ell} = 0$ for $\ell \neq i$, i.e. $\mathbf{M}^{-1}_{ki}$ is the only nonzero element in the k-th row of $\mathbf{M}^{-1}$. But also $\mathbf{M}^{-1}\mathbf{M} = \mathbf{I}$ which implies that the off-diagonal entries in the k-th row of $\mathbf{M}^{-1}\mathbf{M}$ must be zero, i.e. for all $\ell \neq k$

$$0 = \left(\mathbf{M}^{-1}\mathbf{M}\right)_{k\ell} = \sum_{r=1}^{m} \mathbf{M}^{-1}_{kr}\mathbf{M}_{r\ell} = \mathbf{M}^{-1}_{ki}\mathbf{M}_{i\ell}. \tag{D.2}$$

Thus $\mathbf{M}_{ik}$ is in fact the *only* nonzero element in the i-th row. As the considered row i was arbitrary, every row of $\mathbf{M}$ contains only one nonzero element. Because $\mathbf{M}$ is invertible, two nonzero elements cannot occur in the same column of $\mathbf{M}$ and $\mathbf{M}$ must be a scaled permutation matrix and can thus be written in the form $\mathbf{M} = \mathbf{D}\mathbf{P}$ (or $\mathbf{M} = \mathbf{P}\mathbf{D}$), where $\mathbf{P}$ and $\mathbf{D}$ are properly chosen permutation and diagonal matrices. □

Proof of Lemma 6.5. Let $\mathbf{M}$ be an invertible matrix for which $\mathcal{B}(x,y)\mathbf{M}$ and $\mathbf{M}^{-1}\mathbf{U}$ satisfy the constraints (6.5). Since the elements of $\mathcal{B}(x,y)\mathbf{M}$ are nonnegative for all $(x,y) \in A_{\text{top}}$, the entries of the matrix

$$\begin{bmatrix} \mathcal{B}(x_1,y_1)\mathbf{M} \\ \mathcal{B}(x_2,y_2)\mathbf{M} \\ \vdots \\ \mathcal{B}(x_m,y_m)\mathbf{M} \end{bmatrix} = \begin{bmatrix} \mathcal{B}(x_1,y_1) \\ \mathcal{B}(x_2,y_2) \\ \vdots \\ \mathcal{B}(x_m,y_m) \end{bmatrix} \mathbf{M} = \begin{bmatrix} c_1 & 0 & \cdots & 0 \\ 0 & c_2 & \cdots & 0 \\ \vdots & \vdots & \ddots & \vdots \\ 0 & 0 & \cdots & c_m \end{bmatrix} \mathbf{M}, \tag{D.3}$$

must be nonnegative, which implies that the entries of $\mathbf{M}$ are nonnegative. Similarly, since the elements of $\mathbf{M}^{-1}\mathbf{U}$ are nonnegative, the entries of the matrix

$$\begin{bmatrix} \mathbf{M}^{-1}\mathbf{u}_{j_1} & \mathbf{M}^{-1}\mathbf{u}_{j_2} & \cdots & \mathbf{M}^{-1}\mathbf{u}_{j_m} \end{bmatrix} =$$

$$\mathbf{M}^{-1}\begin{bmatrix} \mathbf{u}_{j_1} & \mathbf{u}_{j_2} & \cdots & \mathbf{u}_{j_m} \end{bmatrix} = \mathbf{M}^{-1}\begin{bmatrix} d_1 & 0 & \cdots & 0 \\ 0 & d_2 & \cdots & 0 \\ \vdots & \vdots & \ddots & \vdots \\ 0 & 0 & \cdots & d_m \end{bmatrix}, \tag{D.4}$$

are nonnegative, which implies that all entries of $\mathbf{M}^{-1}$ are nonnegative. Lemma 6.4 now implies that $\mathbf{M} = \mathbf{DP}$. □

Proof of Lemma 6.7. It will be useful to observe that

$$\begin{bmatrix} 1 & 0 \\ -\beta & 1 \end{bmatrix}^{-1} = \begin{bmatrix} 1 & 0 \\ \beta & 1 \end{bmatrix}, \qquad \begin{bmatrix} 1 & \beta \\ 0 & 1 \end{bmatrix}^{-1} = \begin{bmatrix} 1 & -\beta \\ 0 & 1 \end{bmatrix}. \tag{D.5}$$

First consider the case when elements of $\mathcal{B}(x,y)$ are not boundary close. It is then possible to select indices $1 \le i_1, i_2 \le m$, $i_1 \ne i_2$ and to find a $\beta > 0$ such that $B_{i_1}(x,y) - \beta B_{i_2}(x,y) \ge 0$ for all $(x,y) \in \partial\Omega_{\text{top}}$. Now construct a matrix $\mathbf{M}$ by setting $\mathbf{M}_{ii} = 1$ for $1 \le i \le m$, $\mathbf{M}_{i_2 i_1} = -\beta$ and all other entries zero. For this matrix $\mathbf{M}$, it follows that $(\mathcal{B}(x,y)\mathbf{M})_{i_1} = B_{i_1}(x,y) - \beta B_{i_2}(x,y)$ and $(\mathcal{B}(x,y)\mathbf{M})_i = B_i(x,y)$ for $i \ne i_1$. By assumption, all entries of $\mathcal{B}(x,y)\mathbf{M}$ are thus nonnegative. Using the first identity in (D.5), it follows that the inverse $\mathbf{M}^{-1}$ has entries $\mathbf{M}^{-1}_{ii} = 1$, $\mathbf{M}^{-1}_{i_2 i_1} = \beta$, and all other entries zero. As all the entries of $\mathbf{M}^{-1}$ are nonnegative, the entries of $\mathbf{M}^{-1}\mathbf{U}$ are nonnegative.

The proof for the case when the rows of $\mathbf{U}$ are not boundary close is similar. It is then possible to select $1 \le i_1, i_2 \le m$, $i_1 \ne i_2$ and to find a $\beta > 0$ such that $u_{i_1,j} - \beta u_{i_2,j} > 0$ for all $1 \le j \le n$. The matrix $\mathbf{M}$ is now constructed by setting $\mathbf{M}_{ii} = 1$ for $1 \le i \le m$, $\mathbf{M}_{i_1 i_2} = +\beta$, and all other entries zero. As all entries of $\mathbf{M}$ are nonnegative, the shapes $\mathcal{B}(x,y)\mathbf{M}$ are nonnegative. As $\mathbf{M}^{-1}$ is equal to $\mathbf{M}$ apart from the entry $\mathbf{M}^{-1}_{i_1 i_2} = -\beta$ (see the second identity in (D.5)), only the i_1-th rows of $\mathbf{U}$ and $\mathbf{M}^{-1}\mathbf{U}$ differ. The i_1-th row of $\mathbf{M}^{-1}\mathbf{U}$ has entries $u_{i_1,j} - \beta u_{i_2,j}$, which are nonnegative. The matrix $\mathbf{M}^{-1}\mathbf{U}$ thus also has only nonnegative entries. □

D.2 Parameters for the barrier function $\mathcal{J}_2$

In this appendix, the values of the power p and the weight w appearing in the cost functional $\mathcal{J}_0 + w\mathcal{J}_2$ with $\mathcal{J}_0$ as in (6.7) and $\mathcal{J}_2$ as in (6.21) will be determined. The approach is very similar to the approach in Appendix C.1 for the wafer heating problem from Chapter 5.

The power p should be chosen such that J_2 increases 'fast enough' near the edge of the admissible set. In particular, it is desired that the integrand in (6.21) is approximately zero for load cases j and at points (x, y) for which there is enough margin in (6.6) and that the integrand in (6.21) is large for load cases j and points (x, y) where the margin in (6.6) is small. The margin in the constraints (6.6) is considered large when

$$\delta - |T_j(x, y) - T^*| < \varepsilon_1 \delta, \tag{D.6}$$

and is considered small when

$$\delta - |T_j(x, y) - T^*| > \varepsilon_2 \delta, \tag{D.7}$$

where $0 < \varepsilon_1 < \varepsilon_2 < 1$. Note that equations (D.6) and (D.7) are equivalent to

$$\frac{(T_j(x, y) - T^*)^2}{\delta^2} > (1 - \varepsilon_1)^2, \qquad \frac{(T_j(x, y) - T^*)^2}{\delta^2} < (1 - \varepsilon_2)^2, \tag{D.8}$$

and that the integrand in (6.21) can be rewritten as

$$-1 + \left(\frac{\delta^2}{\delta^2 - (T_j(x, y) - T^*)^2} \right)^p = \left(1 - \frac{(T_j(x, y) - T^*)^2}{\delta^2} \right)^{-p} - 1. \tag{D.9}$$

Since the integrand is monotonically increasing in $(T_j - T^*)$, the integrand for a small margin as in (D.6) is at least $M \gg 1$ times larger than the integrand for a large margin as in (D.7) if

$$\left(1 - (1 - \varepsilon_1)^2\right)^{-p} - 1 > M \left(\left(1 - (1 - \varepsilon_2)^2\right)^{-p} - 1 \right). \tag{D.10}$$

Using that $M > 1$, it is easy to see that this inequality is satisfied when

$$\left(1 - (1 - \varepsilon_1)^2\right)^{-p} > M \left(1 - (1 - \varepsilon_2)^2\right)^{-p}. \tag{D.11}$$

Some straightforward algebra now shows that this condition is equivalent to

$$p > \frac{\log(M)}{\log(2\varepsilon_2 - \varepsilon_2^2) - \log(2\varepsilon_1 - \varepsilon_1^2)}. \tag{D.12}$$

The power p is now determined based on the parameter values $M = 1000$, $\varepsilon_1 = 0.05$, and $\varepsilon_2 = 0.5$, which were also used in Appendix C.1. For these values

(D.12) becomes $p > 3.3858$. This requirement is indeed satisfied by the value of $p = 3.5$ used in Section 6.4.

The weight w should be chosen such that the magnitude of the barrier function $w\mathcal{J}_2$ approaches the magnitude of $\mathcal{J}_0$ when the margin in (6.6) becomes 'small' as in (D.6). To find a value of w for which this will happen, typical magnitudes of the integrands in (6.7) and (6.21) are needed. The magnitude of the integrand in (6.7) is estimated based on the idea that the actuation heat loads $Q_{\mathrm{act},j}(x, y)$ will be of similar magnitude as the heat load induced by the projecting light $Q_{\mathrm{EUV},j}(x, y)$. When the margin in (6.6) becomes 'small' as in (D.6), the typical magnitude of the integrand in (6.21) is $(1 - (1 - \varepsilon_1)^2)^{-p} - 1$. The weight w should thus be chosen such that

$$\left(\max_{1 \le j \le n} \max_{(x,y) \in A_{\mathrm{top}}} Q_{\mathrm{act},j}(x, y) \right)^2 \approx w \left((1 - (1 - \varepsilon_1)^2)^{-p} - 1 \right). \tag{D.13}$$

With $\max_{1 \le j \le n} \max_{(x,y) \in A_{\mathrm{top}}} Q_{\mathrm{act},j}(x, y) = 408\ \mathrm{W/m^2}$, this yields $w = 48$. This is also the value of w used in Section 6.4.

D.3 Sensitivity analysis

This appendix contains details regarding the computation of the gradients $\nabla_{\mathbf{B}} J$ and $\nabla_{\mathbf{U}} J$ and the directional Hessians $H_{\mathbf{B}}$ and $H_{\mathbf{U}}$. The first two subsections consider a cost functional J of the general form (6.41). The specific expressions $J = J_1$ and $J = J_0 + wJ_2$ are only considered in the third subsection.

D.3.1 The gradients

Consider a cost functional $J(\mathbf{X})$ that depends on a matrix $\mathbf{X} \in \mathbb{R}^{K \times L}$. The gradient $\nabla_{\mathbf{X}} J(\mathbf{X}_0)$ of J w.r.t. $\mathbf{X}$ in the point $\mathbf{X} = \mathbf{X}_0$ is an $K \times L$ matrix defined by the requirement that

$$\lim_{h \to 0} \frac{J(\mathbf{X}_0 + h\tilde{\mathbf{X}}) - J(\mathbf{X}_0)}{h} = \left\langle \nabla_{\mathbf{X}} J(\mathbf{X}_0), \tilde{\mathbf{X}} \right\rangle_X \tag{D.14}$$

for any direction $\tilde{\mathbf{X}} \in \mathbb{R}^{K \times L}$. Here, $\langle \cdot \ \cdot \rangle_X$ denotes the chosen inner product on the space of $K \times L$-matrices. To rewrite the LHS of (D.14), consider first a direction $\tilde{\mathbf{X}} = \tilde{\mathbf{X}}^{(k,\ell)}$ of which only the element (k, ℓ) is nonzero. In this case, the chain rule shows that

$$\left\langle \nabla_{\mathbf{X}} J(\mathbf{X}_0), \tilde{\mathbf{X}}^{(k,\ell)} \right\rangle_X = \lim_{h \to 0} \frac{J(\mathbf{X}_0 + h\tilde{\mathbf{X}}^{(k,\ell)}) - J(\mathbf{X}_0)}{h} = \frac{\partial J}{\partial \mathbf{X}_{k\ell}}(\mathbf{X}_0) \tilde{\mathbf{X}}^{(k,\ell)}_{k,\ell}, \tag{D.15}$$

where $\partial J / \partial \mathbf{X}_{k\ell}(\mathbf{X}_0)$ denotes the partial derivative of $J(\mathbf{X})$ w.r.t. the element (k, ℓ) of $\mathbf{X}$ evaluated in the point $\mathbf{X} = \mathbf{X}_0$. As differentiation is a linear operation,

the derivative of $J(\mathbf{X})$ in any direction $\tilde{\mathbf{X}}$ can be obtained by summing the contributions of the components of $\tilde{\mathbf{X}}$, i.e.

$$\left\langle \nabla_{\mathbf{X}} J(\mathbf{X}_0), \tilde{\mathbf{X}} \right\rangle_X = \lim_{h \to 0} \frac{J(\mathbf{X}_0 + h\tilde{\mathbf{X}}) - J(\mathbf{X}_0)}{h} = \sum_{k=1}^{K} \sum_{\ell=1}^{L} \frac{\partial J}{\partial \mathbf{X}_{k\ell}}(\mathbf{X}_0) \tilde{\mathbf{X}}_{k,\ell}, \tag{D.16}$$

With the introduction of the $L \times K$-matrix

$$\frac{\partial J}{\partial \mathbf{X}}(\mathbf{X}_0) = \begin{bmatrix} \frac{\partial J}{\partial \mathbf{X}_{11}}(\mathbf{X}_0) & \frac{\partial J}{\partial \mathbf{X}_{21}}(\mathbf{X}_0) & \cdots & \frac{\partial J}{\partial \mathbf{X}_{K1}}(\mathbf{X}_0) \\ \frac{\partial J}{\partial \mathbf{X}_{12}}(\mathbf{X}_0) & \frac{\partial J}{\partial \mathbf{X}_{22}}(\mathbf{X}_0) & \cdots & \frac{\partial J}{\partial \mathbf{X}_{K2}}(\mathbf{X}_0) \\ \vdots & \vdots & & \vdots \\ \frac{\partial J}{\partial \mathbf{X}_{1L}}(\mathbf{X}_0) & \frac{\partial J}{\partial \mathbf{X}_{2L}}(\mathbf{X}_0) & \cdots & \frac{\partial J}{\partial \mathbf{X}_{KL}}(\mathbf{X}_0) \end{bmatrix}, \tag{D.17}$$

equation (D.16) can be rewritten as

$$\left\langle \nabla_{\mathbf{X}} J(\mathbf{X}_0), \tilde{\mathbf{X}} \right\rangle_X = \sum_{k=1}^{K} \sum_{\ell=1}^{L} \left(\frac{\partial J}{\partial \mathbf{X}}(\mathbf{X}_0) \right)_{\ell,k} \tilde{\mathbf{X}}_{k,\ell} = \operatorname{trace}\left(\frac{\partial J}{\partial \mathbf{X}}(\mathbf{X}_0) \tilde{\mathbf{X}} \right). \tag{D.18}$$

The general result in (D.18) can now be applied to the situation where $\mathbf{X}$ is the matrix of spatial shapes $\mathbf{B}$ and to the situation where $\mathbf{X}$ is the matrix of intensities $\mathbf{U}$

$$\left\langle \nabla_{\mathbf{B}} J(\mathbf{B}, \mathbf{U}), \tilde{\mathbf{B}} \right\rangle_B = \operatorname{trace}\left(\frac{\partial J}{\partial \mathbf{B}}(\mathbf{B}, \mathbf{U}) \tilde{\mathbf{B}} \right), \tag{D.19}$$

$$\left\langle \nabla_{\mathbf{U}} J(\mathbf{B}, \mathbf{U}), \tilde{\mathbf{U}} \right\rangle_U = \operatorname{trace}\left(\frac{\partial J}{\partial \mathbf{U}}(\mathbf{B}, \mathbf{U}) \tilde{\mathbf{U}} \right). \tag{D.20}$$

Since these equations must hold for all directions $\tilde{\mathbf{B}}$ and $\tilde{\mathbf{U}}$, the definitions of the inner products in (6.40) now show that

$$\nabla_{\mathbf{B}} J(\mathbf{B}, \mathbf{U}) = \mathbf{E}_0^{-1} \left(\frac{\partial J}{\partial \mathbf{B}}(\mathbf{B}, \mathbf{U}) \right)^{\top}, \quad \nabla_{\mathbf{U}} J(\mathbf{B}, \mathbf{U}) = \left(\frac{\partial J}{\partial \mathbf{U}}(\mathbf{B}, \mathbf{U}) \right)^{\top}. \tag{D.21}$$

To find an expression for $\partial J / \partial \mathbf{U}$, note that (D.17) shows that

$$\frac{\partial J}{\partial \mathbf{U}} = \begin{bmatrix} \frac{\partial J}{\partial u_{1,1}} & \frac{\partial J}{\partial u_{2,1}} & \cdots & \frac{\partial J}{\partial u_{m,1}} \\ \frac{\partial J}{\partial u_{1,2}} & \frac{\partial J}{\partial u_{2,2}} & \cdots & \frac{\partial J}{\partial u_{m,2}} \\ \vdots & \vdots & & \vdots \\ \frac{\partial J}{\partial u_{1,n}} & \frac{\partial J}{\partial u_{2,n}} & \cdots & \frac{\partial J}{\partial u_{m,n}} \end{bmatrix} = \begin{bmatrix} \frac{\partial J}{\partial \mathbf{u}_1} \\ \frac{\partial J}{\partial \mathbf{u}_2} \\ \vdots \\ \frac{\partial J}{\partial \mathbf{u}_n} \end{bmatrix}, \tag{D.22}$$

where $\mathbf{u}_j$ denotes the j-th column of $\mathbf{U}$ and the partial derivatives $\partial J / \partial \mathbf{u}_j$ w.r.t. the column $\mathbf{u}_j$ are row vectors. For a cost functional J of the form (6.41) this

expression can be further simplified as

$$\frac{\partial J}{\partial \mathbf{U}} = \begin{bmatrix} \frac{\partial f_1}{\partial \mathbf{q}_{\mathrm{act},1}}(\mathbf{q}_{\mathrm{act},1})\frac{\partial \mathbf{q}_{\mathrm{act},1}}{\partial \mathbf{u}_1} \\ \frac{\partial g f_2}{\partial \mathbf{q}_{\mathrm{act},2}}(\mathbf{q}_{\mathrm{act},2})\frac{\partial \mathbf{q}_{\mathrm{act},2}}{\partial \mathbf{u}_2} \\ \vdots \\ \frac{\partial g f_n}{\partial \mathbf{q}_{\mathrm{act},n}}(\mathbf{q}_{\mathrm{act},n})\frac{\partial \mathbf{q}_{\mathrm{act},n}}{\partial \mathbf{u}_n} \end{bmatrix} = \begin{bmatrix} \frac{\partial f_1}{\partial \mathbf{q}_{\mathrm{act},1}}(\mathbf{q}_{\mathrm{act},1}) \\ \frac{\partial f_2}{\partial \mathbf{q}_{\mathrm{act},2}}(\mathbf{q}_{\mathrm{act},2}) \\ \vdots \\ \frac{\partial f_n}{\partial \mathbf{q}_{\mathrm{act},n}}(\mathbf{q}_{\mathrm{act},n}) \end{bmatrix} \mathbf{B} = \mathbf{G}(\mathbf{B},\mathbf{U})\mathbf{B}, \quad \text{(D.23)}$$

with $\mathbf{G}(\mathbf{B},\mathbf{U})$ as in (6.43).

The derivative $\partial J/\partial \mathbf{B}$ is a bit harder to compute. Consider therefore first only the derivative w.r.t. the i-th column $\mathbf{B}_i$ of $\mathbf{B}$, which yields

$$\begin{aligned} \frac{\partial J}{\partial \mathbf{B}_i} &= \sum_{j=1}^{n} \frac{\partial f_j}{\partial \mathbf{q}_{\mathrm{act},j}}(\mathbf{q}_{\mathbf{act},j})\frac{\partial \mathbf{q}_{\mathrm{act},j}}{\partial \mathbf{B}_i} = \sum_{j=1}^{n} \frac{\partial f_j}{\partial \mathbf{q}_{\mathrm{act},j}}(\mathbf{q}_{\mathbf{act},j})\mathbf{I}_{N_{\mathrm{top}}} u_{i,j} \\ &= \sum_{j=1}^{n} u_{i,j} \frac{\partial f_j}{\partial \mathbf{q}_{\mathrm{act},j}}(\mathbf{q}_{\mathrm{act},j}) = \begin{bmatrix} u_{i,1} & u_{i,2} & \cdots & u_{i,n} \end{bmatrix} \begin{bmatrix} \frac{\partial f_1}{\partial \mathbf{q}_{\mathrm{act},1}}(\mathbf{q}_{\mathrm{act},1}) \\ \frac{\partial f_2}{\partial \mathbf{q}_{\mathrm{act},2}}(\mathbf{q}_{\mathrm{act},2}) \\ \vdots \\ \frac{\partial f_n}{\partial \mathbf{q}_{\mathrm{act},n}}(\mathbf{q}_{\mathrm{act},n}) \end{bmatrix}. \quad \text{(D.24)} \end{aligned}$$

As the rows of $\partial J/\partial \mathbf{B}$ are the derivatives of J w.r.t. to the columns of $\mathbf{B}$ (see also (D.17)), it now follows that

$$\frac{\partial J}{\partial \mathbf{B}} = \begin{bmatrix} \frac{\partial J}{\partial \mathbf{B}_1} \\ \frac{\partial J}{\partial \mathbf{B}_2} \\ \vdots \\ \frac{\partial J}{\partial \mathbf{B}_m} \end{bmatrix} = \mathbf{U} \begin{bmatrix} \frac{\partial f_1}{\partial \mathbf{q}_{\mathrm{act},1}}(\mathbf{q}_{\mathrm{act},1}) \\ \frac{\partial f_2}{\partial \mathbf{q}_{\mathrm{act},2}}(\mathbf{q}_{\mathrm{act},2}) \\ \vdots \\ \frac{\partial f_n}{\partial \mathbf{q}_{\mathrm{act},n}}(\mathbf{q}_{\mathrm{act},n}) \end{bmatrix} = \mathbf{U}\mathbf{G}(\mathbf{B},\mathbf{U}), \quad \text{(D.25)}$$

with $\mathbf{G}(\mathbf{B},\mathbf{U})$ again as in (6.43). Inserting the formulas (D.25) and (D.23) into (D.21) now yields (6.42). Explicit expressions for the derivatives $\partial f_j/\partial \mathbf{q}_{\mathrm{act},j}$ will be given in Subsection D.3.3.

D.3.2 The Hessians

To compute the directional Hessians of a cost functional J of the form (6.41) w.r.t. $\mathbf{B}$ and $\mathbf{U}$, it will be convenient to introduce the $N_{\mathrm{top}} \times n$-matrix

$$\begin{aligned} \mathbf{Q}_{\mathrm{act}} := \mathbf{B}\mathbf{U} &= \begin{bmatrix} \mathbf{q}_{\mathrm{act},1} & \mathbf{q}_{\mathrm{act},2} & \cdots & \mathbf{q}_{\mathrm{act},n} \end{bmatrix} \\ &= \begin{bmatrix} q_{1,1} & q_{1,2} & \cdots & q_{1,n} \\ q_{2,1} & q_{2,2} & \cdots & q_{2,n} \\ \vdots & \vdots & & \vdots \\ q_{N_{\mathrm{top}},1} & q_{N_{\mathrm{top}},2} & \cdots & q_{N_{\mathrm{top}},n} \end{bmatrix}. \quad \text{(D.26)} \end{aligned}$$

Note that the columns of $\mathbf{Q}_{\mathrm{act}}$ are the $\mathbf{q}_{\mathrm{act},j}$ as defined in (6.30) and that the cost functional J in (6.41) can thus be considered as a function of $\mathbf{Q}_{\mathrm{act}}$. Now consider the composition $J(\mathbf{Q}_{\mathrm{act}}(h))$ of a general cost function $J(\mathbf{Q}_{\mathrm{act}})$ and a function $\mathbf{Q}_{\mathrm{act}}(h)$ depending on a scalar parameter h and compute

$$\begin{aligned}\frac{\partial^2 J(\mathbf{Q}_{\mathrm{act}}(h))}{\partial h^2} &= \frac{\partial}{\partial h}\left(\sum_{\ell=1}^{N_{\mathrm{top}}}\sum_{k=1}^{n}\frac{\partial J}{\partial q_{\ell,k}}(\mathbf{Q}_{\mathrm{act}}(h))\frac{\partial q_{\ell,k}}{\partial h}(h)\right)\\ &= \sum_{\ell,\ell'=1}^{N_{\mathrm{top}}}\sum_{k,k'=1}^{n}\frac{\partial^2 J}{\partial q_{\ell,k}\partial q_{\ell',k'}}(\mathbf{Q}_{\mathrm{act}}(h))\frac{\partial q_{\ell,k}}{\partial h}(h)\frac{\partial q_{\ell' k'}}{\partial h}(h)\\ &\qquad + \sum_{\ell=1}^{N_{\mathrm{top}}}\sum_{j=1}^{n}\frac{\partial J}{\partial q_{\ell,k}}(\mathbf{Q}_{\mathrm{act}}(h))\frac{\partial^2 q_{\ell k}}{\partial h^2}(h). \end{aligned} \tag{D.27}$$

Using the form of J in (6.41) and assuming that $\mathbf{Q}_{\mathrm{act}}(h) = \mathbf{Q}_{\mathrm{act},0} + h\tilde{\mathbf{Q}}_{\mathrm{act}}$ depends linearly on h, it follows from (D.27) that

$$\begin{aligned}\left.\frac{\partial^2 J(\mathbf{Q}_{\mathrm{act}}(h))}{\partial h^2}\right|_{h=0} &= \sum_{j=1}^{n}\sum_{\ell,\ell'=1}^{N_{\mathrm{top}}}\sum_{k,k'=1}^{n}\frac{\partial^2 f_j}{\partial q_{\ell,k}\partial q_{\ell',k'}}(\mathbf{q}_{\mathrm{act},0,j})\tilde{q}_{\ell,k}\tilde{q}_{\ell',k'}\\ &= \sum_{j=1}^{n}\sum_{\ell,\ell'=1}^{N_{\mathrm{top}}}\frac{\partial^2 f_j}{\partial q_{\ell,j}\partial q_{\ell',j}}(\mathbf{q}_{\mathrm{act},0,j})\tilde{q}_{\ell,j}\tilde{q}_{\ell',j},\\ &= \sum_{j=1}^{n}\tilde{\mathbf{q}}_{\mathrm{act},j}^{\top}\frac{\partial^2 f_j}{\partial \mathbf{q}_{\mathrm{act},j}^2}(\mathbf{q}_{\mathrm{act},0,j})\tilde{\mathbf{q}}_{\mathrm{act},j}, \end{aligned} \tag{D.28}$$

where $\mathbf{q}_{\mathrm{act},0,j}$ and $\tilde{\mathbf{q}}_{\mathrm{act},j}$ denote the j-th column of $\mathbf{Q}_{\mathrm{act},0}$ and $\tilde{\mathbf{Q}}_{\mathrm{act}}$, respectively, $\tilde{q}_{\ell,k}$ denotes the element (ℓ,k) of $\tilde{\mathbf{Q}}_{\mathrm{act}}$, and

$$\frac{\partial^2 f_j}{\partial \mathbf{q}_{\mathrm{act},j}^2} = \begin{bmatrix} \frac{\partial^2 f_j}{\partial q_{1,j}^2} & \frac{\partial^2 f_j}{\partial q_{1,j}\partial q_{2,j}} & \cdots & \frac{\partial^2 f_j}{\partial q_{1,j}\partial q N_{\mathrm{top}},j} \\ \frac{\partial^2 f_j}{\partial q_{2,j}\partial q_{1,j}} & \frac{\partial^2 f_j}{\partial q_{2,j}^2} & \cdots & \frac{\partial^2 f_j}{\partial q_{2,j}\partial q_{N_{\mathrm{top}},j}} \\ \vdots & \vdots & \ddots & \vdots \\ \frac{\partial^2 f_j}{\partial q_{N_{\mathrm{top}},j}\partial q_{1,j}} & \frac{\partial^2 f_j}{\partial q_{N_{\mathrm{top}},j}\partial q_{2,j}} & \cdots & \frac{\partial^2 f_j}{\partial q_{N_{\mathrm{top}},j}^2} \end{bmatrix}. \tag{D.29}$$

Note that the second identity in (D.28) follows because f_j only depends on the j-th column of $\mathbf{Q}_{\mathrm{act}}(h)$ and the third identity from (D.29).

The directional Hessian $H_{\mathbf{B}}$ in the point $(\mathbf{B},\mathbf{U})$ for the detection $\tilde{\mathbf{B}}$ is now obtained by setting

$$\mathbf{Q}_{\mathrm{act}}(h) = (\mathbf{B} + h\tilde{\mathbf{B}})\mathbf{U}, \qquad \Rightarrow \qquad \tilde{\mathbf{q}}_{\mathrm{act},j} = \tilde{\mathbf{B}}\mathbf{u}_j. \tag{D.30}$$

Using the formulas for $\partial^2 f_j/\partial \mathbf{q}_{\mathrm{act},j}^2$ that will be determined in Subsection D.3.3, $H_{\mathbf{B}}$ now follows from (D.28).

The directional Hessian $H_{\mathbf{U}}$ in the point $(\mathbf{B}, \mathbf{U})$ for the detection $\tilde{\mathbf{U}}$ is now obtained by setting

$$\mathbf{Q}_{\mathrm{act}}(h) = \mathbf{B}(\mathbf{U} + h\tilde{\mathbf{U}}), \qquad \Rightarrow \qquad \tilde{\mathbf{q}}_{\mathrm{act},j} = \mathbf{B}\tilde{\mathbf{u}}_j, \tag{D.31}$$

where $\tilde{\mathbf{u}}_j$ denotes the j-th column of $\tilde{\mathbf{U}}$. The directional Hessian $H_{\mathbf{U}}$ can now be computed from (D.28) and the formulas for $\partial^2 f_j/\partial \mathbf{q}_{\mathrm{act},j}^2$ that will be determined in Subsection D.3.3.

D.3.3 Explicit expressions for the derivatives of f_j

The cost functional J_1 in (6.36) can be written as a function of the applied actuation heat loads $\mathbf{q}_{\mathrm{act},j}$ by eliminating $\boldsymbol{\theta}_{\mathrm{top},j}$ using (6.30). The resulting cost functional J_1 can then be written in the form (6.41) by setting (for $1 \leq j \leq n$)

$$f_j(\mathbf{q}_{\mathrm{act},j}) = \mathbf{w}_{\mathrm{top}}^\top \left[\left(\boldsymbol{\theta}_{\mathrm{EUV},j} + \boldsymbol{\Gamma}\mathbf{q}_{\mathrm{act},j} - T^*\mathbf{1} \right)^2 - \delta^2 \mathbf{1} \right]^+. \tag{D.32}$$

Differentiating the expression to $\mathbf{q}_{\mathrm{act},j}$ now yields

$$\frac{\partial f_j}{\partial \mathbf{q}_{\mathrm{act},j}}(\mathbf{q}_{\mathrm{act},j}) = \left(\mathbf{w}_{\mathrm{top}} \circ \mathbf{1}_j^+ \circ 2\left(\boldsymbol{\theta}_{\mathrm{EUV},j} + \boldsymbol{\Gamma}\mathbf{q}_{\mathrm{act},j} - T^*\mathbf{1} \right) \right)^\top \boldsymbol{\Gamma}. \tag{D.33}$$

where $\circ$ denotes the componentwise (Hadamard) product of vectors and

$$\left(\mathbf{1}_j^+\right)_\ell = \begin{cases} 1 & \text{when } \left| (\boldsymbol{\theta}_{\mathrm{EUV},j} + \boldsymbol{\Gamma}\mathbf{q}_{\mathrm{act},j})_\ell - T^* \right| > \delta, \\ 0 & \text{otherwise.} \end{cases} \tag{D.34}$$

Differentiating this expression again w.r.t. $\mathbf{q}_{\mathrm{act},j}$ shows that

$$\frac{\partial^2 f_j}{\partial \mathbf{q}_{\mathrm{act},j}^2}(\mathbf{q}_{\mathrm{act},j}) = \boldsymbol{\Gamma}^\top \mathrm{diag}(\mathbf{w}_{\mathrm{top}} \circ \mathbf{1}_j^+) \boldsymbol{\Gamma}, \tag{D.35}$$

where $\mathrm{diag}(\mathbf{v})$ denotes a matrix with the components of $\mathbf{v}$ on the diagonal.

The cost functional J_2 in (6.37) can be written in the form (6.41) with

$$f_j(\mathbf{q}_{\mathrm{act},j}) = \mathbf{w}_{\mathrm{top}}^\top \left(\left(\frac{\delta^2 \mathbf{1}}{\delta^2 \mathbf{1} - (\boldsymbol{\theta}_{\mathrm{EUV},j} + \boldsymbol{\Gamma}\mathbf{q}_{\mathrm{act},j} - T^*\mathbf{1})^2} \right)^p - \mathbf{1} \right). \tag{D.36}$$

Note that $\boldsymbol{\theta}_{\mathrm{top},j}$ has again been eliminated using (6.30). To compute the derivatives of $f_j(\mathbf{q}_{\mathrm{act},j})$, first consider the function $g : \mathbb{R} \to \mathbb{R}$ given by

$$g(T) = \left(\frac{\delta^2}{\delta^2 - (T - T^*)^2} \right)^p - 1, \tag{D.37}$$

and note that the chain rule for differentiation shows that

$$\begin{aligned}\frac{\partial g}{\partial T}(T) &= p\left(\frac{\delta^2}{\delta^2-(T-T^*)^2}\right)^{p-1}\frac{-\delta^2}{(\delta^2-(T-T^*)^2)^2}\left(-2(T-T^*)\right)\\ &= \frac{2p}{\delta^2}\left(\frac{\delta^2}{\delta^2-(T-T^*)^2}\right)^{p+1}(T-T^*),\end{aligned} \tag{D.38}$$

$$\begin{aligned}\frac{\partial^2 g}{\partial T^2}(T) &= \frac{2p(p+1)}{\delta^2}\left(\frac{\delta^2}{\delta^2-(T-T^*)^2}\right)^{p}\frac{-\delta^2\left(-2(T-T^*)\right)}{(\delta^2-(T-T^*)^2)^2}(T-T^*)\\ &\quad+\frac{2p}{\delta^2}\left(\frac{\delta^2}{\delta^2-(T-T^*)^2}\right)^{p+1}\\ &= \frac{2p}{\delta^2}\left(\frac{\delta^2}{\delta^2-(T-T^*)^2}\right)^{p+1}\left(1+2(p+1)\frac{(T-T^*)^2}{\delta^2-(T-T^*)^2}\right).\end{aligned} \tag{D.39}$$

Using these results it is now easy to see that

$$\frac{\partial f_j}{\partial \mathbf{q}_{\mathrm{act},j}}(\mathbf{q}_{\mathrm{act},j}) = \left(\mathbf{w}_{\mathrm{top}}\circ\mathbf{a}_j\circ(\boldsymbol{\theta}_{\mathrm{top},j}-T^*\mathbf{1})\right))^\top\boldsymbol{\Gamma}, \tag{D.40}$$

$$\frac{\partial^2 f_j}{\partial \mathbf{q}_{\mathrm{act},j}^2}(\mathbf{q}_{\mathrm{act},j}) = \boldsymbol{\Gamma}^\top\mathrm{diag}(2\mathbf{w}_{\mathrm{top}}\circ\mathbf{d}_j)\boldsymbol{\Gamma}, \tag{D.41}$$

where $\boldsymbol{\theta}_{\mathrm{top},j} = \boldsymbol{\theta}_{\mathrm{EUV},j} + \boldsymbol{\Gamma}\mathbf{q}_{\mathrm{act},j}$ as in (6.30) and

$$\mathbf{a}_j = \frac{2p}{\delta^2}\left(\frac{\delta^2\mathbf{1}}{\delta^2\mathbf{1}-(\boldsymbol{\theta}_{\mathrm{top},j}-T^*\mathbf{1})^2}\right)^{p+1}, \tag{D.42}$$

$$\mathbf{b}_j = \mathbf{a}_j\circ\left(\mathbf{1}+2(p+1)\frac{(\boldsymbol{\theta}_{\mathrm{top},j}-T^*\mathbf{1})^2}{\delta^2-(\boldsymbol{\theta}_{\mathrm{top},j}-T^*\mathbf{1})^2}\right). \tag{D.43}$$

Appendix E

Appendices to Chapter 7

E.1 Derivation of the transfer functions

E.1.1 One-dimensional spatial domain

As the system (7.1)–(7.2) is considered on the unbounded domain $x \in \mathbb{R}$, it is translation invariant in x, i.e. shifting all input and output locations over the same distance results does not change the input-output behavior. The transfer functions of the infinite-dimensional system (7.1)–(7.2) are thus of the form (7.3) in which $G(s, x_0)$ is the transfer function of the system

$$\frac{\partial T}{\partial t}(x,t) = v\frac{\partial T}{\partial x}(x,t) + D\frac{\partial T^2}{\partial x^2}(x,t) - hT(x,t) + \frac{1}{c}\delta(x)u_0(t), \tag{E.1}$$

with input $u_0(t)$ and output $y_0(t) = T(x_0, t)$ and zero initial conditions. The transfer function $G(s, x_0)$ will be determined by searching for a solution $T(x,t) = T_0(x,s)e^{st}$ resulting from the input $u_0(t) = e^{st}$, see [Curtain and Zwart, 1995] and also [Curtain and Morris, 2009]. Because $y_0(t) = T(x_0, t)$, the output resulting from the input $u_0(t) = e^{st}$ is $y_0(s) = T_0(x_0, s)e^{st}$ and the transfer function $G(s, x_0)$ can thus be determined from $T_0(x, s)$ as $G(s, x_0) = T_0(x_0, s)$. Substituting the expressions for $T(x,t)$ and $u_0(t)$ into (7.1) and dividing the resulting equation by e^{st}, it follows that

$$sT_0(x,s) = v\frac{\partial T_0}{\partial x}(x,s) + D\frac{\partial^2 T_0}{\partial x^2}(x,s) - hT_0(x,s) + \frac{1}{c}\delta(x). \tag{E.2}$$

For $x \neq 0$, $T_0(x,s)$ is equal to a homogeneous solution of the form

$$T_{0,\mathrm{hom}}(x,s) = A(s)e^{x\lambda_+(s)} + B(s)e^{x\lambda_-(s)}, \tag{E.3}$$

where $A(s)$ and $B(s)$ do not depend on x and

$$\lambda_+(s) = \frac{-v + \sqrt{v^2 + 4D(h+s)}}{2D}, \qquad \lambda_-(s) = \frac{-v - \sqrt{v^2 + 4D(h+s)}}{2D}. \quad \text{(E.4)}$$

Because $T_0(x,s)$ should be equal to a homogeneous solution on the domains $x < 0$ and $x > 0$, it follows that

$$T_0(x,s) = \begin{cases} A_-(s)e^{x\lambda_+(s)} + B_-(s)e^{x\lambda_-(s)} & \text{for } x < 0, \\ A_+(s)e^{x\lambda_+(s)} + B_+(s)e^{x\lambda_-(s)} & \text{for } x > 0, \end{cases} \quad \text{(E.5)}$$

for some $A_-(s)$, $B_-(s)$, $A_+(s)$, and $B_+(s)$ that do not depend on x.

Recall that it is assumed that $v \geq 0$. Because $\mathrm{Re}(\sqrt{\zeta}) \geq 0$ for all $\zeta \in \mathbb{C}$ it thus follows that $\mathrm{Re}(\lambda_-(s)) < 0$ for all $s \in \mathbb{C}$. Furthermore, observe that $\lambda_+(s) > 0$ for $s > 0$, i.e. for s on the positive real axis of the complex plane. There thus exists an open subset $V \subset \mathbb{C}$ containing the positive real axis such that $\lambda_+(s) > 0$ for all $s \in V$.

The transfer function $G_{yw}(s)$ will first be determined on this subset V. Because $\mathrm{Re}(\lambda_+(s)) > 0$ for $s \in V$ it follows that $e^{x\lambda_+(s)} \to \infty$ for $x \to \infty$. Since $T_0(x,s)$ should remain bounded for $x \to \infty$, (E.5) shows that $A_+(s) = 0$. Similarly, $e^{x\lambda_-(s)} \to \infty$ for $x \to -\infty$ because $\mathrm{Re}(\lambda_-(s)) < 0$, so that $B_-(s) = 0$.

The remaining constants $A_-(s)$ and $B_+(s)$ are determined such that $T_0(x,s)$ is a weak solution of (E.2) near $x = 0$. To this end, (E.2) is multiplied by a smooth test function $f(x)$ and integrated over the interval $x \in (-\varepsilon, \varepsilon)$. After bringing all terms containing $T_0(x,s)$ to the LHS, it follows that

$$\int_{-\varepsilon}^{\varepsilon} f(x) \left(-D\frac{\partial^2 T_0}{\partial x^2}(x,s) - v\frac{\partial T_0}{\partial x}(x,s) + (h+s)T_0(x,s) \right) \mathrm{d}x = \frac{f(0)}{c}. \quad \text{(E.6)}$$

The LHS is rewritten by integrating by parts twice,

$$\begin{aligned} & f(x)\left(-D\frac{\partial T_0}{\partial x}(x,s) - vT_0(x,s) \right)\Big|_{x=-\varepsilon}^{\varepsilon} \\ & \quad + \int_{-\varepsilon}^{\varepsilon} \left(\frac{\partial f}{\partial x}(x)\left(D\frac{\partial T_0}{\partial x}(x,s) + vT_0(x,s) \right) + f(x)(h+s)T_0(x,s) \right) \mathrm{d}x \\ & = f(x)\left(-D\frac{\partial T_0}{\partial x}(x,s) - vT_0(x,s) \right)\Big|_{x=-\varepsilon}^{\varepsilon} + \frac{\partial f}{\partial x}(x)DT_0(x,s)\Big|_{x=-\varepsilon}^{\varepsilon} \\ & \quad + \int_{-\varepsilon}^{\varepsilon} \left(-\frac{\partial^2 f}{\partial x^2}(x)D + \frac{\partial f}{\partial x}(x)v + f(x)(h+s) \right) T_0(x,s)\, \mathrm{d}x = \frac{f(0)}{c}. \end{aligned} \quad \text{(E.7)}$$

As $f(x)$ is smooth and $T_0(x,s)$ is bounded, the integral over x vanishes when taking the limit $\varepsilon \downarrow 0$. Using the smoothness of $f(x)$, it thus follows that

$$f(0)\lim_{\varepsilon\downarrow 0}\left(-D\frac{\partial T_0}{\partial x}(x,s) - vT_0(x,s) \right)\Big|_{x=-\varepsilon}^{\varepsilon} + \frac{\partial f}{\partial x}(0)\lim_{\varepsilon\downarrow 0} DT_0(x,s)\Big|_{x=-\varepsilon}^{\varepsilon} = \frac{f(0)}{c}. \quad \text{(E.8)}$$

Since this equation must hold for any smooth test function $f(x)$, the terms on the LHS and RHS multiplied by $\partial f/\partial x(0)$ and $f(0)$ must match. Therefore,

$$\lim_{\varepsilon\downarrow 0} T_0(\varepsilon, s) - \lim_{\varepsilon\uparrow 0} T_0(\varepsilon, s) = 0, \qquad \lim_{\varepsilon\downarrow 0} \frac{\partial T_0}{\partial x}(\varepsilon, s) - \lim_{\varepsilon\uparrow 0} \frac{\partial T_0}{\partial x}(\varepsilon, s) = \frac{-1}{cD}. \quad \text{(E.9)}$$

Using the form $T_0(x, s)$ in (E.5) with $A_+(s) = B_-(s) = 0$, it thus follows that

$$B_+(s) - A_-(s) = 0, \qquad B_+(s)\lambda_-(s) - A_-(s)\lambda_+(s) = \frac{-1}{cD}, \quad \text{(E.10)}$$

which implies that

$$B_+(s) = A_-(s) = \frac{1}{cD(\lambda_+(s) - \lambda_-(s))}. \quad \text{(E.11)}$$

Inserting these expressions back into (E.5) it thus follows that

$$T_0(x, s) = \frac{1}{Dc(\lambda_+(s) - \lambda_-(s))} \begin{cases} e^{x\lambda_+(s)} & \text{for } x < 0, \\ e^{x\lambda_-(s)} & \text{for } x > 0. \end{cases} \quad \text{(E.12)}$$

$$= \frac{1}{c\sqrt{v^2 + 4D(h+s)}} \begin{cases} e^{x\lambda_+(s)} & \text{for } x < 0, \\ e^{x\lambda_-(s)} & \text{for } x > 0, \end{cases} \quad \text{(E.13)}$$

$$= \frac{e^{-xv/2D}}{c\sqrt{v^2 + 4D(h+s)}} e^{-|x|\sqrt{v^2+4D(h+s)}/2D}, \quad \text{(E.14)}$$

where the last two identities follow from the expressions for $\lambda_+(s)$ and $\lambda_-(s)$ in (E.4). Using (E.1), it now follows that $y_0(t) = T(x_0, s) = e^{st}T_0(x_0, s)$, so that

$$G(s, x_0) = \frac{y_0(t)}{u_0(t)} = T_0(x_0, s) = \frac{e^{-x_0 v/2D}}{c\sqrt{v^2 + 4D(h+s)}} e^{-|x_0|\sqrt{v^2+4D(h+s)}/2D}. \quad \text{(E.15)}$$

Note that this expression for the transfer function has been derived under the assumption that $s \in V$. However, (E.15) defines a holomorphic function on every subset of the complex plane that does not contain the line $s < -h - v^2/(4D)$ (i.e. $\{s \in \mathbb{C} \mid \mathrm{Re}(s) < -h - v^2/(4D), \mathrm{Im}(s) = 0\}$). In particular, formula (E.15) defines the transfer function on the open right half plane which is the required domain for a transfer function in $\mathcal{H}_\infty$, see Definition 7.1. Formula (E.15) thus defines the transfer function of (E.1).

E.1.2 Two-dimensional spatial domain

On the 2-D spatial domain a similar approach can be used. Again, the considered spatial domain is unbounded which means that shifting all input and output locations over the same displacement vector does not change in the input-output behavior. This implies that the transfer functions of the system (7.19)–(7.20) are of the form (7.21) in which $G(s, \mathbf{x}_0)$ is the transfer function of the system

$$\frac{\partial T}{\partial t}(\mathbf{x}, t) = v\frac{\partial T}{\partial x_1}(\mathbf{x}, t) + D\left(\frac{\partial^2 T}{\partial x_1^2}(\mathbf{x}, t) + \frac{\partial^2 T}{\partial x_2^2}(\mathbf{x}, t)\right) - hT(\mathbf{x}, t) + \frac{1}{c_2}\delta(\mathbf{x})u_0(t), \tag{E.16}$$

with input $u_0(t)$ and output $y_0(t) = T(\mathbf{x}_0, t)$ and zero initial conditions. Again following the approach from [Curtain and Zwart, 1995; Curtain and Morris, 2009], the transfer function of this system is determined by searching for a solution $T(\mathbf{x}, t) = e^{st}T_0(\mathbf{x}, s)$ resulting from the input $u_0(t) = e^{st}$. Substituting this expression into (E.16) and dividing by e^{st}, it follows that $T_0(\mathbf{x}, s)$ is the solution of the elliptic equation

$$sT_0(\mathbf{x}, s) = v\frac{\partial T_0}{\partial x_1}(\mathbf{x}, s) + D\left(\frac{\partial^2 T_0}{\partial x_1^2}(\mathbf{x}, s) + \frac{\partial^2 T_0}{\partial x_2^2}(\mathbf{x}, s)\right) - hT_0(\mathbf{x}, s) + \frac{1}{c_2}\delta(\mathbf{x}), \tag{E.17}$$

Note that the solution $T_0(\mathbf{x}, s)$is not radially symmetric around $\mathbf{x} = \mathbf{0}$ due to the advective transport term. To obtain a radially symmetric problem, write

$$T_0(\mathbf{x}, s) = e^{-x_1 v/2D}T_1(\mathbf{x}, s), \tag{E.18}$$

where the function $T_1(\mathbf{x}, s)$ will turn out to be radially symmetric. This transformation is taken from [Hahn and Ozisik, 2012]. Inserting this expression into (E.17) and dividing by $e^{-x_1 v/2D}$ now shows that

$$\begin{aligned} sT_1(\mathbf{x}, s) &= v\left(\frac{\partial T_1}{\partial x_1}(\mathbf{x}, s) + \frac{-v}{2D}T_1(\mathbf{x}, s)\right) + D\frac{\partial^2 T_1}{\partial x_2^2}(\mathbf{x}, s) + \\ &D\left(\frac{\partial^2 T_1}{\partial x_1^2}(\mathbf{x}, s) + 2\frac{-v}{2D}\frac{\partial T_1}{\partial x_1}(\mathbf{x}, s) + \frac{v^2}{4D^2}T_1(\mathbf{x}, s)\right) - hT_1(\mathbf{x}, s) + \frac{e^{x_1 v/2D}}{c_2}\delta(\mathbf{x}) \\ &= D\left(\frac{\partial^2 T_1}{\partial x_1^2}(\mathbf{x}, s) + \frac{\partial^2 T_1}{\partial x_2^2}(\mathbf{x}, s)\right) - \left(h + \frac{v^2}{4D}\right)T_1(\mathbf{x}, s) + \frac{1}{c_2}\delta(\mathbf{x}). \end{aligned} \tag{E.19}$$

The solution $T_1(\mathbf{x}, s)$ of this equation is thus indeed radially symmetric. After transformation to polar coordinates (r, θ) through $x_1 = r\cos(\theta)$ and $x_2 = r\sin(\theta)$, it thus follows that, away from $r = 0$, $T_1(r, \theta, s) = T_1(r, s)$ satisfies

$$\frac{D}{r}\frac{\partial}{\partial r}\left(r\frac{\partial T_1}{\partial r}(r, s)\right) - \left(s + h + \frac{v^2}{4D}\right)T_1(r, s) = 0. \tag{E.20}$$

This is an ODE in r of which the solution is given by, see e.g. [Gray and Mathews, 1952],

$$T_1(r, s) = A(s)I_0(\gamma(s)r) + B(s)K_0(\beta(s)r), \tag{E.21}$$

where $A(s)$ and $B(s)$ do not depend on r, and $I_0(r)$ and $K_0(r)$ denote the modified Bessel functions of the first and second kind, and

$$\beta(s) = \sqrt{\frac{1}{D}\left(s + h + \frac{v^2}{4D}\right)} = \frac{\sqrt{v^2 + 4D(h+s)}}{2D}. \tag{E.22}$$

Because $I_0(r) \to \infty$ for $r \to \infty$, it follows that $A(s) = 0$. The function $B(s)$ follows from the requirement that $T_1(r, \theta, s) = T_1(r, s)$ in (E.21) is a weak solution of (E.19) near $\mathbf{x} = \mathbf{0}$. A weak solution $T_1 = T_1(\mathbf{x}, s)$ of (E.19) should satisfy

$$\iint_\Omega \left(f(\mathbf{x}) D \nabla^2 T_1(\mathbf{x}, s) - f(\mathbf{x}) \left(s + h + \frac{v^2}{4D} \right) T_1(\mathbf{x}, s) \right) \, \mathrm{d}\mathbf{x} + \frac{1}{c_2} f(\mathbf{0}) = 0, \tag{E.23}$$

for any smooth test function $f(\mathbf{x})$ and any $\Omega \subseteq \mathbb{R}^2$. Here, ∇^2 denotes the Laplacian. The first term on the LHS is rewritten using one of Green's identities to find

$$\begin{aligned} \int_{\partial\Omega} f(\mathbf{x}) D \nabla T_1(\mathbf{x}, s) \cdot \mathbf{n} \, \mathrm{d}\ell - \iint_\Omega \nabla f(\mathbf{x}) \cdot D \nabla T_1(\mathbf{x}, s) \, \mathrm{d}\mathbf{x} \\ - \iint_\Omega f(\mathbf{x}) \left(s + h + \frac{v^2}{4D} \right) T_1(\mathbf{x}, s) \, \mathrm{d}\mathbf{x} + \frac{1}{c_2} f(\mathbf{0}) = 0, \end{aligned} \tag{E.24}$$

where $\mathbf{n}$ denotes the outward pointing normal to the edge $\partial\Omega$ and ∇ denotes the gradient. Now taking Ω as the disk of radius ε centred at $\mathbf{x} = \mathbf{0}$ and transforming to polar coordinates, it follows that

$$\begin{aligned} \int_0^{2\pi} f(\varepsilon, \theta) D \frac{\partial T_1}{\partial r}(\varepsilon, s) \varepsilon \, \mathrm{d}\theta - \int_0^\varepsilon \int_0^{2\pi} \frac{\partial f}{\partial r}(r, \theta) D \frac{\partial T_1}{\partial r}(r, s) r \, \mathrm{d}\theta \, \mathrm{d}r \\ - \int_0^\varepsilon \int_0^{2\pi} f(r, \theta) \left(s + h + \frac{v^2}{4D} \right) T_1(r, s) r \, \mathrm{d}\theta \, \mathrm{d}r + \frac{1}{c_2} f(0, 0) = 0. \end{aligned} \tag{E.25}$$

To determine the constant $B(s)$ in $T_1(r, s) = B(s) K_0(\beta(s) r)$, again the limit $\varepsilon \to 0$ should be considered. This requires the following characterization of the behavior of $K_0(r)$ near $r = 0$ from [Gray and Mathews, 1952]

$$K_0(r) = -\left(\log\left(\frac{r}{2}\right) + \gamma \right) + O(r), \tag{E.26}$$

where $\gamma = 2.718\ldots$ is the Euler-Mascheroni constant. It thus follows that $r T_1(r, s)$ is bounded near $r = 0$, which implies that the third term in (E.25) vanishes when taking the limit $\varepsilon \to 0$. Differentiating (E.26) yields

$$\frac{\partial K_0}{\partial r}(r) = \frac{-1}{r} + O(1). \tag{E.27}$$

It thus follows that $r\partial T_1/\partial r(r,s)$ is also bounded near $r = 0$ and the second term in (E.25) also vanishes in the limit $\varepsilon \to 0$. For the first term, note that

$$\lim_{\varepsilon \to 0} \frac{\partial T_1}{\partial r}(\varepsilon, s)\varepsilon = \lim_{\varepsilon \to 0} B(s) \left(\frac{-1}{\beta(s)\varepsilon} + O(1) \right) \beta(s)\varepsilon = -B(s) \tag{E.28}$$

Taking the limit $\varepsilon \to 0$ in (E.25) thus shows that

$$-2\pi f(0,0)DB(s) + \frac{1}{c_2} f(0,0) = 0, \tag{E.29}$$

so that $B(s) = 1/(2\pi c_2 D)$. Since $T_1(r,s) = B(s)K_0(\beta(s)r)$ and $r = \|\mathbf{x}\|$, it follows now from (E.18) and (E.22) that

$$T_0(\mathbf{x}, s) = \frac{e^{-x_1 v/2D}}{2\pi c_2 D} K_0 \left(\frac{\sqrt{v^2 + 4D(h+s)}\|\mathbf{x}\|}{2D} \right). \tag{E.30}$$

Finally, note that the output $y_0(t)$ resulting from the input $u_0(t) = e^{st}$ is given by $y_0(t) = T(\mathbf{x}_0, t) = T_0(\mathbf{x}_0, s)e^{st}$, so that $G(s, \mathbf{x}_0) = T_0(\mathbf{x}_0, s)$ and (7.22) follows.

E.2 Dynamic controllers

In this appendix, it will be shown that the thermal control systems on the 1-D and 2-D spatial domains considered in Chapter 7 do not have any fundamental performance limitations. In other words, it will be shown that the closed-loop transfer function can be made arbitrarily small by a stabilizing (dynamic) feedback controller.

Both on the 1-D and 2-D spatial domain, the considered plant is of the form

$$\begin{bmatrix} Z(s) \\ Y(s) \end{bmatrix} = \begin{bmatrix} G_{zw}(s) & G_{zu}(s) \\ G_{yw}(s) & G_{yu}(s) \end{bmatrix} \begin{bmatrix} W(s) \\ U(s) \end{bmatrix}. \tag{E.31}$$

Under the (dynamic) feedback control $U(s) = -K(s)Y(s)$, the closed-loop transfer function from $W(s)$ to $Z(s)$ is

$$M(s) = G_{zw}(s) - \frac{G_{zu}(s)K(s)G_{yw}(s)}{1 + K(s)G_{yu}(s)} = G_{zw}(s) - G_{zu}(s)Q(s)G_{yw}(s), \tag{E.32}$$

where $Q(s)$ denotes the Youla parameter

$$Q(s) = \frac{K(s)}{1 + K(s)G_{yu}(s)}. \tag{E.33}$$

If the plant is stable, i.e. if the transfer functions $G_{zw}(s)$, $G_{zu}(s)$, $G_{yw}(s)$, and $G_{yu}(s)$ are in $\mathcal{H}_\infty$ (see Definition 7.1), the controller $K(s)$ is stabilizing when

$Q(s)$ is an element $\mathcal{H}_\infty$, see e.g. [Doyle et al., 1992]. A stabilizing controller $K(s)$ can thus be designed by designing the Youla parameter $Q(s)$. By rewriting (E.33), the corresponding controller is then given by

$$Q(s) - K(s)G_{yu}(s)Q(s) = K(s) \qquad \Leftrightarrow \qquad K(s) = \frac{Q(s)}{1 - G_{yu}(s)Q(s)}. \quad \text{(E.34)}$$

Note that $Q(s) \in \mathcal{H}_\infty$ does not imply that $K(s) \in \mathcal{H}_\infty$. It will also *not* be required in the following that $K(s) \in \mathcal{H}_\infty$. However, it will be required that $K(s)$ represents a causal system, i.e. that $K(s)$ is proper. An irrational transfer function is called proper if $|K(s)|$ does not grow unbounded when $|s| \to \infty$ in the right half of the complex plane, see also e.g. [Curtain and Zwart, 1995]. Similarly, a transfer function $K(s)$ is called strictly proper if $|K(s)| \to 0$ for $|s| \to \infty$ in the right half of the complex plane.

To design $Q(s)$, note that the closed-loop transfer function $M(s)$ in (E.32) can be made zero by setting $Q(s)$ equal to

$$Q_0(s) = \frac{G_{zw}(s)}{G_{zu}(s)G_{yw}(s)}. \quad \text{(E.35)}$$

However, setting $Q(s) = Q_0(s)$ can be problematic for two reasons: 1) $Q_0(s)$ is not necessarily an element of $\mathcal{H}_\infty$, and 2) the corresponding controller $K(s)$ in (E.34) might not be proper. There are generally two reasons for Problem 1: 1a) $G_{zu}(s)$ or $G_{yw}(s)$ have zeros in the right half of the complex plane, or 1b) $Q_0(s)$ is not bounded at infinity. Problem 1a never occurs for the transfer functions considered in Chapter 7 because they do not have zeros. It will be demonstrated below that Problems 1b and 2 can be circumvented by setting

$$Q(s) = Q_0(s)Q_{\text{LP}}(s), \quad \text{(E.36)}$$

where $Q_{\text{LP}}(s)$ is a suitably designed low-pass filter.

E.2.1 1-D spatial domain

Inserting the expressions for the transfer functions in (7.3)–(7.4) into (E.35) shows that

$$Q_0(s) = c\frac{\sqrt{v^2 + 4D(s+h)}}{e^{-(x_y - x_u)v/2D}} e^{(|x_z - x_u| + |x_y - x_w| - |x_z - x_w|)\sqrt{v^2+4D(s+h)}/2D}, \quad \text{(E.37)}$$

so that $Q_0(s)$ is an element of $\mathcal{H}_\infty$ when

$$|x_z - x_u| + |x_y - x_w| < |x_z - x_w|. \quad \text{(E.38)}$$

Otherwise, the additional low-pass filter $Q_{\text{LP}}(s)$ can be defined as

$$Q_{\text{LP}}(s) = e^{-(|x_z - x_u| + |x_y - x_w| - |x_z - x_w| + \varepsilon)(\sqrt{\omega_c/D} - \sqrt{(\omega_c + s)/D})}, \quad \text{(E.39)}$$

with parameter $\varepsilon > 0$ and cut-off frequency ω_c. Note that $Q_{\mathrm{LP}}(s) \approx 1$ for $|s| \ll \omega_c$ and that this choice of $Q_{\mathrm{LP}}(s)$ makes $Q(s)$ in (E.36) proper. Inserting (E.36) into (E.32) yields

$$M(s) = G_{zw}(s)(1 - Q_{\mathrm{LP}}(s)). \tag{E.40}$$

Since $G_{zw}(s)$ is strictly proper, $\|M\|_\infty$ can be made arbitrarily small by increasing ω_c. Also note that the resulting controller $K(s)$ in (E.34) is strictly proper because $Q(s)$ and $G_{yu}(s)$ are strictly proper.

E.2.2 2-D spatial domain

Inserting the transfer functions on the 2-D spatial domain from (7.21)–(7.22) into (E.35) shows that

$$Q_0(s) = \frac{2\pi c_2 D}{e^{-(x_{y,1}-x_{u,1})v/2D}} \frac{K_0(\beta(s)\|\mathbf{x}_z - \mathbf{x}_w\|)}{K_0(\beta(s)\|\mathbf{x}_z - \mathbf{x}_u\|)K_0(\beta(s)\|\mathbf{x}_y - \mathbf{x}_w\|)}, \tag{E.41}$$

with $\beta(s)$ as in (E.22). As $K_0(\zeta)$ has no zeros for $\zeta \in \mathbb{C}$ with $\mathrm{Re}(\zeta) \geq 0$, see e.g. [Gray and Mathews, 1952], it remains to check that $Q_0(s)$ is proper. To study the behavior of $Q_0(s)$ for $|s| \to \infty$ with $\mathrm{Re}(s) \geq 0$, the asymptotic expansion (7.25) is used. In particular, note that for $|s| \to \infty$ with $\mathrm{Re}(s) \geq 0$

$$G(s, \mathbf{x}) \to \tilde{G}(s, \mathbf{x}) = \frac{C_1}{\sqrt[4]{v^2 + 4D(h+s)}} e^{-\|\mathbf{x}\|\sqrt{v^2+4D(s+h)}/2D}, \tag{E.42}$$

with $G(s, \mathbf{x})$ as in (7.22), $\tilde{G}(s, \mathbf{x})$ as in (7.27), and C_1 a constant that does not depend on s. From the formula for $Q_0(s)$ in (E.35) and the form of the transfer functions in (7.21), it thus follows that for $|s| \to \infty$ with $\mathrm{Re}(s) \geq 0$

$$\begin{aligned} Q_0(s) \to \tilde{Q}_0(s) &:= \frac{\tilde{G}_{zw}(s)}{\tilde{G}_{zu}(s)\tilde{G}_{yw}(s)} \\ &= C_2 \sqrt[4]{v^2 + 4D(h+s)} e^{(\|\mathbf{x}_z - \mathbf{x}_u\| + \|\mathbf{x}_y - \mathbf{x}_w\| - \|\mathbf{x}_z - \mathbf{x}_w\|)\sqrt{v^2+4D(s+h)}/2D}, \end{aligned} \tag{E.43}$$

where C_2 is a constant that does not depend on s. The Youla parameter $Q_0(s)$ is thus an element of $\mathcal{H}_\infty$ if

$$\|\mathbf{x}_z - \mathbf{x}_u\| + \|\mathbf{x}_y - \mathbf{x}_w\| < \|\mathbf{x}_z - \mathbf{x}_w\|. \tag{E.44}$$

If this condition is not satisfied, an additional low pass filter $Q_{\mathrm{LP}}(s)$ needs to be designed. As the expression for $\tilde{Q}_0(s)$ is very similar to (E.37), the design of the low-pass filter $Q_{\mathrm{LP}}(s)$ can be done similarly as for the 1-D case. Note that it is still possible to make $\|M\|_\infty$ arbitrarily small because $G_{zw}(s)$ is strictly proper.

Remark E.1. *Note that the conditions* (E.38) *and* (E.44) *have the nice physical interpretation that the distance between the disturbance $w(t)$ and the performance variable $z(t)$ is longer than the path from $w(t)$ to $z(t)$ through the controller, i.e. the sum of the distance between $w(t)$ and the sensor $y(t)$ and the distance between the actuator input $u(t)$ and $z(t)$. Intuitively, this seems to indicate a good control system design and the results in this appendix indeed show that the design of the feedback controller is easier in this case. It is also worth noting that the ideal control architecture suggested in [Bernstein, 2002] with $u(t)$ and $z(t)$ collocated and $w(t)$ and $y(t)$ collocated makes the LHSs of* (E.38) *and* (E.44) *zero.*

E.3 A 1-D thermomechanical control problem

In this appendix, a 1-D thermomechanical control system is considered. The difference with the problem considered in Section 7.2 is that the performance variable $z(t)$ is now the displacement in a point $x = x_z$, and not the temperature. The disturbance $w(t)$ and the actuator input $u(t)$ are still heat loads at the points $x = x_w$ and $x = x_u$, respectively, and the measured output $y(t)$ is still the temperature at the point $x = x_y$. This situation is inspired by the wafer heating application in which it might be possible to use optical temperature measurements of the wafer surface to reduce the influence of thermal disturbances on the overlay error.

E.3.1 System and transfer functions

The considered system on the unbounded spatial domain $x \in \mathbb{R}$ that consists of the thermal model (7.1) together with the mechanical model

$$\frac{\partial^2 d_x}{\partial x^2} - \tilde{k}_s d_x = \alpha \frac{\partial T}{\partial x}, \tag{E.45}$$

where $d_x = d_x(x,t)$ [m] denotes axial displacement, $\tilde{k}_s$ [1/m^2] accounts for the stiffness of the connection to the environment, and α [1/K] denotes the Coefficient of Thermal Expansion (CTE). Furthermore, the output equation (7.2) is replaced by

$$y(t) = T(x_y, t), \qquad z(t) = d_x(x_z, t). \tag{E.46}$$

As the considered spatial domain $x \in \mathbb{R}$ is unbounded, shifting all input and output locations over the same distance does not change the input-output behavior. The input-output relations thus take the form

$$\begin{bmatrix} Z(s) \\ Y(s) \end{bmatrix} = \begin{bmatrix} H(s, x_z - x_w) & H(s, x_z - x_u) \\ G(s, x_y - x_w) & G(s, x_y - x_u) \end{bmatrix} \begin{bmatrix} W(s) \\ U(s) \end{bmatrix}, \tag{E.47}$$

with $G(s,x)$ as in (7.4) and $H(s,x_0)$ the transfer function from a point heat load at $x = 0$ to the displacement at a point $x = x_0$ that still needs to be determined.

To determine $H(s, x_0)$, consider (E.1) together with (E.45) and the output equation

$$z_0(t) = d_x(x_0, t). \tag{E.48}$$

Similarly as in Appendix E.1, the transfer function $H(s, x)$ will be determined by computing the output $z_0(t)$ resulting from the input $u_0(t) = e^{st}$ and noting that $z_0(t) = H(s, x)u_0(t)$. In Appendix E.1.1, it has been shown that the steady-state temperature field resulting from the input $u_0(t) = e^{st}$ is $e^{st}T_0(x, s)$ with $T_0(x, s)$ as in (E.13). The resulting displacement field takes the form $e^{st}d_{x,0}(x, s)$, where $d_{x,0}(x, s)$ is the solution of (E.45) with T replaced by $T_0(x, s)$. The solution $d_{x,0}(x, s)$ consists of a particular solution $d_{x,0,\text{part}}$ and a homogeneous solution $d_{x,0,\text{hom}}$, i.e.

$$d_{x,0}(x, s) = d_{x,0,\text{part}}(x, s) + d_{x,0,\text{hom}}(x, s). \tag{E.49}$$

As $T_0(x, s)$ is of the form (E.13), the particular solution takes the form

$$d_{x,0,\text{part}}(x, s) = \frac{\alpha}{c\sqrt{v^2 + 4D(h + s)}} \begin{cases} \frac{\lambda_+(s)}{\lambda_+^2(s) - \tilde{k}_s} e^{x\lambda_+(s)} & \text{for } x < 0, \\ \frac{\lambda_-(s)}{\lambda_-^2(s) - \tilde{k}_s} e^{x\lambda_-(s)} & \text{for } x > 0, \end{cases} \tag{E.50}$$

with $\lambda_-(s)$ and $\lambda_+(s)$ as in (E.4). Note that $d_{x,0,\text{part}}(x, s)$ is not continuous at $x = 0$. The homogeneous solution of (E.45) therefore takes the form

$$d_{x,0,\text{hom}}(x, s) = \frac{\alpha}{c\sqrt{v^2 + 4D(h + s)}} \begin{cases} A(s)e^{x\sqrt{\tilde{k}_s}} & \text{for } x < 0, \\ B(s)e^{-x\sqrt{\tilde{k}_s}} & \text{for } x > 0, \end{cases} \tag{E.51}$$

for some functions $A(s)$ and $B(s)$ independent of x. Note that it was used here that the homogeneous solution should remain bounded for $x \to \pm\infty$. The factor $\alpha/(c\sqrt{v^2 + 4D(h + s)})$ was included to simplify the following calculations. The functions $A(s)$ and $B(s)$ are now determined by requiring that $d_{x,0}(x, s)$ in (E.49) is a weak solution of (E.45) near $x = 0$, which means that the displacement $d_{x,0}$ and the strain $\partial d_{x,0}/\partial x$ must be continuous at $x = 0$. These two requirements lead to two equations for $A(s)$ and $B(s)$. The solution of these equations is

$$A(s) = -\frac{1}{2}\left(1 + \frac{\lambda_+(s)}{\sqrt{\tilde{k}_s}}\right)\frac{\lambda_+(s)}{\lambda_+^2(s) - \tilde{k}_s} + \frac{1}{2}\left(1 + \frac{\lambda_-(s)}{\sqrt{\tilde{k}_s}}\right)\frac{\lambda_-(s)}{\lambda_-^2(s) - \tilde{k}_s}, \tag{E.52}$$

$$B(s) = +\frac{1}{2}\left(1 - \frac{\lambda_+(s)}{\sqrt{\tilde{k}_s}}\right)\frac{\lambda_+(s)}{\lambda_+^2(s) - \tilde{k}_s} - \frac{1}{2}\left(1 - \frac{\lambda_-(s)}{\sqrt{\tilde{k}_s}}\right)\frac{\lambda_-(s)}{\lambda_-^2(s) - \tilde{k}_s}. \tag{E.53}$$

Now $H(s, x_0)$ follows by noting that the input $u_0(t) = e^{st}$ results in the output $z_0(t) = d_{x,0}(x_0, s)e^{st}$, with $d_{x,0}(x, s)$ as in (E.49)–(E.51), so that $H(s, x_0) = z_0(t)/u_0(t) = d_{x,0}(x_0, s)$.

It is worth noting that an analytic expression for the transfer function from a point heat load to the displacement field on the 2-D spatial domain $\mathbb{R}^2$ can be derived in a similar way as the steady-state displacement fields on $\mathbb{R}^2$ derived in [Overkamp, 2017].

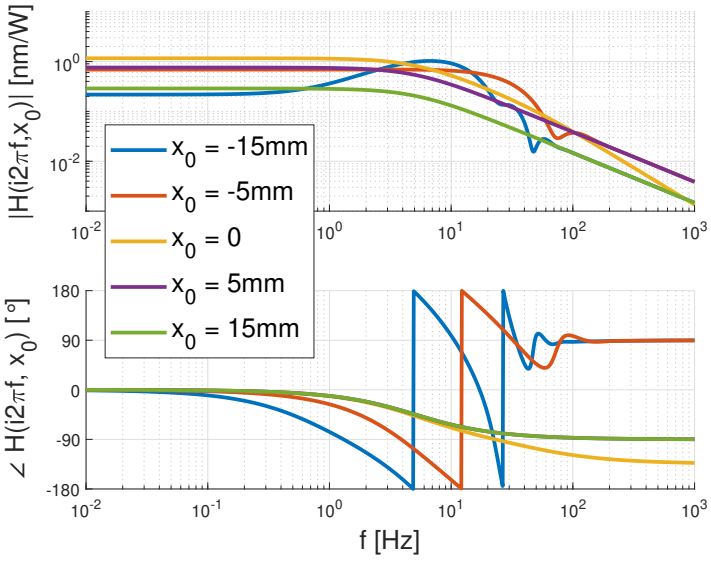

Figure E.1. Bode plots of $H(s, x_0)$ for varying values of x_0

E.3.2 Numerical results

The parameter values used in this subsection are $c = 33$ [J/K/m], $v = 0.33$ [m/s], $D = 91 \cdot 10^{-6}$ [m^2/s], $h = 1$ [1/s], $\tilde{k}_s = 9.34 \cdot 10^3$ [1/m^2], and $\alpha = 2.6 \cdot 10^{-6}$ [1/K] and are based on the wafer heating problem considered in Section 3.5.

A Bode plot of $H(s, x_0)$ is shown in Figure E.1 for several values of x_0. The two Bode plots for $x_0 = 5$ mm and $x_0 = 15$ mm differ practically only by a scaling factor. To understand this better, note that $|e^{x\lambda_-(s)}| < e^{-xv/D}$ (see also Remark 7.2) meaning that length scale at which the magnitude of the particular solution $d_{x,0,\text{part}}(x, s)$ in (E.50) decays for $x > 0$ is $D/v = 0.28$ mm. The homogeneous solution $d_{x,0,\text{hom}}(x, s)$ in (E.51) decays at a much longer length scale $1/\sqrt{\tilde{k}_s} = 10.3$ mm. Therefore, $H(s, x_0) \approx B(s)e^{-x_0\sqrt{\tilde{k}_s}}$ for $x_0 = 5$ mm and $x_0 = 15$ mm, which explains why these two Bode plots differ practically only by a scaling factor. Furthermore, observe that the other Bode plots clearly show that, in contrast to the thermal control problem from Chapter 7, it does not necessarily hold that $\|H(\cdot, x_0)\|_\infty = H(0, x_0)$.

Using the expression for the transfer functions (E.47), the same numerical approach as in Chapter 7 can be used to determine the smallest possible $\|M\|_\infty$ achievable by proportional feedback control for given locations x_w, x_u, x_z, and x_y. The obtained graphs for varying x_y with fixed x_u, x_w, and x_z are shown in Figures E.2 and E.3. Note that all six possible orderings of x_u, x_w, and x_z are

considered in contrast to the advection-dominated thermal control problem from Section 7.2, in which situations where $x_w < x_z$ or $x_u < x_z$ were not relevant.

Because of the complex expression for the transfer function $H(s, x_0)$, it not straightforward to derive analytic expressions for the potential optimal sensor locations similar to the ones in Lemmas 7.3 and 7.4. However, a physical explanation for the optimal sensor locations in Figures E.2 and E.3 can be found for Subfigures E.2b, E.2c, E.3b, and E.3c using the insights from the thermal control problem considered in Section 7.2. The connection with the thermal control problem is also visible in the close match between the optimal sensor locations in Subfigures E.2b and E.2c and Figure 7.3.

The optimal location in Figure E.2b can be understood from Remark 7.8: if $x_y = x_u$ the temperature increase resulting from the disturbance $w(t)$ can be made arbitrarily small at all locations $x < x_y = x_u$ by high-gain feedback. This high-gain feedback will therefore also reduce the deformation at $x = x_z$ significantly, although some deformation will remain due to the temperature increase at locations $x > x_y = x_u$.

For Figure E.2c, recall from Section 7.2 that choosing $x_y = x_w$ is the optimal sensor location for any thermal performance variable at $x < x_w < x_u$. It seems thus natural to expect that choosing $x_y = x_w$ will lead to the best reduction of the influence of the disturbance $w(t)$ on the temperature increase at locations $x < x_w$. Because x_z is relatively far behind x_w in the considered example in Figure E.2c, it is also not surprising that this also reduces the influence of $w(t)$ on the deformation at $x = x_z$.

The results in Subfigure E.3b and E.3c can be understood by noting that one always should choose $x_y < x_w$ in advection-dominated problems (otherwise $G_{yw} \approx 0$, see Remark 7.2). If x_w is behind x_z and x_u (i.e. if $x_w < x_z$ and $x_w < x_u$) as in Figures E.3b and E.3c, it is thus natural that choosing $x_y = x_w$ is optimal because this is the sensor location $x_y < x_w$ that is closest to x_w, x_u, and x_z.

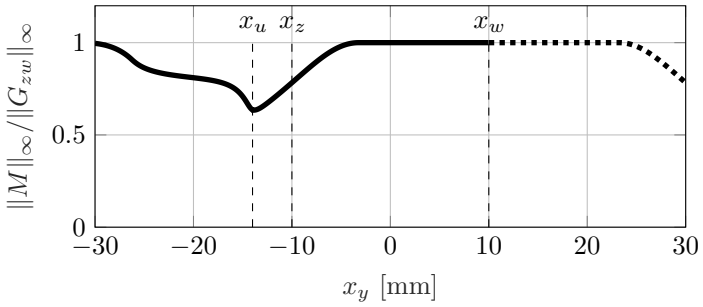

(a) $x_u = -14$ mm, $x_z = -10$ mm, $x_w = 10$ mm

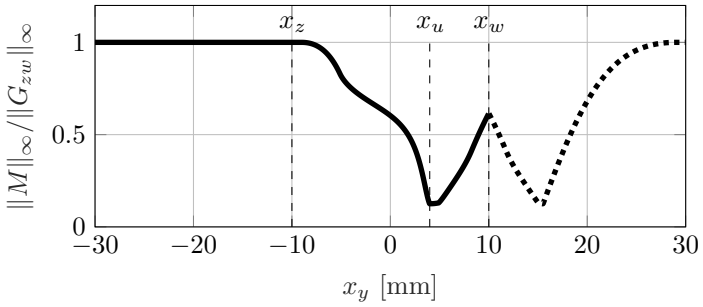

(b) $x_z = -10$ mm, $x_u = 4$ mm, $x_w = 10$ mm

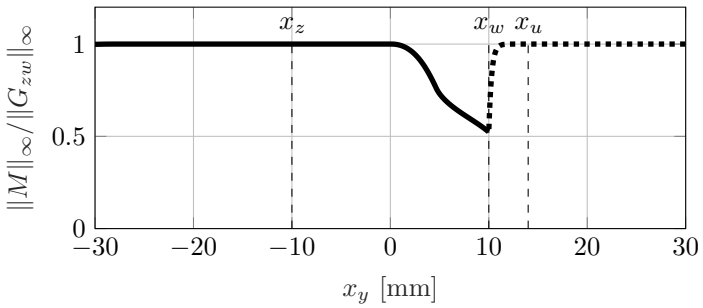

(c) $x_z = -10$ mm, $x_w = 10$ mm, $x_u = 14$ mm

Figure E.2. The improvement in closed-loop performance $\|M\|_\infty$ relative to the open-loop performance $\|G_{zw}\|_\infty$ for varying sensor location x_y for three choices of x_w, x_u, and x_z. The dotted lines indicate locations x_y where feedback control is not effective because $G_{yw} \approx 0$.

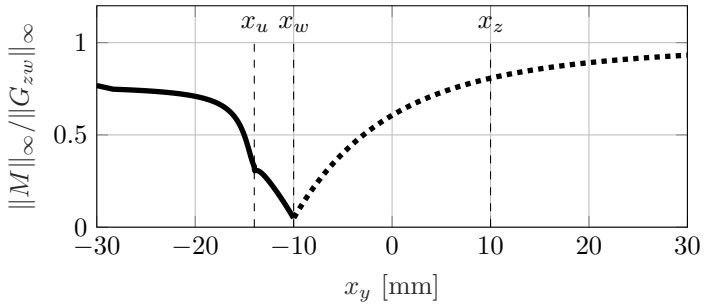

(a) $x_u = -14$ mm, $x_w = -10$ mm, $x_z = 10$ mm

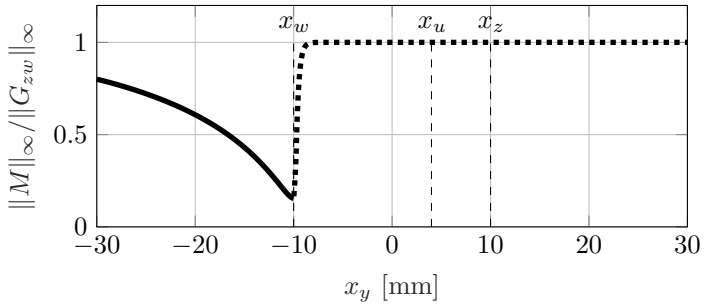

(b) $x_w = -10$ mm, $x_u = 4$ mm, $x_z = 10$ mm

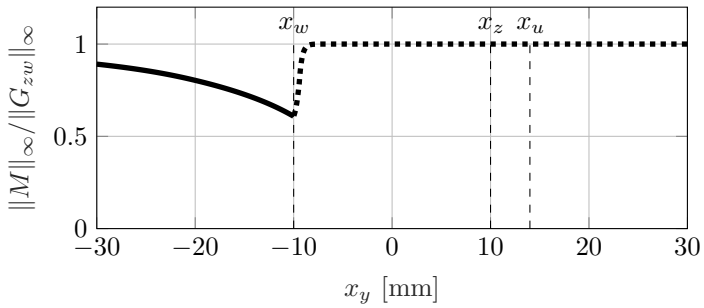

(c) $x_w = -10$ mm, $x_z = 10$ mm, $x_u = 14$ mm

Figure E.3. The improvement in closed-loop performance $\|M\|_\infty$ relative to the open-loop performance $\|G_{zw}\|_\infty$ for varying sensor location x_y for three choices of x_w, x_u, and x_z. The dotted lines indicate locations x_y where feedback control is not effective because $G_{yw} \approx 0$.

Bibliography

Abbott, S. (2015). *Understanding Analysis*. New York, NY: Springer.

Absil, P.-A., Mahony, R. and Sepulchre, R. (2008). *Optimization Algorithms on Matrix Manifolds*. Princeton, NJ: Princeton University Press.

Al-Sulaiman, F. and Zaman, S. (1994). 'Actuator placement in lumped parameter systems subjected to disturbance'. *Computers & Structures*, volume 52, number 1, pages 41 –47.

Anderson, D. L. (1989). *Theory of the Earth*. Oxford: Blackwell.

Antoulas, A. C. (2005). *Approximation of Large-Scale Dynamical Systems*. Advances in Design and Control, volume 6. Philadelphia, PA: SIAM.

Apel, T. and Flaig, T. G. (2012). 'Crank-Nicolson schemes for optimal control problems with evolution equations'. *SIAM Journal on Numerical Analysis*, volume 50, number 3, pages 1484–1512.

Armaou, A. and Demetriou, M. A. (2006). 'Using spatial $\mathcal{H}_2$-norm for sensor placement in parabolic partial differential equations'. In: *Proceedings of the 2006 American Control Conference*, pages 1467–1472.

ASML (2018). *ASML provides strategy and financial update at Investor Day in Veldhoven*. URL: `www.asml.com/en/news/press-releases` (visited on 27/09/2019).

— (2019a). *ASML reports EUR 10.9 billion net sales and EUR 2.6 billion net income in 2018*. URL: `www.asml.com/en/news/press-releases` (visited on 11/08/2019).

— (2019b). *TWINSCAN NXE:3400B*. Datasheet. URL: `www.asml.com` (visited on 26/08/2019).

— (2019c). *TWINSCAN NXT:2000i*. Datasheet. URL: `www.asml.com` (visited on 26/08/2019).

Aung, N., Chung, W. J., Samudrala, P., Gao, H., Gao, W., Brown, D., He, G., Park, B., Hsieh, M., Hao, X., Chen, Y.-J., Zhou, Y., Park, D., Gutjahr, K., Krumanocker, I., Jock, K. and Gomez, J. M. (2018). 'Overlay control for 7nm technology node and beyond'. In: *Proceedings of the 2018 SPIE Conference*

on Optical Microlithography XXXI. Volume 10587. San Jose, CA, pages 62 –73.

Bernstein, D. S. (2002). 'What makes some control problems hard?' *IEEE Control Systems Magazine*, volume 22, number 4, pages 8–19.

Berry, M. W., Browne, M., Langville, A. N., Pauca, V. P. and Plemmons, R. J. (2007). 'Algorithms and applications for approximate nonnegative matrix factorization'. *Computational Statistics & Data Analysis*, volume 52, number 1, pages 155 –173.

Besselink, B., Tabak, U., Lutowska, A., Wouw, N. van de, Nijmeijer, H., Rixen, D. J., Hochstenbach, M. E. and Schilders, W. H. A. (2013). 'A comparison of model reduction techniques from structural dynamics, numerical mathematics and systems and control'. *Journal of Sound and Vibration*, volume 332, number 19, pages 4403 –4422.

de Best, J. (2015). *Thermo-mechanical modeling with a reticle heating case study*. Technical report PIR D0000391429. ASML.

Bhatia, H., Norgard, G., Pascucci, V. and Bremer, P. (2013). 'The Helmholtz-Hodge decomposition—a survey'. *IEEE Transactions on Visualization and Computer Graphics*, volume 19, number 8, pages 1386–1404.

Bikcora, C. (2013). 'Modeling and prediction of thermally induced imaging errors in deep- and extreme-ultraviolet lithography'. PhD thesis. Eindhoven: Technische Universiteit Eindhoven.

Bikcora, C., Weiland, S. and Coene, W. M. J. (2014). 'Thermal deformation prediction in reticles for extreme ultraviolet lithography based on a measurement-dependent low-order model'. *IEEE Transactions on Semiconductor Manufacturing*, volume 27, number 1, pages 104–117.

Bilski, B., Zimmermann, J., Roesch, M., Liddle, J., Setten, E. van, Bottiglieri, G. and Schoot, J. van (2019). 'High-NA EUV imaging: challenges and outlook'. In: *Proceedings of the SPIE 11177, 35th European Mask and Lithography Conference (EMLC 2019)*, pages 64 –73.

Biot, M. A. (1956). 'Thermoelasticity and irreversible thermodynamics'. *J. Appl. Phys.*, volume 27, pages 240–253.

Bittner, B., Iliew, R., Pauls, W., Schneider, R., Schneider, S., Warba, N. and Wagner, H. (2012). Mirror arrangement for an EUV projection exposure apparatus, method for operating the same, and EUV projection exposure apparatus. Patent number CN104487899A.

Boley, B. A. and Weiner, J. H. (1960). *Theory of Thermal Stresses*. New York: Wiley.

Borzì, A. and Schulz, V. (2012). *Computational Optimization of Systems Governed by Partial Differential Equations*. Computational Science & Engineering, volume 8. Philadelphia, PA: SIAM.

Bos, K. M. W. J., Heck, D. J. F., Heertjes, M. F. and van der Kall, R. (2018). 'IO linearization, stability, and control of an input non-affine thermoelectric

system'. In: *Proceedings of the 2018 American Control Conference (ACC)*, pages 526–531.

Boulanger, A.-C. and Trautmann, P. (2017). 'Sparse optimal control of the KdV-Burgers equation on a bounded domain'. *SIAM Journal on Control and Optimization*, volume 55, number 6, pages 3673–3706.

Boyd, S. and Vandenberghe, L. (2004). *Convex Optimization*. Cambridge: Cambridge University Press.

Bryan, G. H. (1890). 'An application of the method of images to the conduction of heat'. *Proceedings of the London Mathematical Society*, volume 1, number 1, pages 424–430.

Bunting, K. A. and Cornfield, G. (1975). 'Toward a general theory of cutting: a relationship between the incident power density and the cut speed'. *ASME Journal of Heat transfer*, volume 97, number 1, pages 116–122.

Burns, J. A. and Rautenberg, C. N. (2015a). 'Solutions and approximations to the Riccati integral equation with values in a space of compact operators'. *SIAM Journal on Control and Optimization*, volume 53, number 5, pages 2846–2877.

— (2015b). 'The infinite-dimensional optimal filtering problem with mobile and stationary sensor networks'. *Numerical Functional Analysis and Optimization*, volume 36, number 2, pages 181–224.

Burns, J. A. and Rubio, D. (1997). 'A distributed parameter control approach to sensor location for optimal feedback control of thermal processes'. In: *Proceedings of the 36th IEEE Conference on Decision and Control*. Volume 3. IEEE, pages 2243–2247.

Cao, Y., Biss, D. and Perkins, J. D. (1996). 'Assessment of input-output controllability in the presence of control constraints'. *Computers & Chemical Engineering*, volume 20, number 4, pages 337 –346.

Carslaw, H. S. and Jaeger, J. C. (1959). *Conduction of Heat in Solids*. 2nd edition. London: Oxford University Press.

Chen, K. K. and Rowley, C. W. (2011). '$\mathcal{H}_2$ optimal actuator and sensor placement in the linearised complex Ginzburg-Landau system'. *Journal of Fluid Mechanics*, volume 681, pages 241–260.

Cohen, J. E. and Rothblum, U. G. (1993). 'Nonnegative ranks, decompositions, and factorizations of nonnegative matrices'. *Linear Algebra and its Applications*, volume 190, pages 149–168.

Crank, J. and Nicolson, P. (1947). 'A practical method for numerical evaluation of solutions of partial differential equations of the heat-conduction type'. *Mathematical Proceedings of the Cambridge Philosophical Society*, volume 43, number 1, pages 50–67.

Curtain, R. F. and Morris, K. A. (2009). 'Transfer functions of distributed parameter systems: A tutorial'. *Automatica*, volume 45, number 5, pages 1101 –1116.

Curtain, R. F. and Zwart, H. J. (1995). *An Introduction to Infinite-Dimensional Linear Systems Theory*. Texts in Applied Mathematics, volume 21. New York: Springer.

Darivandi, N., Morris, K. A. and Khajepour, A. (2013). 'An algorithm for LQ optimal actuator location'. *Smart Materials and Structures*, volume 22, number 3, page 035001.

De Young, C. (2019). 'EUV: Enabling cost efficiency, tech innovation and future industry growth'. In: *BAML 2019 APAC TMT Conference*.

Demetriou, M. A. (2005). 'Robust sensor location optimization in distributed parameter systems using functional observers'. In: *Proceedings of the 44th IEEE Conference on Decision and Control*, pages 7187–7192.

— (2017). 'Sensor selection and static output feedback of parabolic PDEs via state feedback kernel partitioning using modification of Voronoi tessellations'. In: *Proceedings of the 2017 American Control Conference*. Seattle, WA, pages 2497–2503.

Dias, C. J. (2015). 'A method of recursive images to solve transient heat diffusion in multilayer materials'. *International Journal of Heat and Mass Transfer*, volume 85, pages 1075 –1083.

— (2016). 'Transient heat diffusion in multilayered materials with thermal contact resistance'. *International Journal of Heat and Mass Transfer*, volume 97, pages 1001–1009.

Doman, D., Warkentin, A. and Bauer, R. (2009). 'Finite element modeling approaches in grinding'. *International Journal of Machine Tools and Manufacture*, volume 49, number 2, pages 109 –116.

Donoho, D. and Stodden, V. (2004). 'When does non-negative matrix factorization give a correct decomposition into parts?' In: *Advances in Neural Information Processing Systems 16*. Edited by S. Thrun, L. K. Saul and B. Schölkopf. Camebridge, MA: MIT Press, pages 1141–1148.

Dorosti, M., Fey, R., Heertjes, M. and Nijmeijer, H. (2018a). 'Iterative pole–zero model updating: a combined sensitivity approach'. English. *Control Engineering Practice*, volume 71, pages 164–174.

Dorosti, M., Fey, R., Heertjes, M., van de Wal, M. and Nijmeijer, H. (2018b). 'Iterative pole-zero finite element model updating using generic parameters'. English. *Mechatronics*, volume 55, pages 180–193.

Doyle, J. C., Francis, B. A. and Tannenbaum, A. R. (1992). *Feedback Control Theory*. New York: Macmillan.

Duhamel, J.-M. C. (1837). 'Second memoire sur les phenomenes thermo mecaniques'. *Journal de l'Ecole Polytechnique*, volume 15, number 25, pages 1–57.

Edalatzadeh, M. S. (2019). 'Optimal Actuator Design for Nonlinear Systems'. PhD thesis. Waterloo: University of Waterloo.

Edelman, A., Arias, T. A. and Smith, S. T. (1999). 'The geometry of algorithms with orthogonality constraints'. *SIAM Journal on Matrix Analysis and Applications*, volume 20, number 2, pages 303–353.

Elsen, M. V., Baelmans, M., Mercelis, P. and Kruth, J.-P. (2007). 'Solutions for modelling moving heat sources in a semi-infinite medium and applications to laser material processing'. *International Journal of Heat and Mass Transfer*, volume 50, number 23, pages 4872 –4882.

Evans, L. C. (2010). *Partial Differential Equations*. 2nd edition. Graduate Studies in Mathematics, volume 19. Providence, Rhode Island: American Mathematical Society.

Evers, E., de Jager, A. G. and Oomen, T. A. E. (2018). 'Improved local rational method by incorporating system knowledge: with application to mechanical and thermal dynamical systems'. English. *IFAC-PapersOnLine*, volume 51, number 15, pages 808–813.

Evers, E., Lamers, R. and Oomen, T. A. E. (2019a). 'Thermally induced deformations in electron microscopy: challenges and opportunities for system identification'. English. *Mikroniek*, number 2, pages 12–18.

Evers, E., van de Wal, M. M. J. and Oomen, T. A. E. (2019b). 'Beyond decentralized wafer/reticle stage control design: A double-Youla approach for enhancing synchronized motion'. *Control Engineering Practice*, volume 83, pages 21 –32.

Fachinotti, V. D., Anca, A. A. and Cardona, A. (2011). 'Analytical solutions of the thermal field induced by moving double-ellipsoidal and double-elliptical heat sources in a semi-infinite body'. *International Journal for Numerical Methods in Biomedical Engineering*, volume 27, number 4, pages 595–607.

Fathy, H. K., Reyer, J. A., Papalambros, P. Y. and Ulsoy, A. G. (2001). 'The coupling between the plant and controller optimization problems'. In: *Proceedings of the 2001 American Control Conference (ACC)*. Arlington, VA, pages 1864–1869.

Feng, P. and van de Wal, M. (2014). *Advanced thermal feedback control of a wafer table: An exploration of various techniques*. Technical report D000256195. ASML.

Flint, T. F., Francis, J. A., Smith, M. C. and Vasileiou, A. N. (2018). 'Semi-analytical solutions for the transient temperature fields induced by a moving heat source in an orthogonal domain'. *International Journal of Thermal Sciences*, volume 123, pages 140 –150.

Floudas, C. A. and Visweswaran, V. (1990). 'A global optimization algorithm (GOP) for certain classes of nonconvex NLPs – Part I. Theory'. *Computers & Chemical Engineering*, volume 14, number 12, pages 1397 –1417.

Frazier, W. E. (2014). 'Metal additive manufacturing: a review'. *Journal of Materials Engineering and Performance*, volume 23, number 6, pages 1917–1928.

Fung, Y.-c. and Tong, P. (2001). *Classical and Computational Solid Mechanics*. Advanced Series in Engineering Science, volume 1. Singapore: World scientific.

Gawronski, W. (2004). *Advanced Structural Dynamics and Active Control of Structures*. New York: Springer.

Geers, M. G. D., Baaijens, F. P. T. and Schreurs, P. J. G. (2011). Continuum Mechanics for Advanced Manufacturing Technologies. Lecture Notes. Eindhoven: Eindhoven University of Technology.

van Gerven, P. (2016a). 'ASML for beginners'. *Bits & Chips*, number 9.

— (2016b). 'What makes an EUV scanner tick'. *Bits & Chips*, number 9.

van Gils, R., Speetjens, M., Zwart, H. and Nijmeijer, H. (2012). 'Feedback stabilisation of a two-dimensional pool-boiling system by modal control'. *International Journal of Thermal Sciences*, volume 61, pages 38 –49.

Goebel, R., Sanfelice, R. G. and Teel, A. R. (2009). 'Hybrid dynamical systems'. *IEEE Control Systems Magazine*, volume 29, number 2, pages 28–93.

Goldak, J., Chakravarti, A. and Bibby, M. (1984). 'A new finite element model for welding heat sources'. *Metallurgical Transactions B*, volume 15, number 2, pages 299–305.

Gorski, J., Pfeuffer, F. and Klamroth, K. (2007). 'Biconvex sets and optimization with biconvex functions: a survey and extensions'. *Mathematical Methods of Operations Research*, volume 66, number 3, pages 373–407.

Gray, A. and Mathews, G. (1952). *A Treatise on Bessel Functions and Their Applications to Physics*. 2nd edition. London: McMillan.

Grier, D. A. (2006). 'The innovation curve'. *Computer*, volume 39, number 2, pages 8–10.

Grubb, G. (2009). 'Distributions. Examples and Rules of Calculus'. In: *Distributions and Operators*. New York, NY: Springer, pages 27–54.

Habets, M., Scholten, J., Weiland, S. and Coene, W. (2016). 'Multi-mirror adaptive optics for control of thermally induced aberrations in extreme ultraviolet lithography'. In: *Proceedings of the SPIE 9776, Extreme Ultraviolet (EUV) Lithography VII*.

Hahn, D. W. and Ozisik, M. N. (2012). *Heat Conduction*. Chapter 11. Chichester: Wiley.

Hanema, J. (2018). 'Anticipative model predictive control for linear parametervarying systems'. PhD thesis. Eindhoven: Technische Universiteit Eindhoven.

Heertjes, M. F., van der Velden, B. and Oomen, T. A. E. (2016). 'Constrained iterative feedback tuning for robust control of a wafer stage system'. *IEEE Transactions on Control Systems Technology*, volume 24, number 1, pages 56–66.

van der Heijden, J. J. M. (2018). 'Model Order Reduction for Moving Heat Loads'. Master's thesis. Eindhoven: Technische Universiteit Eindhoven.

Hekner, S. (2016). 'Optimal Experiment Design for Improved Parameter Estimation in Thermo-Mechanical Feedforward Models'. Chapter 7. Master's thesis. Delft: Delft University of Technology.

Hengeveld, D. W., Mathison, M. M., Braun, J. E., Groll, E. A. and Williams, A. D. (2010). 'Review of modern spacecraft thermal control technologies'. *HVAC&R Research*, volume 16, number 2, pages 189–220.

Herber, D. R. and Allison, J. T. (2019). 'Nested and simultaneous solution strategies for general combined plant and control design problems'. *Journal of Mechanical Design*, volume 141, number 1.

Herzog, R., Stadler, G. and Wachsmuth, G. (2012). 'Directional sparsity in optimal control of partial differential equations'. *SIAM Journal on Control and Optimization*, volume 50, number 2, pages 943–963.

Hetnarski, R. and Eslami, M. (2009). *Thermal Stresses: Advanced Theory and Applications*. Solid Mechanics and its Applications, volume 158. Springer.

Hinze, M., Pinnau, R., Ulbrich, M. and Ulbrich, S. (2009). *Optimization with PDE Constraints*. Volume 23. Mathematical Modelling: Theory and Applications. Springer, New York.

Hooijkamp, E. C. and van Keulen, A. (2018). 'Topology optimization for linear thermo-mechanical transient problems'. *International Journal for Numerical Methods in Engineering*, volume 113, number 8, pages 1230–1257.

van den Hurk, D., Weiland, S. and van Berkel, K. (2018). 'Modeling and localized feedforward control of thermal deformations induced by a moving heat load'. In: *Proceedings of the 2018 International Symposium on Control Systems of the Society of Instrument and Control Engineers (SICE-ISCS)*. Tokyo, Japan, pages 171–178.

Irwin, J. and Michaleris, P. (2015). 'A line heat input model for additive manufacturing'. *Journal of Manufacturing Science and Engineering*, volume 138, number 11, pages 66 –72.

John, F. (1938). 'The ultrahyperbolic differential equation with four independent variables'. *Duke Mathematical Journal*, volume 4, number 2, pages 300–322.

Kalise, D., Kunisch, K. and Sturm, K. (2018). 'Optimal actuator design based on shape calculus'. *Mathematical Models and Methods in Applied Sciences*, volume 28, number 13, pages 2667–2717.

Kasinathan, D. and Morris, K. A. (2013). '$\mathcal{H}_\infty$-optimal actuator location'. *IEEE Transactions on Automatic Control*, volume 58, number 10, pages 2522–2535.

King, W. E., Anderson, A. T., Ferencz, R. M., Hodge, N. E., Kamath, C., Khairallah, S. A. and Rubenchik, A. M. (2015). 'Laser powder bed fusion additive manufacturing of metals; physics, computational, and materials challenges'. *Applied Physics Reviews*, volume 2, number 4, page 041304.

Komanduri, R. and Hou, Z. (2001). 'Thermal analysis of the laser surface transformation hardening process'. *International Journal of Heat and Mass Transfer*, volume 44, number 15, pages 2845 –2862.

Kovalenko, A. D. (1969). *Thermoelasticity – Basic Theory and Applications*. Groningen: Wolters-Noordhoff.

de Kraker, B. (2004). *A Numerical-Experimental Approach in Structural Dynamics*. Maastricht: Shaker.

Kunisch, K., Pieper, K. and Vexler, B. (2014). 'Measure valued directional sparsity for parabolic optimal control problems'. *SIAM Journal on Control and Optimization*, volume 52, number 5, pages 3078–3108.

Kurusa, (1991). 'A characterization of the Radon transform's range by a system of PDEs'. *Journal of Mathematical Analysis and Applications*, volume 161, number 1, pages 218 –226.

Laurberg, H., Christensen, M. G., Plumbley, M. D., Hansen, L. K. and Jensen, S. H. (2008). 'Theorems on positive data: On the uniqueness of NMF'. *Computational intelligence and neuroscience*, volume 2008.

Lebedev, L. P., Cloud, M. J. and Eremeyev, V. A. (2010). *Tensor Analysis with Applications in Mechanics*. Singapore: World Scientific.

Lee, D. D. and Seung, H. S. (1999). 'Learning the parts of objects by non-negative matrix factorization'. *Nature*, volume 401, number 6755, pages 788–791.

— (2001). 'Algorithms for non-negative matrix factorization'. In: *Advances in neural information processing systems*, pages 556–562.

Levinson, H. J. (2010). *Principles of Lithography*. 3rd edition. Washington: SPIE Press.

Lowisch, M., Kuerz, P., Conradi, O., Wittich, G., Seitz, W. and Kaiser, W. (2013). 'Optics for ASML's NXE:3300B platform'. In: *Proceedings of the SPIE 8679, Extreme Ultraviolet Lithography IV*. San Jose, CA, pages 404 –412.

Lubarda, V. A. (2004). 'On thermodynamic potentials in linear thermoelasticity'. *International Journal of Solids and Structures*, volume 41, number 26, pages 7377–7398.

Majumdar, J. D. and Manna, I (2011). 'Laser material processing'. *International Materials Reviews*, volume 56, number 5-6, pages 341–388.

Manton, J. H., Mahony, R. and Hua, Y. (2003). 'The geometry of weighted low-rank approximations'. *IEEE Transactions on Signal Processing*, volume 51, number 2, pages 500–514.

Markovsky, I. and van Huffel, S. (2007). 'Left vs right representations for solving weighted low-rank approximation problems'. *Linear Algebra and its Applications*, volume 422, number 2, pages 540 –552.

Maugin, G. A. (2014). 'Duhamel's pioneering work in thermo-elasticity and its legacy'. In: *Continuum Mechanics Through the Eighteenth and Nineteenth Centuries: Historical Perspectives from John Bernoulli (1727) to Ernst Hellinger (1914)*. Cham: Springer, pages 69–75.

McGee, T. D. (1988). *Principles and Methods of Temperature Measurement*. New York: John Wiley & Sons.

Merks, R. W. H. (2015). 'Thermal Control for Projection Optics in Extreme Ultraviolet Lithography'. Master's thesis. Eindhoven: Technische Universiteit Eindhoven.

— (2019). 'Towards control relevant system design and constrained order controller synthesis: with a thermal control application in immersion lithography'. PhD thesis. Eindhoven: Technische Universiteit Eindhoven.

Mestrom, R. M. C. (2009). 'Multiphysics modelling and experimental validation of microelectromechanical resonator dynamics'. English. PhD thesis. Eindhoven: Technische Universiteit Eindhoven.

van der Meulen, S. H., Tousain, R. L. and Bosgra, O. H. (2008). 'Fixed structure feedforward controller design exploiting iterative trials: application to a wafer stage and a desktop printer'. *Journal of Dynamic Systems, Measurement, and Control*, volume 130, number 5.

Minoux, M. (1986). *Mathematical Programming – Theory and Algorithms*. Chichester: Wiley.

Moore, G. E. (1965). 'Cramming more components onto integrated circuits'. *Electronics*, volume 38, number 8, pages 33–35.

— (1975). 'Progress in digital integrated electronics'. In: *Electron Devices Meeting*. Volume 21, pages 11–13.

— (1995). 'Lithography and the future of Moore's law'. In: *Proceedings of the International Society for Optics and Photonics (SPIE)*. Volume 2439, pages 2–17.

— (2003). 'No exponential is forever: but "Forever" can be delayed!' In: *Proceedings of the IEEE International Solid-State Circuits Conference (ISSCC)*. Volume 1, pages 20–23.

Morishima, T., Ostayen, R. van, Eijk, J. van and Schmidt, R.-H. M. (2015). 'Thermal displacement error compensation in temperature domain'. *Precision Engineering*, volume 42, pages 66 –72.

Morris, K. A. (1998). 'Noise reduction in ducts achievable by point control'. *Journal of Dynamic Systems, Measurement, and Control*, volume 120, number 2, pages 216–223.

— (2011). 'Linear-quadratic optimal actuator location'. *IEEE Transactions on Automatic Control*, volume 56, number 1, pages 113–124.

Moulik, P. N., Yang, H. T. Y. and Chandrasekar, S. (2001). 'Simulation of thermal stresses due to grinding'. *International Journal of Mechanical Sciences*, volume 43, number 3, pages 831 –851.

MSS (Material Science Service) (2019). Inside of A 7 nm technology node application processor. Presentation.

Naidu, D. S. (2002). *Optimal Control Systems*. Boca Raton, FL: CRC press.

Nemchinsky, V. (2016). 'Temperature created by a moving heat source that heats and melts the metal plate (plasma arc cutting)'. *ASME Journal of Heat transfer*, volume 138, number 12.

Nesterov, Y. and Nemirovskii, A. (1994). *Interior-Point Polynomial Algorithms in Convex Programming*. Studies in Applied Mathematics, volume 13. Philadelphia, PA: SIAM.

Nguyen, N. (2004). 'Analytical approximate solution for double ellipsoidal heat source in finite thick plate'. *Welding journal*, volume 83, page 82.

Nguyen, N., Ohta, A, Matsuoka, K, Suzuki, N and Maeda, Y (1999). 'Analytical solutions for transient temperature of semi-infinite body subjected to 3D moving heat sources'. *Welding Journal*, volume 78, pages 265–274.

Nouwens, S. A. N. (2020). 'Optimal actuator design for mirror heating'. DC 2020.006. Master's thesis. Eindhoven: Eindhoven University of Technology.

Nowacki, W. (1962). *Thermoelasticity*. Reading, Massachusetts: Addison-Wesley.

Nowinski, J. (1978). *Theory of Thermoelasticity with Applications*. Mechanics of Surface Structures, volume 3. Alphen aan de Rijn: Springer.

Oh, S. and Ki, H. (2017). 'Prediction of hardness and deformation using a 3-D thermal analysis in laser hardening of AISI H13 tool steel'. *Applied Thermal Engineering*, volume 121, pages 951 –962.

Oomen, T. A. E., Grassens, E. and Hendriks, F. B. J. W. M. (2015). 'Inferential motion control : identification and robust control for positioning an unmeasurable point of interest'. English. *IEEE Transactions on Control Systems Technology*, volume 23, number 4, pages 1602–1610.

Oomen, T. A. E., van Herpen, R. M. A., Quist, S., van de Wal, M. M. J., Bosgra, O. H. and Steinbuch, M. (2014). 'Connecting system identification and robust control for next-generation motion control of a wafer stage'. *IEEE Transactions on Control Systems Technology*, volume 22, number 1, pages 102–118.

Overkamp, J. (2017). *Wafer heating analytical expression*. Technical report PIR D000479973/10. ASML.

Ozisik, N. (1994). *Finite difference methods in heat transfer*. Boca Raton, FL: CRC press.

Parkus, H. (1976). *Thermoelasticity*. 2nd edition. Vienna: Springer.

Patil, N., Pal, D., Khalid Rafi, H., Zeng, K., Moreland, A., Hicks, A., Beeler, D. and Stucker, B. (2015). 'A generalized feed forward dynamic adaptive mesh refinement and derefinement finite element framework for metal laser sintering – Part I: Formulation and algorithm development'. *Journal of Manufacturing Science and Engineering*, volume 137, number 4, pages 041001–15.

Pinnau, R. (2008). 'Model reduction via proper orthogonal decomposition'. In: *Model Order Reduction: Theory, Research Aspects and Applications*. Mathematics in Industry, volume 13. Berlin: Springer, pages 95–109.

Prasad, N. S. and Narayanan, S. (1996). 'Finite element analysis of temperature distribution during arc welding using adaptive grid technique'. *Welding Journal (USA)*, volume 75, number 4, page 123.

Privat, Y., Trélat, E. and Zuazua, E. (2015). 'Optimal shape and location of sensors for parabolic equations with random initial data'. *Archive for Rational Mechanics and Analysis*, volume 216, number 3, pages 921–981.

— (2017). 'Actuator design for parabolic distributed parameter systems with the moment method'. *SIAM Journal on Control and Optimization*, volume 55, number 2, pages 1128–1152.

Racke, R. and Jiang, S. (2000). *Evolution Equations in Thermoelasticity*. Monographs in pure and applied mathematics. Volume 112. Boca Raton, Florida: CRC Press.

Ramesh, R., Mannan, M. A. and Poo, A. N. (2000). 'Error compensation in machine tools — a review: Part II: thermal errors'. *International Journal of Machine Tools and Manufacture*, volume 40, number 9, pages 1257 –1284.

Rice, B. (2014). 'Extreme ultraviolet (EUV) lithography'. In: *Nanolithography*. Edited by M. Feldman. Philadelphia, PA: Woodhead, pages 42 –79.

Riordan, M. and Hoddeson, L. (1997). *Crystal Fire: The Birth of the Information Age*. Sloan Technology Series. New York: Norton.

Roberts, I. A., Wang, C. J., Esterlein, R., Stanford, M. and Mynors, D. J. (2009). 'A three-dimensional finite element analysis of the temperature field during laser melting of metal powders in additive layer manufacturing'. *International Journal of Machine Tools and Manufacture*, volume 49, number 12—13, pages 916 –923.

de Roover, D. and Bosgra, O. H. (2000). 'Synthesis of robust multivariable iterative learning controllers with application to a wafer stage motion system'. *International Journal of Control*, volume 73, number 10, pages 968–979.

Rosenthal, D. (1946). 'The theory of moving sources of heat and its application of metal treatments'. *Transactions of ASME*, volume 68, pages 849–866.

Rubingh, R. (2007). 'An introduction to photolithography: imaging'. *ASML Images*, spring edition.

Rulison, L. (2017). *Chip firms walking away from landmark SUNY Poly program*. URL: `https://www.timesunion.com/news/article/` (visited on 12/08/2019).

Runnemalm, H. and Hyun, S. (2000). 'Three-dimensional welding analysis using an adaptive mesh scheme'. *Computer Methods in Applied Mechanics and Engineering*, volume 189, number 2, pages 515 –523.

Saathof, R. (2013). 'Adaptive Optics to Counteract Thermal Aberrations: System Design for EUV-Lithography with Sub-nm Precision'. PhD thesis. Delft: Technische Universiteit Delft.

Saathof, R., Wansink, M. V., Hooijkamp, E. C., Spronck, J. W. and Schmidt, R. H. M. (2016). 'Deformation control of a thermal active mirror'. *Mechatronics*, volume 39, pages 12 –27.

Samsung (2019). *Samsung successfully completes 5nm EUV development to allow greater area scaling and ultra-low power benefits*. URL: `https://news.samsung.com/global/` (visited on 26/08/2019).

van der Schaft, A. J. (2006). 'Port-Hamiltonian systems: an introductory survey'. In: *Proceedings of the 2006 International Congress of Mathematicians*. Madrid, pages 1339–1365.

Schaller, R. R. (1997). 'Moore's law: past, present and future'. *IEEE Spectrum*, volume 34, number 6, pages 52–59.

van Schoot, J., Troost, K., Bornebroek, F., van Ballegoij, R., Lok, S., Krabbendam, P., Stoeldraijer, J., Loopstra, E., Benschop, J. P., Finders, J., Meiling, H., Setten, E. van, Kneer, B., Kuerz, P., Kaiser, W., Heil, T., Miguraa, S. and Neumann, J. T. (2017). 'High-NA EUV lithography: enabling Moore's law in the next decade'. In: *Proceedings of the SPIE*. Volume 10450. International Conference on Extreme Ultraviolet Lithography.

Schwalbach, E. J., Donegan, S. P., Chapman, M. G., Chaput, K. J. and Groeber, M. A. (2019). 'A discrete source model of powder bed fusion additive manufacturing thermal history'. *Additive Manufacturing*, volume 25, pages 485 –498.

Shilov, A. (2018). *Samsung foundry roadmap: EUV-based 7LPP for 2018, 3 nm incoming*. URL: `https://www.anandtech.com/show/12795/` (visited on 12/08/2019).

SIA (Semiconductor Industry Association) (2019). *Global Semiconductor Sales Increase 13.7 Percent to $468.8 Billion in 2018*. URL: `www.semiconductors.org` (visited on 11/08/2019).

Skogestad, S. and Postlethwaite, I. (2007). *Multivariable Feedback Control: Analysis and Design*. Chichester: Wiley.

Stadler, G. (2009). 'Elliptic optimal control problems with L^1-control cost and applications for the placement of control devices'. *Computational Optimization and Applications*, volume 44, number 2, pages 159–181.

Steur, M. M. A. (2017). 'Design of an active wafer clamp for wafer machines'. PhD thesis. Eindhoven: Technische Universiteit Eindhoven.

Subramany, L., Chung, W. J., Samudrala, P., Gao, H., Aung, N., Gomez, J. M., Minghetti, B. and Lee, S. (2016). 'Analysis of wafer heating in 14nm DUV layers'. In: *Proceedings of the 2016 SPIE Conference on Metrology, Inspection, and Process Control for Microlithography XXX*. Volume 9778. International Society for Optics and Photonics. San Jose, CA, pages 275 –281.

Tallents, G., Wagenaars, E. and Pert, G. (2010). 'Lithography at EUV wavelengths'. *Nature Photonics*, volume 4, number 12, pages 809–811.

Theis, T. N. and Wong, H.-S. P. (2017). 'The end of Moore's law: a new beginning for information technology'. *Computing in Science & Engineering*, volume 19, number 2, pages 41–50.

Thomas, L. B. (1974). 'Problem 73-14 – Rank factorization of nonnegative matrices'. *SIAM Review*, volume 16, number 3, pages 393–394.

TSMC (2019). *7nm Technology*. URL: `https://www.tsmc.com/english/dedicatedFoundry/technology/7nm.htm` (visited on 11/08/2019).

Turns, S. R. (2006). *Thermodynamics: Concepts and Applications*. Cambridge: Cambridge University Press.

Vaidya, U., Rajaram, R. and Dasgupta, S. (2012). 'Actuator and sensor placement in linear advection PDE with building system application'. *Journal of Mathematical Analysis and Applications*, volume 394, number 1, pages 213 –224.

Veendrick, H. J. (2017). *Nanometer CMOS ICs*. Springer.

Veldman, D. W. M., Fey, R. H. B., Zwart, H., van de Wal, M. M. J., van den Boom, J. D. B. J. and Nijmeijer, H. (2018). 'Semi-analytic approximation of the temperature field resulting from moving heat loads'. *International Journal of Heat and Mass Transfer*, volume 122, pages 128 –137.

— (2019a). 'Optimal actuator shape design with input and state constraints for a wafer heating application'. In: *Proceedings of the 2019 American Control Conference*. Philadelphia, PA, pages 3789–3794.

— (2019b). Optimal thermal actuation for mitigation of heat-induced wafer deformation. *To appear in IEEE Transactions on Control Systems Technology*.

— (2020a). 'Sensor and actuator placement for proportional feedback control in advection-diffusion equations'. *IEEE Control Systems Letters*, volume 4, number 1, pages 193–198.

— (2020b). The method of images in thermoelasticity with an application to wafer heating. *In preperation*.

Viganò, T. F. (2013). 'Control for thermoelastic disturbance rejection in immersion optical lithography systems'. Master's thesis. Milan: Politecnico di Milano.

van der Vorst, H. A. (2003). *Iterative Krylov Methods for Large Linear Systems*. Cambridge monographs on applied and computational mathematics, volume 13. Cambridge: Cambridge University Press.

Waldrop, M. M. (2016). 'More than moore'. *Nature*, volume 530, number 7589, pages 144–148.

van de Wal, M. M. J. and de Jager, A. G. (2001). 'A review of methods for input/output selection'. *Automatica*, volume 37, number 4, pages 487 –510.

van de Wal, M. M. J., Baars, G. E. van, Sperling, F. B. and Bosgra, O. H. (2002). 'Multivariable H_∞/μ feedback control design for high-precision wafer stage motion'. *Control Engineering Practice*, volume 10, number 7, pages 739 –755.

Watson, G. N. (1966). *A Treatise on the Theory of Bessel Functions*. 2nd edition. Camebridge: Cambridge University Press.

Wen, Z. and Yin, W. (2013). 'A feasible method for optimization with orthogonality constraints'. *Mathematical Programming*, volume 142, pages 397–434.

Wesseling, P. (1992). *An Introduction to Multigrid Methods*. Chichester: Wiley.

Wikichip (2018). *A12X Bionic - Apple*. URL: `en.wikichip.org/wiki/apple/ax/a12x` (visited on 12/08/2019).

Wortmann, F. and Flüchter, K. (2015). 'Internet of Things'. *Business & Information Systems Engineering*, volume 57, number 3, pages 221–224.

Zeiss (2020). *Extreme Ultra Violet (EUV) Lithography*. URL: `https://stories.zeiss.com/en/` (visited on 10/02/2020).

Zener, C. (1937). 'Internal friction in solids. I. Theory of internal friction in reeds'. *Physical Review*, volume 52, number 3, pages 230–235.

— (1938). 'Internal friction in solids II. General theory of thermoelastic internal friction'. *Physical Review*, volume 53, number 1, pages 90–99.

Zhang, L, Reutzel, E. W. and Michaleris, P (2004). 'Finite element modeling discretization requirements for the laser forming process'. *International Journal of Mechanical Sciences*, volume 46, number 4, pages 623 –637.

Zhang, M. and Morris, K. A. (2018). 'Sensor choice for minimum error variance estimation'. *IEEE Transactions on Automatic Control*, volume 63, number 2, pages 315–330.

Zienkiewicz, O., Taylor, R. and Nithiarasu, P. (2014). 'Chapter 2 - Convection-Dominated Problems: Finite Element Approximations to the Convection-Diffusion-Reaction Equation'. In: *The Finite Element Method for Fluid Dynamics*. Edited by O. Zienkiewicz, R. Taylor and P. Nithiarasu. Seventh Edition. Oxford: Butterworth-Heinemann, pages 31 –85.

Zienkiewicz, O., Taylor, R. and Zhu, J. (2013). *The Finite Element Method: its Basis and Fundamentals*. Seventh Edition. Oxford: Butterworth-Heinemann.

About the author

Daniël Veldman was born on June 9, 1990 in Nijmegen, the Netherlands. After finishing his secondary eduction at the Karel de Grote College in Nijmegen in 2008, he started studying Mathematics at Utrecht University (UU) in Utrecht, the Netherlands, which he combined with Mechanical Engineering at Eindhoven University of Technology (TU/e) in Eindhoven, the Netherlands, since 2009. He received his Bachelor of Science and Master of Science degrees in Mathematics from the UU in 2012 and 2016, respectively, and his Bachelor of Science and Master of Science degrees in Mechanical Engineering from the TU/e in 2012 and 2015, respectively. His Master's thesis in Mathematics is entitled 'Degenerate Bogdanov-Takens Bifurcations in Fusion Plasma Models' and was supervised by Youri Kuznetsov (UU, University of Twente), Hugo de Blank (Dutch Institute for Fundamental Energy Research, TU/e), and Mark Pékker (a.k.a. Mark Friedman, University of Alabama). His Master's thesis in Mechanical Engineering is entitled 'Controlling Nonlinear Resonances of Rectangular Plates' and was supervised by Rob Fey and Hans Zwart (University of Twente, TU/e).

In February 2016, Daniël started his Ph.D. in the Dynamics and Control group at Department of Mechanical Engineering at the Eindhoven University of Technology. Under supervision of Rob Fey, Hans Zwart, Henk Nijmeijer, Marc van de Wal (ASML), and Joris van den Boom (ASML), he worked on the modeling and control of thermomechanical systems. This thesis contains the main results of this research, which was carried out as part of the Impulse II research program of the High Tech Systems Center of the Eindhoven University of Technology and is financially supported by ASML, Veldhoven, the Netherlands.

List of publications

Peer-reviewed journal articles

- D.W.M. Veldman, R.H.B. Fey, H.J. Zwart, M.M.J. van de Wal, J.D.B.J. van den Boom, H. Nijmeijer. The method of images in thermoelasticity with an application to wafer heating. *In preperation.*
- — Optimal thermal actuation for mitigation of heat-induced wafer deformation. *To appear in IEEE Transactions on Control Systems Technology.*
- — (2020). Sensor and actuator placement for proportional feedback control in advection-diffusion equations. *IEEE Control Systems Letters*, volume 4, number 1, pages 193-198. The contents of this paper were also selected by the 58th IEEE Conference on Decision and Control (CDC 2019) Program Committee for presentation at the conference.
- — (2018). Semi-analytic approximation of the temperature field resulting from moving heat loads. *International Journal of Heat and Mass Transfer*, volume 122, pages 128-137.
- D.W.M. Veldman, R.H.B. Fey, H.J. Zwart (2017). Impulsive steering between coexisting stable periodic solutions with an application to vibrating plates. *Journal of Computational and Nonlinear Dynamics*, volume 12, number 1.
- H.J. de Blank, Yu.A. Kuznetsov, M.J. Pekkér, D.W.M. Veldman (2016). Degenerate Bogdanov-Takens bifurcations in a one-dimensional transport model of a fusion plasma. *Physica D : Nonlinear Phenomena*, volume 331, pages 13–26.

Peer-reviewed articles in conference proceedings

- D.W.M. Veldman, R.H.B. Fey, H.J. Zwart, M.M.J. van de Wal, J.D.B.J. van den Boom, H. Nijmeijer (2019). Optimal actuator shape design with

input and state constraints for a wafer heating application. In: *Proceedings of the 2019 American Control Conference (ACC 2019)*, 10-12 July 2019, Philadelphia, Pennsylvania, USA.

- D.W.M. Veldman, R.H.B. Fey, H.J. Zwart (2017). Switching between co-existing stable periodic solutions by impulsive forces with an application to a vibrating plate. In: *Proceedings of the 9th European Nonlinear Dynamics Conference (ENOC 2017)*, 25-30 June 2017, Budapest, Hungary.

Non peer-reviewed abstracts in conference proceedings

- D.W.M. Veldman, R.H.B. Fey, H.J. Zwart, M.M.J. van de Wal, J.D.B.J. van den Boom, H. Nijmeijer (2020). Extending the method of images to thermomechanical systems. In: *Book of Abstracts of the 39th Benelux Meeting on Systems and Control*, Elspeet, the Netherlands.

- — (2019). Placement of temperature sensors in a one-dimensional thermal system. In: *Book of Abstracts of the 38th Benelux Meeting on Systems and Control*, Lommel, Belgium.

- — (2018). Design of distributed thermal actuators for a one-dimensional thermomechanical model. In: *Book of Abstracts of the 37th Benelux Meeting on Systems and Control*, Soesterberg, the Netherlands.

- — (2017). Finite element and semi-analytic modeling of the temperature field of a wafer with moving heat loads. In: *Book of Abstracts of the 36th Benelux Meeting on Systems and Control*, Spa, Belgium.

Posters

- D.W.M. Veldman, S.V.N. Nouwens, R.H.B. Fey, H.J. Zwart, M.M.J. van de Wal, J.D.B.J. van den Boom, H. Nijmeijer (2019). Optimization of IR heater shapes for mirror temperature control in wafer scanners. In: *Symposium Book of the 22nd Engineering Mechanics Symposium*, Arnhem, The Netherlands.

- D.W.M. Veldman, R.H.B. Fey, H.J. Zwart, M.M.J. van de Wal, J.D.B.J. van den Boom, H. Nijmeijer (2018). Optimization of actuator shapes for a wafer heating application. In: *Symposium Book of the 21st Engineering Mechanics Symposium*, Arnhem, The Netherlands.

- — (2017). Semi-analytic approximation of moving heat load response applied to wafer scanners. In: *Symposium Book of the 20th Engineering Mechanics Symposium*, Arnhem, The Netherlands.

- — (2016). Integral thermal/mechanical modeling and control design. In: *Symposium Book of the 19th Engineering Mechanics Symposium*, Arnhem, The Netherlands.

Dankwoord

De laatste paginas van dit proefschrift zijn voor de mensen die mij de afgelopen vier jaar op allerlei manieren hebben geholpen en die ik graag wil bedanken.

Rob en Hans, sinds ik bijna zes jaar geleden mijn afstudeerproject begon zijn jullie mijn dagelijkse begeleiders geweest en ik had me geen betere kunnen wensen. Bedankt voor onze prettige wekelijkse bijeenkomsten en het precieze lezen en becommentariëren van de vele verslagen waarmee ik jullie bijna wekelijks heb bestookt. Ik heb daar ontzettend veel van geleerd. Rob, bedankt dat ik altijd bij je binnen kon lopen en de aandacht waarmee je mijn werk hebt bestudeerd en verbeterd. Daarnaast natuurlijk ook bedankt voor de vele gezellige momenten: de koffiepauzes, de vrijdagmiddagborrels, de steppegras events, etc. Hans, bedankt voor je precieze commentaar, het met me meedenken, en de leuke gesprekken over wiskunde. Ook bedankt voor je altijd kritische en behulpzame blik op mijn presentaties waar ik veel aan heb gehad.

Henk, bedankt voor je altijd goed geplaatste opmerkingen die de essentie van het probleem raken. Vaak weet jij subtiele maar essentiele problemen te vinden die veel andere mensen niet zouden zijn opgevallen, maar die wel tot substantiële verbeteringen leiden.

Marc en Joris, bedankt voor al die keren dat jullie naar de TU/e zijn gekomen voor mijn progress meetings. Marc, bedankt voor je vele kritische opmerkingen en vragen. Zonder die zouden onze progress meetings maar half zo nuttig zijn geweest. Ook bedankt voor het opzetten van het afstudeerproject voor Sven. Joris, bedankt voor de rustige en heldere antwoorden op de ASML gerelateerde vragen, het aandachtig lezen van mijn papers en natuurlijk ook voor het managen van TPB.

I would also like to thank Enrique Zuazua, Fred van Keulen, and Siep Weiland for being part of my defense committee.

De afgelopen jaren heb ik ook prettig samengewerkt met veel mensen van ASML. Een paar wil ik hier expliciet noemen. Jeroen, bedankt voor je introductie in het eindige elementen pakket dat een perfect startpunt vormde voor

mijn project. Jim, bedankt voor de prettige discussies die me enorm hebben geholpen bij het bepalen van de richting van mijn project. Victor, bedankt voor de levendige discussies over mirror heating die erg verhelderend voor mij waren.

Ik wil ook graag de studenten bedanken die ik de afgelopen jaren heb mogen begeleiden en die hebben geholpen deze thesis vorm te geven. Giel, bedankt voor je goede werk en doorzettingsvermogen waarmee je je een moeilijk onderwerp eigen hebt gemaakt. Ik heb nog regelmatig dingen opgezocht in jouw thesis. Joris, bedankt voor je harde werk, de intelligente discussies, en de goede samenwerking. Door tijdgebrek moet een hoofdstuk over jouw werk helaas ontbreken. Sven, bedankt voor je harde werk, enthousiasme en de scherpe discussies die me vaak voorbij de grenzen van mijn kennis dwongen. Hoofdstuk 6 is grotendeels jouw werk. Ik had me geen betere master student kunnen wensen.

Daarnaast wil mijn collegas uit de DC en CST groepen bedanken met wie ik de afgelopen jaren zoveel gezellige momenten heb beleefd. Ik denk bijvoorbeeld aan de vrijdagmiddagborrels (met als vaste gasten o.a. Michiel, Jurgen, Lennart, Stefan, Robbert, Robert, Ruud, Igor, Rob) die af en toe wel eens 'uit de hand liepen', de discolampen en rookmachines op de Benelux meetings, de andere conferenties, de meerkamp en de groepsuitjes. Maar ook van serieuzere activiteiten zoals de discussies over Dynamica tentamens (Mark, Frans, Robbin, Brandon, Camiel, Rinus, Ruud), het organiseren van het lunchcolloquium (Fahim) en de discussies over thermische problemen (David, Ruben, Amritan, Tomas) heb ik genoten. Then there also the sportive activities such as the futsal matches with Atlético Bitterballen (Fahim, Rishi, Frans, Tom, Wouter, Jijju, Roeland, and Leroy(?) to name a few) and the weekly boulder evenings (Igor and Wouter), that formed a pleasant distraction from the mental labor that comes with a PhD. Geertje en Ingrid, bedankt voor oplossen van mijn administratieve problemen. Brandon, bedankt voor je interesse in het vouwen van temperatuurvelden die belangrijk is geweest voor het ontstaan van Hoofdstuk 3. Rinus, bedankt voor je scherpe opmerkingen die een grote invloed op Hoofdstuk 2 hebben gehad. Roeland, bedankt voor de literaire gesprekken. Chyannie, thank you for the music.

I especially want to thank my roommates: Elise, Hefeng, Muttalip, Igor, Andy, Sajad, and Ruud. Muttalip, thank you for the amazing stories about all the trouble you got into. Igor, thank you for your friendship, for the many evenings at the boulder wall, the many beers, the occasional beer, and the board game nights. Andy, thank you for your openness and kindness, even when you went through difficult times. I hope you can leave your troubles behind and you will be able to finish your PhD soon. Sajad, your sense of humor is unparalleled and I enjoyed the many running jokes you invented (e.g. open the window, the Iranian counter, the box from Norway, the cow search). I also liked our more serious conversations on model reduction and the situation in Iran, which were very insightful for me. Ruud, bedankt voor de vele interessante gesprekken over boeken, communisme, (on)gelijkheid, (positieve?) discriminatie, het deugen van

mensen en (het daarbij vergeleken simpele onderwerp) Bessel functies, waarin we het vaak eens waren.

Dan wil ik nog een paar vrienden bedanken. Frank en Marijke, Koen, Nico en Wing, bedankt voor de gezellige activiteiten en etentjes die altijd een welkome afwisseling waren. Koen, bedankt voor je enthousiasme, gezelligheid en eigenwijsheid, die we nu zullen moeten missen. Diederik en Jeroen, bedankt voor de mooie Risk momenten waar we er veel te weinig van weten te organiseren.

Tenslotte wil ik mijn familie bedanken. Papa, mama en Liesbeth, bedankt voor jullie interesse en steun en de benodigde afwisseling van de technische omgeving waarin ik zoveel tijd doorbreng. Jullie hebben mij een thuis geboden waar ik altijd op terug kan vallen.

Zonder jullie had ik dit proefschrift niet kunnen schrijven.

Eindhoven, juli 2020